CERN Yellow Reports: Monographs CERN-2020-010

High-Luminosity Large Hadron Collider (HL-LHC)

Technical design report

Editors: I. Béjar Alonso
O. Brüning
P. Fessia
M. Lamont
L. Rossi
L. Tavian
M. Zerlauth

CERN Yellow Reports: Monographs
Published by CERN, CH-1211 Geneva 23, Switzerland

ISBN	978-92-9083-586-8 (paperback)
ISBN	978-92-9083-587-5 (PDF)
ISSN	2519-8068 (Print)
ISSN	2519-8076 (Online)
DOI	https://doi.org/10.23731/CYRM-2020-0010

This volume should be cited as:
High-Luminosity Large Hadron Collider (HL-LHC): Technical design report,
I. Béjar Alonso et al. (Eds.)
CERN Yellow Reports: Monographs, CERN-2020-010 (CERN, Geneva, 2020),
doi:10.23731/CYRM-2020-0010.

A contribution in this report should be cited as:
[Author name(s)], in High-Luminosity Large Hadron Collider (HL-LHC): Technical design report,
I. Béjar Alonso et al. (Eds.)
CERN-2020-010 (CERN, Geneva, 2020), pp. [first page]–[last page],
doi:10.23731/CYRM-2020-0010.[first page].

Executive editor: Isabel.BejarAlonso@cern.ch.
Accepted in December 2020 by the CERN Reports Editorial Board (contact Carlos.Lourenco@cern.ch).
Published by the CERN Scientific Information Service (contact Jens.Vigen@cern.ch).
Indexed in the CERN Document Server and in INSPIRE.
Published Open Access to permit its wide dissemination, as knowledge transfer is an integral part of the mission of CERN.

High-Luminosity Large Hadron Collider (HL-LHC)

Technical design report

O. Aberle[f], C. Adorisio[f], A. Adraktas[f], M. Ady[f], J. Albertone[f], L. Alberty[f], M. Alcaide Leon[f], A. Alekou[w,f], D. Alesini[p], B. Almeida Ferreira[f], P. Alvarez Lopez[f], G. Ambrosio[l], P. Andreu Munoz[f], M. Anerella[c], D. Angal-Kalinin[a], F. Antoniou[α,f], G. Apollinari[l], A. Apollonio[f], R. Appleby[w], G. Arduini[f], B. Arias Alonso[f], K. Artoos[f], S. Atieh[f], B. Auchmann[f], V. Badin[f], T. Baer[f], D. Baffari[f], V. Baglin[f], M. Bajko[f], A. Ball[h], A. Ballarino[f], S. Bally[h], T. Bampton[f], D. Banfi[k], R. Barlow[y], M. Barnes[f], J. Barranco[k], L. Barthelemy[g], W. Bartmann[f], H. Bartosik[f], E. Barzi[l], M. Battistin[f], P. Baudrenghien[f], I. Bejar Alonso[f], S. Belomestnykh[c], A. Benoit[f], I. Ben-Zvi[c], A. Bertarelli[f], S. Bertolasi[f], C. Bertone[f], B. Bertran[f], P. Bestmann[f], N. Biancacci[f], A. Bignami[o], N. Bliss[v], C. Boccard[f], Y. Body[f], J. Borburgh[f], B. Bordini[f], F. Borralho[f], R. Bossert[l], L. Bottura[f], A. Boucherie[f], R. Bozzi[f], C. Bracco[f], E. Bravin[f], G. Bregliozzi[f], D. Brett[w], A. Broche[f], K. Brodzinski[f], F. Broggi[o], R. Bruce[f], M. Brugger[f], O. Brüning[f], X. Buffat[f], H. Burkhardt[f], J. Burnet[f], A. Burov[l], G. Burt[z], R. Cabezas[f], Y. Cai[u], R. Calaga[f], S. Calatroni[f], O. Capatina[f], T. Capelli[f], P. Cardon[g], E. Carlier[f], F. Carra[f], A. Carvalho[f], L.R. Carver[α,f], F. Caspers[f], G. Cattenoz[f], F. Cerutti[f], A. Chancé[e], M. Chastre Rodrigues[f], S. Chemli[f], D. Cheng[r], P. Chiggiato[f], G. Chlachidze[l], S. Claudet[f], JM. Coello De Portugal[f], C. Collazos[f], J. Corso[f], S. Costa Machado[f], P. Costa Pinto[f], E. Coulinge[f], M. Crouch[w], P. Cruikshank[f], E. Cruz Alaniz[α,f], M. Czech[f], K. Dahlerup-Petersen[f], B. Dalena[e], G. Daniluk[f], S. Danzeca[f], H. Day[f], J. De Carvalho Saraiva[f], D. De Luca[f], R. De Maria[f], G. De Rijk[f], S. De Silva[s], B. Dehning[f], J. Delayen[s], Q. Deliege[f], B. Delille[f], F. Delsaux[f], R. Denz[f], A. Devred[f], A. Dexter[z], B. Di Girolamo[h], D. Dietderich[r], J.W. Dilly[λ,f], A. Doherty[z], N. Dos Santos[f], A. Drago[p], D.Drskovic[f], D. Duarte Ramos[f], L. Ducimetière[f], I. Efthymiopoulos[f], K. Einsweiler[f], L. Esposito[f], J. Esteban Muller[f], S. Evrard[f], P. Fabbricatore[n], S. Farinon[n], S. Fartoukh[f], A. Faus-Golfe[m], G. Favre[f], H. Felice[r], B. Feral[f], G. Ferlin[f], P. Ferracin[f], A. Ferrari[f], L. Ferreira[f], P. Fessia[f], L. Ficcadenti[f], S. Fiotakis[f], L. Fiscarelli[f], M. Fitterer[f], J. Fleiter[f], G. Foffano[f], E. Fol[ι,f], R. Folch[f], K. Foraz[f], A. Foussat[f], M. Frankl[f], O. Frasciello[p], M. Fraser[f], P. Freijedo Menendez[f], J-F. Fuchs[f], S. Furuseth[k,f], A. Gaddi[f], M. Gallilee[f], A. Gallo[p], R. Garcia Alia[f], H. Garcia Gavela[f], J. Garcia Matos[i], H. Garcia Morales[δ], A. Garcia-Tabares Valdivieso[f], C. Garino[g], C. Garion[f], J. Gascon[f], Ch. Gasnier[g], L. Gentini[f], C. Gentsos[f], A. Ghosh[c], L. Giacomel[f], K. Gibran Hernandez[f], S. Gibson[δ], C. Ginburg[l], F. Giordano[ζ,f], M. Giovannozzi[f], B. Goddard[f], P. Gomes[f], M. Gonzalez De La Aleja Cabana[f], P. Goudket[a], E. Gousiou[f], P. Gradassi[f], A. Granadeiro Costa[f], L. Grand-Clément[f], S. Grillot[f], JC. Guillaume[f], M. Guinchard[f], P. Hagen[f], T. Hakulinen[f], B. Hall[z], J. Hansen[f], N. Heredia Garcia [f], W. Herr[f], A. Herty[f], C. Hill[v], M. Hofer[λ,f], W. Höfle[f], B. Holzer[f], S. Hopkins[f], J. Hrivnak[f], G. Iadarola[f], A. Infantino[f], S. Izquierdo Bermudez[f], S. Jakobsen[f], M.A. Jebramcik[κ,f], B. Jenninger[f], E. Jensen[f], M. Jones[f], R. Jones[f], T. Jones[v], J. Jowett[f], M. Juchno[f], C. Julie[f], T. Junginger[f], V. Kain[f], D. Kaltchev[x], N. Karastathis[f], P. Kardasopoulos[f], M. Karppinen[f], J. Keintzel[κ,f], R. Kersevan[f], F. Killing[f], G. Kirby[f], M. Korostelev[α], N. Kos[f], S. Kostoglou[f], I. Kozsar[f], A. Krasnov[b], S. Krave[l], L. Krzempek[f], N. Kuder[f], A. Kurtulus[f], R. Kwee-Hinzmann[δ], F. Lackner[f], M. Lamont[f], A.L. Lamure[f], L. Lari[m], M. Lazzaroni[f], M. Le Garrec[f], A. Lechner[f], T. Lefevre[f], R. Leuxe[f], K. Li[f], Z. Li[u], R. Lindner[h], B. Lindstrom[f], C. Lingwood[z], C. Löffler[f], C. Lopez[f], LA. Lopez-Hernandez[g], R. Losito[f], F. Maciariello[f], P. Macintosh[a], E.H. Maclean[f], A. Macpherson[f], P. Maesen[f], C. Magnier[f], H. Mainaud Durand [f], L. Malina[f], M. Manfredi[g], F. Marcellini[p], M. Marchevsky[r], S. Maridor[f], S. Maridor [f], G. Marinaro[f], K. Marinov[a], T. Markiewicz[u], A. Marsili[f], P. Martinez Urioz[f], M. Martino[f], A. Masi[f], T. Mastoridis[d], P. Mattelaer[g], A. May[a], J. Mazet[f], S. Mcilwraith[g], E. McIntosh[f], L. Medina Medrano[f], A. Mejica Rodriguez[f], M. Mendes[f], P. Menendez[f], M. Mensi[f], A. Mereghetti[f], D. Mergelkuhl[f], T. Mertens[f], L. Mether[f], E. Métral[f], M. Migliorati[β], A. Milanese[f], P. Minginette[f], D. Missiaen[f], T. Mitsuhashi[q], M. Modena[f], N. Mokhov[l], J. Molson[w], E. Monneret[f], E. Montesinos[f], R. Moron-Ballester[f], M. Morrone[f], A. Mostacci[β], N. Mounet[f], P. Moyret[f], P. Muffat[f], B. Muratori[a], Y. Muttoni[f], T. Nakamoto[q], M. Navarro-Tapia[f], H. Neupert[f], L. Nevay[δ], T. Nicol[l], E. Nilsson[f], P. Ninin[f], A. Nobrega[l], C. Noels[f], E. Nolan[v], Y. Nosochkov[u], FX. Nuiry[f], L. Oberli[f], T. Ogitsu[q], K. Ohmi[q], R. Olave[s], J. Oliveira[f], Ph. Orlandi[f], P. Ortega[g], J. Osborne[g], T. Otto[f], L. Palumbo[β], S. Papadopoulou[f], Y. Papaphilippou[f], K. Paraschou[ε,f], C. Parente[f], S. Paret[r], H. Park[s], V. Parma[f], Ch. Pasquino[f], A. Patapenka[f], L. Patnaik[f], S. Pattalwar[a], J. Payet[e], G. Pechaud[f], D. Pellegrini[f], P. Pepinster[f], J. Perez[f], J. Perez Espinos[f], A. Perillo Marcone[f], A. Perin[f], P. Perini[f], T.H.B. Persson[f], T. Peterson[l], T. Pieloni[f], G. Pigny[f], J.P. Pinheiro de Sousa[f], O. Pirotte[f], F. Plassard[f], M. Pojer[f], L. Pontercorvo[h], A. Poyet[η,f], D. Prelipcean[f], H. Prin[f], R. Principe[f], T. Pugnat[e,f], J. Qiang[r], E. Quaranta[f], H. Rafique[y], I. Rakhno[l], D. Ramos Duarte[f], A. Ratti[l], E. Ravaioli[f], M. Raymond[h], S. Redaelli[f], T. Renaglia[f], D. Ricci[f], G. Riddone[f], J. Rifflet[e], E. Rigutto[f], T. Rijoff[f], R. Rinaldesi[f], O. Riu Martinez[f], L. Rivkin[k], F. Rodriguez Mateos[f], S. Roesler[f], I. Romera Ramirez[f], A. Rossi[f], L. Rossi[f], V. Rude[f], G. Rumolo[f], J. Rutkovksi[f], M. Sabate Gilarte[f], G. Sabbi[r], T. Sahner[f], R. Salemme[f], B. Salvant[f],

F. Sanchez Galan[f], A. Santamaria Garcia[f], I. Santillana[f], C. Santini[t], O. Santos[f], P. Santos Diaz[f], K. Sasaki[q], F. Savary[f], A. Sbrizzi[f], M. Schaumann[f], C. Scheuerlein[f], J. Schmalzle[c], H. Schmickler[f], R. Schmidt[f], D. Schoerling[f], M. Segreti[e], M. Serluca[w], J. Serrano[f], J. Sestak[f], E. Shaposhnikova[f], D. Shatilov[b], A. Siemko[f], M. Sisti[f], M. Sitko[f], J. Skarita[c], E. Skordis[f], K. Skoufaris[θ,f], G. Skripka[f], D. Smekens[f], Z. Sobiech[f], M. Sosin[f], M. Sorbi[o], F. Soubelet[f], B. Spataro[p], G. Spiezia[f], G. Stancari[l], M. Statera[o], J. Steckert[f], G. Steele[f], G. Sterbini[f], M. Struik[f], M. Sugano[q], A. Szeberenyi[f], M. Taborelli[f], C. Tambasco[f], R. Tavares Rego[f], L. Tavian[f], B. Teissandier[f], N. Templeton[v], M. Therasse[f], H. Thiesen[f], E. Thomas[h], A. Toader[y], E. Todesco[f], R. Tomás[f], F. Toral[i], R. Torres-Sanchez[f], G. Trad[f], N. Triantafyllou[α,f], I. Tropin[l], A. Tsinganis[f], J. Tuckamantel[f], J. Uythoven[f], A. Valishev[p], F. Van Der Veken[f], R. Van Weelderen[f], A. Vande Craen[f], B. Vazquez De Prada[f], F. Velotti[f], S. Verdu Andres[c], A. Verweij[f], N. Vittal Shetty[f], V. Vlachoudis[f], G. Volpini[o], U. Wagner[f], P. Wanderer[c], M. Wang[u], X. Wang[r], R. Wanzenberg[j], A. Wegscheider[f], S. Weisz[f], C. Welsch[α], M. Wendt[f], J. Wenninger[f], W. Weterings[f], S. White[f], K. Widuch[f], A. Will[f], G. Willering[f], D. Wollmann[f], A. Wolski[α], J. Wozniak[f], Q. Wu[c], B. Xiao[c], L. Xiao[u], Q. Xu[q], Y. Yakovlev[l], S. Yammine[f], Y. Yang[γ], M. Yu[l], I. Zacharov[k], O. Zagorodnova[j], C. Zannini[f], C. Zanoni[f], M. Zerlauth[f], F. Zimmermann[f], A. Zlobin[l], M. Zobov[p], I. Zurbano Fernandez[f]

[a]ASTeC, STFC, Daresbury Laboratory, UK, [b]BINP, Budker Institute of Nuclear Physics, Russia,
[c]BNL, Brookhaven National Laboratory, USA, [d]CalPoly, California Polytechnic State University, USA,
[e]CEA/SACLAY, DSM/Irfu/SACM, France, [f]CERN, Accelerators and Technology sector, Switzerland,
[g]CERN, Finance and Human Resources sector, [h]CERN, Research and Computing sector, Switzerland,
[i]CIEMAT, Center for Energy, Environmental and Technological Research, Spain,
[j]DESY, Deutsches Elektronen-Synchrotron, Germany,
[k]EPFL, Swiss Federal Institute of Technology in Lausanne, Switzerland,
[l]Fermilab, Fermi National Accelerator Laboratory, USA, [m]IFIC, Institute for Corpuscular Physics, Spain,
[n]INFN, Genova section, Italy, [o]INFN-LASA, Italy, [p]INFN-LNF, Italy, [q]KEK, Japan,
[r]LBNL, Lawrence Berkeley National Laboratory, USA, [s]ODU, Old Dominion University, USA,
[t]Polytechnic University of Milan, Italy, [u]SLAC National Accelerator Laboratory, USA,
[v]STFC, Daresbury Laboratory, UK, [w]UMAN, The University of Manchester, and the Cockcroft Institute, UK,
[x]TRIUMF, Accelerator Physics Group, Canada, [y]UHUD, University of Huddersfield, UK,
[z]University of Lancaster, UK and Cockcroft Institute Sci-Tech Daresbury, UK,
[α]University of Liverpool, UK,[β]University of Rome "La Sapienza", Italy, [γ]SOTON, University of Southampton, UK,
[δ]URHL, Royal Holloway, UK, [ε]Aristotle University of Thessaloniki, Greece, [ζ]INFN, Naples section, Italy,
[η]UGA, Grenoble Alpes University, France, [θ]UoC, University of Crete, Greece, [ι]Goethe University, Germany,
[κ]TUW, Vienna University of Technology, Austria, [λ]Humboldt University of Berlin, Germany

Abstract

The Large Hadron Collider (LHC) is one of the largest scientific instruments ever built. Since opening up a new energy frontier for exploration in 2010, it has gathered a global user community of about 9000 scientists working in fundamental particle physics and the physics of hadronic matter at extreme temperature and density. To sustain and extend its discovery potential, the LHC will need a major upgrade in the 2020s. This will increase its instantaneous luminosity (rate of collisions) by a factor of five beyond the original design value and the integrated luminosity (total number of collisions) by a factor ten. The LHC is already a highly complex and exquisitely optimised machine so this upgrade must be carefully conceived and will require new infrastructures (underground and on surface) and over a decade to implement. The new configuration, known as High Luminosity LHC (HL-LHC), relies on a number of key innovations that push accelerator technology beyond its present limits. Among these are cutting-edge 11–12 Tesla superconducting magnets, compact superconducting cavities for beam rotation with ultra-precise phase control, new technology and physical processes for beam collimation and 100 metre-long high-power superconducting links with negligible energy dissipation, all of which required several years of dedicated R&D effort on a global international level.

The present document describes the technologies and components that will be used to realise the project and is intended to serve as the basis for the detailed engineering design of the HL-LHC

Preface

The High Luminosity LHC (HL-LHC) Project was setup in 2010 by the CERN Director for Accelerators and Technology, Dr. Steve Myers, following a change of strategy and subsequent merging of the LHC upgrade Phase I and Phase II into one unique project. To this end, CERN in consortium with 15 European Institutions applied in November 2010 to the call for European funding under the 7th Framework Programme Design Study category: the application was approved with full budget in 2011 with the name FP7 High Luminosity Large Hadron Collider Design Study (also known as HiLumi LHC, grant no. 284404).

The European Strategy for Particle Physics (ESPP), adopted by the special CERN Council of Brussels on 30 May 2013, placed the HL-LHC as a first priority project for the next decade. Consequently, CERN management inserted the project in the Medium-Term Plan (5-year plan) and a kick-off meeting of the HL-LHC as a construction project was organized in Daresbury on 11 November 2013. The central high priority role of the HL-LHC project within the European Strategy for Particle Physics got underlined and reinforced in the latest update of the ESPP in 2020.

The HL-LHC project is accompanied by upgrade projects of all LHC experiments and by the LHC Injector Upgrade Project (LIU). The upgrade of the experiments is under the responsibility of the respective international collaborations. The LIU project has a separate management, project structure, budget and plans for a complete implementation during Long Shutdown 2 (LS2). The experiments upgrade and LIU projects are not covered by this technical design report (TDR).

A Cost and Schedule Review series (C&SR), reviewing both the HL-LHC and LIU projects and reporting to the CERN Director of Accelerators and Technology, Dr. Frédérick Bordry, started in March 2015, with C&SR-I. Following the very positive results of the review, the CERN management endorsed the cost and planning. In September 2015 the CERN Council approved the medium-term plan (MTP) 2016–2020, containing the funding for the project for that period and envisaging the full Cost-to-Completion (CtC) of the project by 2026. The CERN Council approved the High Luminosity LHC project in June 2016. The Council allocated the required budget for the upgrade of the collider and the related infrastructure until 2026. The approved budget for CtC was set to 950 MCHF, to which the cost of CERN personnel comes in addition.

In August 2016, a re-baselining of the HL-LHC project was approved by CERN management in order to keep the CtC ceiling while accommodating extra cost in the technical infrastructure (mainly in the civil engineering). Following the fourth C&SR-IV in November 2019, the HL-LHC project extended its scope by adding three additional upgrade items to its baseline, mainly financed through in-kind contributions, increasing the total CtC of the project to 989.1MCHF. The present TDR reflects the design of the project with the modifications introduced in the re-baselining exercise in summer 2016, the various changes and optimization carried since the TDR V0.1[1] and with the added scope items approved after the C&SR-IV in November 2019. The report does not take into consideration any impact related to the COVID-19 pandemic causing social and economic disruption on a global scale.

The project leadership is particularly grateful to the CERN management for its continuous support and encouragement and in particular to the CERN Director of Accelerators and Technology, Dr. Frédérick Bordry for his continuous support and guidance from the beginning of the project, to former Director-General Dr. Rolf Heuer for his engagement in having the project initiated and ensured funding during his mandate, as well as to the present Director-General Dr. Fabiola Gianotti, for having pursued and obtained the full approval of the entire HL-LHC project by the Council in June 2016, the first CERN project with such status after the LHC.

CERN, 31 August 2020

Lucio Rossi, Former HL-LHC Project Leader

Oliver Brüning, HL-LHC Project Leader

[1] High-Luminosity Large Hadron Collider (HL-LHC) : Technical Design Report V. 0., 1, CERN-2017-007-M

Table of contents

Chapter 1

High-luminosity Large Hadron Collider

O. Bruning[1*] *and L. Rossi*[1,2*]

[1]CERN, Accelerators and Technology sector, Switzerland
[2] University of Milano and INFN-LASA, Italy
[*]Corresponding authors

1 High-luminosity Large Hadron Collider HL-LHC

1.1 Introduction

The Large Hadron Collider (LHC) was successfully commissioned in 2010 for proton–proton collisions with a 7 TeV centre-of-mass (c.o.m.) energy. It delivered 8 TeV c.o.m. proton collisions from April 2012 until the end of Run 1 in 2013. Following the Long Shutdown 1 (LS1) in 2013–2014, it operated with 13 TeV c.o.m. proton collisions during Run 2 from 2015 until the end of 2018, reaching a peak luminosity twice the nominal design value. At present (2020), the LHC is in Long Shutdown 2 (LS2) during which further consolidation measures (insulation and retrofitting of the protection diode connections) are being pursued; these should enable the LHC to reach its nominal design beam energy of 7 TeV. As a consequence of the coronavirus pandemic, LS2 will last almost one year longer than foreseen, with Run 3 now planned to start at the beginning of 2022.

The truly impressive performance of the LHC has reconfirmed CERN as a European and global centre for high-energy physics, and as an important incubator of knowledge and technology development. After the discovery of the long-awaited Higgs boson in 2012 by the LHC experiments ATLAS [1] and CMS [2], the LHC continues to act as catalyst for a global effort unrivalled by any other branch of science: out of the 12 thousand CERN users, more than 9 thousand are scientists and engineers using the LHC, half of which are from countries outside the EU [3].

The LHC will remain the highest energy accelerator in the world for at least the next two decades. Its full exploitation was the highest priority of the European Strategy for Particle Physics Update (ESPPU) of 2013 [4]. The high priority has been confirmed by the recent 2020 ESPPU [5]. The above referenced strategy deliberations, as well as those of the Snowmass process of 2013–2015 [6], recognized that to extend its discovery potential, the LHC will need a major upgrade in the 2020s, firstly to extend its operability by another decade or more, and secondly to increase its collision rate and thus the delivered integrated luminosity. The upgrade design goal is a fivefold increase of the instantaneous collision rate and a tenfold increase of the integrated luminosity with respect to the LHC nominal design values. The necessary developments required a dedicated research effort lasting more than 10 years; studies included prototype developments and the manufacture of ground-breaking equipment. The machine configuration of the upgrade, the high-luminosity LHC (HL-LHC), relies on new operation modes (e.g. levelled luminosity operation with dynamic optics adjustments) and a number of innovative, profoundly challenging, technologies. These include: cutting-edge 11 to 12 T superconducting magnets; novel magnet designs (e.g. canted cosine theta and super-ferric magnet designs), very compact superconducting RF cavities for beam rotation with ultra-precise phase control; new technologies and materials for beam collimation; and high-current superconducting links with almost zero energy dissipation.

HL-LHC federates the efforts and R&D of a large international community towards its ambitious objectives and contributes to establishing CERN as a focal point of global research cooperation and leadership in frontier knowledge and technologies. HL-LHC relies on strong participation from international partners who make important in-kind contributions. These partners include Non-Member States laboratories in the USA, Japan, China, Canada and Russia as well as leading institutions and universities from the Member States: INFN (Genova and Milano-LASA, IT); CIEMAT (Madrid, ES); STFC (UK) and other British universities and institutions; Uppsala University (FREIA Laboratory, SE); and several other partner institutes (see Table 1-2). These participations with in-kind contributions, as well as the participation of other institutes who provide skilled personnel, are key ingredients for the execution of the construction phase. The US LHC Accelerator R&D Program (LARPhas been essential for the development of some of the key technologies for the HL-LHC, such as the large-aperture niobium–tin (Nb_3Sn) quadrupoles and the crab cavities. The governance, initially modelled for a design study phase, was tailored in 2016 to support the construction phase.

1.2 Project overview

The present LHC baseline programme, as defined at the end of 2019 (the consequences of the coronavirus pandemic are included in the present version, with shift of beginning of Run 3, as much as it is known today) is shown schematically in Figure 1-1. During Run 1 the LHC was operated with 50 ns bunch spacing. After the consolidation of the electrical splices between the superconducting magnets (and many other consolidation measures) in LS1, the LHC was operated in Run 2 at 13 TeV centre-of-mass energy. The bunch spacing was reduced to 25 ns, the design value, and the luminosity was progressively increased, attaining the nominal design luminosity of 1×10^{34} cm^{-2} s^{-1} on 26 June 2016. A peak luminosity of 2×10^{34} cm^{-2} s^{-1} was achieved in 2018 thanks to the small emittances of the beam delivered by the injectors and to a smaller than design β* value of 30 cm (cf. 55 cm nominal value). This luminosity is nearly the ultimate value of the original LHC design report, but it has been obtained with around the nominal bunch population (ca. 1.2×10^{11} p/bunch) rather than the ultimate value of 1.7×10^{11} p/b. This high-luminosity and the excellent availability of the machine and injectors have yielded a record annual integrated luminosity of 65 fb^{-1} in 2018. In the Run 3 period from 2022 to 2024 the LHC aims to further increase the integrated luminosity total: the present goal is to reach 350 fb^{-1} by the end of Run 3, well above the initial LHC goal of about 300 fb^{-1}. In 2018 it was experimentally confirmed that the peak luminosity is limited at the value of around 2×10^{34} cm^{-2} s^{-1} by the heat deposition from luminosity debris and the lack of sufficient cooling of the inner triplet magnets.

Figure 1-1: LHC baseline plan for the next decade and beyond showing the collision energy (upper line) and luminosity (lower line). LS2 sees LHC consolidation and the HL-LHC underground excavation, as well as the upgrade the LHC injectors and Phase 1 upgrade of the LHC detectors. After LS3, the machine will be in the high-luminosity configuration. Covid-19 restrictions have led to the shift of the start of Run 3 to February 2022 while the start of LS3 is maintained at end of 2024.

To fully exploit the physics potential of the LHC, CERN established the high-luminosity LHC project at the end of 2010 [7] with the following targets:

- A peak luminosity of 5×10^{34} cm^{-2} s^{-1} with levelling operation;
- An integrated luminosity of 250 fb^{-1} per year, with the goal of 3000 fb^{-1} in the 12 years or so after the upgrade.

This integrated luminosity is about ten times the predicted luminosity reach of the LHC in its initial configuration.

The main equipment upgrades and layout modifications for HL-LHC will be carried out in the 600 m long insertion regions of LHC Point 1 (P1 - ATLAS) and LHC Point 5 (P5 - CMS). Other parts of the LHC need to be modified as well to deal with the upgraded performance yielding a total length of more than 1.2 km of modified machine and with one further 1 km of additional technical services and equipment required by the new components.

The high-luminosity LHC (HL-LHC) project started as a design study with a contribution by the European Union and various partners in the EU, USA and Japan, federated under the *EC-FP7-HiLumi LHC Design Study* (since then *HiLumi* is frequently used as a project nickname). After the approval of the new European Strategy for Particle Physics by CERN Council on 30 May 2013 [4], the HL-LHC project became CERN's major construction project for the next decade. A series of steps have been taken since then to get a complete approval of the HL-LHC:

- Delivery of a complete preliminary design report (PDR) [8] under the EC-FP7-HiLumi LHC Design Study and first full evaluation of the project cost in 2013.
- Insertion of a budget line (covering most of the cost) in the CERN Medium Term Plan (MTP) [9], with indication for the total cost, in June 2014.
- Implementation of a Cost & Schedule Review (international panel of experts, composed by the CERN Machine Advisory Committee complemented by additional experts). The first meeting in March 9-11, 2015 scrutinized the full project as described in Ref. [8]. The report is available upon request (some information is confidential).
- Modification of the layout for civil engineering (with power supplies of magnets and RF in the underground area with a 'double decker' arrangement – new service galleries located above the existing LHC tunnel), more suitable to the actual needs and conditions in 2015.
- Insertion of the whole budget for the years 2016–2020 (the 5 years covered by MTP approved in 2015), with indication of the total CtC (Cost-to-Completion) of the project until full installation into CERN's MTP, in June 2015.

Thanks to the above-mentioned initiatives, the project and its budget for construction were approved as part of the MTP by the Council at its 16 September 2015 Session. The MTP document also reported, for information, the total cost of the project and the yearly budget profile until 2026.

In spring 2016 the CERN management submitted to Council the proposal for a global approval of the HL-LHC, describing the goals of the upgrade, the physics case for the HL-LHC, and the technology challenges. The proposal, described in Ref. [10], covers all the project period including installation and commissioning, and gives a total material cost for the HL-LHC of 950 MCHF. It is to be noted that this figure covers the high-luminosity LHC, i.e. the materials for collider with its infrastructure, while it does not include the cost of detector upgrades. The document was approved in the 181st session of the CERN Council on 16-17 June 2016. It is remarkable that HL-LHC has become the first project approved directly by the CERN Council since the final approval of the LHC in 1996.

Since then, all equipment has been designed with an engineering margin with respect to the instantaneous heat deposition and the integrated radiation dose. The concept of an ultimate performance is

used for an additional performance increase. By using these margins, it should be possible to push the machine peak levelled luminosity 7.5×10^{34} cm^{-2} s^{-1} increasing the average pile-up, i.e. the number of events per bunch crossing, in the detectors up to around 200. This luminosity level should enable to collect 300 to 400 fb^{-1}/year, provided the experiments can digest this pile-up level and the reduction of engineering margins does not impact too severely on the machine reliability. In terms of total integrated luminosity, the ultimate performance could yield about 4000 fb^{-1}.

Similarly, all magnetic circuits have been designed with a 8–10% margin with respect to the powering at nominal beam energy of 7 TeV [11]. By using these margins, one might hope to operate the LHC eventually at a beam energy of 7.5 TeV [12] and the HL-LHC aims at providing sufficient engineering margins for the new elements to be compatible with this 'ultimate' beam energy, or, when these margins cannot easily be integrated within the HL-LHC resource envelope, to identify the required additional upgrades.

The high-luminosity LHC project is also working in close collaboration with the CERN project for the LHC Injector complex Upgrade (LIU) [13], the companion ATLAS and CMS upgrade projects of 2019–2021 and 2025–2027 and the upgrades planned for both LHCb and ALICE in 2019–2021.

1.2.1 Luminosity

The (instantaneous) luminosity, defined as the number of potential collisions per unit area per second, can be expressed for the LHC as:

$$L = \gamma \frac{n_b N^2 f_{rev}}{4\pi \beta^* \varepsilon_n} R; \quad R = 1/\sqrt{1 + \frac{\theta_c \sigma_z}{2\sigma}} \tag{1-1}$$

where γ is the relativistic gamma factor; n_b is the number of bunches per beam colliding at the Interaction Point (IP); N is the bunch population; f_{rev} is the revolution frequency; β^* is the value of the beta function at the collision point; ε_n is the transverse normalized emittance; R is a luminosity geometrical reduction factor from the crossing angle not including the Hourglass effect; θ_c is the full crossing angle between colliding beam; and σ, σ_z are the transverse and longitudinal r.m.s. sizes, respectively.

With the nominal parameter values shown in Table 2-1, a luminosity of 1×10^{34} cm^{-2} s^{-1} is obtained, with an average pile-up per bunch crossing) of $\mu = 27$ (note $\mu = 19$ was the original forecast at LHC approval due to uncertainties in the total proton cross-section at higher energies).

The discovery reach of the LHC ultimately depends on the integrated luminosity defined as: $L_I \equiv \int_{\Delta t} L\, dt$, or, more directly, the total number of events recorded. Integrated luminosity depends on instantaneous performance (the luminosity) and on the availability of the machine, i.e. the operating time in collision mode, Δt in the above equation. Improving availability (a challenge when machine parameters are pushed near to their maximum acceptable values) is as important as increasing the instantaneous luminosity.

1.2.2 Present luminosity limitations and hardware constraints

Before discussing the new configuration of the HL-LHC, it is useful to recall the LHC systems that will need to be changed, and possibly improved, because they either become vulnerable to breakdown and accelerated aging, or because they may become a bottleneck for operation at higher performance levels and in a higher radiation environment. This goes well beyond the ongoing regular LHC consolidation.

- **Low-β inner triplet quadrupoles** (see Chapter 3). After about 300 fb^{-1} some components of the inner triplet quadrupoles and their corrector magnets will have received a dose of 30 MGy, entering into the region of possible radiation damage. The quadrupoles may withstand a maximum of 400 fb^{-1} to 700 fb^{-1}. But some corrector magnets of nested type might already fail above 300 fb^{-1}, though solid figures are not available. The replacement of the triplet magnets and the associated correctors must be envisaged before damage occurs. Furthermore, the current triplet aperture limits the potential β* reach and thus the attainable peak luminosity. As mentioned above, the cooling power of the triplet is also limited to a value corresponding to a peak luminosity of about 2×10^{34} cm^{-2} s^{-1}.

- **Cryogenics** (see Chapter 9). To increase intervention flexibility and in order to provide the required additional cooling power, the cooling of the inner triplets and part of the matching section magnets needs to be upgraded with a dedicated 1.9 K refrigerator. Separating the triplet cooling from the rest of the arc magnets avoids the need to warm-up an entire arc in the case of interventions in the straight sections near the triplet magnets.
- **Collimation** (see Chapter 5). The collimation system has been designed for the operation of the LHC with its nominal parameters. The upgrade of this system considers, among other things, the need for a lower impedance of the jaws, required for the planned increase in beam intensities and a new configuration to protect the new inner triplet magnets.
- **The dispersion suppressor (DS) regions** (see Chapter 11 and Chapter 5) have been identified as a possible LHC performance limitation, because of a leakage of off-momentum particles from the IPs into the first and second main superconducting dipoles. For P1 and P5 a solution has been found through the implementation of orbit bumps and steering the losses away from the active magnets and into the connection cryostat. For P2 a solution has been found by modifying the optics and placing collimators in a special warm by-pass in a suitably modified connection cryostat. For P7, where the leakage is due to the interaction of primary beam with the collimation system, the solution is more elaborate: an LHC main dipole will be substituted by dipoles of equal bending strength (~120 T·m) obtained by a higher field (11 T) and shorter length (11 m) than those of the LHC dipoles (8.3 T and 14.2 m). The space gained is sufficient for the installation of a warm by-pass hosting additional collimators.
- **Superconducting (SC) links** (see Chapter 6A) for the remote powering of cold circuits. A solution is being pursued for the removal of power converters from the LHC tunnel: for the HL-LHC this equipment will be installed in a new underground gallery following a global optimization study that favours the use of a novel technology that exploits MgB_2 superconductors.

Other systems will potentially become problematic with the aging of the machine and the increased radiation level that comes with higher levels of beam current, luminosity, and integrated luminosity, for example, a number of absorbers and the beam dumps. Their replacement in the frame of the HL-LHC project gives the opportunity of improving their performance or to adapt to new requirements from the experiments.

1.2.3 Luminosity levelling and availability

Both the consideration of energy deposition by collision debris in the interaction region magnets, and the necessity to limit the peak pile-up in the experimental detector, impose an a priori limitation on the acceptable peak luminosity. The consequence is that HL-LHC operation will have to rely on luminosity levelling Figure 1-2 left), the luminosity profile without levelling quickly decreases from the initial peak value due to ‘luminosity burn-off’ (protons consumed in the collisions). With luminosity levelling the collider is designed to operate with a constant luminosity at a value below the virtual maximum luminosity. The integrated luminosity achieved is almost the same as that without levelling, (Figure 1-2 right), in an ideal running configuration without premature fill aborts. The advantage, however, is that the maximum luminosity and peak energy deposition are lower. Among the various methods of levelling, the present favoured one is dynamic variation of β^* during the run. However, variation of crab cavity voltage and/or variation of beam separation are also considered.

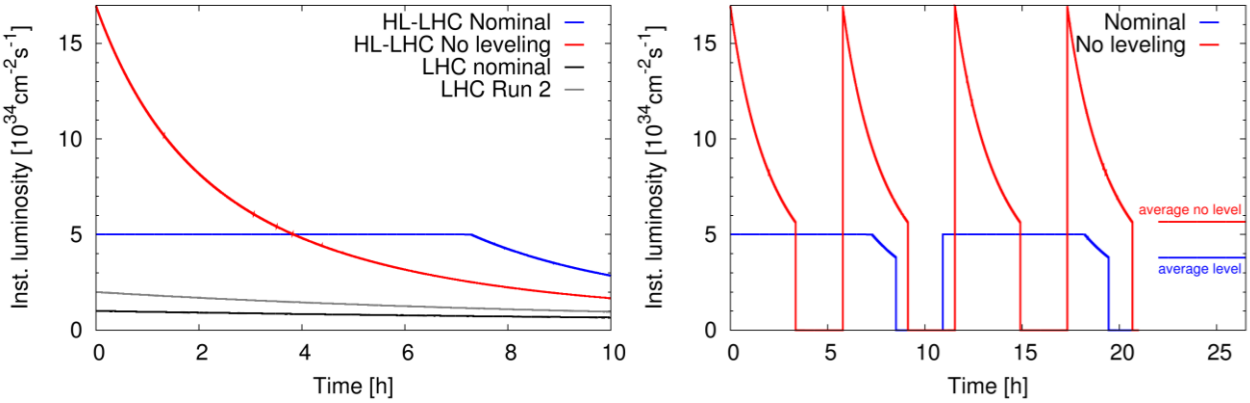

Figure 1-2: (left) Luminosity profile for a single long fill for LHC nominal design and LHC Run 2 operation, as well for HL-LHC with and without levelling. (right) Luminosity profile with optimized run time, without and with levelling, and average luminosity indicated in both cases (solid lines).

A hypothetical 'actual' luminosity cycle for the HL-LHC is depicted in Figure 1-3. With this cycle and assuming 160 days of physics operation per year, the HL-LHC needs a physics efficiency of about 50% in order to reach the 250 fb^{-1} of the nominal design performance, in line with what has been achieved during the last years of the LHC operation, but with twice the beam current. The high-luminosity LHC must therefore also be a high availability machine.

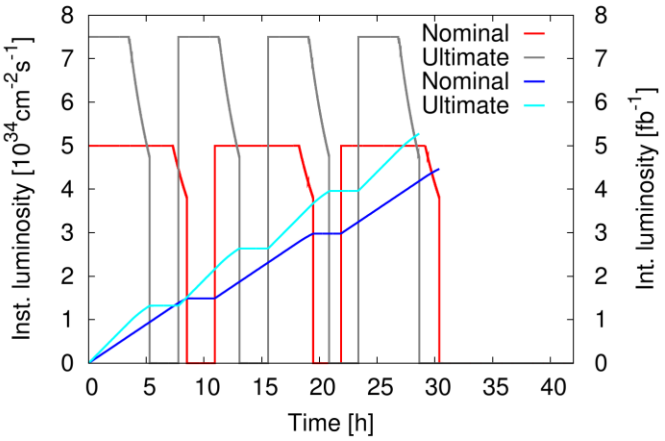

Figure 1-3: Luminosity cycle for HL-LHC with levelling and a short decay (optimized for integrated luminosity) both for nominal levelling (5×10^{34} cm^{-2} s^{-1}) in red and for ultimate levelling (7.5×10^{34} cm^{-2} s^{-1}) in grey. Integrated luminosity is also plotted for both design and ultimate luminosity operation (dark blue and light blue lines respectively).

1.2.4 HL-LHC parameters and main systems for the upgrade

Table 1-1 lists the main parameters foreseen for the HL-LHC operation (a complete list of parameters can be found in Chapter 2). The bunch intensity increases for HL-LHC from 1.15×10^{11} ppb to 2.2×10^{11} ppb, the beam emittance is improved from 3.75 to 2.50 μm and the luminosity reduction factor becomes ca. 0.34 without and 0.72 with crab cavities respectively (compared to ca. 0.84 for the LHC during Run 2). The 25 ns bunch spacing is the baseline operation however, another scheme where each eight bunches with beams are followed by four “empty bunches”, so-called 8b4e the performance with 25 ns bunch spacing. This 8b4e scheme replaces the previous alternative of 50 ns bunch spacing that is disadvantageous from the point of view of pile-up. A slightly different parameter set at 25 ns (batch compression merging and splitting scheme (BCMS)) with very small transverse beam emittance might be interesting for HL-LHC operation in case operation with high beam intensities results in unforeseen emittance blow-up.

Table 1-1: High-luminosity LHC main parameters for proton collisions.

Parameter	Nominal LHC (design report)	HL-LHC 25 ns (standard)	HL-LHC 25 ns (BCMS)	HL-LHC 8b+4e[4]
Number of bunches	2808	2760	2744	1972
Beam current (A)	0.58	1.1	1.1	0.78
Minimum β^* (m)	0.55	0.15	0.15	0.15
Peak luminosity with crab cavities $L_{peak} \times R_1/R_0$ (10^{34} cm^{-2} s^{-1})	(1.18)	17	16.9	12.1
Levelled luminosity for $\mu = 140$ (10^{34} cm^{-2} s^{-1})	-	5.0	5.0	3.8
Events/crossing μ (with levelling and crab cavities)	27	131	132	140
Maximum line density of pile-up events during fill (events/mm)	0.21	1.28	1.29	1.37

The provisional set of parameters of ion beams for the high-luminosity regime of ion collision has also been established, see Chapter 2. The parameters should be able to satisfy the ion integrated luminosity requirements of the ALICE experiment [14]. However, it must be underlined that the beam parameters are being discussed with the LIU project to assess feasibility and optimization. In addition, a discussion with the management of the LHC experiments, arbitrated by CERN management, should also provide clarification on the best sharing of ions collisions between the various experiments. It is worth reminding that the ions luminosity upgrade is available starting from Run 3 in 2021, after the completion of the LIU project.

The HL-LHC upgrade should provide the potential for good performance over a wide range of parameters. The machine and experiments will find the best practical set of parameters in actual operation. The following items are the key variables targeted for optimizing the luminosity performance by the upgrade:

- **Beam current**: the total beam current may be a hard limit in the LHC since many systems are affected by this parameter: RF power system and RF cavities; collimation system and absorbers; cryogenics; vacuum; beam diagnostics; QPS; etc. Radiation effects aside, all existing systems have been designed, in principle, for $I_{beam} = 0.86$ A, the so-called 'ultimate' LHC beam current. However, the ability to go to the ultimate limit is still to be demonstrated in operation and the HL-LHC will need to go 30% beyond ultimate beam current with 25 ns bunch spacing.
- **Beam Brightness**: The beam brightness, the ratio of the bunch intensity to its transverse emittance, is a beam characteristic that must be maximized at the beginning of beam generation and then preserved throughout the entire injector chain and throughout the operation cycle in the LHC itself. The LIU project has as its primary objective increasing the number of protons per bunch by a factor of two above the nominal design value while keeping emittance at the present low value.
- **β* reduction - stronger chromatic aberrations and aperture needs**. A classical route for a luminosity upgrade with head-on collisions is to reduce β* by means of stronger and larger aperture low-β triplet quadrupoles. This reduces the transverse size of the luminous region resulting in a gain in peak luminosity, i.e. the luminosity at the beginning of the fill. The β* reduction comes with an associated increase in beam sizes in the triplet magnets. For operation with a crossing angle, a reduction in β* values also implies an increase in the crossing angle when respecting the requirement for a constant normalized beam separation over the common part of the insertion. The increased crossing angle requires in turn a further increase in the triplet magnet aperture, a larger aperture of the first separation dipole (D1), and further modifications to the matching section. Stronger chromatic aberrations coming from the larger β-functions inside the triplet magnets may furthermore exceed the strength of the existing correction circuits. The peak β-function is also limited by the possibility to match the optics to the regular beta functions of the arcs. A previous study has shown that the practical limit for β* in the nominal LHC is around 30 cm cf. the nominal 55 cm (the LHC operated in 2018 with β* = 30 cm at 6.5 TeV beam energy). However the Achromatic Telescopic Squeeze scheme uses the adjacent arcs as enhanced matching sections. The increase of the beta-functions in these arcs can boost, at constant strength, the

efficiency of the arc correction circuits. In this way a β* value of 15 cm can be envisaged, and flat optics with a β* as low as 10 cm in the plane perpendicular to the crossing plane could be realized. For such a β* reduction the triplet quadrupoles need to double their aperture and require a peak field 50% above those in the present LHC. This implies the use of new, advanced, superconducting technology based on Nb_3Sn. Also, the separation-recombination dipole pair (D1-D2) must have a larger aperture than those in the present LHC, in order to accommodate the larger β and crossing angle coming from the lower β*.

- **Luminosity reduction factor R**. The drawback of very small β^* is that it requires a larger crossing angle θ_c. This causes a severe reduction of the geometrical luminosity reduction factor R. Figure 1-4 shows the reduction factor as a function of β^*, assuming a constant normalized beam separation.

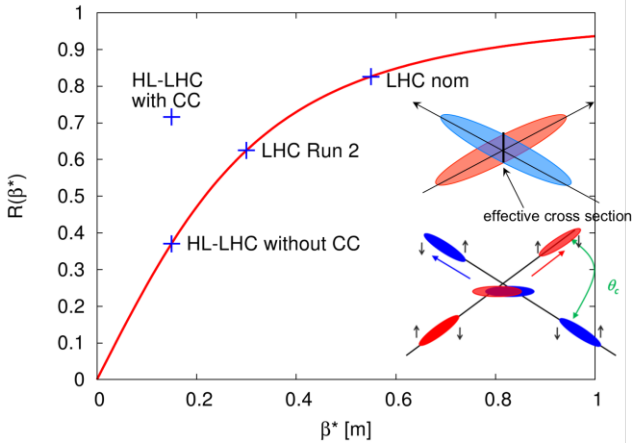

Figure 1-4: Variation of the geometrical luminosity reduction factor with β^* for a constant normalized beam separation with the indication of operational points: nominal LHC, actual LHC Run 2 and HL-LHC with and without crab cavities (CC). The top inset illustrates the bunch crossing overlap reduction effect while the bottom inset shows schematically the effect of CC on beam overlap at collision.

Various methods can be employed to at least partially mitigate this effect. The most efficient and elegant solution for compensating the geometric reduction factor is the use of special superconducting RF crab cavities, capable of generating transverse electric fields that rotate each bunch longitudinally by $\theta_c/2$, such that they effectively collide head on, overlapping perfectly at the collision points, as illustrated in Figure 1-4, see top-right inset. Crab cavities allow access to the full performance reach of the small β^* values offered by the ATS scheme and the larger triplet quadrupole magnets, almost restoring the reduction factor R to values during the nominal LHC operation despite the much larger θ_c. While the crab cavities boost the virtual peak luminosity, β^* variation during the fill – the so-called dynamic β^* squeeze – could be used as levelling mechanism. This would allow optimization of the size of the luminous region and thus the pile-up density throughout the whole fill length. With the chosen baseline of two CC per side and per beam, we achieve R values for the HL-LHC with β* = 15 cm that are higher than those in LHC Run 2, operating at β* = 30 cm.

1.2.5 Baseline hardware summary

The HL-LHC project encompasses the installation of new equipment and the previous de-installation, and removal of the LHC equipment over a length of about 1.2 km. The project, from the first baseline described in the PDR [8] underwent a series of changes and hardware optimization that are described in the two previous TDR versions [16][17]. Here we report only a short, not complete, functional list of the new equipment:

- Almost complete renewal of the insertion region IR1 (around ATLAS experiment) and IR5 (around CMS), from the present TAS to the Q4 quadrupole, passing through the cornerstone of the upgrade, the change of the low-β inner triplet (IT) quadrupoles. The cryogenics, cold powering and warm powering with magnet protection and vacuum systems are completely renewed, too.

- Installation of one new large 1.9 K refrigerator unit at both P1 and P5. The new refrigerators, provide the cooling power needed to absorb the five times larger heat load and, with the adoption of a new cryogenic distribution line QXL, separated from the standard arc QRL, will allow the cooling down or to the warming up of the IR1 and IR5 independently from the arcs.
- Installation of new collimators in IR1 and IR5 as well as the upgrade of most secondary collimators and a few primary ones for impedance reduction.
- Insertion of crab cavities in the Matching sections of IR1 and IR5.
- The addition of collimators in the cold dispersion suppressors regions, DS2 and DS7, in DS7 via the insertion of the 11 T dipole to create the necessary space.
- A modification of the interface to the CMS and ATLAS experiments (VAX region) and addition of a new absorber, the TANB, in IR8 for coping with LHCb increase luminosity.
- Modification of the extraction and injection systems, in particular installation of new upgraded absorbers to cope with injection failures (TDIS)
- Installation of new equipment for Beam Instrumentation (such as, but not only, Beam position monitors (BPM) with high directivity strip lines for the insertion regions, Beam Gas Vertex (BGV) profile monitors and new diagnostics for halo profile measurements), Beam vacuum (like new type of W-shielded beam screen and amorphous carbon coating of the new vacuum components).
- Major civil engineering works both underground and surface in P1 and P5, to host the technical infrastructure, the refrigerators as well as the powering and protection equipment for magnets and cavities. The underground caverns and galleries, about 1 km long in total, will be accessible also during operation with beam, thus increasing the machine availability. On surface a total of ten new buildings will be constructed.
- Three new equipment systems have been recently moved from the status 'options' to the HL-LHC baseline, following a careful preparation and endorsement by dedicated reviews and the recent 4th Cost & Schedule review [18]. They are:
    - Hollow Electron Lenses (HEL) for generating an enhanced particle diffusion in the beam halo and thus their depletion. Extrapolating the beam halo density from the LHC operation during Run 2 to the higher beam intensities of the HL-LHC implies a stored beam energy of more than 35 MJ in the beam halo for particles outside the 3-sigma beam core. This poses a significant risk for the LHC equipment in case of failures and drops in the beam lifetimes. The HEL strongly mitigates this risk and is described in Chapter 5 (as part of the Collimation system).
    - Upgrades of the LHC Beam Dump Kicker system and the main beam dump absorbers. New failure modes observed during the Run 2 operation have highlighted the vulnerability of the machine and potential hardware damage with the existing beam dump system (BDS). Upgrades of power system of the dilution kickers and new windows of the beam dump block were already implemented during LS2. However, the installation of two additional horizontal dilution kickers and a replacement of the entire beam dump absorbers by a new, more robust alternative, solves the problem, as described in Chapter 14, as part of the new BDS for the HL-LHC.
    - Crystal collimators have the potential to significantly boost the cleaning efficiency during ion beam operation. The system has been studied in the LHC with prototype hardware during LHC Run 2. An installation of a minimal configuration (4 crystals, 2 per beam) has been adopted as part of the collimation system in P7 and is described in Chapter 5.

A minor, but useful system that has been recently inserted in the baseline are the inclinometers for measuring vibrations in the machine area near the main experiments.

Now that the project has entered in construction mode there is no room for further options, at least in the present timeframe. However, a few studies are supported for the long-range beam-beam compensator system. Such a system could allow operation with smaller crossing angle and thus increase the available aperture inside the triplet magnets and extend the β^* reach and support the crossing angle compensation via the crab cavity system.

Other options that are considered highly desirable are:

- an upgrade of the power converters for the main dipole and quadrupole circuits of the LHC arcs neighbouring IP1 and IP5, where the ATS optics implies an increase in the average optic functions along the arcs. Such intervention would reduce the tune and optics perturbation due to power converter ripples and noise.
- an additional undulator in IR4 for the generation of synchrotron light for beam diagnostics purposes. The synchrotron light generated in IR4 is being used for the diagnostics of the beam abort gap population, transverse beam profile measurements and beam halo population measurements. The existing light source does not allow a parallel measurement of all the above points throughout the whole LHC cycle. In case such parallel measurements become necessary one could increase the number of available synchrotron light sources through the installation of a second undulator system in IR4.

For the equipment described above, the possible implementation is eventually left to a second stage of HL-LHC consolidation (an exception may be the power converters upgrade, given the moderate cost and the easy implementation).

1.3 Performance

The performance of the upgraded machine has evolved in time as can be seen by the three general scientific reports to the IPAC conference series [7][19][20]. The most updated projected luminosity performance along the whole life of LHC/HL-LHC machine is shown in Figure 1-5 where some “luminosity learning” due to operational experience and staging of some components is included.

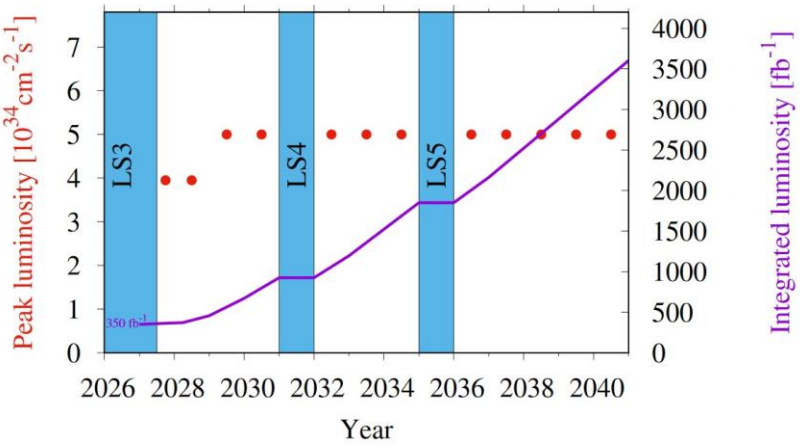

Figure 1-5: Forecast for peak luminosity (red dots) and integrated luminosity (violet line) in the HL-LHC era with nominal HL-LHC parameters.

If the performance of the HL-LHC can go beyond the design levelled luminosity value of $L_{peak} = 5 \times 10^{34}$ cm^{-2} s^{-1}, and if the upgraded detectors will accept a higher pile-up, up to 200 on average, then the performance could eventually reach 7.5×10^{34} cm^{-2} s^{-1} with levelling. With such parameters, a performance about 350 fb^{-1}/year is possible if the days of proton physics per year can be increased after LS4 and LS5. Here one foresees the end of the ALICE ion program after LS4 and a reduced need for machine development time after LS5. This would allow up to 4000 fb^{-1} to be obtained before 2040, as shown in Figure 1-6.

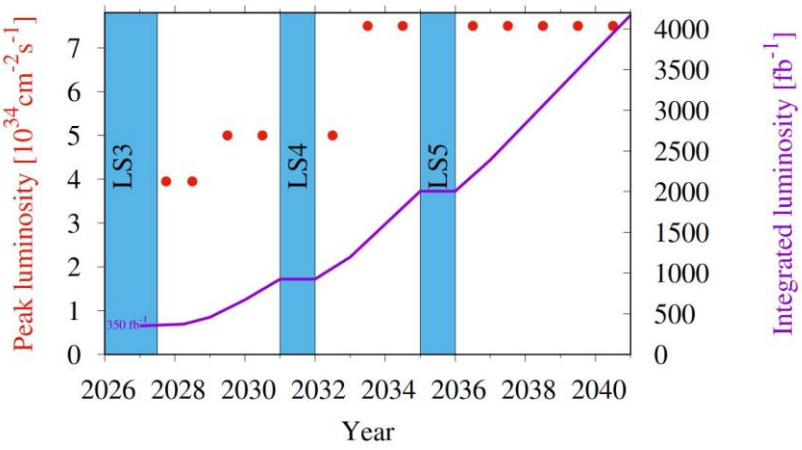

Figure 1-6: Forecast for peak luminosity (red dots) and integrated luminosity (violet line) in the HL-LHC era with ultimate HL-LHC parameters.

The graphs are based on an efficiency in luminosity production of 50%. A more detailed discussion on performance can be found in Chapter 2.

1.4 Planning and cost

1.4.1 Main milestones

The HL-LHC schedule aims at the installation of the main HL-LHC hardware during LS3, together with the final upgrade of the experimental detectors (the so-called Phase II upgrade). However, a few items have been installed or are being installed already during LS2. These include: two new DS collimators integrated in a modified version of the connection cryostat in P2 for ions; a number (40% of the total) of the new low-impedance collimators; the new TANB for P8 as well as modification of the Collider-Experiment interface for P1 and P2 and the injection protection absorbers of new design (TDIS). The 11 T dipole magnets for the new DS collimators in P7 for both ion and proton beams, could also be installed during LS2 o later during an extended technical stop during Run 3.

The HL-LHC time plan comprising past milestones, is summarized below:

- 2010: High-luminosity LHC project established at CERN as Design Study;
- 2011: Approval and start of the FP7 HiLumi LHC Design Study;
- 2014: Preliminary Design Report (PDR) published;
- 2015: First Cost & Schedule Review (C&SR-1); end of FP7-HiLumi, publication of Technical Design Report (TDR_v0);
- 2016: Validation of hardware (components and models); TDR_v0.1 and C&SR-2;
- 2018–2020: Testing of full prototypes and release of final TDR;
- 2019–2024: Construction and test of hardware components;
- 2018–2020: Main underground excavation works;
- 2019–2021: LS2 – Installation of TANB, TDIS, first batch of low impedance collimators; DS collimators in new connection cryostat in P2 and, the DS collimators with 11 T in P7 (this last point maybe completed in an extended technical stop during Run 3 or during LS3). Advancing some installation of collider-experiment interface and prototype installations for Beam instrumentation and Vacuum Work Packages;
- 2021–2023: delivery of all surface buildings;

- 2022–2024: Installation and operation test of the inner triplet string;
- 2025–2027: LS3 –Installation (new magnets, crab cavities, cryo-plants, collimators, SC Links, ancillary equipment, absorbers) and hardware commissioning. This operation is preceded by de-installation of the P1 and P5 insertion regions, as well as by excavation of the cores connecting the new HL underground areas with the LHC tunnel.

1.4.2 Cost

The Cost-to-Completion construction project, as scrutinized and endorsed by the C&SR1 in March 2015, and reconfirmed by the C&SR2 and C&SR3, amounted to about 950 MCHF for materials (including the cost for associate personnel, but excluding some items that are accounted for by the Consolidation project). In the most recent C&SR-4, held at CERN on 11-13 November 2019, an extra cost of 19 MCHF over the previous baseline was presented (the extra-cost is the balance of many cost increase and cost reduction decisions). The project also presented the proposal of adding three new main equipments to the HL-LHC baseline: Hollow Electron Lenses, a new LHC beam dumping system and minimal configuration crystal collimators, as described in the previous section. The material cost associated to this scope increase is 20 MCHF. Both the extra-cost of the previous baseline and the scope increase were endorsed by the C&SR-4 panel, by the CERN management and then inserted into the MTP2020. The total material cost of the HL-LHC construction project as of March 2020 is then 989 MCHF, to which one has to add about 100 MCHF of budget in the HL-LHC Consolidation (budget line for equipment spares and other items related to LHC and HL-LHC operation). The 989 MCHF of HL-LHC construction budget is complemented by almost 2000 FTE-y of CERN staff personnel (the cost of the more than 1300 FTE-y of CERN associated personnel are included in the material budget). At the time of the C&SR-4 about 300 MCHF of HL construction budget were already spent and about 500 MCHF engaged. This CtC is comprehensive of the baseline activities, including a contribution of 10 MCHF to cryogenic testing infrastructure and all civil engineering underground and surface buildings work (both for IP1 and IP5).

The most up-to-date budget profile from the CERN MTP is shown in Figure 1-7.

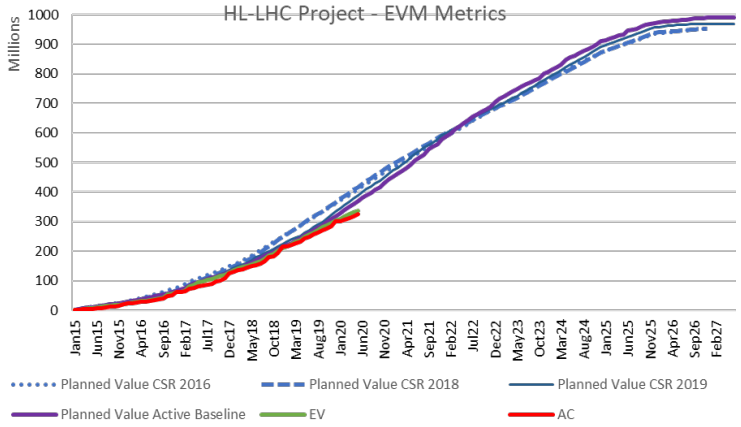

Figure 1-7: The HL-LHC construction project budget allocation as a function of time over 2015–2027, as prepared by the Budget Office for integration in the CERN Medium-Term Plan 2020–2021 with the past and present CtC (active baseline, violet curve). The earned value in June 2020 was 336 MCHF.

1.5 HL-LHC international collaboration

The LHC Luminosity Upgrade was envisioned from the beginning as being an international project. Indeed, US laboratories started to work on it with considerable resources well before CERN. In 2002–2003 a collaboration between the US laboratories and CERN established a first road map for a LHC upgrade 16 [21]. The LARP programme was then set up and approved by the US Department of Energy (DOE). In the meantime, CERN was totally engaged in LHC construction and commissioning: it could only participate in Coordinated

Accelerator Research in Europe (CARE), an EC-FP6 programme, in 2004–2008. CARE contained a modest programme for the LHC upgrade. Then two FP7 programmes (SLH-PP and EuCARD) helped to reinforce the design and R&D work for the LHC upgrade in Europe, although still at a modest level. CERN started in 2008 the project LHC luminosity upgrade phase-1, based on inner triplet quadrupoles with 120 mm aperture (vs. the 70 mm of the present LHC and 150 mm for the HL-LHC), made with Nb-Ti technology, that was stopped in 2010 when HL-LHC was established. KEK in Japan, in the framework of the permanent CERN-KEK collaboration, also engaged from 2008 in activities for the LHC upgrade. LARP remained, until 2011, the main R&D activity in the world for the LHC upgrade.

Finally, with the approval of the FP7 Design Study *HiLumi LHC* in 2011, and the maturing of the main project lines, the HL-LHC collaboration took its present form with participation of various laboratories, also from outside of Europe (KEK was formally part of FP-HiLumi and USA-LARP laboratories were associated to it). Since 2013, efforts have been launched to establish a collaboration framework for the HL-LHC project that continues beyond the EC funded FP7 Design Study and to also address the contribution of actual hardware systems (in-kind contributions). The cornerstone in these efforts is the transformation in 2016 of the US LARP program to a construction project called US HL-LHC Accelerator Upgrade Project (US-AUP). US-AUP will provide to HL-LHC half the Inner Triplet Nb_3Sn quadrupoles (Q1 and Q3 in their cryostat) and half of the crab cavities (the RFD dressed cavities). In addition to these efforts with the USA we have been able to successfully negotiate various in-kind contributions from Laboratories and Institutions in the CERN Member States (MS) and non-member states (NMS). In case of MS Institutions, the baseline is that CERN gives a financial contribution equal to 50% of the material cost of the equipment. For NMS Institution the in-kind is normally at charge of the Institutions (exception for special materials or tooling might be agreed). In addition to the collaborations for in-kinds, there are various collaborations for studies. In general, the participation to the project is expressed by signing the high-luminosity LHC MoU. Institutions that are providing an in-kind contribution are members of the HL-LHC Collaboration Board (see Section 1.6), and institution that collaborates for studies, R&D and with associated personnel are invited to the HL-LHC Collaboration Board as partners. Table 1-2 reports the list of collaborations providing in-kind contribution, design, R&D or providing associated personnel for the project.

Table 1-2: Institutions contributing to the HL-LHC project.

In-Kind	
Lancaster University, Royal Holloway University, Cockcroft Institute – ASTeC, University of Manchester University of Liverpool University of Southampton University of Oxford (UK)	
INFN-Milan-LASA, INFN Genoa (IT)	
BINP, IHEP Kurchatov Institute, PNPI (RU)	
BNL, FNAL, LBNL, SLAC (USA)	
Uppsala University (SE)	KEK (JP)
TRIUMF (CA)	PAEC (PK)
CIEMAT (ES)	IHEP CAS (CN)
University of Belgrade (RB)	

Design, R&D and Associated personnel		
National University of Mar del Plata (AR)	GSI Helmholtz Centre for Heavy Ion Research (D)	Kharkiv Institute of Physics and Technology (UA)
Universidad de Oviedo, Universidad del País Vasco, Universidad de Sevilla, Universidad Politécnica de Madrid, (ES)	Commissariat à l'énergie atomique et aux énergies, Conservatoire National des Arts et Métiers, Centre national de la recherche scientifique (FR)	University of Dundee, University of Huddersfield University of Oxford (UK)
University of Malta (MT)	Lapin Amk (FI)	University of Miskolc (HU)
Université Libre de Bruxelles (BE)	National Technical University of Athens (GR)	Norwegian University of Science and Technology (NO)
Institute of Modern Physics (IMP), Beijing University of Technology, Institute of Plasma Physics (ASIPP) (CN)	Università degli Studi di Napoli Federico II, Politecnico di Torino, Sapienza University of Rome (IT)	VNIIKP, Institut Fiziki Vysokikh Energiy, JINR - Joint Institute for Nuclear Research (RU)
Instituto Superior Técnico (PT)	Jefferson Lab (USA)	Old Dominion University (USA)
Université de Geneve (CH)	École polytechnique fédérale de Lausanne (CH)	Vienna University of Technology (AT)
Cracow University . Technology, Institute of Nuclear Physics, AGH University of Science and Technology, Cracow University of Technology, Lodz University of Technology, National Centre for Nuclear Research NCBJ (PL)		

1.6 Governance and project structure

The HL-LHC is structured in work packages (WPs), each of them subdivided in tasks arranged in a tree-like structure, a structure inherited from the FP7-HiLumi project. In Figure 1-8 the project work package structure is shown, with names of WP Leaders and deputies as well as the main collaborators. Typically, each WP is assigned four to eight tasks. The tasks are the core of the technical work. To be noticed that L. Rossi handed over the Project Leader role to O. Bruning on 1 July 2020.

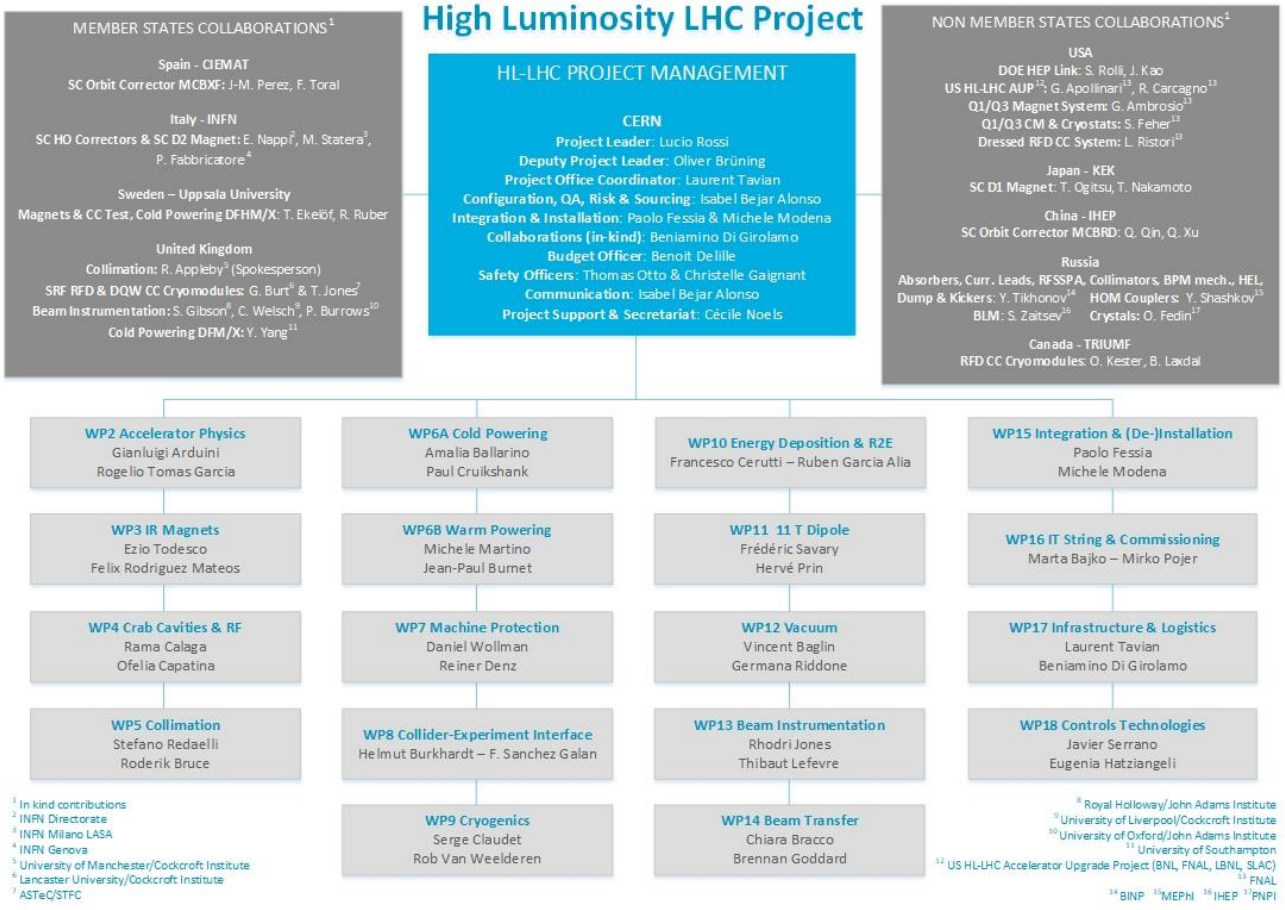

Figure 1-8: The HL-LHC project structure, with management, main collaborators and WP leaders.

The HL-LHC governance and position inside the CERN Accelerator & Technology Sector is shown in Figure 1-9. The Project management holds weekly project management meetings and a monthly special meeting to steer civil engineer works with the SMB department, and uses three main bodies to govern the project:

- HL-LHC Technical Coordination Committee that follows up on the hardware developments and prototype testing;
- HL-LHC Project Steering Committee that meets for each WP two to four times per year with the WP leader, the project office and with the implied group leaders and department management, to supervise budget and planning evolution;
- HL-LHC Coordination Group: high level interface and connection with experiments;

The Collaboration Board meets once a year and recognizes the value and importance of the new collaboration partners with concrete hardware contributions and facilitates the coordination and information flow between the partners. In addition, the HL project management is a member of the Executive Committee,

which looks after decisions that will affect both the LIU and HL-LHC projects with CERN-wide relevance and of the Extended A&T Sector management board (EATSMB).

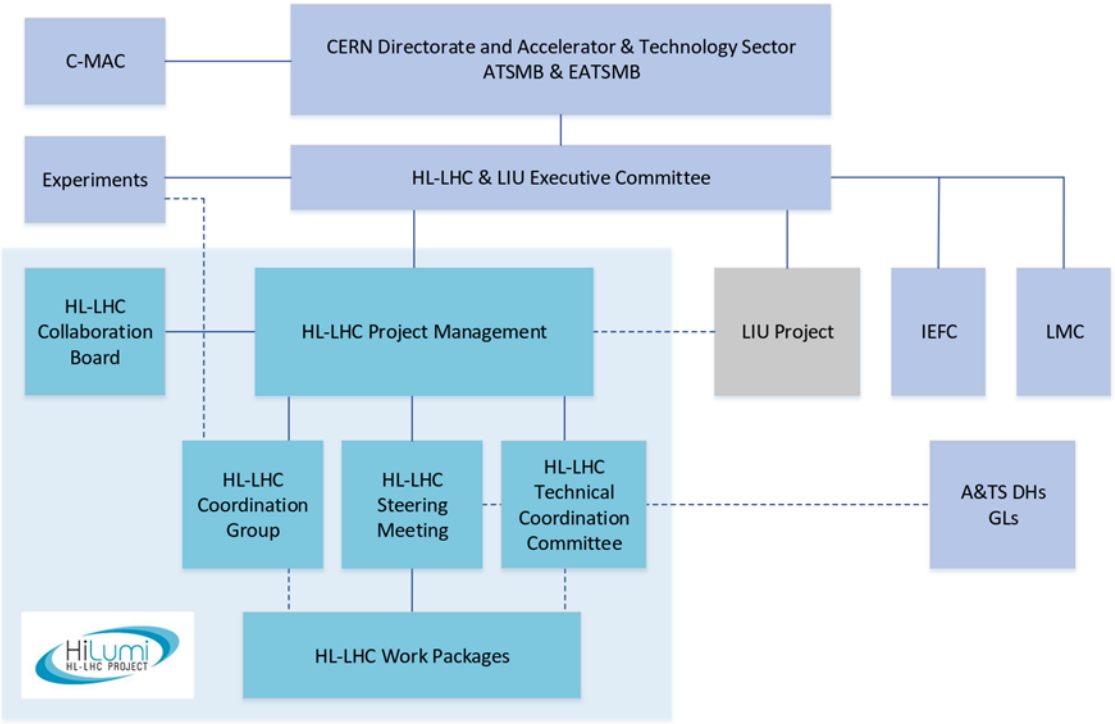

Figure 1-9. The HL-LHC organization in the global CERN Accelerator & Technology Sector structure for the construction phase.

1.7 References

[1] ATLAS Collaboration, “Observation of a new particle in the search for the Standard Model Higgs boson with the ATLAS detector at the LHC”, *Phys. Lett. B*, Volume 716, Issue 1, 17 September 2012, Pages 1–29. DOI: 10.1016/j.physletb.2012.08.020.

[2] CMS collaboration, “Observation of a new boson at a mass of 125 GeV with the CMS experiment at the LHC”, *Phys Lett. B*, Volume 716, Issue 1, 17 September 2012, Pages 30–61. DOI: 10.1016/j.physletb.2012.08.021.

[3] CERN annual report 2018. DOI: 10.17181/RapportAnnuel2018.

[4] The European Strategy for Particle Physics Update 2013, CERN-Council-S/106, adopted at a special session in Brussels on 30 May 2013, CERN (2013).

[5] Deliberation Document on the 2020 Update of the European Strategy for Particle Physics, web page, ISBN: 978-92-9083-576-9 DOI: 10.17181/ESU2020.

[6] Building for Discovery: Strategic Plan for U.S. Particle Physics in the Global Context, US DOE (2014). Reports.

[7] L. Rossi, LHC Upgrade Plans: Options and Strategy, 2nd International Particle Accelerator Conference, San Sebastian, Spain, 4 - 9 Sep 2011, pp.TUYA02, p. 908. CERN-ATS-2011-257.

[8] G. Apollinari, I. Béjar Alonso, O. Brüning, M. Lamont, L. Rossi, High-Luminosity Large Hadron Collider (HL-LHC): Preliminary Design Report, DOI: 10.5170/CERN-2015-005.

[9] Medium-Term Plan for the period 2015–2019 and Draft Budget of the Organization for the sixty-first financial year 2015; CERN/3117, CERN (2014).

[10] The High-Luminosity LHC Project (Director-General) 298th Meeting of Scientific Policy Committee; CERN/3255, CERN (2016).

[11] O. Brüning et al., LHC Full Energy Exploitation Study: Operation at 7 TeV, CERN-ACC-2017-0086

[12] O. Brüning et al., LHC Full Energy Exploitation Study: Operation at Ultimate Energy of 7.5 TeV, CERN-ACC-2019-0015, CERN(2019).

[13] H. Damerau, LHC Injectors Upgrade, Technical Design Report CERN-ACC-2014-0337, CERN-ACC-2016-0041.

[14] J. Jowett, HL-LHC Heavy-Ion Beam Parameters at LHC Injection, EDMS: 1525065.

[15] S. Fartoukh, Achromatic telescopic squeezing scheme and application to the LHC and its luminosity upgrade, DOI: 10.1103/PhysRevSTAB.16.111002.

[16] G. Apollinari, I. Béjar Alonso, O. Brüning, M. Lamont, L. Rossi, D1.10 - Annex 1 - Technical Design Report V0; EDMS: 1558149.

[17] G. Apollinari, I. Béjar Alonso, O. Brüning, P. Fessia, M. Lamont, L. Rossi, L. Tavian, High-Luminosity Large Hadron Collider (HL-LHC) Technical Design Report V. 0.1 DOI: 10.23731/CYRM-2017-004.

[18] 4th HL-LHC/LIU Cost & Schedule Review 2019 Close-out presentation EDMS: 2271479 (Confidential)

[19] O. Brüning, The High-Luminosity LHC Project, IPAC'15, Richmond, USA. DOI:10.18429/JACoW-IPAC2015-FRXC2.

[20] L. Rossi and O. Brüning, Progress with the High-Luminosity LHC Project at CERN, IPAC 2019, Melbourne, AUS, DOI:10.18429/JACoW-IPAC2019-MOYPLM3.

[21] J. Strait et al., Towards a New LHC Interaction Region Design for a Luminosity Upgrade 20th IEEE Particle Accelerator Conference, Portland, OR, USA, 12 -16 May 2003, pp.42-4, CERN-LHC-Project-Report-643, CERN(2003).

Chapter 2

Machine layout and performance

G. Arduini[1*] *R. Bruce*[1], *R. De Maria*[1], *M. Giovannozzi*[1], *G. Iadarola*[1], *J. Jowett*[1], *E. Métral*[1], *Y. Papaphilippou*[1] *and R. Tomás Garcia*[1]

[1]CERN, Accelerator & Technology Sector, Switzerland
[*]Corresponding author

2 Machine layout and performance

2.1 Overview

The goal of the High-luminosity upgrade of the LHC is to deliver an integrated luminosity of at least 250 fb^{-1} per year (assuming at least 160 days of operation at high-luminosity) in each of the two high-luminosity general-purpose detectors, ATLAS and CMS, located at the interaction points (IP) 1 and 5, respectively in Refs. [1][2][3]. The ATLAS and CMS detectors will be upgraded to handle an average pile-up, the number of events per bunch crossing, of at least 140 (ultimately 200), corresponding to an instantaneous luminosity of approximately 5×10^{34} cm^{-2} s^{-1} (ultimately 7.5×10^{34} cm^{-2} s^{-1} [4]) for operation with 25 ns beams consisting of 2760 bunches at 7 TeV, and for an inelastic cross-section σ_{in} = 81 mb [5]. The detectors are also expected to handle a peak line density of pile-up events of at least 1.3 events per mm per bunch crossing and ultimately larger values with limited reduction of the detection efficiency [6][7].

The other two experiments, ALICE and LHCb with detectors located at IP2 and IP8, respectively, will be upgraded to operate at instantaneous luminosities of up to 2×10^{31} cm^{-2} s^{-1} and 2×10^{33} cm^{-2} s^{-1}, respectively. Moreover, they are expecting to collect integrated luminosities of 100 pb^{-1} per year (of proton–proton data) and 5 fb^{-1} to 10 fb^{-1} per year, respectively [1][2][8]. Recently, the LHCb Collaboration has expressed the interest to upgrade the detector even further, to operate at instantaneous luminosities of 1 - 2 × 10^{34} cm^{-2} s^{-1} [9]. Operation for forward physics experiments during high-luminosity operation is being considered [10]. Both these additional requests are not part of the present baseline.

2.2 Performance goals (nominal scheme)

The instantaneous luminosity L for operation with round beams at the IP is given in Ref. [11]

$$L = \frac{n_b N^2 f_{rev} \gamma}{4\pi\beta^* \varepsilon_n} R(\beta^*, \sigma_z, d_{bb}) \qquad (2\text{-}1)$$

where n_b is the number of colliding bunches per beam, N is the bunch population, f_{rev} is the beam revolution frequency, γ is the relativistic gamma factor and the RMS normalized transverse emittance ε_n in collision is assumed here to be equal for the two beams and for the horizontal and vertical planes. The Twiss beta function β^* in collision at the IP determines, together with the normalized emittance, the RMS. beam size $\sigma^* = \sqrt{\varepsilon_n \beta^* / \gamma}$ at the IP (assuming that the contribution to the beam size due to the dispersion and the momentum spread of the beam can be neglected). Here and below it is assumed that the relativistic factor β = 1.

A crossing angle is needed to separate bunches immediately upstream and downstream of the collision point. This leads to a reduced geometric overlap between the colliding beams, and hence to a reduction in luminosity. The crossing angle needs to be increased when reducing the β^* in order to maintain a constant

normalized beam–beam separation d_{bb}, a minimum separation of 10.5 σ is assumed to be sufficiently large. The luminosity is also reduced by the 'hourglass effect' that arises from the increase of the beta function upstream and downstream of the interaction point along the bunch longitudinal distribution. The hourglass effect is enhanced by a reduction in β^* and by an increase in bunch length σ_z. The luminosity reduction factor R in equation (2-1) takes the crossing angle, the hourglass effect and the dispersion at the IP into account.

The HL-LHC project aims to achieve a 'virtual' peak luminosity as close as possible to 2×10^{35} cm^{-2} s^{-1}, considerably higher than the maximum luminosity imposed by the acceptable event pile-up, and to control the instantaneous luminosity during the physics fill ('luminosity levelling') to accumulate the required integrated luminosity [2][12], for a performance efficiency (defined in Refs. [3] [13]) of at least 50%. The latter has been obtained and exceeded during LHC Run 2 [13][14]. Table 2-1 [15][16] shows the machine and beam parameters at collision required to obtain the target 'virtual' peak luminosity, considering the achievable beam parameters in the injectors after their upgrade [13][18][19]. The parameters of Table 2-1 have been updated, as compared to those reported in Ref. [3], after an optimization of the optics, allowing to operate with tighter collimator settings, and a reduction of the acceptable normalized beam-beam long-range separation (from 12.5 to 10.5 σ) enabled by simulation studies and by the experience gained in the LHC during Run 2 [20][21][22]. Collimators at tighter settings, protecting smaller apertures of the magnetic elements in units of the beam σ, and a smaller normalized beam-beam long-range separation have allowed increasing the beam size at the triplet magnets at constant physical aperture and therefore reducing the minimum β* at the high-luminosity IPs down to 15 cm [23] as in Ref. [1].

Table 2-1: HL-LHC nominal parameters for 25 ns operation [15][16] for two production modes of the LHC beam in the injectors described in Ref.[13].

Parameter	Nominal LHC (design report)	HL-LHC (standard)	HL-LHC (BCMS)[#]
Beam energy in collision (TeV)	7	7	7
Particles per bunch, N [10^{11}]	1.15	2.2	2.2
Number of bunches per beam	2808	2760	2744
Number of collisions in IP1 and IP5[*]	2808	2748	2736
N_{tot} [10^{14}]	3.2	6.1	6.0
Beam current (A)	0.58	1.1	1.1
Half-crossing angle in IP1 and IP5 (μrad)	142.5	250	250
Minimum norm. long-range beam–beam separation (σ)	9.4	10.5	10.5
Minimum β^* (m)	0.55	0.15	0.15
ε_n (μm)	3.75	2.50	2.50
Longitudinal emittance ε_L (eVs)	2.50	3.03	3.03
RMS energy spread [10^{-4}] (q-Gaussian distribution)	-	1.1	1.1
RMS energy spread [10^{-4}] (FWHM equiv. Gaussian)	1.13	1.29	1.29
RMS bunch length (cm) (q-Gaussian distribution)	-	7.61	7.61
RMS bunch length (cm) (FWHM equivalent Gaussian)	7.55	9.0	9.0
IBS horizontal (h)	105	16.5	16.5
IBS longitudinal (h)	63	19.2	19.2
Radiation damping (h)	26	26	26
Piwinski parameter	0.65	2.66	2.66
Total reduction factor R_0 without crab cavities at min. β^*	0.836	0.342	0.342
Total reduction factor R_1 with crab cavities at min. β^*	-	0.716	0.716
Beam–beam tune shift/IP [10^{-3}]	3.1	8.6	8.6
Peak luminosity without crab cavities L_{peak} [10^{34} cm^{-2} s^{-1}]	1.00	8.11	8.07
Peak luminosity with crab cavities $L_{peak} \times R_1/R_0$ [10^{34} cm^{-2} s^{-1}]	-	17.0	16.9

Parameter	Nominal LHC (design report)	HL-LHC (standard)	HL-LHC (BCMS)[#]
Events/crossing w/o levelling and without crab cavities	27	212	212
Levelled luminosity [10^{34} cm^{-2} s^{-1}]	-	5.0	5.0
Events/crossing μ (with levelling and crab cavities)[‡]	27	131	132
Max. line density of pile-up events during fill (evts/mm)	0.21	1.28	1.29
Levelling time (h) (assuming no emittance growth)[‡]	-	7.2	7.2
Number of collisions in IP2/IP8	2808	2492/2574[**]	2246/2370[**]
N at injection [10^{11}][††]	1.20	2.30	2.30
Maximum number of bunches per injection	288	288	240
Total beam population per injection [10^{13}]	3.46	6.62	5.52
ε_n at SPS extraction (μm)[‡‡]	3.50	2.10	1.70

[#]BCMS parameters are only considered as a backup scenario set in case of larger-than-expected emittance growth in the HL-LHC during injection, ramp, and squeeze

[*]Assuming one less batch from the PS for machine protection (pilot injection, transfer line steering with 12 nominal bunches) and non-colliding bunches for experiments (background studies, etc.). Note that due to RF beam loading the abort gap length must not exceed the 3 μs design value.

[‡]The total number of events/crossing is calculated with an inelastic cross-section of 81 mb, while 111 mb is assumed as a pessimistic value for calculating the proton burn off and the resulting levelling time [5][17].

[**]The lower number of collisions in IR2/8 compared to the general-purpose detectors is a result of the agreed filling scheme, aiming as much as possible at an equal sharing of collisions between the experiments.

[††]An intensity loss of 5% distributed along the cycle is assumed from SPS extraction to collisions in the LHC.

[‡‡]A transverse emittance blow-up of 10–15% on the average H/V emittance in addition to that expected from intra-beam scattering (IBS) is assumed (to reach 2.5 μm of emittance in collision for 25 ns operation).

The spacing between PS/SPS trains has been reduced to 200/800 ns following the 2017 operational experience [24][25] and the maximum number of bunches per beam and colliding pairs have been updated accordingly. Concerning the BCMS beam, the compatibility of these beam parameters with the protection devices involved in the SPS-LHC transfer has been validated [26].

Based on the LHC experience a light-tailed q-Gaussian* distribution with q = 3/5 [27][28] has been considered to represent the longitudinal distribution. Its Full Width at Half Maximum (FWHM) at high energy has been selected such as to avoid longitudinal instabilities due to loss of Landau damping [29] and the corresponding RMS value (7.61 cm) can be used to estimate luminosity with a Gaussian distribution with good accuracy. However, the calculation of the pile-up event density requires the use of the q-Gaussian distribution.

---

* The q-Gaussian distribution is defined by

$$f(s) = \frac{\sqrt{\beta}}{C_q} \mathrm{e}_q[-\beta s^2],$$

with $q < 3$ and $\beta > 0$

The normalization factor C_q and the q-exponential function in the equation above are given by

$$C_q = \begin{cases} \dfrac{2\sqrt{\pi}\,\Gamma\left(\frac{1}{1-q}\right)}{(3-q)\sqrt{1-q}\,\Gamma\left(\frac{3-q}{2(1-q)}\right)}, & -\infty < q < 1 \\ \sqrt{\pi}, & q = 1 \\ \dfrac{\sqrt{\pi}\,\Gamma\left(\frac{3-q}{2(q-1)}\right)}{\sqrt{q-1}\,\Gamma\left(\frac{1}{q-1}\right)}, & 1 < q < 3 \end{cases},$$

and

$$\mathrm{e}_q = \begin{cases} \exp(s), & q = 1 \\ [1 + (1-q)s]^{\frac{1}{1-q}}, & q \neq 1 \text{ and } 1 + (1-q)s > 0 \\ 0^{\frac{1}{1-q}}, & q \neq 1 \text{ and } 1 + (1-q)s \leq 0 \end{cases}.$$

The RMS of the distribution σ_f is

$$\sigma_f = \begin{cases} \sqrt{\dfrac{1}{\beta(5-3q)}}, & q < \dfrac{5}{3} \\ \infty, & \dfrac{5}{3} \leq q < 2 \\ Undefined, & 2 \leq q < 3 \end{cases}.$$

A detailed description of the corresponding operational scenarios for proton operation is provided in Ref. [30]. Here, only the main parameters in collision are updated together with the corresponding performance estimates.

2.3 Baseline optics and layout

2.3.1 Basic optics and layout choices for the high-luminosity insertions

The historical development of the optics design up to the previous optics version is summarized in Refs. [2][3]. The current baseline optics design (HLLHCV1.5) has evolved from that described in Ref. [3] and it is based on the Achromatic Telescopic Squeeze (ATS) scheme [31], together with the installation of triplet quadrupoles and separation dipoles of larger aperture. Successful validation tests of the ATS with beam were achieved in 2011–2012 and in 2016 [32] and the ATS optics has been implemented in operation in the LHC starting from the 2017 Run [33][34].

In the triplet region (between 20 m and 85 m from the IP in Figure 2-1), the Q1 and Q3 quadrupole magnets (indicated in red) are split in two and the dipole corrector magnets (used to create the crossing and separation schemes and indicated in green) are implemented in a nested configuration for both planes. The corrector package (CP) close to Q3 consists of superferric multipolar corrector magnets (indicated in orange) and of a pair of Nb-Ti dipole corrector magnets in nested configuration (indicated in green). The specifications and performance of the non-linear correctors (used to compensate the field quality effects of the triplets and separation dipoles) [35][36] have been recently updated in Refs. [37][38][39].

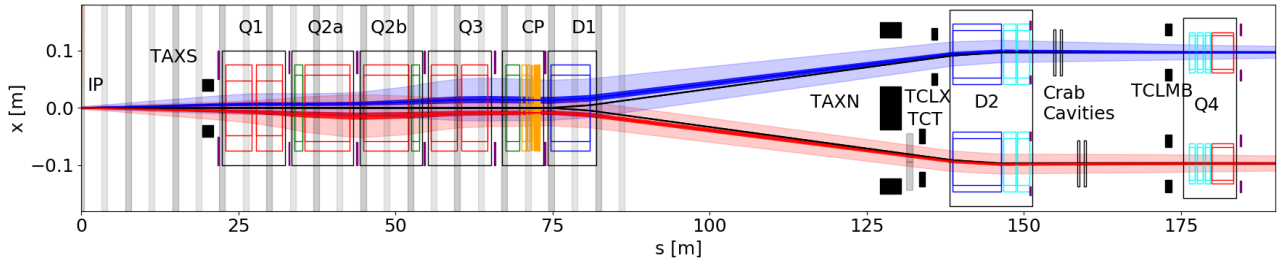

Figure 2-1: Overall layout of the insertion region between the IP and Q4. The dark blue and dark red areas represent the 2 σ beam envelope for the β* = 15 cm round optics. The lighter regions correspond to the 11.9 σ (protected aperture) value of the beam envelope for a normalized emittance of 2.5 μm and including tolerances in β-beating and orbit distortions [40]. The shaded grey areas in the triplet region represent the locations of the parasitic beam–beam encounters in which the BPM (marked in purple) should not be installed. Additional aperture margins are needed in the matching section to be compatible with flat optics operations.

The block of two separation-recombination dipoles D1 and D2 (indicated in blue) has been changed with respect to the nominal LHC layout, decreasing the distance between them. The D2 area is particularly delicate, as there are space constraints because of the need for protection devices, such as the TAXN absorber for neutral debris from the collisions. Moreover, because the transverse aperture separation is not yet the nominal one (see Table 2-3) and because the local values of the beta functions are large, the amount of iron between the two apertures of the D2 is reduced. Downstream of D2, the crab cavities impose tight constraints on the space between D2 and Q4, as well as on the local values of the beta functions.

The HLLHCV1.5 optics [41] features a reduction of the minimum β* for round optics down to 15 cm as in Ref. [1] thanks to the optimization of the phase advance between the beam dump kicker - MKD - and tertiary collimators – TCTs – in IR1 and IR5. This made possible the consequent reduction of the protected aperture (in beam σ) by means of tighter settings of the collimation system [23][42][43][44], as mentioned in Section 2.2. The minimum β* achievable both for the round and flat optics is limited by the triplet aperture [41].

The length of the sextupole, octupole and decapole triplet corrector magnets (normal and skew) has been increased to cope with larger-than-expected multipoles in the triplet quadrupoles [38] (see Section 2.3.2). The length of the skew quadrupole correctors has been reduced [38] based on the updated alignment tolerances of the triplet quadrupole magnets and cold masses [45][46][47].

The implementation of a fully remote alignment system, allowing beam-based remote alignment with safe beams [48][49] (see Chapter 15), has brought a healthy reduction of the strength requirements of the orbit correctors at Q4 and Q5, as well as increased aperture with the possibility of reaching $\beta^* = 7.5$ cm in flat optics, previously limited by Q4 aperture. The existing LHC cold masses can now be used for both the Q4 (MQY + 3 × MCBY) and Q5 (MQML + MCBC) magnets [50], requiring only a re-positioning of the existing magnets and the re-orientation of some of the beam screens. It must be noted that recent concerns about the radiation resistance of the correctors' coils might entail future consolidation needs presently under study but not required before the end of Run 4 [51][52]. Reduction of the operating temperature from 4.5 K to 1.9 K is no longer required [41][53]. The position of the Q4 and Q5 magnets with respect to the IP has been optimized to allow cooling them from the arc cryogenic line with limited modifications. The present optics and layout configuration include an additional lattice sextupole (MS) to be installed in Q10 in IR1 and IR5 [3].

The IR4 optics has been revised and is compatible with the requirements set by beam instrumentation and transverse feedback operation. Furthermore, it fulfils the conditions for the implementation of hollow electron lenses for beam halo collimation [41][54].

The IR6 optics has been optimized and is compatible with the constraints imposed by the TCDQ gap opening [41] and, given the results of tests performed at the end of Run 2, with the operation of Q5.L6 and Q5.R6 at 4.5 K, as in the nominal LHC, up to the beam energy of 7.0 TeV. The upgrade of Q5.L6 to operate at 1.9 K would be only required for operation at 7.5 TeV and could be postponed until the operation at ultimate energy is considered. Hence, the initially planned change of the operational temperature [3] has been removed from the baseline [55][56][57].

The IR7 optics has been revised and adapted to the new layout with a removed MQW magnet in each of the Q5 magnets, which will be implemented during LS2 [58]. In addition, 11T magnets (MBH) and TCLD collimators have been included in both sides of Point 7 replacing a normal dipole (MB) in Cell 9.

Table 2-2 lists the key parameters of the quadrupoles (new or refurbished) to be installed in IR1 and IR5, while Table 2-3 refers to the separation dipoles and orbit correctors for the HL-LHC configuration [59]. Table 2-4 gives the parameters for the superferric correctors. The shape and inner size of the beam screens for the new magnets, which define the region available for the beam, is based on a preliminary design [60]. These have been updated [61] and the estimated mechanical tolerances will have to be refined following the development of hardware prototypes. The minimum β^* reach has been assessed based on the available mechanical aperture of the beam screens (including mechanical tolerances) and considering optics and orbit errors based on the experience gained with LHC operation so far [40]. It has been also assumed that the collimation system can protect a horizontal aperture of 11.9 σ (for a normalized emittance of 2.5 μm) for elements protected by tertiary collimators (TCTs), provided the phase advance between MKD and TCT is below 30° and 11.2 σ in the vertical plane at top energy. Otherwise, for the rest of the machine, 19.4 σ is the limit of protected aperture at top energy and 12.4 σ at injection energy [40]. Mechanical, alignment, and beam tolerances have been added linearly and account for about 15% of the triplet aperture. The reduction of crab cavities per IP side and beam from 4 to 2, implemented in June 2016 [3], prevents changing the crossing-angle plane without major hardware interventions. The crossing-angle planes have been selected to be horizontal in IP1 and vertical in IP5, differently from the LHC, as this provides some additional aperture margins for the baseline round optics while favouring forward physics detectors in IR5, which are not yet part of the HL-LHC baseline. The additional aperture in the crossing plane is also beneficial for the possible installation of the Beam-Beam Long Range (BBLR) wire compensator (presently not in the baseline). Conversely, squeezing β^* in the horizontal plane in IP5 for flat optics requires additional compromises in IR6 optics, thus making a horizontal crossing angle in IP5 more attractive for flat optics scenarios.

The description of the shapes of the beam screens is made by providing the dimensions corresponding to the horizontal (H)/vertical (V) and 45° cuts for octagons; diameter (d) and gap (g) for rectellipses [50]; radius for circles. The orientation of the rectellipse cross-section depends on the IP side and beam and it has been chosen to optimise the beam aperture in collision. The alignment tolerances are represented as a racetrack shape of radius (R), horizontal (H), vertical (V) extent, respectively. The values provided include ground motion and fiducialization tolerances [62], although they are going to be reviewed in the context of the full remote alignment system.

Table 2-2: New or refurbished quadrupoles for the HL-LHC in IR1 and 5. “Beam stay clear” indicates the minimum aperture available for the beam considering the tolerance on the mechanical deformations of the nominal beam screen inner shape.

	Inner triplet (single aperture)			**Matching section (two-in-one)**	
Magnet	**Q1**	**Q2**	**Q3**	**Q4**	**Q5**
Number per side per insertion	2			1	
Type	MQXFA	MQXFB	MQXFA	MQY	MQML
Magnetic length (m)	4.2	7.17	4.2	3.4	4.8
Maximum Gradient (T/m)	132.2			160	160
Coil aperture (mm)	150			70	56
Aperture separation (mm)	NA			194	
Operating temperature (K)	1.9			4.5	
Beam screen shape	Octagon			Rectellipse	
Nominal beam screen aperture (mm)	99.7(H/V)/ 99.7(45°)	119.7(H/V)/ 110.7(45°)		60.2(d) / 50.4 (g)	47.5(d)/37.7(g)
Beam stay clear (mm)	94.94(H/V)/ 94.94(45°)	115.3(H/V)/ 106.3(45°)		57.8(d) / 48 (g)	45.1(d)/35.3(g)
Alignment tolerances (R/H/V) (mm)	0.6/1.0/1.0			0.84/1.26/0.6	
Beam screen orientation (plane of smaller gap)				L.B1: V L.B2: H R.B1: H R.B2: V	

Table 2-3: Separation and corrector dipole magnets for the HL-LHC in IR1 and 5. The order of the correctors has to be considered starting from the IP.

	Separation/recombination dipoles		**Orbit correctors**				
Assembly	**D1**	**D2**	**CP**	**Q2**	**D2**	**Q4**	**Q5**
Number per side per insertion	1	1	1	2	2	3	1
Configuration			HV nested	HV nested	L.B1: VH L.B2: HV R.B1: VH R.B2: HV consecutive	L.B1: VHV L.B2: HVH R.B1: HVH R.B2: VHV consecutive	L.B1: V L.B2: H R.B1: H R.B2: V
Type	MBXF	MBRD	MCBXFA	MCBXFB	MCBRD	MCBY	MCBC
Magnetic length (m)	6.27	7.78	2.2	1.2	1.93	0.9	0.9
Integrated field (T m)	35.08	35.08	4.5	2.5	5.0	2.5	2.33

Assembly	**D1**	**D2**	**CP**	**Q2**	**D2**	**Q4**	**Q5**
Coil aperture (mm)	150	105	150	150	105	70	56
Aperture separation (mm)	NA	188	NA	NA	188	194	194
Operating temperature (K)	1.9					4.5	
Beam screen shape	Octagon	Octagon	Octagon	Octagon	Octagon	Rectellipse	Rectellipse
Nominal beam screen aperture (mm)	119.7 (H/V)/ 110.7 (45°)	87.45 (H/V)/ 77.55 (45°)	119.7(H/V)/ 110.7 (45°)	119.7 (H/V)/ 110.7 (45°)	87.45 (H/V)/ 77.55 (45°)	60.2 (d) / 50.4 (g)	47.5 (d)/ 37.7(g)
Beam stay clear	115.3 (H/V)/ 106.3 (45°)	82.7 (H/V)/ 72.5 (45°)	115.3(H/V)/ 106.3(45°)	115.3 (H/V)/ 106.3 (45°)	82.7 (H/V)/ 72.5 (45°)	57.8 (d) / 48 (g)	45.1 (d)/ 35.3(g)
Alignment tolerances (R/H/V) (mm)	0.6/1.0/1.0	0.84/1.36/1.0	0.6/1.0/1.0	0.6/1.0/1.0	0.84/1.36/1.0	0.84/1.26/0.6	
Beam screen orientation (plane of smaller gap)						L.B1: V L.B2: H R.B1: H R.B2: V	

Table 2-4: New superferric correctors for the HL-LHC [38][39]. The order (from left to right) follows the order of installation from the IP.

Number	1	1	1	1	1	1	1	1	1
Number of poles	4	12	12	10	10	8	8	6	6
Normal/skew	Skew	Normal	Skew	Normal	Skew	Normal	Skew	Normal	Skew
Name	MQSXF	MCTXF	MCTSXF	MCDXF	MCDSXF	MCOXF	MCOSXF	MCSXF	MCSSXF
Magnetic length (m)	0.401	0.470	0.099	0.146	0.146	0.145	0.145	0.167	0.167
Integrated field (mT m) at 50 mm	700	86	17	37	37	69	69	95	95
Aperture (mm)	150								
Operating temp.(K)	1.9								
Beam screen shape	Octagon								
Nominal beam screen aperture (H/V) (mm)	119.7(H/V)/ 110.7(45^0)								
Beam stay clear (mm)	115.3(H/V)/ 106.3(45°)								
Alignment tolerances (R/H/V) (mm)	0.6/1.0/1.0								

As already mentioned, protection devices are required for the new layout of the IR1 and IR5 regions. The current LHC layout has a TAS in front of Q1, to protect this magnet from collision debris, and a TAN to protect D2 from the neutrals produced at the IP. For the HL-LHC, these two devices will have to be upgraded to withstand much larger luminosities and to be suitable for the new layouts and flexible optics configurations. Furthermore, additional masks are envisaged to protect other magnets in the matching section. A summary with the characteristics of these devices can be found in Table 2-5.

Table 2-5: New absorbers for the HL-LHC. TAXS alignment tolerances include the IP displacement. Mechanical tolerances are not known yet therefore a conservative fiducialization tolerance has been used (2 mm).

	Inner triplet (single aperture)	**Matching section (two-in-one)**			
Function	Main secondary absorber	Main neutral absorber	Mask Q4	Mask Q5	Mask Q6
Aperture	1	2	2	2	2
Type	TAXS	TAXN	TCLMB	TCLMB	TCLMC
L (m)	1.8	3.332	1.0		
Aperture separation (mm)	NA	151–161	194		
Aperture shape	Circle	Circle	Rectellipse		
Nominal aperture (mm)	60	85	60.2 (d)/50.4 (g)	60.2 (d)/50.4 (g)	47.5 (d)/37.7 (g)
Beam stay clear (mm)	58	82	57.8 (d)/48 (g)	57.8 (d)/48 (g)	45.1 (d)/35.3 (g)
Alignment tolerances (R/H/V) (mm)	2.0/2.5/2.5	0.84/1.36/1	0.6/1/1		

Table 2-6 gives the main sets of β* values (including the optical parameters corresponding to the ion runs). Since IR2 and IR8 are running with increased strength of the triplets at injection, an optics transition is applied before reaching top energy to reduce the required strength of the triplets. It is also planned to perform the squeeze down to $\beta^* = 64$ cm (which is the initial value of the β^* required to level at the nominal luminosity of 5×10^{34} cm^{-2}s^{-1}) in IP1 and IP5 for the high-luminosity IR optics and to $\beta^* = 1.5$ m for Point 8 during the ramp to minimize the turn-around time [30]. Additional optics scenarios for the end of the ramp with different combinations of β^* and ATS factor are being studied to optimize the Landau damping and allow a smooth increase of luminosity as required by the cryogenic system.

Table 2-6: Available optical configurations for the baseline layout. IR3 and IR7 are not included as they have static optics from injection to collision and do not take part in the ATS scheme. IR4 and IR6 take part in the ATS and this is highlighted here, where the "No ATS" configuration corresponds to an injection-compatible optics kept constant up to top energy. The telescopic indexes [63] are indicated in parenthesis. Flat alternative configurations are also shown, assuming V/H crossing in IP1/5, respectively.

Optics	**IR1**	**IR5**	**IR2**	**IR8**	**IR4**	**IR6**
Injection	$\beta^* = 6$ m	$\beta^* = 6$ m	$\beta^* = 10$ m	$\beta^* = 10$ m	No ATS	No ATS
End of ramp	$\beta^* = 6$ m	$\beta^* = 6$ m	$\beta^* = 10$ m	$\beta^* = 10$ m	No ATS	No ATS
Pre-squeeze	$\beta^* = 50$ cm	$\beta^* = 50$ cm	$\beta^* = 10$ m	$\beta^* = 1.5$ m	No ATS	No ATS
Collision round	$\beta^*_{ATS} = 15$ cm	$\beta^*_{ATS} = 15$ cm	$\beta^* = 10$ m, ATS (3.33×, 3.33×)	$\beta^* = 1.5$ m, ATS (3.33×, 3.33×)	ATS (3.33×, 3.33×)	ATS (3.33×, 3.33×)
Collision ions	$\beta^* = 50$ cm	$\beta^* = 50$ cm	$\beta^* = 50$ cm	$\beta^* = 1.5$ m	No ATS	No ATS
Collision VDM	$\beta^* = 30$ m	$\beta^* = 30$ m	$\beta^* = 30$ m	$\beta^* = 30$ m	No ATS	No ATS
Alternative configurations						
Collision Flat	β^*_{ATS} = 7.5/30 cm	β^*_{ATS} = 30/7.5 cm	$\beta^* = 10$ m, ATS (6.66×, 1.66×)	$\beta^* = 1.5$ m, ATS (6.66×, 1.66×)	ATS (1.66×, 6.66×)	ATS (1.66×, 6.66×)
Collision FlatCC	β^*_{ATS} = 7.5/18 cm	β^*_{ATS} = 18/7.5 cm	$\beta^* = 10$ m, ATS (6.66×, 2.77×)	$\beta^* = 1.5$ m, ATS (6.66×, 2.77×)	ATS (2.77×, 6.66×)	ATS (2.77×, 6.66×)

2.3.2 Target field quality, dynamic aperture, and correction schemes

The Dynamic Aperture (DA) specifies the minimum stable amplitude in terms of RMS beam size over a given number of turns in the machine. It has been used since the initial steps of the design of the LHC [50] to determine the required field quality of the various magnet classes. The methods used for DA computation in

the HL-LHC are described in Refs. [12][37][50]. For reference, the multipole expansion used to describe the magnetic field is given as in Ref. [50]:

$$B_y + iB_x = B_{\mathrm{ref}} \sum_{n=1}^{\infty} (b_n + \mathrm{i}a_n) \left(\frac{x+\mathrm{i}y}{r_0}\right)^{n-1}, \qquad (2\text{-}2)$$

where B_x, B_y, and B_{ref} are the transverse magnetic field components and the reference field, respectively. The coefficients a_n, b_n are the skew and normal field components, and r_0 is the reference radius. The magnetic errors are split into three components, namely systematic (*S*), uncertainty (*U*), and random (*R*), such that a given multipole is obtained by:

$$b_n = b_{n_S} + \frac{\xi_U}{1.5} b_{n_U} + \xi_R b_{n_R}, \qquad (2\text{-}3)$$

where ξ_U, ξ_R are Gaussian-distributed random variables cut at 1.5 σ and 3 σ, respectively. The ξ_U variable is the same for all magnets of a given class and manufacturer, but changes from seed to seed and for the different multipoles, whereas ξ_R also changes from magnet to magnet. In the numerical simulations, the best knowledge of the measured magnetic errors is assigned to the magnets as installed, while, for the magnets that will be replaced according to the upgrade plans, the expected error table, with statistical assignment of errors, is used. The expected field quality for the new HL-LHC magnets is reported in Annex A-7. Given the large aperture, estimates for the fringe fields have been provided for the triplet magnets and are used in simulations.

The layout HLLHCV1.0 [64] has been extensively used and it has been the reference for the DA studies, so far [37]. Given the CPU-time required for these studies, it is not always possible to keep them synchronised with the development and evolution of the layout. It is expected that the differences introduced by layout and optics changes since HLLHCV1.0 should not have a significant impact on DA. Nonetheless, DA studies for HLLHCV1.4 are ongoing.

The minimum acceptable DA value differs between injection and collision energies. At injection, where the beam–beam effects can be neglected, the focus is on the impact of magnetic field quality. For the LHC design [50], a minimum DA value of 12 σ (for a normalized emittance of 3.75 μm) was assumed. The best model of the LHC, including the measured field quality of the magnets and the magnets sorting, provides a DA slightly lower than 11 σ [65], but no signs of DA-related limitations have been observed during operation or dedicated studies in Run 1 and Run 2. Hence, for the HL-LHC a target value of 12 σ has been assumed, but for the lower nominal emittance of 2.5 μm.

At top energy, and in particular in collision, beam–beam effects are dominant and the DA has to be evaluated including magnetic field imperfections as well as head-on and long-range beam–beam effects (see Section 2.4.2). Hence, the impact of the various multipolar errors on DA is first verified without beam-beam effects and eventually these effects are included, providing the final DA value, also verifying that the impact of field quality remains negligible in this configuration. Note that the acceptable minimum DA was set to 10 σ (for a normalized emittance of 3.75 μm) at top energy for the LHC [50]. Based on the LHC experience the acceptance criteria for the field quality of the HL-LHC magnets have been defined to guarantee a minimum DA of 8 σ (for a normalized emittance of 2.5 μm) in the absence of beam-beam effects and of 6 σ in collision when beam-beam effects are included (see Section 2.4.2).

The simulation studies have confirmed that the target field quality at injection is consistent with the LHC DA target mentioned above for low values of the chromaticity (Q' = + 3) and when the Landau Octupoles are not powered. The expected field quality at high energy gives a minimum DA of about 8.5 σ (for the clockwise rotating beam - Beam 1) and 7.5 σ (for the anti-clockwise rotating beam - Beam 2) for the round optics at the minimum β* of 15 cm, provided that the field errors are properly compensated by the high-order triplet correctors [37]. The difference of DA between Beam 1 and 2 is already present for the LHC [65] and such a difference is observed also in the HL-LHC [37]. Note that the phase advances over the various insertions are not the same for the two beams as well as the global phase advance between IP1 and IP5, which could explain the differences in DA observed. Optimization of the DA by tuning of the phase advance between IP1 and IP5 is being pursued [37]. Although the simulations including beam-beam effects (see Section 2.4.2) indicate that

the operational scenario described in Ref. [30] is compatible with the target DA of 6 σ and this is dominated by beam-beam, it is evident that a close follow-up of the field quality is mandatory and corrective actions are required in case of deviations from the expected one. In that respect, the analysis of the first measurements of the field quality on short models of the triplet quadrupoles, showing larger than expected a_4 and b_5 errors have led to the increase of the length of the sextupole, octupole and decapole correctors (normal and skew), after analysis of the potential impact of these errors on DA [37][38]. The analysis of the effect of a larger than expected b_6 error in the short models of the triplet quadrupoles has led to the decision to act on the MQXF cross-section to optimize b_6 [66][67], rather than increasing the length of the corresponding corrector. Recent results on the field quality of the D2 separation dipole and of the MCBRD correctors are being scrutinized to determine whether mitigation measures are needed. The impact of the field quality of the MCBXF corrector magnets on DA is also being reviewed [68]. Note that the impact of the field quality of the 11 T dipoles on DA has been assessed and found marginal [69].

The knowledge of the transfer functions of the higher-order correctors and of the optical functions at their location has been found to be uncritical. Tolerance of ±1 mm in the relative alignment of the magnetic axis of the non-linear correctors with respect to that of the triplet magnets and of ±1 mrad in the roll angle of the non-linear correctors have been determined [37]. In the absence of multipolar correctors, the minimum DA would be reduced down to about 5.5 σ (Beam 1) and 3.8 σ (Beam 2) [37]. Rapid commissioning of the machine down to low β* will rely on accurate knowledge of the field errors and for that reason an accurate (down to 0.05 units [45]) measurement of the field errors is vital. In addition, the development of strategies for beam-based measurement and correction of field errors is being pursued and actively tested in the LHC [70].

Preliminary estimates of the crab cavity field quality have been provided and are summarized in Annex A-8. DA simulations indicate that the estimated field quality should be good enough to prevent any impact on DA [71][72][73]. Recently, the RF multipoles have been measured for the DQW cavities [69] and the impact on DA was assessed [74] and found to be negligible.

The correction of the linear optics poses significant challenges given the tight requirements, e.g. to ensure a luminosity imbalance lower than 5% between IP1 and IP5, as has been requested in Ref. [75]. Tune stability of about 10^{-5} is needed to achieve the required accuracy of the β function at the IP using k-modulation [76]. The tune stability critically depends on the low frequency (<1 Hz) current stability in the main circuits as confirmed by measurements in the LHC [77]. Extrapolations to the HL-LHC indicate the need of a further improvement of the current stability of the main dipoles in the four sectors adjacent to the two high-luminosity experiments where the telescopic squeeze is applied. The feasibility of such a scheme has been confirmed, although the corresponding upgrade is not included in the baseline yet [78]. Recently, a significantly less demanding power converter upgrade has been found with similar noise level in the low frequency region [79]. In order to precisely determine the optics at the interaction point, K-modulation techniques need to be applied on the first of the two magnets in the Q1 assembly. Hence, a trim circuit to modulate the current of the first magnet in Q1 has been added [77][78]. On the other hand, the trim circuit allowing to vary independently the current circulating in the two magnets in the Q2 assembly has been suppressed based on the expected alignment tolerances and the precision of the measurement of the transfer functions of the MQXF magnets [45]. The new triplet circuit configuration is represented in Figure 6.4. Note that a detailed and global review of the specifications of the new electrical circuits has been carried out recently [81].

The Nb_3Sn technology features unavoidable thermo-magnetic instabilities, called flux jumps, that, coupled to the voltage and current control of the magnet, result in a change of the integrated magnetic field. Recent studies in the HL-LHC magnet prototypes suggest that flux jumps could lead to average variations in the integrated magnetic field of about 0.002% within 46 ms [82] during the energy ramp. Simulations assuming these preliminary values indicate that flux jumps during the energy ramp are not a concern for emittance growth [82] although orbit excursions could occasionally lead to beam dumps [83].

2.4 Performance

2.4.1 Beam stability

The LHC effective impedance is larger at high energy, when the collimators become its dominant contributors, over a wide range of frequencies, because of their small gaps [84] and it can affect beam stability. Among them, the primary (TCP) and secondary collimators (TCSG) are the main contributors to the transverse impedance and particularly those in the betatronic collimation section in LSS7, because of their smaller gaps. During Run 2, systematic measurements have been performed to characterize the present LHC impedance model. These agree with expectations, with an uncertainty that is estimated to be less than 50% [85][86][87]. Concerning beam stability measurements through Landau octupoles, a good agreement was also obtained [88], but only when stability is considered on short time scales (shorter than few minutes). For longer time scales, typical of transition times between different phases of the cycle, noise sources acting on the beam and inducing dipolar oscillations at the level of 10^{-4} σ are observed to affect beam stability. The origin of this noise and the mechanisms leading to transverse instabilities are being investigated [89][90][91][92].

During LS2, new low-impedance collimators will be installed to replace and enhance, with the addition of embedded beam position monitors, the functionality of the existing ones, as part of the HL-LHC and Consolidation Projects. During LS3, up to 5 additional low-impedance secondary collimators per beam will be installed, depending on the beam-based measurements during Run 3.

The impedance reduction with Mo-coated Mo-Gr collimators has been tested and validated through extensive laboratory and beam-based measurements [85][86]. The resulting impedance reduction will guarantee transverse stability in all phases of the HL-LHC cycle, compatibly with the maximum strength of the Landau octupoles and the present performance of the transverse feedback in terms of damping time and bandwidth, still providing sufficient DA for large values of the chromaticity [85][93][94]. The scenarios for operation at nominal and ultimate luminosity are described in Ref. [30] and they consider the experience gained during Run 1 and Run 2 [89][94][96][97]. The effects of beam coupling impedance, electron cloud, head-on and long-range beam-beam forces, realistic transverse feedback and machine optical parameters like tunes, linear coupling [98], linear and non-linear chromaticity, Landau octupole strength and other non-linearities and more recently the effect of noise [89][92][99] have been or are gradually being taken into account [2][12] and mitigated, still a factor 2 stronger Landau octupoles are required as compared to expectations.

Requirements on the ramp and acceleration rates of the dipole correctors determining the separation bump have been elaborated in order to guarantee transverse stability during the collapse of the separation bump [78][100].

Attention must be paid to the impedance of new pieces of equipment, in particular for those being installed in regions with high β functions (e.g. crab cavities), which are enhancing the effects of transverse impedance. Their design is being closely followed-up by the impedance team in collaboration with the designers. For the crab cavities, a limit of 1 MΩ/m (depending on the frequency) on the transverse shunt impedance of each HOM has been chosen as a guideline to avoid that this equipment visibly affects the corresponding stability thresholds, expressed by the additional Landau octupole strength required to stabilize the corresponding transverse instabilities [101]. An overall description of the studies carried out and the status of the guidelines concerning the design of new pieces of equipment to minimize impedance and the corresponding actions is available in Ref. [84].

The operation with 25 ns beams relies heavily on beam-induced scrubbing and the pace of the intensity ramp-up after LS1 (when practically all LHC beam screens and vacuum chambers were vented to air for interventions) was determined by electron cloud effects, both from the implied heat load (see Section 2.4.3) and beam stability point of views [102][103], as expected. Although a significant reduction of the Secondary Electron Yield (SEY) has been obtained during Run 2 through scrubbing, significant differences in the final value of the SEY, inferred from measurements of the heat load, have been observed in different sectors, in different cryogenic cells and between magnets within the same sector and cryogenics cell, as a result of

different surface properties [104][105][106]. Coherent beam instabilities are expected and observed [89] in the LHC at injection as a result of the residual electron cloud, in particular in the quadrupoles. Machine settings with high chromaticity and Landau octupoles [30] are considered to be sufficient to stabilize the HL-LHC beam, even assuming the same SEY pattern observed in Run 2, considering the non-monotonic dependence of the electron cloud density as a function of the bunch population [107][108][109][110][111].

Amorphous carbon coating of the beam screens of the superconducting magnets from the IP up to Q5 (included) in IR1 and IR5 and of the triplet and D1 magnets in IR2 and IR8, as well as of the Q4, D2, Q5 and Q6 cold masses R2 and L8 is part of the baseline. This and the non-monotonic dependence of the electron cloud density on the bunch population should prevent electron cloud instabilities at high energy after scrubbing for SEY < 1.3 and in particular at the higher bunch populations [110][111]. However, due to the non-monotonic dependence of the electron cloud on the bunch population, instabilities driven by e-cloud [112] could be observed in the HL-LHC at the end of long physics fills (so-called “pop-corn instabilities”) due to the increase of electron density in the centre of the dipole magnets as the bunch intensities become smaller. If this occurs, the beams can be stabilized by increasing the chromaticity up to 15-20 units [109].

The longitudinal beam parameters of the HL-LHC beams in collision listed in Table 2-1, and more generally those described in Ref. [30] for the various phases of the HL-LHC cycle, have been updated with respect to those listed in Ref. [3] to guarantee the longitudinal beam stability.

2.4.2 Beam–beam effects

The beam–beam interaction is known to be an important factor limiting the performance reach of present particle colliders [12]. Beam–beam interactions induce particle losses, beam size blow-up and an increase in the beam halo population and therefore lower luminosity lifetime, due to crossing of excited resonances, enhanced by the large beam-beam tune-spread and by noise. The rapid depletion of the beam halo when going in collision because of the sudden reduction of the DA can lead to loss spikes and unwanted beam dumps taking into account that the energy stored in the beam halo particles above 3.5 σ is expected to reach 35 MJ in the HL-LHC assuming the same halo densities measured in the LHC during Run 1 and Run 2. For that reason, it has been proposed to install hollow-electron lenses to control halo population down to 3 to 4 σ during the whole cycle. The resulting transverse beam distribution has been considered in the definition of the operational scenario [30].

In the evaluation of the HL-LHC, the criteria used for establishing satisfactory beam dynamics behaviour during operation with beam collisions were similar to those in the LHC design study. The target value for the one-million turn DA is 6 σ for operation (for the nominal HL-LHC emittance of 2.5 μm) or more for a particle with relative momentum deviation of 2.7×10^{-4}, in order to guarantee that the beam lifetime is dominated by luminosity burn-off. The motivation for the choice is explained in Ref. [113] and it has been validated with experiments in the LHC [21][114][115][116].

Multi-parametric DA studies have validated the operational scenario [30] both for nominal and ultimate luminosity with a constant total crossing angle of 500 μrad in IP1 and 5, including the margins for reducing it during the collision process, through tune optimisation [22][117][118]. Operation at high-luminosity of LHCb (1.5×10^{34} cm^{-2} s^{-1}) appears also to be compatible with the above DA target, although it might limit the possibility of further optimizing the crossing angle throughout the levelling phase by reducing it further for $\beta^* > 15$ cm as indicated in Ref. [3]. PACMAN effects have been evaluated and shown not to have a significant impact on DA and luminosity [119].

A more significant mechanism of emittance degradation can be related to the interplay between the nonlinearity of the beam–beam interaction and various sources of noise. The effects of the ripple in the phase and amplitude of crab cavities and in the current of magnet power supplies have been studied. Current estimates for white random phase and relative voltage amplitude noises in the crab cavities, suggest RMS values of 3.4×10^{-5} rad and 4.9×10^{-5}, respectively [120]. This would cause an integrated luminosity loss of about 2% for the baseline scenario in the presence of a transverse feedback with a damping time of 50 turns

[120][121][122][123]. Nevertheless, recent measurements in the SPS suggest that these estimates could be too pessimistic by about a factor 2 or 3 [124]. The main specification for the crab cavities including expected multi-pole components [74] are summarized in Annex A-8.

Magnet power converter current noise can also lead to an increase of losses and emittance blow-up. The requirements have been summarized in Refs. [80][125][126][127][128]. The observed noise on the dipole main power converters at frequencies between 7-8 kHz is of concern, its origin is not yet clear and its amplitude should be reduced in view of the HL-LHC to avoid any significant reduction of the DA [126][127].

The concept of beam-beam long range compensation by means of current bearing wires [117][129][130][131] has been successfully demonstrated in the LHC [132][133] and could enhance the HL-LHC performance allowing a reduction of the crossing angle for the baseline scenario [134][135][136] or open the way to alternative scenarios (see Section 2.5). Although not in the baseline, possible implementations are being studied and a space reservation between Q4 and Q5 has been granted.

2.4.3 Beam-induced heat load

The circulating beam can deposit a significant amount of power on the structures exposed to it mainly through three different mechanisms: synchrotron radiation, impedances, and electron cloud. The impedance-induced heat loads with the HL-LHC beam parameters [16] have been summarized in Ref. [84] for several key systems. The design of the various components is being closely followed-up and at present no showstoppers have been identified for the HL-LHC operation. In the analysis, it is assumed that no forward physics detectors will be installed during the HL-LHC era. This might have to be reviewed if proposals for forward physics at the HL-LHC will be submitted.

In the superconducting arcs, an important contribution to the heat load on the beam screens is given by synchrotron radiation, which amounts to 1.92 kW/arc for HL-LHC beam parameters, whereas the longitudinal impedance of the beam screen introduces a further contribution of 1.90 kW/arc.

The remaining contribution from electron cloud will depend on the SEY of the beam screen surface that can be achieved through beam-induced scrubbing. Although a significant reduction of the SEY has been obtained through scrubbing during Run 2, significant differences in the final value have been observed in different sectors [104][105][106]. Figure 2-2 shows the simulated beam induced heat load on the beam screens of the LHC arcs for the nominal 25 ns bunch pattern at 7 TeV, as a function of the bunch population, for a SEY_{max} parameter of 1.25 and 1.35, respectively. Details about the simulation model can be found in Ref. [138]. The contributions to the heat deposition given by the impedance of the beam screen, the synchrotron radiation and the electron cloud in the different magnets have been displayed separately in different colours. The chosen SEY values of 1.25 and 1.35 correspond to the estimated values of SEY in the best (S34) and worst (S12) sectors, based on heat load measurements taken in Run 2 (August 2017, average over the arc) [139]. The cooling capacity provided by the cryogenic system for the arc beam-screens is expected to be 8 kW/arc (corresponding roughly to 160 W/half-cell) in the design cryogenic configuration. During Run 2, the LHC cryogenic system has been operated in an optimized configuration (using one cold-compressor unit to serve two consecutive sectors) profiting from the lower than expected heat loads on the cold masses at 1.9 K. The compatibility of this optimized configuration with the HL-LHC operational scenarios is being verified. With this optimized configuration, a higher cooling capacity becomes available for the arc beam screens [140], as indicated by the blue line in Figure 2-2, which is very close to the heat load expected for the sectors showing higher SEY (Figure 2-2 right).

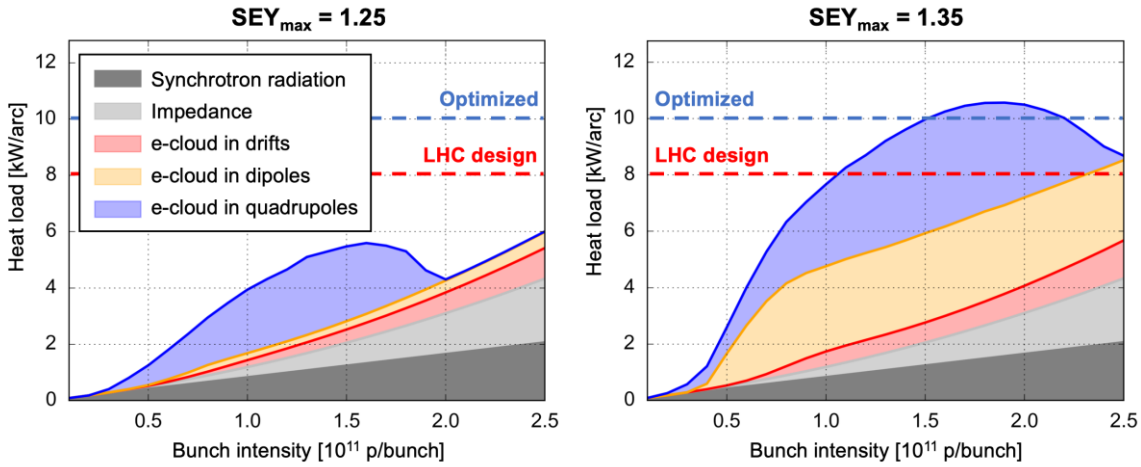

Figure 2-2: Simulated heat load in the LHC arcs for 25 ns bunch spacing and 7 TeV as a function of the bunch intensity for a SEY of 1.25 (left) and 1.35 (right). The heat load values are in kW/arc and include the effect of the two beams. The different contributions are highlighted in different colours, as labelled. The expected cooling capacity, in the LHC design configuration and in the optimized configuration, are shown by the dashed lines.

In case the intensity limitations from the heat loads on the beam screens are found to be stronger than expected, electron cloud effects can be mitigated by using specially conceived filling patterns. The underlying idea is to use the flexibility of the injector complex to build bunch trains with long enough gaps interspersed, to prevent the build-up of electron cloud along the beam. An alternative scenario (referred to as 8b+4e [141]) based on very short trains with 25 ns spacing has been conceived to reduce the electron cloud effects in the HL-LHC and has been considered as part of the HL-LHC operational scenarios [13]. Hybrid schemes allowing to maximize the number of bunches compatibly with the maximum acceptable heat load can also be envisaged [97]. The effectiveness of the 8b+4e scheme for electron cloud suppression as well as that of the hybrid schemes has been proven experimentally in the LHC [142][143][144]. The performance for these schemes is presented in Section 2.5.

The expected heat loads on the beam screen of the elements of the insertion regions are summarized in Refs. [145][146]. The impact of the shielding of the pumping holes (“baffles”) has been studied showing that the electrons impacting on the cold bore (without baffle plates) contribute significantly to the multipacting inside the chamber. The resulting additional heat load on the cold bore would be non-negligible and therefore shielding baffles will be installed behind the pumping slots in the design of the beam screen for the new HL-LHC superconducting magnets [147].

The above estimates rely strongly on the dependence of the SEY on the electron energy [148] that determines, among others, the scaling of the heat load on the bunch population. A direct experimental validation requires employing long bunch trains and will be possible only after the implementation of the LIU upgrade during LS2. Tests with short bunch trains with bunch populations up to 1.9×10^{11} p/bunch were conducted in 2018. The measured dependence of the heat loads on the bunch intensity has been found to be consistent with simulations, especially for the arcs showing the highest heat loads [108][144].

The effects of electron cloud formation have been studied also for other equipment that will be installed for the HL-LHC upgrade. In particular, for the low-impedance collimators no electron cloud formation is expected for the operational collimator gaps [149]. For the TDIS injection absorbers, coating with amorphous carbon will be applied on the beam screen in order to suppress multipacting [150][151][152].

2.4.4 Luminosity performance

The peak performance at 7 TeV has been estimated in Table 2-1. The estimate of the integrated luminosity requires determining the luminosity evolution during a fill. The beam intensity evolution has been estimated

by calculating the burn-off due to luminosity with a cross-section of 111 mb corresponding to the total cross-section [5].

The emittance evolution has been determined including intra-beam scattering (IBS) and radiation damping. A finite difference method in steps of 10 min has been implemented to model the beam parameters during a physics fill [123]. Figure 2-3 shows the evolution of the main parameters for the nominal and ultimate scenarios for the standard filling scheme with parameters listed in Table 2-1. The crossing angle is assumed to be constant during the fill. β^* levelling has been considered as levelling mechanism and it has been applied when the pile-up deviates by more than 2% from the target value. Levelling by separation (with full separations smaller than 0.6 σ at IP1 and IP5) can be used between β^* levelling steps to minimize the number of optics steps to about 10. Alternative matching schemes are also being studied to guarantee controlled optics transitions that minimize β-beating during ramp, squeeze and during levelling [153]. It is also assumed that longitudinal blow-up is applied to keep the longitudinal emittance and RMS bunch length constant throughout the fill which results in a q-Gaussian density distribution in the longitudinal direction [123].

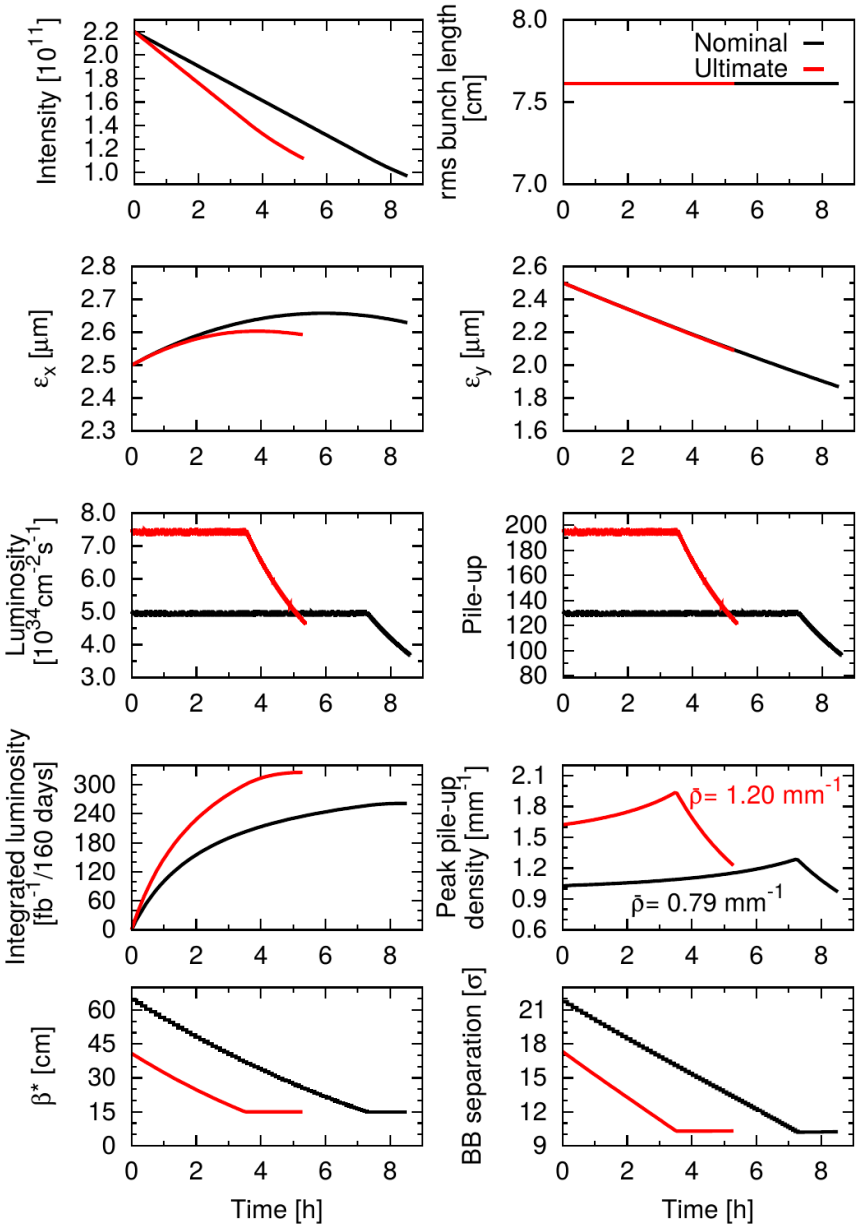

Figure 2-3: Evolution of the main beam and machine parameters for the nominal and ultimate scenarios.

2.5 Alternative operational scenarios

The HL-LHC project includes the study of various alternatives to the present baseline configuration with the aim either of improving the potential performance or of providing options for addressing possible limitations or changes in parameters [123]. These are briefly described in the following Sections and summarized in Table 2-7.

2.5.1 8b+4e and hybrid filling schemes

The 8b+4e filling scheme [141] consists of PS trains of 56 bunches, providing similar bunch parameters as the other 25 ns schemes with about 30% fewer bunches. The four empty slots are expected to highly suppress the formation of the electron cloud, as discussed in Section 2.4. The lower number of bunches of the 8b+4e scheme implies a lower peak luminosity at the same number of pile-up events per crossing, μ. The single bunch parameters evolve as for the baseline during the physics fill. Therefore, integrated luminosity simply scales linearly with the number of bunches. To maximize luminosity, it is possible to mix 8b+4e trains with BCMS ones to adapt the heat-load to the available cryogenic power.

2.5.2 Other filling schemes

The number of bunches in the PS trains could be increased from 72 to 80 in order to increase the integrated luminosity without affecting peak pile-up density [154]. In Ref. [155], various fillings schemes have been considered offering an increase in integrated luminosity above 1.9% for all IPs. The only drawback of the 80-bunch filling scheme is the slightly larger number of bunches per injection (from 288 to 320) to be considered for machine protection matters in the SPS and the TI2 and TI8 transfer lines.

2.5.3 Flat optics with crab cavities

A flat optics might be used with β^* of 7.5 cm and 18 cm in the separation and crossing planes, respectively, to improve the performance. The achievement of the above β^* might require the change of the crossing plane in IP1 and IP5 with respect to the present baseline unless significant improvements on tolerances are achieved. A normalized beam-beam long range separation of 11.4 σ could be reached at the end of the fill for bunch populations of 1.1×10^{11} p/bunch applying approximate scaling from DA studies [117][156][157][158]. The operation at ultimate luminosity might not be possible unless β^* is increased or beam-beam long-range compensation schemes are implemented. The performance for this configuration is shown in Figure 2-4 and it exceeds the HL-LHC nominal performance in terms of integrated luminosity and pile-up density. Further studies are necessary to validate the performance of this configuration.

2.5.4 Flat optics without crab cavities

Although crab-cavities have been successfully operated with beam in the SPS [159][160], a back-up scenario has been developed in case of a major crab cavity RF failure in the HL-LHC. In this scenario, it is possible to partially recover the performance loss by resorting to flat optics with larger beam size in the crossing plane at the IP. The IP β functions that maximize luminosity are 7.5 cm and 31.5 cm. These β functions will require the change of the crossing plane in IP1 and IP5 with respect to the present baseline unless significant improvements on tolerances are achieved. Current bearing wires [117][131][132][133][134][135][136] could compensate for the long-range interactions allowing for a reduction of the crossing angle and therefore increasing the luminous region. Without any mitigation, i.e. keeping round optics and no compensating wires, the nominal integrated luminosity would decrease by 13% with double peak pile-up density in case of a crab cavity failure. In the ultimate levelling scenario, the performance would drop by 23% with a peak pile-up density reaching 4.1 events/mm in such an event.

Assuming flat optics, the absence of crab cavities reduces the performance by 5% in the nominal and 12% in the ultimate scenarios. The beam-beam long-range compensation could allow reducing the normalized

long-range beam-beam separation from 12.6 to 11.0 σ improving the integrated luminosity from 249 fb^{-1} to 252 fb^{-1}. Performance improvements of the same order have been obtained also for round optics [137].

Table 2-7: Parameters of the HL-LHC baseline scenarios and main alternatives.

Parameter	Baseline	Flat with CC	8b+4e	No CC	
				Round	Flat
Beam energy in collision (TeV)	7	7	7	7	7
Particles per bunch, N [10^{11}]	2.2	2.2	2.2	2.2	2.2
Number of bunches per beam	2760	2760	1972	2760	2760
Number of collisions in IP1 and IP5	2748	2748	1960	2748	2748
N_{tot} [10^{14}]	6.1	6.1	4.3	6.1	6.1
Beam current (A)	1.10	1.10	0.78	1.10	1.10
Half-crossing angle in IP1 and IP5 (μrad)	250	245	250	250	206
Min. norm. long-range beam–beam sep. (σ)	10.5	11.4	10.5	10.5	12.6
Minimum β^* in the crossing plane (cm)	15	18	15	15	31.5
Minimum β^* in the separation plane (cm)	15	7.5	15	15	7.5
ε_n [μm]	2.50	2.50	2.50	2.50	2.50
Longitudinal emittance ε_L (eVs)	3.03	3.03	3.03	3.03	3.03
RMS energy spread [10^{-4}] (q-Gaussian distribution)	1.1	1.1	1.1	1.1	1.1
RMS energy spread [10^{-4}] (FWHM equiv. Gaussian)	1.29	1.29	1.29	1.29	1.29
RMS bunch length (cm) (q-Gaussian distribution)	7.61	7.61	7.61	7.61	7.61
RMS bunch length (cm) (FWHM equivalent Gaussian)	9.0	9.0	9.0	9.0	9.0
IBS horizontal (h)	16.5	16.5	16.5	16.5	16.5
IBS longitudinal (h)	19.2	19.2	19.2	19.2	19.2
Radiation damping (h)	26	26	26	26	26
Piwinski parameter	2.66	2.42	2.66	2.66	1.52
R_0 w/o crab cavities at min. β^*	0.342	0.362	0.342	0.342	0.507
R_1 with crab cavities at min. β^*	0.716	0.690	0.716	N/A	N/A
Beam–beam tune shift/IP [10^{-3}]	8.6	8.7	8.6	3.2	4.1
Peak luminosity w/o CC [10^{34} cm^{-2} s^{-1}]	8.11	11.1	5.78	8.11	9.00
Peak luminosity with CC [10^{35} cm^{-2} s^{-1}]	1.70	2.12	1.21	N/A	N/A
Events/crossing w/o levelling and without crab cavities	212	290	212	212	307
Levelled luminosity [10^{34} cm^{-2} s^{-1}]	5.0	5.0	3.8	5.0	5.0
Events/crossing μ (with levelling and crab cavities)	131	131	140	131	131
Max. line density of pile-up events during fill (evts/mm)	1.3	1.34	1.4	2.7	1.8
Levelling time [h] (assuming no emittance growth)	7.2	8.2	6.4	3.5	5.7
Integrated luminosity (fb^{-1})/160 days	261	267	195	228	249
Number of collisions IP2	2492	2492	1178	2492	2492
Number of collisions IP8	2574	2574	1886	2574	2574
N at injection [10^{11}]	2.3	2.3	2.3	2.3	2.3
Maximum n. of bunches per injection	288	288	224	288	288
Total beam population per injection [10^{13}]	6.62	6.62	5.15	6.62	6.62
ε_n at SPS extraction (μm)	2.1	2.1	1.7	2.1	2.1

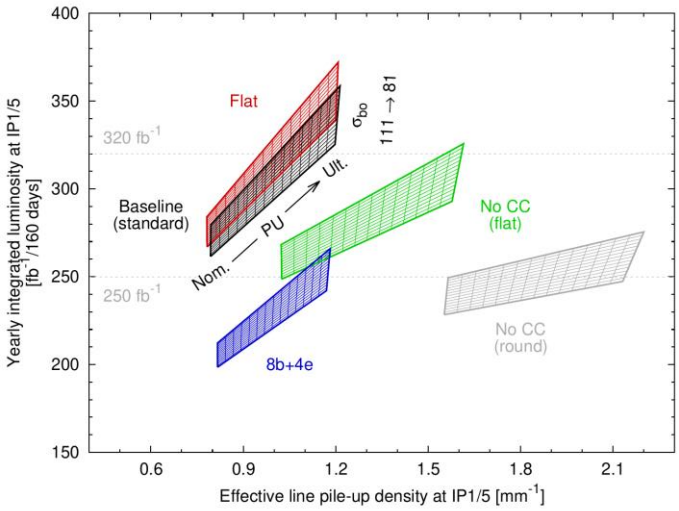

Figure 2-4: Summary chart showing integrated luminosity per year versus effective pile-up density for the various scenarios considered. The impact of assuming less conservatively a cross-section of 81 mb (inelastic cross-section) instead of 111 mb (total cross-section), for the estimate of the burn-off lifetime is also shown, (height of the boxes) indicating the importance of minimizing losses due to reduced DA and the potential gain in integrated luminosity.

2.6 The HL-LHC as a nucleus–nucleus collider

The LHC's second major physics programme provides nucleus–nucleus (fully stripped lead ions $^{208}Pb^{82+}$) and proton–nucleus collisions to ALICE, ATLAS and CMS, during typically about one month per year and up to LS4 in the current HL-LHC baseline schedule. All upgrades of the injectors, collider (upgrade of the collimation system described in Chapter 5) and experiments relevant to this heavy-ion programme are expected to be implemented during LS2, so the full "HL-LHC" performance is considered to be already available in Run 3. It should be noted that LHCb has also taken heavy-ion data since the 2012 p-Pb pilot run and 2015 Pb-Pb Run and is expected to continue to take data after LS2 and during the HL-LHC operating period.

The overall goals of the programme were initially set according to Ref. [161]. The central component was the accumulation 13 nb^{-1} of Pb-Pb luminosity in the ALICE experiment between LS2 and LS4 at a (levelled) peak luminosity of 7×10^{27} cm^{-2} s^{-1} [162][163][164][165]. Similar luminosities would be delivered to ATLAS and CMS with filling schemes adjusted to provide a smaller level to LHCb, where a target of 2 nb^{-1} is set [166]. The presently approved CERN planning also includes a short p-Pb run (whose goals were already far exceeded in 2016) and a p-p reference run before the end of LHC Run 4 in 2030. Although no further heavy-ion runs beyond Run 4 are approved yet, a revised proposal for Runs 3 and 4 and plans to extend the LHC nuclear programme beyond Run 4 have been formulated [166] and are presently under review. An extension of the ion program beyond Run 4 will evidently reduce the time available for proton-proton operation and will thus imply a reduction of the performance reach of the HL-LHC. These new plans envisage a similar Pb-Pb luminosity but more time spent on p-Pb and p-p reference runs and also collisions of lighter nuclei, e.g. Ar, O or Kr [166][167] with the potential to reach higher nucleon-nucleon luminosities. The accelerator and injector scenarios for these lighter ion species remain to be worked out in detail.

In 2018, an integrated Pb-Pb luminosity of 1.8 nb^{-1} was reached in ATLAS and CMS (c.f., the ~ 3 nb^{-1} per one-month run that would achieve the HL-LHC goals), 0.9 nb^{-1} in ALICE and 0.23 nb^{-1} in LHCb. This excellent performance was made possible through many improvements in the LHC and the injector chain. In particular, the average colliding bunch intensity was up to about 2.3×10^8 Pb/bunch, which is more than 3 times the LHC design value. Peak luminosities of more than 6.1×10^{27} cm^{-2} s^{-1} were achieved in ATLAS and CMS, which is a factor 6 larger than the nominal peak luminosity [50] and almost at the HL-LHC target. ALICE and LHCb were levelled at the LHC design value of 1×10^{27} cm^{-2} s^{-1}. This was the intrinsic limit of detector

saturation for ALICE during Run 2. The detector upgrade to be implemented in LS2 aims to increase this limit by enabling a 50 kHz event rate [161] and it is therefore assumed that luminosity levelling can be performed at 6.4×10^{27} cm^{-2} s^{-1}. Thanks to the special bunch spacing of 75 ns used in 2018, many more colliding bunch-pairs could be given to LHCb compared to operation with the usual 100 ns. This required LHCb luminosity levelling at the same value as ALICE for reasons of quench mitigation and luminosity sharing. While the LHC could already provide peak luminosities close to the HL-LHC design, the integrated luminosity per run must be increased to reach the requested target in the available time. Since optics and bunch intensities in 2018 reached or exceeded already the HL-LHC specifications, slip-stacking [168], enabled by the LS2 upgrades of the low-level RF system in the SPS, remains as the last significant upgrade to be implemented for the heavy-ion programme. Slip-stacking will increase the total number of circulating bunches from the current 733 bunches with 75 ns bunch spacing to 1240 bunches spaced by 50ns.

The increased peak luminosity in the ALICE experiment will significantly increase the local beam losses in IR2 after LS2. Ultra-peripheral electromagnetic interactions of colliding Pb nuclei create secondary beams with altered magnetic rigidity emerging from the collision points. These are lost locally in the downstream dispersion suppressor. The most critical one (bound-free pair production – BFPP) carries a significant power that can quench the impacted magnet [169][170][171][172]. The resulting luminosity limit in IR1 and IR5 is mitigated through local orbit bumps that deviate these losses into the empty connection cryostat. This technique was successfully proven close to the HL-LHC design luminosity in the 2018 Pb-Pb run. In IR2 this method does not work because of the opposite quadrupole polarities. Instead installation of new collimators (TCLD) on the outgoing beam on each side of the ALICE experiment will allow the losses to be safely absorbed, as discussed in more detail in Chapter 5.

The collimation of nuclear beams has been demonstrated to be about two orders of magnitude worse than for protons because of the more complicated nuclear interactions with collimators [173][174][175][176]. This could lead to beam dumps or magnet quenches in case of sudden beam losses. To increase the collimation efficiency and withstand a temporary drop of the beam lifetime to 12 minutes with the full HL-LHC intensity, new TCLD collimators will be installed in the dispersion suppressors of IR7, as described in detail in Chapter 5. Each TCLD in IR7 will be part of a 15 m assembly, containing two new 11 T dipoles with the TCLD in the middle, which will replace a present main dipole. A system of Crystal collimators will also be installed as an additional measure.

The HL-LHC baseline parameters for Pb beams are summarised in Table 2-8. These parameters, initially given in Ref. [164] and later updated in Ref. [165] and further in Ref. [177], apply to both Run 3 and Run 4, where the performance will be similar. The luminosity performance in a single fill has been simulated in Ref. [177] using two independent codes, the Collider Time Evolution program [178] and the Multi-Bunch Simulation [179], assuming colliding Pb-Pb beams in all experiments and different options for how the luminosity is shared between them through the filling scheme. The time evolution of the luminosity is shown in Figure 2-5. With an average turnaround of about 200 min, the optimum fill length is about 4 h for the studied scenarios. Assuming an operational efficiency of 50% (defined in Refs. [14] [3]) an integrated luminosity of 2.2 - 2.8 nb^{-1} over a 24-day Pb-Pb physics run is expected at ATLAS, ALICE, and CMS, depending on filling scheme, and up to 0.5 nb^{-1} at LHCb. With these assumptions, the HL-LHC target of 13 nb^{-1} at the end of Run 4 can be met in about five Pb-Pb runs. It should be noted that meeting this target relies on the 50 ns bunch scheme and hence on the successful implementation of slip-stacking in the SPS. As a backup scheme, the 75 ns scheme deployed in 2018 could be used, which would cause a decrease in integrated luminosity by 30-40%.

Operation with p-Pb was not foreseen in the original LHC design but, in the meantime, it has been successfully demonstrated in the LHC [180]. For the HL-LHC, the Pb beam in Table 2-8 is assumed, matched with a proton beam of the same filling scheme and about 3×10^{10} protons per bunch. The same optics as for the Pb-Pb runs are used. The luminosity is assumed to be levelled in ALICE at 5×10^{29} cm^{-2} s^{-1}, while no levelling is needed in ATLAS and CMS. The luminosity evolution has been simulated for a single fill as shown in Figure 2-6. Assuming an operational efficiency of 50% during a typical 24-day run, a total integrated

luminosity of 0.53 - 0.68 pb^{-1} is reached in ATLAS and CMS depending on filling scheme, about 0.31 pb^{-1} in ALICE, and up to about 0.15 pb^{-1} in LHCb.

Table 2-8: Key LHC design parameters for Pb operation from Ref. [177] compared with the achieved parameters in 2018 and the HL-LHC design values.

Parameters	**Nominal LHC (design report)**	**2018 achieved**	**HL-LHC (LIU baseline)**
Beam energy in collision (Z TeV)	7	6.37	7
Particles per bunch, N [10^7]	7	23	18
Number of bunches per beam	592	733	1240
Colliding pairs at IP1/5	< 592	733	976 - 1240[1]
Colliding pairs at IP2	592	702	976 - 1200[1]
Colliding pairs at IP8	0	468	0-716[1]
Total intensity N_{tot} [10^9]	41.4	169	223
Beam current (mA)	6.12	24.9	33.0
Stored beam energy (MJ)	3.8	13.9	20.5
Minimum β^* (m)	0.5	0.5	0.5
Normalized emittance ε_n (µm)	1.5	2.3	1.65
Longitudinal emittance ε_L (eVs/charge)	2.50	2.33	2.42
RMS energy spread [10^{-4}]	1.08	1.06	1.02
RMS bunch length (cm)	8.07	8.24	8.24
Half-crossing angle at IP2 (µrad) (external,net)	110,40	137,60	170,100
Peak luminosity [10^{27} cm^{-2} s^{-1}]	1.0	-	-
Levelled luminosity IP1/5 [10^{27} cm^{-2} s^{-1}]	-	6.13	6.4
Levelled luminosity IP2 [10^{27} cm^{-2} s^{-1}]	-	1.0	6.4
Levelled luminosity IP8 [10^{27} cm^{-2} s^{-1}]	-	1.0	1.0
Typical levelling time IP2 (h)	-	7	1.5
Maximum number of bunches per injection	54	42	56

[1]The values give the range over the filling schemes considered in Ref. [177].

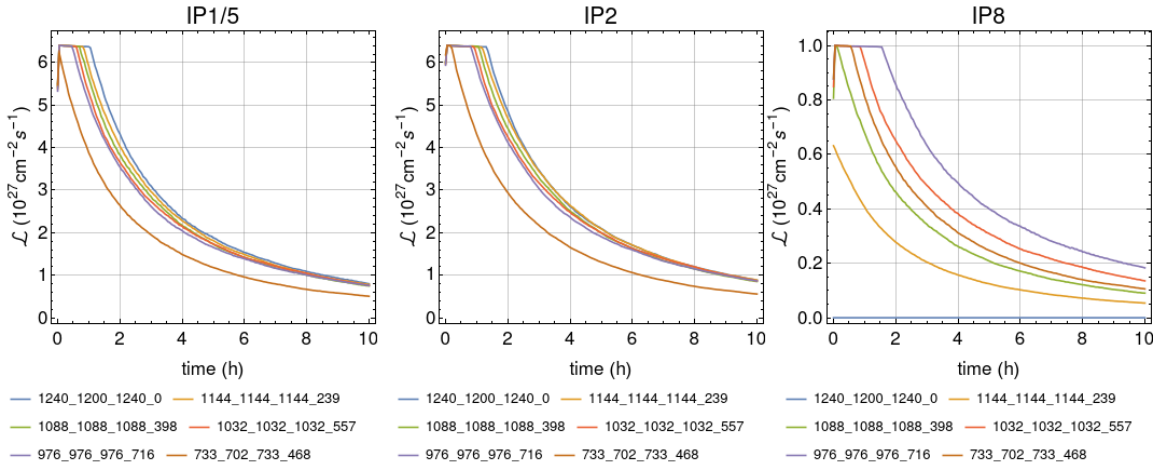

Figure 2-5: The Pb-Pb luminosity evolution over time [177], simulated with the CTE code [178], in the ATLAS and CMS experiments (left), in ALICE (middle) and in LHCb (right) for a typical fill in the HL-LHC, assuming the baseline parameters in Table 2-8. Each line represents a different filling scheme from [177], named by the convention where the first number shows the total number of bunches, the second number the collisions at IP1/5, the third number the collisions at IP2 and the last number the collisions at LHCb.

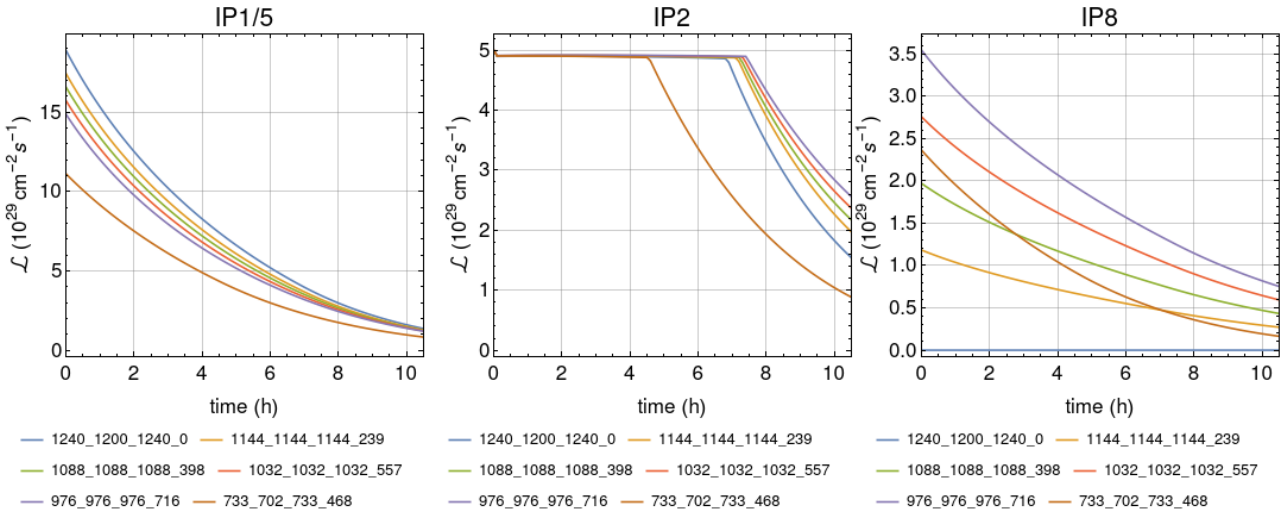

Figure 2-6: The p-Pb luminosity evolution [177], simulated with the MBS code [179], in the ATLAS and CMS experiments (left), in ALICE (middle) and in LHCb (right) for a typical p-Pb fill in HL-LHC. It is assumed that ALICE is levelled at 5×10^{29} $cm^{-2}s^{-1}$, while no levelling is applied in the other experiments. Each line represents a different filling scheme from [177], named by the convention where the first number shows the total number of bunches, the second number the collisions at IP1/5, the third number the collisions at IP2 and the last number the collisions at LHCb.

2.7 References

[1] G. Apollinari, I. Bejar Alonso, O. Brüning, M. Lamont, L. Rossi, eds., High-luminosity Large Hadron Collider (HL-LHC): Preliminary Design Report, DOI: 10.5170/CERN-2015-005.

[2] O. Brüning, L. Rossi, eds., The High-luminosity Large Hadron Collider: the new machine for illuminating the mysteries of Universe, Advanced Series on Directions in High Energy Physics: Volume 24 (2015), World Scientific, DOI: 10.1142/9581.

[3] G. Apollinari, I. Bejar Alonso, O. Brüning, P. Fessia, M. Lamont, L. Rossi, L. Tavian (Eds.) High-Luminosity Large Hadron Collider (HL-LHC): Technical Design Report V.0.1, DOI: 10.23731/CYRM-2017-004.

[4] L. Rossi, Short recap of recent changes to baseline, 16th HL-LHC Parameter and Layout Committee Meeting, 16th July 2015, EDMS: 1567268.

[5] The ATLAS and CMS Collaborations, Expected pile-up values at HL-LHC, 30 September 2013, 2013, ATL-UPGRADE-PUB-2013-014.

[6] R. Tomás Garcia et al., Experimental Data Quality, 8th HL-LHC Collaboration Meeting, 15-18 October 2018, CERN, INDICO: 742082.

[7] R. Tomás Garcia et al., Experimental Data Quality Working Group Indico Page, INDICO: 7932.

[8] R. Jacobsson, Future wishes and constraints from the experiments at the LHC for the proton–proton programme, ICFA Mini-Workshop on Beam-Beam Effects in Hadron Colliders (BB2013), CERN, Geneva, Switzerland, 18 - 22 Mar 2013, Eds. W. Herr and G. Papotti, DOI: 10.5170/CERN-2014-004.167.

[9] The LHCb Collaboration, Physics Case for an LHCb Upgrade II, CERN-LHCC-2018-027.

[10] M. Deile on behalf of the CMS collaboration, CMS Forward Physics Detectors: Plans for HL-LHC, 8th HL-LHC Collaboration Meeting, 15-18 October 2018, CERN, INDICO: 742082.

[11] W. Herr, B. Muratori, Concept of Luminosity, CAS – CERN Accelerator School: Intermediate Course on Accelerator Physics, Zeuthen, Germany, 15-26 Sep 2003, DOI: 10.5170/CERN-2006-002.361.

[12] O. Brüning, L. Rossi, eds., The High-luminosity Large Hadron Collider: the new machine for illuminating the mysteries of Universe, 2nd Edition, Advanced Series on Directions in High Energy Physics: Volume XX (20XX), World Scientific. (Pending publication)
[13] G. Arduini, O. Brüning, R. De Maria, R. Garoby, S. Gilardoni, B. Goddard, B. Gorini, M. Meddahi, G. Rumolo and R. Tomás Garcia, Beam parameters at LHC injection,2014, CERN-ACC-2014-0006.
[14] B. Todd, LHC & Injectors, availability Run 2, 9th Evian Workshop on LHC Beam Operation, Evian, France, 30 January-1 February 2019, INDICO: 751857.
[15] R. Tomás Garcia, Update of HL-LHC parameters and operational scenarios (protons), 104th Technical Coordination Committee, 28th May 2020, INDICO: 921722.
[16] HL-LHC Technical Coordination Committee Parameter Table v. 7.1.1 (29/07/2020) HL-LHC Parameter Table
[17] D. Contardo, private communication, 3 December 2014.
[18] J. Coupard, H. Damerau, A. Funken, R. Garoby, S. Gilardoni, B. Goddard, K. Hanke, A. Lombardi, D. Manglunki, M. Meddahi, B. Mikulec, G. Rumolo, E. Shaposhnikova, M. Vretenar, eds., LHC Injectors Upgrade, Technical Design Report – Volume I: Protons, 2014, CERN-ACC-2014-0337.
[19] G. Rumolo et al., LIU baseline for protons, LHC Performance Workshop 2017, Chamonix, France, 23–27 January 2017, INDICO: 580313.
[20] Y. Papaphilippou *et al.*, Long Range Beam-Beam effects for HL-LHC, LHC Performance Workshop 2018, Chamonix, France, 29 January – 2 February 2018, INDICO: 676124.
[21] D. Pellegrini *et al.*, Incoherent beam-beam effects and lifetime optimization, 8th Evian Workshop on LHC Beam Operation, Evian, France, 12-14 December 2017, INDICO: 663598.
[22] N. Karastathis and Y. Papaphilippou, Beam-beam simulations for optimizing the performance of the High-luminosity Large Hadron Collider Proton Physics, 2020, CERN-ACC-NOTE-2020-0026.
[23] G. Arduini, S. Redaelli, HL–LHC ECR Optics configuration change, EDMS: 1832081.
[24] R. Tomás Garcia et al., HL-LHC beam parameters for protons, LHC Performance Workshop 2017, Chamonix, France, 23–27 January 2017, INDICO: 580313.
[25] R. De Maria *et al.*, What can be learnt in Run 2 for Run 3 and HL-LHC runs?, Proc. of the 7th Evian Workshop, 13-15 December 2016, Evian, France, Eds. S. Dubourg, B. Goddard, G. Trad, CERN-ACC-2017-094, pp. 255-264.
[26] Minutes of the LIU-SPS BLPTL WG Meeting, 8th November 2017, INDICO: 671463.
[27] E. Shaposhnikova, J.E. Müller, Bunch length and particle distribution for (HL-)LHC, 82nd HiLumi WP2 meeting, CERN, 12/01/2017, INDICO: 572439.
[28] R. Tomás Garcia, L. Medina, Parameter update for the nominal HL-LHC: Standard, BCMS and 8b+4e, 26th HL-LHC TCC meeting, CERN, 16/03/2017, INDICO: 590415.
[29] E. Shaposhnikova and J.E. Müller, Longitudinal stability limits and bunch length specifications, 78th HiLumi WP2 meeting, CERN, 23/09/2016, INDICO: 563288.
[30] E. Métral *et al.*, Update of the HL-LHC operational Scenarios for Proton Operation, CERN-ACC-NOTE-2018-0002.
[31] S. Fartoukh, Achromatic telescopic squeezing scheme and application to the LHC and its luminosity upgrade, Phys. Rev. Spec. Top. Accel. Beams 16, 2013, DOI: 10.1103/PhysRevSTAB.16.111002.
[32] S. Fartoukh, Experience with the ATS optics, Proc. of the 7th Evian Workshop, 13-15 December 2016, Evian, France, Eds. S. Dubourg, B. Goddard, G. Trad, pp. 93-104, CERN-ACC-2017-094.
[33] B. Salvachua, M. Albert, R. Alemany-Fernandez, T. Argyropoulos, E. Bravin, H. Burkhardt, G. Crockford, J.C. Dumont, S. Fartoukh, K. Fuchsberger, R. Giachino, M. Giovannozzi, G.H. Hemelsoet, W. Höfle, J.M. Jowett, Y. Borgne, D. Nisbet, M. Pojer, L. Ponce, S. Redaelli, M. Solfaroli, R. Suykerbuyk, D.J. Walsh, J. Wenninger, M. Zerlauth et al., LHC Operational Scenarios During 2017

Run, 9th International Particle Accelerator Conference, Vancouver, Canada, 29 April - 4 May 2018, DOI: 10.18429/JACoW-IPAC2018-MOPMF051.

[34] M. Pojer, M. Albert, R. Alemany-Fernandez, T. Argyropoulos, E. Bravin, A. Calia, G. Crockford, S. D. Fartoukh, K. Fuchsberger, R. Giachino, M. Giovannozzi, G.-H. Hemelsoet, W. Höfle, M. Hostettler, Y. Le Borgne, D. Nisbet, L. Ponce, S. Redaelli, B. Salvachua, M. Solfaroli, R. Suykerbuyk, D. J. Walsh, J. Wenninger, M. Zerlauth, LHC Operational Experience of the 6.5 TeV Proton Run with ATS Optics, 9th International Particle Accelerator Conference, Vancouver, Canada, 29 April - 4 May 2018, DOI: 10.18429/JACoW-IPAC2018-MOPMF050.

[35] M. Giovannozzi, S. Fartoukh and R. De Maria, Specification of a system of correctors for the triplets and separation dipoles of the LHC upgrade, Proc. 4th International Particle Accelerator Conference, Shanghai, China, 12 - 17 May 2013, pp. 2612-2614. CERN-ACC-2013-0168.

[36] M. Giovannozzi, S. Fartoukh and R. De Maria, Initial models of correction systems, 2014, CERN-ACC-2014-0010.

[37] Y. Cai, R. De Maria, M. Giovannozzi, Y. Nosochkov, F. Van Der Veken, Dynamic aperture studies for HL-LHC V1.0, CERN-ACC-2018-0054.

[38] E. Todesco, M. Sorbi, HL–LHC ECR - WP3 Change of quadrupole, sextupole, octupole and decapole correctors integrated field - LHC-M-EC-0002, EDMS: 1963788.

[39] J. Oliveira, M. Amparo Gonzalez De La Aleja Cabana, Final confirmation of dimension of magnetic length of Corrector Package, INDICO: 774098.

[40] R. Bruce, C. Bracco, R. De Maria, M. Giovannozzi, S. Redaelli, R. Tomas, F. Velotti, J. Wenninger, Updated parameters for HL-LHC aperture calculations for proton beams, CERN-ACC-2017-0051.

[41] R. De Maria, Status of optics V1.5, 161st WP2 meeting, 29th October 2019, INDICO: 858460.

[42] R. Bruce, Aperture in case of an asynchronous beam dump with ATS optics, 5th Joint HiLumi LHC-LARP Annual Meeting 2015, CERN, 26-30 October 2015, INDICO: 400665.

[43] R. De Maria, Review on aperture (N1 + mechanical) between D1 and Q6 in HLLHC IR1/5, 67th ColUSM Meeting (5/02/2016), INDICO: 493012.

[44] S. Fartoukh, Asynchronous free ATS optics for LHC & HL-LHC, 61st HiLumi WP2 Task Leader Meeting, 27 November 2015, INDICO: 402184.

[45] R. Carcagno, P. Ferracin, G. Sabbi, US HL-LHC AUP - ACCEPTANCE CRITERIA PART A: MQXFA MAGNET (US-HiLumi-doc-1103), EDMS: 2031083.

[46] R. Carcagno, S. Feher, U.S. HL-LHC Accelerator Upgrade Project LMQXFA COLD MASS FUNCTIONAL REQUIREMENTS SPECIFICATION, EDMS: 1686197.

[47] R. Carcagno, U.S. HL-LHC Accelerator Upgrade Project MQXFA MAGNETS FUNCTIONAL REQUIREMENTS SPECIFICATION, EDMS: 1535430.

[48] P. Fessia, Remote alignment options and solutions, 61st HL-LHC TCC meeting, CERN, 15/11/2018, INDICO: 772120.

[49] S. Claudet, P. Fessia, HL-LHC ECR - WP1. Full Remote Alignment and New Matching section Optimisation, LHC-_-EC-0041, EDMS: 2083813.

[50] O. S. Brüning, P. Collier, P. Lebrun, S. Myers, R. Ostojic, J. Poole and P. Proudlock (Eds.), LHC Design Report, v.1: The LHC Main Ring,2012, DOI: 10.5170/CERN-2004-003-V-1.

[51] Minutes of the 69th Technical Coordination Committee, 28th February 2019, INDICO: 802179.

[52] Minutes of the 111th Technical Coordination Committee, 13th August 2020, INDICO: 945883.

[53] R. De Maria et al., Possible further simplification of the matching section, LHC Performance Workshop 2018, Chamonix, France, 29 January – 2 February 2018, INDICO: 676124.

[54] R. De Maria, Optics conditions in IR4 for instrumentation and e-lenses, 115th HiLumi WP2 meeting, CERN, 06/03/2018, INDICO: 706991.

[55] R. De Maria, M. Pojer, M. Solfaroli Camillocci, Operating temperature of Q5 in Point 6 based on 2018 hardware tests, 63rd Technical Coordination Committee, 13th December 2018, INDICO: 779650.
[56] Minutes of the 64th Technical Coordination Committee, 19th December 2018, INDICO: 781668.
[57] HL-LHC ECR - WP3. Change of operational temperature in Q5 IR6 from 1.9 K to 4.5 K, EDMS: 2117079.
[58] S. Redaelli, R. Bruce, A. Mereghetti, Installation of new passive absorbers (TCAPM) for warm magnet protection in IR7, LHC-TCAP-EC-0001, EDMS: 1973905.
[59] D. Gamba et al., IP Orbit Correction Update for HL-LHC, 9th International Particle Accelerator Conference, Vancouver, Canada, 29 April - 4 May 2018, Eds. S. Koscielniak, T. Satogata, V.R.W. Schaa, J. Thomson, pp. 3048-3051. DOI: 10.18429/JACoW-IPAC2018-THPAF039.
[60] C. Garion, R. Kersevan, N. Kos, Preliminary Design of the HiLumi-LHC Triplet Area Beam Screen, 5th International Particle Accelerator Conference, Dresden, Germany, 15 - 20 Jun 2014, pp.2378. DOI: 10.18429/JACoW-IPAC2014-WEPME048.
[61] C. Garion, "Update on the beam screen/cold bore tolerances and apertures in the triplet area", 7th HL-LHC Technical Coordination Committee, 28th April 2016, INDICO: 515629.
[62] J.-B. Jeanneret, Geometrical tolerances for the qualification of LHC magnets, 2007, LHC Project Report 1007.
[63] S. Fartoukh et al., About a flat telescopic optics for the future operation of the LHC, CERN-ACC-2018-0018.
[64] R. De Maria, S. Fartoukh, A. Bogomyagkov and M. Korostelev, HLLHCV1.0: HL-LHC layout and optics models for 150 mm Nb3Sn Triplets and local crab-cavities, Proc. 4th International Particle Accelerator Conference, Shanghai, China, 12 - 17 May 2013, pp.1358-1360, CERN-ACC-2013-0129.
[65] S. Fartoukh and M. Giovannozzi, Dynamic aperture computation for the as-built CERN Large Hadron Collider and impact of main dipoles sorting, Nucl. Instrum. Methods Phys. Res., A 671 (2012) 10–23, DOI: 10.1016/j.nima.2011.12.052.
[66] M. Giovannozzi, F. Van der Veken, Update on dynamic aperture in the presence of b6 triplet field errors, 128th HiLumi WP2 meeting, CERN, 28/08/2018, INDICO: 751331.
[67] E. Todesco, Fine tuning of MQXF cross-section to optimize b6, 56th Technical Coordination Committee, 30th August 2018, INDICO: 751364.
[68] F. Van der Veken, Field quality of MCBRD D2 correctors and its impact on DA, 141st WP2 Meeting, 5 February 2019, INDICO: 788835.
[69] L. Fiscarelli et al., Field Quality of MBH 11-T Dipoles for HL-LHC and Impact on Beam Dynamic Aperture, IEEE Trans. Appl. Supercond. 28, 2018, DOI: 10.1109/TASC.2018.2792424.
[70] R. Tomás Garcia et al., Optics Measurements and Correction Challenges for the HL-LHC, CERN-ACC-2017-0088.
[71] J. Barranco García et al., Study of multipolar RF kicks from the main deflecting mode in compact crab cavities for LHC, Proc. 3rd International Particle Accelerator Conference 2012, New Orleans, LA, USA, 20 - 25 May 2012, pp.1873-1875. CERN-ATS-2012-120.
[72] D. R. Brett et al., Comparison of Taylor maps with RF multipoles in a thin lens 6D tracking code, Proc. 4th International Particle Accelerator Conference, Shanghai, China, 12 - 17 May 2013, Eds. Z. Dai, C. Petit-Jean-Genaz, V. Schaa, C. Zhang, pp. 2687-2689. CERN-ACC-2013-0052.
[73] R. Appleby et al., Modelling and long term dynamics of crab cavities in the LHC, Proc. 5th International Particle Accelerator Conference, Dresden, Germany, 15 - 20 June 2014, pp. 1578-1580. CERN-ACC-2014-0173.
[74] E. Cruz Alaniz, Y. Papaphilippou and C. P. Welsch, RF multipoles deliverable, 2020, CERN-ACC-NOTE-2020-0031.

[75] E. Meschi, Luminosity comparison for ATLAS and CMS, 129th LHC Machine Committee meeting, 18 April 2012, LMC: 129.
[76] M. Hofer et al., K-modulation in future high energy colliders, Proc. 10th International Particle Accelerator Conference, Melbourne, Australia, 19 - 24 May 2019, DOI:10.18429/JACoW-IPAC2019-MOPMP022.
[77] D.W. Wolf, Analysis of tune modulation in the LHC, CERN-THESIS-2018-251.
[78] D. Gamba et al., Beam dynamics requirements for HL–LHC electrical circuits, CERN-ACC-2017-0101.
[79] M. Martino et al., Upgrade of LHC class 1 power converter precision measurement systems: class 0.5, EDMS: 2379888.
[80] R. Tomás Garcia, Trim in Q1 for the beta* measurements, 27th Technical Coordination Committee, 30th March 2017, INDICO: 590417.
[81] D. Gamba et al., Update of beam dynamics requirements for HL-LHC electrical circuits, CERN-ACC-2019-0030.
[82] J. Coello et al., Impact of flux jumps in future colliders, Phys. Rev. Accel. Beams **23**, 011001, 2020. DOI: 10.1103/PhysRevAccelBeams.23.011001.
[83] D. Gamba et al., Update on WP2 flux jumps studies, 99th HL-LHC TCC, INDICO: 907316.
[84] D. Amorim, S. Antipov, N. Biancacci, B. Salvant et al., HL-LHC impedance and related effects, CERN-ACC-NOTE-2018-0087.
[85] E. Métral, Impedance models, operational experience and expected limitations, International Review of the HL-LHC Collimation System, 11-12 February 2019, CERN, INDICO: 780182.
[86] S.A. Antipov, C. Accettura, D. Amorim, A. Bertarelli, N. Biancacci, R. Bruce, E. Carideo, F. Carra, J. Guardia Valenzuela, A. Mereghetti , E. Métral, S. Redaelli, B. Salvant, and D. Valuch, Transverse Beam Stability with Low-Impedance Collimators in the High-luminosity Large Hadron Collider: Status and Challenges, Phys. Rev. Accel. Beams 23, 2020, DOI: 10.1103/PhysRevAccelBeams.23.034403.
[87] D. Amorim et al., Comparison of LHC impedance model predictions to beam-based measurements, CERN HSC meeting, 18/02/2019, INDICO: 795854.
[88] L. Carver et al., Current status of instability threshold measurements in the LHC at 6.5 TeV, Proc. 7th International Particle Accelerator Conference 2016, Busan, South Korea, 8-13 May 2016, pp. 1434-1437, DOI: 10.18429/JACoW-IPAC2016-TUPMW011.
[89] X. Buffat et al., Transverse instabilities, 9th Evian Workshop on LHC Beam Operation, Evian, France, 30 January-1 February 2019, INDICO: 751857
[90] X. Buffat, Noise, latency and transverse instabilities, 353rd LHC Machine Committee Meeting, 11th July 2018, INDICO: 743309.
[91] X. Buffat, Impact of noise on beam stability, 8th HL-LHC Collaboration Meeting, 15-18 October 2018, CERN, INDICO: 742082.
[92] S. Furuseth, Noise Driven Instabilities, 388th LHC Machine Committee Meeting, 4th December 2019, INDICO: 868659.
[93] X. Buffat, HL-LHC stability limits for positive octupole current, CERN HSC meeting, 21/01/2019, INDICO: 783125.
[94] N. Karastathis et al., DA with positive octupole polarity, 141st HiLumi WP2 meeting, CERN, 05/02/2019, INDICO: 788835.
[95] E. Métral et al., Summary of the half-day internal review of LHC performance limitations (linked to transverse collective effects) during run II (CERN, 29/11/2016), CERN-ACC-NOTE-2017-0005.
[96] E. Métral, Beam stability from impedance (including effect of coating) and overall summary for the nominal scenario including all effects, 7th HL-LHC Collaboration Meeting, 13-16 November 2017, Madrid, INDICO: 647714.

[97] G. Iadarola, Digesting the LIU high brightness beam: is this an issue for HL-LHC?, LHC Performance Workshop 2018, Chamonix, France, 29 January – 2 February 2018, INDICO: 676124.
[98] L.R. Carver et al., Transverse beam instabilities in the presence of linear coupling in the Large Hadron Collider, DOI: 10.1103/PhysRevAccelBeams.21.044401.
[99] X. Buffat, Transverse beams stability studies at the Large Hadron Collider, Ph.D. thesis (6321), EPFL, 2015 CERN-THESIS-2014-246.
[100] C. Tambasco, Specification of separation collapsing speed, 67th HiLumi WP2 Task Leader Meeting, 26th April 2016, INDICO: 512381.
[101] S. Antipov et al., Effect of crab cavity high order modes on the coupled-bunch stability of High-Luminosity Large Hadron Collider, CERN-ACC-NOTE-2019-0009.
[102] K. Li et al., Electron cloud observations during LHC operation with 25 ns beams, Proc. 7th International Particle Accelerator Conference 2016, Busan, South Korea, 8-13 May 2016, pp. 1458-1461, DOI: 10.18429/JACoW-IPAC2016-TUPMW017.
[103] G. Rumolo et al., Electron cloud in the CERN accelerator complex, Proceedings of the 57th ICFA Advanced Beam Dynamics Workshop on High-Intensity and High-Brightness Hadron Beams, Malmö, Sweden, 3-8 July 2016, Eds. D. Gous, M. Marx, R. Mueller (GSI, Germany), J. Olander, V.R.W. Schaa, G. Trahern, pp. 266-271, DOI: 10.18429/JACoW-HB2016-TUAM4X01.
[104] G. Iadarola, G. Rumolo, Ph. Dijkstal, L. Mether, Analysis of the beam induced heat loads on the LHC arc beam screens during Run 2, CERN-ACC-NOTE-2017-0066.
[105] G. Iadarola et al., Beam-induced heat loads on the LHC arc beam screens with different beam and machine configurations: experiments and comparison against simulations, CERN-ACC-NOTE-2019-0057.
[106] G. Iadarola et al., Heat loads in the LHC arcs: observations from Run 1 and Run 2, LHC Machine Committee, CERN, 12 September 2018, INDICO: 756727.
[107] K. Li et al., Update on Landau octupoles settings at injection, 65th LHC Beam Operation Committee meeting, CERN, 23rd August 2016, INDICO: 564033.
[108] G. Iadarola, Electron Cloud & Heat Loads, 9th Evian Workshop on LHC Beam Operation, Evian, France, 30 January - 1 February 2019, INDICO: 751857.
[109] A. Romano, Electron cloud formation in CERN particle accelerators and its impact on the beam dynamics, CERN-THESIS-2018-299.
[110] G. Iadarola, E. Métral, G. Rumolo, Beam induced heat loads on the beam-screens of the twin-bore magnets in the IRs of the HL-LHC, CERN-ACC-2016-0112.
[111] G. Iadarola, L. Mether, E. Métral and L. Sabato, Electron cloud instabilities at injection, 173rd HiLumi WP2 Task Leader Meeting, 21st April 2020, INDICO: 903324.
[112] A. Romano, O. Boine-Frankenheim, X. Buffat, G. Iadarola, G. Rumolo, Electron cloud buildup driving spontaneous vertical instabilities of stored beams in the Large Hadron Collider, Phys. Rev. Accel. Beams 21, 2018, DOI: 10.1103/PhysRevAccelBeams.21.061002.
[113] Y. Luo and F. Schmidt, Dynamic aperture studies for LHC optics Version 6.2 at Collision, LHC-PROJECT-NOTE-310.
[114] W. Herr, X. Buffat, R. Calaga, R. Giachino, G. Papotti, T. Pieloni and D. Kaltchev, Long range beam-beam effects in the LHC, Proc. ICFA Mini-Workshop on Beam-Beam Effects in Hadron Colliders, CERN, Geneva, Switzerland, 18-22 March 2013, Eds. W. Herr and G. Papotti, DOI:10.5170/CERN-2014-004.
[115] S. Papadopoulou, Transverse emittance blow-up, 9th Evian Workshop on LHC Beam Operation, Evian, France, 30 January -1 February 2019, INDICO: 751857.

[116] S. Kostoglou, Luminosity, lifetime and modelling, 9th Evian Workshop on LHC Beam Operation, Evian, France, 30 January -1 February 2019, INDICO: 751857.
[117] N. Karastathis et al., Beam-beam simulations in the HL-LHC, 8th HL-LHC Collaboration Meeting, 15-18 October 2018, CERN, INDICO: 742082.
[118] N. Karastathis et al., Refining the HL-LHC Operational Settings with Inputs from dynamic aperture simulations. A Progress Report, 9th International Particle Accelerator Conference, Vancouver, Canada, 29 Apr - 4 May 2018, pp. 188-191, DOI: 10.18429/JACoW-IPAC2018-MOPMF041.
[119] A. Ribes Metidieri, Studies of PACMAN effects in the HL-LHC, 123st WP2 Meeting, 12 June 2018, INDICO: 733521.
[120] Ph. Baudrenghien, Expected performances of the CC in terms of voltage and (phase) noise, 96th WP2 Meeting, 13 June 2017, INDICO: 645814.
[121] J. Qiang et al., Simulation of beam–beam interaction with crab cavities for LHC upgrade, Nucl. Instrum. Methods Phys. Res., A 900, 53-59, 2018, DOI: 10.1016/j.nima.2018.05.055.
[122] X. Buffat, Review of the tolerances to CC phase noise (emittance blowup, ...), 96th WP2 Meeting, 13 June 2017, INDICO: 645814.
[123] L. Medina et al., Assessment of the performance of High-luminosity LHC operational scenarios: integrated luminosity and effective pile-up density, Canadian Journal of Physics, DOI: 10.1139/cjp-2018-0291.
[124] P. Baudrenghien, LLRF lessons learned from SPS tests, observed emittance growth, 8th HL-LHC collaboration meeting 2018, CERN, INDICO: 742082
[125] D. Gamba, Amendment to HL-LHC circuit specifications, 137th WP2 Meeting, 11 December 2018, INDICO: 773002.
[126] S. Kostoglou, Summary of observations on noise for LHC and projections for HL-LHC, 63rd Technical Coordination Committee, 13th December 2018, INDICO: 779650.
[127] S. Kostoglou**,** et al., Impact of the 50 Hz harmonics on the beam evolution of the Large Hadron Collider, 2020, arXiv:2003.00140.
[128] S. Kostoglou**,** et al., Tune modulation effects in the High-luminosity Large Hadron Collider, 2020, arXiv:2003.00960.
[129] J.P. Koutchouk, Principle of a Correction of the Long-Range Beam-Beam Effect in LHC using Electromagnetic Lenses, CERN, 2000, LHC-Project-Note 223.
[130] S. Fartoukh, A. Valishev, D. Shatilov, An alternative High-luminosity LHC with flat optics and long-range beam-beam compensation, Proc. 6th International Particle Accelerator Conference, Richmond, USA, 3 - 8 May 2015, Eds. S. Henderson, E. Ayers, T. Satogata, V.R.W. Schaa, pp. 2199-2202.
[131] S. Fartoukh, Compensation of the long-range beam-beam interactions as a path towards new configurations for the high-luminosity LHC, Phys. Rev. Spec. Top. Accel. Beams 18, 2015, DOI: 10.1103/PhysRevSTAB.18.121001.
[132] G. Sterbini et al., Results of the BBLR compensation experiments in the LHC, 62nd Technical Coordination Committee, 29th November 2018, INDICO: 776391.
[133] G. Sterbini et al., Results of the BBLR compensation experiments in the LHC, 10th International Particle Accelerator Conference, Melbourne, Australia, 19 - 24 May 2019, DOI: 10.18429/JACoW-IPAC2019-WEYYPLM3.
[134] K. Skoufaris et al., Simulations for wire BBLR compensation in HL-LHC, 8th HL-LHC Collaboration Meeting, 15-18 October 2018, CERN, INDICO: 742082.
[135] K. Skoufaris et al., Numerical optimization of DC wire compensation in HL-LHC, 10th International Particle Accelerator Conference, Melbourne, Australia, 19 - 24 May 2019, DOI: 10.18429/JACoW-IPAC2019-MOPMP053.

[136] K. Skoufaris et al., Simulations for HL-LHC configuration, 9th HL-LHC Collaboration Meeting, Fermilab 2019, WP2/WP13 HL-LHC Satellite Meeting - Wire Compensation, INDICO: 844153.
[137] Y. Papaphilippou et al., Scenarios and timeline for wire compensation in the HL-LHC, 9th HL-LHC Collaboration Meeting, Fermilab 2019, WP2/WP13 HL-LHC Satellite Meeting - Wire Compensation, INDICO: 844153.
[138] P. Dijkstal et al., Simulation studies on the electron cloud build-up in the elements of the LHC arcs at 6.5 TeV, CERN-ACC-NOTE-2017-0057.
[139] G. Iadarola et al., Summary of the overall heat load estimates, 40th HL-LHC Technical Coordination Committee, 2nd November 2017, INDICO: 676089.
[140] K. Brodzinski, Measurement of available beam screen cooling capacity on cryoplants, LHC Machine Committee, 10th Apr 2019, INDICO: 812689.
[141] H. Damerau et al., LIU: Exploring Alternative Ideas, Proc. Review of LHC and Injector Upgrade Plans Workshop (RLIUP), Archamps, France, 29–31 October 2013, Eds. B. Goddard and F. Zimmermann, pp. 127-137, DOI: 10.5170/CERN-2014-006.127.
[142] G. Iadarola, H. Bartosik, K. Li, L. Mether, A. Romano, G. Rumolo, M. Schenk, Performance limitation from electron cloud in 2015, Proc. 6th Evian Workshop on LHC beam operation, Evian, France, 15-17 June 2016, Eds. B. Goddard, S. Dubourg, INDICO: 434129.
[143] H. Bartosik et al., MD421: Electron cloud studies on 25 ns beam variants (BCMS, 8b+4e), CERN-ACC-NOTE-2017-0028.
[144] G. Iadarola, Heat load studies, LHC Studies Working Group meeting, 29 November 2018, INDICO: 772189.
[145] G. Iadarola, E. Metral, G. Rumolo, Expected heat load for the two bore magnets in the IRs of the HL-LHC, CERN-ACC-2016-0112.
[146] G. Skripka, G. Iadarola, Beam-induced heat loads on the beam screens of the inner triplets for the HL-LHC, CERN-ACC-NOTE-2018-0009.
[147] A. Romano et al., Effect of the LHC beam screen baffles on the electron cloud buildup, Proc. 7th International Particle Accelerator Conference 2016, Busan, South Korea, 8-13 May 2016, pp. 1454-1457. CERN-ACC-2016-256.
[148] R. Cimino, I. R. Collins, M. A. Furman, M. Pivi, F. Ruggiero, G. Rumolo, and F. Zimmermann, Can Low-Energy Electrons Affect High-Energy Physics Accelerators?, Phys. Rev. Lett., vol. 93, p. 014801, Jun 2004, DOI: 10.1103/PhysRevLett.93.014801.
[149] G. Iadarola and E. Wulff, Update on e-cloud validation of the new materials, ColUSM meeting #111, CERN 18 Jan 2019, INDICO: 788917.
[150] G. Skripka and G. Iadarola, Electron cloud studies for the LHC TDI and HL-LHC TDIS, CERN-ACC-NOTE-2018-0060.
[151] P. Ribes Metidieri et al., TDIS pressure profile simulations after LS2, CERN-ACC-NOTE-2018-0075.
[152] C. Bracco et al., The New Injection Protection Dump TDIS, Engineering Change Request, EDMS: 1936580.
[153] R. De Maria, HL-LHC Optics Transition, 33rd HL-MCF Meeting, 17th April 2018, INDICO: 721822.
[154] H. Bartosik et al., Other Means to increase the SPS 25 ns Performance - Transverse Plane, Proc. Chamonix 2014 Workshop on LHC Performance, Chamonix, France, 22–25 September 2014, Ed. M. Draper, pp. 180-184, DOI: 10.5170/CERN-2015-002.
[155] G. Iadarola, HL-LHC filling schemes: possible optimization, 140th HiLumi WP2 Task Leader Meeting, 29 January 2019, INDICO: 788818.
[156] A. Valishev, S. Fartoukh and D. Shatilov, BBLR compensation for HL-LHC, 3rd Joint HiLumi LHC–22nd LARP Collaboration Meeting, 7–8 May 2014, BNL, USA, INDICO: 17058.

[157] D. Banfi, J. Barranco, T. Pieloni, A. Valishev, Update on crossing angle scaling with bunch intensity , 20th HiLumi WP2 Task Leader Meeting, 25 October 2013, CERN, INDICO: 278765.

[158] D. Banfi, J. Barranco, T. Pieloni, A. Valishev, Beam-beam effects for round and flat optics: DA simulations, 4th Joint HiLumi LHC - LARP Annual Meeting, 17-21 November 2014, KEK, Japan, INDICO: 1711470.

[159] R. Calaga, Crab cavities: SPS test results, design advancement, plans for production, 8th HL-LHC Collaboration Meeting, 15-18 October 2018, CERN, INDICO: 742082.

[160] L. Carver and R. Calaga, Update on SPS crab cavity tests, 363rd LHC Machine Committee Meeting, 3rd October 2018, INDICO: 762684.

[161] ALICE upgrade Letter of Intent endorsed by the LHCC on 27 Sep 2012 and approved by the Research Board on 28 Nov 2012, CERN-DG-RB-2012-433.

[162] J.M. Jowett et al., Heavy ion operation from run 2 to HL-LHC, Proc. Review of LHC and Injector Upgrade Plans Workshop (RLIUP), Archamps, France, 29–31 October 2013, Eds. B. Goddard and F. Zimmermann, CERN–2014–006, DOI: 10.5170/CERN-2014-006.167.

[163] J.M. Jowett, R. Alemany-Fernandez, R. Assmann, P. Baudrenghien, G. Bellodi, S. Hancock, M. Lamont, D. Manglunki, S. Redaelli, M. Sapinski, M. Schaumann, M. Solfaroli, R. Versteegen, J. Wenninger and D. Wollmann, Heavy ions in 2012 and the programme up to 2022, Proc. Chamonix 2012 Workshop on LHC Performance, Chamonix, France, 6–10 Feb 2012, Ed. C. Carli, pp. 200-215, 2012, DOI: 10.5170/CERN-2012-006.200.

[164] J. Jowett, Functional Specification HL-LHC Heavy-Ion Beam Parameters at LHC Injection, EDMS: 1525065.

[165] J.M. Jowett, HL-LHC beam parameters for ions, LHC Performance Workshop (Chamonix 2017), Chamonix, France, 23–27 January 2017, INDICO: 580313.

[166] Z. Citron et al., Future physics opportunities for high-density QCD at the LHC with heavy-ion and proton beams, Proceedings of the HL/HE-LHC Workshop: Workshop on the Physics of HL-LHC, and Perspectives at HE-LHC Geneva, Switzerland, June 8-20, 2018, DOI: 10.23731/CYRM-2019-007.1159.

[167] J. Jowett. HL-LHC performance: Update for HE-LHC and light ions, Workshop on the physics of HL-LHC, and perspectives at HE-LHC. CERN. Geneva, Switzerland, June 18-20, 2018, INDICO: 686494.

[168] J. Coupard, H. Damerau, A. Funken, R. Garoby, S. Gilardoni, B. Goddard, K. Hanke, D. Manglunki, M. Meddahi, R. Scrivens, G. Rumolo, E. Shaposhnikova, eds., LHC Injectors Upgrade Technical Design Report – Volume II: Ions, EDMS: 1626950.

[169] R. Bruce, D. Bocian, S. Gilardoni and J.M. Jowett, Beam losses from ultra-peripheral nuclear collisions between $^{208}Pb^{82+}$ ions in the large hadron collider and their alleviation, Phys. Rev.ST Accel. Beams 12, 2009, DOI: 10.1103/PhysRevSTAB.12.071002.

[170] J.M. Jowett, H.-H. Braun, M.I. Gresham, E. Mahner and A.N. Nicholson, et al., Limits to the performance of the LHC with ion beams, Proc. 9th European Particle Accelerator Conference, Lucerne, Switzerland, 5 – 9 July 2004, Eds. J. Chrin, C. Petit-Jean-Genaz, J. Poole, C. Prior, H.-A. Synal, pp. 578–580.

[171] M. Schaumann et al., LHC BFPP Quench Test with Ions, 2015, CERN-ACC-NOTE-2016-0024.

[172] J.M. Jowett et al., Bound-free pair production in LHC Pb-Pb operation at 6.37 Z TeV per beam, Proc. 7th International Particle Accelerator Conference 2016, Busan, South Korea, 8-13 May 2016, pp. 1497, CERN-ACC-2016-245.

[173] H.-H. Braun, R.W. Assmann, A. Ferrari, J.-B. Jeanneret, J.M. Jowett and I.A. Pshenichnov, Collimation of heavy ion beams in LHC, Proc. 9th European Particle Accelerator Conference, Lucerne, Switzerland, 5 – 9 July 2004, Eds. J. Chrin, C. Petit-Jean-Genaz, J. Poole, C. Prior, H.-A. Synal, pp. 551–553.

[174] H.-H. Braun, A. Fassò, A. Ferrari, J.M. Jowett, P.R. Sala and G.I. Smirnov, Hadronic and electromagnetic fragmentation of ultrarelativistic heavy ions at LHC, Phys. Rev. ST Accel. Beams 17, 2014, DOI: 10.1103/PhysRevSTAB.17.021006.

[175] P. Hermes et al., Measured and simulated heavy-ion beam loss patterns at the CERN Large Hadron Collider, Nucl. Instrum. Methods Phys. Res. A 819 (2016) 73 – 83, DOI: 10.1016/j.nima.2016.02.050.

[176] N. Fuster et al., Cleaning performance of the collimation system with Xe beams at the Large Hadron Collider, Proc. 7th International Particle Accelerator Conference 2016, Vancouver, Canada, 29 Apr - 4 May 2018, pp 176, DOI: 10.18429/JACoW-IPAC2018-MOPMF038.

[177] R. Bruce et al., HL-LHC operational scenario for Pb-Pb and p-Pb operation, 2020, CERN-ACC-2020-0011.

[178] R. Bruce et al., Time evolution of the luminosity of colliding heavy-ion beams in BNL Relativistic Heavy Ion Collider and CERN Large Hadron Collider, Phys. Rev. ST Accel. Beams 13, 091001, 2010, DOI: 10.1103/PhysRevSTAB.13.091001.

[179] M.A. Jebramcik, “Beam Dynamics of Proton-Nucleus Collisions in the Large Hadron Collider,” Ph.D. dissertation, Johann Wolfgang Goethe-Universität, Frankfurt am Main, Germany, 2019. CERN-THESIS-2020-075.

[180] J.M. Jowett et al., Proton-nucleus Collisions in the LHC, Proc. 4th International Particle Accelerator Conference 2013, Shanghai, China, May 12-17, pp 49, 2013, CERN-ACC-2013-0057.

Chapter 3

Insertion magnets

E. Todesco[1*] *and P. Ferracin*[1]

[1]CERN, Accelerator & Technology Sector, Switzerland
[*]Corresponding author

3 Insertion magnets

3.1 Overview

The layout of the HL-LHC insertion magnets is shown in Figure 3-1 and compared to those of the LHC in Figure 3-2.

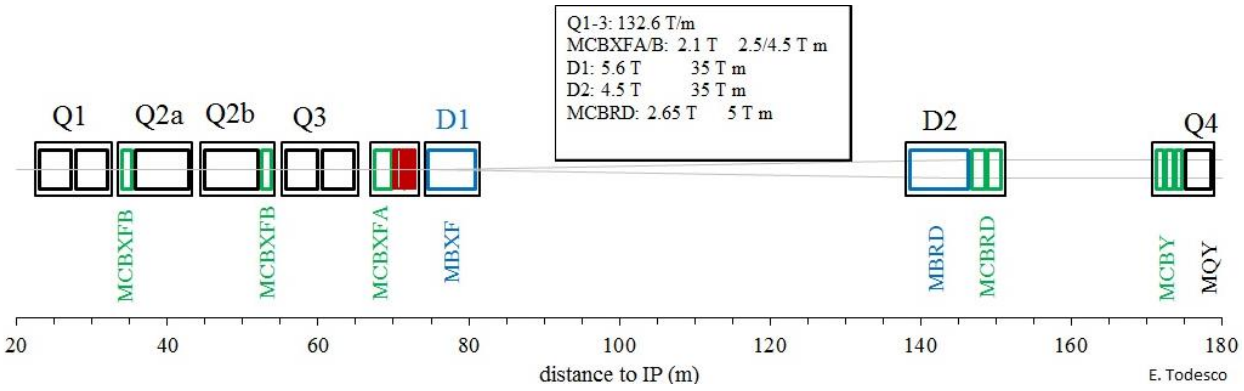

Figure 3-1: Schematic layout of the magnets in the Insertion Region (IR) region till Q4 of the HL-LHC. Thick boxes are magnets, thin boxes are cryostats.

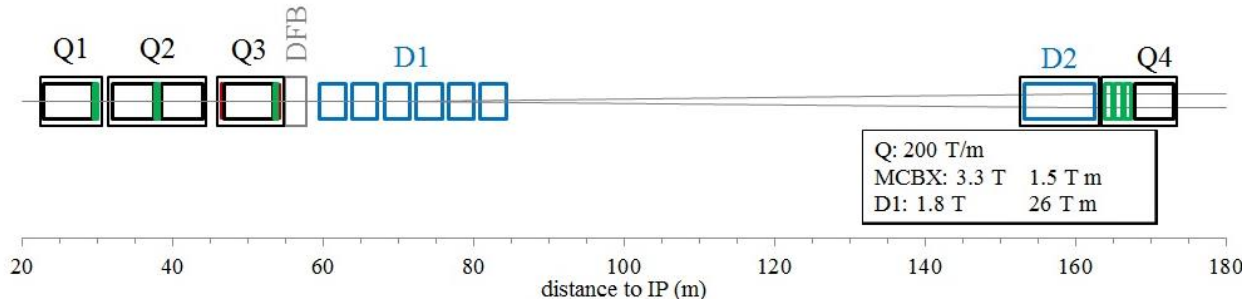

Figure 3-2**:** Schematic layout of the magnets in the current IR region till Q4 of the LHC. Thick boxes are magnets, thin boxes are cryostats.

The main technical choices can be summarized as follows [1][2]:

- Maintain the distance from the first magnet to the collision point at 23 m. This allows preserving the most critical boundaries with the detectors and the tunnel transition to the experimental cavern.

- Increase the quadrupole triplet coil aperture from 70 mm to 150 mm to allow a smaller β^* and to be able to integrate a 8/16-mm-thick tungsten (W) shielding attached to the outer surface of the beam screen; this allows reducing the effect of collision debris (heat load and radiation damage) in the magnet cold masses to the present LHC levels notwithstanding 5 times larger peak luminosity and a 10 times larger integrated luminosity.
- Select the Nb_3Sn technology for the quadrupoles [3], allowing doubling the aperture at constant integrated gradient without a too large increase in the triplet length that would make impossible the integration in the LHC tunnel. To keep the length increase below 30% while minimizing risks and costs, the following steps were taken:
    - Use in the triplet a large coil width (about 36 mm, arranged in two layers of 18-mm-wide cable) to reach maximum performance in terms of gradient [1, 4].
    - Select a working point on the loadline at 77% of short sample for nominal operation at 7 TeV [5][6][7]. This gives a 5% larger margin with respect to the LHC triplet magnets, and 9% larger margin with respect to the LHC main dipoles.
    - Fix the critical current specification to a conservative value of 1280 A/mm^2 at 15 T and 4.2 K, to avoid significant rejection of strand during production.
- Three steps are taken to recover the 10 m of additional space required by the triplet and the correctors, and to gain further space to insert the crab cavities (see Chapters 2 and 4):
    - Increase the strength of the separation/recombination dipoles from 26 T·m to 35 T·m, thus reducing the distance between the D1 and D2 centres from 90 to 75 m and recovering ~15 m.
    - Replace the 20-m-long normal conducting magnet D1 operating at 1.28 T with a superconducting 6.27 m long magnet, operating at 5.6 T [8], thus recovering ~15 m.
    - Connect the triplet busbars to the D1 through a service module on the non-IP side of D1 (not shown in Figure 3-1) instead of connecting them through a feedbox placed between D1 and the triplet as in the LHC (indicated by DFB in Figure 3-2), thus shifting the D1 towards the IP by a few metres.
- Increase the apertures of D1 and D2 dipoles and associated correctors: D1 from 60 mm to 150 mm, D2 from 80 mm to 105 mm. For the new dipoles D1 and D2, Nb-Ti superconductor has been chosen [1][2], since requirements are within reach of this technology, and the potential performance improvement given by Nb_3Sn is not sufficient to justify the additional cost and complexity. Using the LHC cable allows to reduce the risks (the cable properties are well known), to ease the schedule (lengths are already available) at the price of a larger operational current.
- Increase the strength of the three horizontal/vertical orbit correctors required in the triplet from 1.5 T·m (LHC value) to 2.5 T·m for the correctors close to Q2a/b, and to 4.5 T·m for the corrector close to Q3. The position with respect to the quadrupole magnets is the same as in the LHC layout, with the exception of the corrector between Q2a and Q2b, which is moved to between Q2b and Q3. Correctors are nested (like in the present LHC), providing both horizontal and vertical field in the same longitudinal location, to keep a compact triplet layout.
- Use a skew quadrupole to correct the triplet tilt, as in the LHC. Non-linear correctors of order 3, 4, 5, and 6 are required, both normal and skew. With respect to the LHC layout, normal and skew decapole correctors [order 5] and a skew dodecapole corrector [order 6] are added. Experience with LHC operation and field quality of the triplet short models will confirm whether these correctors are needed. In any case, the longitudinal space required for a single corrector is about 15 cm, and therefore it does not have a large impact on the layout.
- Add horizontal and vertical orbit correctors close to D2 (not present in the LHC) with a nominal strength of 5 T·m.

The main parameters of the magnets are listed in Table 3-1 and Table 3-2

Table 3-1: Overview of the main parameters of the insertion magnets – see the text for definitions of footnotes.

	Unit	MQXFA	MQXFB	MCBXFB	MCBXFA	MBXF	MBRD	MCBRD
Order		2	2	1	1	1	1	1
Aperture[1]	(mm)	150	150	150	150	150	105	105
Central field	(T)			2.10		5.58	4.50	2.59
Central gradient[a]	(T/m)	132.2						
Magnetic length[2a]	(m)	4.200	7.174	1.200	2.200	6.270	7.778	1.930
Integrated field	(T m)	556.9	948.1	2.500	4.500	35.08	35.08	5.000
Number of apertures		1	1	1	1	1	2	2
Aperture distance[2]	(mm)						188	188
Number of circuits		4 mains + 4*2		8 H + 8 V	4 H + 4 V	4	4	8 H +
Units needed (magnets)		16	8	8	4	4	4	8
Spares (magnets)		4	2	4	2	2	2	4
Cable								
Material		Nb_3Sn		Nb-Ti		Nb-Ti	Nb-Ti	Nb-Ti
Strand diameter	(mm)	0.850		0.480		0.825	0.825	0.825
Cu/No_Cu		1.20		1.75		1.95	1.95	1.30
N. strands		40		18		36	36	
Cable thickness inner[3]	(mm)	1.530		0.819		1.362	1.362	
Cable thickness outer[3]	(mm)	1.658		0.871		1.598	1.598	
Cable width[3]	(mm)	18.363		4.37		15.10	15.10	
Ins. thickness radial[4]	(mm)	0.145		0.105		0.155	0.100	0.085
Ins. thickness	(mm)	0.145		0.105		0.135	0.100	0.085
Filling factor[5]		0.294		0.229		0.243	0.253	0.132
Coil								
Number of layers		2		2		1	1	
Number of turns/pole		50		140 / 191		44	31	3650
Cable length/pole		431	721	390 / 515	670 / 900	556	530	2200
Operational parameters								
Peak field[6]	(T)	11.41		4.13		6.58	5.26	2.94
Temperature	(K)	1.9		1.9		1.9	1.9	1.9
Current[a]	(kA)	16.23		1.625/1.474	1.584/1.402	12.11	12.33	0.394
Overall current	(A/mm^2)	469		314 / 285	306 / 271	449	478	702
Loadline fraction[8]		0.77		0.51	0.50	0.77	0.68	0.47
Temperature margin	(K)	5.0		4.1	4.1	2.4	3.0	4.2
Stored energy/m	(MJ/m)	1.17		0.064/0.119	0.061/0.109	0.340	0.291	0.074
Inductance/m	(mH/m)	8.21		48.7 / 105		3.97	3.52	480
Stored energy[9]	(MJ)	4.91	8.37	0.077/0.143	0.134/0.239	2.13	2.26	0.143
Mechanical structure								
Forces x	(MN/m)	2.47		0.322		1.52	0.67	
Forces y	(MN/m)	-3.48		0.402		-0.65	-0.57	
Midplane stress[10]	(MPa)	108		25		91	51	
Protection								
Circuit inductance[11]	(mH)	255		58.4 /124.8	107.1/232.3	24.9	27.4	920
Coil energy density[12]	(J/mm^3)	0.078		0.027	0.025	0.071	0.045	0.122
Dump resistor	(mΩ)			0.15	0.15			1.4
Heater circuits[13]		8	8			4	8	

[1]Aperture is the coil inner diameter at room temperature, excluding ground insulation, cold bore, and beam screen.
[2]Distance between apertures and magnetic length are given at 1.9 K.
[3]Strand/cable dimensions are given at room temperature, in the case of Nb_3Sn after reaction.
[4]Insulation dimensions are given at room temperature.

[5]Filling factor is defined as the fraction of superconductor in the insulated cable.
[6]Peak field in the coil is given including the contribution of the strand where the peak is located (self-field correction).
[7]Overall current density is the average over the whole cross-section of the insulated cable (i.e. including voids or impregnation and insulation, but not copper wedges); for the MCBRD overall current density is referred to the cross-sectional area of the slot.
[8]Load line fraction is the ratio between the operational current and the critical current on the load line.
[9]Stored energy is given for the whole magnet: in the case of independently powered apertures or nested magnets, stored energy is given for both circuits powered with maximum nominal current.
[10]Midplane stress is an estimate given by the accumulation of the azimuthal Lorentz forces at nominal current divided by the coil radial width – the impact of the structure, preload, and bending is not considered.
[11]Circuit inductance is the differential inductance of the circuit at nominal current.
[12]Energy density is given over the coil volume, including insulation but not coil parts such as copper wedges and pole pieces.
[13]Heater circuit are the available number of heater circuits per magnet; to know how many are actually used, see Chapter 7.
[a] Values for the nominal current, gradient in the straight section and magnetic length for the Q1, Q2 and Q3 magnets based on present results.

Table 3-2**:** Overview of the main parameters of the triplet corrector magnets.

	Unit	**MQSXF**	**MCSXF/ MCSSXF**	**MCOXF/ MCOSXF**	**MCDXF/ MCDSXF**	**MCTXF**	**MCTSXF**
Order		2	3	4	5	6	6
Aperture	(mm)	150	150	150	150	150	150
Integrated strength[1]	(T m)	0.700	0.095	0.069	0.037	0.086	0.017
Coil length[2]	(mm)	456.8	191.5	171.5	171.7	498.3	123.3
Gradient	(T/m^{n-1})	34.8	224	3680	40480	585600	550400
Number of apertures		1	1	1	1	1	1
Number of circuits		1	2	2	2	1	1
Units needed		4	8	8	8	4	4
Spares		2	4	4	4	2	2
Cable data							
Material		Nb-Ti	Nb-Ti	Nb-Ti	Nb-Ti	Nb-Ti	Nb-Ti
Strand diameter	(mm)	0.700	0.500	0.500	0.500	0.500	0.500
Insulation thickness	(mm)	0.070	0.070	0.070	0.070	0.070	0.070
Cu/No_Cu		2.1	2.1	2.1	2.1	2.1	2.1
Coil design							
N. turns/pole		754	288	372	228	432	432
Cable length/pole	(m)	1230	104	105	59	439	112
Operational parameters							
Coil peak field	(T)	3.60	2.23	2.09	1.63	1.57	1.50
Temperature	(K)	1.9	1.9	1.9	1.9	1.9	1.9
Current	(A)	174	99	102	92	85	84
j overall[3]	(A/mm^2)	314	308	317	286	264	261
Loadline fraction	(a dim)	0.44	0.31	0.31	0.26	0.27	0.27
Temperature margin	(K)	4.3	4.9	4.9	5.2	5.0	5.0
Differential	(mH)	1530	213	220	120	805	177
Stored energy	(kJ)	30.8	1.72	1.55	0.668	3.627	0.732

[1]Integrated strength is defined as the field at the 50 mm reference radius times the magnetic length.
[2]Coil length refers to the physical coil length, and not to magnetic length.
[3]The overall current density includes 0.07 mm thick strand insulation and the coil ground insulation.

After TDR 0.1 [9] several design decisions were adopted:

- MQXF shimming in order to modify the systematic harmonics b6 of the MQXF quadrupole [47].
- Increase of the iron yoke hole diameter from 60 to 61 mm for heat exchangers in D1 and MCQSXF [49].

- Triplet protection: after validation on short models and prototypes, CLIQ has been selected as baseline for protection with outer layer heaters [10].
- Nested corrector protection: a 0.15 Ω dump resistor adopted for both MCBXFA and MCBXFB [10].
- Triplet circuit: the 120 A trim on Q2a has been removed, since the spread between the integrated transfer function of the quadrupoles was deemed to be well within the tolerance range, and sorting could be used as an additional way to reduce this spread.
- Triplet circuit: a 35 A trim on Q1a has been added for beam optics measurements [10].
- High order correctors: to better correct the measured triplet errors there has been one iteration on the corrector strengths, keeping the same length of the cold mass, with a 30% reduction of the skew quadrupole and by 50% increase of sextupole, octupole and decapole (normal and skew) [44].
- Q4 and Q5: both the Q4 LHC cold mass and the Q5 LHC cold masses shall be reused for the HL-LHC, with operational temperature of 4.5 K as in the LHC.
- Q5 in IR6: no modifications with respect to the LHC layout [46].
- A consolidation action of the resistive magnet has been carried out, adding shielding to reduce the radiation damage. This removes the need of construction of new resistive magnets initially foreseen [48].
- Implementation of the Fully Remote Alignment system allowing to reduce the required correctors strength [43].
- Optimization of the alignment of the D1 to maximize the beam aperture [42].

3.2 Low-β triplet quadrupoles

Function, operational modes, and powering: The triplet magnets, denoted by MQXF, ramp with the energy of the LHC, with a nominal gradient of 8.5 T/m at 450 GeV, and a maximal operational gradient of 132.2 T/m at 7 TeV. During squeeze, its gradient is constant or decreases by not more than 10%. The triplet quadrupoles, Q1-Q2a-Q2b and Q3, are powered in series, with a 2 kA powering trim acting on Q1 and another one on Q3. The quadrupoles Q1 and Q3 are produced by the USA DOE project HL-LHC AUP (see Chapter 1) and Q2a and Q2b by CERN.

Conductor: The Nb_3Sn cable has 40 strands, with 0.85 mm diameter [7]. The main specifications are:

- A minimum non-copper critical current density of 1280 A/mm^2 at 15 T and 4.2 K; this value has been lowered in 2015 with respect to the initial specification of 1400 A/mm^2 to avoid the rejection of a significant part of the production.
- The cable keystone angle has been fixed to a conservative value of 0.40° to reduce the critical current degradation of cabling below the 5% specified value; this value has been reduced from the initial 0.55° to reduce cabling degradation for PIT strand.
- RRR larger than 100 after cabling.
- Cu/no Cu ratio of 1.2 (54.5% of copper in the strand) to have a good compromise between critical current density and protection.
- The cable has S2^{TM} glass braided insulation, whose thickness is 145 µm at 5 MPa before reaction.
- The cable contains a 12-mm-wide, 25-µm-thick stainless-steel core to control and reduce the dynamic effects.

Coil, current density, and margin: Having two coil layers, one can reach the operational gradient of 132.2 T/m at 77% of the short sample limit on the load line (i.e. 23% of load line margin). Each layer has a copper wedge to tune field quality.

Lengths and transverse size: The triplet is made of Q1 and Q3 magnets, each unit requiring a magnetic length of 8.4 m; plus Q2 with a 14.3-m-long magnetic length. In the initial phase of the project, US-AUP decided to split both Q1 and Q3 into two 4.2-m-long magnets, assembled in the same cold mass, to reduce the risks associated to manufacturing long magnets. CERN decided to split the Q2 into two 7.17-m-long magnets called Q2a and Q2b. The Q1, Q2, and Q3 cross-sections are identical, and make use of the same design, technologies, and (almost all) components. The cold mass cross-section has a 630 mm diameter, i.e. 60 mm more than the LHC dipoles including the stainless-steel vessel.

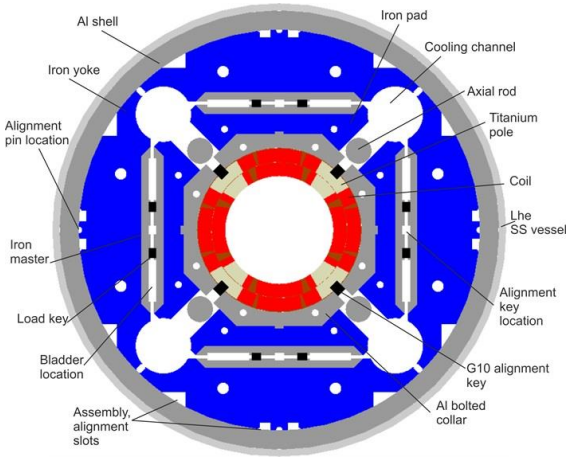

Figure 3-3: Sketch of triplet quadrupole magnet cross-section.

Mechanical structure: The quadrupole makes use of a shell-based structure developed at LBNL and within the LARP collaboration with a series of short models called TQS [11]. The structure scale-up to a length of 3.4 m, was demonstrated in the LARP LR and LQ quadrupole models [12], and features to assure alignment in operational conditions have been included in the 120 mm aperture HQ short model quadrupole [13]. The MQXF cross-section is a scale up of the HQ design. Coils are mainly pre-stressed by the Al shell during cool-down, acting as the structure to contain the Lorentz forces. The level of stress is fine-tuned during the loading of the coil, which is done at room temperature using water-pressurized bladders and interference keys. Typically, one has ~70 MPa of azimuthal coil compression at room temperature, which becomes ~150 MPa at 1.9 K thanks to the interplay of the thermal contractions of the different components. The structure keeps the coil under compression up to the ultimate current, corresponding to 143.2 T/m (7.5 TeV operation).

Protection: The energy density in the coil is ~0.08 mJ/mm^3 (with coil volume including insulation, but excluding wedges), which is ~50% larger than the LHC main magnets [14]. This makes quench protection challenging. Since the circuit inductance is of about 250 mH, only a small fraction (~5%) of the energy can be extracted on a dump resistor. Therefore, we have to rely on quench heaters on the outer layer of the coil, and no dump resistor is included in the circuit. Quench heaters are 25 µm stainless steel strips with a 50 µm polyimide layer to ensure proper insulation. The heaters will have heating stations of 40 mm length, separated by 120 mm sections with lower resistance due to a 10 µm copper cladding (see Figure 3-4). The width of the heating stations is 20 mm, and a 7.17-m-long magnet will have ~40 heating stations. Two independently powered strips will cover the two blocks of the outer layer. The typical time needed to quench the coil at nominal current is of the order of 15–20 ms following heater firing [15]. Assuming 5 ms for detection time, a validation window of 10 ms and a few ms for switch opening, this brings the hotspot temperature to ~350 K [16]. To reduce this value and to ensure some redundancy, we also use the CLIQ system [17], recently developed at CERN, based on coil heating induced by an induced oscillating current in the magnet. The CLIQ system has the interesting feature of acting rapidly on the inner layer and is therefore complementary to the outer layer quench heaters. It has been validated on all short models and on the US prototypes, allows reducing the hotspot temperature of about 70 K, i.e. from 350 K (outer layer quench heaters) to 280 K (outer layer quench heaters and CLIQ). However, CLIQ is less effective at low current and cannot protect the magnet at injection current.

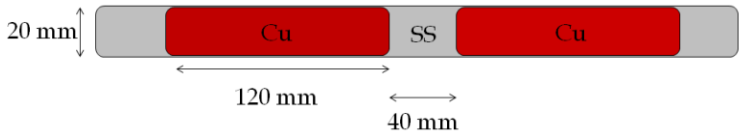

Figure 3-4: Quench heaters for the outer layer. Stainless steel (SS) in grey and copper cladding in red. A ~300 mm long portion, out of the 4/7 m long strip, is shown.

Field quality: Allowed field harmonics (b_6, b_{10}) are optimized for operation at high field, and are expected to be below one unit in absolute value. Contributions from the coil ends are also taken into account and compensated when possible through the straight part [18]. Random components are estimated for a 25 μm random error in the block positioning for non-allowed, and 100 μm for allowed; most critical components are low-order harmonics (b_3, a_3, b_4, a_4). To minimize these components we opted for a strategy similar to that used in the RHIC magnets [19], with magnetic shims to be inserted in the bladder location [20]. This allows correcting (i) ±5 units of b_3; (ii) ±5 units of a_3; (iii) ±3 units of b_4; (iv) ±1 units of a_4, for a maximum of two harmonics at the same time, through an asymmetric magnetic shimming. A fine-tuning of b_6 has been done at the beginning of the prototype phase, to increase it from -4 to 0 units through the addition of a 125 μm shim in the coil pole and a reduction of 125 μm shim in the midplane.

Cooling: The magnet is in a static bath of pressurized HeII, with a welded stainless-steel shell placed outside the Al structure acting as a helium vessel. Cooling is ensured via two heat exchangers of 68 mm inner diameter, in which a saturated HeII bath is formed, housed in the 77 mm diameter holes of the iron located in the upper part, see Figure 3-3 [21]. The heat exchanger cools the triplet and the short orbit correctors MCBXFB, with the separation dipole and corrector package on a different circuit. With this design, one can comfortably remove ~800 W of heat load from the triplet, i.e. 675 W at ultimate luminosity on the cold mass given by debris (see Table 3-1), plus a 125 W budget for other loads (among them the 25 W load of collision debris ending on interconnections), at the ultimate peak luminosity. To cope with these high heat loads, a low pressure pumping is added between Q2a and Q2b to keep the two-phase vapour flow velocity below 7 m/s, above which the Heat exchangers (HXs) would not function correctly [50].

For the Nb-Ti coils in the LHC, the peak heat deposition target was set at 4 mW/cm^3; this has a factor of 3 safety on 12 mW/cm^3, which was considered to be the hard limit. Later experience showed that the hard limit is at least a factor of two larger. In the HL-LHC, thanks to the tungsten shielding, we are always below the 4 mW/cm^3 target, as shown in Table 3-1. The Nb_3Sn superconductor in the present MQXF design is expected to have a peak power limit of the order of about 70 mW/cm^3, i.e. one order of magnitude larger than the load in the HL-LHC. The heat loads from the coils, from the cold mass and from the beam-pipe area can only be evacuated to the two heat exchangers by means of pressurized HeII. To this aim the cold mass design incorporates the required helium passages: 1.5 mm annular spacing between cold bore and inner coil-block, and free passage through the coil pole and subsequent G10 alignment key. The free passage needed through the coil pole and G10 alignment key in the transverse direction is given by 8 mm diameter holes repeated every 50 mm.

The beam screen receives ~500 W in the triplet–correctors–D1 region (including 55 W from the interconnections). Given the 100 W budget for the residual effect of electron cloud, and the 50% margin for getting to ultimate luminosity, the system has to remove ~1000 W over 55 m, i.e. ~17 W/m. Heat is removed at 60-80 K [41]. The cooling tubes inner diameter is ~7 mm, due to an increase of the pressure of the helium to 18 bar. This choice is more challenging for the piping system but allows minimization of the space taken by the cooling pipes, which reduce the aperture available to the beam.

Cryostat: Independent cryostats are used for Q1, Q2a, Q2b, and Q3. The Q1 and Q3 cryostats contain two 4.2-m-long magnets. The Q2a and Q2b cryostats contain each one 7.17-m-long magnet plus the orbit correctors described below. The cryostat size should be able to accommodate the cold mass, the thermal shielding, and the cooling pipes. The LHC standard vacuum vessel size of 980 mm (including flanges) is a tight fit for all of

these components. To solve this problem, we use asymmetric centering to make room for the piping in the upper part of the cryostat (see Figure 3-5).

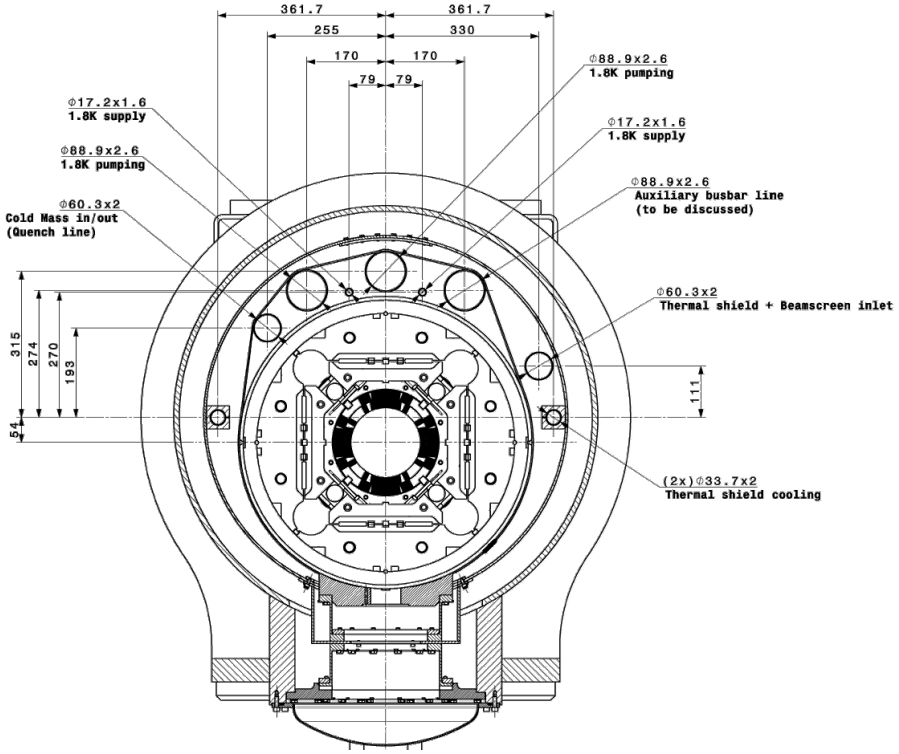

Figure 3-5: Cross-section of the cryostat.

3.3 Nested orbit correctors

Function, operational modes and powering: The orbit correctors are single-aperture magnets. Two versions are required, providing 2.5 T·m and 4.5 T·m integrated fields. To have a more compact layout in this region where longitudinal space affects performance, a nested design has been adopted, with the horizontal and vertical dipole coil in the same cross-section (see Figure 3-6). The field in each plane has been limited to 2.1 T, giving a maximum combined field of 3 T. Powering will be allowed in a square in the horizontal/vertical plane, with both positive and negative currents. These magnets generate the crossing angle and correct the quadrupole misalignment.

Orbit corrector prototypes have been developed by CIEMAT (Madrid, ES), which provides the series magnets in the framework of a collaboration agreement [23].

Conductor: The 4.5-mm-wide Nb-Ti cable developed for the SLHC corrector [24] has been adopted. This is based on a 0.48-mm-diameter strand, arranged in a Rutherford cable with 18 strands. The cable is insulated with a braided S2-glass as the MQXF.

Coil, current density and margin: The magnets have two-layer coils per dipole direction; this allows reaching the operational field of 2.1 T simultaneously in both planes at less than 50% of the load line. The coil has a large number of turns (up to 200) and it is impregnated with CTD-101K® as the MQXF to ensure a proper control of the dimension and to allow magnet assembly.

Lengths and transverse size: The magnetic length is 1.2 m for the short version (MCBXFB) and 2.2 m for the long one (MCBXFA). The magnet cross-section has a 630 mm diameter, including the stainless steel helium vessel (not shown in Figure 3-6), i.e. as in the HL-LHC triplet.

Mechanical structure: The magnet makes use of self-supporting collars. Stainless steel collars are used for keeping the inner and outer coils in place. Their thickness is 25 mm. Due to the nested coil arrangement, a

complex collaring based on two consecutive steps (first the inner, then the outer) is needed. The inner collars are closed with two round pins; the outer ones will be kept in place by four prismatic keys. A particular difficulty is that when both horizontal and vertical coils are powered, electromagnetic forces push the inner coil towards the centre of the aperture: for this reason, the preload must exceed the compression due to e.m. forces.

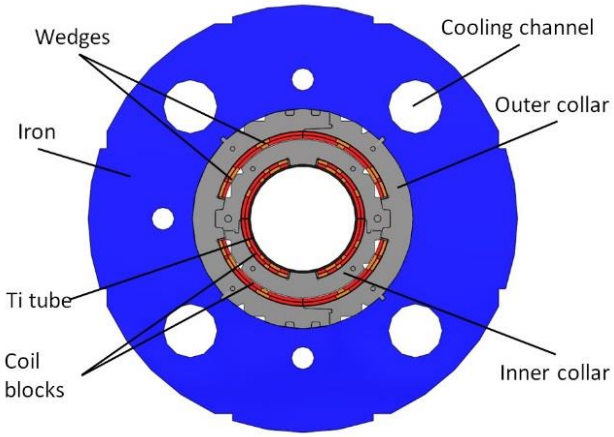

Figure 3-6: Orbit corrector cross-section (both MCBXFA and MCBXFB).

Protection: The magnets are protected via a 0.15 Ω dump resistor, keeping hotspot temperatures within 250 K.
Field quality: The magnet multipoles shall be within a window of ±20 units at maximum current in one field direction for all powering configurations of the other field direction. This is ensured by the cross-section and proper shaping of the iron.
Cooling: The MCBXFB magnet will share the same cold mass of the triplet Q2a/Q2b; cooling is ensured via the 68-mm-diameter heat exchangers placed in the 77-mm-diameter iron hole at 45º; a minimum of 1.5 mm gap between cold bore and magnet is also guaranteed for heat extraction.
The MCBXFA magnet will share the cold mass with the high order correctors; simulations show that a solution with one (or more) heat exchangers cooling the whole string triplet–corrector package-D1 is not viable. Therefore, a second system of heat exchangers is used to cool the corrector package and D1. Here the baseline is to have two heat exchangers of 49 mm inner diameter, reusing the LHC ones, able to remove 250 W. One heat exchanger would provide only 125 W.
Cryostat: The cryostat of the corrector package will have a similar design and features as the triplet cryostat, described in 3.2.

3.4 High-order correctors

Function, operational modes and powering: The high-order correctors (skew quadrupole, normal and skew sextupole, octupole, decapole, and dodecapole) are specified based on the expected field quality and alignment errors of the triplet magnets and separation-recombination dipoles (see Chapter 2), with a safety factor of 2 for the quadrupole, sextupole, and octupole, and 1.5 for the decapole and dodecapole components. The magnets will operate with nominal settings based on the measured field errors of the triplet and of the separation dipole. To ease operation, a non-nested layout (see Figure 3-7) has been adopted, using a superferric technology (see Figure 3-8 and Figure 3-9), already developed for the SLHC-PP [25]. Nb-Ti racetrack coils provide the ampere-turns, with iron giving the required field shape. The aperture is 150 mm, as for the triplet and D1.

The high-order corrector prototypes have been developed by the LASA laboratory of INFN (Milano, IT), which also provides the series magnets in the framework of a collaboration agreement.

Conductor: The cable is a single Nb-Ti strand, of 0.7-mm-diameter for the quadrupole and of 0.5 mm diameter for the higher order multipoles. Insulation is made with a 0.07-mm-thick S2 glass. Ground insulation is added on the external side of the coil.

Coil, current density, and margin: We chose to operate at 25% to 45% on the load line. The optimized current density is of the order of 300 A/mm^2 [26], with peak fields on the coil in the range of 1.5-2.3 T for the nonlinear correctors and 3.6 T for the skew quadrupole (see Table 3-2). Coils are dry-wound and then vacuum impregnated with CTD-101K®. Currents are below 120 A for all correctors to be able to reuse the LHC power converters, with the exception of the quadrupole corrector that requires 200 A.

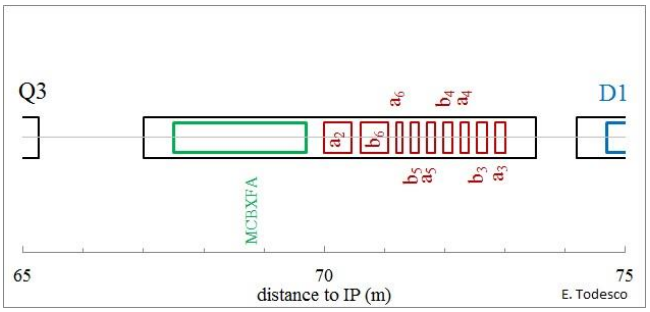

Figure 3-7**:** Layout of the corrector region.

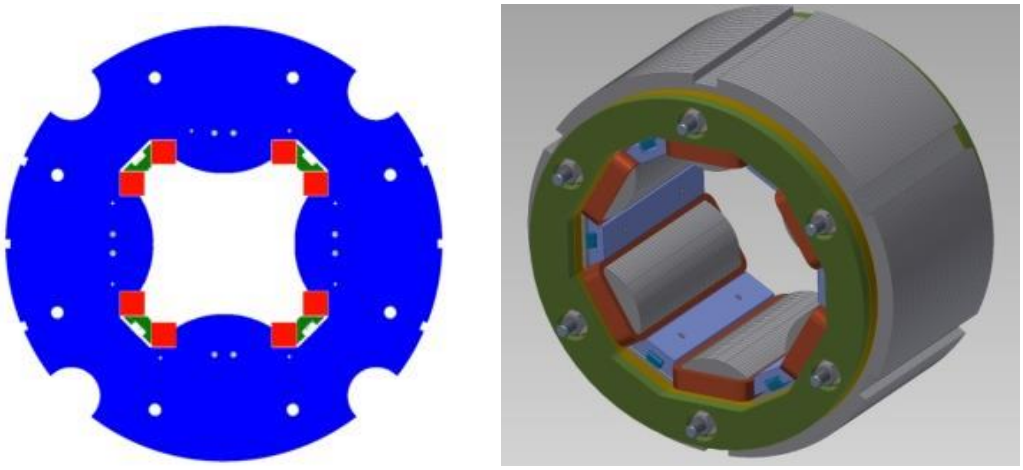

Figure 3-8**:** Cross-section of the skew quadrupole and 3D view of a sextupole (right).

Lengths and transverse size: The magnet lengths are 200 to 250 m for the sextupole, octupole, decapole, and skew dodecapole (see Table 3-2). The normal dodecapole and the skew sextupole require greater strengths, giving a magnet length of about 600 mm. The skew quadrupole needs a 460 mm diameter iron yoke that has to include indents for the cooling pipes for the heat exchanger. The nonlinear correctors can have an iron yoke diameter of 320 mm, which fits inside the cooling pipes. Spacers are required to match the transverse size of the correctors to the same value of the MCBXFA orbit correctors, and to maintain alignment within the cold mass. Heat exchangers will go through these spacers to cool the whole cold mass.

Mechanical structure: The mechanical support is guaranteed by wedges screwed to the structure (in green in the figures). The forces are of the order of 60 kN/m for the quadrupole and 10-30 kN/m for the other magnets.

Protection: The skew quadrupole protection relies on a dump resistor of 0.7 Ω; for the other magnets, the quench propagation is enough to protect the magnet with a hotspot below 200 K.
Field quality: Field quality requirement is to have all harmonics below 100 units at the reference radius of 50 mm. By design the harmonics are 10 times lower.
Cooling: Cooling of the helium bath is ensured by heat exchangers as described in 3.3. No requirement is needed on the stacking factor of the laminations. A wide gap between the Nb-Ti coils and the cold bore ensure free He passage in the inner part of the magnet.
Cryostat: As described in 3.3.

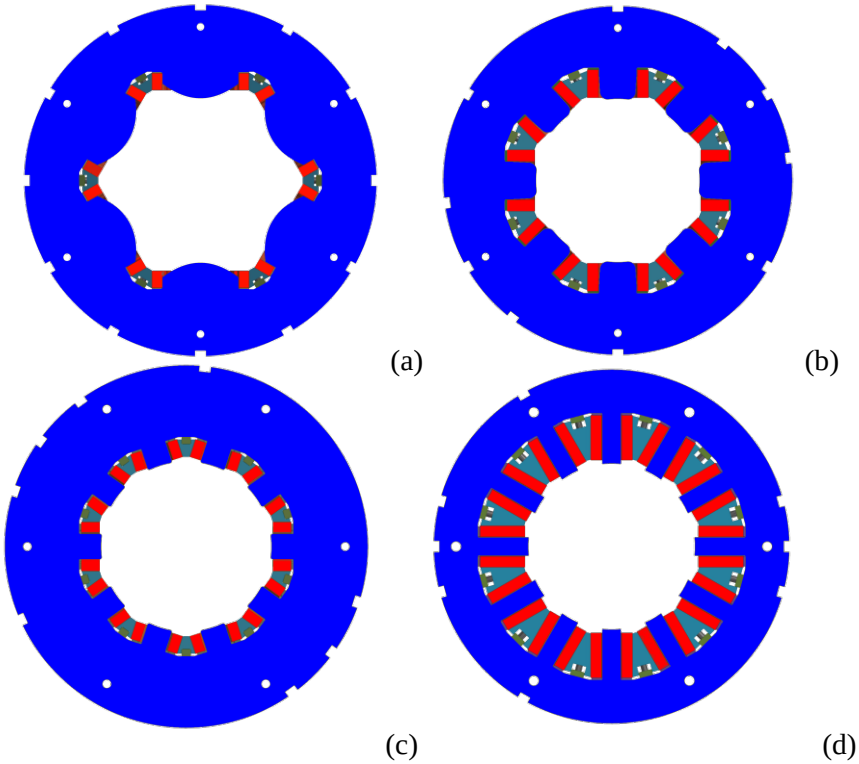

Figure 3-9: Sketch of nonlinear corrector cross-sections of (a) normal sextupole; (b) normal octupole; (c) normal decapole; (d) normal dodecapole correctors.

3.5 Separation dipole D1

Function, operational modes and powering: The separation dipole is ramped with the energy of the LHC and is constant during squeeze. D1 is individually powered.

The separation dipole short models and prototypes have been developed by KEK (Tsukuba, JP), which also provides the series magnets as in-kind contribution.

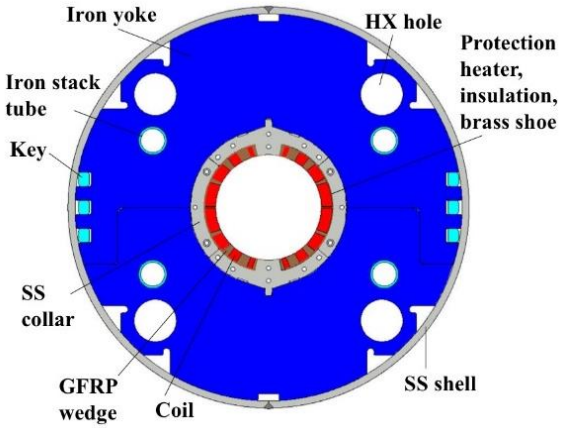

Figure 3-10: Cross-section of the MBXF magnet.

Conductor: The 15-mm-width Nb-Ti cable used for the outer layer of the main LHC dipole is adopted. The required unit length is about 2/3 of the main LHC dipole outer cable unit length (780 m).

Coil, current density and margin: With the initial choice of 70% operational level, the magnet length was slightly longer than the KEK test station [8][27]. We therefore fixed the operational current at 77% of the load

line, with a bore field of 5.6 T: this allowed fitting the vertical test station without significantly increasing the risk related to the lower margin.

Lengths and transverse size: Magnetic length is 6.27 m. The magnet cross-section has a 570 mm diameter, including the stainless-steel vessel, i.e. the same as the LHC dipoles. A larger diameter has been excluded to be able to reuse the yoking tooling used for J-PARC at KEK.

Mechanical structure: Forces are contained by the iron yoke, with thin spacers between the iron and the coil, as the J-PARC [28], RHIC magnets [29], and LHC Q1/Q3 [30]. Here the pre-stress is given by the iron laminations, horizontally split, that are locked through keys (see Figure 3-10). A thin stainless-steel collar acts as a spacer between the coil and the iron yoke. An alignment notch at 90° and 270° has been added after a first collaring test. An average pre-stress of 90 MPa is given at room temperature during the so-called 'yoking'. During cool-down the pre-stress lowers to 70 MPa, which is enough to counteract the Lorentz forces during powering.

Protection: The magnet shall be protected with quench heaters based on the same LHC technology and no energy extraction; hotspot temperature shall be within 300 K.

Field quality: The main issue here is the saturation component [8], which is optimized via the iron shaping. Following the analysis given in Refs. [31][32], the random components are estimated through random positioning of the coil block with different amplitudes for each family of harmonics, namely 40 µm for the allowed b_{2n+1}, 30 µm for the even skew a_{2n}, 15 µm for the odd skew a_{2n+1},and 10 µm for the even normal multipoles b_{2n}.

Cooling: The magnet is in a static bath of pressurized HeII, with a stainless-steel shell acting as a helium vessel. First baseline, showed in Figure 3-10, had cooling is ensured via two heat exchangers, of 49 mm inner diameter, housed in the 60 mm diameter holes through the iron. The position of the heat exchanger is the same as in the triplet to ease the interconnections.

Cryostat: The cryostat has the same geometry as the triplet cryostat (see Figure 3-5).

3.6 D1-DFX connection module (DCM)

Function: The DCM is the module that connects D1 to the distribution feedbox (DFX, see Chapter 6A), see Figure 3-11 and Figure 3-12. The module has on the one side the connection to the D1 cryostat, and on the other side the lambda plate with the transition from 1.9 K to 4.2 K. The module contains the five busbars of the 18 kA circuit, including trims, the two busbars of the 13 kA circuit of the D1, and the six busbars of the nested correctors MCBXFA/B. These busbars go through the lambda plate, where they are joint to the Nb-Ti busbars of the cold powering(see Figure 3-11). After the insertion of the "cold" diodes in the triplet circuit, this module has also the function of housing the stack of four diodes in a chimney whose position is optimized to minimize the radiation dose.

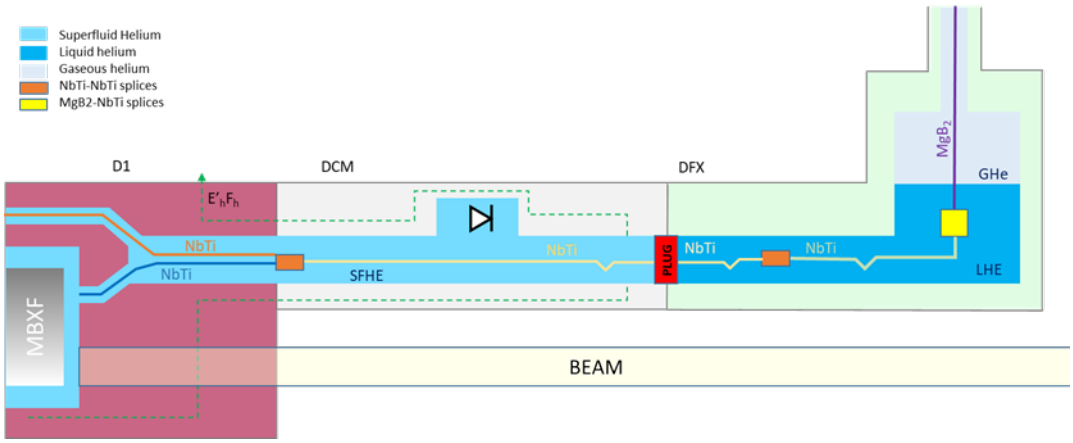

Figure 3-11: Conceptual design of the D1-DFX connection module

Conductor: All busbars are based on the same round cable using Nb-Ti strands used in WP6a (see Chapter 6A).

Lengths and transverse size: The module is 8 m long, thus requiring an adequate mechanical support and careful treatment of the fixed points and thermal contractions.

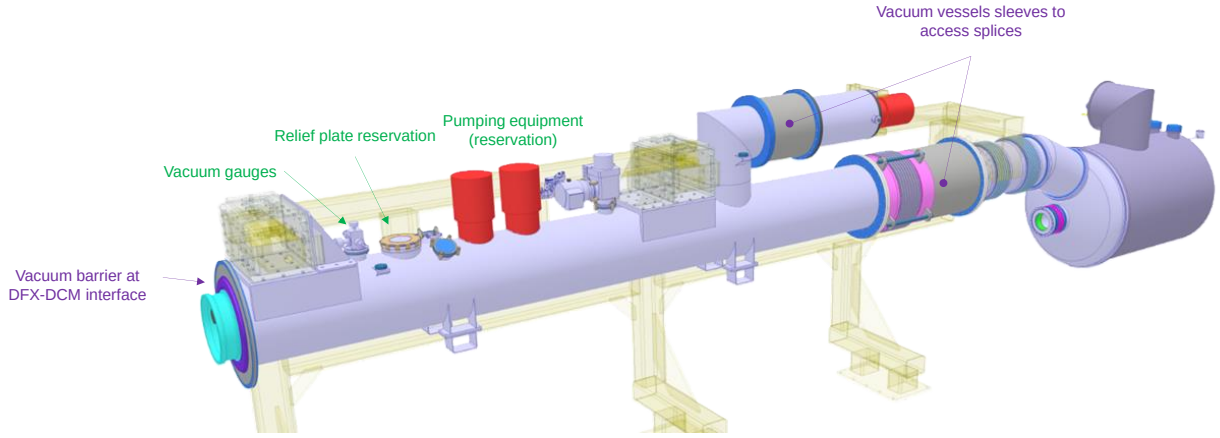

Figure 3-12: Engineering design of the D1-DFX connection module

3.7 Recombination dipole D2

Function, operational modes and powering: The recombination dipole is ramped with the energy of the LHC and is constant during squeeze. The two D2 apertures are in series. In D2, the fields point in the same direction in both apertures; this makes field quality control much more challenging than in the LHC dipoles, where the fields point in opposite directions.

The recombination dipole short model and prototype have been developed by INFN (Genova, IT), which also provides the series magnets in the framework of a collaboration agreement.

Conductor: The 15-mm-wide Nb-Ti cable used for the outer layer of the main LHC dipole is adopted. The required unit length about 2/3 of the LHC main dipole's outer layer unit length (780 m).

Coil, current density and margin: We selected a conservative margin, operating at 68% of the load line with a 15-mm-width coil, and an operational field of 4.5 T. In these conditions, the approach used in the present D2 design, that is using iron to magnetically decouple the two apertures, leads to large saturation effects. An alternative approach using left–right asymmetric coils was therefore adopted [33] to compensate for the cross-talk between the two apertures (see Figure 3-13). A very careful optimization is needed to find the best solution. After several iterations, a cross-section was found where the left–right asymmetry is only given by the angles of the blocks, but the number of cables per block is the same [34]. This allows for much simpler coil heads.

Lengths and transverse size: The magnetic length is 7.78 m. The magnet requires an adequate iron thickness to reduce the fringe field. An elliptical iron yoke is proposed, of 570 mm vertically and 630 mm horizontally.

Mechanical structure: The accumulation of Lorentz forces corresponds to a pressure in the midplane of about 40 MPa. A self-supporting stainless-steel collar, one per aperture, is considered. The two apertures are then inserted in an Al skin providing the relative alignment. The whole pack is inserted in the iron. Peak stress during collaring is of the order of 100 MPa [35].

Protection: Protection will be based on quench heaters using the standard LHC dipole technology (used also in D1). Hotspot temperature is estimated to be below 250 K.

Field quality: This is the main issue for this magnet: the square design of the central aperture in the iron and its elliptical shape is imposed by field quality optimization, namely the reduction of the field harmonics due to saturation. Cross-talk is optimized via the asymmetric cross-section, and the saturation through an iron shaping. In absence of iron and for a collared coil in stand-alone mode, quadrupole and sextupole components are of

the order of 200 units. The compensation due to the presence of the other coil and of the iron shaping allows to reduce these components within few units, i.e. has to work with a precision of the order of 1%.

Cooling: The magnet is in a static bath of pressurized HeII. Direct cooling is ensured via a cold finger.

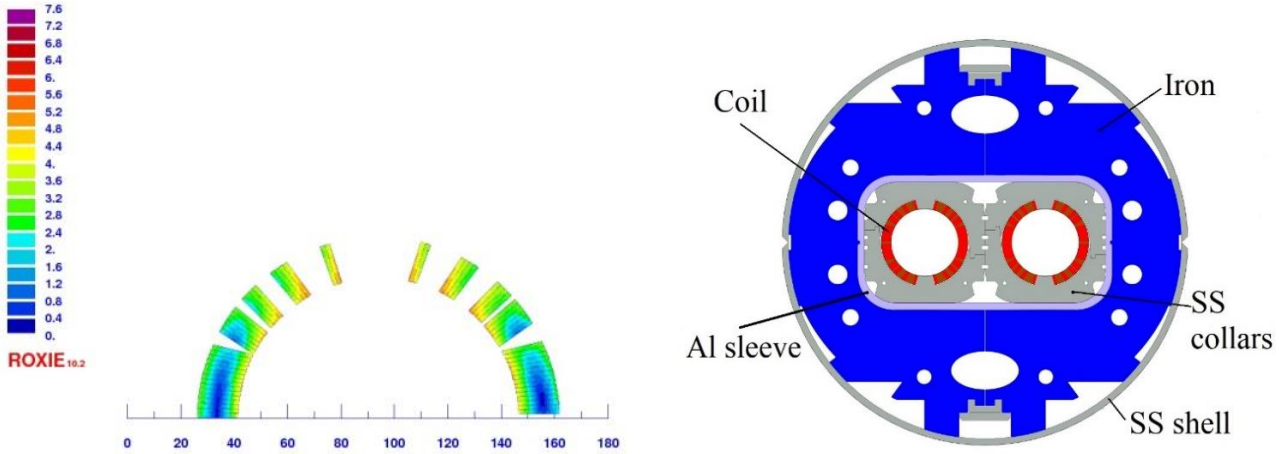

Figure 3-13: Sketch of recombination dipole cross-section. Asymmetric coil (left) and magnet cross-section (right). Note the elliptical shape of the yoke.

Cryostat: The cryostat has the same geometry as the triplet cryostat (see Figure 3-5).

3.8 D2 correctors

Function, operational modes and powering: D2 orbit correctors have to be installed for each beam and each plane (horizontal and vertical), with an integrated strength of 5 T·m, and an aperture of 105 mm. These correctors are used to control the crossing angle and to correct the closed orbit, and therefore they should be powered in a wide range of configurations. The large electromagnetic coupling and the stringent field quality requirement (all harmonics within 10 units for all combinations of currents) limit the main field to 2.60 T; this gives a magnetic length is 1.92 m. Horizontal and vertical correctors share the same longitudinal position for beam 1 and 2 respectively, and are followed by a vertical (beam1) and horizontal (beam2) corrector. In this configuration the magnetic cross-talk is less severe than in a case with horizontal-horizontal (or vertical/vertical) correctors in both beams (see Figure 3-14). These requirements make the D2 corrector as the ideal test bed for the canted cos-theta design, which provides the advantage of low operational current, and simple components and assembly procedures [36]. It will be the first time that a magnet based on this design will be used in a high energy physics accelerator.

The D2 corrector prototypes have been developed in CERN and shall be provided as in-kind contribution by a by IHEP (Beijing, CN), with the support of other Institutes.

Conductor: a 0.825 mm diameter Nb-Ti strand with characteristics similar to the LHC shall be used. Strand will be manufactured in China.

Coil, current density, and margin: Ten strands are wound in the groove, with 365 turns per magnet. The inclination of the winding of the top of the groove is 30º with respect to beam axis. The nominal bore field is 2.60 T, the peak field is 2.94 T, the operational current is ~400 A with a loadline fraction ~50%. Ten wires are wound in the same groove; the former+wire is then impregnated with CTD-101K®.

Lengths and transverse size: The magnet has a mechanical length of 2.2 m. The diameter is the same of the D2 cold mass, i.e. 614 mm.

Mechanical structure: In this design, the former is providing the position of the cable and the mechanical support. Each layer (in the two opposite direction of the angle, see Figure 3-14) is a 10 mm thick tube with a 5.2 mm deep and 1.1 mm width groove to house the ten strands. The two tubes contacting the two windings are surrounded by a third 10-mm-thick tube to limit the deformations due to Lorentz forces within 0.1 mm.

Protection: The low-current / large inductance of this type of design requires the use of a dump resistor. The resistance is set at 1.4 Ω, allowing to keep the voltages well below 1000 V. Even with this large value of resistance, energy extraction and quench propagation are not enough to keep the hotspot temperature below a safe value of 250 K. The magnet protection has to rely on the quench back induced in the former by the initial *dI/dt* given by the energy extraction. This mechanism is very effective and has been verified on short models and prototypes.

Field quality: The challenge in these magnets is the cross-talk between the apertures. Since for D2 the beam distance is 188 mm, and the aperture is 105 mm, little space is left for the iron to decouple the two apertures [37]. No optimization can be made through the coil cross-section as is the case in D2 since these magnets have to be powered with any combination of currents. The solution is to keep a thin coil, and to maximize the iron thickness. Requirements on field quality are to have all multipoles below 10 units.

Cooling: The magnets will share cooling with D2, so will have heat exchangers in the same position.

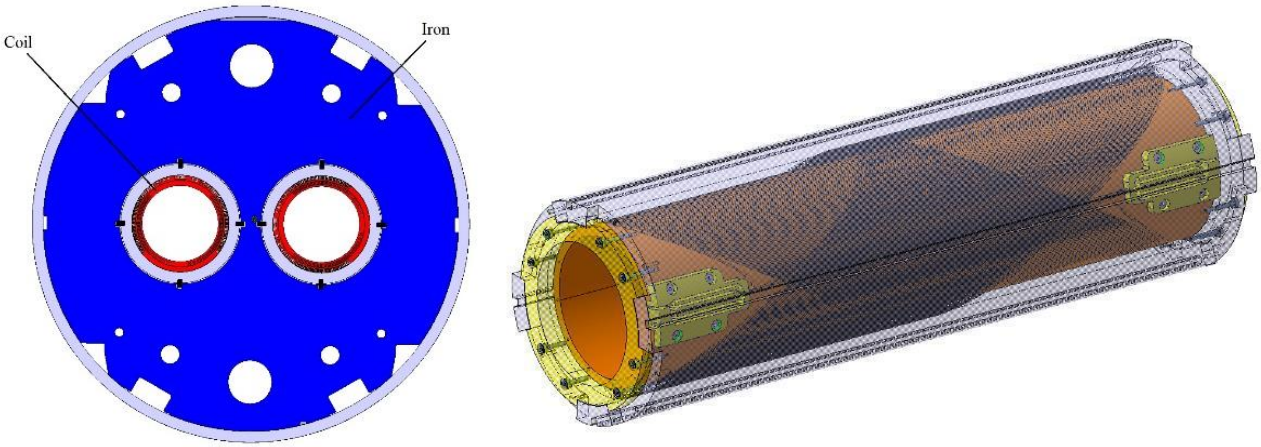

Figure 3-14: Cross-section of D2 orbit corrector (left) and 3D view of the short model coil (right).

3.9 Q4, Q5 and Q6

Both Q4 and Q5 will be moved from their positions in the LHC layout by about 10 m in the opposite direction of the interaction point to adapt to the new optics of the HL-LHC; they will work in the same operational conditions as in the LHC. In the first version of the project, a larger Q4 of 90 mm aperture was planned (MQYY) whose cross-section is shown in Figure 3-15. A short model magnet has been built in collaboration with CEA (Saclay-France); moreover, two full length prototypes are in construction in the industry with a European initiative (EC-H2020-QUACO). The Q6 magnet will not be modified and will be operated at 4.5 K as it is today in the LHC.

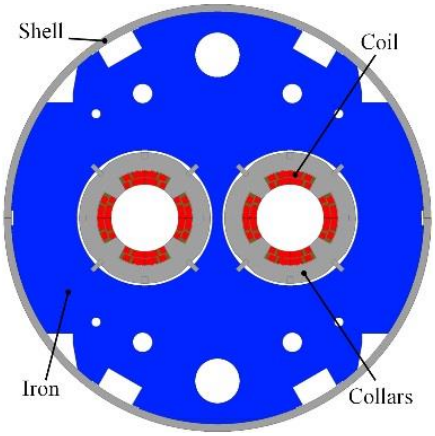

Figure 3-15: MQYY 90 mm aperture cross-section. This magnet is not anymore in the HL-LHC baseline.

3.10 Other modifications for the upgrade: sextupole (MS) in Q10 and magnets in IR3-IR7

The four cold masses of Q10 around IP1 and IP5 require a modification to include a lattice sextupole (MS) corrector. In the first version of the project, the two Q5 in IR6 were replaced by a new cold mass with two MQY each. In a second iteration the present LHC Q5 was kept for the HL-LHC, but the operational temperature was lowered from 4.5 K to 1.9 K to allow a larger strength. Further optimizations of the optics allowed to also avoid this modification, and in the present baseline the Q5 in IR6 has no modifications.

A Few of the MBW and MQW in IR3 and IR7 will have in the HL LHC era a radiation dose above the safe limit [40]. Consolidation actions have been taken to make these magnets able to survive the expected integrated luminosity of the HL-LHC; therefore, the initial plan of manufacturing radiation-hard MBW and MQW has been abandoned.

3.11 Magnets test plan

In general, magnets will be tested individually in a vertical test station, and then horizontally in the final cold mass assembly within the final cryostat, with the exception of Q2 and D2 whose length does not allow vertical testing. Many power tests will be done in laboratories collaborating with CERN (BNL for vertical test of Q1/Q3, FNAL for horizontal test of Q1/Q3, KEK for vertical test of D1, LASA for vertical test of high order correctors, IMP (Lanzhou-China) for vertical test of D2 correctors, FREIA (Univ. of Uppsala, Sweden) for vertical test of MCBXFB. For the D2 correctors and for the high order correctors, performance shall be assessed in LASA and IMP at 4.5 K.

All test will require reaching the so-called ultimate current, corresponding to operation in the HL-LHC at 7.5 TeV. All main magnets will undergo a thermal cycle to verify the training. A string including the magnets from Q1 to D1 will be assembled in the CERN test facility (SM18) and tested prior to the installation of the HL-LHC components in the LHC tunnel (See Chapter 16).

3.12 References

[1] O. Bruning, L. Rossi, Eds. “The High Luminosity Large Hadron Collider”, Advances Series on Directions in High Energy Physics **24,** (World Scientific, Singapore 2015), DOI: 10.1142/9581.

[2] E. Todesco *et al.*, A first baseline for the magnets in the high luminosity LHC insertion regions, *IEEE Trans. Appl. Supercond.* **24** (2014) 4003305, DOI: 10.1109/TASC.2013.2288603.

[3] G. Sabbi, Nb_3Sn IR Quadrupoles for the High Luminosity LHC, *IEEE Trans. Appl. Supercond.* **23**, 2013, DOI: 10.1109/TASC.2003.812635.

[4] L. Rossi and E. Todesco, Electromagnetic design of superconducting quadrupoles, *Phys. Rev. Spec. Top. Accel. Beams* **9** *(2006)* 102401, CERN-AT-2006-016-MCS.

[5] A. Tollestrup *et al.*, The development of superconducting magnets for use in particle accelerators: from Tevatron to the LHC, *Rev. Accel. Sci. Technol.* **1** (2008) 185-210, DOI: 10.1142/S1793626808000101.

[6] P. Ferracin *et al.*, Limits to high field magnets for particle accelerators, *IEEE Trans. Appl. Supercond.* **22** (2012) 4003106, DOI: 10.1109/TASC.2011.2181143.

[7] P. Ferracin *et al.*, Magnet design of the 150 mm aperture low-beta quadrupoles for the high luminosity LHC, *IEEE Trans. Appl. Supercond.* **24** (2014), DOI: 10.1109/TASC.2013.2284970.

[8] Q. Xu *et al.*, Design optimization of the new D1 dipole for HL-LHC upgrade, *IEEE Trans. Appl. Supercond.* **24** (2014) 4000104, DOI: 10.1109/TASC.2013.2280812.

[9] G. Apollinari, I. Bejar Alonso, O. Brüning, M. Lamont, L. Rossi, eds., High Luminosity Large Hadron Collider (HL-LHC): Preliminary Design Report. CERN-2015-005, DOI: 10.5170/CERN-2015-005.

[10] HL-LHC ECR WP3. Baseline for the Inner Triplet Main Circuit, EDMS: 1832082 and HL-LHC ECR WP7, energy extraction systems for HL-LHC RCBX circuits, EDMS: 2360296.

[11] S. Caspi *et al.*, Test results of LARP Nb_3Sn quadrupole magnets using a shell-based support structure (TQS), *IEEE Trans. Appl. Supercond.* **19** (2009) 1221–1225, DOI: 10.5170/CERN-2009-001.117.

[12] G. Ambrosio *et al.*, Test results of the First 3.7 m long Nb_3Sn quadrupole by LARP and future plans, *IEEE Appl. Supercond.* **21** (2011) 1858–1862, DOI: 10.1109/TASC.2010.2089586.

[13] H. Felice *et al.*, Design of HQ – A high field, large bore Nb_3Sn Quadrupole Magnet for LARP, *IEEE Trans. Appl. Supercond.* **19** (2009) 1235–1239, DOI: 10.1109/TASC.2009.2019105.

[14] E. Todesco, Quench limits in the next generation of magnets, CERN Yellow Report 2013-006, 2013, DOI: 10.5170/CERN-2013-006.10.

[15] T. Salmi *et al.*, Modeling heat transfer from quench protection heaters to superconducting cables in Nb_3Sn magnets, *CERN Yellow Report* **2013-006** (2013) p. 30–37, DOI: 10.5170/CERN-2013-006.30.

[16] V. Marinozzi *et al.*, Study of quench protection for the low β quadrupole for the LHC luminosity upgrade. *IEEE Trans. Appl. Supercond*. **25** (2015) 4002905, DOI: 10.1109/TASC.2014.2383435.

[17] E. Ravaioli *et al.*, New coupling loss induced quench protection system for superconducting accelerator magnets, *IEEE Trans. Appl. Supercond.* **24** (2014) 0500905, DOI: 10.1109/TASC.2013.2281223.

[18] S. Izquierdo Bermudez *et al.*, Coil end optimization of the low β quadrupole for the high luminosity LHC, Applied Superconductivity Conference 2014, IEEE Trans. Appl. Supercond. 25 (2015), CERN-ACC-2015-0023.

[19] R. Gupta, Tuning shims for high field quality in superconducting magnets, *IEEE Trans. Magn.* **32** (1996) 2069–2073, DOI: 10.1109/20.508569.

[20] P. Hagen, Study of magnetic shimming in triplet magnets, Milestone Report 36 of HiLumi project.

[21] R. Van Weelderen, Superfluid helium cooling, Milestone Report 42 of HiLumi project.

[22] D. Duarte Ramos *et al.*, talk given at WP3 meeting on 28 January 2014.WP3 Web page.

[23] J. Garcia Matos *et al.*, talk given at WP3 meeting on 17 July 2014. WP3 Web page.

[24] M. Karppinen, Corrector magnets for the LHC upgrade phase-1, CERN EDMS 1039976, and R. Ostojic *et al.*, Conceptual design of the LHC interaction region upgrade: Phase I, LHC Project Report **1163** (2008) p. 42.

[25] F. Toral *et al.*, Development of radiation resistant superconducting corrector magnets for the LHC upgrade, *IEEE Trans. Appl. Supercond.* **23** (2013), DOI: 10.1109/TASC.2013.2239698.

[26] G. Volpini *et al.*, Nb-Ti superferric corrector magnets for the LHC luminosity upgrade, *IEEE Trans. Appl. Supercond.* **25** (2015), DOI: 10.1109/TASC.2014.2378377.

[27] T. Nakamoto *et al.*, Model magnet development of D1 beam separation dipole for the HL-LHC upgrade, *IEEE Trans. Appl. Supercond.* **25** (2015) 4000505, DOI: 10.1109/TASC.2014.2361404.

[28] T. Nakamoto *et al.*, Construction of superconducting magnet system for the j-PARC neutrino beam line, *IEEE Trans. Appl. Supercond.* **20** (2010) 208–213, DOI: 10.1109/TASC.2009.2038800.

[29] M. Anerella *et al.*, The RHIC magnet system, *Nucl. Instrum. Meths. A* **499** (2003) 280–315, DOI: 10.1016/S0168-9002(02)01940-X.

[30] Y. Ajima *et al.*, The MQXA quadrupoles for the LHC low-beta insertions, *Nucl. Instrum. Meths. A* **550** (2005) 499–513, DOI: 10.1016/j.nima.2005.04.092.

[31] B. Bellesia, J. P. Koutchouk and E. Todesco, Field quality in low-beta superconducting quadrupoles and impact on the beam dynamics for the Large Hadron Collider, *Phys. Rev. STAB* **10**, 2007, DOI: 10.1103/PhysRevSTAB.10.062401.

[32] B. Bellesia, C. Santoni and E. Todesco, Random errors in superconducting dipoles, 10th European Particle Accelerator Conf. (2006) 2601–2603, CERN-AT-2006-010-MAS.

[33] V. Kashikhin, *et al.*, Design study of 2-in-1 large aperture IR dipole (D2) for the LHC luminosity upgrade Particle Accelerator Conference (2007) 464-6, and G. Sabbi *et al.*, Conceptual Design Study of the High Luminosity LHC Recombination Dipole, 5th International Particle Accelerator Conf., (2014) 2712-4, DOI: 10.1109/PAC.2007.4440246.

[34] P. Fabbricatore *et al.*, talk given at WP3 meeting on 17 September 2014.

[35] S. Farinon *et al.*, talk given at WP3 meeting on 17 September 2014, WP3 Web page.

[36] G. Kirby, J. Rysti, *et al.*, Hi-Lumi LHC Twin-Aperture Orbit Correctors Magnet System Optimisation, *IEEE Trans. Appl. Supercond.* **27** (2017), DOI: 10.1109/TASC.2016.2633424.

[37] J. Rysti *et al.*, talk given at WP3 meeting on 17 September 2014.

[38] G. Kirby *et al.*, Performance of the 1-m model of the 70 mm twin aperture superconducting quadrupole for the LHC insertions, *IEEE Trans. Appl. Supercond.* **11** (2001) 1641.P. P. Granieri *et al.*, Thermally enhanced cable insulation for the Nb-Ti high luminosity LHC inner triplet model, *IEEE Trans. Appl. Supercond.* **22** (2012) DOI: 10.1109/77.920095 and DOI: 10.1109/TASC.2012.2183669.

[39] M. Segreti *et al.*, A Nb-Ti 90 mm double aperture quadrupole for the high luminosity LHC upgrade, *IEEE Trans. Appl. Supercond.* **25** (2015) 4001905, DOI: 10.1109/TASC.2014.2366517.

[40] N. Mariani, P. Fessia, et al., talk given at WP3 meeting on 31 August 2016, WP3 Web page.

[41] HL-LHC ECR - WP12 - Shielded Beam Screens Operating Temperature for the Triplets (Q1,Q2,Q3), correctors package and D1, EDMS: 2112891.

[42] HL-LHC ECR WP15-WP3: Alignment of the D1 separation dipole in IR1 and 5 to maximize available beam aperture, EDMS: 2374033.

[43] HL-LHC ECR - WP15.4 Remote Alignment, EDMS: 1823448.

[44] HL-LHC ECR - WP3 Change of Quadrupole, Sextupole, Octupole and Decapole Correctors Integrated Field, EDMS: 1963788.

[45] HL-LHC ECR - WP3. Need of a connection module LDQD (D1-DFX), EDMS: 2210558.

[46] HL-LHC ECR - WP3. Change of operational temperature in Q5 IR6 from 1.9 K to 4.5K, EDMS: 2117079.

[47] HL-LHC Decision management: WP3 - fine tuning of b6, EDMS: 2019517.

[48] HL-LHC ECR - WP3. Change of Baseline for HL-LHC Warm magnets, EDMS: 1832073.

[49] HL-LHC ECR - WP3 Increase of iron yoke holes diameter from 60 to 61 mm for heat exchangers in D1 and MCQSXF, EDMS: 1865591.

[50] US HL-LHC AUP - MQXFA Final Design Report [US-HiLumi-doc-948], EDMS: 2031097.

Chapter 4

RF systems

R. Calaga[1*], *P. Baudrenghien*[1], *Ofelia Capatina*[1], *Erk Jensen*[1] *and Eric Montesinos*[1]

[1]CERN, Accelerator & Technology Sector, Switzerland
[*]Corresponding author

4 RF systems

4.1 Introduction

The HL-LHC beams are injected, accelerated, and stored to their nominal energy of 7 TeV by the existing 400 MHz superconducting RF system of the LHC.

A novel superconducting RF system consisting of eight cavities per beam for transverse deflection (aka crab cavities) of the bunches will be used to compensate the geometric loss in luminosity due to the non-zero crossing angle and the extreme focusing of the bunches in the HL-LHC.

Due to doubling of the beam currents in the HL-LHC era, an optimal detuning scheme (aka full-detuning) is required to cope with the transient beam loading effects [1][2]. A modulation of the klystron and cavity phase make the phase of bunches with respect to the RF clock to progressively slip along the bunch train, but then recover during the abort gap. With this scheme the klystron power is independent of the beam current and maintained constant over one full turn at the expense of bunch-to-bunch phase modulation. This scheme was experimentally tested in 2016 and operational since then in the LHC during the acceleration ramp and flat-top [3]. During injection of the HL-LHC beams from the SPS in to the LHC, the original half-detuning scheme to strictly preserve the bunch-to-bunch spacing is a pre-requisite [4]. The total available voltage with HL-LHC beams is therefore limited to approximately 6 MV with the available RF power at injection.

Second harmonic RF system at 800 MHz for Landau damping and lower frequency accelerating RF system at 200 MHz in conjunction with the exiting 400 MHz cavities for improved capture from the SPS for intense and longer bunches were studied but are no longer considered for the HL-LHC.

4.2 Crab Crossing and hardware considerations

The HL-LHC will use a 45 m common focusing channel plus a 21 m common drift space and a 6.7 m long common dipole channel on each side of the interaction region (IR), where the two counter-rotating beams share the same beam pipe and have to be separated transversely to avoid parasitic collisions. Separation is accomplished by introducing a crossing angle at the interaction point (IP), which needs to increase with the inverse of the transverse beam size at the collision point in order to maintain a constant normalized beam separation. The non-zero crossing angle implies an inefficient overlap of the colliding bunches at the IP. The luminosity reduction compared to that of a zero crossing angle (head-on collision), assuming a Gaussian distribution, can be conveniently expressed by a reduction factor,

$$R_{\Phi} = \frac{1}{\sqrt{1+\Phi^2}} \ , \qquad (4\text{-}1)$$

where $\Phi = \sigma_z \varphi / \sigma_x$ is the aspect ratio of the longitudinal (σ_z) to the transverse (σ_x) beam sizes multiplied by the half crossing angle φ; Φ is also known as the Piwinski angle [5]. Alternatively, the reduction can be viewed as an increase in the transverse beam size at the collision point to effective beam size given by $\sigma_{\text{eff}} = \sqrt{\sigma_x^2 + \sigma_z^2 \varphi^2}$ and a reduction of the luminous region. For the HL-LHC beam parameters, the reduction compared to the case of a head-on collision can be 70% or larger, depending on the final β^* value and the beam emittance. Therefore, the effective gain in luminosity by simply reducing the beam size at the collision point diminishes rapidly.

To recover the loss, it was proposed [6][7] to use RF deflectors. The time-dependent transverse kick from an RF deflecting cavity is used to perform a bunch rotation, in the crossing plane about the barycentre of the bunch (see Figure 4-1). The kick is transformed to a relative displacement of the head and the tail of the bunch at the IP to impose a head-on collision while maintaining the required beam separation to minimize parasitic collisions. In a local compensation scheme, a downstream RF deflector is used to reverse the kick of the upstream RF deflector to confine the bunch rotation to within the IR. The crab crossing scheme in a global compensation using only a single cavity per beam was successfully implemented at the e^+e^- collider at KEKB in Japan to achieve record luminosity performance [8].

Figure 4-1: Bunches colliding with a crossing angle without crab crossing (left); with the crab crossing (right).

Since the luminosity gain is substantial, the crab crossing scheme is adopted as a baseline for the HL-LHC upgrade. The time-dependent transverse kick can equally be used to adjust the bunch overlap at the IP and therefore allows for a natural knob to control the total number of events per crossing (luminosity levelling), a feature highly desired by the experiments. Levelling by means of collision offsets is already used at LHCb and ALICE. However, a luminosity levelling by a simple variation of the crossing collision angle at the IP will not change the pile-up density, another important parameter for the optimization of the data production for the experiments. More sophisticated means of levelling to control both the instantaneous luminosity and the density of the events along the luminous region by means of crab cavities had been studied for a configuration with 4 crab cavities in 2 cryo-modules per beam and IP side with horizontally and vertically deflecting crab cavities for both beams [9]. However, after the re-scoping exercise in 2016, the crab-kissing scheme studied in Ref. [9] is no longer possible with only horizontally deflecting crab cavities in IR1 and only vertically deflecting crab cavities in IR5.

Since the crossing plane in the two experiments is different, a local crab cavity system is mandatory. The nominal configuration will use a two-cavity cryomodule as the basic unit providing a deflecting voltage of 6.8 MV (3.4 MV per cavity). A total CC voltage of ca. 11-12 MV is required at 400.79 MHz per IP side per beam to perform the complete bunch rotation. Assuming a maximum voltage of 3.4 MV per cavity, four cavities per side per beam per collision point, i.e. a total of 32 cavities is needed for full compensation. However, only half the system, 16 cavities, are to be installed after the re-baselining in 2016, allowing a partial compensation if the crab cavities cannot exceed the design voltage of 3.4MV.

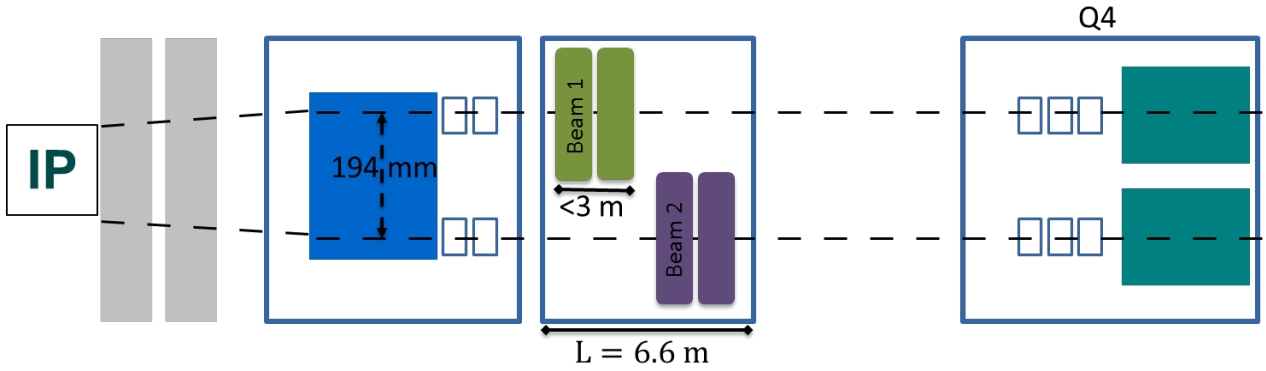

Figure 4-2: Schematic layout of the crab cavities in the LHC Point 1 and 5 w.r.t the interaction point.

Two types of cavities are required: the Double Quarter Wave (DQW), which will be installed around IP 5 for vertical crabbing, and the Radiofrequency Dipole (RFD) which will be installed around IP 1 for horizontal crabbing. The low frequency of 400.79 MHz is required to minimize the RF curvature for the long LHC bunches. The machine constraints near the interaction region require cavities with a transverse dimension compatible with the location of the adjacent beam pipe, which is only 194 mm centre to centre. The RF and machine parameters directly relevant to the crab cavities are shown in Table 4-1. An operating temperature of 2 K is chosen as a baseline. A pressure stability on the cavity surface should be minimized to less than 1 mbar. The static and dynamic heat load is expected to be approximately 30 W to the 2 K bath for a two-cavity module. A cavity vacuum level to better than 10^{-10} mbar is required to assure stable performance.

An input power of 40 kW per cavity is required in CW, up to 80 kW peak may be needed to cope with transients and potential beam loading caused by beam offset. This is provided with an Inductive Output Tube (IOT) amplifier, which can provide 80 kW during up to 1 ms. The low level RF (LLRF) will include a regulation loop around the IOT amplifier (to reduce the RF amplitude and phase noise in a band extending to a few tens of kHz), plus an RF feedback to control the vector sum precisely on the two sides of the interaction region to cancel the crab kick elsewhere in the ring. Eight longitudinal pickups located close to the crab cavities (one per IP per side and per beam) are used to regulate the slow drifts of the deflecting voltage with respect to the average bunch centre. To stay within the specified RF power limits, the total orbit offset including mechanical tolerances must not exceed 1 mm with stable beams at flat-top. The cavity is kept on tune at all times. The resonant frequency should be precisely controlled by a tuning system to a level well below 80 Hz (approximately one tenth of the cavity bandwidth) to be compatible with the RF power limits. To cope with the RF power limits a novel alignment system using the Frequency Scanning Interferometry (FSI) system will monitor the independent cavity positions in all three dimensions to ensure that the mechanical centres between the two cavities after cool-down are aligned within the 0.5 mm tolerance.

Table 4-1: Relevant RF parameters for the HL-LHC crab cavities.

Characteristics	Units	Value
Resonance frequency	MHz	400.79
Bunch length	ns	1.0 (4 σ)
Maximum cavity radius	mm	$\leq$ 145
Nominal kick voltage	MV	3.4
R/Q (assumed, linac convention)	Ω	430
Q_0		$\geq 1 \times 10^{10}$
Q_{ext} (fixed coupling)		5×10^5
RF power (1 cavity)	kW	40
LLRF loop delay	μs	$\approx$ 1
Cavity detuning (if parked, optional)	kHz	$\approx$ 1.0

The cavities are housed in individual titanium helium tanks connected by a 100 mm diameter two-phase He pipe placed above the cavities, along with a 20 mm diameter cool-down bypass lines placed below the tanks. The two-phase pipe ensures that the liquid is fed to the cavities by gravity and is also used as a pumping line for gaseous helium. A saturated helium bath maintains the cavities operating temperature at 2 K. Liquid helium is supplied to the two-phase pipe through a 10 mm supply line. It is proposed to fill the cryostat from one single point at the extremity opposite to the pumping outlet of the two-phase pipe, and to control the He level at about half of the two-phase pipe diameter.

The bottom bypass of 20 mm diameter will be used during cool-down for parallel helium distribution to two helium tanks, allowing for progressive cavity cool-down from the bottom to the top. This bypass will also have the function to equilibrate the quantity of helium between the two tanks in cases when the two-phase pipe will be out of this function (transients – e.g. filling, special tests). The static plus dynamic heat loads are expected to be approximately 30 W to the 2 K bath for a two-cavity module. The cryogenic limits in the LHC are not precisely known at this time. However, the 15 W per cavity heat load at 2 K is small compared to the LHC heat load capacity; the total heat load of the LHC crab cavity systems is estimated at 0.5 kW at 2 K.

The crab cavity system has three independent types of vacuum systems: the cavity vacuum, the adjacent beam pipe, and the cryostat. The two-cavity common vacuum is pumped at room temperature with two ion pumps mounted at each end of the modules. However, at 2 K, the cryogenic pumping of the cavity walls is the dominating feature, with a pumping speed of 10 000 L/s. The background pressure without RF is expected to be much better than 10^{-10} mbar and likely limited by the measurement devices such as Penning gauges. Pressure signals provided for RF control are a hardware interlock from the ion pumps to cut the high voltage and readout from the Penning gauges, one per coupler, to limit the RF power. The cavity vacuum can be isolated by four all-metal valves at the ends of each module (two interior and two exterior to the cryomodule), to maintain vacuum during transport and installation.

The second beam pipe for the non-deflected beam has to pass through the cavity helium vessel due to its proximity. It is planned that this will be made of a standard HL-LHC cold vacuum chamber configuration using a beam screen. The use of carbon coating in the warm regions near the crab cavities to reduce the pressure and to avoid electron cloud effects is currently under study; the SPS experience revealed no observable contamination of the cavities. A new solution for RF continuity at the cryostat extremities using deformable RF bridges and corresponding vacuum instrumentation is used.

The insulation vacuum is less demanding in terms of pressure, the modules being pumped to 10^{-5} mbar before being cooled down. When cold, the insulation vacuum also benefits from the cryogenic pumping of the cold surfaces and the operating pressure will decrease to10^{-7} mbar. Turbo molecular pumps are used, and pressures are measured using Penning gauges.

Due to the large stored energy of the beam (>700 MJ), the transient behaviour of the crab cavities is of concern. The crab cavity system will be equipped with several levels of interlocks both for machine protection and to protect the RF system itself. Slow and fast interlocks, including specific RF interlocks (reflected power, signal level, arc detection, etc.) will ensure safe operation under all conditions and cope with transients; the interlock system will be fully embedded in the overall machine interlock system. All RF systems, including amplifiers, circulators, and loads are designed to withstand full reflection in the case of a malfunction in the RF chain.

4.3 Crab cavity RF system

4.3.1 RF cavity

In order to sustain the surface fields at a kick voltage of 3.4 MV per cavity for the LHC in continuous wave (CW), the deployment of superconducting technology is essential. Space restrictions led to the concept of ‘compact’ cavities. An intense R&D programme led to the two present designs for vertical and horizontal kick, the Double Quarter Wave (DQW) and the RF Dipole (RFD).

The final mechanical design of the cavities including all external interfaces is shown in Figure 4-3.

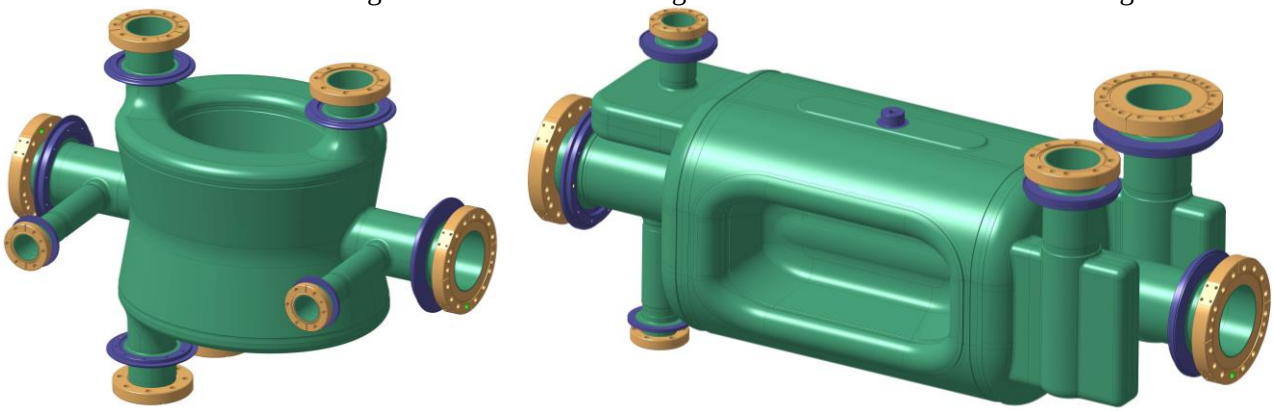

Figure 4-3: Schematic view of the cavity with interfaces (left) DQW; (right) RFD.

The longitudinal impedance of the operating mode of these cavities vanishes on axis, i.e. there is no beam loading for a centred beam; the RF generator does not exchange energy with the beam. The RF power required to maintain the required cavity voltage thus only depends on the cavity wall losses and remains small for a superconducting cavity with large Q_0 and Q_L. The input coupling and thus Q_L should be chosen to just allow sufficient bandwidth for unavoidable frequency transients due to external perturbations.

The situation is different for a beam circulating at an offset Δx. The beam-induced voltage due to an orbit offset is given by

$$\Delta V = I_\mathrm{b} \cdot \frac{R_\mathrm{T}}{Q_0} \cdot Q_L \cdot \Delta x \,, \qquad (4\text{-}2)$$

where I_b is the average beam current, R_T is the transverse shunt impedance in Ω/m. In deflecting cavities operated in the crabbing mode, kick voltage and beam current are in quadrature ($\phi_\mathrm{s} = 0$, synchrotron convention). With the Q_L resulting from the bandwidth requirement discussed above, sufficient RF power is required to compensate for the resulting beam loading caused by unavoidable orbit offsets. Figure 4-4 shows the required forward power as a function of Q_L for a beam that is centred (red), off-centred by 1 mm (green) and 2 mm (blue). It is expected that the orbit will be kept within 0.5 mm at top energy of the LHC; further 0.5 mm should be added for mechanical tolerances. At injection and ramp, the operating voltage is kept at 10-15% of the nominal voltage. Therefore, beam offset tolerance can be relaxed to 3 mm with the available RF power.

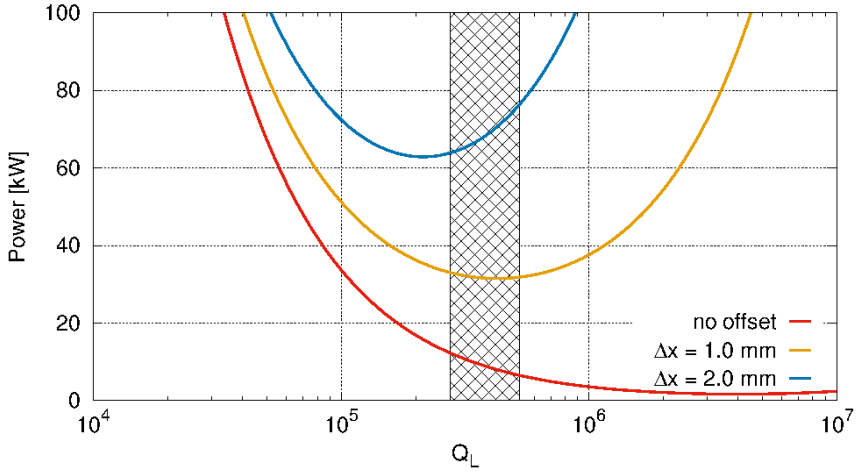

Figure 4-4: Forward power vs. cavity Q_L for centred (red), 1 mm offset (green), and 2 mm offset (blue) beams. Assumed $R_\mathrm{T}/Q = 430\,\Omega$, 3.4 MV RF, 1.1 A DC.

For a beam offset below 1 mm, the required RF power has a broad minimum ($\leq$ 40 kW) for Q_L in a range of $3.0 \cdot 10^5$ to $1.5 \cdot 10^6$. Selection of an optimal Q_L value in this range is a compromise between the feasible tuning precision and the minimization of the field fluctuations from the amplifier electronics: for larger bandwidth (leading to more stability), lower Q_L values are favoured – the crosshatched area in Figure 4-4 was chosen as a trade-off between bandwidth and required power. A lower Q_L is also favourable for the tuning system as it relaxes the precision needed by a mechanical system. The input RF power of 80 kW specified above will leave enough margin to cope with the specified offset and with short excursions even beyond this limit.

The RF power coupler was designed in view of the HL-LHC requirements; additional mechanical constraints were introduced to limit the variances between the two types of cavities to have a common high power coupler concept. The adopted crab cavity power coupler will use a single coaxial disk-type window to separate the cavity vacuum and the atmospheric pressure. The antenna shape is specific to each cavity type as the coupling mechanisms for the different cavities are not identical. However, a common cavity flange followed by the ceramic and outer tube is imposed. The inner antenna has a 27 mm diameter with an outer coaxial line of 62 mm diameter to sustain a maximum power of approximately 100 kW. The outer tube is made of Stainless Steel 316LN with the inner surface coated with copper. The vacuum-to-ambient pressure separation is achieved with a coaxial ceramic window (Al_2O_3) with an outer flange made of titanium. The rest of the items are built from massive Oxygen Free Electronic (OFE) 3D forged copper blocks. The coupler body is made of a conical with an increased diameter near the ceramic to limit arcing with the primary aim to maximize the ambient pressure side diameter while keeping the 62 mm dimension for the input antenna on the vacuum side. A coaxial-to-waveguide transition is implemented with a half-height WR2300 waveguide with proper impedance matching (see Figure 4-5).

The ambient pressure side of the coupler will be air-cooled while the antenna itself will be water-cooled. The waveguide design includes the possibility of DC polarization in order to suppress multipacting.

Each coupler is equipped with one single port for a vacuum gauge. The vacuum gauge is mandatory to protect the window during conditioning as well as during operation. It will be oriented along the air line in order to minimize the cryomodule flange size.

Special quarter-wave test boxes to condition the couplers were designed (see Figure 4-5) and built. The coupler ports are designed to come out on the top of the cryomodule, perpendicular to the beam axis for ease of integration with the WR2300 waveguide transition. The cavity's helium vessel is designed to withstand the weight of the couplers and the waveguide (approximately 35 kg). The alternating crossing angle scheme will require that the orientation of a coupler assembly be robust for horizontal and vertical deflections.

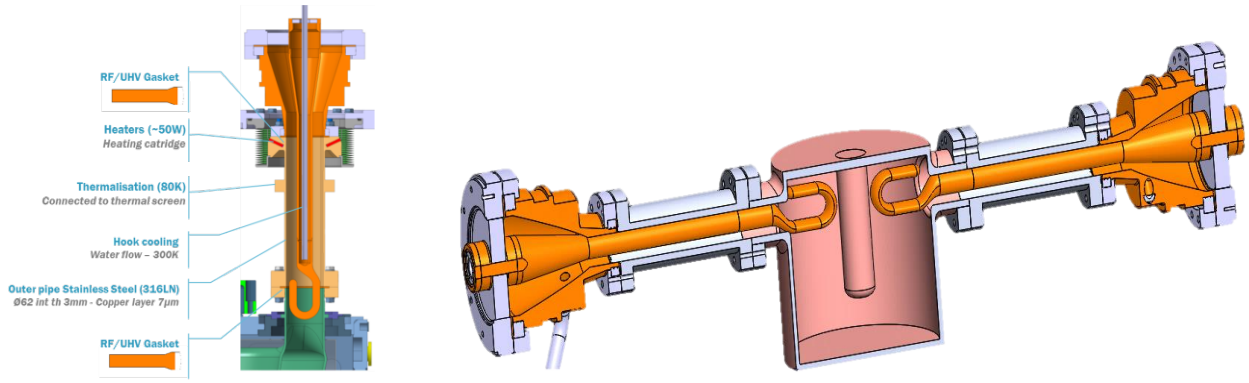

Figure 4-5: (left) Input coupler assembly; (right) quarter wave FPC test box for RF conditioning.

On resonance, the large impedance of the fundamental deflecting (dipole) mode is cancelled between the positive and negative sideband frequencies, which are symmetric around ω_{RF}. The active feedback will reduce the growth rates by a large factor.

For higher order modes (HOMs), both narrowband and broadband impedance should be minimized during the entire machine cycle as the LHC will accelerate and store beams of currents exceeding 1.1 A (DC). Tolerances are set from impedance thresholds estimated from Ref. [11]. The tolerable longitudinal impedance has approximately a quadratic behaviour vs. f in the region of interest with its minimum between 300 and 600 MHz. The total maximum allowed impedance from each HOM, summing over all cavities in one beam, assuming that the HOM fall exactly on a beam harmonic, is specified to be $< 200\ \mathrm{k\Omega}$, so if all 4 cavities have identical HOM frequencies, the longitudinal impedance must not exceed $50\ \mathrm{k\Omega}$ per cavity. The same limit was imposed for higher frequencies. Modes with frequencies above 2 GHz are expected to be Landau-damped due to natural frequency spread and synchrotron oscillations.

In the transverse plane, the impedance threshold is set by the bunch-by-bunch feedback system with a damping time of $\tau_{\mathrm{D}} = 5\ \mathrm{ms}$ [11]. Four effective cavities per beam are assumed due to the two different cavity types with different HOM spectra. The single bunch studies show that integrated R_{T}/Q over the frequency for all the HOMs per cavity should be suppressed to below 4 kΩ/m (without accounting for β-function) from stability considerations [13]. From multi-bunch considerations and assuming the pessimistic case that the HOM frequency coincides with the beam harmonic, the maximum total transverse impedance in each plane is set to be $1\ \mathrm{M\Omega/m}$ [13]. Analogous to the longitudinal modes, frequencies above 2 GHz are expected to be Landau-damped due to natural frequency spread, chromaticity, and Landau octupoles.

Due to the very tight impedance thresholds, the distribution of HOM frequencies as mentioned above due to manufacturing errors can help relax the tolerances. The beam power deposited in the longitudinal HOMs can become significant when the frequencies coincide with bunch harmonics. The HOM couplers were dimensioned to accept a maximum of 1 kW to be able to cope with the HL-LHC beams [12].

The first design goal of the HOM filter is to block the transmission of the main deflecting mode, while transmitting all remaining HOMs. Several HOM coupler designs were developed and optimized for different cavity geometries. High-pass filter designs, incorporating a notch filter at the fundamental frequency, are shown in Figure 4-6 with both HOMs using hook-like antennae to couple to the HOMs. The DQW in addition incorporates a special high frequency antenna on the cavity beam pipe while the RFD uses a second hook like antenna mounted on a waveguide stub to damp transverse modes in the plane perpendicular to the deflecting mode.

Simulations show that the HOM coupler must have a superconductive surface due to the high fields of the fundamental mode. A second design constraint requires that HOM couplers be able to effectively remove the power in the HOMs (up to 1 kW) and the heat dissipated by the fundamental mode in the inner part of the HOM coupler. High purity bulk niobium with sufficient cooling can ensure this. The required cooling may be possible by conduction, but active cooling with superfluid liquid helium or immersion in a small He tank is used.

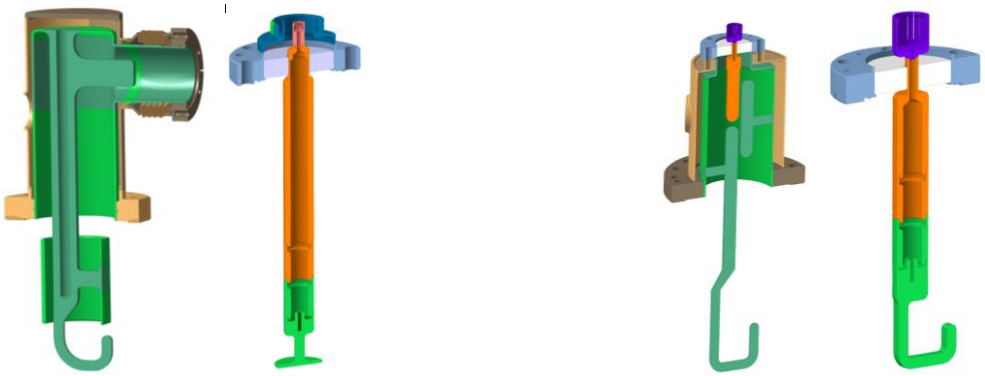

Figure 4-6: HOM couplers for the DQW (left) and the RFD (right).

The main deflecting field of the chosen crab cavity geometries contain higher order components of the main deflecting field dependence due to the lack of azimuthal symmetry. Due to the placement of the cavities

at high beta-function locations, the higher order components of the main deflecting mode can affect long-term particle stability. RF multipole components b_n of the RF deflecting field can be approximated and hence expressed in a similar fashion to magnets [14]:

$$b_n = \int_0^L \frac{1}{qc} F_\perp^n \, dz \ \ [\mathrm{T\,m^{2-n}}] . \qquad (4\text{-}3)$$

The quadrupolar component b_2 is zero in the case of perfect symmetry, but due to fabrication errors and ancillary components it is non-zero in practice. It must be smaller than 10 units resulting in a tune shift in the order of $\Delta Q \approx 10^{-4}$. The first systematic multipole is the sextupolar component, b_3. Long-term simulations with the optical functions of the HL-LHC indicate that the b_3 component should be limited to approximately 1000 ±10% units, which results in an acceptable degradation of the dynamic aperture below $1\ \sigma$ for orbit offsets of 1.5 mm [11]. Both the DQW and the RFD designs are below the specified tolerance for b_3. No specifications are yet provided for higher order terms, but it is expected that they can be controlled to smaller values than the neighbouring D2 dipole magnet.

For $n \geq 4$, assuming a very approximate scaling of the additional kick from an orbit offset via b_n, the b_n must be kept below $\propto O(10^n)$. Better estimates are pending as results from long-term tracking are needed to confirm the exact specifications.

When the cavity contains RF fields, then there is a Lorentz force on the cavity surface resulting from the high radiation pressure on the cavity walls. This results in a detuning of the cavity frequency. The Lorentz force detuning is kept small (≤ 0.6 kHz) at the nominal field.

Another common problem in complex RF structures is multipacting. This is a resonant phenomenon where the electrons will absorb RF power, limiting the field to a finite level and depositing additional heat load in the walls. Multipacting was modelled in all cavities and couplers using two codes with different methodologies to identify multipacting. CST Particle Studio® uses particle tracking with accurate secondary emission models to simulate the growth in electrons with time, while Track3P tracks a single particle in the RF fields and looks for resonant trajectories.

In CST, three secondary electron yield (SEY) models were used to look at the effect of surface cleanliness. The models were for wet-treated, baked, and processed niobium surfaces. While multipacting in all cavities was found for the wet-treated and baked models, no multipacting trajectories were found for the processed surface, suggesting that any multipacting would be soft and easily processed. Similarly, Track3P found multipacting at low field. This is in good agreement with the results from the prototype tests, where multipacting was observed and could be processed away easily.

4.3.2 Dressed cavities

4.3.2.1 Temperature choice

The Bardeen-Cooper-Schrieffer (BCS) resistance of niobium at 4.5 K and 400 MHz is around 50 nΩ, which is more than 10 times larger than the value at 2 K. The complex shapes of the cavities may also be susceptible to microphonics caused by liquid He boil-off, hence operation below the lambda point of He is preferred. For these reasons operation at 2 K is baseline. This will require the provision of liquid He at 2 K to the crab cavity location in the LHC. The dynamic heat load limits for the LHC are specified to be less than 7 W per cavity at 2 K.

4.3.2.2 Cavity interfaces and cold mass

The cavities were dimensioned to cope with several mechanical constraints: ensure elastic deformation during maximum pressure as well as during all transport and handling conditions; maximize tuning range; minimize sensitivity to pressure fluctuation; avoid buckling due to external pressure; and maximize the frequency of the

first mechanical natural mode. The superconducting resonators are fabricated from bulk niobium sheets by electron-beam welding of deep-drawn parts. A final thickness of 4 mm was calculated to be acceptable in order to cope with all the mechanical constraints as well as minimizing the cost of cavity production. The cavities are bath-cooled by saturated superfluid Helium at 2 K. Each cavity is equipped with (aka dressed cavity): a Helium tank, internal magnetic shield, a tuning system, a fundamental RF power coupler, a field probe, and two or three HOM couplers.

4.3.2.3 Helium vessel and dressed cavity unit

The Helium tank will contain saturated superfluid Helium at 2 K. The geometry of the Helium tank has been determined to maximize heat extraction while optimizing the quantity of the Helium to be used.

The Titanium grade 2 was chosen as the optimum material for the Helium tank, allowing for rigid connection of cavity ports to the Helium vessel. The tank is bolted with additional leak proof welds to minimize the stress on the cavity during the assembly of the Helium vessel Figure 4-7.

The Helium tank has a structural role, and its rigid connection to the cavity ports ensures optimum boundary conditions for the cavity during mechanical loading, in particular during maximum pressure loading and tuning. The Helium tank geometry was chosen to limit the maximum stress on the cavity to tolerable values [11]. Figure 4-7 shows a qualitative stress distribution in the cavity wall during maximum pressure for the DQW cavity. The red colour indicates only small areas of high stress, which are tolerable. This distribution, as well as the maximum values, are directly influenced not only by the cavity geometry but also by the Helium tank configuration.

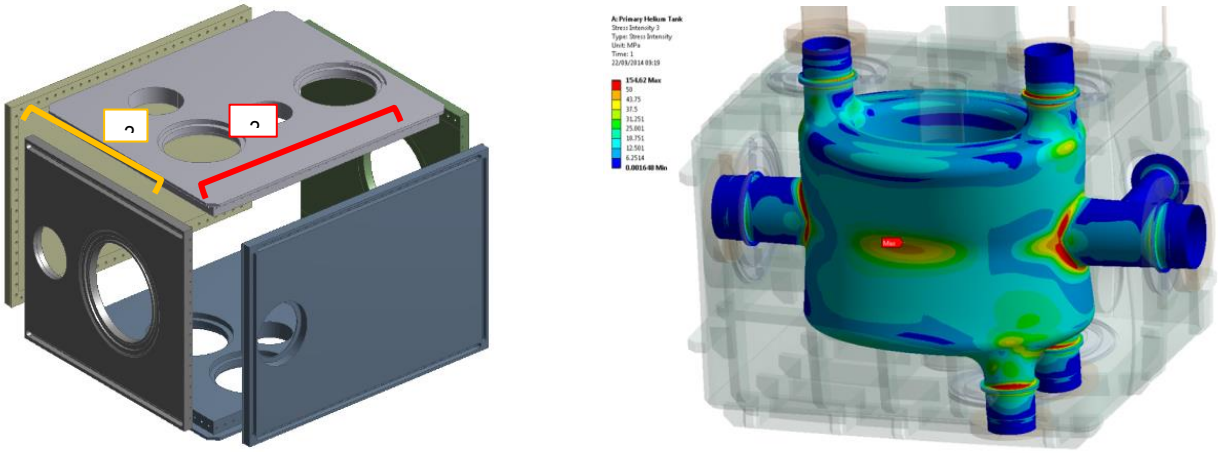

Figure 4-7: Schematic of the Helium vessel assembly of the bolted design (left). Mechanical stress induced by maximum pressure on the DQW cavity inside its Helium tank (right). Red indicates regions with highest stress, which can be tolerated if confined to small areas.

A major concern for the mechanical design was the transitions from the Helium tank to all of the adjacent components, in particular the main coupler, HOM couplers, and the flanges for connection to the beam pipes and Helium pipes. All flange connections are stainless steel to stainless steel connections. Due to its proximity, the second beam pipe had to be integrated inside the Helium vessel and consequently will be at 2 K; it will use the standard HL-LHC cold vacuum chamber configuration with a beam screen. A schematic view of the dressed DQW and RFD cavities inside their Helium tanks and equipped with the required ancillary equipment are shown in Figure 4-8 and Figure 4-9.

Figure 4-8: (left) The DQW cavity inside its Helium tank with the field probe port (front), beam port (right) and tuner frame around. (right) Sectional view of the DQW cavity inside its Helium tank with the power coupler (top right, orange), HOM coupler (left, top and bottom), and tuner (centre, top, and bottom). Colour coding with cavity in green, HOM couplers and field antenna in magenta, Helium vessel in light-blue, power coupler in orange, tuner frame in blue, actuation system in yellow

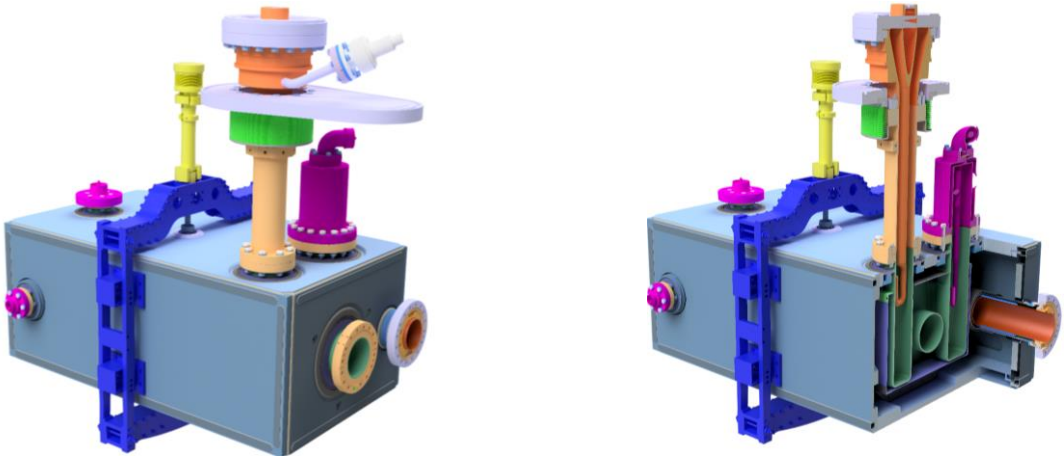

Figure 4-9: (left) The RFD cavity inside its Helium tank with the field probe port (centre left), beam port (centre right), tuner frame around Helium vessel and tuner actuation (top centre). (right) Schematic sectional view of the RFD cavity inside its Helium tank with the power coupler (orange) and HOM couplers (violet).

4.3.2.4 Frequency tuning

The final resonance frequency of the cavity will depend on a number of fabrication and handling steps and cool-down (shifts by hundreds of kHz). A ‘slow’ mechanical tuning system is required to compensate for the uncertainties of the above steps by altering the cavity shape – this will dominate the tuner requirement. At 2 K it must be possible to tune the cavity to $f_{\mathrm{res}} = f_{\mathrm{operation}} \pm \Delta f_{\mathrm{LFD}}$, where Δf_{LFD} denotes Lorentz force detuning occurring during cavity filling. The operational tuning range required in the LHC is approximately a few kHz. A large tuning range (≈ ±200 kHz) is specified to cope with frequency variations from cool-down and other mechanical deformations. However, the resolution of the tuner should allow at least ten steps inside the cavity bandwidth (≈ 800 Hz); backlash and hysteresis must be small. Both the large tuning range and resolution was successfully demonstrated in the SPS beam tests with the DQW cryomodule.

The tuning system, similar for both cavities (DQW and RFD), is shown in Figure 4-8 and Figure 4-9. It consists of an actuation system that is placed outside the cryomodule, and operated at room temperature and at atmospheric pressure, which makes it accessible and thus maintainable. The actuation system consists of a

stepper motor, a harmonic gearbox, a roller screw, and linear guide bearings. The concept is based on a design developed and already in use at JLAB. The details of the prototype actuation system are shown in Figure 4-10. Since the cavity will be operated in continuous wave mode and frequency variations are expected to be small, active tuning is not needed in the final design.

A symmetric deformation is thus applied simultaneously to the top and bottom of the cavity.

A stepper motor drives with a high resolution (1.8 deg/step) a harmonic gearbox with a 100:1 ratio. A roller screw, transforms the rotation into a linear motion, guided by linear roller bearings on precision guides. The estimated mechanical resolution of the tuning system at the connection to the cavity is estimated to be in the order of 10nm or less, which is equivalent to a few tens of Hz for both cavities, allowing for at least 10 micro-steps inside the cavity RF frequency bandwidth. The cryostat vacuum exerts a non-negligible force on the tuner mechanism, as it remains floating with respect to the vacuum vessel. A pressure compensation feature is added to minimize this force.

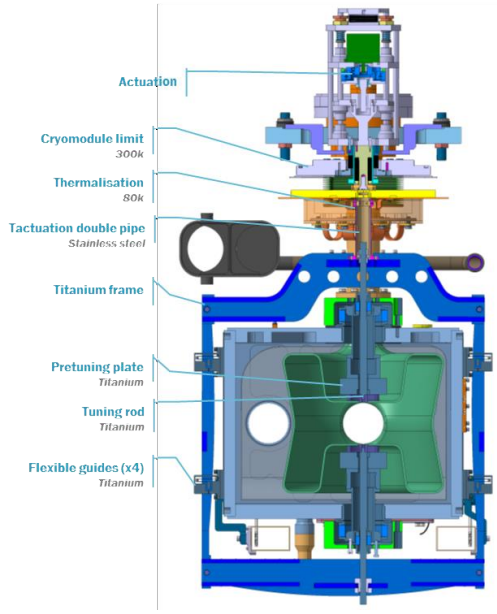

Figure 4-10: (a) Cross-sectional view of the tuning system for the DQW cavity. (b) Actuation system of the prototype tuning system for DQW and RFD cavities.

Low frequency mechanical resonances (below 150 Hz) should be avoided to minimize cavity perturbation due to both Helium pressure fluctuations $\mathcal{O}(1\ \mathrm{mbar})$ and external noise sources. Resonances above 150 Hz are considered to be benign.

4.3.3 Cryomodule

Machine architecture and integration studies for the LHC led to the choice of housing two individual cavities in one stand-alone cryomodule, individually connected to a cryogenic distribution line cryostat running in parallel with the main line. The nominal configuration will use a two-cavity cryomodule as a basic unit. As a consequence, a total of eight cold-to-warm transitions for the beam tube and two connections to the cryogenic distribution line are required for one side of an LHC interaction region (Figure 4-11).

The length of the cryomodule depends on the cavity type and, for the longest cavity, results in a total required space of 7.4 m for four cavities in 2 cryomodules (6.9 m for four cavities DQW) per side of the LHC interaction region for both beams including gate valves from the interconnection plane, as shown in Figure 4-11. For each two-cavity module, two gate valves outside the cryomodule vacuum (see Figure 4-12 right) and corresponding vacuum equipment for pumping and monitoring outside at ambient temperature are foreseen.

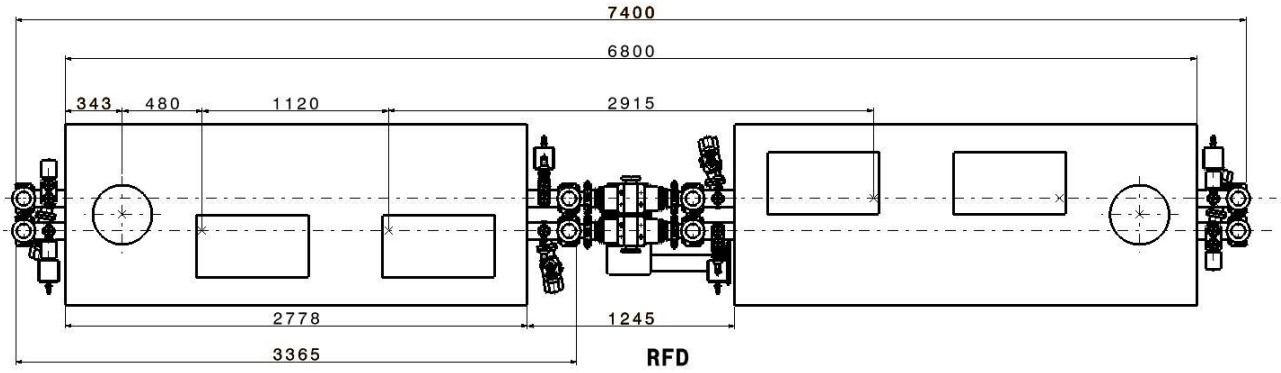

Figure 4-11: Cryomodule layout for one side of the interaction region in the LHC for the RFD cryomodule.

A detailed view of the cryomodule containing two DQW and RFD cavities is illustrated in Figure 4-12. The fixed RF coaxial coupler, with a single ceramic window, providing 40 kW average power, is mounted onto the cavity via a ConFlat® flange assembly equipped with a specific vacuum/RF seal designed at CERN and widely used elsewhere.

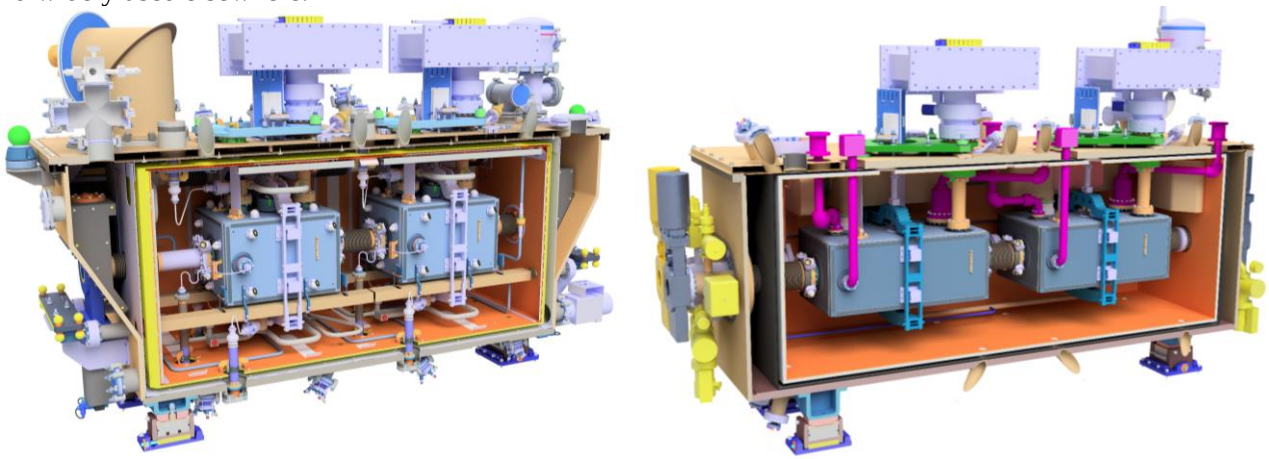

Figure 4-12: Cross-section view of the cryomodules for DQW cavity (left) used for the SPS tests; Conceptual design of the RFD cryomodule of HL-LHC configuration (right). Note that the RF, cryogenic, vacuum and survey circuits are under development not explicitly shown.

The RF coupler is mounted on the cavity in the clean room, constraining the assembly of subsequent components of the cryomodule due to its size. The vacuum vessel allows the possibility of cavity alignment with optical devices (laser trackers, for example) while making fine adjustments through the adjustable supports before closing the cryomodule.

The cavity supporting concept uses the external conductor of the RF coupler as the main mechanical support of the dressed cavities. An additional supporting point is used to keep cavity alignment stability within requirements. In the RFD cavity, the power coupler is transversely offset from the cavity axis, which requires additional vertical support, as shown in Figure 4-12.

The cryomodules are designed to have a rectangular outer vacuum vessel with removable side panels such that the dressed cavities remain accessible [15]. All external connections except the beam pipes are on the top of the cryomodule. The cavities are supported by the power coupler outer tube. This allows easy access to the cavities and ancillaries, as required for a prototype. The designs for both cavity variants are kept as similar as possible.

4.3.4 Magnetic and thermal shielding.

Assuming a cavity geometric factor G ≈ 100 Ω, the additional surface resistance due to trapped flux R_{mag} is required to be below 1–2 nΩ in order to stay in the shadow of the total surface resistance specification of 10 nΩ. To achieve this, magnetic shielding in the cryostat should reduce the external magnetic field on the outer surface of the cavity by a factor of at least 100 (reducing the effective earth's magnetic field to <1 μT).

The external warm magnetic shield is made of 3 mm thick mu-metal and will be directly attached to the vacuum vessel. This layer on its own, is not sufficient to completely shield the earth's magnetic field to the required level. Figure 4-13 (right) shows the magnetic field amplitude inside a two-cavity cryomodule without an internal shield for an applied external field of 60 μT in the longitudinal direction. A second shield is required close to the cavity. In order to reduce the size of the holes in the internal shield the cold magnetic shielding will be integrated inside the Helium vessel, as presented in Figure 4-13. The internal shield is 1 mm thick and will be made from Cryoperm® or Aperam Cryophy®. Magnetization of both materials is adversely affected by mechanical stress. Hence, degradation of the shielding material during assembly and handling should be carefully studied and monitored. The stress on the shield is kept to less than 150 MPa. It is possible that this may affect the magnetization locally, but the effect is comparable to that of a small hole in the shield. Simulation results from OPERA, assuming the worst-case field orientation, show that the use of the proposed two-layer shielding solution to achieve magnetic fields well below 1 μT is feasible, as shown in Ref. [16].

The absence of mechanical contact between the shield and the string of cavities eliminates the risk of interference with the alignment of the cavities induced by differential contractions and cooling transients. The cryomodule contains a single thermal shield, actively cooled in the LHC between 50 and 80 K by a cryogenic cooling line containing pressurized Helium gas. A 30-layer prefabricated Multi-Layer Insulation (MLI) blanket protects the thermal shield whereas a 10-layer blanket is mounted around each Helium vessel.

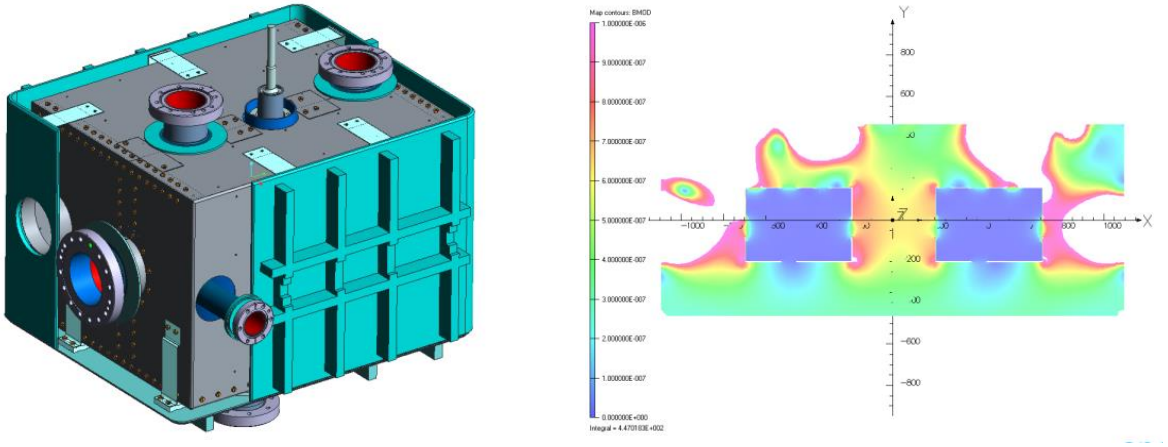

Figure 4-13: (left): Concept of the cold magnetic shielding inside the Helium vessel; (right): magnetic field amplitude inside the two-cavity CM without the second internal cold magnetic shield, scale 0 to 1 μT. An external field of 60 μT in the direction parallel to *X* (longitudinal) is used.

4.3.4.1 Cavity Alignment and support

Successful operation of the RF cavities depends on their correct position. The transverse and longitudinal alignment tolerances described in the LHC performance requirements [11] define the configuration constraints:

- Cavity rotation in the X-Y plane ("roll", Rz, Figure 4-14) – it is required that this rotation has to be < 0.3º= 5.2 mrad (2 σ) per cavity;
- Cavity "yaw" (R_Y) and "pitch" (R_X) with respect to the cryostat axis should be less than < 1 mrad = 0.057º (3 σ), Figure 4-14;

- Transverse displacement of cavities w.r.t each other inside a cryomodule: intra-cavity alignment in the transverse plane with respect to the cryostat axis should not exceed the 0.5 mm (3 σ) tolerance set by beam loading and multipolar specifications.

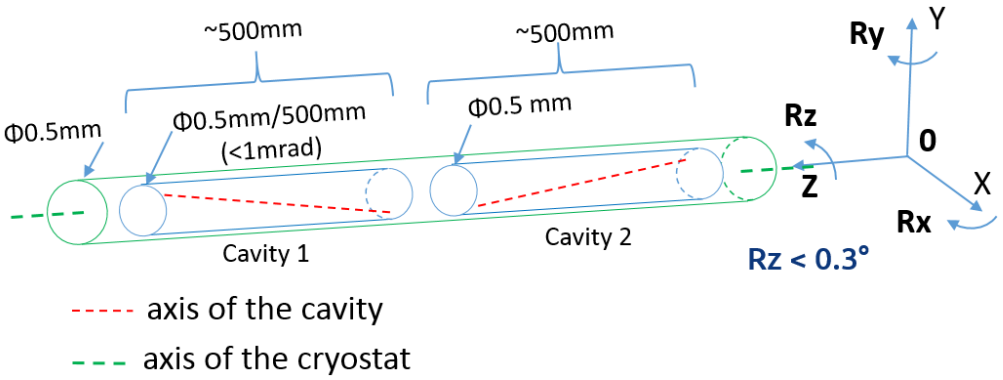

Figure 4-14: Crab-cavities alignment tolerances inside the cryostat.

The dressed cavity's geometry can only be measured accurately by means of Coordinate Measurement Machines (CMM) at room temperature. After cool-down, the CMM data is corrected through models using the materials contraction coefficients. The temperature gradient between the sensor head and the object may have impact on the result of the measured values. Therefore, non-contact methods are preferred. The components of the monitoring system will have to be radiation hard and keep stable properties over time. Before operation, the orientation and position of the cavity is adjusted by means of a plate rigidly connected to the dressed cavity. Such a plate is supported isostatically in 3 points (Figure 4-15). Its position and altitude can be modified by setting the position of these 3 support points. The rigid connection between the cavity and the alignment plate is obtained by means of the fundamental power coupler (FPC) and a set of additional supports as shown in Figure 4-15.

A 'blade' type flexure arrangement is used for the supporting system on the dressed cavities. This arrangement gives an increase in overall stiffness whilst still allowing for thermal contraction on cool-down to 2 K towards the fixed point, which is the input coupler.

The FSI system is chosen as a baseline solution crab cavity alignment system in the LHC [18]. The FSI system offers absolute interferometric distance measurement capability at sub-micron level. Only passive components (mirror, collimator, fibres) are needed at the points of measurement, which makes the application suitable for a high radiation level of operation. FSI is a measurement technique that allows the determination of absolute distances (0.2-20 m) with high accuracy with a measurement uncertainty (95%) of 0.5 µm/m. The FSI unit consists of a reference interferometer and a measurement interferometer that use tuneable lasers (from 1410 nm to 1510 nm). Each cavity features several FSI heads and several lengths between the FSI system heads and all the reflective targets are measured in order to determine the position of the dressed cavities (Figure 4-15). To verify the performance of the FSI system during the preliminary prototype tests, a second solution based on the Brandeis CCD Angle Monitor (BCAM) was used in the SPS DQW tests [19]. An improvement from the SPS system using multiple targets for added reliability and robust targets is under study for the eventual use in the HL-LHC.

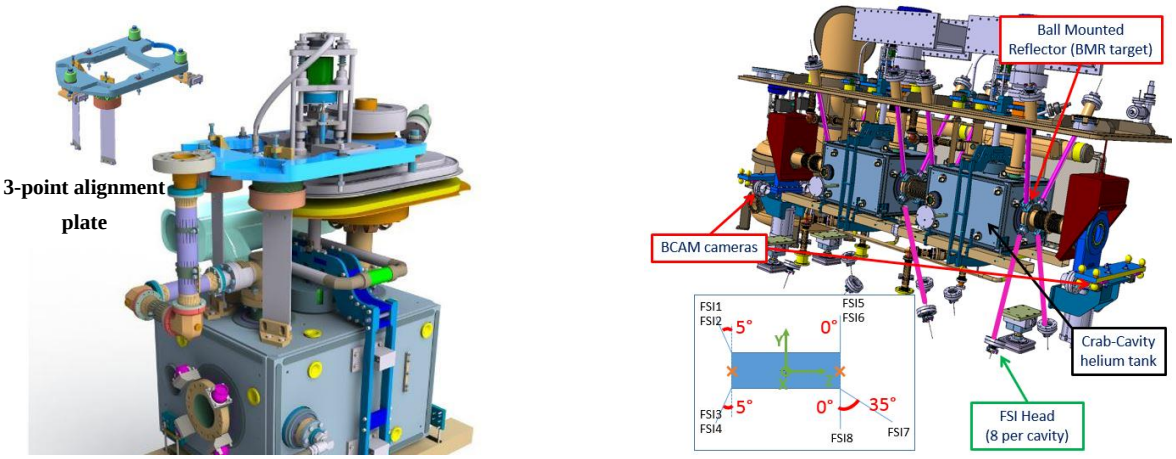

Figure 4-15: (left) Alignment plate in blue with the supports used for attitude and position actuation. (right) Frequency scanning interferometry (FSI) system for alignment monitoring.

4.3.4.2 Vacuum vessel

The main constraints in the design of the vacuum vessel are the integration steps. The shape and the openings must allow the assembly and positioning of all systems in their right location. The dimensions of the vessel have to conform to the maximum available envelope in the LHC tunnel, including all systems external to the vacuum vessel, Figure 4-16:

- 3365 mm longitudinally for the RFD, 3110 mm for the DQW.
- 1080 mm laterally (and proper position with respect to the beam for both axis).
- 2350 mm height (1400 mm above the beams, 950 mm below).

The detailed design also depends on the deformation induced by the difference of pressure between the outside (atmosphere) and the inside (vacuum); the design should limit the deformation to a minimum. Special care is required at each interface with the dressed cavity through the support and alignment. Figure 4-17 shows a trapezoidal concept adopted for the SPS tests with a top plate assembly of the dressed cavity string which is lowered into the vacuum vessel.

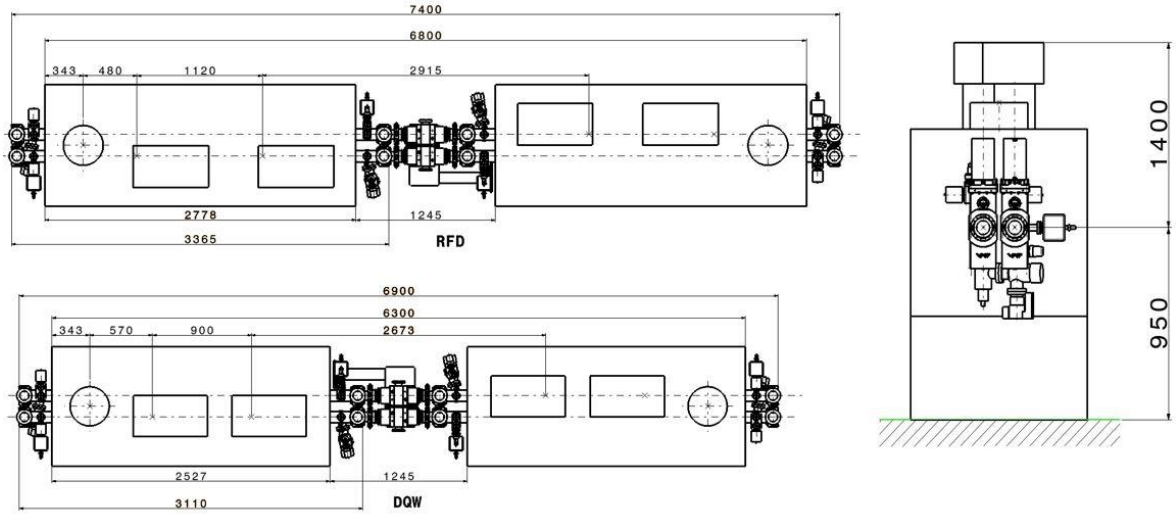

Figure 4-16: A section layout in the LHC for Beam 2 and Beam 1 with a two-cavity cryomodule (left). Maximum vertical envelope for the cryomodules including the RF and cryogenic services with interfaces on the top (right).

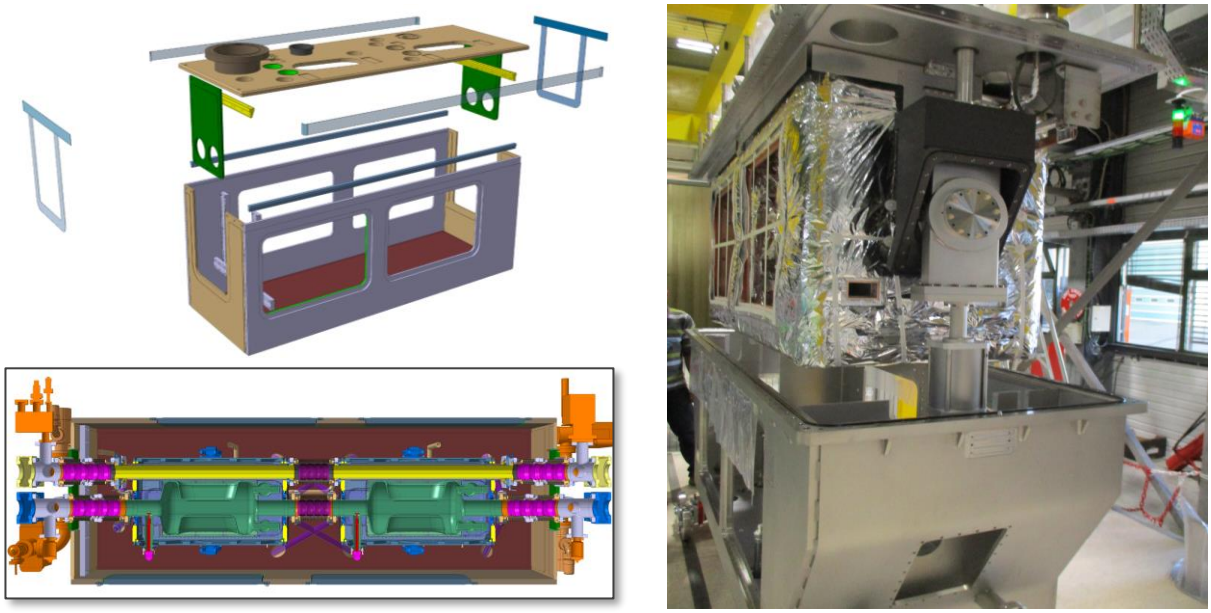

Figure 4-17: The design of the vacuum vessel for the HL-LHC using a welded design including the provision for the adjacent beam pipe (left top); Cross-sectional view of the cryomodule including the vacuum interfaces and cold-to-warm transitions (left bottom); Assembly concept of the SPS-DQW dressed cavity string on the top plate of the vacuum vessel (right).

4.3.5 RF powering and control architecture

The overall architecture and approximate volume of the RF infrastructure is shown schematically in Figure 4-18. A common underground service gallery will host the ensemble of the RF services (see Chapter 15). The circulators and RF loads are placed in an RF service gallery directly above the LHC tunnel with 1m diameter pits connecting the RF power lines. The circulator to cavity transmission lines will be waveguide WR2300 whilst amplifiers to circulators transmission lines will be coaxial lines. The RF gallery is then connected to the main service gallery via a perpendicular tunnel, which is used to host power amplifiers and LLRF and also used for passage (see Figure 4-19). The caverns shall be accessible at any time and adequate shielding is foreseen.

An independent powering system using SPS-type 400 MHz IOT, of 40 kW-CW with 80 kW peak is assumed for the integration studies including the transmission line losses of approximately 0.8 db. Recent advances in solid-state technology is being developed have opened the door for a baseline change as the baseline for the crab cavity RF powering, to providing a flexible platform based on solid-state technology while retaining a potential back up option of IOTs as used for the SPS tests.

The IOTs provide adequate power overhead in a compact footprint. This scheme would also allow for fast and independent control of the cavity set point voltage and phase to ensure accurate control of the closed orbit and the crossing angle in the multi-cavity scheme. Most importantly, fast control of the cavity fields will minimize the risk to the LHC during an abrupt failure of one of the cavities, ensuring machine protection before the beams can be safely extracted. For such fast and active feedback, a short overall loop delay between the RF system and the cavity is required [10].

To provide strong feedback, the low-level RF system requires the total loop delay to be approximately < 2μs, including the group delay from the driver, amplifier, circulator, and cable delays. Therefore, a distance of less than 100 m is desired for the separation between the amplifier, electronics, and the cavity in the tunnel. Such a short delay is already in place for the Acceleration Cavities main RF system (ACS) in P4 (650 ns loop delay) with a service gallery running parallel to the tunnel.

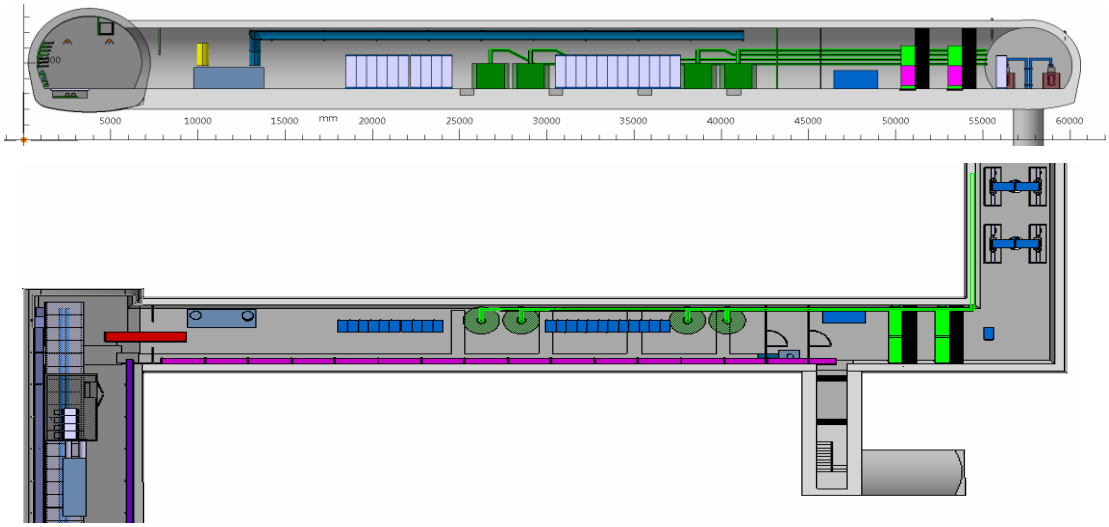

Figure 4-18: Schematic of the RF system layout (four per IP side) in the underground cavern above the LHC tunnel lateral view (top); and top view (bottom); Note that these are only estimated values of space requirements.

The controls and driver electronics are required to be located in a radiation-minimized zone. Assuming one IOT per cavity to provide 80 kW and electronics racks required for drivers, PLC, LLRF, and fast interlocks for eight cavities per IP side, an area of approximately 100 m^2 is needed near the cavities. The high-voltage power supplies and the power controls would need an additional 85 m^2. Both the high power and the low level control systems are placed in the nearby underground gallery (UA). The proximity of the circulator and RF loads in the present configuration allows for smaller RF transmission lines from the amplifier to the circulators. The required electrical interfaces are specified in Ref. [17]. Despite the reduction of cryomodules to be installed after the re-baselining in 2016 the space required for a full installation will be maintained.

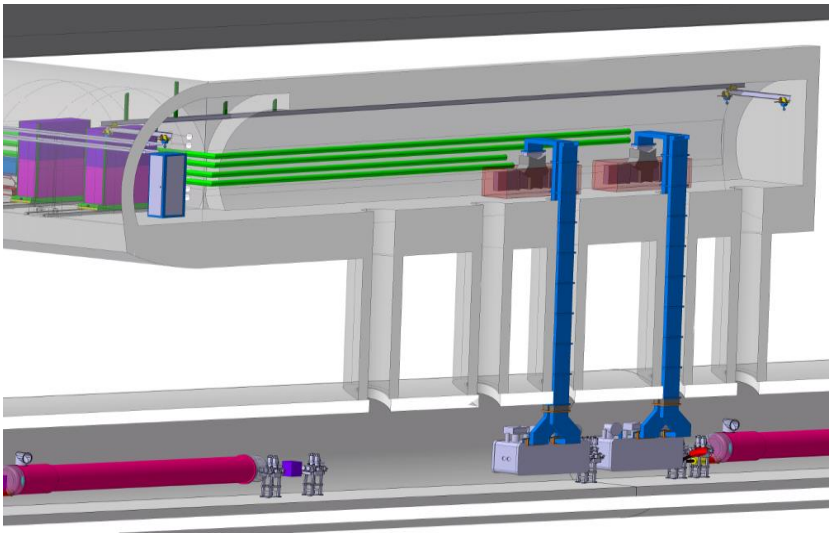

Figure 4-19: Preliminary sketch of a high-power RF, controls and LLRF layout in the underground RF cavern.

The RF control system, also commonly referred to as the low level RF system (LLRF), includes several functionalities. First, a tuning control is required to keep the cavity resonant frequency on-tune with the beam during the crabbing operation. If required, the LLRF also has to ensure that the cavity is safely parked at an optimal detuned position during filling, ramping, and collisions without crabbing. This system also synchronizes the phase of the RF kicks with the exact passage of the bunches for both beams. The LLRF

includes a regulation loop around the amplifier (to reduce the RF amplitude noise and phase noise in a band extending to a few tens of kHz), plus an RF feedback to precisely control the cavity field. The feedback loop consists of both a local loop around the cavity-amplifier and a global loop regulating the vector sum of voltages on the two sides of the interactions' regions. The global loop will reduce beam perturbation following a single cavity trip, by quickly reducing the field in the companion cavities to track the uncontrolled voltage in the faulty cavity. The beam dump system has a three-turn (270 μs) response delay.

For each ring, the eight accelerating cavities are driven from a single reference generated in a surface building above IP4. These two signals must be sent over phase-compensated links to IP1 (ATLAS) and IP5 (CMS). The up to four crab cavities of a given ring at each IP are coupled with a 4-in, 4-out multi-cavity feedback (MFB). Figure 4-20 shows the proposed architecture.

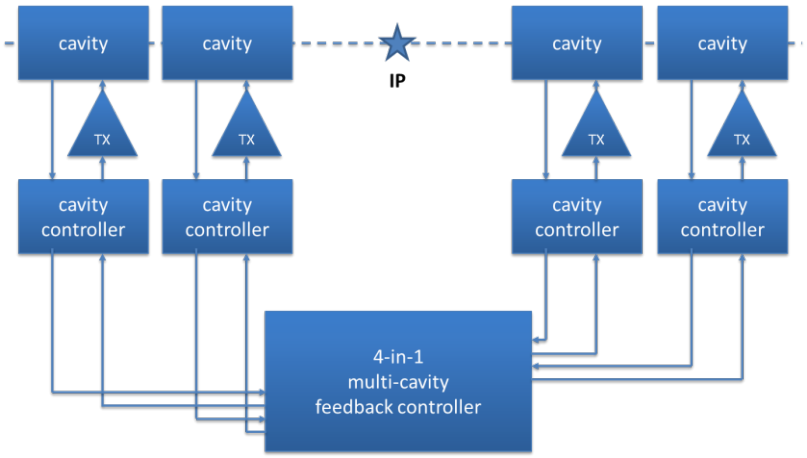

Figure 4-20: Proposed LLRF architecture for one ring at one IP for operation with an installation of four cavities per IP per beam.

A central controller receives measurements from all relevant cavities on each ring and IP and makes corrections to the drive of each individual RF transmitter (TX). If the field starts changing in a cavity, the MFB will adjust the field in the other cavities on both sides of the IP, such that the orbit distortions remain local. As described in Section 4.3.6 on flat-top, counter-phasing is nulled while keeping the voltage set point small. The RF feedback keeps the cavity impedance small (beam stability) and compensates for beam loading as the cavity moves to resonance. The voltage set points are ramped to synchronously change the voltage in all crab cavities as desired. Any levelling scheme is possible. With a circulator between amplifier and cavity, the TX response is not affected by the cavity tune.

In the early stages of LHC operation the spacing between LHC bunches within a batch was maintained to be strictly constant along the ring. A large amount of RF power is used in the ACS system to fully compensate the transient beam loading caused by the 3 μs long abort gap and the smaller gaps required for the injection kicker ('half detuning'). This scheme cannot be extended into the HL-LHC era as it would require excessive RF power. The power required is minimized by optimally detuning the cavity ('full detuning') and adapting the cavity set-point phases bunch by bunch. It results in bunch arrival time modulation of up to ± 42 ps [20]. This was demonstrated and in operation since 2016. There is no effect on the luminosity as the modulation is identical in both beams, only the collision point vertex position is modulated around the nominal vertex by a maximum of 1 μm over one turn. The bunch-to-bunch variation within a batch is at least an order of magnitude smaller. If not, the LLRF must synchronize the bunch-by-bunch crabbing field with the actual phase modulation.

4.3.6 Operation scenarios of the RD acceleration system

The crab cavities must cope with the various modes of the collider cycle: filling, ramping, and physics. During filling of the nominally 2760 bunches into the LHC, energy ramping, or operation without crab cavities, the

system will be inhibited by making the cavities transparent to the beam (crabbing off). Since more than one cavity is used, counter-phasing to make the effective kick voltage zero while always keeping accurate control of the cavity field is used as the baseline scenario. The counter-phasing ensures both zero effective voltage and beam stability on tune – in fact, it was found that this is the preferred scenario [10]. Another possibility to operate with 'crabbing off' can be achieved by detuning the cavity; but a small field should be kept for the required active tuning system. This is referred to as 'parking'. Parking the cavity half the distance between two revolution frequency sidebands would be ideal for stability.

If detuning is used with a positive non-integer tune ($Q_h = 64.3$), the cavity should be tuned above the RF frequency to make the mode $l = -64$ stabilizing [10]. Although RF feedback is not mandatory for stability with a detuned cavity, it is preferred to be active for accurate knowledge about, and control of, the cavity's resonance frequency and field. Active feedback will also keep the beam-induced voltage zero if the beam is off-centred. The RF power is a measure of beam loading to guide beam centring.

On the flat-top detuning can be reduced (while keeping the total kick voltage initially at zero). The RF feedback keeps the cavity impedance small (beam stability) and compensates for beam loading as the cavity moves to resonance. Once the cavity detuning is reduced to zero, we drive then counter-phasing to zero and use the functions to synchronously change the voltage in all crab cavities as desired (crabbing on). The counter-phasing of two crab cavities was successfully demonstrated in the SPS tests. In a LHC physics run, with crabbing on, the active RF feedback will continue to provide precise control of the cavity field. The RF feedback reduces the peak cavity impedance and transforms the high Q resonator to an effective impedance that covers several revolution frequency lines. The actual cavity tune then has no big importance for stability anymore. The growth rates and damping rates are much reduced, and we have no more dominant mode as shown in Figure 4-21.

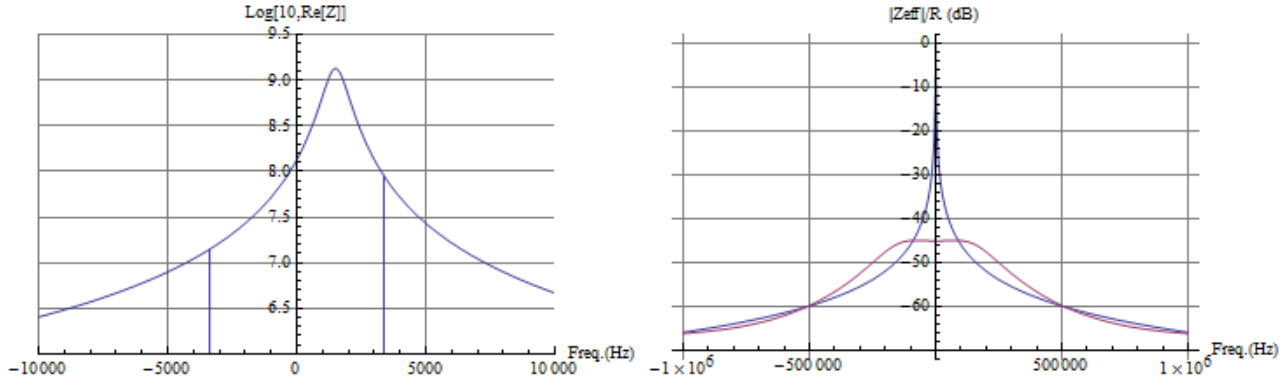

Figure 4-21: (left) Real part of the deflecting mode impedance with a detuning of 1.5 kHz from 400 MHz. The vertical lines represent the difference in $\Re\{Z\}$ evaluated at $\pm 0.3\, f_{rev}$ for the computation of damping rate (mode $l = -64$). (right) Modulus of the cavity impedance seen by the beam with the RF feedback on (red) and off (blue) normalized to the cavity impedance at the fundamental mode.

Injection mismatch at the LHC ring causes beam oscillation along the ring, resulting beam orbit offsets at the LHC crab cavity. Due to transverse oscillations that can reach up to 2 mm, the power requirement exceeds that available power from the 40 kW-CW specification and full compensation of transient beam loading is not possible. A fast transverse damper is used to damp the injections oscillations within 50 turns. Simulations shown that the required crab cavity RF power rapidly converges to the steady state value within 15 turns and should be compatible with the peak power available in the crab cavity RF system [22].

The required klystron power for the accelerating RF system is minimized by using the optimal detuning scheme. As a consequence of the klystron phase modulation, the bunch-to-bunch timing can no longer be perfectly maintained. The phase of bunches with respect to the RF clock progressively slip during the bunch train but then are finally recovered during the abort gap. Perfect operation of the crab cavities requires the RF field to be zero when the centroid of a bunch is at the centre of a cavity. The RF phase of the crab cavities cannot be modulated to follow this phase modulation due to their high loaded quality factors. Due to phase slip

introduced by the full detuning scheme, the bunch centre arrives at the cavity early or late, and the transverse momentum kick is not zero at the bunch centre, resulting in an asymmetric kick. However, the crab cavities are synchronized and for identical bunch phase shifts on the two counter-rotating beams, the bunch centres have the same transverse displacement at the IP. The cumulative effect of this phase shift and the RF curvature was shown in simulations to be negligible [23].

Crab cavity failures can lead to a fast voltage and/or phase change with a short time constant. This can lead to large, global head–tail oscillations, or coherent betatron oscillations with a change in transverse beam trajectories of 1.7 σ for a single cavity failure; the effect is cumulative with the number of failing cavities. These failures can be broadly classified into two categories.

- Fast failures, single or few turns. For example, a sudden cavity quench or breakdown.
- Slow failures, several tens of turns or greater (caused by vacuum degradation, voltage, and phase drifts, or similar).

Due to the relatively high quality factor in the superconducting cavity, the stored energy inside the cavity can typically only be extracted with a time constant determined by Q_L, which results from the coupling to the cavity via the power coupler. The stored energy will decay with a time constant $\tau = 2Q_L/\omega_0$. For $Q_L = 5 \times 10^5$, the time constant is approximately 400 μs. The three-turn delay time (267μs) for a beam dump trigger is an important consideration during a RF source failure, where the cavity field decays to roughly half its value before the beam can be safely aborted. In the case of a quench, the time constant of field decay may be dominated by the quench dynamics rather than Q_L. The situation is similar to strong and sudden electron loading due to multipacting or other phenomena.

Typical superconducting cavity quench mechanisms and the measurements from KEKB crab cavities [21] indicate that typically a quench is a slow thermal process (typically of the order of several milliseconds). Once the temperature of a sufficiently large area exceeds the critical temperature of niobium, the quench can propagate very quickly to completely quench the cavity or cause RF breakdown. However, any change in cavity quality factor well before reaching a critical temperature limit could be easily detected from the requested forward power (fast) or changes in the cavity temperature bath (slow). An interlock on the forward power, except due to induced orbit excursion, can cut the RF to slow down or stop quench propagation. A beam abort, if required, can be triggered simultaneously (a few μs) for machine protection.

The choice of low operating temperature (2 K) and moderate surface field levels allow operation with ample margin over quench temperature and field limits. The significantly better thermal conductivity of superfluid Helium should also improve the thermal performance and stability of the cavity. Additional measures in the cryomodule design are being considered to dimension the Helium enclosures with sufficient margin for heat flux. Cryomodule tests in the SPS have revealed no fast failures leading to RF voltage and phase changes of the time scale of 100 μs.

To minimize the perturbation on the beam during a cavity failure, the MFB will adjust the field in the other cavities on both sides of the IP, such that the orbit distortion remains local. Figure 4-22 shows the cavity control of two cavities across the IP with one cavity failure and the RF controller to adjust the second cavity to follow. The rapid change in field will also result in a detuning of the cavity; however, the mechanical tuning system is unable to adjust the tune within 400 μs. Since a rapid breakdown of a failed cavity may become unpredictable, it is probably safest to ramp down the cavities synchronously. However, small, and slow changes in one of the cavities can be adjusted for without aborting the beam.

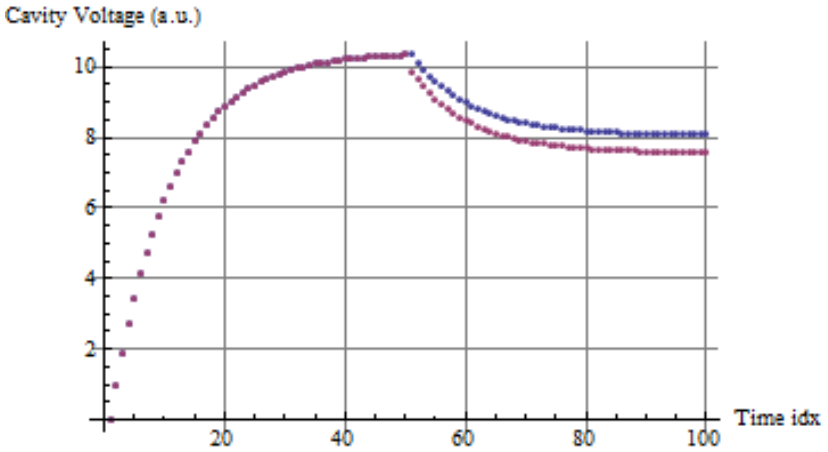

Figure 4-22: Voltage response with strongly coupled cavities across the IP as a function of time [μs]. At 50 μs, one cavity trips (red trace) and the other one is forced by the RF controller to follow (blue trace).

The cavities can be equipped with a fast tuning system such as a piezo mechanism. If the speed of such tuning devices is sufficient, it could compensate for Lorentz force detuning during transients and thus keep the tune within the bandwidth of the feedback system. If the SPS tests show fast tuning to compensate for cavity transients, piezo stacks can be added to the actuation within a limited range.

An additional mitigation to avoid large beam losses (and hence deposited energy) in the case of single or multiple cavity failures is a robust measurement and interlocking of the tail population and eventual head–tail oscillations. The addition of halo depletion methods (e.g. a hollow electron lens) for cleaning of the bunch tails to ensure a low particle density in the beam halo and interlocking with improved diagnostics like fast head–tail monitors and/or fast beam loss monitors (e.g. diamond monitors) are under investigation.

4.4 References

[1] D. Boussard, RF power requirements for a high intensity proton collider, Proceedings of Particle Accelerator Conference (PAC'91) (1991), pp. 2447-2449.

[2] P. Baudrenghien, T. Mastoridis, Proposal for an RF roadmap towards ultimate intensity in the LHC, Proceedings of International Particle Accelerator Conference (IPAC'12) (2012), pp. 154-156.

[3] T. Mastoridis, P. Baudrenghien, J. Molendijk, Cavity voltage phase modulation to reduce the high-luminosity Large Hadron Collider RF power requirements, Phys. Rev. Accel. Beams, 20, 2017, DOI: 10.1103/PhysRevAccelBeams.20.101003.

[4] LHC Design Report, CERN-2004-003-V-3, CERN (2004), DOI: 10.5170/CERN-2004-003-V-3.

[5] A. Piwinski, Nucl. Instr. and Meth. 81, 199 (1970), DOI: 10.1016/0029-554X(70)90631-2.

[6] R. Palmer, Energy scaling, crab crossing and the pair problem, 1988, SLAC-PUB-4707.

[7] K. Oide, K. Yokoya, The crab crossing scheme for storage-ring colliders, 1989, SLAC-PUB-4832.

[8] Y. Funakoshi, Operational Experience with Crab Cavities at KEKB, ICFA Mini-Workshop on Beam-Beam Effects in Hadron Colliders, CERN, Geneva, Switzerland, 18 - 22 Mar 2013, pp.27-36, 2014, DOI: 10.5170/CERN-2014-004.27.

[9] S. Fartoukh, Pile up management at the High Luminosity LHC and introduction to the crab kissing concept, CERN-ACC-2014-0076, 2014, DOI: 10.1103/PhysRevSTAB.17.111001.

[10] P. Baudrenghien, LLRF for Crab Cavities, presented at the 2nd HiLumi-LHC Meeting, Frascati, 2012.

[11] P. Baudrenghien et al., Functional specification of the LHC prototype crab cavity system, 2013, CERN-ACC-Note-2013-003.

[12] R. Calaga, B. Salvant, Comments on crab cavity HOM power, CERN-ACC-NOTE-2015-0024.

[13] N. Biancacci et al., HL-LHC impedance and stability studies, presented at the 4th HiLumi-LHC workshop, KEK, 2014.

[14] M. Navarro-Tapia, R. Calaga, A. Grudiev, RF Multipolar Characterization of the Latest LHC Deflecting Cavities, 4th International Particle Accelerator Conference, Shanghai, China, 12 - 17 May 2013, pp.2402.

[15] S. Pattalwar et al., Key Design features of the Crab-Cavity cryomodule for HiLumi LHC, 5th International Particle Accelerator Conference, Dresden, Germany, 15 - 20 Jun 2014, pp.WEPRI045.

[16] T. Jones et al., presented at the Crab cavity manufacturing readiness meeting, 2014, INDICO: 334041.

[17] L. Arnaudon et al., Conceptual specification of the crab cavity RF system, 2014, EDMS: 1363181.

[18] NPL Dimensional metrology web page.

[19] BCAM “Brandeis CCD Angle Monitor”, web page.

[20] R. Calaga, Chamonix 2014, in the proceedings of the LHC Performance Workshop, Chamonix 2014.

[21] K. Nakanishi et al., Beam Behaviour due to Crab Cavities Break down, in the proceedings of IPAC10, Kyoto, 2010 pp 2938.

[22] E. Yamakawa et al., Beam loading study for HL-LHC and measurements in SPS crab cavities, STFC- Report-2018.

[23] E. Yamakawa et al., Luminosity reduction caused by phase modulations at the HL-LHC crab cavities, Nuclear Inst. and Methods in Physics Research, A 908 (2018), DOI: 10.1016/j.nima.2018.08.074.

Chapter 5

Collimation system

S. Redaelli[1*], *R. Bruce*[1], *A. Lechner*[1] *and A. Mereghetti*[1]

[1]CERN, Accelerator & Technology Sector, Switzerland
[*]Corresponding author

5 Collimation system

5.1 The LHC multi-stage collimation system

5.1.1 Introduction

A variety of processes can cause unavoidable beam losses during normal and abnormal beam operation. Because of the high stored energy of about 700 MJ and the small transverse beam sizes, the HL-LHC beams are highly destructive. Even a local beam loss of a tiny fraction of the full beam in a superconducting magnet could cause a quench, and larger beam losses could cause damage to accelerator components. Therefore, all beam losses must be tightly controlled. For this purpose, a multistage collimation system has been installed [1][2][3][4][5][6][7][8], to safely dispose of beam losses. Unlike other high-energy colliders, where the main purpose of collimation is typically to reduce experimental backgrounds, the LHC and the HL-LHC require efficient beam collimation during all stages of operation from injection to top energy. The requirement to operate efficiently and safely with high-intensity hadron beams at small colliding beam sizes provides significant challenges, which drive the key design aspects of the collimation system at the HL-LHC.

The HL-LHC poses increased challenges to the collimation system. The LHC collimation system was designed to safely withstand beam lifetime drops down to 0.2 h during 10 s at 7 TeV, corresponding to peak losses of up to 500 kW, which increase to 945 kW for the HL-LHC. The ion beam upgrade, with the target of storing more than 20 MJ at 7 Z TeV and producing luminosities above 7×10^{27} cm^{-2} s^{-1} [9], is also very demanding for beam collimation. The collimation system must be upgraded on various fronts to cope with more demanding operation challenges. It is clear that the lifetime control and optimization of beam halo losses will also be crucial for the LHC upgrade (see also Section 5.4). Three main pillars of the collimation system upgrade for the HL-LHC can be identified:

- Re-design of the collimation system of incoming and outgoing beams in the upgraded insertion regions IR1 and IR5.
- Improved protection of the Dispersion Suppressor (DS) regions around IR7 and IR2 to mitigate increased local beam losses.
- Reduction of the collimator-induced impedance to allow the operation with higher brightness beams in the HL-LHC.

Note that the HL-LHC also relies significantly on operational efficiency as it is based on operation with levelled luminosity, so that it becomes even more important to minimize time spent outside physics operation. Improvements of the collimator setup time and minimization of downtimes from collimator faults also call for a consolidation of the present system. This can be seen as an essential “fourth pillar” of the system in light of

the HL-LHC operation. Indeed, to meet the new challenges, the HL-LHC collimation system builds on the existing LHC collimation system, with the addition of several upgrades.

It is also noted that, as a part of the upgrade of the collimation betatron cleaning, two new items were integrated in the baseline upgrade of WP5: hollow electron lenses and crystal collimation. In the previous HL-LHC baseline upgrade [10], WP5 budgets covered the R&D phase for these items, but not their implementation that was subject to the assessment of needs for these technologies and of the demonstration of their feasibility. After several years of studies, these items were incorporated in the WP5 upgrade baseline in Dec. 2019 by the CERN management following the 4th Cost & Schedule review [11]. The incorporation into the baseline was possible thanks to the in-kind contribution by Russia to the HL-LHC project. These new advanced collimation concepts are described in Section 5.6.

5.1.2 The LHC collimation system

The backbone of the HL-LHC collimation system will remain, as for the current LHC, the betatron (IR7) and momentum (IR3) cleaning systems installed in two separated warm insertions [1]. A very efficient halo cleaning is achieved by very precisely placing blocks of materials close to the circulating beams, while respecting a pre-defined collimator hierarchy that ensures optimum cleaning in a multi-stage collimation process. This is illustrated schematically in Figure 5-1 and the list of the LHC collimation system devices is given in Table 5-1.

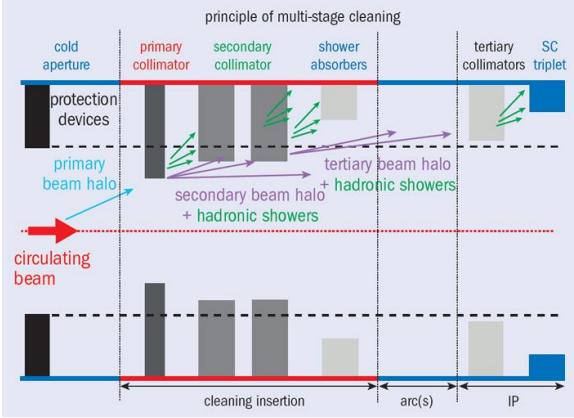

Figure 5-1: Schematic illustration of multi-stage collimation cleaning at the LHC.

Most collimators consist of two movable blocks referred to as ‘jaws’, typically placed symmetrically around the circulating beams. The present IR7 system, used in the LHC proton operation in Run 1 (2010–2013) [12] and Run 2 (2015–2018) [13], provided a cleaning efficiency above 99.99% [2], i.e. it ensures that less than 10^{-4} of primary beam losses reach the superconducting magnets. Highest losses occur in the DSs around IR7, while the rest of the cold elements around the ring are typically a factor 10 lower. The system was significantly upgraded already in the first LHC long shutdown (LS1, between 2013 and 2015), by replacing 18 collimators with new ones based on the new integrated-BPM design (see below), by improving the passive protection of warm magnets in IR3, and by adding 8 new physics debris collimators in IR1/5 [14]. About 30-40% of the present system will have to remain operational throughout the HL-LHC era as part of the collimation system. These collimators will need to be kept fully operational to ensure an efficient operation of the HL-LHC.

The initial LHC collimator design has been improved by adding two beam position monitors (BPM pickups) on both extremities of each jaw [21][22][23][24]. Eighteen operational collimators (16 TCTP and 2 TCSP) were already upgraded with this new design during LS1 [14]. Four additional prototypes with BPMs were included in the system in various yearly stops of the LHC [25][26][27][28]. This concept allows for fast collimator alignment as well as a continuous monitoring of the beam orbit at the collimator with the possibility to interlock the readout of the beam position. The BPM pickups have improved significantly the collimation

performance in terms of operational flexibility and β^* reach [13][29]. In particular, this was one of the key ingredients that allowed β^* values down to 25 cm in 2018 [19][20][29]. The BPM design is now applied to all new collimators regardless of the jaw material.

Table 5-1: Collimators for the LHC Run 2, starting in 2015. For completeness, injection and dump devices are also listed.

Functional type	Name	Plane	Number	Material
Primary IR3	TCP	H	2	CFC
Secondary IR3	TCSG	H	8	CFC
Absorber IR3	TCLA	H, V	8	Inermet 180
Primary IR7	TCP	H, V, S	6	CFC
Secondary IR7	TCSG	H, V, S	22	CFC
Absorber IR7	TCLA	H, V, S	10	Inermet 180
Tertiary IR1/IR2/IR5/IR8	TCTP	H, V	16	Inermet 180
Physics debris absorbers IR1/IR5	TCL	H	12	Cu, Inermet180
Dump protection IR6	TCDQ	H	2	CFC
	TCSP	H	2	CFC
Injection protection (transfer lines)	TCDI	H, V	13	Graphite
Injection protection IR2/IR8	TDI	V	2	hBN, Al, Cu/Be*
	TCLI	V	4	Graphite, CFC
	TCDD	V	1	Copper

*In 2016, the TDI collimator absorbing materials were changed to Gr, Al, CuCrZr

5.2 Baseline upgrades to the LHC collimation system

In this Section, for each upgrade pillar, we present the WP5 upgrade baseline. The two new upgrade items that were added to the WP5 baseline in Dec. 2019 – hollow electron lenses and crystal collimation – are discussed in Section 5.6.

The detailed scope of the collimation baseline upgrade can be summarized as follows (details of all items are discussed in the subsequent Sections):

- IR collimation upgrade:
  - 4 tertiary collimators per beam and per high-luminosity IR are needed to protect the inner triplet and the matching section from losses on the incoming beam, amounting to a total of 16 tertiary collimators.
  - 3 physics debris collimators and 3 fixed masks per beam and per high luminosity IR are needed to protect matching section and DS from collision debris in IR1/5, amounting to a total of 12 collimators and 12 masks.

Note that 8 collimators can be recuperated from the existing pool of operational collimators (i.e., the 8 tertiary collimators presently used in IR1 and IR5, built in LS1) or spare collimators of type “TCTP” (Inermet 180 jaws with pick-ups). Thus, 20 rather than 28 new collimators are needed to be designed and built.

The IR collimation upgrade is deployed during LS3 when IR1/5 will be upgraded for the HL-LHC.

- Dispersion suppressor upgrade:

- Addition of DS collimators TCLD in the DSs around IR7 for proton and ion operation, with the addition of 11 T dipoles: 1 collimator per beam in cell 9 per side of P7;
- Addition of DS collimators TCLD in the DSs around IR2 for ion operation, without 11 T dipoles: 1 collimator per beam in cell 11 at each side of P2 at the location of the connection cryostat.

Note that the losses in the DSs of IR1/5 during ion operation are mitigated by local bumps in the DS that move losses to the location of the connection cryostat, without need for dedicated collimators. The complete DS collimation upgrade takes place in LS2.

- Low-impedance upgrade:
  - Replacement of 9 secondary collimators per beam, out of the present 11 per beam, with a new low-impedance design; in total 18 new low impedance collimators.
  - Contribution to the construction on new primary collimators (renewed under the Consolidation project) by providing the low-impedance material for the jaws.

  The low-impedance upgrade of the system takes place in two phases:
  - Four new secondary collimators and two primary collimators per beam are installed in LS2.
  - The rest of the five secondary collimators per beam are installed in LS3.

The detailed list of collimators to be produced for the WP5 upgrade of the collimation system is given in Table 5-2.

Two baseline changes have taken place with respect to the previous TDR:

- The change of location for the TCLD collimators around IR7, from cell 8 to cell 9.
- The scope reduction by 4 units of the low-impedance collimators to be installed in LS3. In addition, a further change of scope – the WP5 contribution to the procurement of low-impedance material for the consolidated primary collimators – was also approved [18].

Table 5-2: List of the new HL-LHC collimators. The IR upgrade will require 28 operational collimators in IR1/5, 8 of which are planned to be recuperated from the existing TCTP collimators.

Collimator description	**Names**	**LS2 installation**			**LS3 installation**		
		Operational	**Production**	**Spares**	**Operational**	**Production**	**Spares**
Tertiary collimators	TCTPXH, TCTPXV, TCTPM, (TCTP)	--	--	--	16	12	2
Physics debris collimators	TCLP, TCLPX, (TCTP)	--	--	--	12	8	2
Physics debris collimator masks	TCLM	--	--	--	12	12	3
DS collimators	TCLD	4	4	1	--	--	--
Low-Impedance secondary collimators	TCSPM	8	8	2	10	10	2

5.3 Collimation upgrade in the high-luminosity interaction regions: IR Collimation

With the increased beam intensity and luminosity of the HL-LHC, the protection of the IR superconducting magnets and experiments becomes even more challenging. In order to provide adequate protection, the HL-LHC collimation layout in IR1 and IR5 includes two pairs of TCTs (horizontal and vertical) on each incoming

beam, as well as three physics debris absorbers (TCLs) and three fixed masks on each outgoing beam. This is illustrated in Figure 5-2, showing the HL-LHC layout in IR1 together with the nominal LHC layout. The layout in IR5 is similar and contains the same upgrades. The upgrades for the incoming and outgoing beams, as well as the newly developed collimator designs, will be discussed in more detail in the following Sections.

5.3.1 Upgrades to the collimation of the incoming beam in the experimental IRs

The present tertiary collimators (target collimator tertiary with pick-up, TCTP) are located at positions that protect the triplet; in order to provide the necessary absorbance, they are made of a heavy tungsten alloy (Inermet 180). They effectively protect the elements downstream, but are not robust against high beam losses, in particular during very fast beam failures that might occur if the beam dumping system does not trigger synchronously with the abort gap (an asynchronous beam dump). With the increase in bunch intensity of the HL-LHC, this accident scenario becomes even more critical. Settings margins are added to the collimator hierarchy to minimize the risk of exposure of these collimators to beam losses in case of such failures [3][19]. These margins have been reduced in Run 2 using a new optics with a specially matched phase advance between the extraction kickers and the TCTs [20], which was used to push further the β^* performance of the LHC. A TCT design with improved robustness would allow an alternative way to reduce the hierarchy margins without introducing constraints on the optics. This gives more flexibility in the optics design, which is useful in particular for the HL optics baseline that features many other constraints.

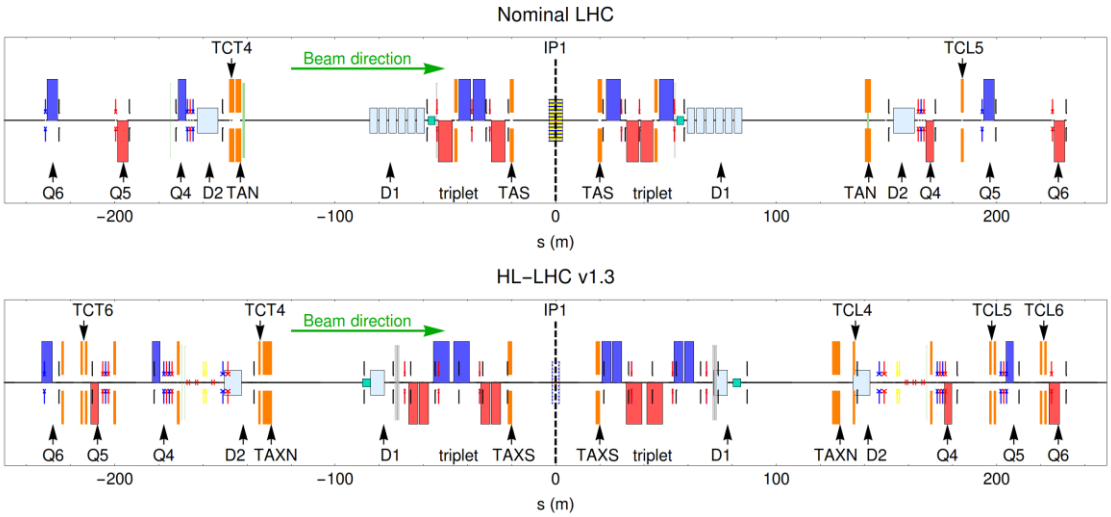

Figure 5-2: Schematic layout in experimental insertion IR1 for LHC (top) and the HL-LHC v1.3 (bottom). Collimators are indicated in orange, quadrupoles in blue and red for the two polarities, and dipoles in cyan.

The experimental experience of beam impacts on collimator material samples at HiRadMat [36], where several new materials were studied, indicates that molybdenum graphite (MoGr) can improve the TCTP robustness by a factor of several hundreds, while copper-diamond (CuCD) features higher density (and hence better cleaning efficiency) and larger electrical conductivity and still gives about a factor 15 improvement in robustness [37]. In order to keep a good absorption, the baseline is therefore to use CuCD in the horizontal TCTs, while the vertical ones are still made of Inermet 180, since the critical losses from an asynchronous beam dump occur only in the horizontal plane.

In addition to improvements from increased robustness, the HL-LHC layout has additional aperture constraints [2][3] because the optics functions at the magnets up to Q5 planned at the HL-LHC reduce the normalized aperture. Thus, additional tertiary collimators are required in IR1/IR5 to protect the Q4 and Q5 quadrupole magnets. The present baseline includes a pair of new TCTP collimators in front of Q5, including one horizontal and one vertical, and another pair of TCTPs just upstream of the TAXN to protect the triplet, as for the nominal LHC.

The expected beam losses in the experimental insertions have been verified in simulations. Tracking simulations using SixTrack [38][39] show that the proposed layout provides adequate protection of all magnets against cleaning losses [40][41]. Simulations of asynchronous beam dumps show that no direct losses are to be expected on the magnets, and losses of up to about 2×10^{10} protons [42] could occur on the TCTs [43]. Those losses are spread-out secondary protons, scattered out of upstream collimators, about a factor 5 below the onset of plastic deformation even for Inermet 180. This result relies on a matched fractional phase advance below 30° between the extraction kickers and the TCTs, as implemented in the HL-LHC v1.3. Under these conditions the heat deposition in SC magnets and in experimental detector is quite safe with respect to damage.

5.3.2 Outgoing beam cleaning: physics debris in the matching section

The collimators on the outgoing beams, downstream of the high-luminosity experiments, must intercept both scattered primary beam particles and secondary particles generated by the collisions, in order to protect the magnets downstream. The protection of the triplet from luminosity debris is discussed in Chapter 10, and here the focus is instead on the protection of the matching section. In Run 1, protection of the matching section was done by a single horizontal collimator in Cell 5, called TCL5. For Run 2, the system was upgraded with additional TCLs in cells 4 and 6 (8 new collimators), to cope with the higher luminosities and requirements from forward-physics experiments.

In the HL-LHC, the levelled luminosity of 5 to 7.5 $\times 10^{34}$ cm^{-2} s^{-1} will be about a factor four higher than the peak achieved during Run 2 in the LHC, which is a significant challenge for the collimation of physics debris. In addition, the absorber TAXN (the upgrade of the TAN, see Chapter 8) is less effective, in fact, because of the geometry of the reference trajectory and crossing angle, a significantly larger fraction of the scattered particles can pass through its opening than in the LHC [47].

In order to cope with these challenging conditions, several improvements are foreseen for the HL-LHC. The TCL4 needs to be upgraded to have thicker jaws [47] in order to intercept a larger fraction of the particles that have passed through the TAXN opening. This new collimator is called TCLX, and a sketch of the increased coverage in the transverse plane, compared with the present, thinner TCL, is shown in Figure 5-3. It should be noted that the jaw material is changed from copper to tungsten heavy alloy for better protection. In addition, fixed masks have to be installed on the IP side of Q4, Q5, and Q6, with the aperture well aligned and matching the beam screen of each magnet. Furthermore, the TCL5 and TCL6 are still needed. Using this new layout, the highest power loads in any magnet coil in the matching section stays below 1 mW/cm^3 [46], which is far below the estimated quench limits. It should be noted also that the TCTs play a role in protecting the incoming beam bore from the collision debris.

5.3.3 Collimator designs for IR collimation

The design of the new IR collimators is challenging. Due to the larger β-functions in the HL-LHC high-luminosity insertions, the TCTs and TCLs in cell 4 have to be opened to rather large gaps in mm to achieve the smaller normalized design openings in σ. To keep a maximum operational flexibility, it is thus demanded that the stroke should be as large as 15 σ for the baseline optics with β^*=15 cm. In this case, a half gap of 34 mm is needed for the most critical, vertical, collimator, which goes up to 40 mm for flat optics [49][50]. The half gap is limited to 30 mm in the present collimator design, so modifications are necessary. Similar considerations apply also to the TCLs. This calculation includes imperfections from orbit, optics, and ground motion, but also a gain of several mm thanks to remote alignment capabilities, described in Chapter 15. Without the gain from the new remote alignment system, the present design would have to be changed to meet the design specifications in terms of jaw strokes.

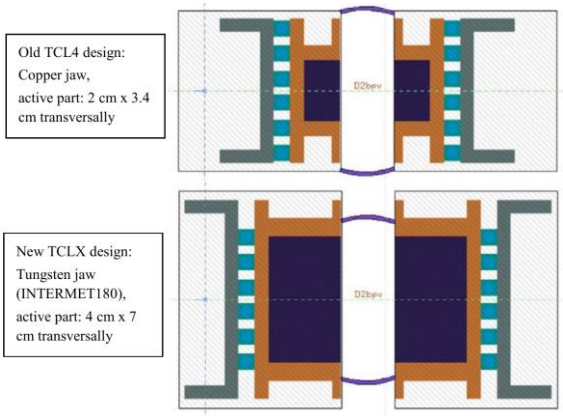

Figure 5-3: A schematic of the transverse cross-section of the present TCL design, as implemented in FLUKA (top), together with a first guess on the TCLX design (bottom), including thicker jaws, where the jaw material should be changed from copper to tungsten heavy alloy. Figure from Ref. [48].

In addition, the region in cell 4 between the D2 separation dipole and the TAXN, where the beams are recombined in a common vacuum chamber, is particularly critical from the integration point of view. In order to provide the needed stroke and still fit in the horizontal space, a new two-in-one collimator design for the horizontal TCT and the TCL4 has been developed. In this design, a single vacuum tank houses at the same location the movable jaws acting on one beam and the vacuum chamber of the opposing, non-collimated, beam. Details like the vacuum coupling of the two beams as well as the impedance budget of this design need to be studied in detail, but this proposed solution seems suitable for the HL-LHC. A 3D model of this design is shown in Figure 5-4. For the vertical TCT in Cell 4, a two-in-one design is not needed, however, a special design still has to be developed to implement the larger stroke up to 40 mm. These collimators with special designs will all have a letter “X” in the name. A summary of the technical key parameters is given in Table 5-3 for the different collimator types, and Figure 5-5 shows a 3D model of the proposed layout in the region between the TAXN and the D2.

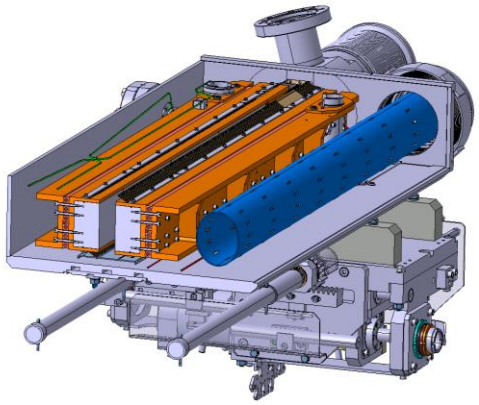

Figure 5-4: Design of new two-in-one collimator with a common vacuum tank housing both the movable jaws (left part) and the vacuum chamber of the opposing beam.

For the TCLs in cell 5 and 6, and the TCT in Cell 6, the standard 30 mm stroke of the present collimator design is sufficient. It is important to note that some of these collimators should re-use the present TCTP collimators with BPM that are essentially of the same design and using Inermet 180 as active material. It is believed that up to 8 collimators can be recuperated from those built for the present LHC (units installed in the machine or operational spares). It is planned to use these collimators in the vertical TCT slot in Cell 6 (not exposed to beam dump failures at top energy) and as single-beam horizontal TCLs in cells 5 or 6 that are at settings above 10 σ. For the horizontal TCTs in Cell 6, new collimators using CuCD as active material will be

built, as well as the remaining TCLs. A total of 20 movable collimators and 12 fixed masks have to be built for the IR1 and IR5 installations in the HL-LHC.

Table 5-3: Equipment parameters of the new TCTs and TCLs to be installed in cell 4.

Characteristics	Units	TCLX	TCTPXH	TCTPXV
Jaw active length	mm	1000	1000	1000
Jaw material	-	Inermet 180	Copper-diamond	Inermet 180
Flange-to-flange distance	mm	1556	1556	1480
Number of jaws	-	Two	Two	Two
Orientation	-	Horizontal	Horizontal	Vertical
Number of motors per jaw	-	Two	Two	Two
Number of BPM buttons per jaw	-	Two	Two	Two
RF damping	-	Fingers	Fingers	Fingers
Cooling of the jaw	-	Yes	Yes	Yes
Cooling of the vacuum tank	-	Yes	Yes	Yes
Maximum half gap	mm	> 39	> 33	> 40
Stroke across zero	mm	>5	>5	>5
Angular adjustment	-	Yes	Yes	Yes
Jaw coating	-	No	No	No
Transverse jaw movement (fifth axis)	-	No	No	No

Despite being less critical because of the larger β^* values, upgraded TCTPs are under consideration also for IR2/8 because various luminosity scenarios in these IRs require the usage of tertiary collimators, although at relaxed settings compared to IR1 and IR5. For the time being, new collimators in IR2/8 are not considered part of the baseline.

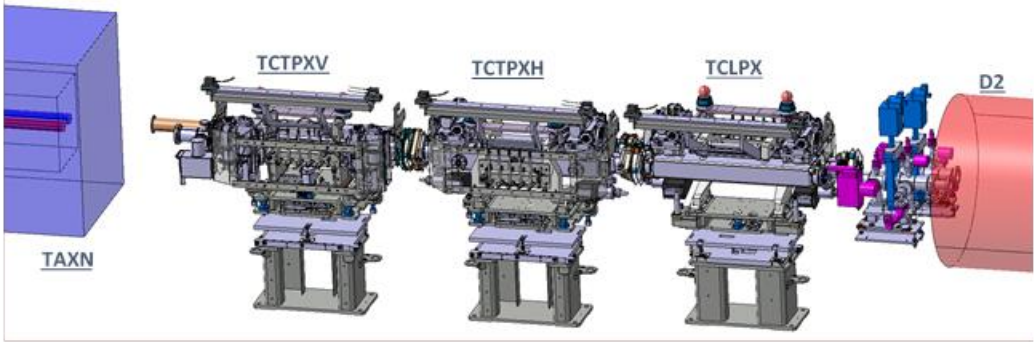

Figure 5-5: Layout in the region in Cell 4 between the TAXN and the D2.

5.4 Dispersion suppressor collimation upgrades

5.4.1 Introduction

The necessity of cleaning upgrades in the DSs for the HL-LHC is primarily driven by the increased risk of quenches arising from off-momentum losses. The source of dispersive losses can be halo particles intercepted in the collimation system or collision products from the interaction points. Extensive tracking and shower simulations, as well as experimental quench tests were carried out in Run 1 and Run 2 in order to determine the expected power loads and quench margins both for proton and heavy ion operation. The results, summarized in the following Sections, indicate that upgrades of the collimation cleaning hardware are needed in the DSs next to IR7 (for Pb operation and probably also for proton operation), and in the DSs around IR2 (for Pb operation). Note that steering of loss peaks into the connection cryostats of IR1 and IR5 successfully mitigates losses in these IR's without the need for hardware upgrades.

The DSs around IR7 are the main bottleneck in the LHC in terms of collimation leakage both for protons and heavy ions. The design goal for the present LHC collimation system was to avoid quenches and beam dumps for a beam lifetime of 0.2 h for up to 10 s, or 1 h for extended time periods [1]. The same specification is maintained for the HL-LHC, which implies that the cleaning system must sustain a higher power loss due to the higher beam intensity. The need for upgrades depends on the level of losses eventually encountered in the HL-LHC operation and the quench limit of superconducting magnets. In this design phase, where there are significant uncertainties for the scaling to higher energy, it is important to take appropriate margins. To mitigate the risk of quenches due to IR7 leakage, it is foreseen to add local collimators, referred to as TCLDs, in the DSs, where the dispersion has already started rising. In order to make space for the new collimators, it is envisaged to replace, for each TCLD, an existing main dipole with two shorter 11 T dipoles [53].

The need for a cleaning upgrade in the DS also arises for heavy ion collisions in IP2. Secondary ion beams with different magnetic rigidity are created, which are lost in the adjacent DS and would induce a quench of magnets at the HL-LHC Pb-Pb target luminosity of $7 \times 10^{27} \mathrm{cm}^{-2}\,\mathrm{s}^{-1}$ [9]. A similar solution, based on TCLDs, will therefore be adopted in IR2, with the difference that the collimator will be installed at the location of the connection cryostat in Cell 11, thanks to a dedicated cryogenics bypass.

5.4.2 Dispersion suppressors around IR7

A small fraction of protons interacting with the collimators in IR7 escapes from the IR with a modified magnetic rigidity. These protons, which are mainly single diffractive protons emerging from the TCPs, represent a source of local heat deposition in the cold DS magnets downstream of IR7, where the dispersion starts to increase (see [52] and references therein). These losses are among the highest losses in cold magnets around the ring. In case of large drops in the beam lifetime, in particular for the case of the HL-LHC where the stored energy is almost doubled compared to the nominal LHC, the impacted magnets risk quenching and the beams should be dumped before based on the BLM readings. This would result in costly downtime and reduced the HL-LHC availability and have a negative impact on physics production. The same applies to secondary ion fragments produced in IR7 collimators during heavy ion operation. Although the intensities of heavy-ion beams are lower, they undergo numerous nuclear and electromagnetic interactions with the material of the primary collimators, creating an abundance of secondary ions with different mass and charge. Collimation of heavy-ion beams is therefore much less efficient than that of proton beams.

In order to probe the acceptable losses in the DSs around IR7, experimental quench tests have been performed with protons and Pb ions at different beam energies between 3.5 TeV and 6.5 TeV [54][55][56][57][58][59]. The proton quench tests, in particular the latest one at 6.5 TeV, did not result in a quench [58], however, the heavy-ion test with a 6.37 Z TeV Pb beam resulted in a quench of the dipole MB.B9L7 [59][60]. Table 5-4 summarizes the corresponding peak power densities in the MB coils, obtained with FLUKA [61][62] shower simulations. The FLUKA simulations were based on multi-turn tracking simulations [63][64] performed with the FLUKA-SixTrack coupling [60][65][66], for the configuration deployed in the quench tests [67]. The table also includes results of another quench test performed in IR5, based on Bound-Free Pair Production (BFPP) ions produced by the collision of Pb beams at 6.37 Z TeV [57]. This test also achieved a dipole quench. The losses exhibited different time profiles in the different tests, which affected the minimum power density needed to induce a quench. According to electro-thermal simulations, the minimum quench power density in $\mathrm{mW/cm^3}$ can be a factor of two, or more, higher if the losses are rising than if the losses are constant in time. This can possibly explain why the maximum power density was found to be somewhat higher for the Pb collimation quench test than for the BFPP test. It should nevertheless be stressed that these numbers are computed in complex simulations that have a non-negligible range of uncertainty and therefore a certain margin needs to be considered for the power density estimates reconstructed by the simulations.

Table 5-4: Simulated peak power densities in MB dipole coils for different quench tests. The values are radially averaged over the coil radius. The results for the collimation quench tests include an empirical correction based on BLM signals, which accounts for the underestimation of particles leaking to the DS.

Loss term	**Beam particles**	**Energy**	**Time profile of losses**	**Quench**	**Reconstructed maximum power density MB coils**	**Complexity of simulations**
Betatron collimation leakage (DS next to IR7)	Protons	6.5 TeV	Losses rising for 5 sec	No	23 mW/cm3	High
Betatron collimation leakage (DS next to IR7)	Pb ions	6.37 ZTeV	Losses rising for 12 sec	Yes	25-30 mW/cm3	High
Secondary ions from IP (DS next to IR5)	Pb ions	6.37 ZTeV	Losses rising for 20 sec	Yes	20 mW/cm3	Low-medium

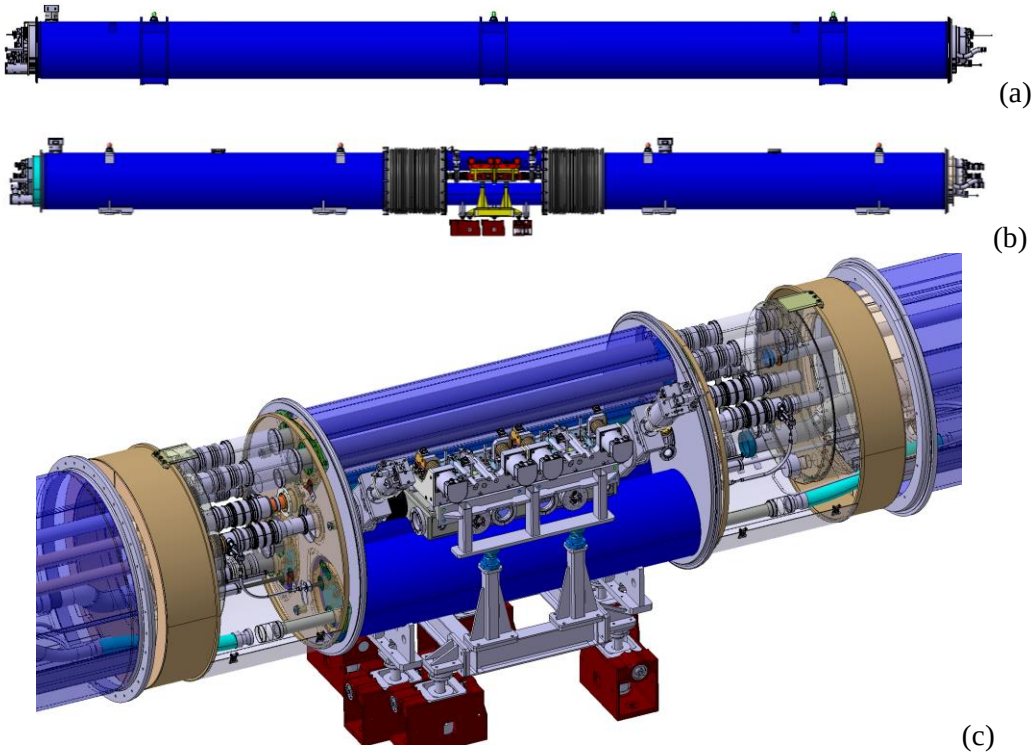

Figure 5-6: (a–b) Schematic view of the assembly of two shorter 11 T dipoles with a collimator in between, which can replace one standard main dipole. (c) 3D model showing the collimator (in grey, at the centre), the two dipole cryostats and the connection cryostat (courtesy of L. Gentini).

For comparison, Table 5-5 summarizes FLUKA results of the peak power density in DS magnets for the HL-LHC beam parameters at 7 Z TeV, i.e. 2760 proton bunches with a bunch intensity of 2.3×10^{11} and 1248 Pb bunches with a bunch intensity of 2.1×10^{8} ions [68] (previous results can be found in Refs. [69] [70] [71] [72]). These proton beam parameters are only expected in Run 4 whereas the upgraded ion beams are already expected in Run 3. The table shows results [69] for different layouts, including the case without TCLD and with TCLD at the MB.B8 in Cell 8 or at the MB.A9 in Cell 9. Inputs are from Refs. [73] [74]. The collimator settings for protons (ions), specified for a normalized emittance of 3.5×10^{-6} m rad, are: TCP at 5.7σ (6.0σ), TCSGs at 7.7σ (7.0σ), TCLAs at 10σ (10σ) and TCLD at 14σ (14σ) [63][64].

Table 5-5: Simulated peak power densities in superconducting coils of DS magnets in cells 8/9 and 11, expressed in mW/cm^3, respectively for a beam energy of 7 Z TeV. The values are radially averaged over the coil radius. Results for different layouts are shown (no TCLD, TCLD at the location of the present MB.B8 and the MB.A9). The nominal HL-LHC beam parameters are used and an empirical correction factor of 3 accounting for the underestimation of particles leaking to the DS in the simulation is applied.

		PROTONS (mW/cm^3)					**IONS (mW/cm^3)**				
		Cell 8/9			**Cell 11**		**Cell 8/9**			**Cell 11**	
		MB	**MQ**	**11T**	**MB**	**MQ**	**MB**	**MQ**	**11T**	**MB**	**MQ**
No TCLD	0.2 h	21	9.9	-	12	13	57	27	-	57	36
	1 h	4.2	2.0		2.4	2.6	11	5.4	-	11	7.2
MB.B8	0.2 h	6.6	8.1	11	8.7	13	5.4	15	21	36	33
	1 h	1.3	1.6	2.2	1.7	2.6	1,1	3	4.2	7.2	6.6
MB.A9	0.2 h	6.0	8.1	48	< 0.3	< 0.3	6.0	3.6	33	< 0.003	< 0.003
	1 h	1.2	1.6	9.6	< 0.06	< 0.06	1.2	0.7	6.6	< 0.0006	< 0.0006

For Pb ions, the simulations indicate that, with the present DS layout without TCLD, the peak power density in the most loaded IR7 DS magnet reaches almost 60 mW/cm^3 during a 0.2 h lifetime drop. This is higher than the peak power density reached in both the BFPP and the Pb collimation quench tests at 6.37 Z TeV, indicating that a cleaning upgrade is needed at 7 Z TeV, with magnets with even lower quench limits that at 6.5 ZTeV. A similar conclusion can be reached by simply scaling the acceptable power load determined in the Pb collimation quench test.

It should be recalled that full mitigation of the losses from heavy-ion collimation would ideally require two collimators on each side of IR7. This solution would consistently cure the two main loss clusters in cell 8/9 and cell 11, and in addition would suppress efficiently the off-momentum halo that leaves IR7 after interactions with the collimators, causing losses in other locations around the ring. As a result of the re-baselining in 2016, it was decided to have only 1 TCLD collimator per beam. This decision was to a large extend determined by cost constraints, but also by the clear understanding that the need for the additional TCLD collimators per DS side was not 100% certain and that it would not have been possible to produce more than 4 new dipoles in time for installation in LS2. Possible further installations might be considered later on. The results in

indicate that, if the TCLD is located in Cell 8, a risk remains that a quench occurs in Cell 11, where the collimator is less effective. A much better cleaning in Cell 11 can be achieved by placing the TCLD in Cell 9, but with the disadvantage that the heat load in the 11 T magnet upstream of the collimator increases by about a factor 2 [48 mW/cm^3 during proton operation instead of 21mW/cm^3 during ion operation]. Recently updated studies [77] suggest that the quench level of the 11 T magnets is significantly higher than that of the MB, reaching about 70 mW/cm^3 [78]. The higher heat load in the 11 T magnets seems therefore acceptable, although the remaining margin is moderate.

For protons, the predicted peak power density for the HL-LHC beams with a 0.2 h lifetime and without TCLD is about a factor of three lower than that for ions, reaching about 20 mW/cm^3 at 7 TeV. Nevertheless, this value is comparable to the power density reached in the steady-state BFPP quench test at 6.37 *Z* TeV. Based on these results and considering the simulation uncertainty, it is estimated that the TCLDs might be needed in Run 4 even for safe proton operation. Like for ions, one can achieve a better cleaning if the collimator is located in Cell 9. The addition of a TCLD in Cell 9 improves the loads on standard dipoles by more than a factor 3, bringing losses to the level of 6 mW/cm^3, but again with the disadvantage of a locally higher heat load in the 11 T. For a 12 minutes lifetime, the power density in the 11 T coils is predicted to reach almost 50 mW/cm^3. It is to be noted that this power density is reached in the 11 T magnet upstream of the TCLD and hence the TCLD settings have no influence on this value. It is also worth noting that the 50 mW/cm^3 in the 11 T coils is about a factor of two higher than that in the MB.A9 replaced by the 11 T magnets. This can mainly be attributed to the higher dipole field, which leads to an enhancement of off-momentum proton impacts on the 11 T beam screen as compared to the MB. The predicted power density in the 11 T is still lower than the

above quoted 11 T quench level, although a smaller safety margin remains. Losses are localized towards the end of the 11 T dipole upstream of the TCLD and various mitigation measures are under study to reduce further the load (optimized alignment of the 11 T dipole, effect of local bumps).

In conclusion, it seems at this stage that one TCLD per beam is acceptable for the performance. On the other hand, this should be reviewed later in light of the Run 3 performance.

5.4.3 Dispersion suppressors around IR2

Secondary ion beams produced with a modified magnetic rigidity are generated in ion collisions and represent a source of local heat deposition in the adjacent DS regions where the dispersion function starts rising. The dominating processes are bound-free pair production (BFPP), where electron–positron pairs are created and one (BFPP1) or two (BFPP2) electrons are caught in a bound state of one of the colliding nuclei, thus changing its charge, and 1- or 2-neutron electromagnetic dissociation (EMD1 and EMD2) where one nucleus emits one or two neutrons, thus changing mass. An example of ion beams produced in collisions of $^{208}Pb^{82+}$ nuclei in IR2 is given in Figure 5-7.

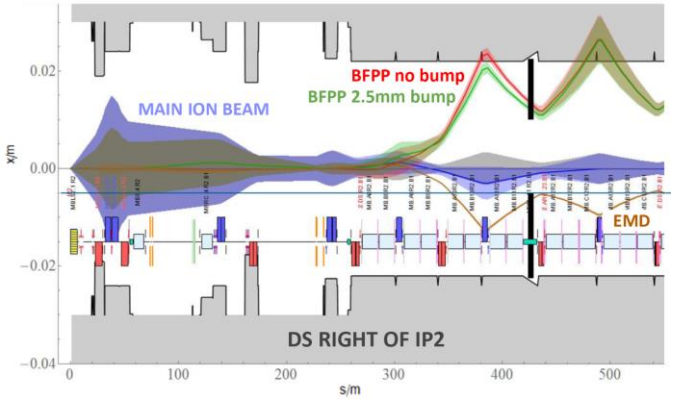

Figure 5-7: 1 σ envelope of the main Pb^{82+} beam (violet) together with the dispersive trajectories of ions undergoing BFPP1 (red) and EMD1 (brown), coming out of IP2. Black lines indicate the TCLD jaws. The green line indicates the shifted BFPP1 orbit using a closed orbit bump, which is necessary to intercept the beam with the collimator. The EMD1 beam can be intercepted with the other jaw.

After the LS2 ALICE upgrade, aiming at a peak luminosity of 7×10^{27} cm^{-2} s^{-1} (about seven times higher than the nominal one), the dominant BFPP1 beam can carry about 180 W, resulting in a power load in the coils of the MB.B10 dipole of about 50 mW/cm^3 [71][81][82] on both sides of ALICE. Similar ion losses also occur in the DS regions around ATLAS and CMS (see next Section).

A beam loss experiment carried out during the 2015 Pb-Pb run at 6.37 Z TeV [57] confirmed the long-standing presumption that BFPP1 ions risk to quench magnets [79][80]. The experiment was carried out around CMS because of the higher peak luminosity than in ALICE. During standard operation, special bumps were deployed around ATLAS and CMS to steer the BFPP1 losses into the connection cryostats. In the quench experiment, BFPP1 losses were deliberately shifted inside a dipole using an orbit bump, and the heat deposition in the magnet was increased in steps by reducing the beam separation. The dipole eventually quenched at a luminosity of 2.3×10^{27} cm^{-2} s^{-1}. Results from particle shower simulations indicate that the peak power density achieved during the test was around 15-20 mW/cm^3. The test is planned to be repeated in another location in Run 3 to further reduce the quench level uncertainty. These results scaled to 7 TeV – taking into account the changes of quench limits from 6.37 TeV to 7 TeV – confirmed that BFPP1 ions would limit the luminosity to less than 2.0×10^{27} cm^{-2} s^{-1}, well below the HL-LHC target of 7×10^{27}cm^{-2} s^{-1} and therefore would limit the full exploitation of the ALICE upgrade.

To eliminate any risk of ion-induced quenches in the DS next to IR2, it is foreseen to install TCLD collimators, as shown schematically in Figure 5-7. One collimator per side of the ALICE experiment is

sufficient to intercept the secondary beams from the most dominant processes (BFPP1 and EMD1) in a location where these ions are well separated from the main beam. The baseline for IR2 is to install the collimator in the connection cryostat in Cell 11 and to implement a closed orbit bump. The bump makes the BFPP1 beam miss the aperture at the first maximum of the locally generated dispersion since IP2 and redirects the beam onto the TCLD jaw. At the same time, the EMD1 beam, which carries ~65 W at a luminosity of $7 \times 10^{27} \mathrm{cm}^{-2}\ \mathrm{s}^{-1}$, could be intercepted with the other jaw. The feasibility of operating with closed orbit bumps of a few mm over more than 100 m has been successfully demonstrated in the 2015 Pb-Pb run [83], as well as in the 2018 Pb-Pb run [84].

The collimator length (60 cm) and material (Inermet 180) are the same as for the TCLDs around IR7 to optimize the TCLD production and spare plans. Particle shower simulations suggest that, with such jaws, the power deposition density in the coils of downstream magnets is expected to remain below 1 $\mathrm{mW/cm^3}$ if the BFPP1 and EMD1 beams impact at least 2 mm from the collimator edges. Hence there is no risk that the showers escaping from the jaws induce a quench of the downstream magnets or of the bus bars [82][85].

5.4.4 Dispersion suppressors around IR1/5

The ATLAS and CMS target luminosity for heavy ion operation in the HL-LHC is the same as for ALICE ($7 \times 10^{27} \mathrm{cm}^{-2}\ \mathrm{s}^{-1}$) [9]. The situation in IR1/5 is, however, different from IR2 since the BFPP1 ions produced in IP1/5 are lost towards the end of the last dipole in Cell 11. As the loss location is close to the connection cryostat, the risk of quenches can be mitigated by redirecting the losses onto the cryostat beam screen using local orbit bumps [57]. Such bumps have been routinely used in the 2015 [83] and 2018 [84] Pb-Pb runs at 6.37 Z TeV, enabling peak luminosities up to $6.2 \times 10^{27}\ \mathrm{cm}^{-2}\ \mathrm{s}^{-1}$. This is a robust solution, providing sufficient margin for the HL-LHC goal [81][82]. Losing the ions in the connection cryostat also reduces the total heat load to be evacuated by the cryogenic system. A significant fraction of the power is expected to be deposited in the Pb shielding of the connection cryostat, which is less critical than the power deposited in the cold mass of magnets as the Pb shielding is mainly thermalized to the thermal screen (~60-65K) [81][82].

Losses in the DS regions also occur during proton operation. Power deposition studies however indicate that there is no risk that these protons quench DS magnets in the HL-LHC operation. At the HL-LHC proton-proton design luminosity of $5 \times 10^{34}\ \mathrm{cm}^{-2}\ \mathrm{s}^{-1}$, the predicted power density in DS magnet coils is 1-2 $\mathrm{mW/cm^3}$, which is safely below the magnet quench level [47]. This remains true for the ultimate luminosity value of $7.5 \times 10^{34}\ \mathrm{cm}^{-2}\ \mathrm{s}^{-1}$ that caused 50% larger peak losses. The long-term dose in the magnet coils reaches about 20 MGy for an integrated luminosity of 3000 fb^{-1} [47]. Also, this is considered acceptable since magnets are expected to sustain a peak dose up to about 30 MGy. The proton simulation studies for the DS are discussed in more detail in Chapter 10. Based on these results, it is concluded that, like for heavy ions, no DS collimators around IR1/5 are needed for proton operation. These collimators are therefore not part of the HL-LHC baseline.

5.4.5 Dispersion suppressor collimator design

The TCLD (see Figure 5-8) consists of two parallel jaws collimating the beam in the horizontal plane. The TCLD design is identical for IR7 and IR2. Some design choices are driven by the more constrained installation between 11T dipoles around IR7. In both cases, the active material of the jaws was chosen to be the heavy tungsten alloy Inermet 180 because the TCLD will rarely be exposed to a large beam load, hence there is no need at this stage to consider advanced materials, while optimising the absorption in the given longitudinal constraints is important. As for all new collimators, the design includes BPMs. The jaws are water cooled, using squared 9 mm pipes. In this compact design, the maximum jaw opening reaches 25 mm from the beam centre, 5 mm less than for standard collimators. The TCLD will be integrated in a specially designed assembly, containing a beam pipe for the other beam, as well as a cryo-bypass (see Refs. [86] [87] and references therein).

Table 5-6: Key parameters of TCLD collimators

Characteristics	Units	Value
Jaw active length	mm	600
Jaw absorbing material	-	Inermet 180
Flange-to-flange distance	mm	1080
Number of jaws	-	Two
Orientation	-	Horizontal
Number of BPMs per jaw	-	Two
RF damping	-	RF fingers
Cooling of the jaw	-	Yes
Cooling of the vacuum tank	-	No
Minimum gap	mm	< 2
Maximum gap	mm	50
Stroke across zero	mm	5
Number of motors per jaw	-	Two
Angular adjustment	-	Yes
Transverse jaw movement (fifth axis)	-	No

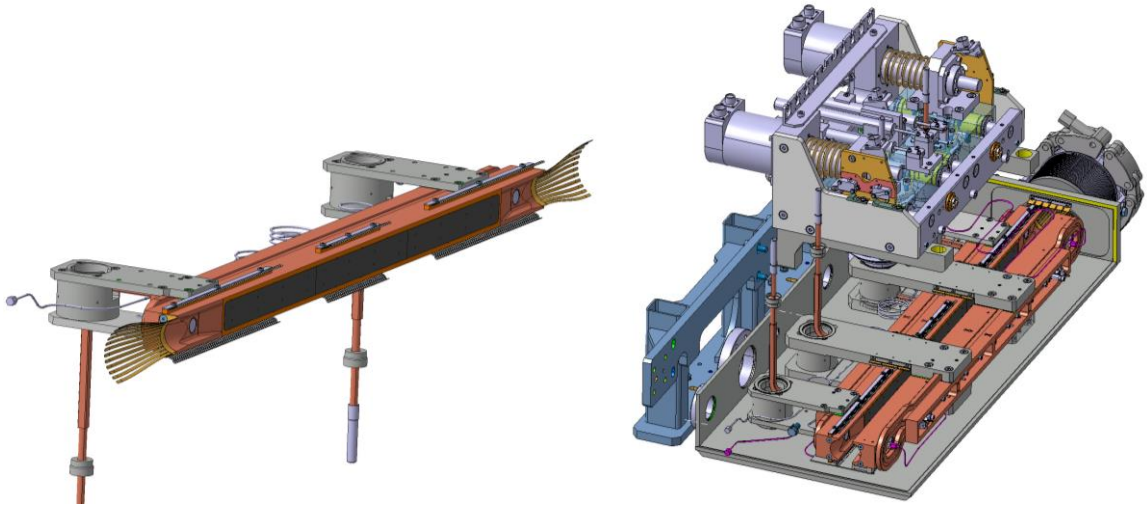

Figure 5-8: TCLD collimator jaw. The present design foresees a 60 cm-long jaw made of tungsten heavy alloy. The figure also shows RF fingers, cooling pipes and BPMs. Courtesy of L. Gentini.

5.5 Upgrades for impedance improvement

5.5.1 Introduction and rationale

The LHC impedance budget is largely dominated by the contribution of the LHC collimators [1] that amounts to more than 90% in the frequency of interest. For this reason, the present collimation system has been conceived in a way that it can be easily upgraded to reduce the impedance, since every secondary collimator slot TCSG in IR3 and IR7 features a companion slot TCSM for the future installation of a low-impedance secondary collimator [1]. A total of 22 slots (IR7) and 8 slots (IR3) are already cabled* for a quick installation

* Present installations include cabling for the collimator controls, but not for the read-out of the in-jaw BPMs, which were not part of the collimator design when these slots for system upgrade were prepared. Also missing are the last meters of radiation-hard cabling from the tunnel cable trails to the collimators.

of new collimators – referred to as TCSPM – that can either replace or supplement the present TCSG collimators. A partial preparation of these slots was done in LS1.

The importance of minimizing the machine impedance for the HL-LHC has been emphasized in Refs. [89] [90] [91], and in the 2013 LHC collimation review [76]. It is also important to stress that each new TCS collimator will also add the BPM functionality for a faster setup, We therefore foresee that, by the time of the full HL-LHC implementation (LS3), some or all of the available TCSM slots will be equipped with advanced collimators using new jaw materials with thin coating layers, to reduce the machine impedance. A staged installation using LS2 and LS3 is the present installation baseline (see Section 5.5.2). Simulations predict that beam stability can be re-established for all the HL-LHC scenarios if the CFC of present secondary collimators is replaced, at least in the betatron cleaning insertion, with a jaw material having an electrical conductivity a factor of 50 to 100 higher than CFC [89][90].

Secondary collimators in IR7 play a crucial role in LHC machine protection and might be exposed to large beam losses. Therefore, collimator materials and designs must also be robust against beam failure (at least those exposed to horizontal losses). The driving requirements for the development of new materials are thus: (i) low resistive-wall impedance to avoid beam instabilities; (ii) high cleaning efficiency; (iii) high geometrical stability to maintain the extreme precision of the collimator jaw during operation despite temperature changes; and (iv) high structural robustness in case of accidental events like single-turn losses. The latter requirement rules out the possibility to deploy high-Z metals because of their relatively low melting point and comparatively large thermal expansion that impairs their resistance to thermal shocks [92]. The present baseline for the upgraded secondary collimators relies on novel carbon-based materials such as molybdenum carbide-graphite (MoGr), a ceramic composite, jointly developed by CERN and Brevetti Bizz (IT), in which the presence of carbides and carbon fibres strongly catalyses the graphitic ordering of carbon during high temperature processing, enhancing its thermal and electrical properties [93][94]. To further improve their surface electrical conductivity, these materials will be coated with pure molybdenum.

In addition to the impedance improvements, the new TCSPM design also features a number of improvements in the mechanical design (see Figure 5-9) [95]. They incorporate the BPM button design. The key hardware parameters are listed in Table 5-7.

Table 5-7: Parameters of TCSPM collimators

Characteristics	**Units**	**Value**
Jaw active length	mm	1000
Jaw material	-	MoGr
Flange-to-flange distance	mm	1480
Number of jaws	-	2
Orientation	-	Horizontal, vertical, skew
Number of motors per jaw	-	Two
Number of BPM buttons per jaw	-	Two
RF damping	-	Fingers
Cooling of the jaw	-	Yes
Cooling of the vacuum tank	-	Yes
Minimum gap	mm	< 1
Maximum gap	mm	60
Stroke across zero	mm	5
Angular adjustment	-	Yes
Jaw coating	-	Yes: Mo
Transverse jaw movement (fifth axis)	mm	± 10

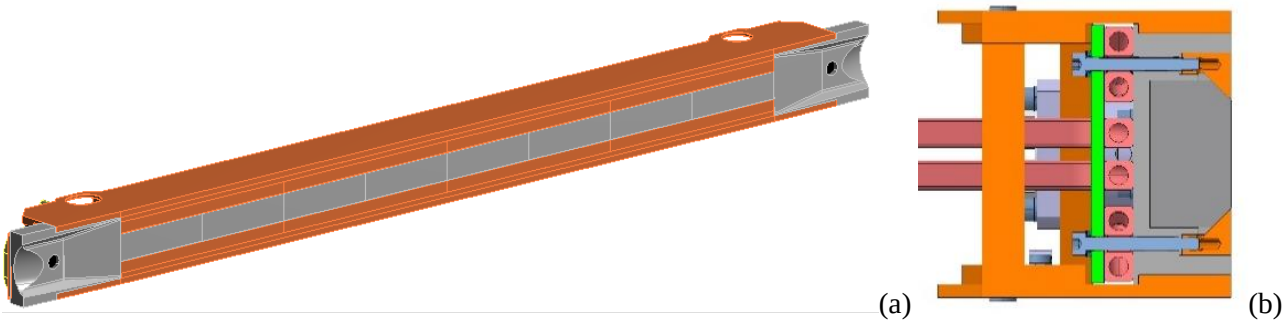

(a) (b)

Figure 5-9: The 3D view of the TCSMP jaw (a) and its cross-section (b).

5.5.2 Staged installation

The present low-impedance upgrade baseline foresees the installation of TCSPM collimators in 9 out of 11 TCSM slots per beam. Two slots out of the original upgrade pool have been dropped for cost optimisation, in light of recent estimates that indicate that this revised baseline is compatible with the HL-LHC goals. Each TCSM slot sits immediately downstream of the respective TCSG slot, where regular TCSG collimators are installed. The installation is foreseen in two stages: a first installation in the Long Shutdown 2 (LS2), involving 4 TCSPM collimators per beam, followed by a second installation in LS3, when the remaining 5 collimators per beam will be installed. Assets of this choice are:

- It provides an important reduction of the collimator impedance already for the LHC Run 3, when the upgraded beam parameters from the LHC Injector Upgrade (LIU) program will progressively become available. This allows studying the impedance limitations for the HL-LHC.
- It allows possible further iterations on the new collimator design for LS3.
- It allows distributing resources that would otherwise have to be made available in LS3, when WP5 will be focused on the IR1/5 upgrade.

The choice of the slots for installation during LS2 [96] was mainly driven by maximising the impedance reduction for the first upgrade phase with the limited pool of upgraded collimators; the expected thermo-mechanical loads on the new collimators in case of regular or abnormal losses have also been taken into account. In terms of cleaning inefficiency, numerical simulations have shown that all the considered options are equivalent. The optimisation process highlighted that:

- The first two skew collimators were not selected. They are the most loaded secondary collimators and are exposed to large jaw deformations in the HL-LHC. A new design that mitigates jaw deformation is necessary for these collimators.

The risk of damage for the present slots, in case of injection failures or asynchronous dumps, is considered tolerable [96].Table 5-8 details the installation slots of the TCSPM collimators in LS2. In general, the installation slots are always the TCSM ones and the present TCSGs are kept operational, with the only exceptions being those slots where test hardware is already installed and foreseen for future use (e.g. in D4L7.B1 and D4R7.B2). The choice of the two TCSG that will not be replaced is being studied by exploring various options.

Table 5-8: Installation slots of the TCSPM collimators in LS2, along with the collimation angle [96].

B1 slot	B2 slot	Angle [deg]
TCSG.D4L7.B1	TCSG.D4R7.B2	90.0
TCSM.B4L7.B1	TCSM.B4R7.B2	0.0
TCSM.E5R7.B1	TCSM.E5L7.B2	130.5
TCSM.6R7.B1	TCSM.6L7.B2	0.5

5.5.3 Validation of new design

The new collimator design [95] along with novel materials and coating solutions must be validated for operation in the LHC. For this purpose, a rich program of validation tests has been carried out involving mechanical engineering prototyping, validation of new materials for operation with HUV and at high radiation doses, and tests with high radiation doses (e.g. at BNL and GSI) [101]. HiRadMat tests [99][100] demonstrated among other things that a full-scale MoGr jaw could withstand the most challenging design failure scenario (injection error) without apparent damage and that the Mo-coating layer exhibited only a small, non-catastrophic surface scratch which can be compensated for by exposing an undamaged surface to the beam using the 5th axis functionality[†]. Furthermore, tests with circulating beam in the LHC have been carried out in 2017–2018 with a special prototype built with MoGr bulk and with three stripes with different surface (uncoated MoGr, Mo coating and TiN coating [102][103]. The measured tune shift confirms a significantly lower impedance, although a discrepancy with numerical simulations can be explained by the quality of the microstructure of the coating and of the jaw roughness. This aspect has been improved for the series production. The prototype collimator was successfully used in regular operation throughout 2018 without issues [104][105].

5.5.4 Reduction of impedance of primary collimators

The WP5 impedance upgrade includes a contribution to the procurement of low-impedance material for the primary collimators that are otherwise renewed under the Consolidation project. In LS2, 4 primary collimators of IR7, the horizontal one and the vertical one for both beams, will be replaced with the new design called TCPPM that adds [106]: (1) MoGr absorbing material, without coating; (2) BPM functionality. For the case of primary collimators continuously exposed to primary beam losses, coating the active jaw part is not considered a viable option. The MoGr provides an improvement of about a factor 5 in resistivity compared to CFC, while ensuring a similar robustness against beam failure. Five TCPPM are built in LS2, 4 for the machine and one spare. The HL-LHC-WP5 contributes by procuring material for 3 collimators.

5.6 Advanced concepts for collimation upgrade recently integrated into the baseline

In this Section we discuss two new collimation concepts and designs that were integrated in the WP5 upgrade baseline in Dec. 2019: crystal collimation for heavy-ion beams and hollow electron lenses (HELs). These two items, which are schematically illustrated in Figure 5-10, were part of the approved studies within WP5 and became in 2019 part of the HL-LHC Baseline through in-kind contributions from Russia. Focus was put in recent years to review the needs for these upgrades for the HL-LHC and to demonstrate the required technology in tests without and with beam. Both crystal collimation and HELs address, in different ways, further improvements of the betatron collimation system.

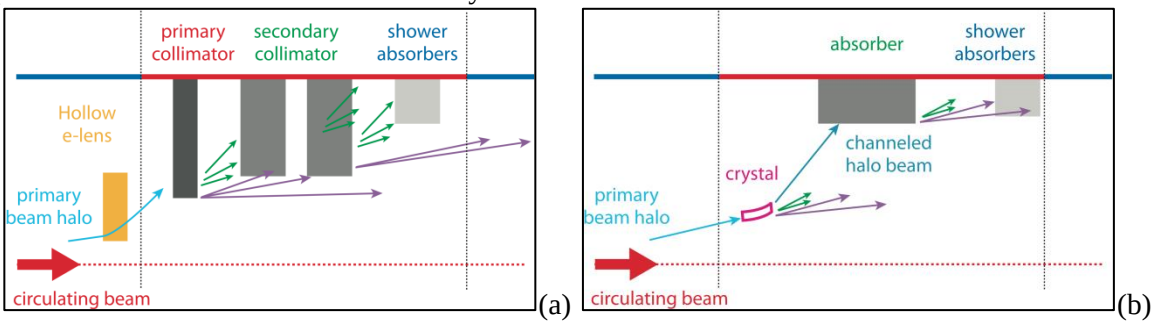

Figure 5-10: Illustrative view (a) of the collimation system with integrated hollow e-lens or equivalent halo diffusion mechanism; (b) an ideal crystal-based collimation.

[†] Observations of jaw surface damage are not straightforward. In case of failure, dedicated beam measurements (e.g., check of alignment positions found with beam-based techniques, impedance measurements) will be setup to see if any detrimental effect is observed compared to the reference system.

5.6.1 Hollow electron lenses for enhanced halo collimation

Operational experience in 2012 indicates that the LHC collimation would profit from halo control mechanisms. The operation of Run 2 at 6.5 TeV showed a less severe impact from halo losses [107]; however, scaling them to HL-LHC beam parameters is still a source of concerns. In particular, the presence of over-populated tails in the LHC beams was consistently observed in dedicated measurements at the LHC [107]. Simple extrapolations to the HL-LHC beam intensities lead to the estimate that more than 30 MJ can be stored at transverse amplitudes between 3.5-4.0 σ and the aperture of primary collimators. This scenario, in particular considering that crab-cavities might produce new fast-loss failures at the HL-LHC, requires the need for an active control of tail population at the HL-LHC. The HEL described in this Section are the most promising solution to achieve this goal. These aspects were reviewed in various international WP5 reviews that recommended the insertion of HEL in the WP5 upgrade baseline [108][109].

In a HEL, a hollow electron beam runs parallel and concentrically to the proton or ion beam. The hollow beam produces an electromagnetic field only affecting halo particles above a given transverse amplitude determined by its inner radius, changing their transverse diffusion speed. The conceptual working principle and its integration into the collimation system are illustrated in Figure 5-10 (a). A solid experimental basis achieved at the Tevatron indicates that this solution is promising for the LHC ([110] and references therein). The potential advantages of the electron lens collimation are several:

- Control of the primary loss rates, with potential mitigation of peak loss rates in the cold magnets, for a given collimation cleaning. Peak power losses on the collimators themselves can be optimized as well.
- Controlled depletion of beam tails (mitigate risk of damage with tens of MJ in the tails).
- Mitigation of loss spikes in the case of orbit drifts.
- Scrape the beam at very low amplitudes (>3 σ) without the risk of damage, as one would have for bulk scrapers.
- Tuning of the impact parameters on the primary collimators with a possible improvement in cleaning efficiency (in particular for ions).
- Possibility to tighten primary collimator settings for a smaller β^* reach, through reduced beam tails.

IR4 is considered to be the best candidate for installing the two HEL devices due to the larger than standard inter-beam distance that eases integration aspects, cryogenics availability, low-radiation environment, and quasi-round beams.

The HEL is targeted at enabling active control of beam tails above 3 to 4 real beam sigmas, with tail depletion efficiencies of the order of 90% over times of tens of seconds. This should be possible, ideally, in all phases of the operational cycle, but specifically at top energy. No specific loss problems are expected at injection energy, but the possibility to use HELs at 450 GeV is considered as a key asset for an efficient commissioning of these complex devices, that is required to be able to perform tail depletion during the beam energy ramp before reaching 7 TeV. The present parameters of the HL-LHC lenses, optimized for 7 TeV, are given in Table 5-9. Note that the HEL design should ensure: (i) the possibility of pulsing the current turn-by-turn (as required to drive linear resonances in the machine before beams are in collision); (ii) a train-by-train selective excitation (leaving ‘witness’ trains with populated halos for diagnostics and machine protection purposes). The present design of the HL-LHC lenses is shown in Figure 5-11, and a preliminary integration in IR4 is given in Figure 5-12.

Table 5-9: Hollow electron beam equipment parameters

Parameter	Value
Geometry	
Length of the interaction region, L (m)	3
Desidered transverse scraping range (σ, ε= 2.5 µm)	3.5 – 7.1
Inner/outer electron beam radii at 7 TeV (mm)	1,1 – 2.2
Inner/outer cryostat diameter (mm)	132/ ≈ 500
Inner vacuum chamber diameter (mm)	60
Magnetic fields at 7 TeV and magnet parameters	
Main solenoid field, B_m (T)	5
Gun solenoid field, B_g (T)	0.35
Bending Solenoid field (T)	3.5
Compresor factor $\sqrt{B_m/B_g}$	3.8
Maximum current in main solenoid (A)	250 - 300
Electron gun	
Inner/outer cathode diameters (mm)	8.0 – 16.0
Peak yield at 10 kV, I (A)	5
High-voltage modulator	
Cathode-anode voltage (KV)	10
Cathode-ground voltage (KV)	15
Rise time (10% - 90%) (ns)	200
Repetiotion rate (kHz)	35

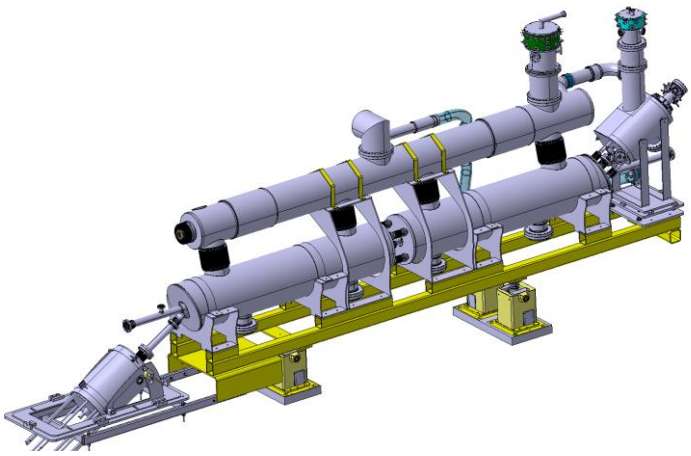

Figure 5-11: 3D design of the HL-LHC hollow e-lens. An ‘S’ shape is proposed. Courtesy of D. Perini.

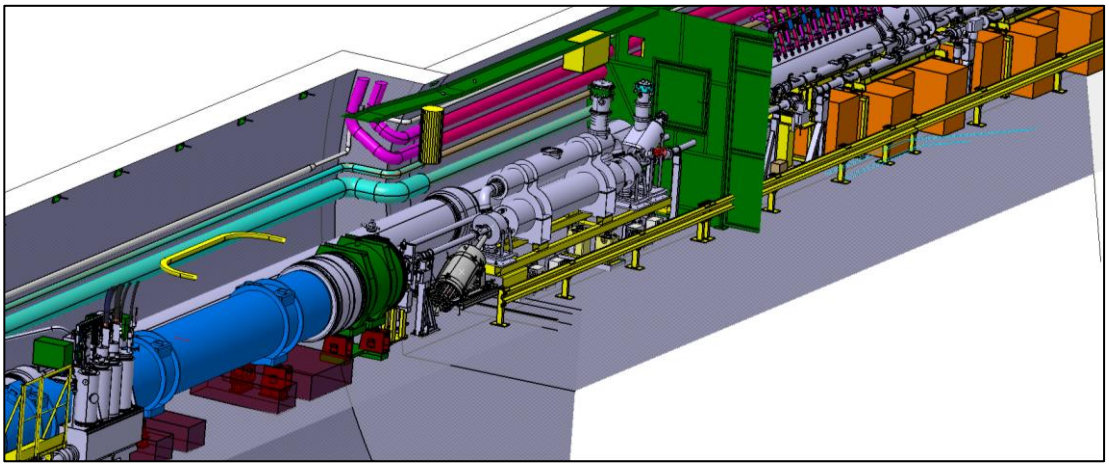

Figure 5-12: 3D integration in P4 for the HEL of beam 1 [109].

5.6.2 Crystal collimation

Highly pure bent crystals can be used to steer high-energy particles that get trapped by the potential of parallel lattice planes. Equivalent bending fields of up to hundreds of Tesla can be achieved in crystals with a length of only a few mm, which allows, in principle, steering halo particles to a well-defined point where dedicated absorbers are located. This scheme is shown schematically in Figure 5-10 (b). As opposed to the standard multi-stage collimation system based on amorphous materials, requiring several secondary collimators and absorbers to catch the products developed through the interaction with matter (see Figure 5-1), one single absorber per collimation plane is in theory sufficient in a crystal-based collimation system.

Simulations indicate a possible gain in cleaning efficiency for proton beams by a factor 5 to 10 [112], even for a layout without an optimized absorber design. In the present layout, this can only be achieved with low beam intensities because deploying crystal collimation for proton beam would require adding in IR7 new – to be designed – absorbers for the ~ 1 MW halo. The crystal collimation option is particularly interesting for collimating heavy-ion beams, where more stringent limitations are expected (see Section 5.4.2) and where the implied losses in IR7 are compatible with the existing hardware and layout in IR7. The recent R&D program on crystal collimation has been focused on ion beam performance, to demonstrate the feasibility of this concept. A unique crystal collimation test stand has been available for beam tests at high energy in the LHC during Run 2 [112]. A summary of the main results can be found in the contributions to the Crystal Collimation Day organized on October 18th, 2018 [114] (see Refs. [115] [116] [117]). Additional important results were achieved during the 2018 heavy ion run, in November 2018, showing an improvement of ion collimation cleaning by up to a factor 7 [118][119]. The LHC beam tests also validated critical hardware components like the high-precision goniometer and its controls that allow maintaining the crystal angular orientation at the optimum value for channelling with sub-μrad resolution. Continuous channelling was achieved during energy ramp and betatron squeeze.

The specifications of the crystal devices are given in Ref. [112] and summarized in Table 5-10. The present IR7 layouts include two different design versions, with the newest design installed in 2016 and 2017 featuring improvements obtained after the first installation in 2015. A newer, final version is now available [121] and it is being prototyped during LS2. For a complete system, it is ideally required to have a total of eight crystals: two per beam and per plane, allowing one to confine possible orbit drifts of both signs while ensuring a good cleaning performance. The test stand in IR7 only has 4, with one crystal only per beam plane.

During LS2, it was decided to integrate crystal collimation in the upgrade baseline in order to cope with potential schedule issues with the production of the new 11 T dipoles for IR7 (see Section 5.4.2). The proposal was approved by the management in Dec. 2019, thanks to the possibility to build the new required hardware through an in-kind contribution by Russia. The detailed scope of this upgrade consists in preparing 4 new

crystal primary collimators (TCPCs) that can replace the existing 4 devices installed in IR7[‡]. The latter were conceived for MD studies and not for regular operations, which calls for an improvement of their design. The controls also need to be upgraded in order to adapt the operational modes to the standards used by the rest of the collimation system for operations with high intensity beams. The WP5 teams are presently working on a schedule for a possible installation of the new devices before the end of LS2, with the fall-back option to install them (or complete the installation, if fewer can be installed in LS2) in a subsequent end-of-year shutdown.

Table 5-10: Crystal equipment parameters.

Parameter	Value
Crystal length along the beam	4 ± 0.1 mm
Total height	< 55 mm
Total weight	< 150 g[§]
Channeling plane	<110>
Channeling axis	<111> or <110>
Miscut for planar channeling	< 40 μrad
Torsion	< 1 μrad/mm
Bending	50.0 ± 2.5 μrad
Miscut for axial channeling	0 ± 18 mrad
Dislocation density	< 1 cm^2

5.7 Other collimators from the present system required in the HL-LHC

It is important to realize that several devices of the present LHC collimators, which are not to be modified or replaced in the collimation upgrade baseline described above, must remain reliably operational for the HL-LHC era. A summary is given in Table 5-11. These items are subject of consolidation of the system that is not discussed as part of this document.

Table 5-11: Collimators of the present system that remains operational in Run 3 and Run 4.

Functional type	Type	Plane	Material	BPM	Run 2	Run 3	Run 4
Primary IR3	TCP	H	CFC	No	2	2	2
Secondary IR3	TCSG	H	CFC	No	8	8	8
Absorber IR3	TCLA	H, V	W alloy	No	8	8	8
Primary IR7	TCP	H, V, S	CFC	No	6	2	2
Secondary IR7	TCSG	H, V, S	CFC	No	22	14	4
Absorber IR7	TCLA	H, V	W alloy	No	10	10	10
Tertiary IR1/2/5/8	TCTP	H, V	W alloy	Yes	16	16	16
Physics debris absorbers IR1/5	TCL	H	Cu, W alloy	No	12	12	0

5.8 Acknowledgements

This Chapter reports on important contributions by several people who, across the years, participated to the collimation upgrade studies. The authors who took the role to summarize all these contributions on behalf of the WP5 teams, would like to kindly acknowledge all the work done by these teams over the year.

5.9 References

[1] O. Brüning (Ed.) *et al.*, LHC Design Report Vol. 1 (2004). DOI: 10.5170/CERN-2004-003-V-1.

[2] R. Assman *et al.*, The final collimation system for the LHC, CERN-LHC-PROJECT-REPORT-919.

[‡] As a part of the in-kind contributions, devices for a 8-TCPC system will be built, but the IR7 upgrade baseline does not include CERN budget for the infrastructure preparation.

[§] 300 g might be accepted following the results on goniometer studies.

[3] R. Bruce *et al.*, LHC Operation Workshop, Evian, 2011. INDICO: 155520.

[4] R. Bruce, et al., Sources of machine-induced background in the ATLAS and CMS detectors at the CERN Large Hadron Collider, Nucl. Instrum. Methods Phys. Res. A729 DOI: 10.1016/j.nima.2013.03.058.

[5] G. Valentino *et al.*, Beam diffusion measurements using collimator scans in the LHC, *Phys. Rev. Spec. Top. Accel. Beams* **16** (2013) 021003. DOI: 10.1103/PhysRevSTAB.16.021003.

[6] K. H. Mess and M. Seidel, Collimators as diagnostic tools in the proton machine of HERA, *Nucl. Instrum. Meth.* A351 (1994) 279–285. DOI: 10.1016/0168-9002(94)91354-4.

[7] H. Burkhardt, *et al.* Collimation System, Conference (2013). DOI: 10.5170/CERN-2015-005.109.

[8] S. Redaelli *et al.*, LHC Collimator Controls for a Safe LHC Operation, wepmu020.

[9] Z. Citron *et al.*, Future physics opportunities for high-density QCD at the LHC with heavy-ion and proton beams, CERN-LPCC-2018-07 (2018).

[10] G. Apollinari, I. Béjar Alonso, O. Brüning, P. Fessia, M. Lamont, L. Rossi, L. Tavian, High-Luminosity Large Hadron Collider (HL-LHC) Technical Design Report V. 0.1 DOI: 10.23731/CYRM-2017-004.

[11] 4th HL-LHC/LIU Cost & Schedule Review 2019 Close-out presentation EDMS: 2271479 (Confidential)

[12] B. Salvachua Ferrando *et al.*, Cleaning performance of the LHC collimation system up to 4 TeV mopwo048.

[13] N. Fuster *et al.*, Collimation, Proc. 9th LHC Operations Evian Workshop, Evian, France (2019).

[14] S. Redaelli *et al.*, Replacement of TCT in IR1, IR2, IR5 and of TCSG Collimators in IR6 with Collimators with Embedded BPM Buttons, EDMS: 1251162, CERN, Geneva, Switzerland (2013).

[15] A. Bertarelli *et al.*, The Mechanical Design for the LHC Collimators, moplt008.

[16] S. Redaelli *et al.*, Final Implementation and Performance of the LHC Collimator Control System, Proc. PAC09, Vancouver (CA). Conference: C09-05-04, FR5REP007.

[17] A. Bertarelli *et al.*, Mechanical design for robustness of the LHC collimators, Proc. PAC2005, Knoxville. TPAP004.

[18] S. Redaelli, Change of number of low-impedance secondary collimators for HL-LHC EDMS: 2165931.

[19] R. Bruce, R.W. Assmann and S.Redaelli, Calculations of safe collimator settings and β* at the Large Hadron Collider, *Phys. Rev. ST Accel. Beams* **18**, (2015). DOI : 10.1103/PhysRevSTAB.18.061001.

[20] R. Bruce *et al.*, Reaching record-low β^* at the CERN Large Hadron Collider using a novel scheme of collimator settings and optics, *Nucl. Instrum. Methods Phys. Res. A* **848** (2017). DOI: 10.1016/j.nima.2016.12.039.

[21] F. Carra *et al.*, LHC collimators with embedded beam position monitors: A new advanced mechanical design, Proc. IPAC2011, San Sebastian, IPAC-2011-TUPS035 (2011).

[22] D. Wollmann *et al.*, Beam feasibility study of a collimator with in-jaw beam position monitors, *Nucl. Instrum. Methods Phys. Res., Sect. A* **768**, 62, (2014). DOI: 10.1016/j.nima.2014.09.024.

[23] G. Valentino *et al.*, Successive approximation algorithm for BPM-based LHC collimator alignment, *Phys. Rev. ST Accel. Beams* **17**, 021005 (2014). DOI: 10.1103/PhysRevSTAB.17.021005.

[24] G. Valentino *et al.*, Final implementation, commissioning, and performance of embedded collimator beam position monitors in the Large Hadron Collider, *Phys. Rev. Accel. Beams* **20**, 081002 (2017) DOI: 10.1103/PhysRevAccelBeams.20.081002.

[25] R. Bruce *et al.*, Installation of a primary collimator with orbit pickups (TCPP) replacing a TCP, LHC-TC-EC-0005, EDMS: 1705737, CERN, Geneva, Switzerland (2016).

[26] R. Bruce and S. Redaelli, Installation of a low-impedance secondary collimator (TCSPM) in IR7, LHC-TC-EC-0006, EDMS: 1705738, CERN, Geneva, Switzerland (2016).

[27] A. Rossi *et al.*, Installation of two wire collimators in IP1 for Long Range Beam-Beam compensation, LHC-TC-EC-0009, EDMS: 1832270, CERN, Geneva, Switzerland (2017).

[28] A. Rossi *et al.*, Installation of two wire collimators in IP5 for Long Range Beam-Beam compensation, LH-TC-EC-0007, EDMS: 1705791, CERN, Geneva, Switzerland (2018).

[29] R. Bruce *et al.*, Machine Configuration, Proc. 9th LHC Operations Evian Workshop, Evian, France (2019), in publication.

[30] D. Wollmann *et al.*, First beam results for a collimator with in-jaw beam position monitors, Proc. IPAC2011. THPZ027.

[31] D. Wollmann *et al.*, Experimental verification for a collimator with in-jaw beam position monitors, Proc. HB2012. mop242.

[32] R. Bruce *et al.*, Sources of machine-induced background in the ATLAS and CMS detectors at the CERN Large Hadron Collider, *Nucl. Instrum. Methods Phys. Res., Sect. A* **729**, 825 (2013). DOI: 10.1016/j.nima.2013.03.058.

[33] ATLAS Collaboration, Characterisation and mitigation of beam-induced backgrounds observed in the ATLAS detector during the 2011 proton-proton run, *J. Instrum.* **8**, P07004 (2013). DOI: 10.1088/1748-0221/8/07/P07004.

[34] ATLAS Collaboration, Comparison of simulated and observed LHC beam backgrounds in the ATLAS experiment at E_{beam} = 4 TeV, *J. Instrum.* **13**, P12006 (2018). DOI: 10.1088/1748-0221/13/12/P12006.

[35] R. Bruce *et al.*, Collimation-induced experimental background studies at the CERN Large Hadron Collider, *Phys. Rev. Accel. Beams* **22**, 021004 (2019). DOI: 10.1103/PhysRevAccelBeams.22.021004.

[36] A. Bertarelli *et al.*, An experiment to test advanced materials impacted by intense proton pulses at CERN HiRadMat facility, *Nucl. Instr. Meth. B* **308** (2013) 88. CERN-ATS-Note-2013-005 TECH.

[37] G. Gobbi *et al.*, Novel LHC collimator materials: High-energy Hadron beam impact tests and nondestructive postirradiation examination, *Mechanics of Advanced Materials and Structures* 1-13, DOI: 10.1080/15376494.2018.1518501.

[38] R. De Maria *et al.*, SixTrack V and Running Environment, *Int. J. Mod. Phys. A*, DOI: 10.1142/S0217751X19420351.

[39] A. Mereghetti *et al.*, SixTrack for cleaning studies: 2017 updates, Proc. 8th Int. Particle Accelerator Conf. (IPAC'17), Copenhagen, Denmark, 2017. DOI: 10.18429/JACoW-IPAC2017-THPAB046.

[40] D. Mirarchi *et al.*, "Cleaning Performance of the Collimation System of the High Luminosity Large Hadron Collider", in Proc. 7th Int. Particle Accelerator Conf. (IPAC'16), Busan, Korea, May 2016, pp. 2494-2497. DOI: 10.18429/JACoW-IPAC2016-WEPMW030.

[41] H. Garcia Morales *et al.*, Beam cleaning of the incoming beam in experimental IRs in HL-LHC, CERN-ACC-NOTE-2017-0023, 2017.

[42] E. Quaranta *et al.*, Modeling of beam-induced damage of the LHC tertiary collimators, *Phys. Rev. Accel. Beams* **20**, 091002 (2017). DOI: 10.1103/PhysRevAccelBeams.20.091002.

[43] R. Bruce *et al.*, Triplet and TCT protection during asynchronous dump in HL-LHC, presentation at the 7th HL-LHC annual meeting 2017, CIEMAT, Madrid, Spain.

[44] A. Tsinganis *et al.*, Impact on the HL-LHC triplet region and experiments from asynchronous beam dumps on tertiary collimators, Proc. 8th Int. Particle Accelerator Conference, Copenhagen, Denmark, (2017). DOI: 10.18429/JACoW-IPAC2017-MOPAB011.

[45] C. Bertella *et al.*, Study of damages induced on ATLAS silicon by fast extracted and intense proton beam irradiation, *Nucl. Instrum. Methods Phys. Res., Sect. A* **924**, pp. 236-240 (2019). DOI: 10.1016/j.nima.2018.06.043.

[46] M. Mentink, Conservative Quench Scenario Considerations in the IT Main Circuit and Impact on Voltages to Ground, presentation at the Magnet circuit forum 20th February 2018, CERN, INDICO: 704894.

[47] F. Cerutti *et al.*, IR collimation upgrades - outgoing beam, presentation at the International Review of the HL-LHC collimation system 2019, INDICO: 780182.

[48] L.S. Esposito and F. Cerutti, "Energy deposition for HL-LHC v1.1: TAN/D2/Q4", Presentation at the 4th Joint HiLumi LHC-LARP Annual Meeting, Tsukuba Japan, 2014.

[49] R. de Maria, Update on tolerance for remote alignment in IR1/5 for HL-LHC, presentation at the Collimation Upgrade Specification Meeting #108, 2018, INDICO: 757667.

[50] P. Fessia, Remote alignment options and solutions, Presentation at the 61st HL-LHC TCC, 15th November 2018, INDICO: 772120.

[51] 67th Collimation Upgrade Specification Meeting (ColUSM), Feb. 6th, 2016. INDICO: 493012.

[52] HiLumi-WP5 deliverable document 5.4. Available on the collimation page web page.

[53] Web site: Review of 11 T dipoles and cold collimation. INDICO: 155408.

[54] R. W. Assmann *et al.*, Collimator losses in the DS of IR7 and quench test at 3.5 TeV, CERN-ATS-Note-2011-042-MD (2011).

[55] R. W. Assmann *et al.*, Pb ions Collimator losses in the DS of IR7 and quench test at 3.5 Z TeV, CERN-ATS-Note-2012-081-MD (2012).

[56] B. Salvachua *et al.*, Collimation quench test with 4 TeV proton beams, CERN-ACC-NOTE-2014-0036.

[57] J.M. Jowett *et al.*, "Bound-free pair production in LHC Pb-Pb operation at 6.37 Z TeV per beam", Proceedings of IPAC2016, Busan, Korea. DOI: 10.18429/JACoW-IPAC2016-TUPMW028.

[58] B. Salvachua *et al.*, Collimation quench test with 6.5 TeV proton beams, CERN-ACC-NOTE-2016-0015 (2016).

[59] P. D. Hermes *et al.*, LHC Heavy-Ion Collimation Quench Test at 6.37Z TeV, CERN-ACC-Note-2016-0031 (2016).

[60] P. D. Hermes, Heavy-ion collimation at the Large Hadron Collider - Simulations and measurements, Ph.D. thesis, University of Munster, DE (2016) CERN-THESIS-2016-230.

[61] A. Ferrari, P.R. Sala, A. Fasso`, and J. Ranft, FLUKA: a multi-particle transport code, (2005), DOI: 10.2172/877507, 10.5170/CERN-2005-010.

[62] G. Battistoni *et al.*, Overview of the FLUKA code, *Annals of Nuclear Energy* **82**, 10-18 (2015) DOI: 10.1016/j.anucene.2014.11.007.

[63] P. D. Hermes, Tracking simulations of heavy ions quench test, presentation at the 201st LHC Collimation Working Group, 7th March 2016, INDICO: 504706.

[64] A. Mereghetti, Tracking simulations of protons quench test, presentation at the 201st LHC Collimation Working Group, 7th March 2016, INDICO: 504706.

[65] E Skordis *et al.*, FLUKA coupling to SixTrack, Proc. ICFA Mini-Workshop on Tracking for Collimation in Particle Accelerators, CERN, Geneva, Switzerland (2015). DOI: 10.23732/CYRCP-2018-002.205

[66] A. Mereghetti, Performance evaluation of the SPS scraping system in view of the High Luminosity LHC, Ph.D. Thesis, University of Manchester, UK (2015). CERN-THESIS-2015-116.

[67] E. Skordis *et al.*, Impact of Beam Losses in the LHC Collimation Regions, Proceedings of IPAC15, Richmond, VA, USA (2015). CERN-ACC-2015-271.

[68] C. Bahamonde Castro *et al.*, Energy deposition from collimation losses in the DS region at P7, Presentation at the 8th HL-LHC Collaboration Meeting, CERN (2018).

[69] C. Bahamonde Castro *et al.*, Update on energy deposition for IR7 for HL-LHC, presentation at the 7th HL-LHC Collaboration Meeting, Madrid, Spain (2017).

[70] G. Steele *et al.*, Heat load scenarios and protection levels for ions, presentation at the 2013 LHC Collimation Project review. INDICO: 251588.

[71] A. Lechner *et al.*, Energy deposition with cryo-collimators in IR2 (ions) and IR7, presentation at the 3rd Joint HiLumi LHC-LARP Annual Meeting, Daresbury (UK), 2013. INDICO: 257368.

[72] E. Skordis, Updated power deposition simulations for DS collimators in IR7 (proton operation), presentation at the 51st Collimation Upgrade Specification Meeting. INDICO: 366694.

[73] P. D. Hermes, Ion simulations for different TCLD layouts, presentation at the 89th ColUSM, June 16th, 2017. INDICO: 646799.

[74] D. Mirarchi, Proton Simulations for different TCLD layouts, presentation at the 94th ColUSM, Sep. 29th, 2017. INDICO: 666560.

[75] LHC Collimation Review 2009. INDICO: 55195.

[76] 2013 Collimation Project Review. INDICO: 251588.

[77] L. Bottura *et al.*, Expected performance of 11 T and MB dipole considering the cooling performance, presentation at the 8th HL-LHC Collaboration Meeting, CERN, 2018.

[78] L. Bottura *et al.*, Quench performance and assumptions: magnets and cryogenics, presentation at the International Review of the HL-LHC Collimation System (2019). INDICO: 780182.

[79] J.M. Jowett *et al.*, Heavy ion beams in the LHC, Proc. PAC 2003, Portland (2003), TPPB029.

[80] R. Bruce *et al.*, Beam losses from ultraperipheral nuclear collisions between $^{208}Pb^{82+}$ ions in the Large Hadron Collider and their alleviation, *Phys. Rev. ST Accel. Beams* **12** (2009) DOI: 10.1103/PhysRevSTAB.12.071002.

[81] A. Lechner *et al.*, "BFPP losses in the connection cryostat: power deposition and dose estimates for Run 2 (and some outlook to HL-LHC)", Presentation at the LMC Meeting, Sept 2015, INDICO: 442208.

[82] C. Bahamonde Castro *et al.*, Power deposition in LHC magnets due to bound-free pair production in the experimental insertions, Proceedings of IPAC2016, Busan, Korea. DOI: 10.18429/JACoW-IPAC2016-TUPMW006.

[83] J.M. Jowett *et al.*, "The 2015 heavy-ion run of the LHC", Proceedings of IPAC16, Busan, Korea, TUPMW027, pp. 1493-1496. DOI: 10.18429/JACoW-IPAC2016-TUPMW027.

[84] J.M. Jowett *et al.*, "Overview of ion runs during run 2", Proc. 9th LHC Operations Evian Workshop, Evian, France (2019).

[85] C. Bahamonde Castro *et al.*, "Needs for shielding in the connection cryostats in IR2 DS", Presentation at the 14th Meeting of the HL-TCC, Sept 2016, INDICO: 559125.

[86] R. Bruce, A. Mereghetti and S. Redaelli, Installation in IR2 of Dispersion Suppressor Collimators (TCLD), LHC-TC-EC-0012, EDMS: 1973010, CERN, Geneva, Switzerland (2018).

[87] R. Bruce, A. Mereghetti and S. Redaelli, Installation in IR7 of Dispersion Suppressor Collimators (TCLD), LHC-TC-EC-0013, EDMS: 1973028, CERN, Geneva, Switzerland (2018).

[88] G. Steele *et al.*, Preliminary results of the FLUKA TCLD study (IR7), presentation at the Collimation Upgrade Specification Meeting , 18th October 2013, INDICO: 278104.

[89] N. Mounet, Transverse impedance in the HL-LHC era, presentation at the 3rd HiLumi Annual meeting, Daresbury, (2013). INDICO: 257368.

[90] N. Biancacci, presentation at the 55th meeting of the Collimation Upgrade Specification working group INDICO: 390114.

[91] HiLumi WP2 milestone document M29, Initial estimate of machine impedance. CERN-ACC-2014-0005.

[92] A. Bertarelli, Beam Induced Damage Mechanisms and Their Calculation, proceedings of the Joint International Accelerator School on Beam Loss and Accelerator Protection, Newport Beach, DOI: 10.5170/CERN-2016-002.

[93] A. Bertarelli *et al.*, Novel Materials for Collimators at LHC and its Upgrades, HB2014, East Lansing, 2014. CERN-ACC-2015-0173.

[94] A. Bertarelli *et al.*, Development and testing of novel advanced materials with very high thermal shock resistance, Tungsten, Refractory and Hard metals Conference, Orlando, 2014.

[95] F. Carra *et al.*, Mechanical engineering and design of novel collimators for HL-LHC, IPAC2014, Dresden, (2014). DOI: 10.18429/JACoW-IPAC2014-MOPRO116.

[96] S. Antipov *et al.*, Staged implementation of low-impedance collimation in IR7: plans for LS2, CERN-ACC-2019-0001, CERN, Geneva, Switzerland (2019). CERN-ACC-NOTE-2019-0001.

[97] E. Metral, *et al.*, Impedance models, operational experience and expected limitations, presentation at the International Review of the HL-LHC Collimation System (2019). INDICO: 780182.

[98] X. Buffat *et al.*, MD3288 – Instability latency with controlled noise, presentation at the LSWG meeting, 3rd July 2018, CERN, Geneva, Switzerland.

[99] E. Quaranta *et al.*, Towards optimum material choices for HL-LHC collimation upgrade, IPAC2016, wepmw031.

[100] 96th Collimator Upgrade Specification Meeting, 8th November 2017, CERN, Geneva, Switzerland. INDICO: 676105.

[101] E. Quaranta *et al.*, Radiation-induced effects on LHC collimator materials under extreme beam conditions, IPAC2016, wepmw032.

[102] R. Bruce and S. Redaelli, Installation of a low-impedance secondary collimator (TCSPM), LHC-TC-EC-0006, EDMS: 1705738.

[103] S. Antipov *et al.*, Single-collimator tune shift measurement of the three-stripe collimator at LHC, Proceedings of IPAC2018, Vancouver, BC, Canada. DOI: 10.18429/JACoW-IPAC2018-THPAF035.

[104] M. Patecki and A. Mereghetti, Operational experience with the TCSPM prototype, presentation at the 239th LHC Collimation Working Group Meeting, 4th February 2019, INDICO: 792567.

[105] A. Mereghetti *et al.*, Performance of new designs deployed in Run II and plans for Run III, Presentation at the International Review of the HL-LHC Collimation System, INDICO: 780182.

[106] R. Bruce, A. Mereghetti and S. Redaelli, LHC-TC-EC-0016, EDMS: 1973590 (2018).

[107] B. Salvachua Ferrando *et al.*, Beam losses, lifetime and operational experience at 6.5 TeV, Presentation at the International Review of the HL-LHC Collimation System, INDICO: 780182.

[108] Review of the needs for a hollow e-lens for the HL-LHC, 6th – 7th October 2016, CERN, Geneva, Switzerland. INDICO: 567839.

[109] International review on the e-lens concept readiness for integration into the HL-LHC baseline, 19th – 20th October 2017, CERN, Geneva, Switzerland. INDICO: 648237.

[110] G. Stancari, Electron-lens experience at Tevatron and RHIC, International review on the e-lens concept readiness for integration into the HL-LHC baseline, 19th – 20th October 2017, CERN, Geneva, Switzerland.

[111] M. Fitterer, *et al.*, Resonant and random excitations on the proton beam in the Large Hadron Collider for active halo control with pulsed hollow electron lenses arXiv:1804.07418.

[112] D. Mirarchi *et al.*, Design and implementation of a crystal collimation test stand at the Large Hadron Collider, *The European Physical Journal C* **77:424** (2017). DOI: 10.1140/epjc/s10052-017-4985-4.

[113] C. Bahamonde Castro *et al.*, Simulations of energy deposition for crystal collimation, Presentation at the 106th ColUSM Meeting, INDICO: 740297.

[114] HL-LHC Crystal Collimation Day, INDICO: 752062.

[115] D. Mirarchi *et al.*, Recent results on crystal collimation for a low-background physics run at the LHC, Presentation at the HL-LHC Crystal Collimation Day, INDICO: 752062.

[116] M. D'Andrea *et al.*, LHC operational experience with proton beams, Presentation at the HL-LHC Crystal Collimation Day, INDICO: 752062.

[117] R. Rossi *et al.*, LHC operational experience with heavy ion beams, Presentation at the HL-LHC Crystal Collimation Day, INDICO: 752062.

[118] D. Mirarchi *et al.*, Crystal collimation for lead ion beams, Presentation at the International Review of the HL-LHC Collimation System, INDICO: 780182.

[119] M. D'Andrea *et al.*, Preliminary results from crystal collimation studies in 2018, Presentation at the 70th HL-LHC TCC, INDICO: 804616.

[120] W. Scandale et al., Observation of channeling for 6500 GeV/ c protons in the crystal assisted collimation setup for LHC, *Phys. Lett. B* **758** (2016) 129-133.DOI: 10.1016/j.physletb.2016.05.004.

[121] I. Lamas Garcia *et al.*, "Update on mechanical design for crystal collimators", Presentation at the 111th ColUSM Meeting, INDICO: 788971.

[122] R. Bruce, A. Mereghetti and S. Redaelli, LHC-TCAP-EC-0001, EDMS: 1973905 (2018).

[123] P. Fessia *et al.*, LHC-MW-EC-0002, EDMS : 1321045.

Chapter 6

Circuit layout, powering, and protection

F. Rodríguez Mateos[1*], *T. D. Catalão Rolhas da Rosa*[1], *F. Menéndez Cámara*[1], *S. Yammine*[1] *and M.Zerlauth*[1]

[1]CERN, Accelerator & Technology Sector, Switzerland
[*]Corresponding author

6 Circuit layout, powering and protection

During LS2 and LS3, the HL-LHC upgrade will impose many changes to the magnet circuits of the LHC long-straight sections at points 1 and 5. Figure 6-1 depicts the new layout of magnets as required for the HL-LHC insertion regions. These magnets will be installed in the machine during LS3. In addition to these changes, during LS2, two main dipole magnets (MB) will be replaced by 11T cryo-assemblies (MBH) in order to allow the addition of two extra collimators at warm to intercept dispersive beam losses originating from the collimation system installed in point 7. The two concerned dipole magnets that are to be replaced are MBB.A9L7 and MBA.A9R7. Figure 6-2 and Figure 6-3 show the circuit upgrade for the 11T cryo-assemblies. The next paragraphs will detail each of the circuits concerned.

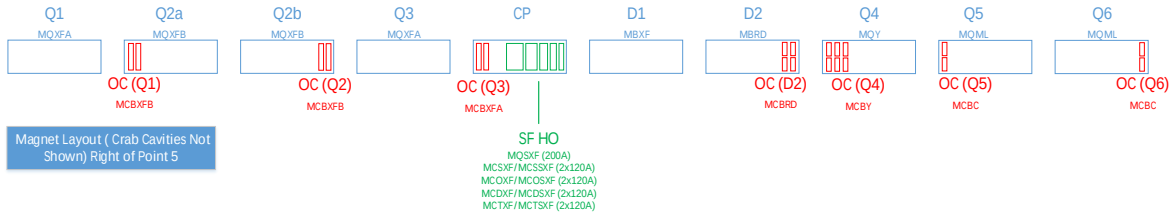

Figure 6-1: Magnet representation for the HL-LHC insertion region at right of point 5.

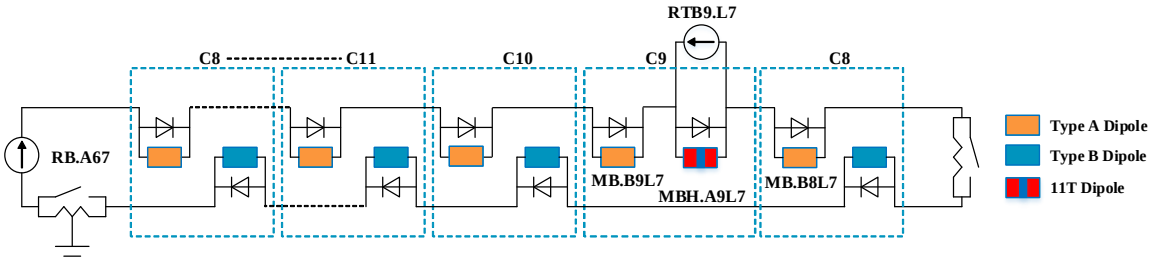

Figure 6-2: 11T cryo-assembly replacement of an MB magnet for circuit RB.A67.

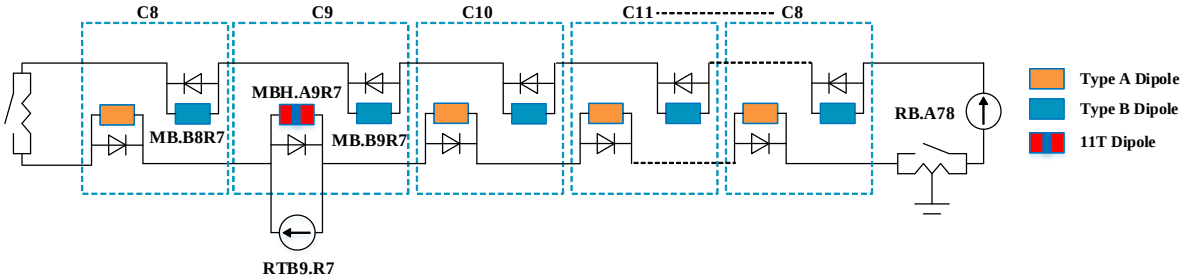

Figure 6-3: 11T cryo-assembly replacement of an MB magnet for circuit RB.A78.

6.1 Inner triplet main circuit

For the HL-LHC, the new MQXFA and MQXFB will replace the MQXA and MQXB magnets as Q1-Q2a/b-Q3 low-β triplet around the high-luminosity experiments ATLAS and CMS. In addition, the layout relies on one main circuit with additional trim circuits for Q1a, Q1 and Q3 as shown in Figure 6-4. Figure 6-5 shows the electrical schematic of the inner triplet main circuit with the main powering components and magnets. The changes of the inner triplet main circuit with respect to TDR V0.1 are summarized in an engineering change request [1]

- **Power converters**: The main power converter of the Inner Triplet circuit will have a rating of 18 kA. R&D work is being done to develop a new type of 2-quadrant power converter in order to apply positive and negative voltages to the magnets which is mandatory to allow for the ramp-down the current in the shadow of the main LHC dipole magnets. Two trim power converters will allow to superimpose trim currents up to 2 kA for Q1 and Q3. In addition, one 35 A power converter will be connected to the first half of Q1 magnet (i.e. Q1a) for K-modulation purposes.
- **Cold Powering:** A superconducting link dedicated for the inner triplet circuits (Q1 till D1) will be used to transport the current to the superconducting magnets through the UL galleries. The interface between the superconducting link and the warm powering is at the level of the DFHX boxes in the UR galleries whereas, the interface between the sc link and the magnets is at the level of the DFX box located in the tunnel.
- **DC Cabling:** Water-cooled cables and copper bus bars will be installed between the power converters, the Circuit Disconnector Boxes (CDB) and the current leads of the DFHX, all placed inside the UR galleries. Cable length and resistance estimations are detailed in Chapter 17.
- **Quench Protection**: The magnets of the main inner triplet circuits will be protected by means of outer layer quench heaters, CLIQ units and cold diodes (CD)[2][3][4]. The CLIQ units are electrically connected to the circuit as shown on Figure 6-4. Quench heaters are the primary baseline protection system. As second protection system, useful to reduce the hot spot and necessary to mitigate risk in a multiple fault event, the innovative CLIQ system is chosen in the baseline after a series of very successful validation tests on stand-alone magnets. Furthermore, cold diodes are introduced to the baseline in order to balance voltages during quench and mitigate the possible delays in firing the quench protection systems between different magnets. The protection strategy of the main inner triplet circuit is the simultaneous firing of all the quench protection systems (quench heaters and CLIQ) when a quench is detected in any superconducting element of the circuit (i.e. magnet, bus-bars, sc link, current leads). The quench protection details are shown in paragraph 7.3.

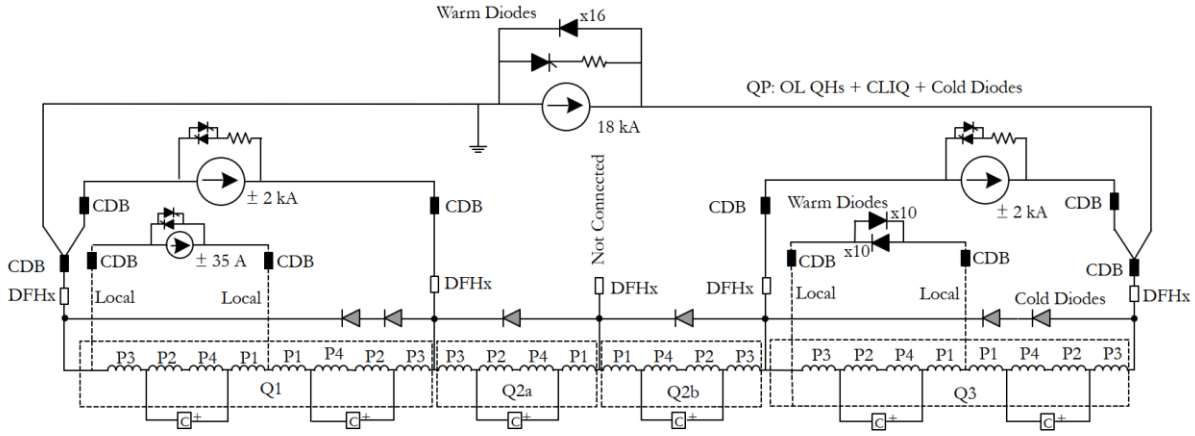

Figure 6-4: Circuit layout of the HL-LHC inner triplet.

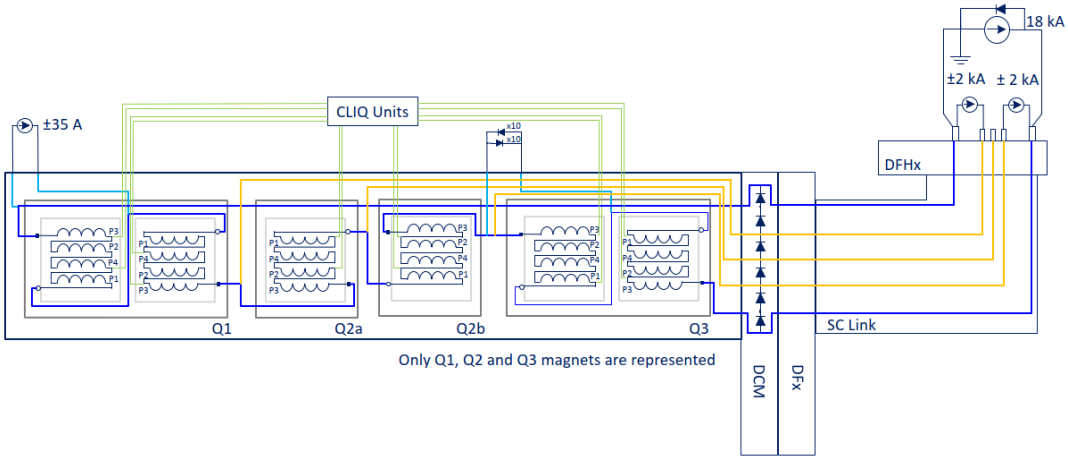

Figure 6-5: General schematic of the HL-LHC inner triplet circuit powering and magnet elements.

6.2 Triplet orbit correctors

For the inner triplet circuit, there will be a total of 6 dipole orbit correctors installed (1 vertical and 1 horizontal in Q2a, Q2b and the corrector package cold masses respectively). These new circuits have a rating of ± 2 kA. The circuit layout of these correctors is shown on Figure 6-6.

- **Power converters:** One 4-quadrant power converter per circuit rated at ±2 kA.
- **Cold Powering:** The MCBXF correctors will be powered via the sc link, the DFHX and the DFX boxes.
- **DC Cabling:** Water-cooled and air-cooled cables will be installed between the power converters, the CDB and the current leads of the DFHX.
- **Quench Protection:** The baseline for quench protection includes the installation of energy extraction systems for both, the long magnets (MCBXFA) as well as the shorter magnets (MCBXFB) [5][6].

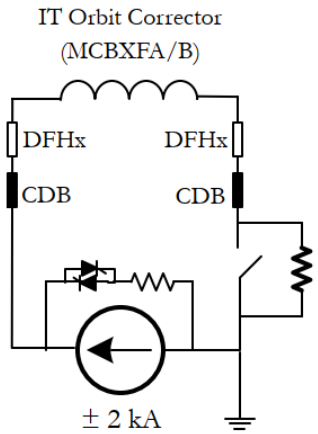

Figure 6-6: Circuit layout of the Inner triplet dipole orbit corrector circuit (MCBXF[A/B]).

6.3 Inner triplet high order correctors

Nine high-order correctors (skew quadrupole, normal and skew sextupole, octupole, decapole and dodecapole) are required for the compensation of magnetic effects in the main inner triplet magnets. The quadrupole corrector circuit has a rating of ±200 A whereas all the eight other correctors have a rating of ±120 A. The circuit layout of these correctors is shown in Figure 6-7.

- **Power converters:** One power converter per circuit (total of 9 circuits) of rating ±200A or ±120A will be used. The power converters will be located in LHC infrastructure (UL14, UL16, USC55 and UL557).
- **Cold Powering:** The cold powering interface of the high order correctors will be at the level of the corrector package cryostat (i.e. local powering) [7].
- **DC Cabling:** Air-cooled copper cables will be placed between the power converters and the current lead feedthroughs on the corrector package cryostat.
- **Quench Protection:** All magnets except the skew quadrupole are self-protected. The power converter crowbar resistance (80 mΩ) contributes to the dissipation of the coil's energy in the case of a quench or overvoltage in the current leads. For the skew quadrupole, an energy extraction system is required to protect the magnets with the earth detection system connected to the midpoint of the extraction resistor to limit the magnet voltage to ground during a quench [8].

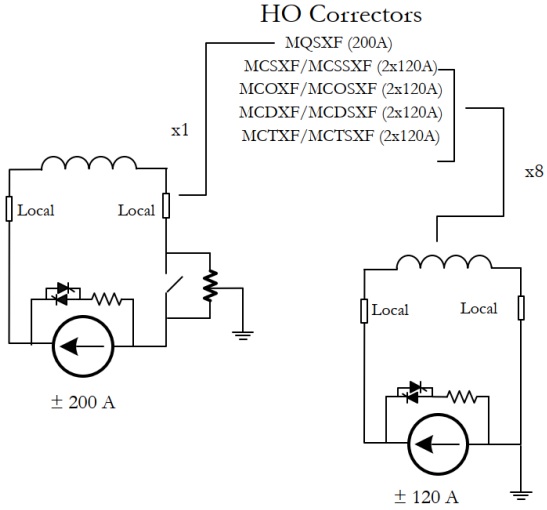

Figure 6-7: Superferric, higher order correctors' circuit layout.

6.4 Separation dipole D1

For the HL-LHC, D1 in points 1 and 5 is a sc magnet in contrast with the LHC configuration where D1 is a series of 6 warm magnets on either side of the IP. The circuit layout is shown on Figure 6-8.

- **Power converters:** One power converter per circuit rated at 14 kA. This converter will be 1-quadrant type since no ramp-down issues are foreseen for this circuit.
- **Cold Powering:** The D1 circuit will be powered via the sc link, the DFHX and the DFX boxes.
- **DC Cabling:** Water-cooled cables and copper bus bars will be placed between the power converters, the CDB and the current leads of the DFHX. Cable lengths and resistances are shown in Chapter 17.
- **Quench Protection:** The baseline for quench protection is quench heaters [9].

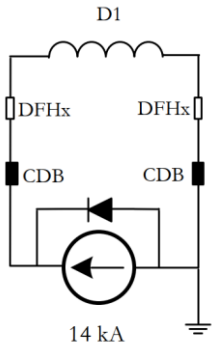

Figure 6-8: D1 magnet circuit layout.

6.5 Recombination dipole D2

The new recombination dipole magnet D2 will be a superconducting magnet with two beam apertures. The two aperture coils are powered in series. The circuit layout is shown on Figure 6-9.

- **Power converters:** One power converter per circuit rated at 14 kA. This converter will be 1-quadrant type since no ramp-down issues are foreseen for this circuit.
- **Cold Powering:** The D2 circuit will be powered via the DFHM, sc link and DFM (dedicated matching section link).
- **DC Cabling:** Water-cooled cables and copper bus bars will be placed between the power converters, the CDB and the current leads of the DFHM (matching section electrical feed-box), all placed inside the UR galleries.
- **Quench Protection:** The baseline for quench protection is quench heaters [10].

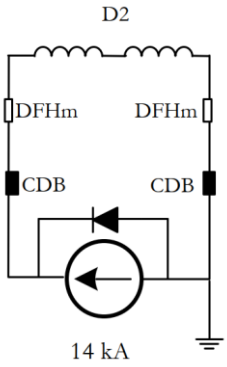

Figure 6-9: D2 magnet circuit layout.

6.6 D2 orbit correctors

Four orbit correctors are needed for the D2 recombination magnets (one vertical and one horizontal for each aperture). These corrector magnets will have a rating of ±600 A. The circuit layout of these correctors is shown on Figure 6-10.

- **Power converters:** One power converter per circuit rated ±600 A.
- **Cold Powering:** The D2 orbit corrector circuits will be powered via the DFHM, sc link and DFM (dedicated matching section link).
- **DC Cabling:** Air-cooled copper cables will be placed between the power converters, the CDBs and the current leads of the DFHM. Cable lengths and resistances are shown in Chapter 17.

- **Quench Protection:** The magnet will be protected by means of an energy extraction system [11][12].

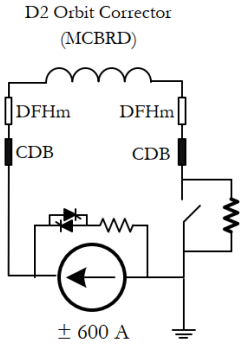

Figure 6-10: D2 correctors' circuit layout.

6.7 Individually powered quadrupoles Q4, Q5 and Q6 and correctors

The Q4, Q5 and Q6 magnets will have the same circuit configuration as in the LHC following the optimization and the introduction of the full remote alignment system to the matching sections [13]. However, since the Q4 and Q5 will be displaced towards the arcs by around 10 m, modifications on the DSL and the corresponding cryogenic infrastructure should be done. Figure 6-11 and Figure 6-12 show the circuit layout of the Q4, Q5 and Q6 magnets and their correctors.

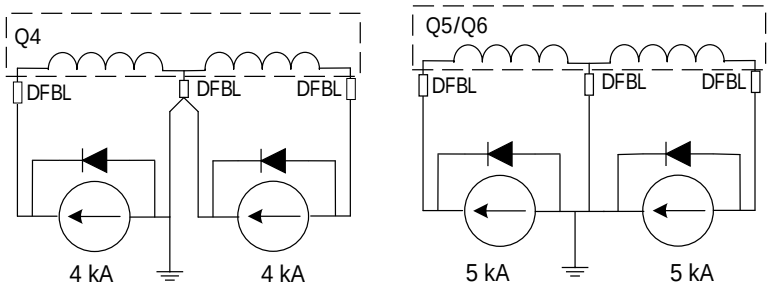

Figure 6-11: Q4, Q5 and Q6 circuit layout (no change with respect to the present LHC layout).

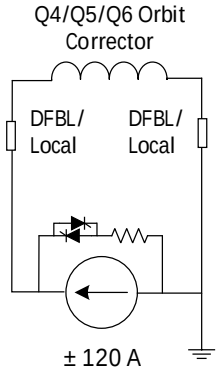

Figure 6-12: Circuit layout of each of the 10 corrector circuits for Q4, Q5 and Q6 (no change with respect to the present LHC layout).

6.8 11T trim circuit

Two main dipole magnets (MB) will be replaced by 11T cryo-assemblies in order to allow for the addition two warm collimators in between the two 5.5 m long 11T MBH magnets. The two concerned magnets are MB.A9L7 and MB.A9R7 (refer to Figure 6-2 and Figure 6-3).

- **Power converters:** One power converter per circuit rated at ± 250 A, see Figure 6-13.
- **Cold Powering:** The cold powering interface will be at the level of the 11T cryostat (i.e. local powering) with two current leads per polarity.
- **DC Cabling:** Copper cables will be placed between the power converters placed in RR73 and RR77 and the local current leads of the 11T with two cables per polarity due to the number of current leads.
- **Quench Protection:** The protection scheme used for the 11T magnet includes solely quench heaters [14][15]. The existing energy extraction system will extract the energy of the RB circuit (11T is in series with the MB magnets in this circuit). The trim superconducting bus-bars and the current leads are included in the quench protection of the 11T magnet. When an overvoltage is detected on these elements, the quench heaters of the 11T magnet are fired as well as the two energy extraction systems of the RB circuit, on either side of the long arc cryostat.

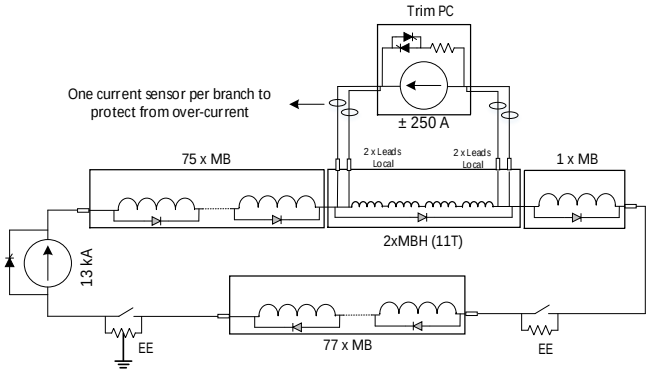

Figure 6-13: Circuit layout of the 11T trim circuit.

6.9 Circuit parameters

Table 6-1 and Table 6-2 regroup the main circuit parameters of the HL-LHC circuits from Q1 to D2 and the 11T circuit. For the complete and dynamically updated set of circuit parameters, please see Ref. [16].

Table 6-1: HL-LHC Circuit Parameters (1/2). (version 9.1)

	Circuits	Magnet Type	Circuit Name	circuits IP side	Number circuits	I_nominal (kA)	I_ultimate (kA)	L per circuit (mH)	R per circuit (mΩ)	Precision Class	Ramp rate (A/s)	Acceleration rate (A/s²)
Inner Triplet	Triplet Q1, Q2a, Q2b, Q3	MQXFA / MQFXB	RQX	1	4 (IR1/5)	16.23	17.5	255	0.15	0	14.6	0.73
	Trim Q1	-	RTQX1	1	4 (IR1/5)	2	2	69	1.45	2	2.09	0.16
	Trim Q1a	-	RTQXA1	1	4 (IR1/5)	0.035	0.035	34.5	227.08	4	3.32	0.35
	Trim Q3	-	RTQX3	1	4 (IR1/5)	2	2	69	1.3	2	2.09	0.11
	Orbit correctors Q1/2 -H/I	MCBXFB	RCBXH [1,2]	2	8 (IR1/5)	1.625	1.741	58.4	2.38	2	15	5
	Orbit correctors Q1/2 - V/O	MCBXFB	RCBXV [1,2]	2	8 (IR1/5)	1.474	1.579	124.8	2.42	2	15	5
	Orbit correctors Q3 - H/I	MCBXFA	RCBXH3	1	4 (IR1/5)	1.584	1.702	107.1	1.99	2	15	5
	Orbit correctors Q3 - V/O	MCBXFA	RCBXV3	1	4 (IR1/5)	1.402	1.502	232.3	1.98	2	15	5
	Superferric, order 2	MQSXF	RQSX3	1	4 (IR1/5)	0.174	0.197	1530	18.12	3	2.42	0.48
	Superferric, order 3, normal and skew	MCSXF / MCSSXF	RCS[S]X3	2	8 (IR1/5)	0.099	0.112	213	54	4	1.4	0.28
	Superferric, order 4, normal and skew	MCOXF / MCOSXF	RCO[S]X3	2	8 (IR1/5)	0.102	0.115	220	54	4	1.4	0.28
	Superferric, order 5, normal and skew	MCDXF / MCDSXF	RCD[S]X3	2	8 (IR1/5)	0.092	0.106	120	54	4	1.4	0.28
	Superferric, order 6	MCTXF	RCTX3	1	4 (IR1/5)	0.085	0.097	805	54	4	1.4	0.28
	Superferric, order 6, skew	MCTSXF	RCTSX3	1	4 (IR1/5)	0.084	0.094	177	54	4	1.4	0.28
D1	Separation dipole D1	MBXF	RD1	1	4 (IR1/5)	12.11	13.231	24.9	0.41	0	12	2
D2	Recombination dipole D2	MBRD	RD2	1	4 (IR1/5)	12.33	13.343	27.4	0.18	0	12	2
	Orbit correctors D2	MCBRD	RCBRD[V,H]4	4	16 (IR1/5)	0.394	0.422	920	1.36	3	2	1
11T	11T dipole, MBH	MBH	RB.A67-RB.A78	-	2 (IR7)	11.85	12.798	15734	1	1	10	1
	Trim circuit	-	RTBH9	-	2 (IR7)	0.25	0.25	127.1	30.96	3	1	0.1

Table 6-2: HL-LHC Circuit Parameters (2/2). (version 9.1)

	Circuits	Cold powering feedbox	Envelope max currents (kA)	Maximum thermal load [MIIT]	Maximum dI/dt* (kA/s)	PC Location	PC quad number	PC rated current [kA]	Maximum estimated ultimate voltage (V)	PC rated voltage (V)	Crowbar Resistance (mΩ)	Quench Protection
Inner Triplet	Triplet Q1, Q2a, Q2b, Q3	DFHX	17.82	32	250	UR	2	18	6.82	± 10	0.5	OL QHs, CLIQ, CD
	Trim Q1	DFHX	6.8	5	250	UR	4	±2	4.17	± 10	2	OL QHs, CLIQ, CD
	Trim Q1a	Local	4.1	1.5	250	UR	4	±0.06	7.99	± 10	2	OL QHs, CLIQ, CD
	Trim Q3	DFHX	6.8	5	250	UR	4	±2	3.76	± 10	2	OL QHs, CLIQ, CD
	Orbit correctors Q1/2 -H/I	DFHX	2	1	20	UR	4	±2	5.02	± 10	25	Energy Extraction
	Orbit correctors Q1/2 - V/O	DFHX	2	1	20	UR	4	±2	5.7	± 10	25	Energy Extraction
	Orbit correctors Q3 - H/I	DFHX	2	1	20	UR	4	±2	5	± 10	25	Energy Extraction
	Orbit correctors Q3 - V/O	DFHX	2	1	20	UR	4	±2	6.46	± 10	25	Energy Extraction
	Superferric, order 2	Local	0.2	0.44	0.01	UL, USC55	4	±0.6	7.28	± 10	50	Energy Extraction with Earth at Midpoint
	Superferric, order 3, normal and skew	Local	0.12	0.01	0.08	UL, USC55	4	±0.12	6.35	± 10	80	Self-Protected
	Superferric, order 4, normal and skew	Local	0.12	0.02	0.07	UL, USC55	4	±0.12	6.52	± 10	80	Self-Protected
	Superferric, order 5, normal and skew	Local	0.12	0.01	0.12	UL, USC55	4	±0.12	5.9	± 10	80	Self-Protected
	Superferric, order 6	Local	0.12	0.03	0.02	UL, USC55	4	±0.12	6.37	± 10	80	Self-Protected
	Superferric, order 6, skew	Local	0.12	0.01	0.08	UL, USC55	4	±0.12	5.33	± 10	80	Self-Protected
D1	Separation dipole D1	DFHX	13.3	42.5	130	UR	1	14	5.71	8	-	QHs
D2	Recombination dipole D2	DFHM	13.4	42.5	130	UR	1	14	2.74	8	-	QHs
	Orbit correctors D2	DFHM	0.6	1.01	0.04	UR	4	±0.6	2.42	± 10	50	Energy Extraction
11T	11T dipole, MBH	DFBA					2	13	170.14	± 190	-	QHs
	Trim circuit	Local	0.25	0.16	250	RR73,RR77	4	±0.3	9.14	± 10	60	NA

6.10 Circuit disconnector boxes

The Circuit Disconnector Boxes (CDBs) have been approved for inclusion into the baseline for the HL-LHC circuits [17]. These systems would provide for an easier connection/reconnection of power cables around the HL-LHC current leads. In particular, the disconnectors would feature safer and easier preparations for the Electrical Quality Assurance tests.

The CDBs are today proposed for the following circuits:

- Inner triplet main circuit (RQX, RTQX1, RTQX3 and RTQXA1)
- Triplet Orbit Correctors (RCBX[V,H] [1][2][3])
- Separation Dipole D1 (RD1)
- Recombination Dipole D2 (RD2)
- D2 Orbit Correctors (RCBRD[V,H]4.B [1][2])

6.11 Electrical design criteria for magnets and cold powering equipment

Electrical tests are performed on all individual components belonging to the superconducting magnet chains in order to verify that the integrity of insulation and electrical parameters across the systems are within the expected nominal limits. Electrical tests are also required, among others, in the process to certify acceptance before cryostating, at reception at the test station or before installation of components in the tunnel. Defining realistic testing conditions requires the understanding of both the design of components and their operational aspects.

Usually, insulation materials used in cryogenic systems are highly dielectric, having rather large breakdown voltages, with a large margin with respect to operation (e.g. a layer of 125 μm of polyimide withstands more than 15 kV).

Liquid helium has also a high breakdown voltage. At conditions T = 1.9 K and p = 920 mbar, liquid helium has a dielectric strength of about 10 kV/mm. However, insulation layers are never totally hermetic and creep paths through helium can be created in case of generation of helium bubbles or warm gas volumes (e.g. during a quench). This is particularly relevant in case of resin potted coils when fissures are created in the resin allowing helium to penetrate them.

The voltages that a magnet should withstand at every required Electrical Quality Assurance (ElQA) step is calculated from the maximum voltage that a component is expected to experience during accelerator operation conditions. From this value, the electrical test levels are obtained by applying factors regarding the different environments and temperature-pressure conditions under which the magnet will be tested.

We define two distinct main stages at which the electrical integrity of the magnets must be qualified:

- Manufacturing Facilities and Test Stations: This stage comprises all the tests performed on a single magnet, from the final test after assembly through the reception of the magnet at a test facility up to the acceptance of the magnet in test stations at cold.
- Tunnel: Tests performed on a magnet or a circuit (once the magnet is connected) during installation in the machine and further commissioning and operation.

The electrical qualification shall be performed in several steps, within the two stages, these steps are denominated as Electrical Quality Assurance (ElQA).

6.11.1 Electrical tests strategy

The magnet or superconducting element must be designed according to the voltages that it should withstand during operation. The voltages are calculated through the simulation of worst-case conditions, including single failures of some of the protection elements.

It is important to mention that worst-case calculations are conducted at nominal current. It is a policy stated by the HL-LHC Project that conditions at ultimate current should be covered by the margin in the design of components without applying safety factors.

Moreover, we have considered that some exceptional conservative cases will follow the same rule as ultimate conditions, i.e. no safety margins will apply onto those extreme (realistic but with very low likelihood of happening) cases.

From worst-case simulations, during a quench at nominal current, maximum coil-to-ground and coil-to-heater voltages (if applicable) are calculated and used as reference for the test voltages defined.

6.11.2 Test conditions

The ElQA tests required to qualify the magnet shall be performed at two different conditions, equally valid for both stages:

- at Nominal Operating Conditions (NOC). These conditions are the ones equivalent to 1.9 K superfluid helium in the cold mass, with all the ancillary components (e.g. instrumentation capillary tube and feedthrough) at the corresponding local conditions;
- at warm (room temperature in air with T = 20±3 °C and humidity lower than 60%) (RT).

An additional test step at gaseous helium conditions is included for the qualification of the 11 Tesla dipole and the Main Inner Triplet magnets. The temperature of gaseous helium is obtained from simulations, according to the expected worst-case conditions during a quench, while the pressure is derived \ from discussions with the magnet designers and tests on short models. For the 11 Tesla Dipole magnet the reference value is T = 200±20 K and the pressure during tests shall be 3.0±0.2 bar. For the Inner Triplet Main magnets, the test shall be performed at T = 100±20 K and 1.2±0.2 bar. This test is only applicable within the test stations stage.

To qualify the electrical integrity of the components under test, several factors are applied to the maximum expected coil voltages during quench, henceforth named V_{sim} both for coil-to-ground and quench heater for the purpose of explaining the rationale behind the test voltages. These factors consider either the safety margins or the scaling ratios that changes in test conditions (e.g. presence of helium) bring together.

6.11.2.1 Test levels at NOC

Electrical qualification at NOC shall be performed by applying the test levels defined in this Chapter. The test voltage to apply depends only on the stage.

At *'Manufacturing Facilities and Test Stations'* stage, the test voltage shall follow the formula $V_{test1} = a * V_{sim} + b$, with *a* equal to 2 and *b* to 500. These values are based on the IEEE Standard 95-177 which suggests the same factor *a* equal to 2 and *b* between 1000 and 2000 V. This norm has been frequently applied to superconducting systems, although it was defined for electrical devices in general. Nevertheless, in the case of the LHC [18], CERN followed already the latter standard. For the HL-LHC Project, it has been agreed that the same standard, with the same minor modifications, shall be followed:

$$V_{test1} = 2 * V_{sim} + 500 \ [V] \quad (6\text{-}1)$$

This value should be used whenever the magnet needs to be qualified at NOC in test stations.

For series magnets, once they have been through the acceptance tests at the previous stage and proceed to *'Tunnel'* stage, V_{test1} shall no longer be applied. Therefore, whenever the magnet needs to be tested at NOC in the machine, the following test voltage shall be applied:

$$V_{test4} = 1.2 * V_{sim} \ [V] \quad (6\text{-}2)$$

6.11.2.2 Test levels at warm

For testing the magnet at room temperature two values are also defined. The chosen test value must consider the presence of helium in the magnet due to previous tests in a helium bath.

Prior to the first time the magnet is immersed in helium, i.e. after assembly and at reception of the magnet assembly at test stands, qualification at warm shall be performed at $V_{test2} = c*(a*V_{sim} + b)$, whereby *c* is a scaling factor to consider the influence of density according to Paschen's law, between nominal cryogenic conditions and room temperature in dry air. A scaling factor of 2 has been proposed, hence the voltage level at warm for a magnet which has not yet been in a helium bath is:

$$V_{test2} = 2 * (2 * V_{sim} + 500) = 2 * V_{test1} \ [V] \quad (6\text{-}3)$$

Once the components have been exposed in a previous stage to helium, V_{test2} cannot be longer applied as the presence of helium may weaken the insulation by creating creepage paths. Thus, a second test at warm is defined for whenever the magnet needs to be tested at room temperature after being operated in helium, which shall be applied at acceptance after cold testing and during the following stages of installation and commissioning in the machine. This value, V_{test3}, is also obtained from a scaling of the value at NOC, V_{test1}. Nonetheless, due to the risk of helium pockets, a factor *c* of 1/5 is applied:

$$V_{test3} = \frac{(2*V_{sim}+500)}{5} = \frac{V_{test1}}{5} \ [V] \quad (6\text{-}4)$$

The test voltage V_{test3} shall also be applied after assembly and at reception, if the magnet returned from a test station to manufacturing for modifications.

6.11.2.3 Test level at gaseous helium conditions

The test in gaseous helium intends to qualify the magnet on the test stations at conditions closely resembling the ones encountered during a quench. This test shall be performed after the magnet has been immersed in superfluid helium, during the magnet warm up, in order to guarantee that only gaseous helium is present within the magnet, including possible pockets inside the insulation. The specified temperature and pressure conditions shall be kept stable during the execution of the test.

The test value is calculated following a different rationale than the already mentioned tests and shall cover the value at ultimate current without margin, $V_{sim\ (I\ ultimate)}$. The test level, V_{test5}, is therefore calculated from:

$$V_{test5} = \max\{\ 1.2 * V_{sim(I\ nominal)}\ ;\ V_{sim(I\ ultimate)}\ \}\ [V] \qquad (6\text{-}5)$$

6.11.3 Diagram and flowchart for the test strategy

Figure 6-14 summarizes in a block diagram the strategy for the calculation of test voltages (it is important to note that it does not reflect the temporal sequence of tests which is instead detailed in Figure 6-15). The diagram allows to identify the factors between different test levels and the stage in which they shall be applied. It should be noticed that the test voltage at warm after the magnet has been in presence of helium – V_{test3} – is applicable for both stages.

Figure 6-15 presents a summarized flowchart of the test sequences and possible scenarios over time, starting from the final manufacturing step to machine powering and operation. The flowchart intends to clarify the test levels to apply whenever an ElQA test [19] – represented as hexagons in the flowchart – is required, and the applicable test value. The *End* output represents the closure of a short model or prototype magnet test programme, which will not proceed to *'Tunnel'* stage, contrarily to a series magnet.

The flowchart also includes the approach for magnets required to return back to manufacturing for refurbishment or replacement of some parts. To notice that, despite the several flowchart cycles in the *'Manufacturing Facilities and Test Stations'* stage which a magnet could experience, the test level at warm V_{test2} should not be performed except for the initial test after magnet assembly. If testing at warm after prior immersion in a helium bath is required, even when returning to manufacturing, it is recommended that the magnet should be tested at the less stringent test level V_{test3}.*

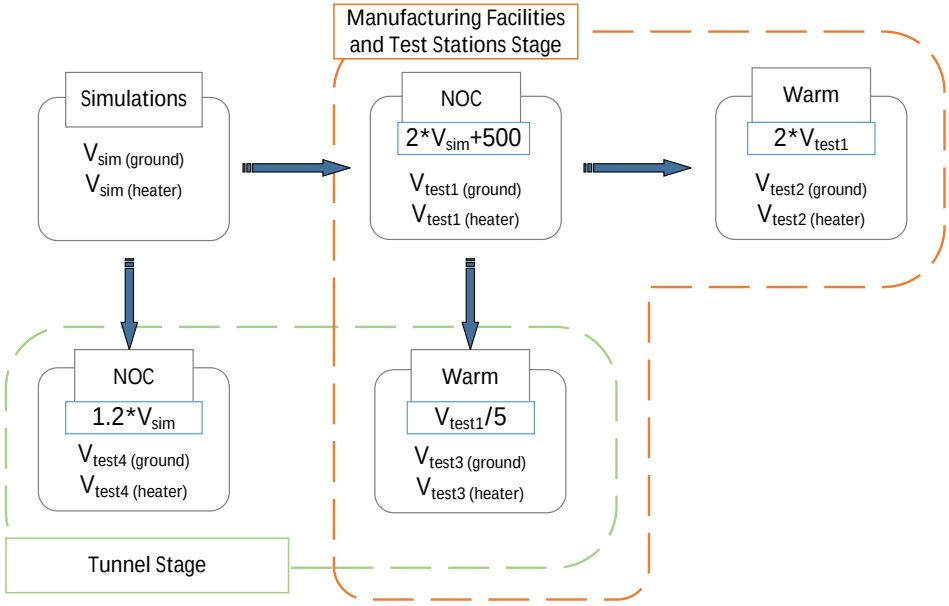

Figure 6-14: Test voltages diagram.

* The test levels at room temperature for a refurbished magnet, where part of the coils have been in helium and another part has not, needs to be addressed in the future after proper studies are conducted. As for today there is no final decision on the applicable procedures.

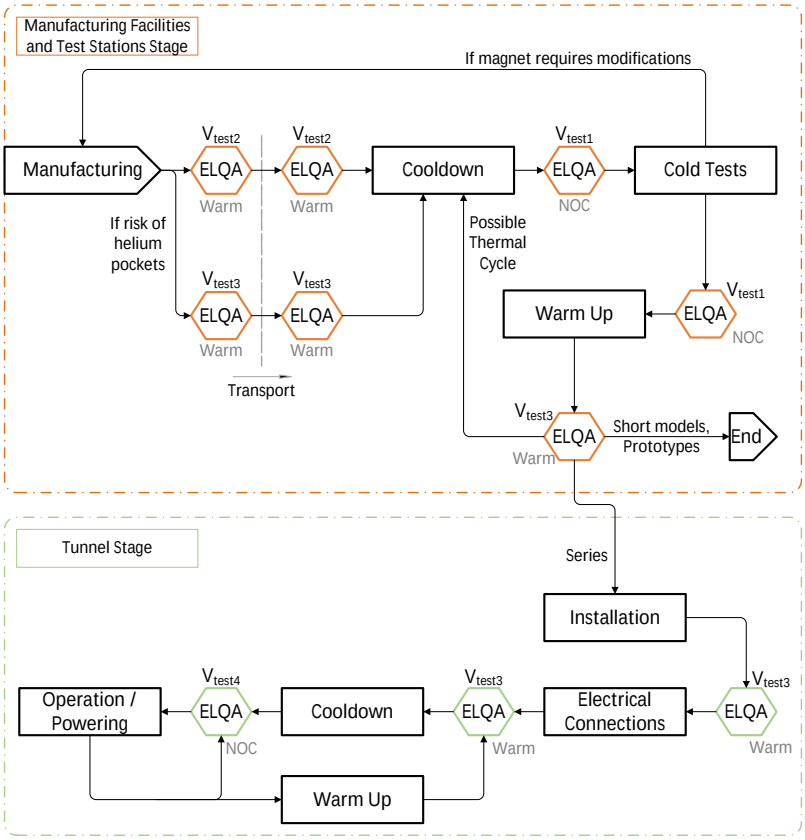

Figure 6-15: Flowchart of the defined stages and test levels to apply at each ElQA step.

6.11.4 Summary of test levels

Table 6-3 summarizes the rationale behind the test levels previously defined. As mentioned, the test strategy is equally applicable for coil-to-ground and coil-to-heater voltage. A description of the table inputs is below presented:

- **Maximum expected coil voltage at quench**: This value is obtained running simulations on the worst-case scenarios for each magnet or circuit.
- **Test voltage at NOC at *'Manufacturing Facilities and Test Stations'* stage**: Is the voltage level that the magnet should withstand whenever it is tested at NOC during this stage, in order to make sure that the dielectric material properties are not modified/damaged during the cooldown process and after the cold test programme.
- **Test voltage at warm before first helium bath**: It is the test value that must be applied at warm, after manufacturing and at reception, if the magnet has not been previously immersed in helium. This test value shall not be applied if any magnet component has been previously introduced in helium.
- **Test voltage at warm after helium bath**: This will be the value to consider whenever the magnet needs to be tested at warm once the components have been immersed in helium (risk of helium pockets).
- **Test voltage at NOC at *'Tunnel'* stage**: Once the magnet has been tested and qualified at the first stage, this will be the value to consider whenever the components need to be tested at NOC in the 'Tunnel' stage.
- **Test voltage at gaseous helium conditions:** It is the test value at which the magnet shall be qualified in helium gas conditions at the test station. The test shall be performed after the magnet has been

immersed in liquid helium to ensure the presence of gaseous helium within the coils and insulation layers.

Table 6-3: Expressions to obtain the test voltage levels.

Maximum expected coil voltage at quench (V)	**To ground**	$V_{sim\ (ground)}$
	To quench heater	$V_{sim\ (heater)}$
Test voltage at NOC at *'Manufacturing Facilities and Test Stations' stage* (V)	**To ground**	$V_{test1\ (ground)} = 2 * V_{sim\ (ground)} + 500$
	To quench heater	$V_{test1\ (heater)} = 2 * V_{sim\ (heater)} + 500$
Test voltage at warm* before first helium bath (V)	**To ground**	$V_{test2\ (ground)} = 2 * V_{test1\ (ground)}$
	To quench heater	$V_{test2\ (heater)} = 2 * V_{test1\ (heater)}$
Test voltage at warm[(1)] after helium bath (V)	**To ground**	$V_{test3\ (ground)} = V_{test1\ (ground)} / 5$
	To quench heater	$V_{test3\ (heater)} = V_{test1\ (heater)} / 5$
Test voltage at NOC at *'Tunnel' stage* (V)	**To ground**	$V_{test4\ (ground)} = 1.2 * V_{sim\ (ground)}$
	To quench heater	$V_{test4\ (heater)} = 1.2 * V_{sim\ (heater)}$
Test voltage at gaseous helium conditions (V)	**To ground**	$V_{test5} = \max\{1.2 * V_{\max(I\ nominal)}; V_{\max(I\ ultimate)}\}$
	To quench heater	

[(1)] Air at T = 20±3 °C and humidity lower than 60%.

The detailed test levels for the HL-LHC magnets (including short models, prototypes and series) and cold components are defined in Refs. [20][21][22][23][24][25][26].

6.12 References

[1] F. R. Mateos et al., "HL-LHC ECR WP3. Baseline for the Inner Triplet Main Circuit", EDMS: 1832082.

[2] M. Mentink, "Conservative Quench Scenario Considerations in the IT Main Circuit and Impact on Voltages to Ground", presented at HL-MCF Meeting no.29, INDICO: 704894.

[3] E. Ravaioli, "Quench Protection Studies for the HL-LHC Inner Triplet Circuit", EDMS: 1760496.

[4] E. Ravaioli, "Table with voltages and temperatures on QXF magnets", presented at the International Review of HL-LHC Magnet Circuits, INDICO: 835702.

[5] S. Yammine, "HL-LHC ECR - WP7. Energy Extraction Systems for HL-LHC RCBX Circuits", EDMS: 2360296.

[6] E. Todesco, "Modification of the Energy Extraction Resistance for the MCBXF Magnets", presented at HL-MCF Meeting no.60, INDICO: 896408.

[7] F. R. Mateos, "HL-LHC ECR - WP6A Local Powering of Correctors in the Inner Triplets of HL-LHC", EDMS: 1832068.

[8] M. Prioli, S. Mariotto, M. Sorbi and M. Statera, "Quench Protection Study of High Orbit Corrector Magnets", EDMS: 2370274.

[9] S. Kento, "Quench simulation and results for the MBXF magnet", EDMS: 2257328.

[10] P. Fabbricator, "Quench and Protection of D2 Magnet (MBRD) for the High Luminosity Upgrade of LHC", EDMS: 2222536.

[11] M. Mentink, "Quench Protection of the HL-LHC RCBRD Circuits", EDMS: 2222746.

[12] E. Ravaioli, "HL-LHC magnet Circuit Forum Meeting no. 58: Update on the RCBRD Protection Studies and Circuit Layout", Minutes in EDMS: 2360705.

[13] S. Claudet, B. Delille and P. Fessia, “HL-LHC ECR - WP1. Full Remote Alignment and New Matching Section Optimisation”, EDMS: 2083813.

[14] M. Maciejewski, “Modified RB with 11T Dipoles and Trim Circuit Simulations,” presented at HL-MCF Meeting no. 44, INDICO: 777024.

[15] M. Maciejewski, “Updated Quench Simulation Results on the 11T MBH,” presented at HL-MCF Meeting no.59, INDICO: 892290.

[16] “HL-LHC Magnet Circuit Forum - Reference Circuit Parameters Table,” [Online access].

[17] S. Yammine, “HL-LHC ECR WP6B - Circuit Disconnector Boxes”, EDMS: 2317207.

[18] F. R. Mateos, “Voltage Withstand Levels for Electrical Insulation Tests on Components and Bus Bar Cross Sections for the Different LHC Machine Circuits”, EDMS: 90327.

[19] M. Bednarek *et al*., “ElQA Qualification of the Superconducting Circuits During Hardware Commissioning”, EDMS: 788197.

[20] T. D. C. R. da Rosa and F. Rodríguez Mateos, “HL-LHC Electrical Design Criteria for the IT magnets”, EDMS: 1963398.

[21] T. D. C. R. da Rosa, “HL-LHC Electrical Design Criteria for the D1 Dipole”, EDMS: 2187266.

[22] T. D. C. R. da Rosa and M. J. Bednarek, “INFN - MBRD - D2 - Electrical Design Criteria”, EDMS: 2363904.

[23] T. D. C. R. da Rosa, F. Menendez Camara and F. Rodríguez Mateos, “Electrical Design Criteria for the HL-LHC 11T Dipole”, EDMS: 1995595.

[24] T. D. C. R. da Rosa and M. J. Bednarek, “CIEMAT - MCBXF - Electrical Design Criteria”, EDMS: 2363905.

[25] T. D. C. R. da Rosa and M. J. Bednarek, “IHEP - MCBRD - Electrical Design Criteria”, EDMS: 2363906.

[26] T. D. C. R. da Rosa and M. J. Bednarek, “HL-LHC Electrical Design Criteria for the High Order Corrector Magnets”, EDMS: 2060633.

Chapter 6A

Cold powering of the superconducting circuits

A. Ballarino[1*], *P. Cruikshank*[1*], *J. Fleiter*[1], *Y. Leclercq*[1], *V. Parma*[1] *and Y.* Yang[2]

[1]CERN, Accelerator & Technology Sector, Switzerland
[2]SOTON, University of Southampton, UK
[*]Corresponding authors

6A. Cold powering the superconducting circuits

6A.1 Overview

For the HL-LHC project, a novel concept for the cold powering of superconducting magnets has been developed. It is based on a new type of superconducting lines (hereafter referred to as Superconducting (SC) Links) that have been developed to transfer the current to the new HL-LHC insertion region magnets from remote distances [1]. Power converters and current leads will in fact be located in the new underground areas (UR) excavated for the HL-LHC (technical galleries running aside the LHC tunnel), and the SC Links will provide the electrical connection between the current leads and the magnets – the latter being located in the LHC main tunnel [2]. Each SC Link has a length of more than 100 m and transfers a total current of up to about |120| kA.

The benefits of the remote powering of the HL-LHC magnets via SC links are several and can be summarized as follows:

- Access of personnel for maintenance, routine tests and specific interventions on power converters, current leads and associated cryogenic/electrical equipment can be located in areas far away from the LHC ring and therefore radiation free, in accordance with the principle of radiation protection that optimizes doses to personnel exposed to radiation by keeping them As Low As Reasonably Achievable (ALARA);
- Current leads and associated cryostats (in LHC called Distribution Feedboxes, DFBs) are removed from the accelerator ring, thus leaving space in the main tunnel for other equipment. In the HL-LHC Interaction Regions (IR) around P1 and P5, no space has been reserved for DFB-type cryostats with current leads, which are now located in the new UR galleries. Connection to the magnets' bus-bar is made at 4.2 K via short connection cryostats.;
- The new technical galleries are areas with less restrictive access for personnel. Access to these galleries may be granted under certain conditions even during operation of the accelerator with beam, with the advantage of reduced time for interventions on the equipment which is located there.

The HL-LHC Cold Powering work-package (WP) conceived, developed, and is producing:

- High Temperature Superconducting (HTS) current leads (DFLH), based on High Temperature Superconducting (HTS) REBCO technology;
- SC Links (DSH) based on MgB_2 technology;
- Cryostats in the LHC main tunnel (DF) containing the Nb-Ti cables from/to the magnets and the electrical splices to the SC Links;

- Cryostats (DFH) in the new technical galleries containing the splices between MgB_2 and the HTS;
- Technologies specific to the HL-LHC Cold Powering Systems, e.g. electrical splices between HTS and MgB_2, MgB_2 and Nb-Ti, Nb-Ti and Nb-Ti;
- Cryogenic and electrical instrumentation;
- Definition of operating parameters (cryogenic flow and related control) and protection requirements (interlocks, protection strategy and thresholds of resistive and superconducting components).

The Cold Powering Systems for the HL-LHC includes: a system for the Inner Triplets, one for the Matching section magnets and finally the upgrade of the DLS in order to power the Q4, Q5 and Q6.

6A.2 Cold powering systems

The Cold Powering Systems for the HL-LHC Triplets and for the Matching sections have different layouts, lengths, and routing in the LHC underground areas. The number and type of superconducting cables and current leads required for each system type are summarized in Chapter 6.

The SC Links connect the current leads, placed in the technical galleries, to the Nb-Ti bus-bar located inside the DF cryostats (DFX for the Triplets and DFM for the Matching sections) which are placed in the LHC main tunnel. Their routing – through the UL galleries – respects a specified minimum bending radius of 1.5 m and includes a vertical height change of about 8 m.

The SC Links for the Triplet magnets transfer the current from/to the technical galleries to feed the following magnets: Q1, Q2 and Q3 (i.e. the main low-β quadrupole circuit along with the 2 kA trim circuits), D1 and the associated orbit correctors. The higher order multiple correctors operating at currents ≤ 200 A and the k-modulation circuit on Q1 are not fed via the SC Links. Their cold powering is instead provided by conduction-cooled resistive current leads located directly in the magnets' cryostats [3]. Their design is based on the development done for the LHC dipole orbit corrector current leads [5], and it takes into account the specific boundary conditions including routing and cooling possibilities. Differently from the LHC corrector current leads, which rely on two thermalization points, only one thermalization, provided by the HL-LHC beam screen cryogenic circuit, is available.

The SC Links for the Matching Sections transfer from/to the technical galleries the current feeding D2 and its orbit correctors.

The DFX and DFM cryostats interface with the cryostats of the D1 and D2 magnets, respectively. A schematic of the layout of a Cold Powering System in the underground areas of LHC Point 1 is shown in Figure 6A-1.

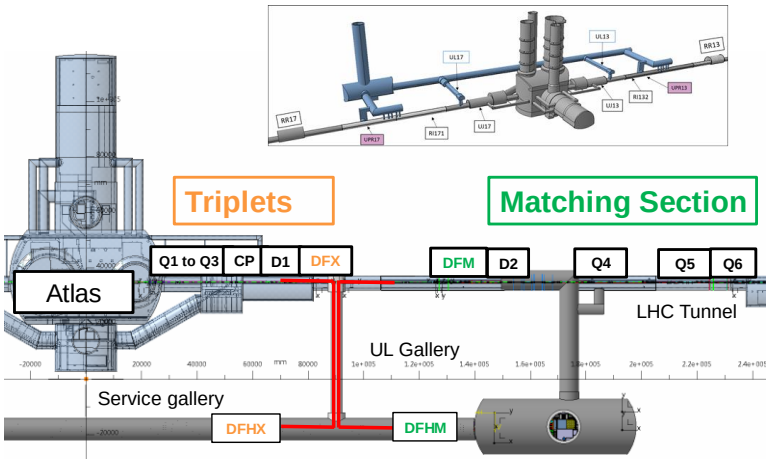

Figure 6A-1: Schematic routing of the SC Links (red lines) at LHC Point 1

The cryogenic cooling of the Cold Powering Systems relies on a forced-flow of helium gas generated by boil-off of liquid helium in the DF cryostats [6]. The amount of helium flowing through a SC Link is defined by the cooling needs of the current leads: the SC Links are not only electrical lines, but also cryogenic lines that transfer the helium required for the cooling of the current leads from the LHC main tunnel to the technical galleries. The He gas absorbs the static heat load of the SC Link cryostat and consequently warms-up over the length of the link up to the maximum operating temperature of the MgB_2 (17 K, T1 in Figure 6A-2). From the DFH, it is then distributed among the installed current leads. The maximum operating temperature of the HTS (T2 in Figure 6A-2) is 50 K. After having cooled the current leads, the helium gas is recovered at room temperature in the technical galleries.

Superconductors used throughout in the HL-LHC Cold Powering Systems are: Nb-Ti inside the DF cryostats, MgB_2 in the SC Links and HTS REBCO material in the current leads. In nominal operating conditions, the superconducting part of the system spans the temperature range from 4.5 K up to 50 K – with Nb-Ti at 4.5 K, MgB_2 at up to 17 K, and HTS at up to 50 K. However, the MgB_2 system is designed for operating at up to 25 K, and the REBCO at up to 60 K. The generous temperature margin ($\geq$ 7 K) and the operating temperature much higher than in previous cold powering system working at 4.5 K, made possible by the use of MgB_2 and HTS superconducting components, renders the HL-LHC Cold Powering Systems very robust against thermal disturbances and transients to ensure reliable operation in the LHC machine.

The HL-LHC Cold Powering System consists of several HTS current leads optimized for different current ratings, a DFH cryostat, a SC Link, and a DF cryostat. It contains cryogenic equipment (helium valves, level gauges) and all cryogenic and electrical instrumentation needed for operation of the system and for protection of the superconducting and resistive components. The protection strategy of the HTS REBCO material relies on the development and experience gained from operation of the HTS BSCCO 2223 in the LHC current leads [7].

By design choice, the Nb-Ti cables and the MgB_2 to Nb-Ti splices in the DF cryostats are submerged in liquid helium (LHe) and operated in pool-boiling conditions.

Figure 6A-2 shows a schematic of a Cold Powering System with the respective nominal operating temperatures. Interfaces with the HL-LHC Work Packages are also indicated. Main interfaces with the other HL-LHC systems are at the level of the λ-plate, which is part of the magnets WP, of the He gas recovery lines with the valves controlling the flow through the current leads, which are part of the cryogenics WP, and of the room temperature power cables, which are part of warm powering and technical infrastructures WPs. The electronics for the protection of all superconducting components and current leads is the responsibility of the Machine protection Work package, based on performance specification and electrical instrumentation installed by the Cold powering Work package.

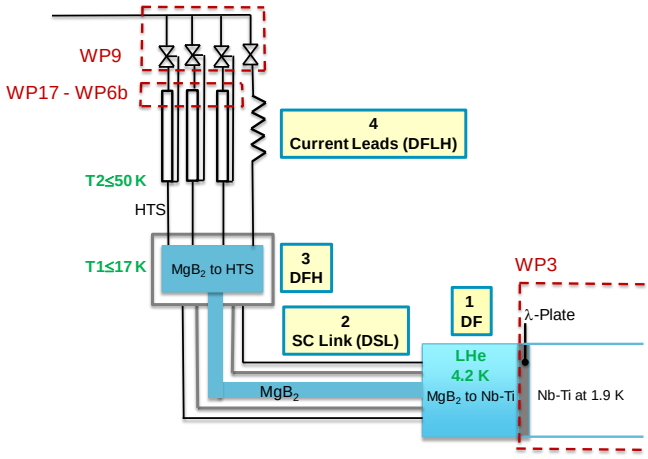

Figure 6A-2: Components of a Cold Powering System and naming conventions. Operating temperatures are indicated, as well as interfaces with other HL-LHC Work Packages

6A.2.1 Superconducting links (DSH)

The SC link is an electrical transfer line that consists of a long, semi-flexible cryostat and MgB_2 cables. The latter are housed inside the cold mass of the flexible cryostat.

The cryostat consists of two corrugated concentric pipes (2-wall configuration, see Figure 6A-3): the inner pipe houses the superconducting cables, while the outer pipe is the vacuum insulation envelope. Initially, the SC Link cryostat incorporated a He- gas cooled thermal shield (4-wall configuration). Following the evolution of the HL-LHC project and the reduction of length of the SC Links, the possibility of simplifying the cryostat design was identified, and the development of 2-wall cryostats with high thermal performance was launched with industry. As a result of this effort, low static heat load 2-wall flexible cryostats of the size required for the Cold Powering Systems of the HL-LHC Triplets were extensively and very successfully qualified at CERN. The challenging project specification (static heat load in nominal cryogenic conditions - 4.5 K to 17 K - of the order of 1.5 W/m) was met by each of the three industrial partners that produced a 60 m long prototype. The achievement of the target performance on the three prototypes enabled the adoption of the 2-wall design. The benefits of the 2-wall cryostat are: a global simplification of the Cold Powering System at the level of DFH design and system operation, a lower weight and higher flexibility of the SC Links. The latter facilitate spooling and routing operations.

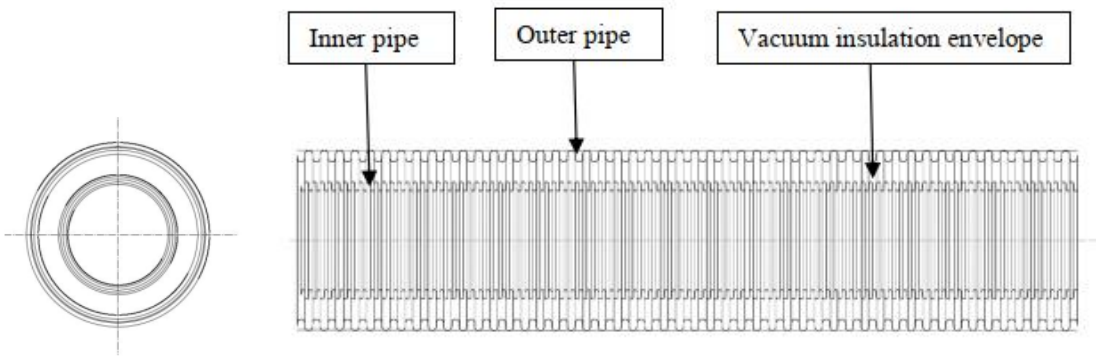

Figure 6A-3: Schematic cross-section (left) and longitudinal section (right) of the flexible cryostat for the SC Links. The diameter of the outer pipe, for the Triplets, is about 170 mm. The minimum bending radius is 1.5 m. The weight of the cryostat is of the order of 10 kg/m.

The MgB_2 cables inside the flexible cryostats are complex assemblies made from different cable types. Each cable type is optimized for the current rating of the corresponding circuit. There are two different cable assemblies: one for Triplets and one for the Matching sections. Their total current capability is about |120| kA and |61| kA respectively.

The cables are made from round ex-situ Powder-In-Tube (PIT) MgB_2 wire specifically developed for this project in collaboration between CERN and ASG Superconductors. The development aimed at producing long lengths (> 500 m) of MgB_2 wire with mechanical properties enabling cabling after reaction. Different wire layouts were produced in industry and characterized in-depth at CERN. The layout retained is a 1 mm diameter multi-filamentary wire, with Monel matrix and copper stabilizer that is electro-chemically deposited around the external surface. Superconducting filaments in the wire have an equivalent diameter of less than 60 µm, and are twisted with a pitch of 100 mm.

At the end of the development, unit lengths of wire exceeding 2 km were produced. The minimum specified critical current is 480 A at 20 K and 0.5 T, and 320 A at 25 K and 0.5 T. The main characteristics of the adopted wire design are summarized in Table 6A-1. The total production of MgB_2 wire for the project is about 1130 km.

Table 6A-1: Main characteristics of the MgB_2 wire. Mechanical properties refer to a reacted wire. Ic is the critical current of the wire, whereas RRR is the Residual Resistivity Ratio of the copper stabilizer in the MgB_2 wire.

Wire diameter	**mm**	**1±0.2**
Wire ovality	mm	≤ 0.15
Copper fraction in the wire	%	> 12
Filaments equivalent diameter	µm	≤ 60
Filaments twist pitch	mm	100±5
Tensile stress at room temperature	%	≥ 0.26
Bending radius	mm	≤ 100
Unit length	m	≥ 500
RRR of copper	-	> 100
Ic (25 K, 0.9 T)	A	≥ 186
Ic (25 K, 0.5 T)	A	≥ 320
Ic (20 K, 0.5 T)	A	≥ 480
n-value at 25 K and 0.9 T	-	> 20

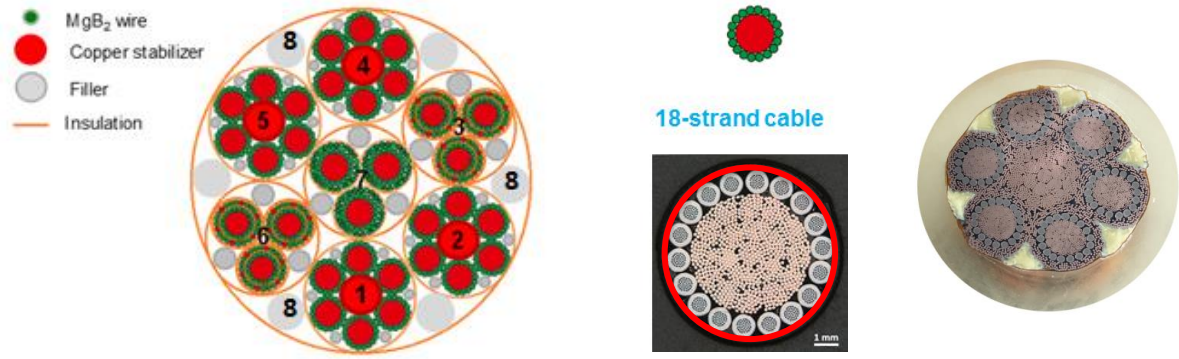

Figure 6A-4: Left: Schematic of MgB_2 cable assembly for the HL-LHC Triplet string [4]. 1,2,4 and 5: 18 kA cables; 3 and 6: triplets of concentric 3- kA cables; 7: triplet of 7- kA cables. 8: bundles of instrumentation wires. The external diameter of the cable assembly is ~ 90 mm. Current capability is specified at 25 K and in an external field of 0.9 T. Center: schematic (top) and cross-section (bottom) of a base cable made from 18 MgB_2 wires. The core of the cable is made from copper strands. The external diameter of the base cable is about 8 mm. Right: cross-section of 18- kA cable. The external diameter of the cable is 27.6 mm.

The MgB_2 cables have a round geometry. The layout of the cable assemblies was conceived in such a way that it could be produced in the final required lengths using industrial large industrial cabling equipment [4]. Cable development and characterization were done at CERN. The high-current cables are derived from a base cable layout. The base cable is made from eighteen MgB_2 wires twisted around a central multi-strand copper core (see Figure 6A-4, left). Six base cables twisted around a central multi-strand copper core form a 18- kA cable; a base cable with an additional second layer of MgB_2 wire forms a 7- kA cable; a base cable electrically insulated and with an additional second layer of MgB_2 wires around the electrical insulation forms a co-axial 3- kA cable (see Figure 6A-4). The 7- kA cables and the 3- kA cables are twisted together to form triplets. The 18- kA cables, the triplets of 7- kA cables and the triplets of 3- kA cables are twisted together to form the final cable assembly for the Triplets (see Figure 6A-4 left). Electrical insulation is provided by polyimide tape wrapped around each cable type with appropriate overlapping that enables achieving the high-voltage electrical insulation requirements. Each cable type contains sufficient copper to limit heating in case of resistive transitions to temperatures not exceeding 50 K.

Each MgB_2 cable assembly is cabled in its final length and then pulled inside the long flexible cryostat to produce a SC Link. MgB_2 cable assemblies, SC Link cryostats and final SC Links are transported spooled on drums of from about 1.5 m to 3.5 m internal diameter, and an external diameter of less than 4 m. In particular, the SC links are conceived for being lowered into the LHC underground areas spooled on drums with dimensions and weight compatible with a descent from the surface through the HL-LHC PM shafts. The new and compact design of the DFH enables lowering the SC Links after connection to the DFH cryostats. Integration studies in this direction are being performed. Unspooling and routing of the SC Links to the final location is done in the underground galleries. The minimum bending radius of the SC Links is 1.5 m. The weight of the 120- kA SC Link for the Triplets – cryostat with cable assembly – is about 40 kg/m.

At one termination, each MgB_2 cable type is soldered to a Nb-Ti cable with an equivalent current capacity at 4.5 K. This connection is done at the surface, after having pulled the MgB_2 cable assemblies into their flexible cryostats. This is the termination of the SC Link that is destined to be located in a DF cryostat (see Figure 6A-2). The Nb-Ti cables are connected, in the tunnel, to the Nb-Ti bus coming from the 1.9- K magnet cold mass after passing through the λ-plate.

The SC Links incorporate all instrumentation required for the protection of the superconducting cables as well as for the monitoring of all electrical splices within the systems. The instrumentation wires are first cabled together to form round cables, and then twisted with the MgB_2 cables in order to be an integral part of the final cable assembly – instrumentation signals occupy three of the six locations of the most external fillers in Figure 6A-4.

6A.2.2 Current leads and DFH

The HTS current leads rely to a large extend on the technologies developed for the LHC HTS leads [8]. The main difference is the use, for the superconducting part, of REBCO tape superconductor instead of BSCCO 2223 Ag-Au tape, and the HTS part is a flexible cable instead of an assembly of stacks of superconducting tapes vacuum soldered onto a metallic structure. Also, the cryogenic cooling is different. The LHC HTS section terminates with its Nb-Ti extension in a saturated liquid helium bath at 4.5 K and is self-cooled up to a temperature of about 50 K. The resistive copper section receives helium gas at about 20 K from an independent LHC cryogenic line [8]. The cryogenic cooling of the HL-LHC Cold Powering Systems relies entirely on forced flow of helium gas: the HL-LHC HTS current leads receive gas from the SC Link at about 17 K and return it at room temperature at the level of the UR after the cooling of the resistive section. As in the LHC, the helium flow through each current lead is controlled by the temperature of the HTS warm-end termination, which should never exceed 50 K.

The electrical connection between each MgB_2 cable type and the corresponding HTS current lead is done inside the DFH cryostat (see Figure 6A-2). The cryostat houses the electrical splices between the MgB_2 cables in the SC Link and the HTS cold-end termination of the current leads. The design of the DFH assures a reliable and secure routing of the superconducting cables. The development of low-resistance splices between MgB_2 and REBCO has successfully been done at CERN. For the 18- kA splices, contact resistances of a few nΩ have been measured in nominal operating conditions , in line with the specified electrical resistance of not more than 2.5 nΩ for the high current (18 kA and 13 kA) circuits [9]. Electrical resistances of not more than 15 nΩ are specified for 3- kA circuits. The design of the DFH cryostat assures effective cooling of the splices via the helium gas delivered by the SC Link.

6A.2.3 Cryostats interfacing to the LHC machine

The DF cryostats are located in the LHC main tunnel between the SC Links and the magnet cold masses (see Figure 6A-2). Two types of DF cryostats are required: the DFX for the Triplets – for the connection of the SC Link to the D1 - and the DFM for the Matching sections – for the connection of the SC Link to the D2. The main functionalities of these cryostats consist in: a) receiving and routing the Nb-Ti termination of the SC Link; b) host the splices between the Nb-Ti terminations of the SC Link and the Nb-Ti bus-bar coming from the magnets via the λ-plate; c) maintaining an appropriate volume and level of liquid helium in order to cover

emerge the Nb-Ti cables and splices; d) producing, via liquid helium boil-off, the mass flow rate passing through the SC Link and cooling the current leads; e) extracting the instrumentation (voltage taps and temperature sensors) required for operation and protection aspects. Table 6A-2 summarizes the main design parameters of the two types of cryostats.

Table 6A-2: Design parameters of the DFX and DFM cryostats.

Helium volume	**Unit**	**DFX**	**DFM**
Approximate volume	litres	650	360
Nominal temperature	K	4.5	4.5
Design pressure	bara	3.5	3.5
Nominal He mass flow rate produced	$g.s^{-1}$	5	2
Maximum heat loads to the helium volume	W	30	20
Insulation Vacuum volume	**Unit**	**DFX**	**DFM**
Nominal pressure level	mbar	10^{-5}	10^{-5}

The DF cryostats and the SC Link share common helium volumes and are hydraulically separated from the superfluid helium volume of the magnets via a λ-plate (plug in Figure 6A-5). The controlled gaseous mass flow is produced by vaporising liquid helium via electrical heaters and/or a heat exchanger integrated inside the DF cryostat. The liquid helium level, measured by superconducting level gauges, is controlled through an inlet cryogenic valve. In case of unforeseen interruption in the supply of liquid helium, the helium inventory in the DF ensures a cooling autonomy for a period of about ten minutes, sufficient to enable re-establishment of nominal cryogenic conditions without impacting operation of the LHC machine. Since the DF cryostats are not constrained by stringent thermal heat loads, a thermal shield is not incorporated, permitting a simple, compact, and economic design. Cold surfaces are covered by 30-layers of Multi-Layers-Insulation (MLI) blankets to limit the radiation heat load and reduce heat inleak in the case of accidental venting.

Following the study of different layouts, the vertical integration option has been retained as the most appropriate design concept: the SC Link (DSHX in Figure 6A-5) terminates in the HL-LHC vertical shaft cores. The DFX receives the Nb-Ti termination of the SC Link in its vertical section, and routes it into the horizontal section. The MgB_2 cables and the MgB_2 to Nb-Ti splices are located in the vertical section. A schematic of the DFX cryostat is shown in Figure 6A-5 [9].

The DFX cryostats are located under the UL vertical cores, at about 90 m distance from the Interaction Points. The DFM cryostats are installed in the LHC tunnel at about 45 meters distance from the PM shaft.

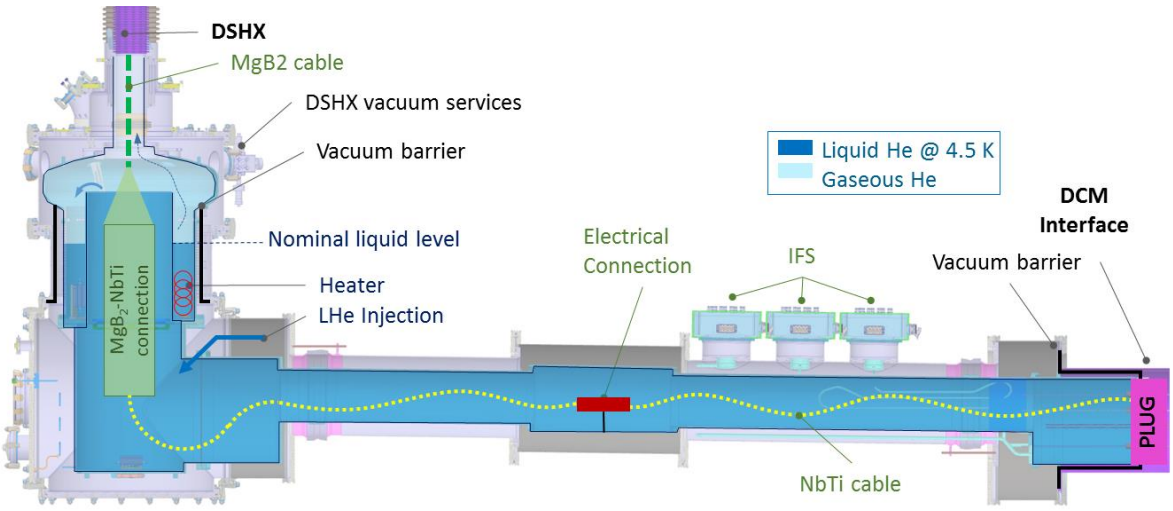

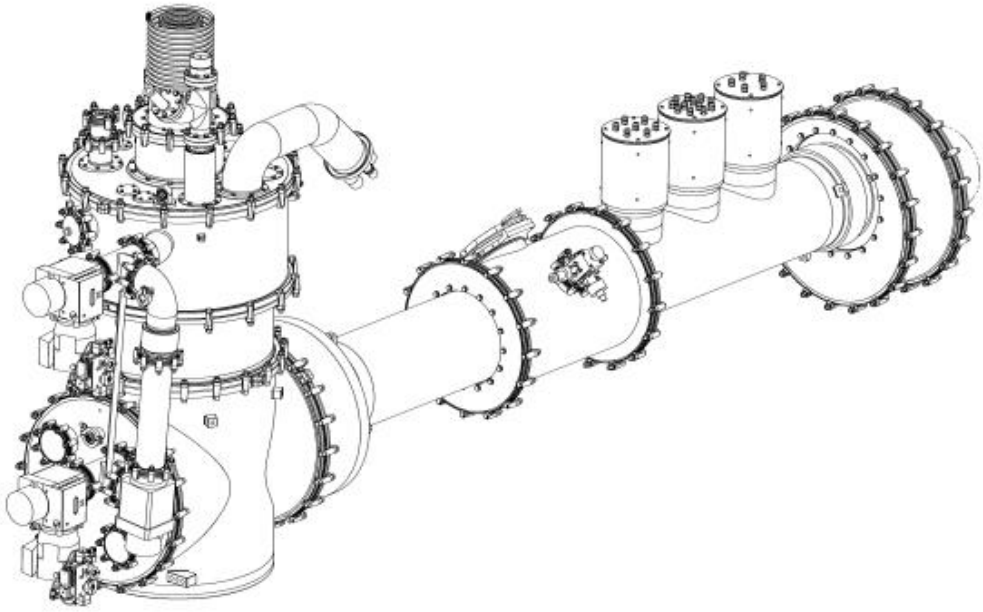

Figure 6A-5**.** Schematic (top) and 3D drawing (bottom) of DFX cryostat. The SC Link (DSHX) terminates in the vertical section of the cryostat, where the MgB_2 to Nb-Ti splices are located. The instrumentation signals are routed out from electrical connectors (IFS) located in the horizontal section of the DFX. The electrical connection between the Nb-Ti extension of the SC Link and the Nb-Ti cables coming from the magnets and passing through the λ-plate (plug) is also indicated. The horizontal length of the DFX, flange to flange, is about 4 m.

6A.3 Control, protection and electrical insulation

Operation of the Cold Powering System relies on maintaining two nominal temperatures, i.e. not more than 17 K at the location, in the SC Link, of the splices between MgB_2 and REBCO in the SC Link (T1 in Figure 6A-2) and not more than 50 K at the warm end of the REBCO section (T2 in Figure 6A-2) [4]. These two operating conditions define the amount of helium mass flow rate that is needs to be produced in the DF cryostat for the cooling of the system. Appropriate override of the two controllers is devised in order to have them working correctly in tandem. In nominal operating conditions, the total amount of helium flow circulating in the system is imposed by the requirements of the current leads and of the bypass valve. The helium gas is recovered, at room temperature, in the technical galleries from the current leads and the DFH.

A quench in the superconducting part of the system or a thermal run-away of the resistive heat exchanger of a current lead is detected by the quench detection system and will result in the firing of the corresponding magnet protection system (CLIQ, quench heaters and energy extraction systems as a function of the protected circuit). Each MgB_2 cable, REBCO cable and Nb-Ti cable is independently protected in case of resistive transition. The protection threshold of the REBCO cables is in the order of a few mV and relies on the experience gained from operation of the HTS current leads in the LHC machine [7] as well as the DEMO2 tests. The MgB_2 cables are protected at a voltage threshold of about 100 mV [10]. The amount of copper stabilizer in the MgB_2 and in the Nb-Ti cables is such that in case of a resistive transition the peak temperature never exceeds 50 K. Each MgB_2 to Nb-Ti splice and MgB_2 to REBCO splice is monitored and their protection is incorporated in the corresponding overall protection scheme of the corresponding circuits. Each resistive section of a current lead is independently protected at voltages of the order of 100 mV.

The Cold Powering Systems are designed in order to withstand the high voltage requirements imposed by the magnets' circuits [4]. In view of the operation in helium gas, the high voltage test levels, which are

specified for the magnets in liquid helium, are performed in helium gas environment at room temperature and atmospheric pressure.

6A.4 References

[1] A. Ballarino, Development of Superconducting Links for the LHC Machine, Superconductor Science and Technology, vol. 27, 2014, DOI: 10.1088/0953-2048/27/4/044024.

[2] I. Bejar Alonso, HL-LHC: Decision Management - CE works P1 and P5 underground, EDMS: 1515107.

[3] A. Ballarino and S. Yammine, Number of components and current rating of the current leads and superconducting cables feeding the HL-LHC Triplets and D1, EDMS: 1821907.

[4] A. Ballarino, WP6a: HL-LHC Cold Powering, International Review of HL-LHC Magnet Circuits, September 2019, INDICO: 835702.

A. Ballarino, Conduction-Cooled 60 A resistive current leads for the LHC dipole correctors, 2004, LHC Project Report 691.

[5] U. Wagner, A. Ballarino, Y. Yang, Cryogenic Scenarios for the Cold Powering System, HiLumi LHC Milestone Report MS57, FP7 High Luminosity Large Hadron Collider Design Study, 2014, CERN-ACC-2014-0065.

[6] A. Ballarino, K. H. Meβ, S. A. March, Commissioning of the LHC current leads, Proceedings of EPAC08, Genoa, Italy, 2008, WEPD018.

[7] A. Ballarino, HTS Current Leads for the LHC magnet powering systems, Physica C 372-376, 1413-1418, 2002, DOI: 10.1016/S0921-4534(02)01042-0.

[8] CERN: World-record current in a superconductor,

[9] Y. Yang et al, Distribution Feedbox for the Superconducting Link (SCLink) and Magnets of HL-LHC, Proceedings of EUCAS 2019, September 2019, Glasgow, DOI: 10.1088/1742-6596/1559/1/012076.

[10] S. Giannelli, G. Montenero and A. Ballarino, Quench propagation in helium gas cooled MgB_2 cables, IEEE Transactions on Applied Superconductivity 26(3):1, 2016, DOI: 10.1109/TASC.2016.2524449.

Chapter 6B

Warm powering of the superconducting circuits

M. Martino[1*], *J-P Burnet*[1*], *M. Cerqueira Bastos*[1], *V.R. Herrero Gonzales*[1], *N. Kuczerowski*[1], *S. Pittet*[1], *H. Thiesen*[1], *Y. Thurel*[1], *B. Todd*[1] *and S. Yammine*[1]

[1]CERN, Accelerator & Technology Sector, Switzerland
[*]Corresponding authors

6B Warm powering of the superconducting circuits

6B.1 Overview

The warm powering of the HL-LHC involves the new circuits of the Inner Triplets and the Separation/Recombination magnets in Point 1 and Point 5, the powering of the 11 T magnets in Point 7, and the final R2E consolidation phase in LS3. The LHC was built with modular power converters to facilitate maintenance and integrate the redundancy principle [1][2]. Redundancy was foreseen in power converters rated above 600 A. This has proven to be a real asset during operation. The $n + 1$ redundancy indeed allows the converter to be operated even with one module in fault. The advantages are: (i) in case of fault, only one sub-converter is not operational and usually this does not generate a beam dump; (ii) the LHC can run with some faulty sub-converters and all interventions for repairing can be performed during a technical stop of the machine. With the exception of dipole circuits (whose power converters are based on thyristors technology), switch-mode technology was chosen for the LHC power converters in order to minimize their size and assure low output voltage ripple. All LHC power converters rated at currents above 120 A are water-cooled, inducing a size reduction of the hardware. All these design principles will be maintained for the new HL-LHC power converters and the use of switch-mode technology extended to all new designs. The R&D aspects involved in the Warm Powering are discussed in Ref. [3] and will not be addressed here. The main changes with respect to TDR v.0.1 are summarised in Table 6B-1.

Table 6B-1: Summary of the main changes with respect to TDR v.0.1.

	TDR v.0.1	**TDR v.1**	**Reference**
Inner Triplet 18 kA Main PC	Rated voltage: ±8 V	Rated voltage: ±10 V	
Inner Triplet Q2a Trim PC	Ratings: ±120A±10V	no Q2a trim circuit	EDMS 1682952
Inner Triplet Q1a Trim PC	no Q1a trim circuit	Ratings: ±60A±10V	EDMS 1682952
PCs of RD1, RD2 circuits	Rated Current: 13 kA	Rated Current: 14 kA	EDMS 1973948
PCs of Q4/Q5 correctors (*)	8 additional ±120A±10V	no additional circuits	ECR LHC-_-EC-0041
Powering of Super-ferric High Order correctors (**)	from UR15 (by SC-link) from UR55 (by SC-link)	from UL14 & UL16 from UL557 & USC55	ECR LHC-D-EC-0002
Control Electronics	FGC4	FGC3.2	EDMS 1973217
Precision Performance	Table 6B-5	Table 6B-7	CERN-ACC-2019-0030
DCCTs Remote Calibration	IT Main, RD1, RD2	None: manual calibration	CERN-ACC-2019-0030
Circuit Disconnector Boxes		Baseline	LHC-RP-EC-0005

(*) Per IP side: from 8 MCBY to 6 MCBY for Q4, from 6 MCBY to 2 MCBC for Q5.

(**) Local powering.

6B.2 Powering of the new HL-LHC circuits

The circuit layouts for the Insertion Regions in Point 1 and Point 5 together with the 11 T circuits in Point 7 are described in detail in Chapter 6; the corresponding new power converters are presented in detail in 6B.4.

6B.3 Powering upgrade to face new level of radiations after LS3

The present LHC power converters are installed in underground areas. Of the 1710 total units, 1065 are exposed to radiation. During machine operation up to 2013, the power converters generated a number of beam-dumps due to single event effect (SEE). The faults due to SEE represented about 20% of the total power converter failures (which decreased to about 12.5 % during Run 2). The R2E (Radiation To Electronics) Project was launched in 2010 to mitigate radiation issues for the whole LHC machine. In this framework, all power converters connected to the present DFBX (that feeds the Inner Triplet magnets) were relocated to reduce their exposure to radiations. More shielding was added inside the RR alcoves to reduce particle fluences. A new radiation-tolerant version of the FGC (Function Generator/Controller [11]) digital controller system, called FGClite, was developed and deployed in the machine in 2017 (details in 6B.6).

The power converters currently in the RR alcoves will be replaced with radiation-tolerant converters. The consolidation during Long Shutdown 2 (LS2) concerns the 600 A and the 4 kA and the 6 kA families. The new power converters will be able to withstand the doses and the fluences expected during the HL-LHC operation. These radiation-tolerant converters will be used to power the Q4-Q5-Q6 of the new HL-LHC configuration (as conceived by the Matching section Optimization outcome). No extra costs are foreseen for this part of the machine.

The 120 A power converters were not included in the R2E project foreseen in LS2. These converters are installed in the RR galleries: RR13, RR17, RR53 and RR57 from where the matching sections are powered, but also in the RR73 and RR77. A new radiation-tolerant version, called R2E-HL-LHC120A-10V, will be needed to guarantee a good availability of the LHC machine after LS3; high availability will be guaranteed by means of $n + 1$ redundancy. In addition, the present 60 A converters will not be able to withstand the doses estimated during the HL-LHC operation. They were designed for tolerating a maximum total dose of about 50 Gy, and the power converters placed in or close to the matching sections will receive a dose not compatible with their design limits. It was therefore decided to replace about 55% of the 60 A power converters in the ARCs by the new radiation tolerant one, called R2E-HL-LHC60A-10V. This new design comes with a withstanding limit of 200 Gy total dose and $n + 1$ redundancy which is crucial for the availability of the machine. The replacement of 55% of the units will include the converters installed in areas close to cells 12 to 16 where the highest exposition to radiation is foreseen. It is worth noting that the new 60 A and 120 A converters will be based upon the same power source in order to optimize the design effort, a power module rated: ±60 A/±10 V. Two of such modules will be used for the 60 A converters, whereas three will be needed for 120 A converters.

6B.4 General requirements for power converters

The design of power converters for particle accelerator superconducting magnets needs to consider several criteria such as:

- large inductive loads, with time constants up to several hundred seconds that often require power converters to be able to recover the magnet energy (dissipate it, store it, or re-inject it to the grid);
- very high precision performance which also implies very low electromagnetic interference (which impacts on the choice of the topology);
- magnet, and more in general, circuit protection (as also discussed in 6B.4.5); sometimes, as in the case of the LHC 60A correctors, the protection of the Current Leads is fully delegated to power converters.

Because of all these requirements, sometimes together with very specific earth leakage current detection systems, the design of these power converters is often fully carried out “in house” at CERN. The list of circuits

and corresponding power converters needed for the HL-LHC Inner Triplet and Separation/Recombination magnets (of LHC Point 1 and Point 5) is reported in Table 6B-2. A summary of the corresponding quantities needed in operation and details of the power converters installation location is reported in Table 6B-9. Two additional circuits: RTB9.L7 and RTB9.R7 are foreseen in operation for the trim of the 11 T magnets MBH.A9L7 and MBH.A9R7 that will replace the MB.A9L7 and MB.A9R7 respectively. The maximum current will be ± 250 A, but the rated current of the power converter will be ± 600 A. As these converters are going to be installed in RR73 and RR77 they will need to be radiation tolerant; furthermore given the trim function of the circuits (used to match the so-called transfer function of the new magnets with respect to the old ones) there are special requirements in terms of operation with common-mode voltage (±85 V in normal operation, 500 V during Energy Extraction, up to 1200V if also an Earth fault happens), as the trim circuits will "sit" on top of the LHC dipole ones as shown in Chapter 6 (Figure 6-13).

Table 6B-2: Inner Triplet and Separation/Recombination circuits and their corresponding Power Converters. The reported value of differential inductance refers to nominal current [4].

Power Converter Equipment Code	Circuit Name	Circuit Description	Main Circuit Parameters		Nominal Current 7 TeV (kA)	Ultimate Current 7.5 TeV (kA)	Converter Rated Current (kA)	Converter Rated Voltage (V)
			L (mH)	R (mΩ)				
HCRPAFE	RQX	Triplet Q1, Q2a, Q2b, Q3	255.4	0.15	16.23*	17.500*	18.000	±10
HCRPBAB	RTQX1	Trim Q1	69.0	1.45	±2.000	±2.000	±2.000	±10
HCRPBAB	RTQX3	Trim Q3	69.0	1.30	±2.000	±2.000	±2.000	±10
HCRPLAD	RTQXA1	Trim Q1a	34.5	227.10	±0.035	±0.035	±0.060	±10
HCRPBAA	RCBXV[1,2]	Orbit correctors Q1/2 – Vert./Inner	58.4	2.38	1.625	1.741	±2.000	±10
HCRPBAA	RCBXH[1,2]	Orbit correctors Q1/2 – Hor./Outer	124.8	2.42	1.474	1.579	±2.000	±10
HCRPBAA	RCBXV3	Orbit correctors Q3 – Vert./Inner	107.1	1.99	1.584	1.702	±2.000	±10
HCRPBAA	RCBXH3	Orbit correctors Q3 – Hor./Outer	232.3	1.98	1.402	1.502	±2.000	±10
HCRPMB	RQSX3	Superferric, order 2	1530.0	18.12	0.174	0.197	±0.600	±10
HCRPLBC	RCS[S]X3	Superferric, order 3, normal [skew]	213.0	54.00	0.099	0.112	±0.120	±10
HCRPLBC	RCO[S]X3	Superferric, order 4, normal [skew]	220.0	54.00	0.102	0.115	±0.120	±10
HCRPLBC	RCD[S]X3	Superferric, order 5, normal [skew]	120.0	54.00	0.092	0.106	±0.120	±10
HCRPLBC	RCTX3	Superferric, order 6	805.0	54.00	0.085	0.097	±0.120	±10
HCRPLBC	RCTSX3	Superferric, order 6, skew	177.0	54.00	0.084	0.094	±0.120	±10
HCRPAFF	RD1	Separation/recomb. dipole D1	24.9	0.41	12.11	13.231	14.000	8
HCRPAFF	RD2	Separation/recomb. dipole D2	27.4	0.18	12.33	13.343	14.000	8
HCRPMBF	RCBRD[V,H]4	Orbit correctors D2	920.0	1.36	0.394	0.422	±0.600	±10

* Values for the nominal current, gradient in the straight section and magnetic length for the Q1, Q2 and Q3 magnets based on present results.

6B.4.1 Power converters architecture

The architecture of modern power converters for particle accelerator is highly modular; different parts will be designed and produced separately, power converters being finally integrated in a housing rack. There are three main parts:

- High precision current measurement chain (described in 6B.4.5) based on DCCT (DC Current Transformer) sensors able to measure currents at the required, often very challenging, precision down to DC.
- Digital control electronics (described in 6B.6) based on a digital controller (FGC) (that is also used to interface with the accelerator control infrastructure by means of WorldFip or dedicated Ethernet protocol).

- Power part: power modules and protection modules.

The power converter internal architecture is illustrated in Figure 6B-1 (left) together with the different "interfaces" with "services" such as Cooling and Ventilation, AC powering, Technical Network and other systems such as Machine Protection. This architecture, including the $n + 1$ parallel implementation of the power part (on the right) is common to all power converters for the HL-LHC.

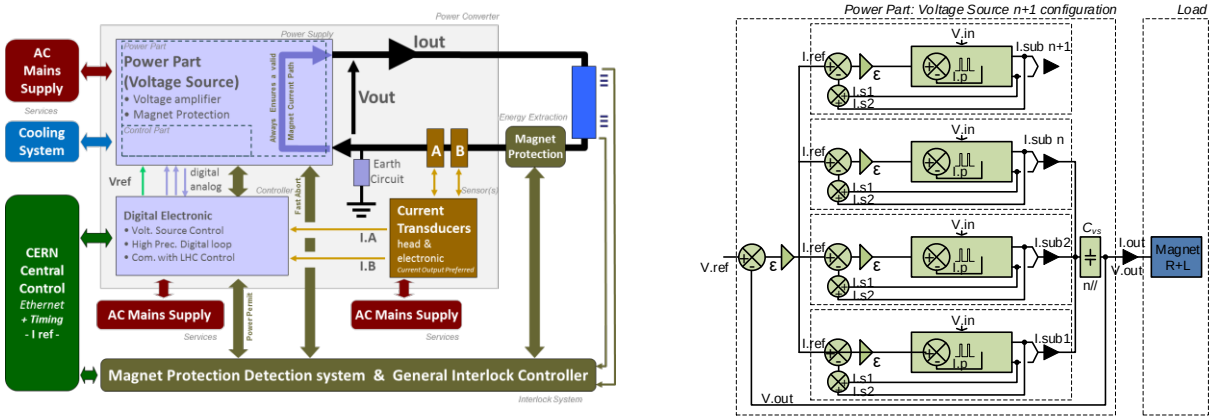

Figure 6B-1: Power converter internal architecture common to all families (on the left): field buses can either be based on WorldFIP or on dedicated Ethernet. Illustration of the parallelization of $n + 1$ power sources to supply the final current to the load (on the right).

6B.4.2 HL-LHC18kA-10V

In the LHC, the energy stored in the Inner Triplets magnets is not being recovered, and during the ramp-down phase, it is dissipated in the copper cables during a free-wheeling process, whose internal resistance together with magnet's inductance, define the time constant of the circuit. With the new layout, there is almost no resistance in the magnet circuit, so the power converter has to recover the magnet energy during the ramp down to limit it to about 20 minutes or to reduce it to less. Therefore, a new 2-quadrant design, based on Switch-Mode technology, is required including $n + 1$ redundancy to obtain high-reliability. Furthermore, it is proposed to include Energy Storage inside the converter in order to maximize the overall system efficiency and to limit the peak power drawn from the network (minimizing the cost of electrical infrastructure). The development of the HL-LHC18kA-10V will also aim at guaranteeing a lifetime expectancy of 20 years assuming 1000 cycles per year (including physics runs and all additional cycles).

Table 6B-3: Summary of HL-LHC18kA-10V power source features.

Equipment Code	Converter name	Quadrants	# Sub-Converters × Ratings	I_{POWER} Installed	I_{DCCT} Rated	Full $n + 1$ Redundancy	Controller
HCRPAFE	HL-LHC18kA-10V	2	10 × ±2kA ±10V	20 kA	18 kA	7.5 TeV	FGC3.2

6B.4.3 HL-LHC14kA-08V

The separation and recombination dipoles (D1 and D2) currently installed in the LHC will be replaced by a new pair, both of them being superconducting. The relatively low inductance of these new magnets allows a natural decrease of the current in the shadow of the Inner Triplets discharge time. The new power converter HL-LHC14kA-08V has therefore being defined as 1st quadrant converter (in the I-V plane). Its design aims at providing a Switch-Mode solution achieving low noise and high-reliability by means of $n + 1$ redundancy.

Table 6B-4: Summary of HL-LHC14kA-08V power source features.

Equipment Code	Converter name	Quadrants	# Sub-Converters × Ratings	I_{POWER} Installed	I_{DCCT} Rated	Full $n + 1$ Redundancy	Controller
HCRPAFF	HL-LHC14kA-08V	1	8 × 2kA -08V	16 kA	14 kA	7.5 TeV	FGC3.2

6B.4.4 4-Quadrant power converters

As already mentioned, in order to achieve the very high reliability required by physics operation, $n + 1$ redundancy is foreseen (since it has already proven to be the right approach in LHC) despite the increased design complexity. For 4-quadrant converters, implementing this feature is challenging, as some of the parallel power modules could be absorbing the current supplied by some of the other ones hence producing a malfunction of the overall converter. Furthermore, some of the new 4-quadrant converters would need to be radiation tolerant; this will be guaranteed by means of a specific design and qualification process in dedicated CERN facilities like CHARM.

Table 6B-5: Summary of the 4-Quadrant Power Converters.

Equipment Code	Converter name	# Sub-converters × Ratings	I_{POWER} Installed	I_{DCCT} Rated	Full $n + 1$ Redundancy	Controller	R2E
HCRPBAA	HL-LHC2kA-10V	6 × ±400A ±10V	2400 A	2000 A	7.5 TeV	FGC3.2	N
HCRPBAB	HL-LHC2kA-10V	6 × ±400A ±10V	2400 A	2000 A	7.5 TeV	FGC3.2	N
HCRPMBF	HL-LHC600A-10V	2 × ±400A ±10V	800 A	600 A	7.0 TeV (*)	FGC3.2	N
HCRPLAD	R2E-HL-LHC60A-10V	2 × ±60A ±10V	120 A	60 A (**)	7.5 TeV	FGC3.2	N
HCRPMBE	R2E-HL-LHC600A-10V	2 × ±400A ±10V	800 A	600 A	7.5 TeV	FGCLite	Y
HCRPMBD	R2E-LHC600A-10V	2 × ±400A ±10V	800 A	600 A	7.5 TeV	FGCLite	Y
HCRPLBC	R2E-HL-LHC120A-10V	3 × ±60A ±10V	180 A	120 A	7.5 TeV	FGCLite	Y
HCRPLAC	R2E-HL-LHC60A-10V	2 × ±60A ±10V	120 A	60 A (**)	7.5 TeV	FGCLite	Y

(*): the HCRPMBF will power the D2 correctors (MCBRD magnets) for which the nominal current at 7 TeV is 394 A. However even at 7.5 TeV (ultimate current of 422 A) the correctors will likely be operating below 400 A so $n + 1$ redundancy will be guaranteed most of time.

(**): DCCT of 120A with two turns.

HL-LHC2kA-10V Protection Module | R2E-LHC600A-10V Control Module | R2E-LHC600A-10V Power Module

Figure 6B-2: Examples of 4-Q power converters modules that build up the full power converter.

6B.4.5 Power converters and circuits protection

During circuit discharges, the power converter is designed to ensure a safe path of the magnet current. The crowbar existing in every power converter is the system responsible for this safe path to protect the elements in the connected circuit (power converter, DC cables, superconducting link, superconducting bus-bars and the magnet). The crowbar could be constituted by free-wheeling diodes (FWDs) in the case of 1 quadrant power converters, free-wheeling thyristors (FWTs) in case of 2 quadrant converters or free-wheeling thyristors in an anti-parallel configuration for 4 quadrant power converters. In some cases, a resistance is added in series with the free-wheeling elements in order to discharge the circuit faster. Even though the power converter is designed to ensure a safe path, in rare events a short circuit could occur over the crowbar system and the installed resistance is not ensured.

- In the case of trim circuits, several considerations have to be considered in order to define the resistance values and the triggering values of the crowbars. These considerations include:
- preventing current looping to limit the currents to the design current value of the sub-circuits,

- in case of the presence of bypass cold diodes in parallel, a very precise system should be used in order to prevent the cold diodes from being brought into conduction by exceeding their characteristic turn-on voltages.

Table 6B-6: Summary of the crowbar values and the energy dissipation capabilities for the HL-LHC circuits.

Power Converter Equipment Code	Power Converter Current Rating (kA)	Crowbar Configuration	Crowbar Resistance Value (mΩ)	Energy Absorption Capability (kJ)	Discharge Time Constant (s)
HCRPAFE	18	FWTs	0.5	42000 (*)	510
HCRPAFF	14	FWDs	0	2300	230
HCRPBAB	2	Anti-parallel FWTs	2	20	510 (**)
HCRPBAA	2	Anti-parallel FWTs	25	80	35
HCRPMB[D,F]	0.6	Anti-parallel FWTs	50	70	20
HCRPMBE	0.6	Anti-parallel FWTs	60	210	110 (***)
HCRPLBC	0.12	Anti-parallel FWTs	80	2	12

(*): estimation assuming circa 25% saturation of the differential inductance at $I_{nominal}$ (and $I_{ultimate}$ [4]) with respect to 0A;
(**): identical to RQX circuit; (***): identical to RB circuit.

6B.5 High precision: requirements, measurement, and regulation technology

Precision requirements are illustrated in Figure 6B-3 and summarized in Table 6B-7; the latest updates are derived from Ref. [5]. The main components of high precision current measurement are depicted in Figure 6B-4; for the HL-LHC the same proven principles adopted in LHC will be implemented [6]. Important R&D activities are being carried out to update and improve the metrological performance of the LHC equipment [3]. Class 1, LHC flagship power converters that currently equip LHC main dipole and quadrupole circuits, proved to perform, in many respects, way better than what was specified during LHC design phase, nevertheless the HL-LHC optics still push this limit a step ahead and the performance required by Class 0 must be further improved by a factor of at least two for some of the metrological figures of merit. One of the main principle of the high precision measurement is the redundancy: all power converters are equipped with two complete measurement “chains”. In normal operation the regulation uses the average of the two measured values of the circuit current. In case of a faulty component in one of the chains the regulation can work with the single measurement supplied by the other one.

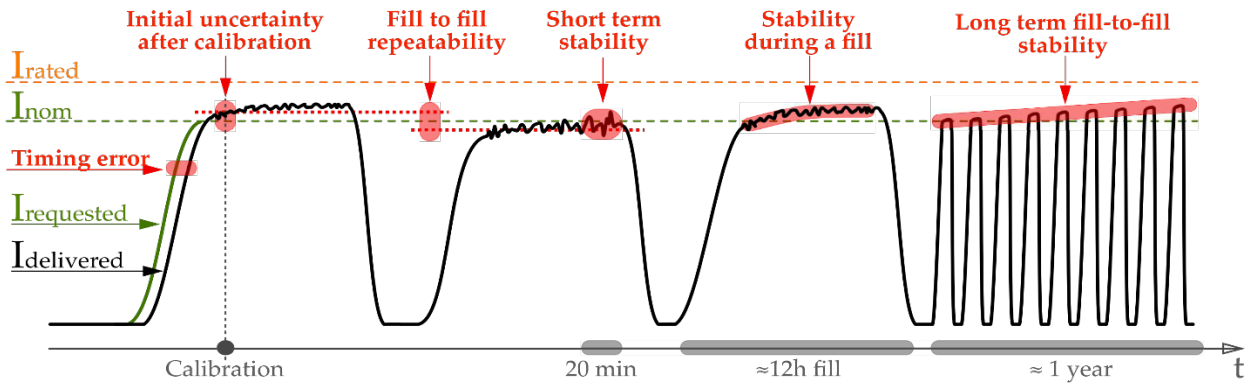

Figure 6B-3: Illustration of the main precision performance figures.

The two main components of the high precision measurement chain are:

- **DCCT:** DC Current Transformer is the transducer at the heart of the high precision measurement chain of the circuit current; DCCTs of different accuracy classes, D0 to D4, will be used.
- **ADC:** the analog-to-digital converter is the other key component of the high precision measurement of the current, its metrological performance combined with the one of the DCCT will determine the overall precision of the power converter (in the low frequency regime where the current regulation is active [7]).

The different types of ADC that will be used for application in the HL-LHC are summarized in Table 6B-8. There will be three main ADCs: FGC3.2 External ADC, FGC3.2 Internal ADC, and FGCLite Internal ADC. An intensive R&D program is being carried to develop FGC3.2 External ADC in order to meet the challenging specifications required by Class 0 [3]. Together with the ADCs themselves finely temperature-controlled racks and software temperature compensation will be used to finally guarantee the required metrological performance for the different classes. A consolidation of the DCCTs test infrastructure and a R&D program for the upgrade of the calibration system [8] (to unprecedented Class 0 performance) are undergoing.

Table 6B-7: Summary of precision requirements per circuit (including LHC mains) [5].

Circuit Name	**Equipment Code**	**I_{DCCT} (kA)**	**Accuracy Class**	**Stability [ppm of $I_{DCCT.rated}$]** expressed as twice the standard deviation		
				Short	**During a fill**	**Long Term fill-to fill**
RB[a]	HCRPTE	13	1	0.4	2	9.5
RQ(D/F)[a]	HCRPHE	13	1	0.4	2	9.5
RQX	HCRPAFE	18	0	0.2	1	9.5
RTQX1	HCRPBAB	2	2	1.2	15.5	26.5
RTQXA1	HCRPALD	0.06	4	5	40	64
RTQX3	HCRPBAB	2	2	1.2	15.5	26.5
RCBX	HCRPBAA	2	2	1.2	15.5	26.5
RQSX[b]	HCRPMBD	0.6	3	2	34	56
RC(S/O)X	HCRPLBC	0.12	4	5	40	64
RC(D/T)X	HCRPLBC	0.12	4	5	40	64
RD(1/2)	HCRPAFF	14	0	0.2	1	9.5
RCBRD	HCRPMBF	0.6	3	2	34	56
RQ4[c]	HCRPHRA	4	2	1.2	15.5	26.5
RCBY	HCRPLBC	0.12	4	5	40	64
RQ(5/6)[c]	HCRPHSB	5	2	1.2	15.5	26.5
RCBC	HCRPLBC	0.12	4	5	40	64
RTB9[d]	HCRPMBE	0.60	3	2	34	56

[a] existing LHC circuits, [b] standard HL-LHC 600 A but I_{max} = 197A in operation, [c] upgraded R2E power converters in LS2 with identical LHC performance, [d] R2E-HL-LHC 600 A but I_{max} = ± 250A in operation.

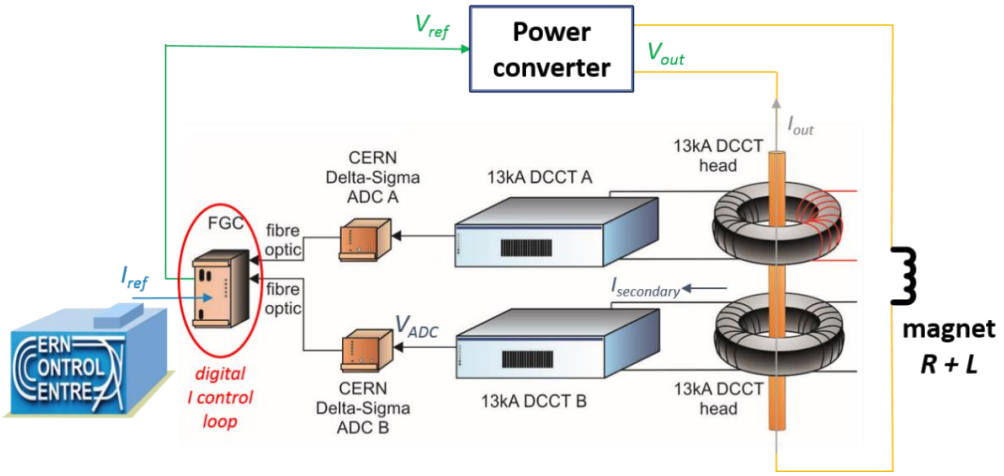

Figure 6B-4: Illustration of the full current measurement chain (main circuits LHC - accuracy Class 1).

Table 6B-8: Summary of measurement equipment for the different converters.

Accuracy Class	Equipment code – Circuit	ADC Configuration	DCCT Ratings	DCCT Class
INNER TRIPLETS and SEPARATION/RECOMBINATION CIRCUITS				
0	HCRPAFE - Main Inner Triplet	FGC3.2 + EXT ADC + AIRCON RACK	18 kA	D0
2	HCRPBAB - Q1 - Q3 trims	FGC3.2 + EXT ADC	2 kA	D2
4	HCRPALD - Q1a trim	FGC3.2 + INTERNAL ADC	120 A (*)	D4
2	HCRPBAA - IT correctors	FGC3.2 + EXT ADC	2 kA	D2
3	HCRPMBD - SuperFerric 2nd order	FGCLITE + INTERNAL ADC + TC COMP	600 A	D3
4	HCRPLBC - HO correctors	FGCLITE + INTERNAL ADC + TC COMP	120 A	D4
0	HCRPAFF - D1 - D2	FGC3.2 + EXT ADC + AIRCON RACK	14 kA	D0
3	HCRPMBF - D2 correctors	FGC3.2 + INTERNAL ADC	600 A	D3
11 T TRIM CIRCUITS				
3	HCRPMBE - 11 T trim	FGCLITE + INTERNAL ADC + TC COMP	600 A	D3
R2E CONSOLIDATION in LS3				
4	HCRPLBC - MS correctors	FGCLITE + INTERNAL ADC + TC COMP	120 A	D4
4	HCRPALC - ARCs correctors	FGCLITE + INTERNAL ADC	120 A (*)	D4

(*): DCCT with two turns to measure (up to) 60 A.

6B.5.1 RST control algorithm

The final component needed to guarantee the demanded precision performance is the control algorithm that elaborates the measured value of the current to calculate the required voltage that the power converter needs to apply to the circuit. As for LHC the control algorithm is a 2-degree-of-freedom polynomial controller (RST) [9]; it will need also to guarantee the required robustness, or stability margins, as magnet (differential) inductances vary a few % from nominal to ultimate. Sometimes the variation is much larger, for the MQSXF indeed, between 0A and ultimate current, differential inductance is expected to change by a factor 3 due to magnetic saturation; in this case a dedicated feature of the control algorithm is needed to handle it [10]. The control for the Inner Triplets, where 4 nested circuits (only 3 in LHC) need to be controlled, is an additional challenge with respect to LHC; a software implemented decoupling strategy is currently being developed [3].

6B.6 Control electronics: FGC3.2 and FGCLite

6B.6.1 Principles and current status

LHC power converter control is based on an “all-digital approach” [11][12][13]. The hardware implementing this is a so-called Function Generator/Controller (FGC). In the LHC, two main variations of FGC are used: FGC2, used in areas without radiation and FGClite, used in areas exposed to radiation (see Figure 6B-6).

The FGClite was a major project combining the challenges of using commercial parts in radiation, with high dependability requirements of the LHC. Around 1700 FGC2/FGCLite are deployed in the LHC, key functions are:

- managing the voltage source state, and providing voltage source diagnostics;
- regulation of the circuit current (by means of an RST control algorithm);
- interfacing with accelerator supervision and controls infrastructure (as depicted in Figure 6B-5).

The communication network interfaces of FGC2 and FGClite are based on the WorldFIP fieldbus. FGC2 uses a MicroFIP transceiver, and FGClite uses CERN’s in-house nanoFIP transceiver. A new version of FGC was developed for use in the injectors, called FGC3.1 (shown in Figure 6B-6 right) [14]. The FGC3.1 uses the same principles as FGC2, but uses modern analogue and digital components. The FGC3.1 network interface is based on a dedicated implementation of 100 Mbps Ethernet called FGC-Ether providing data communication and time synchronization [15]. In addition to the FGC3 control unit, a wider set of dedicated analogue and

digital boards have been developed by the power converter group for low-level converter control under the name of RegFGC3 [16]. These additional dedicated electronics extend the “all-digital” approach to the full control of the power converter, beyond the simple current control.

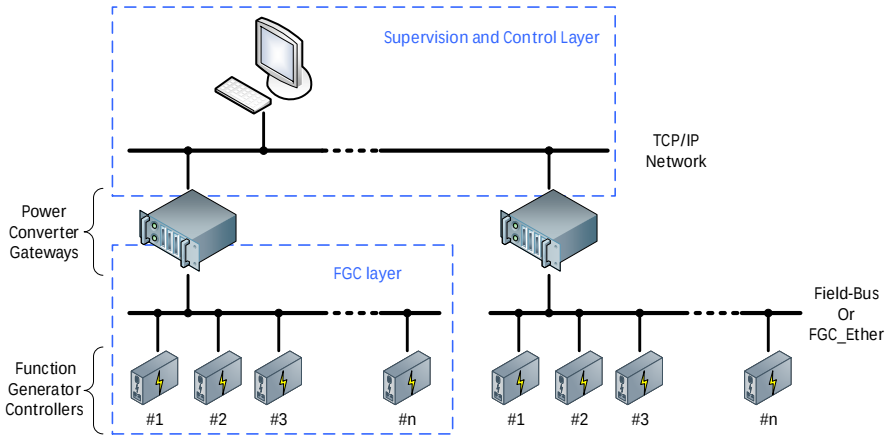

Figure 6B-5: Power Converters Controls Hierarchy

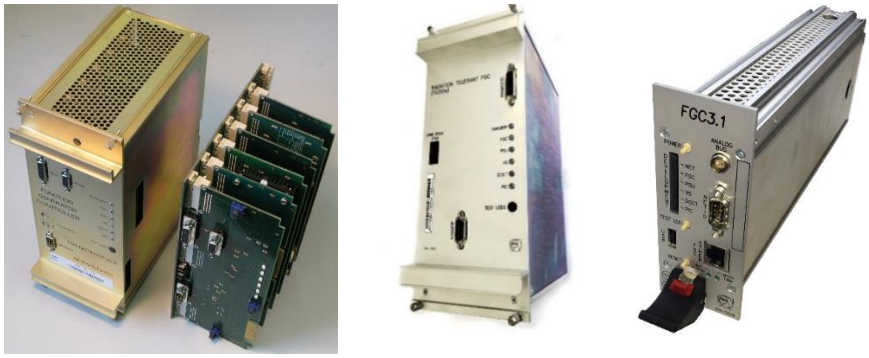

Figure 6B-6: FGC2 (left), FGClite (centre) and FGC3.1 (right) Controller Units

6B.6.2 FGC3.2 control unit for the HL-LHC power converters

The HL-LHC’s installation is foreseen around 2025, by which time the FGC3.1 will be obsolete. A new version, FGC3.2, is under development [17]. FGC3.2 is based on the same principles that have proven effective in LHC, such as direct implementation of current regulation and management/monitoring of the voltage source. FGC3.2 adds more processing power for flexibility in low-level control. In addition to the dependable design of the FGC3.2 control unit itself, one of the main features of RegFGC3 electronics is to be native support of $n + 1$ redundancy introduced in 6B.4.

The larger bandwidth of the 100 Mbps Ethernet allows more detailed monitoring compared to the WorldFIP fieldbuses currently used in the LHC. New capabilities will be implemented both in hardware and in software, such as the development of new libraries, to improve online diagnostics for both operators, and beam physicists. These are designed to improve analysis to speed up commissioning and decrease the time taken for troubleshooting. They will be particularly beneficial for the monitoring and troubleshooting of complex cases, such as nested circuits powering the Inner Triplets magnets.

6B.7 Integration

The power converters for the Inner Triplets (except higher order correctors) and Separation/Recombination circuits as well as the DFHX and DFHM (electrical feed-boxes) will be placed in the UR gallery to reduce the length of water-cooled DC cables, see Figure 6B-7. The superconducting (SC) link will bring the DC current from the UR, through the UL, to the superconducting magnets in the LHC tunnel. The power converters will

be water-cooled to ease heat extraction and reduce the air-conditioning requirements. Two 18 kV line will bring electricity in the UR. Two dedicated 18 kV/400 V transformers will supply all the new power converters separating the feeding of the left and right part of the IP.

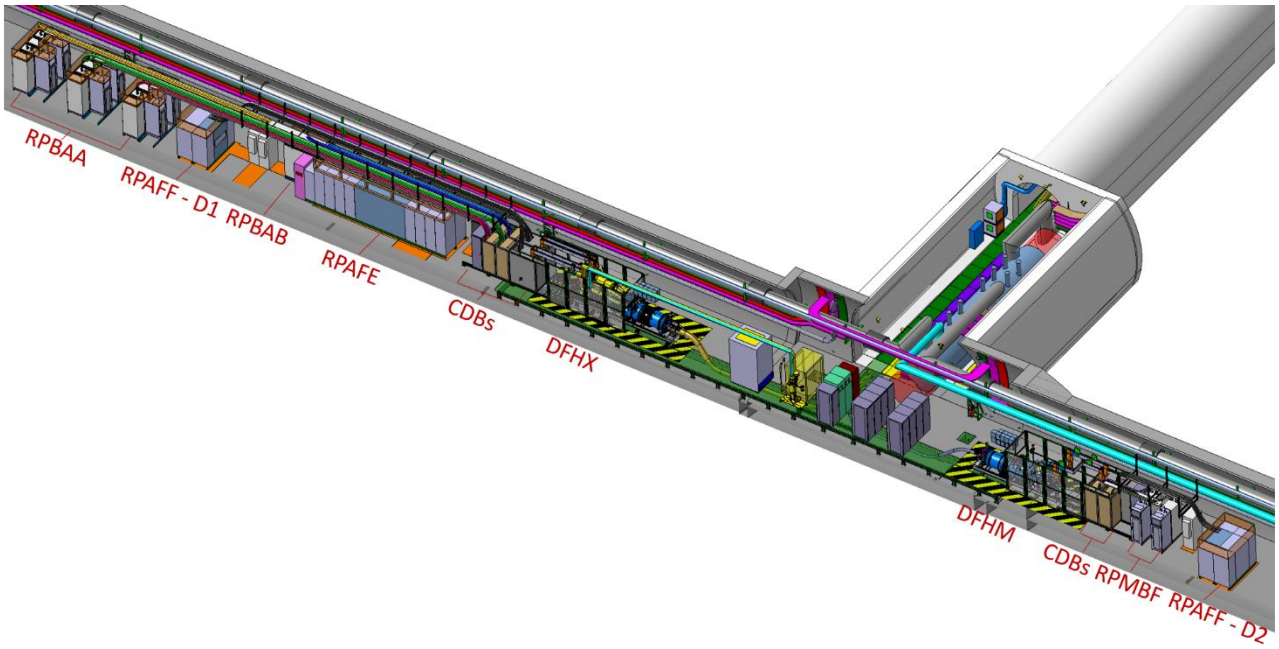

Figure 6B-7: Details of the power converters integration in UR15 right (connection to UL17 is also shown); RYABC (Class 0 measurement) and RYCHB (control) racks and RPLAD power converter (Q1a trim circuit) are shown in the illustration but not explicitly tagged to help readability.

The power converters for the higher order correctors of the Inner Triplets circuits will be placed in the UL14 and UL16 for Point 1 circuits and UL557 and USC55 for Point 5 circuits. The correctors will be powered locally (not through the SC link). It must be noted that during the HL-LHC operation the UL14 and UL16 will require radiation tolerant equipment; it has been therefore decided that also power converters in UL557 and US55 will be radiation tolerant. The 120A power converters were already designed to be radiation tolerant, so the local powering of these circuits only imposed the HCRPMBD to be radiation tolerant (4 converters in total).

More details on the interface of power converters are illustrated in Figure 6B-8 with reference to HL-LHC14kA-08V – HCRPAFF; as a general feature for all power converters: DC connections are foreseen on the top of the racks, cooling water and AC power connections are foreseen at the bottom.

As already mentioned, new power converters will be powering the Matching sections correctors (the quadrupoles power converters will be replaced in LS2 within the scope of R2E Project) and the 11 T trim circuits (new units to be installed also during LS2). Furthermore, all the 120 A corrector circuits powered from the RRs and about 55% of the 60 A correctors powered directly from the ARCs (installed below the dipoles) will have new converters. The main integration information concerning all the new power converters is summarized in Table 6B-9).

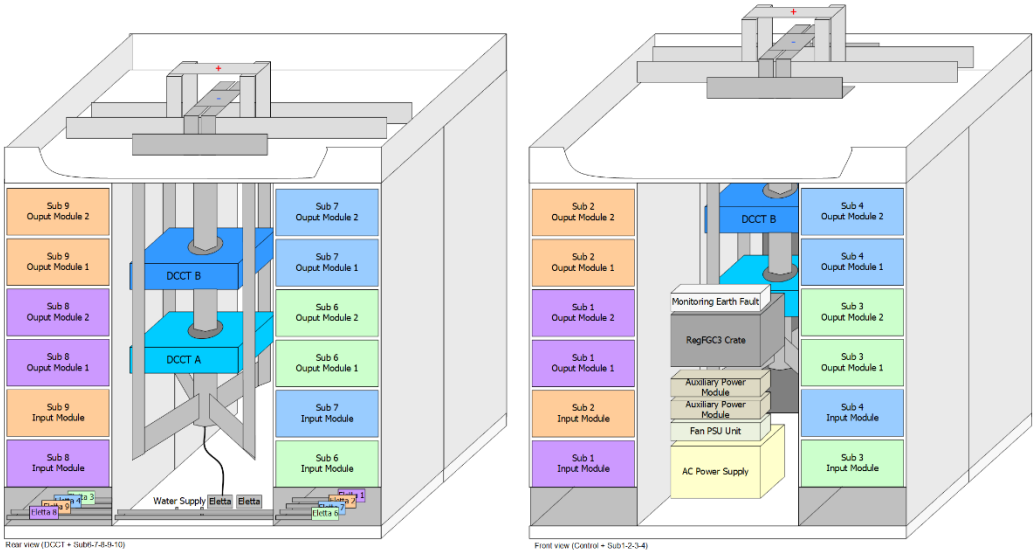

Figure 6B-8: Illustration of the HL-LHC14kA-08V – HCRPAFF power converter. Rear view (on the left) front view (on the right).

Table 6B-9: Main integration parameters. “Standard Racks” are hereby assumed 600 mm x 900 mm. Racks height is not standardized, however all racks will be, at least, 42U tall.

Power Converter Name / Equipment Code	**Integration**					**AC Powering per converter**		**Cooling and Ventilation (**)**	
	Location	**Quantities**		**Dimensions in “Standard Racks”**	**Operational Converters per Rack**	**Load Average (kW)**	**Load Average (kVA)**	**Dissipated Power Water (kW)**	**Dissipated Power Air (kW)**
		Operation	**Equivalent Spare (*)**						
INNER TRIPLETS and SEPARATION/RECOMBINATION CIRCUITS									
HCRPAFE	UR15/55	4	1.4[a]	13 x 2	Multi-rack	45	50	47.5	10.8
HCRPAFF	UR15/55	8	1	4 x 2	Multi-rack	60	75	19.5,15.2	8.3,6.5
HCRPBAA	UR15/55	24	4[b]	2 x 1	Multi-rack	28.8	30.7	<4.7>	<2.5>
HCRPBAB	UR15/55	8						5.7	3.1
HCRPLAD	UR15/55	4	2	1 x 1	1	0.77	0.85	/	0.4
HCRPMBF	UR15/55	16	4	1 x 1	2	9.1	9.6	1.5	0.65
HCRPMBD	UL14/16/557 - USC55	4	4	1 x 1	1	9.1	9.6	1.5	0.65
HCRPLBC	UL14/16/557 - USC55	32	4	1 x 1	3	1.52	1.68	/	0.6
11 T TRIM CIRCUITS									
HCRPMBE	RR73/77	2	3[c]	1 x 1	1	9.1	9.6	1.5	0.65
R2E CONSOLIDATION in LS3									
HCRPLBC	RR13/17/53/57	72	8	1 x 1	3	1.52	1.68	/	0.6
HCRPLBC	RR73/77	20							
HCRPLAC	ARCs	414	22	“4 in a row under LHC dipoles”		0.77	0.85	/	0.4

[a] : 1 full spare unit (in EPC facilities) + 1 x 2kA sub-converter per IP side; [b] : common recommended spare parts + individual crow-bar components; [c] : high quantities of spares due to special/non-standard components.

(*): All power converters are modular, so no full spare converters are foreseen; conversely spare components (power modules, control and measurement electronics, interface equipment) will be installed in dedicated racks in close proximity to the operational converters.

(**): Values estimated at $I_{ultimate}$; value between < > is the average for the HCRPBAA circuits, individual values for HCRPAFE of D1 and D2, respectively.

6B.8 Circuit disconnector boxes

In the LHC powering systems, many compensatory measures and equipment are added to the warm to cold transition to comply with the different electrical standards used for electrical installations (i.e. NF-C18-510 for the lockout procedure, NF-C15-100 and IEC-60364 for the rules on electrical installations and EN-60529 for the Ingress Protection, IP, for enclosures). In addition, disconnection and reconnection of the water-cooled cables, a risky mechanical action, becomes necessary, in average, once a year around the DFBAs (for high current circuits) mostly for the purpose of ElQA tests [18].

For the magnet circuits of the HL-LHC insertion regions, Circuit Disconnector Boxes (CDBs) are foreseen in between the warm and cold powering systems in order to comply with the above-mentioned standards. In addition, this system will eliminate the need for disconnection and reconnection of cables (except for maintenance and/or repairing of current leads). The proposed CDBs include two earthing systems in order to provide a safe intervention environment both on the warm powering side and on the cold powering side according to the electrical safety rules and standards. Moreover, a short circuit connection would make possible to perform specific tests on power converters and provide the possibility to disconnect a sub-circuit (i.e. a trim and the main circuit in the inner triplets) to efficiently perform fault diagnosis on the powering systems. Figure 6B-9 shows the electrical scheme, the possible connections, and the manipulation scheme for the proposed HL-LHC Circuit Disconnector Boxes.

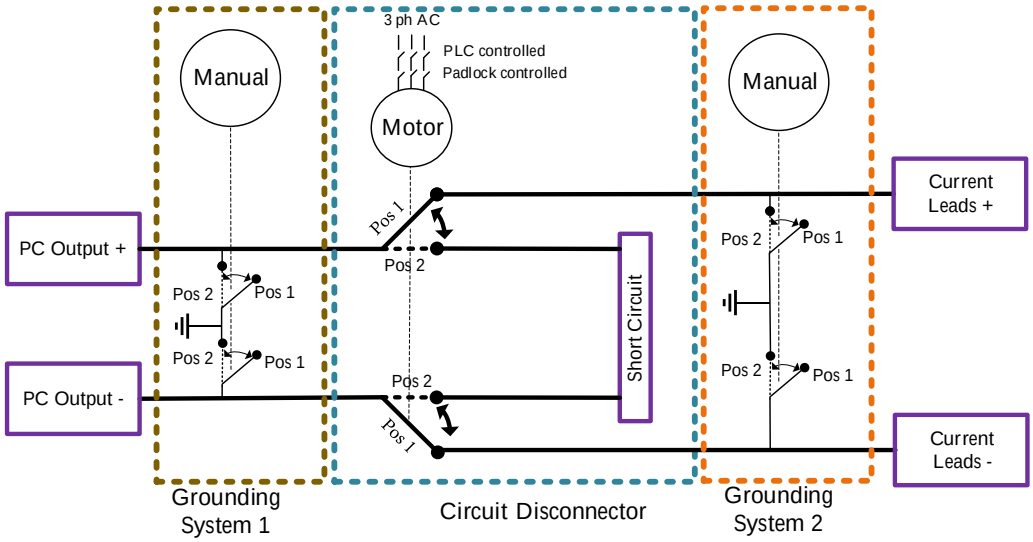

Figure 6B-9: Electrical schematic and the manipulation scheme for the HL-LHC circuit disconnector boxes.

6B.9 Options

6B.9.1 Class 0 upgrade of ATS main dipole circuits power converters

Currently in LHC the eight main dipole circuits are powered by Class 1 Power Converters as indicated in Table 6B-7. Upgrading the four main dipole circuits involved in the Achromatic Telescopic Squeezing ATS (namely RB.A12, RB.A45, RB.A56 and RB.A81) to Class 0, an improvement on tune stability of more than 30% is expected [7]. Such an upgrade will only involve the control and measurement electronics (including the remote calibration capability already available for these converters) whereas the power electronics will not need interventions; this upgrade could therefore also be planned at a later stage (after the start of the HL-LHC operation) if needed.

6B.10 References

[1] F. Bordry, H. Thiesen, LHC Inner Triplet Powering Strategy, 19th IEEE Particle Accelerator Conference, Chicago, IL, USA, 18 - 22 Jun 2001, pp.e-proc. 633 (2001), LHC-Project-Report-476.

[2] F. Bordry, D. Nisbet, H. Thiesen, J. Thomsen, Powering and Control Strategy for the Main Quadrupole Magnets of the LHC Inner Triplet System, 13th European Conference on Power Electronics and Applications, Barcelona, Spain, 8 - 10 Sep 2009, CERN/ATS 2010-022.

[3] O. Brüning and L. Rossi, The High Luminosity Large Hadron Collider: The New Machine for Illuminating the Mysteries of Universe, 1st edition, 2015, DOI: 10.1142/9581.

[4] "HL-LHC Magnet Circuit Forum - Reference Circuit Parameters Table," [Online access].

[5] D. Gamba *et al*., Update of beam dynamics requirements for HL-LHC electrical circuits, 2019, CERN-ACC-2019-0030.

[6] M. Cerqueira Bastos, G. Fernquist, G. Hudson, J. Pett, A. Cantone, F. Power, A. Saab, B. Halvarsson, J. Pickering, High Accuracy Current Measurement in the Main Power Converters of the Large Hadron Collider: Tutorial 53, IEEE Instrumentation & Measurement Magazine, 2014, DOI: 10.1109/MIM.2014.6783001.

[7] D. Gamba *et al*., Beam dynamics requirements for HL-LHC electrical circuits, 2017, CERN-ACC-2017-0101.

[8] F. Bordry, G. Fernquist, B. Halvarsson, J-C. Perreard, J.G. Pett, High-Current Performance Evaluation of DCCT's, Electrical Power Technology in European Physics Research : EP2 Forum '98, Grenoble, France, 21 - 22 Oct 1998, CERN-SL-98-069-PO.

[9] Q. King, K. Lebioda, M. Magrans de Abril, M. Martino, R. Murillo, A. Nicoletti, CCLIBS: The CERN Power converter Control Libraries, 15th International Conference on Accelerator and Large Experimental Physics Control Systems, Melbourne, Australia, 2015, DOI: 10.18429/JACoW-ICALEPCS2015-WEPGF106.

[10] Q. King, S. T. Page, H. Thiesen, M. Veenstra, Function Generation and Regulation Libraries and their Application to the Control of the new Main Power Converter (POPS) at the CERN CPS, 13th International Conference on Accelerator and Large Experimental Physics Control Systems, Grenoble, France, 10 - 14 Oct 2011, pp.WEPMN008.

[11] J.C.L. Brazier, A. Dinius, Q. King, J.G. Pett, The all-digital approach to LHC Power converter Current Control, 8th International Conference on Accelerator and Large Experimental Physics Control Systems, San José, CA, USA, 27 - 30 Nov 2001, pp.e-proc. THBT004.

[12] H. Thiesen, M. Cerqueira-Bastos, G. Hudson, Q. King, V. Montabonnet, D. Nisbet, S. Page, High precision current control for the LHC main Power converters, 1st International Particle Accelerator Conference, Kyoto, Japan, 23 - 28 May 2010, pp.WEPD070.

[13] I. Barnett, D. Hundzinger, Q. King, J.G.Pett, Developments in the high precision control of magnet currents for LHC, 18th Biennial Particle Accelerator Conference, New York, NY, USA, 29 Mar - 2 Apr 1999, pp.e-proc. 3743.

[14] D. Calcoen, Q. King, P.F. Semanaz, Evolution of the CERN Power converter Function Generator/Controller for Operation in Fast Cycling Accelerators, 13th International Conference on Accelerator and Large Experimental Physics Control Systems, Grenoble, France, 10 - 14 Oct 2011, pp.WEPMN026.

[15] S.T. Page, Q. King, H. Lebreton, P.F. Semanaz, Migration from WorldFIP to a Low-Cost Ethernet Fieldbus for Power converter Control, 14th International Conference on Accelerator & Large Experimental Physics Control Systems, San Francisco, CA, USA, 6 - 11 Oct 2013, pp.tuppc096.

[16] M. Di Cosmo, B. Todd, The New Modular Control System for Power Converters at CERN, 2015, CERN-ACC-2015-0137.

[17] B. Todd, M. di Cosmo, D. Nisbet and S. Uznanski, Converter Controls Electronics: Strategy 2035, EDMS: 1772926.

[18] S. Yammine, HL-LHC ECR Circuit Disconnector Boxes, LHC-RP-EC-0005, EDMS: 2317207.

Chapter 7

Machine protection

D. Wollmann[1*], *R. Denz*[1], *B. Lindstrom*[1], *E, Ravaioli*[1], *F. Rodriguez Mateos*[1], *A. Siemko*[1], *J. Uythoven*[1], *A. Verweij*[1], *A. Will*[1] *and M. Zerlauth*[1]

[1]CERN, Accelerator & Technology Sector, Switzerland
[*]Corresponding author

7 Machine protection

Since the previous TDR version 0.1, the hardware development has made significant progress. The universal quench detection system, CLIQ and energy extraction system prototypes have been successfully produced and tested and first units have been successfully deployed and used in SM18. This progress is reflected in the Sections below and some of the previously retained options have therefore been removed. In addition, the development of the quench heater power supplies for the HL-LHC is well advanced, which is shown in the respective Section below. Chapter 6 was updated following the approval of layout changes to the triplet circuit and an additional Section on cold diodes was added, as they have been adopted within the HL-LHC baseline. Finally, two new sources for very fast failures have been identified and studied in the past years, which is presented in the Section on fast failures.

7.1 Overview

The combination of high intensity and high energy that characterizes the nominal beam in the LHC leads to a stored energy higher than in any previous accelerator. For nominal HL-LHC operation, the beam energy will increase by another factor of two compared to standard LHC parameters and, therefore, also significantly increase the damage potential due to accidental beam losses.

The damage limits of superconducting magnets due to instantaneous beam losses are currently under study, with two dedicated experiments performed in CERN's HiRadMat facility. First results clearly indicate that Nb_3Sn magnets are significantly more sensitive to damage by instantaneous beam losses than Nb-Ti magnets. For the latter, the allowed energy deposition to remain below the limit of any irreversible damage to the superconductor due to e.g. injection or dump failures is far beyond the specified 100 J/cm^3[1].

In addition, new beam loss failure scenarios are currently under study due to the experience from LHC Run 2, proposed optics changes, the installation of new accelerator components such as crab cavities or systems that might enter the HL-LHC baseline such as hollow electron beam lenses and long-range beam-beam compensators. Special care is required to define a trade-off between equipment protection and machine availability in view of the reduced operational margins (e.g. lower beam loss thresholds to assure a timely removal of the beam in view of increased beam intensity and tighter collimator settings, UFOs, etc.).

The new HL-LHC circuits will be protected by a newly developed universal quench detection electronics (UQDS), novel Coupling Loss Induced Quench (CLIQ) units, new energy extraction systems using in-vacuum electro-mechanical switches, re-designed quench heater power supplies and a new generation of radiation tolerant cold by-pass diodes.

7.2 New Fast Failures (Protection against uncontrolled beam losses)

Equipment failures or beam instabilities appearing on the timescale of tens of turns (with 1 LHC turn ~ 89 µs) allow for an active interlocking of beam operation by dedicated detection systems. These systems feature detection times of up to several hundred microseconds. The currently fastest detection systems are the LHC beam loss monitors (BLM, 80 µs) and the fast magnet current change monitors (FMCM, 20 µs). Following the detection of a failure, the beam interlock system (BIS) and the LHC beam dumping system (LBDS) will require less than 280 µs, or about three LHC turns, to complete the removal of the concerned beam from the LHC ring. Figure 7-1 depicts the time required, respectively allowed, from the occurrence of a critical failure or unacceptable beam loss until the completion of a beam dump. With this reaction time the accelerator can be protected against damage for failures, which do not cause critical beam loss levels in less than one millisecond or about 10 LHC turns.

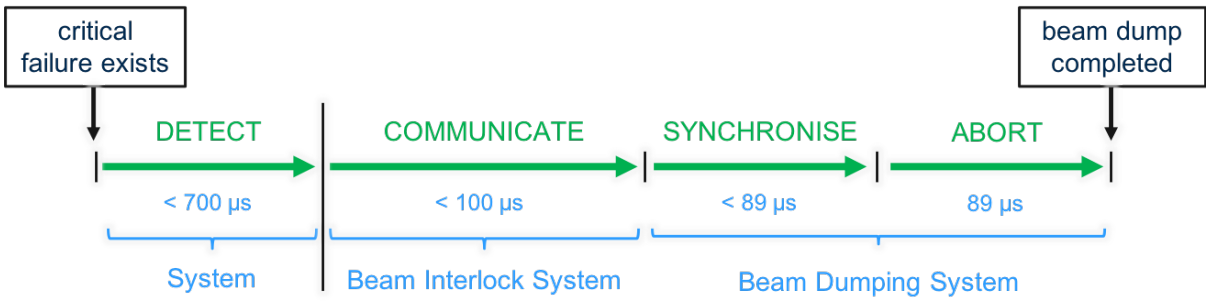

Figure 7-1: Sketch of the required machine protection system response time from existence of a failure to completion of the beam dump. These requirements allow the active interlocking of failures causing critical loss levels not faster than 10 LHC turns.

During LHC Run 2, small orbit oscillations of the circulating beam have been observed following quenches in the main dipole magnets. The magnetic field caused by the firing of the quench heaters, which protect the magnet from damage in case of a quench, has been confirmed in dedicated beam experiments and simulations to identify the origin of this orbit disturbance. Following an extremely fast increase in the first 270 µs these fields rise to the level expected from magnetostatic simulations after 1 ms [3][4]. Studies of the new HL-LHC magnets showed that the effect of their quench heaters on the beam will increase significantly as compared to today's LHC, due to the increased number of quench heaters and the drastically increased β-functions in the straight sections around IP1 and IP5. Therefore, the connection schemes of the quench heater circuits for the new HL magnets were optimised to reduce or, where possible, eliminate the skew dipole field created by the quench heater firing (see Table 7-1). Nevertheless, in case of the HL-LHC triplet magnets the total kick will still be unacceptable and a kick due to the spurious pre-firing of a single quench heater can reach critical levels. Therefore, in the new inner triplets of the HL-LHC it is required that the quench detection system initiates a beam dump before the firing of the quench heater circuits is triggered. A spurious firing of the quench heaters needs also to be interlocked triggering an immediate beam dump within ~ 1ms after the start of the discharge.

Table 7-1: Simulated kicks on the circulating beam due to firing of quench heaters in the LHC Run 2 and the HL-LHC in collision [4]. The values before the arrow in the HL-LHC column give the kick expected before the optimisation and the second value gives the kick after the optimisation.

Magnet (all QH)	LHC Run 2 kick [σ_{nom}]	HL-LHC kick [σ_{nom}]
Main dipole (worst case)	0.3	0.5
D1	1.4	2.0 → 1.4
D2	1.2	2.4 → < 0.3
11 T dipole	0.04	0.4 → 0.03
Triplet	2.5	33
Triplet (single QH – worst case)	0.6	1.2

As discussed in Section 7.3.1 the new HL-LHC triplet magnets are in addition to classical quench heaters protected by the novel CLIQ system. The connection scheme of this system is shown in Chapter 6. The spurious firing of one of the CLIQ systems in Q3 in collision will cause a very fast dI/dt in the different poles of the magnet. As this dI/dt is non-symmetric, it creates a fast-rising strong dipole kick, reaching an offset of about 3 σ_{nom} in the first turn and rising to more than 20 σ_{nom} within the first ten turns after the start of the firing process (see Figure 7-2 – left, Q3) [4]. This is an unacceptable failure which must be considered in the protection scheme. As mitigation, an alternative connection scheme has been identified, with one CLIQ unit protecting each half magnet of Q1 and Q3, as already done for Q2a and Q2b, in combination with a by-pass similar to the k-mod trim in Q1a. For this scheme, critical orbit offsets are reached only after 15 to 20 turns (see Figure 7-2 – right) [4]. Combined with a fast interlocking of a spurious firing of a CLIQ unit this scheme sufficiently reduces the criticality of this failure case to rely on the already foreseen active protection systems.

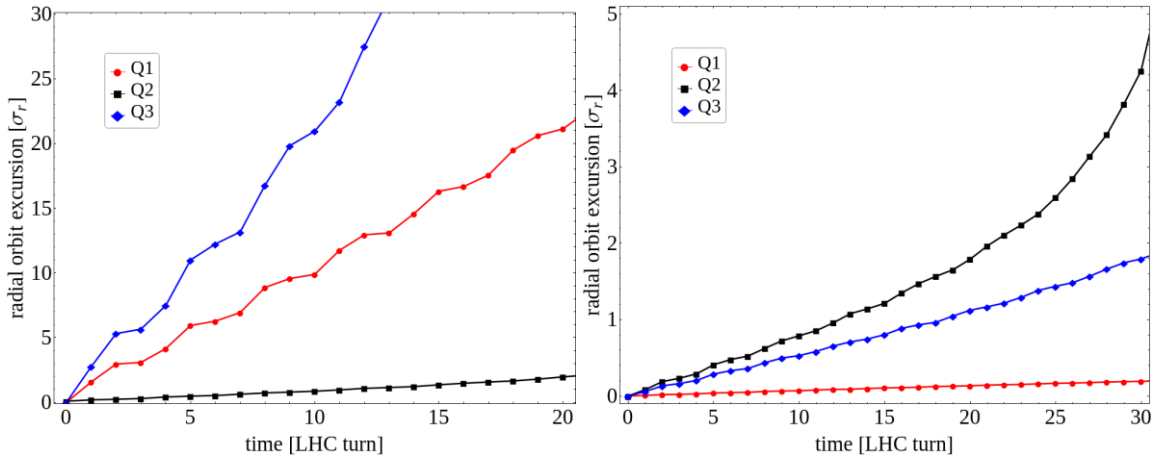

Figure 7-2: Left: The orbit excursion induced by a CLIQ discharge in the three triplet magnets Q1, Q2, and Q3. For each type, only the magnet with the largest kick is shown for the original connection scheme; Right: The orbit excursion induced by a CLIQ discharge using the new baseline in the three triplet magnets Q1, Q2 and Q3. For each type, only the magnet with the largest kick is shown in Ref. [4].

In a similar way as quench heaters and CLIQ, the use of crab cavities will introduce new failure scenarios that can affect the particle beams on timescales in the range of 10 turns [6]. Recent studies identified sudden phase changes in several crab cavities to be most critical, causing damage to the collimation system within less than five LHC turns [5]. Mitigation techniques of crab cavity failures have to include dependable detection of the crab cavity phase and voltage failures within less than 200 μs. In addition, correlated failures of multiple cavities (on one side of an IP) should be avoided through mechanical and cryogenic separation of the individual modules and appropriate design of the low-level RF.

Highly overpopulated transverse tails compared to the expected Gaussian beams were measured in the LHC (beam scrapings with collimators and van-der-Meer scans in the LHC experiments). Based on these observations, the energy stored in the tails beyond 4 σ are extrapolated to correspond to ~30 MJ for the HL-LHC parameters. These levels are significantly beyond the specification of the collimation system, with the present LHC design capable of absorbing up to 1 MJ for very fast accidental beam losses. The criticality of new fast failures can significantly be reduced by a partial depletion of the transverse beam halo, reducing the beam potentially being deflected into the collimation system to acceptable levels. Nevertheless, the impact of the halo depletion on the reaction time of the beam loss monitor system and, therefore, the protection in case of fast beam losses and possible mitigations via witness bunches needs to be carefully studied. In addition, if halo depletion is required for safe HL-LHC operation, it is mandatory to implement a reliable system to measure and interlock on the energy stored in the beam halo (see Chapter 5 on Hollow electron lenses).

7.2.1 Interlock Systems

The Beam Interlock System BIS is at the heart of CERN's accelerator machine protection systems. It is currently used in the LHC, SPS, LINAC4, and other parts of the injector chain at CERN. Its primary objective is to provide a fast and highly reliable link between users requesting a beam abort and the beam dumping system and injection elements. The hardware implementation of the system is based on custom-made electronics, as industrial solutions have not been found to be adequate for the specific requirements of the system, especially regarding the reaction time combined with the geographical distribution of the system. To fulfil the requirements of the HL-LHC, the system will be equipped with additional input channels to connect additional user interfaces and to provide more flexibility in the configuration of the various user inputs, while at the same time addressing shortcomings with the fibre optical links of the current LHC system. The number of required channels is subject to a future functional specification to be provided by the Machine Protection Panel (MPP). The new system will be equipped with advanced diagnostic features for all optical links allowing preventive maintenance, e.g. in the case of degraded performance due to the enhanced radiation load on the optical fibres in the underground areas.

The upgraded Machine Protection System will have to reach at least the same performance level in terms of reliability as the present system. For the Beam Interlock System this qualitatively corresponds to a likelihood of less than 10 % in 1000 years of operation of not transmitting a beam dump request. The safety critical part of the BIS hardware architecture will be based on well-proven principles and solutions but adapted to state-of-the-art electronic components and assemblies. From the availability point of view, the design goal of the new BIS hardware is not to cause more than one spurious beam abort per year, in line with the present operational system design and experience.

The new hardware, based on technologies like Small Form-factor Pluggable (SFP) and recent FPGA generations, will require a major revision of the high-level supervision and controls software and the adaptation to the accelerator controls environment as done at present.

7.3 Magnet circuit protection

The layout, circuit parameters as well as the protection method for the new HL-LHC circuits is described in Chapter 6 of this report. In the following Section, the quench protection of the new triplet circuit and the chosen technical solutions for quench detection systems, quench heater powering, coupling loss induced quench systems, energy extraction systems, cold by-pass diodes and the powering interlock controllers will be discussed.

7.3.1 Quench protection of the new inner triplet circuits

The new triplet quadruple magnets for the HL-LHC are wound using Nb_3Sn Rutherford cables. It was decided to keep the maximum hotspot temperatures below 350 K during quenches in nominal conditions. In rare failure scenarios the hotspot can reach up to 380 K. The quench protection scheme of these triplet circuits is aiming for the lowest possible hot-spot temperatures and thermal gradients, and sufficiently low voltages to ground and inter-turn and inter-layer voltages (see Chapter 6). To achieve these goals, each magnet will be equipped with 16 quench heater strips (8 in the low-field and 8 in the high-field regions), which will be powered in 8 heater circuits. In addition, the circuit will be protected with CLIQ units, which will reduce peak temperatures in the triplet magnets and add diverse redundancy of protection wrt to the quench heater circuits (see 7.3.4). Each single magnet (Q1a, Q1b, Q2a, Q2b, Q3a, Q3b) will be equipped with one CLIQ unit. In total, this corresponds to 48 quench heater circuits and 6 CLIQ units per triplet. Note, that this describes the baseline protection scheme of the new triplet circuits. The performance of the protection systems has so far been validated in short model coils, and on the first MQXFA magnet prototype by US-AUP (4 m long) but remains to be validated for longer prototypes and in the IT string. Cold parallel diodes (see 7.3.6) minimize the voltages in the circuit during a quench in case of non-zero currents in the trim circuits and differing discharge rates in the individual triplet quadrupoles due to tolerances and possible failures.

Detailed quench protection studies, including sensitivity studies of the superconductor parameters and failure cases, have been performed for the triplet circuit, i.e. MQXFA and MQXFB, and are summarized in Refs. [7] [9]. Table 7-2 summarizes the simulated worst-case hot spot temperatures and peak voltages to ground during a quench with nominal protection by quench heaters and CLIQ for the two magnet types. The given parameter range indicates the spread of the simulation results depending on the quench location and the variation of cable parameters within their specifications. It can be clearly seen that the hot spot temperature stays well below the specified 350 K.

Table 7-2: Simulated worst-case hot spot temperature (T_{hot}), peak voltage ($U_{g,peak}$) to ground and peak turn to turn voltage ($U_{t,peak}$) obtained after a quench at nominal and ultimate current for varying copper to superconductor rations, RRR and strand diameter. The range also includes the effect of different quench locations [7]. The ranges presented include MQXFA and MQXFB.

Current	**T_{hot} (K)**	**$U_{g,peak}$ (V)**	**$U_{t,peak}$ (V)**
I_nominal	215 – 248	521 – 658	49 – 90
I_ultimate	237 – 273	664 – 924	61 – 109

Figure 7-3 shows the typical currents in the triplet circuit (main circuit branch, trim Q1, trim Q3 and k-modulation trim) and the cold diodes during a quench at nominal current. The development of the hot spot temperature and the currents in poles P2-P4 and P1-P3 during a quench of magnet Q2a is depicted in the left plot of Figure 7-4. The right plot of Figure 7-4 shows the envelop of the voltages to ground in the coil (min and max) in case of a quench at nominal current.

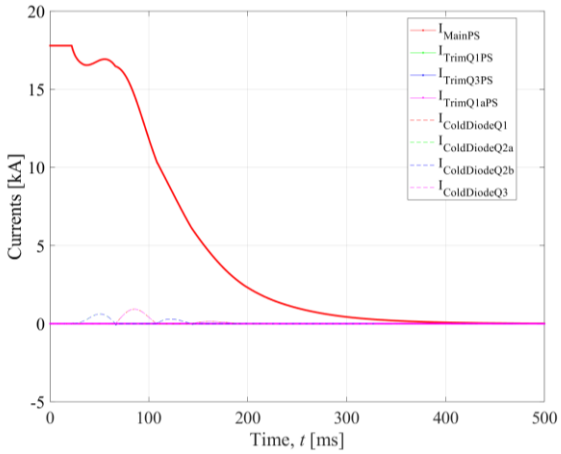

Figure 7-3: Typical current in the different branches of the triplet circuit and the cold diodes during a quench at nominal current. The simulation results were derived from STEAM-COSIM, coupling a STEAM-LEDET [30] magnet model to a PSPICE© electrical circuit model.

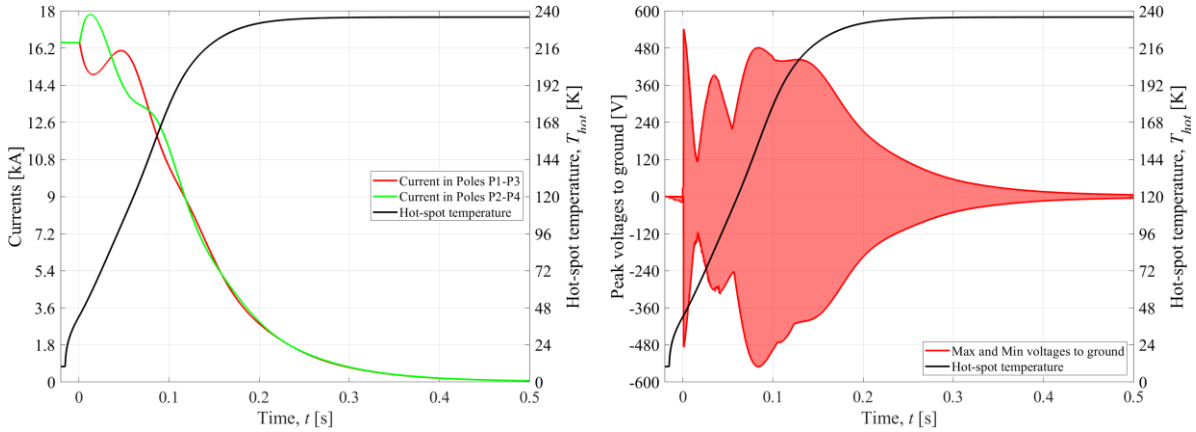

Figure 7-4 Left: currents in poles P1-P3 and P2-P4 during a quench of magnet Q2a (Q2 being of the longest type) and development of the hot spot temperature. Right: Envelop of the voltages to ground in the coil (min and max) and development of hot spot temperature in case of a Q2a quench at nominal current. The simulation results were derived from STEAM-LEDET [30].

7.3.2 Quench detection system

The HL-LHC project will incorporate for its magnet powering system a new generation of superconducting elements such as high field superconducting magnets based on Nb_3Sn conductors and high temperature superconducting links based on MgB_2. In addition, the HL-LHC will also feature new generations of Nb-Ti based magnets. The proper protection and diagnostics of those elements requires the development of a new generation of integrated quench detection and data acquisition systems (QDS). For the HL-LHC QDS, a unified approach, the Universal Quench Detection System (UQDS) described in Ref. [12] will be used.

7.3.2.1 UQDS general architecture

As a flexible and generic system, the UQDS architecture is not bound to a specific quench detection algorithm and can be configured according to the requirements of the protected superconducting element. In case of the HL-LHC, the UQDS can be adapted to the needs of various magnet technologies and provide as well efficient protection for the novel MgB_2 high current cable links. One of the key elements of the UQDS architecture are the analogue front-end channels, which are equipped with a high-resolution analogue to digital converter (ADC) of the successive approximation type. Insulated DC-DC converters and digital isolators for the serial data interfaces provide galvanic isolation of the analogue channels. In the current implementation, up to 16 of such channels connect to a field programmable gate array (FPGA), which processes the acquired data and executes the quench detection algorithms. The isolated nature of the analogue front-end channels allows a flexible usage of the magnet instrumentation, as there is no limitation imposed in the comparison of voltages by differences in common-mode potential. To enhance reliability, UQDS units (see Figure 7-5) are always deployed as a set of two independent units reading signals from two redundant sets of instrumentation voltage taps. Each unit is powered by two independent and monitored power supply units, which are supplied by different uninterruptable power supply (UPS) rails. The UQDS units are equipped with dedicated hardware interlocks for the activation of the protection elements of the magnet circuit such as quench heater discharge power supplies (DQHDS), Coupling Loss Induced Quench units [22] and energy extraction systems. The built-in field-bus interface, either of the WORLDFIP™ or the POWERLINK™ standard, provides the data link to the front-end computers of the accelerator control system.

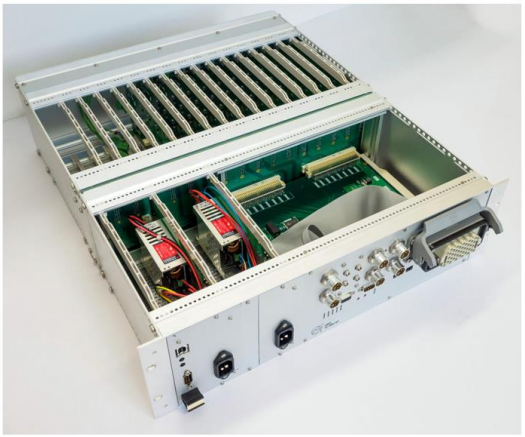

Figure 7-5: UQDS v2.1 crate serving as the baseline prototype for the 11T quench detection system. The crate is not equipped with top covers to illustrate its construction.

7.3.2.2 Quench detection for 11 T dipole magnets

The Nb_3Sn based 11T dipole magnets of type MBH will be installed in series to the main bending dipoles of LHC in sectors 6-7 and 7-8. Located in the dispersion suppressor region of both sides of IP7, the shorter but stronger 11T magnet will provide space to insert additional collimators (see also Chapters 5 and 11). The quench detection algorithm [23] uses a complex scheme, where an insulated channel measures the voltage over each pole and adjacent bus-bars. The bus-bars between the two magnet halves are protected via two additional channels. Comparisons between poles of the physically separated submodules MBHA and MBHB serve as an efficient method to detect aperture symmetric quenches that might arise due to beam losses in this region. To increase the reliability of quench detection, the scheme is implemented in a fully redundant way using the redundant voltage taps on the magnet level (see Figure 7-6). To cover all pieces of superconductor in a redundant scheme, the pole voltages include the adjacent pieces of bus-bars in an overlapping way.

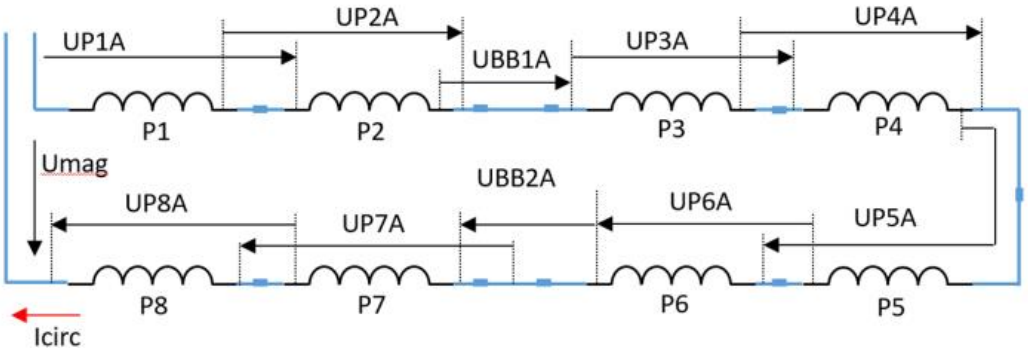

Figure 7-6: Simplified schematic of the 11T magnet circuit. The arrows indicate the voltages measured for one redundancy level. To cover all superconducting elements, the voltage measurements are interleaved.

Nb_3Sn based magnets experience so-called flux jumps [24], which result in voltage spikes on the magnet poles which are also directly seen by the quench detection electronics. The quench detection algorithm needs therefore to be adapted in order to reduce its sensitivity to these transient signals to reduce the likelihood of false positives. Since flux jumps are more dominant at lower currents where protection requirements are less stringent, a suitable solution is the application of current dependent detection settings. For this purpose, the UQDS unit is equipped with an adequate system for reading the circuit current.

In case of the 11T dipole, the 16 quench heater power supplies (DQHDS) feeding the quench heaters [25] are located close to the magnet and are triggered by the UQDS quench controllers. To activate the energy extraction systems and to switch off power converters in case of a quench the QDS system simultaneously opens the quench interlock loop of the main dipole circuit. From an LHC machine protection view, it is important to dump the beams prior to the quench heater activation. To comply with this requirement the quench loop controllers in sectors 6-7 and 7-8 will be upgraded for faster reaction and transmission times towards the subsequent powering and beam interlock systems.

7.3.2.3 11 T trim circuit protection

The resistive current leads and the superconducting bus-bars of the 11 T trim circuits require an active detection system to prevent overheating. The quench detection system measures the voltage drop across the resistive leads including the superconducting bus-bar and verifies the current sharing between the two individual leads of each circuit polarity.

7.3.2.4 Quench protection for new inner triplets in IR1 and IR5

The quench detection algorithms for the inner triplet circuits follow the same principles as for the protection of the 11 T dipoles. Due to the complexity of the triplet circuit, the number of required channels for quench detection is significantly higher (see Table 7-3). All quench detection systems for the inner triplet, the D1 magnet and the corrector package will be installed in the new, shielded underground areas UR1 and UR5 and are therefore not required to be radiation tolerant.

Table 7-3: Signals for Inner Triplet Protection (per circuit). Some channels use also share pole voltage taps. The possible dedicated detection for return bus-bar Q1-Q3 is not yet included.

Signal type	**Vtaps**	**UQDS channels**
Pole voltage	96	48
Bus-bar voltage	20	18[1]
Current	N/A	6
Earth voltage	N/A	6
Corrector voltage	24	16
Corrector bus-bar voltage	16	16
Corrector current	N/A	8
Corrector current derivative sensors	N/A	8
Sum	**156**	**126 (10 units)**

7.3.2.5 Inner triplet quench heater circuit and CLIQ supervision and triggering

The supervision and triggering of the quench heater power supplies (DQHDS) and CLIQ units is managed by a dedicated supervision and trigger controller (DQHSU). The DQHSU records data from quench heater and CLIQ discharges with sampling rates up to 192 kS/s and ensures the timely activation of the DQHDS and CLIQ units. For safe LHC operation, it is mandatory to dump the beams prior to the quench heater activation. A spurious trigger of a CLIQ unit and a DQHDS requires an immediate beam abort combined with a re-trigger of all not yet activated CLIQ and DQHDS units (see Table 7-4).

Table 7-4: Timing of beam abort sequence in case of spurious quench heater or CLIQ activation [10].

Step	**Duration**
Detection DQHDS (di/dt ≈ 4 MA/s)	100 µs
Detection CLIQ (di/dt ≈ 200 kA/s)	< 500 µs
Communication DQHSU → PIC → BIS [x]	12 µs
Beam abort sequence	270 µs
Total	**< 1 ms**

7.3.2.6 Quench detection systems for MgB_2 based high temperature superconducting links

For the protection of the MgB_2 multi-cable assemblies, which incorporate cables with current ratings from 2 kA to 18 kA, dedicated quench detection units will be deployed. The same UQDS electronic is used, while detection algorithms and thresholds will be adapted according to the needs of this new material technology. In case triggered, the UQDS systems trigger a power abort and the active protection systems of the respective circuit such as CLIQ units, DQHDS or energy extraction systems. For each pair of cables, the UQDS triggers on the differential voltage signal as well as on the absolute voltage signal as symmetric quenches in a pair of cables cannot be excluded.

7.3.2.7 Quench detection systems for D1, D2 and D2 orbit correctors

The new Nb-Ti D1 and D2 magnets will also be protected with the UQDS quench detection systems. In addition, separate bus-bar and link protection, enhanced quench heater supervision and current derivative sensors for symmetric quench detection will be installed. Furthermore, the new CCT type D2 correctors require as well, the deployment of a UQDS unit for their protection. For safe LHC operation, it is mandatory to dump the beams prior to the activation of quench heaters in the D1 and the D2.

7.3.2.8 HL-LHC impact on existing quench detection electronics

The enhanced luminosity of the HL-LHC will increase the radiation levels in the dispersion suppressor regions around IP1 and IP5 to levels requiring an upgrade of the quench detection electronics currently installed in those areas. The latest simulations indicate a total integrated dose of up to 100 Gy/year in some locations [8]. For these integrated dose levels, it is still possible to develop enhanced, more radiation tolerant versions of the currently installed QDS electronics using qualified Commercial of the Shelf (COTS) components.

With the high intensity beams of the HL-LHC, the risk of beam induced symmetric quenches in the insertion region magnets is significantly increased. The deployment of the novel current derivative sensors, which allow for an elegant method of quench detection, is considered as an adequate solution to overcome the limitations of the presently installed systems.

Another possible application of current derivative sensors are the quench detection systems for the closed orbit correctors of the inner triplets in IP2 and IP8. In this case, the current derivative sensors will allow better inductive compensation and in consequence higher ramp rates and acceleration for these circuits.

7.3.3 Quench Heater Power Supplies

The Quench Heater Discharge Supplies (DQHDS), widely known as Quench Heater Power Supplies, are the units responsible for energizing the quench heaters strips installed on the magnet coils in order to dissipate the energy stored in the magnet into its full volume, hence limiting the hot-spot temperature at the location of the original quench and preventing damage to the coil.

Every DQHDS consists of a capacitor bank with 6 aluminium electrolytic capacitors (4.7 mF/ 500 V) arranged in two sets of 3 capacitors each, which are connected in series, resulting in a total capacitance of 7.05 mF / 1000 V. The nominal operating voltage of the capacitors will be 450 V and therefore an overall voltage for the capacitor bank of 900 V is expected to deliver ~3.5 kJ to a single quench heater strip when the unit is triggered by the QDS. Figure 7-7 shows a simplified scheme of a DQHDS.

Presently, there are over 6000 DQHDS installed in the LHC and an additional ~320 DQHDS with improved capabilities and higher reliability will be needed for the HL-LHC in order to protect the 11T dipoles, the Inner Triplet quadrupoles and the new separation and re-combination dipoles D1 and D2.

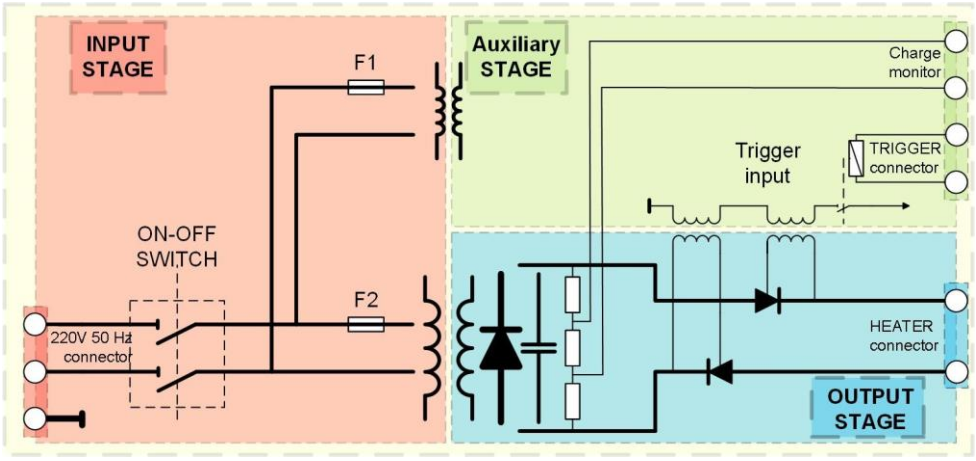

Figure 7-7: Simplified electrical scheme of a DQHDS unit

The 11T cryo-assemblies, as well as the protection racks, will be installed during LS2. Figure 7-8 shows the prototype of the DQHDS units prepared for the 11 T magnet. In the meantime, the series units have been produced and qualified. The DQHDS dedicated to the protection of the Inner Triplet and Matching section will be installed during LS3 and a first prototype is currently under development.

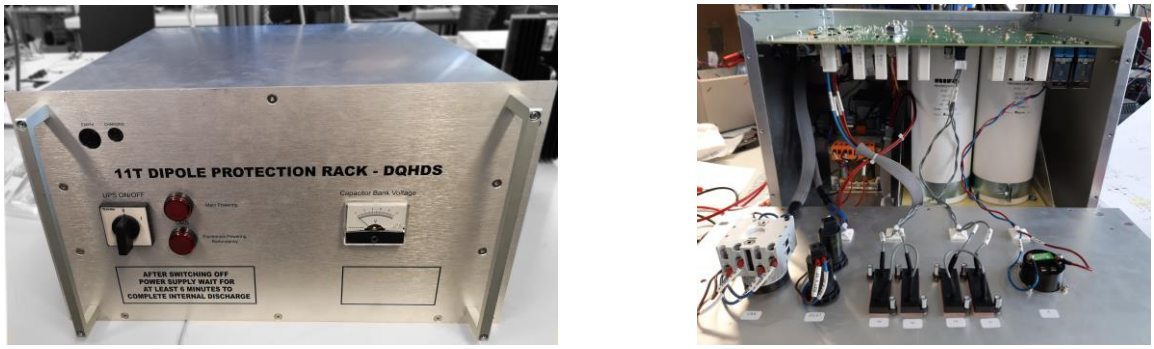

Figure 7-8: Prototype of a DQHDS for the 11T Magnet. In the right picture shows the DQHDS unit with open front face. Two of the total six capacitors can be clearly seen (white cylinders).

7.3.4 Coupling-Loss Induced Quench (CLIQ)

Coupling-Loss Induced Quench (CLIQ) is an innovative method for the protection of superconducting magnets after a quench [13][14][15]. Its fast and effective heating mechanism, utilizing coupling loss between the conductors of the coil, and its robust electrical design makes it a very attractive solution for high-field magnets. The CLIQ technology has been already successfully applied to magnets of different size, coil geometry, and type of superconductor.

The CLIQ system is schematized in Figure 7-9. It is composed of a capacitor bank C, a floating voltage supply S, two additional resistive current leads CL1 and CL2 connecting the system to the magnet, and a Bidirectional Controlled Thyristor (BCT) package, indicated as TH in the figure. The positioning of the connection of the current leads strongly affects the effectiveness of the CLIQ system. These leads carry typically 10% of the nominal magnet current for about 100-200 ms and can therefore have a small cross-section. The capacitor bank is charged by the power supply S with a voltage U_C. Upon quench detection, the bi-directional thyristors are activated resulting in a current I_C being discharged through CL2 leading initially to an over-current in P2-P4 and an under-current in P1-P3 as compared to the nominal current in the magnet (see Figure 7-10). The BCT package allows for several oscillations of these currents.

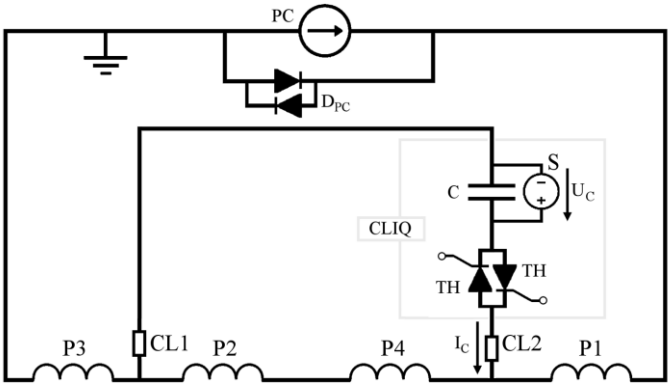

Figure 7-9: Schematic of a CLIQ unit connected to a magnet for its protection [13].

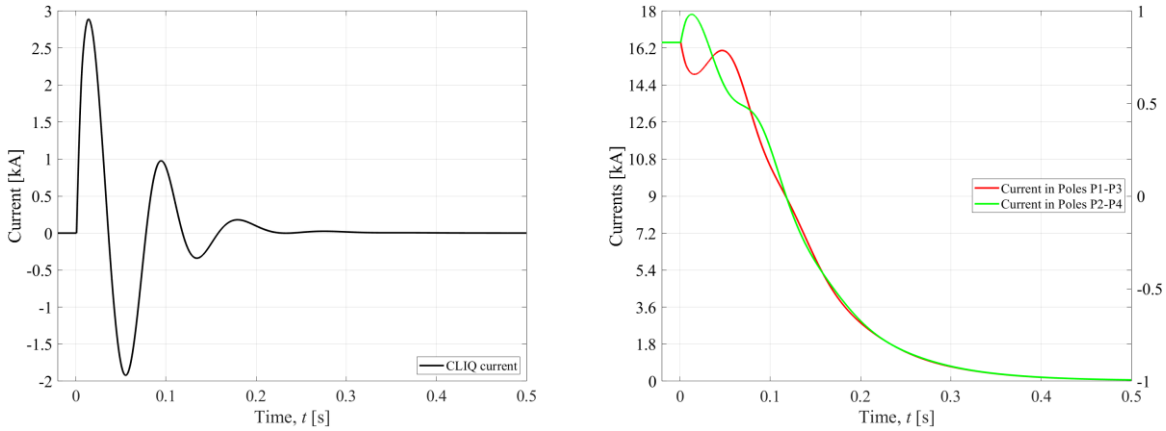

Figure 7-10: Oscillation of the CLIQ current I_c (left) and resulting overall current in the poles of the magnet (right) following the activation of the CLIQ thyristors as simulated with STEAM-LEDET [30].

CLIQ in combination with the DQHDS and quench detection system assures that the peak temperatures and voltages to ground in the MQXF coils are maintained within safe limits. A detailed analysis of the magnet quench protection of the inner triplet circuits can be found in Ref. [15]. The CLIQ units connected to the magnets must comply with the same standards as quench heaters. As the units are directly connected to the magnet potential, every effort must be made for reducing the probabilities of a short circuit across a unit or internally within a unit.

So far 11 CLIQ units of industrial-grade have been manufactured and successfully qualified [17] while the machine version, that will include an improved monitoring and interlock system, enhanced electronics and a higher reliability configuration, is being designed at this moment. Figure 7-11 shows units of the second-generation prototypes, manufactured for the tests of the inner triplet magnets in SM18.

A validation programme using prototype CLIQ units, on the HL-LHC model and prototype magnets, has been successfully carried out within the different magnet test programmes [18][19].

Figure 7-11: CLIQ prototype units of the second generation in the MPE test lab

7.3.5 Energy extraction system

Energy extraction (EE) systems are an important part of the safety-critical quench protection equipment, which are widely used in the existing LHC machine for fast discharge of the energy stored in its superconducting magnet circuits in case of quench. Their design, based on specific and conservative sets of requirements, ensures a reliable dissipation (extraction) of the stored energy that may otherwise overheat and even damage the quenching superconducting parts of the circuit. Currently, 234 energy extraction systems of two distinct types are installed in the LHC machine:

- 202 systems that protect the 600 A-class corrector magnet circuits.
- 32 systems for the main 13 kA dipole and quadrupole circuits.

The existing installations use high-speed electromechanical DC circuit breakers to commutate upon request the circuit current into one or several dedicated energy absorbers (dump resistors). The resistors are permanently connected in parallel to the breakers, passively waiting the opening of the switches to start dissipating the magnet's energy. This basic protection principle is going to be kept the same in the forthcoming HL-LHC.

The present 13kA EE systems will continue their operation after an extensive consolidation program performed on their power and control parts. The dump resistors will be kept the same as well, with resistance values of 2×75 mOhms for dipole systems and 6.8/7.7 mOhms for quadrupole systems. This limits the maximum current decay rate to -125 A/s in the dipole circuits and defines the extraction time constant to 104 sec for dipoles and 37 sec for quadrupoles circuits.

The 600A EE systems will have to be entirely consolidated for the HL-LHC era, introduce at the same time another DC switching technology. Fast vacuum switches will replace the conventional electromechanical devices, providing almost 10 times faster opening times. The new switches will be assembled with two in series, being fully independent from one another. They are practically maintenance-free, requiring only 1 to 2 interventions for the whole of their service life which is estimated to more than 20 000 cycles. The new energy dissipation resistors are composed of two units. They are identical and connected in parallel to the switches. The resistors are industrially made, compact, with low internal inductance devices, each with a resistance of 1.4 Ohms, and a rated energy deposition of 150 kJ. The replacement of the present systems is currently planned in a staged manner between LS3 and LS4.

In parallel with the consolidation and renewal of the existing EE systems, the HL-LHC requires the installation of additional 44 completely new systems for the protection of the MCBXFA/B, MQSXF and MCBRD corrector magnet circuits. The circuits containing MQSXF and MCBRD will be equipped with the 600A vacuum switch-based EE systems as their ultimate current is compatible with this rating. A suitable

resistor in accordance with the circuit specification will be selected and this will be the only different element with respect to the other EE systems using vacuum switches.

Regarding the MCBXFA/B circuits, a third-class EE facility rated for 2kA will be put in operation, as the nominal current flowing in these circuits is 1.6 kA. These EE systems also will be based on vacuum switches with slightly different operational parameters but the same topology as the 600A ones. Four resistors of 0.3 Ohms and 250kJ of nominal energy dissipation capacity will be connected in two parallel branches to provide safe dissipation of the energy when required. Figure 7-12 shows the first prototype of the 2 kA EE system for the HL-LHC.

Figure 7-12: Prototype of 2 kA EE system based on vacuum breakers. Left: rack of first prototype; Right: Zoom on vacuum switch and auxiliary components

The new energy extraction equipment for the HL-LHC will use a new generation of DC switches, which incorporates the latest technology for high-current transmission. The equipment will benefit from improved diagnostics and requires significantly less maintenance.

7.3.6 Cold diodes for the IT circuit

The complexity of the Inner Triplet circuits of the HL-LHC calls for the installation of cold diodes in parallel to magnets Q1, Q2a, Q2b and Q3 (see Fig. 6-4 of the circuit in Chapter 6). These diodes will be located in a dedicated extension cryostat between D1 and the DFX, immersed in superfluid helium, and hence not be located very far from the beam axis. As opposed to the previous option of warm diodes, which would have been located in the new UR cavern, the cold diodes will avoid large over-currents through the superconducting link in case of non-uniform quenches across the different magnets. Furthermore, the cold diodes avoid large voltages in between magnets, and give more robustness to the whole circuit system, allowing to better cope with the differences between magnets and cable parameters (RRR, Cu/SC ratio, strand diameter) as well as increasing the available times for the detection and protection devices (quench detectors, CLIQ, quench heater power supplies).

However, the cold diodes will be exposed to high radiation doses and fluence of neutrons and high energy hadrons, leading to a potential degradation of their characteristics over time. The integrated radiation dose and fluence at the location of the cold diodes is estimated to reach up to 12 kGy and 5×10^{13} n/cm^2 1 MeV equivalent over the HL-LHC lifetime [20].

The radiation tolerance of different types of bypass diodes has been tested at low temperatures at CERN's CHARM irradiation facility during the operational year 2018. The main electrical properties of the diodes (turn-on voltage, forward voltage, reverse blocking voltage and capacitance) have been measured on a

weekly basis, at 4.2 K and 77 K, respectively, as a function of the accumulated dose/fluence. The diodes were submitted to an integrated dose close to 12 kGy and a 1 MeV equivalent neutron fluence of 2.2×10^{14} n/cm^2. After the end of the irradiation campaign, the annealing behaviour of the diodes was tested by increasing the temperature to 300 K. The diodes' electrical properties gave satisfactory results and have been added to the HL-LHC baseline following their successful qualification [21].

7.3.7 Powering interlock system (PIC)

The powering interlock system PIC guarantees the presence of the correct powering conditions for the electrical circuits with superconducting magnets in the LHC. At the same time, it guarantees the protection of the magnet equipment by interfacing the quench protection systems, the beam interlock system, the power converters, the cryogenic system, and technical services such as uninterruptable power supplies (UPS), emergency stop buttons (AUG), and controls. The PIC is a distributed system consisting for the current LHC of 36 individual powering interlock controllers, which manage the powering of each of the 28 powering subsectors [8]. Note, that the arcs require two PICs per powering subsector.

The PIC is a hybrid system consisting of a central, standard PLC connected to deported Input – Output units via a specific electronic board, including an industrial PROFIBUS-DP interface and a CPLD, close to the equipment they are connected to. The PLCs are installed in the UA and UL areas, where acceptable levels of radiation are expected, while the deported Input – Output units in IP1, IP5 and IP7 are installed in the RRs and are subjected to radiation. The PLCs are not radiation tolerant, while the deported I/O units have been successfully tested to withstand low radiation levels, as foreseen in the original design 15 years ago.

At the design luminosity for the HL-LHC (5×10^{34} cm^{-2} s^{-1}), and even more for ultimate, the thermal neutron and high-energy hadron fluencies in the areas close to the tunnel, like the RRs, will increase considerably with respect to the values for which the existing PIC has been designed and tested. In IP1 and IP5, a relocation of the PLCs from the UL/USC areas to the new UR galleries is under study. For IP1, IP5 and IP7 no repositioning of the deported I/Os units from the RRs is foreseen. The estimate of the increased radiation levels for the HL-LHC is above the acceptable level of the deported PIC units. For this reason, a new version of the PIC deported units is foreseen, based on radiation tolerant FPGAs, up to the levels predicted for the HL-LHC with ultimate luminosity operation. The upgrade will also cover the refurbishment of the electronics, which has become obsolete and is expected to reach its end of life in the coming years. The replacement of the central PLC is also under study.

The new PIC system will have exactly the same functional specification as the present PIC and the interfaces to the different systems are not expected to change considerably. The protection of the new 11 T dipole magnets, which includes a new dipole trim circuit, can be covered by the present functionality. This trim circuit will be treated in the same way as other corrector circuits in the LHC.

Table 7-4 summarizes the interlock requirements for the RB circuits 6-7 and 7-8 and the related 11 T trim circuit [27]. The Trim circuit will be considered as essential from the PIC side, which means un-maskable at the level of the beam interlock controller (BIC).

Table 7-4: Interlock requirements for the RB circuits in sectors 6-7 and 7-8 including the 11 T trim circuit [27].

Interlock case	**PIC Action on RB Circuit**	**PIC Action on Trim Circuit**	**Beam Dump**
Quench in RB circuit	Fast Power Abort	Fast Power Abort	Yes
RB Discharge Request	Fast Power Aboort	Fast Power Abort	Yes
Powering Failure in RB Circuit	Slow power Abort	No action	Yes
Current Lead of Trim circuit	No action (Fast Power Abort triggered by QDS)	Fast Power Abort	Yes
Powering Failure in Trim Circuit	No action	Slow Power Abort	Yes
Switch opening request by RB PC	Fast Power Abort	Fast Power Abort	Yes
Cryo-failure	Slow Power Abort	Slow Power Abort	Yes

7.4 References

[1] V. Raginel, M. Bonura, D. Kleiven, K. Kulesz, M. Mentink, C. Senatore, R. Schmidt, A. Siemko, A. Verweij, A. Will, and D. Wollmann, "First Experimental Results on Damage Limits of Superconducting Accelerator Magnet Components Due to Instantaneous Beam Impact", IEEE Trans. Appl. SC, Vol 28(4), June 2018, DOI: 10.1109/TASC.2018.2817346.

[2] V. Raginel, "Study of the Damage Mechanisms and Limits of Superconducting Magnet Components due to Beam Impact", CERN-THESIS-2018-090.

[3] M. Valette, L. Bortot, A. Fernandez Navarro, B. Lindstrom, M. Mentink, E. Ravaioli, R. Schmidt, E. Stubberud, A. Verweij, D. Wollmann, "Impact of superconducting magnet protection equipment on the circulating beam in HL-LHC", IPAC 2018, DOI: 10.18429/JACoW-IPAC2018-THPAF062.

[4] B. Lindstrom, P. Belanger, L. Bortot, R. Denz, M. Mentink, E. Ravaioli, F. Rodriguez Mateos, R. Schmidt, J. Uythoven, M. Valette, A. Verweij, C. Wiesner, D. Wollmann, M. Zerlauth, "Fast failures in the LHC and the future high luminosity LHC", Phys. Rev. Accel. Beams 23 (2020) 081001, DOI: 10.1103/PhysRevAccelBeams.23.081001.

[5] A. Santamaria Garcia, "Experiment and Machine Protection from Fast Losses caused by Crab Cavities in the High Luminosity LHC", CERN-THESIS-2018-142.

[6] T. Baer *et al*., "Very fast crab cavity failures and their mitigation", Proc. IPAC'12, May 2012, pp. 121–123, MOPPC003, CERN-ATS-2012-106.

[7] E. Ravaioli, "Quench protection studies for the high luminosity inner triplet circuit", EDMS: 1760496.

[8] R. Schmidt B.Puccio, M.Zerlauth, "The hardware interfaces between the powering interlock system, power converters and quench protection system", EDMS: 68927.

[9] E. Ravaioli, G. Ambrosio, B. Auchmann, P. Ferracin, M. Maciejewski, F. Rodriguez-Mateos, GL. Sabbi, E. Todesco, A. Verweij: "Quench Protection System Optimization for the High Luminosity LHC Nb_3Sn Quadrupoles", IEEE Trans. on Appl. SC, 2017, DOI: 10.1109/TASC.2016.2634003.

[10] A. Antoine, "Study of the delay time required by the PIC to do a beam dump request", EDMS: 2187812.

[11] L. Rossi, (ed.) and O. Brüning (ed.), "The High Luminosity Large Hadron Collider : the new machine for illuminating the mysteries of Universe", World Scientific, Hackensack, 2015, DOI: 10.1142/9581.

[12] R. Denz, E. de Matteis, A. Siemko, J. Steckert, "Next Generation of Quench Detection Systems for High Luminosity Upgrade of the LHC", ASC'2016, 2016, DOI: 10.1109/TASC.2016.2628031.

[13] E. Ravaioli, CLIQ. "A new quench protection technology for superconducting magnets", PhD thesis University of Twente, 2015, CERN-THESIS-2015-091.

[14] V.I. Datskov, G.Kirby, and E. Ravaioli, "AC-Current Induced Quench Protection System", EP13174323.9, Application Granted 2020-03-25.

[15] E. Ravaioli *et al.,* "Advanced Quench Protection for the Nb_3Sn Quadrupoles for the High Luminosity LHC", IEEE Trans. Appl. Supercond. 26, 2016, DOI: 10.1109/TASC.2016.2524464.

[16] Conceptual Design Review of the Magnet Circuits for HL-LHC, 21.-23.03.2016, CERN, Switzerland. INDICO: 477759.

[17] F. Rodriguez Mateos, S. Balampekou, D. Carrillo, K. Dahlerup-Petersen, M. Favre, J. Mourao and B. Panev, "Design and Manufacturing of the First Industrial-Grade CLIQ Units for the Protection of Superconducting Magnets for the High-Luminosity LHC Project at CERN," in IEEE Transactions on Applied Superconductivity, vol. 28, no. 3, DOI: 10.1109/TASC.2018.2794473.

[18] E. Ravaioli, V. I. Datskov, G. Dib, A.M. Fernandez Navarro, G. Kirby, M. Maciejewski, H. H. J. ten Kate, A. P. Verweij and G. Willering, "First Implementation of the CLIQ Quench Protection System on a 14-m-Long Full-Scale LHC Dipole Magnet" IEEE Trans. On applied Superconductivity, vol. 26, No4, 2016, DOI: 10.1109/TASC.2015.2510400.

[19] E. Ravaioli, G. Ambrosio, H. Bajas, G. Chlachidze, P. Ferracin, S. Izquierdo Bermudez, P. Joshi, J. Muratore, F. Rodriguez-Mateos, GL. Sabbi, S. Stoynev, E. Todesco, and A. Verweij, "Quench

protection performance measurements in the first MQXF magnet models", IEEE Trans. Appl. Supercond., DOI: 10.1109/TASC.2018.2793900.

[20] G. Lerner, R. G. Alia, M. S. Gilarte, A. Tsinganis, and F. Cerutti, "Update on HL-LHC radiation levels on equipment in the IP1-IP5 LSS", presentation at the 9th HL-LHC Collaboration Meeting, Fermilab, USA, 15 October 2019, INDICO: 806637.

[21] A. Will, G. D'Angelo, R. Denz, D. Hagedorn, A. Monteuuis, E. Ravaioli, F. Rodriguez-Mateos, A. Siemko, K. Stachon, A. Verweij, D. Wollmann, A.-S. Mueller, and A. Bernhard, "Characterization of the radiation tolerance of cryogenic diodes for the High Luminosity LHC inner triplet circuit", Physical Review Accelerators and Beams 23, 053502, 2020, DOI: 10.1103/PhysRevAccelBeams.23.053502.

[22] E. Ravaioli, H. Bajas, V. I. Datskov, V. Desbiolles, J. Feuvrier, G. Kirby, M. Maciejewski, G. Sabbi, H. H. J. ten Kate, A. P. Verweij, "Protecting a Full-Scale Nb3Sn Magnet with CLIQ, the New Coupling-Loss-Induced Quench System", IEEE Trans. Appl. Supercond, DOI: 10.1109/TASC.2014.2364892.

[23] J. Steckert *et al*., "Application of the New Generic Quench Detection System for LHC's 11 T Dipole Magnet", IEEE Transactions on Applied Superconductivity, vol., DOI: 10.1109/TASC.2019.2898681.

[24] A. F. Lietzke *et al*., "Differentiation of performance-limiting voltage transients during Nb_3Sn magnet testing" AIP Conf. Proc., vol. 824, pp. 550–557, 2006, DOI: 10.1063/1.2192394.

[25] S. Bermudez et al., "Quench protection studies of the 11T Nb_3Sn dipole for LHC upgrades", IEEE Trans. Appl. Supercond. vol. 26, no. 4, Jun., 2016, DOI: 10.18429/JACoW-IPAC2014-WEPRI098.

[26] R. Garcia Alia, private communication, CERN Geneva, (2019).

[27] A. Antoine, D. Carrillo, R. Denz, F. Menendez Camara, F. Rodriguez Mateos, "Modifications to the protection system hardware to adapt to requirements given by the 11T dipoles installation in LHC", Internal Note 2019_08, EDMS: 2104676.

[28] M. Valette, "Parameters of Quench Heater (QH) circuits for all LHC Run II, Run III and HL-LHC superconducting magnets as well as their associated kicks on the beam", EDMS: 2051527.

[29] B. Lindstroem *et al*, "Fast failures in the LHC and future HL-LHC", DOI: 10.1103/PhysRevAccelBeams.23.081001.

[30] E. Ravaioli *et al*., "Lumped-element dynamic electro-thermal model of a superconducting magnet," Cryogenics, 2016, DOI: 10.1016/j.cryogenics.2016.04.004.

Chapter 8

Collider-experiment interface

F. Sanchez Galan[1*], *H. Burkhardt*[1*], *F. Cerrutti*[1], *A. Gaddi*[1], *J.L. Grenard*[1], *L. Krzempek*[1], *M. Lino Diogo dos Santos*[1], *J. Perez Espinos*[1], *M. Raymond*[1] *and P. Santos Diaz*[1]

[1]CERN, Accelerator & Technology Sector, Switzerland
[*]Corresponding authors

8 Collider-experiment interface

8.1 Overview

The HL-LHC targeted luminosities for the four main experiments (Table 8-1) will require upgrades of multiple subsystems in In particular, the LHCb experiment subsystems as the vertex locator (VELO), the ring-imaging Cherenkov (RICH) detectors and the tracking system will undergo a major upgrade in LS2, and its surrounding protection systems will be upgraded with neutral absorbers (TANB) to allow to reach the HL-LHC foreseen peak luminosity as from Run 3. Also, in LS2, ALICE will replace its beam-pipe for a new one, with smaller diameter and will also replace its tracking system, time projection chamber and will install a new fast interaction trigger detector. In ATLAS and CMS during Long Shutdown 2 (LS2) and Long Shutdown 3 (LS3) the inner tracker, trigger system, calorimeter, and muon detection systems capable of operating at the foreseen pile-up density, increased radiation environment and minimisation of activation will be replaced. [1][2][3] [17].

Table 8-1: Nominal design luminosities for p-p operation for the HL-LHC. In parenthesis, the value envisaged as “ultimate”. The luminosities for the LHC Run 2 are also included for comparison. Total targeted integrated luminosity in CMS and ATLAS is 3000 fb-1 about 10 years after upgrade.

	Peak Luminosity (cm^{-2} s^{-1})		
Experiment	**HL-LHC**	**LHC**	**IP**
ATLAS	$5(7.5) \times 10^{34}$	$1(2) \times 10^{34}$	1
CMS	$5(7.5) \times 10^{34}$	$1(2) \times 10^{34}$	5
ALICE	1×10^{31}	1×10^{31}	2
LHCb	2×10^{33}	2×10^{32}	8

Besides the high-luminosity experiments, the ALICE and LHCb experiments will be upgraded and continue operations during the HL-LHC era. The ALICE experiment, which prepares upgrades of several subsystems and the online–offline system for data acquisition and processing during LS2, will continue the Pb-Pb ion and proton-Pb ion collision program up to LS4, aiming to collect in total 10 nb^{-1} for Pb-Pb collision at top energy plus 3 nb^{-1} for Pb-Pb collision at reduced energy for low-mass dilepton studies and 50 nb^{-1} for p-Pb plus p-p reference runs. As ion beams will still be available during the HL-LHC operation after LS3, the ATLAS and CMS experiments will also participate in the Pb-Pb and p-Pb collision program within the capabilities and constraints from the upgraded inner triplet magnets and available apertures. The LHCb experiment plans for an upgrade during LS2 to allow operating at instantaneous luminosities of 2×10^{33} cm^{-2} s^{-1} (ten times their current design luminosity), that remains compatible with the present magnet layout of the machine in LSS8. This will increase the level of collected data much beyond the Run 2 rate (between 1.7 and 2.2 fb^{-1} per year). The increase in luminosity will mean an increase of collision debris, and

the introduction of a Neutral Absorber (TANB) is planned to protect the D2 separation dipole and the downstream cryogenic magnets. Operating in these conditions, LHCb expects to collect 50 fb^{-1} of data until LS4, when a second major upgrade of the detector might be envisaged that would open the possibility of operating at with a luminosity of around 1.8×10^{34} cm^{-2} s^{-1} to allow the collection of 300 - 500 fb^{-1} of data to fully exploit the flavour physics potential of LHC. This later major upgrade is presently under study within the HL-LHC project, albeit not yet part of the baseline HL-LHC project, in particular to understand the implications on operations and the impact to the ATLAS and CMS experiments, and to anticipate modifications to the installed hardware in LSS8 in view of optimizing interventions before the foreseen increased activation levels.

At present, no forward physics experiment has been officially approved to be operated in the LHC tunnel in LSS1 and LSS5 after LS3, apart the detectors required for the ion operation. The presently installed elastic scattering and diffractive physics experiments TOTEM, ATLAS/ALFA and, AFP are assumed to be dismantled during LS3. To what extend they will be replaced with other projects is still under discussion.

The major changes of the layout of the machine in the high-luminosity regions around IP1 and IP5 also result in significant changes in loss patterns in the experimental insertions and backgrounds to the detectors. This is followed up by continuous efforts organized within the LHC background study working group (LBS) to monitor backgrounds in the present LHC and to understand the observations by matching them to evolving, detailed simulations. The reduction of tolerances in the collimation hierarchy and the increase in aperture for the HL-LHC potentially increases losses on tertiary collimators and losses reaching the detector region. As expected, backgrounds and losses were in fact observed to increase with beam energy and intensity. Under normal conditions, they have remained at comfortably tolerable levels for the experiments. The beam-induced backgrounds observed in the detectors are dominated by beam-gas scattering. Efforts to maintain and if possible, further improve the excellent vacuum conditions around the experiments are important to keep backgrounds low at the HL-LHC.

Studies are ongoing on the possible operation scenarios including crabbing schemes, luminosity levelling, collision crossing angles, etc. The goal is to evaluate the limits from the pile-up density that can be afforded whilst maintaining high efficiency for physics signals. Furthermore, studies on possible accident scenarios and associated risks for the machine and experiments have been initiated (see Chapter 7). The studies address failure scenarios of machine components during operation e.g. crab cavity failures [5][6], asynchronous beam dumps, or rarer events like mechanical failures with obstacles in the beam, to name the major ones. The background and failure scenario studies are being updated to follow modifications in the design details and to examine the impact of any new components. The possible impact of recent updates to the HL-LHC baseline as the hollow electron lens on accidental beam losses and backgrounds has not yet been studied in detail. From what is known so far, it is likely that the hollow electron lens will not result in fast accidental beam losses and that its impact on backgrounds will be minimal.

The hardware and equipment involved in the machine-experiment interface for the HL-LHC operation include:

- The passive absorbers for charged (TAXS) and neutral (TAXN and TANB) particles designed to primarily protect the nearby superconducting magnets from the radiation coming out from the interaction region, and simultaneously provide a background reduction to the experiments from beam interactions in the collimators and beam gas;
- The forward shielding in the experimental caverns, in particular the part that is close to the LHC machine tunnels, designed to minimize the background radiation in the detectors and to protect personnel from the highly activated elements during access and maintenance activities;
- The experimental beam pipes, covering in particular the part around the interaction region but more widely the design, handling, and routine operation procedures for the vacuum sector from Q1-left-to-Q1-right.

The design considerations and required upgrades and modifications for the HL-LHC operation are described in the next Sections.

8.2 The charged particles passive absorber – TAXS – TAXS

The high-luminosity regions of LHC at P1/ATLAS and P5/CMS are equipped with passive absorbers for charged particles (TAS) [10] installed on both sides of the interaction region at the transition of the experimental caverns to the LHC tunnel. Their main function is to reduce the heat load and radiation to the superconducting quadrupoles in the straight section from the collision debris coming out of the interaction region. In parallel, the TAS completes the forward shielding of the experiments and participates in the background reduction to the experiments.

The design of the new TAXS absorbers for the HL-LHC for IP1 and IP5 is based on the existing ones, thus maintaining the same shielding configuration, with the following modifications and improvements:

- The beam pipe aperture increases to 60 mm in diameter from the present 34 mm. This aperture is compatible with all possible beam optics versions foreseen for the HL-LHC operation and impacts on the background conditions for the experiments.
- No internal ionization chamber is foreseen in the TAXS.
- The cooling power increases to dissipate the approx. 780 W deposited in the TAXS during beam operation conditions of the HL-LHC including a safety margin which allows for operation at ultimate luminosity of 7.5×10^{34} cm^{-2} s^{-1} (see Ref. [11]).
- The vacuum chamber inside the TAXS will be amorphous carbon (a-C) coated. No baking will be needed. The design of the TAXS remains compatible with the mechanical and geometrical constraints from the surrounding shielding of the experiments.

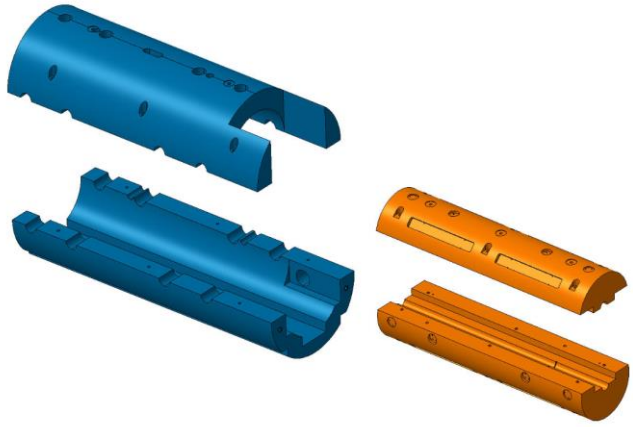

Figure 8-1: Exploded view of the ATLAS TAXS (orange) and its surrounding cradle (blue)

The key design and operation parameters are shown in Table 8-2 and Table 8-3 below.

The exchange from the TAS to TAXS will be done from the experimental caverns and could happen both at the beginning and/or at the end of LS3. Performed simulations regarding estimated radiation levels show that the effect of leaving the TAS in the current location does not affect the dose received by the workers for the routine operations performed in the experimental caverns [15]. The overall procedure is being optimized such as to minimize the exposure of personnel to radiation in compliance with the ALARA principle and the overall planning of the activities in the LHC tunnel and experimental caverns.

Table 8-2: TAXS design parameters from ref. [11].

Characteristics	**Units**	**Value**
Distance from IP1 to front flange	mm	19050
TAXS absorber length	mm	1800
TAXS absorber diameter	mm	500
Nominal beam height from floor	mm	1100 at IP1 and 950 at IP5
Nominal longitudinal tunnel slope		+1.236% at IP1 and -1.236% at IP5
Nominal transverse tunnel slope		0.0%
Maximum floor loading	MPa	<0.5
Beam tube straight absorber section (two beams in one tube) Inner radius	mm	30
Supports range of motion		± 30 mm at installation, ± 5.0 mm horizontal and vertical Stops in z (beam axis) at operation.
Absorber cooling		Water and ambient air

Table 8-3: TAXS operation parameters from ref. [12].

Characteristics	**Units**	**Value**
Aperture diameter	mm	60
Absorbed collision power at 5×10^{34} cm^{-2} s^{-1}	kW	0.5
24 hr average absorbed collision power (80%)	kW	0.4
Maximum internal beam tube temperature at 5×10^{34} cm^{-2} s^{-1}	C	< 50
Peak power density	mW/cm^3	290
Peak dose	GGy	2
Lifetime alignment operations [1 per opening]		20

8.2.1.1 The TAXS absorber and the relocated VAX in ATLAS/P1

The current Vacuum Assemblies for eXperimental Areas (VAX) are installed inside the LHC tunnel, following Q1 and in a dead end and extremely narrow and difficult access environment. Radiation will increase until LS3 and after that during the HL-LHC operation, making the need of improving access and reducing dose to people during eventual interventions a must. Due to the nature of the shielding (massive steel pieces installed previously in the experiments and tunnel infrastructure) mean that the tunnel cross-section cannot be enlarged at these particular locations.

To solve this, all elements belonging to the VAX will be positioned inside a new support structure, cantilevered with respect to a baseplate that is attached on the fixed forward Shielding structures (JN monobloc, shown in blue surrounding the TAXS in Figure 8-2). The VAX support baseplate has an embedded alignment mechanism that can be manipulated from a distance. The new support will also provide support for the last part of the experimental beam pipe (VJ chamber).

Bellows and quick disconnects installed on either side of the vacuum modules inside the support structure will allow for a fast exchange with remote tools in case of problems. The installation of two flanges, one on the experiment side and one towards the machine, will allow for redundancy and easy decoupling of vacuum sections in case of failures. A permanent bake-out system for the modules will be installed.

Figure 8-2 shows the updated layout of the Forward Regions in ATLAS. On the IP side of the TAXS the assembly module of vacuum equipment (VAX) will be installed as previously described. To do so the present forward luminosity detector (LUCID) will have to be moved towards the IP for the HL-LHC. The module consists of two all-metal gate valves (DN80), the VAX module with ports for the ionic pump, the gas (Ne) injection/extraction line, the quick flanges and intermediate bellows as shown in Figure 8-5. The removal of the different modules and its ancillary services will be fully remote controlled.

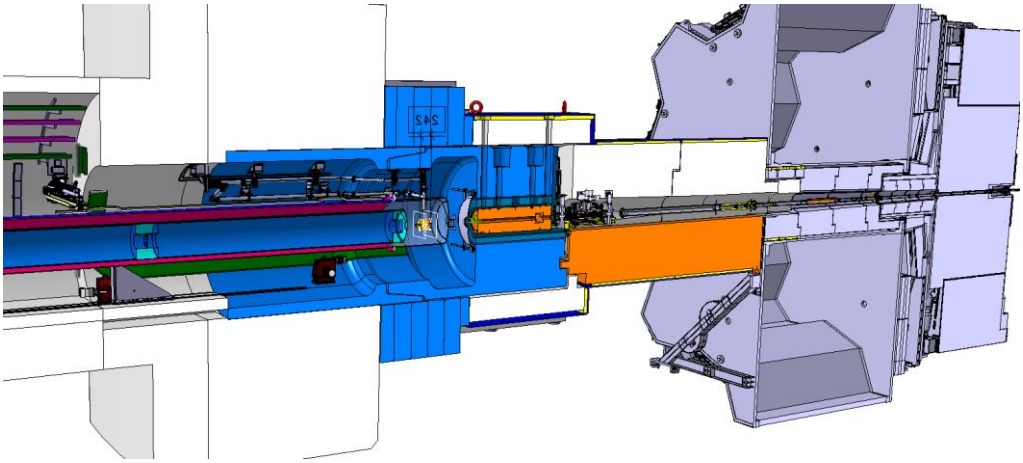

Figure 8-2: 3-D view of the TAXS region from Q1 (machine side, on the left) to ATLAS Endcap toroid (in grey). The layout corresponds to the Run 3 configuration. Q1 is followed by the TAXS absorber (first piece in orange, inside the blue shielding), and the vacuum assembly module (VAX). The foreseen modifications required to host it in the experimental area concern the Forward Shielding (JFC upper shown in white, lower bridge shown in orange) and Endcap Toroid Shielding (JTT in grey).

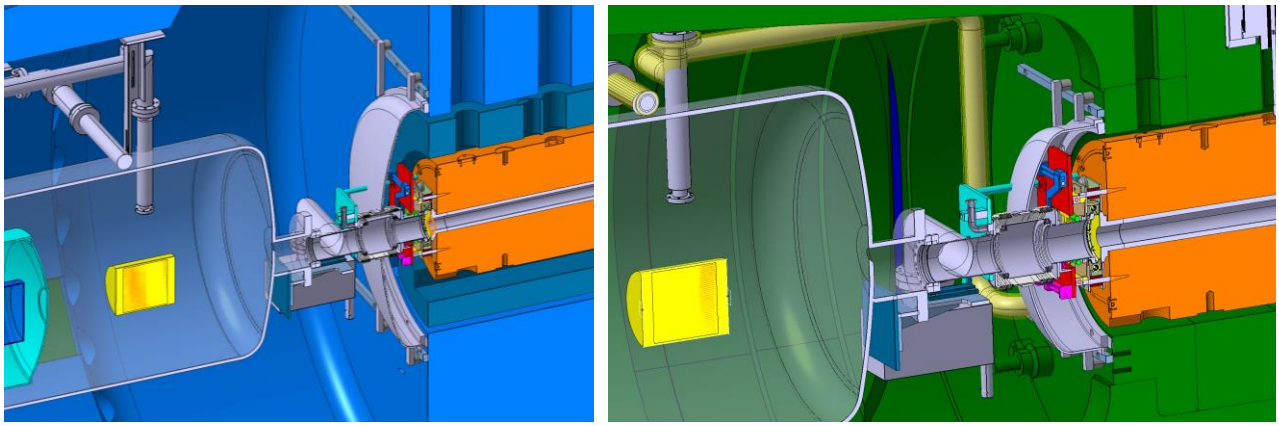

Figure 8-3: [Left]- Zoom into the IP1 Q1-TAXS region as foreseen for the HL-LHC. TAXS (orange) is shown inside its cradle shielding (dark blue). The BPM (yellow) will be placed inside the Q1 secondary vacuum and quick connector, double pump which requires no access and the He tightness dome will remain in the very limited region (grey elements). The gate valves and current VAX assembly will be moved to the experimental caverns. [Right] Zoom on IP5 Q1-TAXS region as foreseen for the HL-LHC.

Modifications of the ATLAS forward shielding elements will be required to integrate the relocated vacuum elements (VAX, all-metal gate-valves). Background studies based on a preliminary geometry of the shielding, have been performed by ATLAS and show that the overall performance is within the current acceptable range. More detailed studies will be performed once a more final shielding geometry is defined, in order to check if additional shielding is required or not.

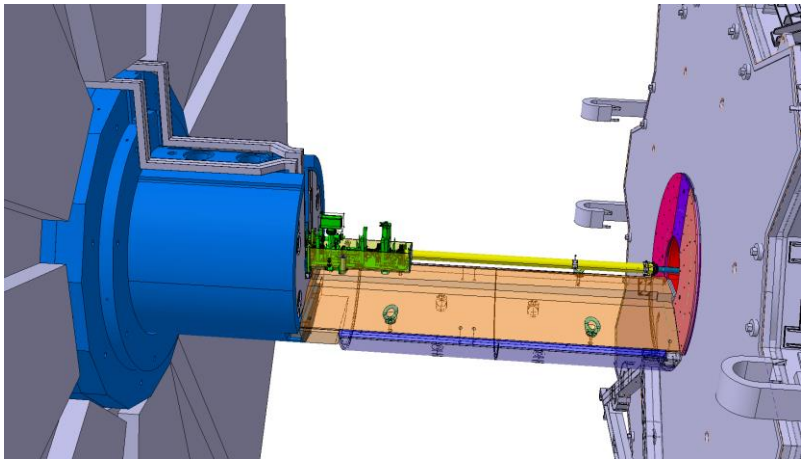

Figure 8-4: 3D view of the forward shielding region with the relocated VAXS and services. The layout corresponds to a phase in the detector access procedure where the octagonal and cylindrical part of the JFC shielding are removed. The passage of the services for the vacuum equipment module (cabling and gas injection/pumping pipes) is shown in grey.

During routine Year-end Technical Stop (YETS) periods, the, ATLAS Endcap Toroid (ECT) opens and slides towards the TX1S shielding without removing the vacuum pipe. At present, all the beamline elements in the region (VJ & VT chambers) are compatible with the inner bore of the ECT, but the size of the new VAX elements will exceed the present envelopes. To allow the full opening of the ATLAS endcap toroid without dismantling any vacuum component, the first disk of the plug shielding is placed inside the toroid inner bore tube (JTT) [8].

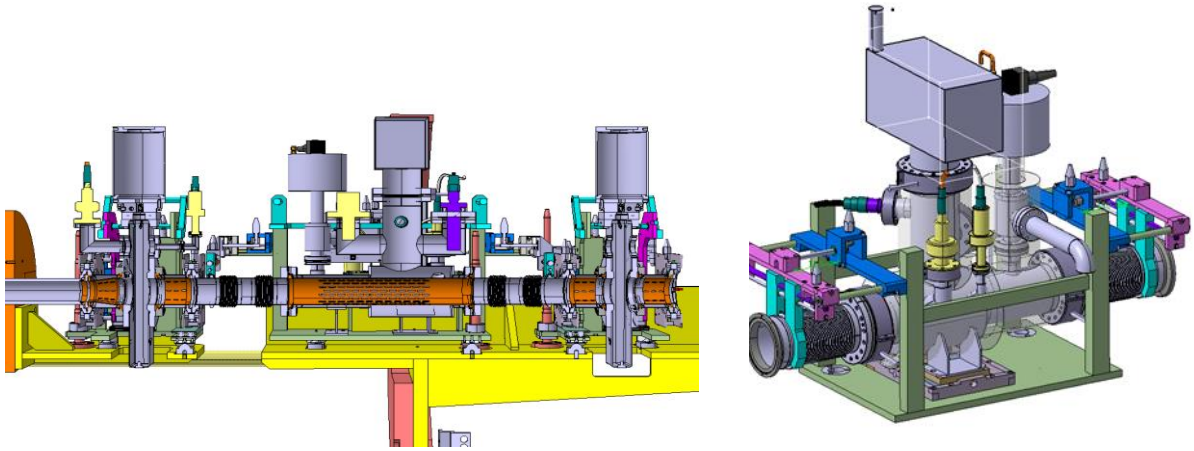

Figure 8-5: [Left] Cut of the Vacuum module assembly (VAX) to be installed on the IP side of the TAXS with all-metal gate valves. Right: the valves are closed in case of remote exchange of the vacuum pump module (Right). Note that the cantilever support structure is not shown in the right picture.

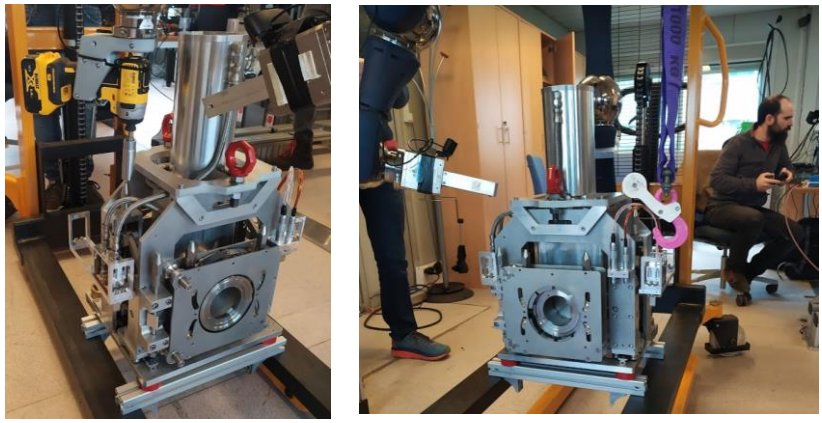

Figure 8-6: Left: All-metal gate sector valve prototype belonging to the vacuum module assembly (VAX) for the IP side of the TAXS. Right: The valves will be remotely disconnected in case of exchange.

The internal bore will be fully compatible with the new vacuum equipment and will provide a safe clearance in case of the detector opening. Shielding performance will be kept by adding extra-material (nose-shape) onto the JFC2. Due to this, the usual opening routine will be only slightly affected.

As the proposed JTT modification preserves the shielding volume, it should be transparent to the operation of the detector. It affects however the support of the experimental vacuum chamber, where a solution is being developed.

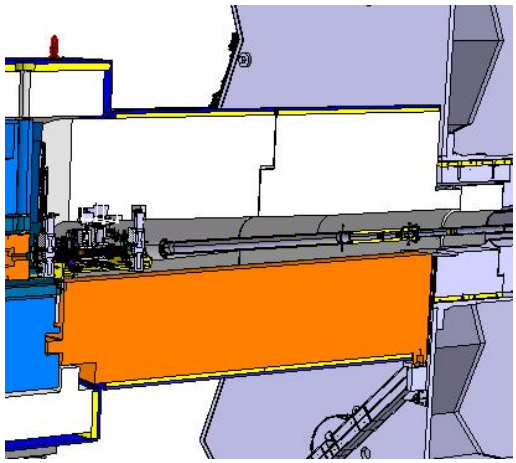

Figure 8-7: Detail cut view of ATLAS forward shielding structures that need to be modified. The shielding consists of two parts: The cylindrical core and the octagonal back. Three pieces called JFC1 ("the bridge", in orange"), JFC2 (white) and JFC3 (white) are used for the core and two pieces called "JFS3 upper" and "JFS3 lower" (on the left, surrounding the blue nose monobloc) are used for the octagonal back.

As the equipment installed on the IP side will be exposed to higher particle fluxes, resulting in higher (× 3) residual doses, the use of optimised material such as Aluminium or low carbon & low cobalt stainless steel will be promoted. Studies on the activation levels and impact to detector background are ongoing, to fully validate this baseline layout [9].

Other shielding modifications (machining) are needed to accommodate the passage of services to the relocated VAX:

- Forward shielding bridge structure “JFC1” (machining below VAX support frame);
- Forward shielding disk at TAS side “JFC2” (machining slots for all-metal gate valve heads and VAX);
- Forward shielding disk at ATLAS Toroid side “JFC3” (include nose for shielding JTT);

- ATLAS Toroid shielding plug “JTT1” (increase bore diameter to host VAX and gate valve heads in ATLAS Standard openings).

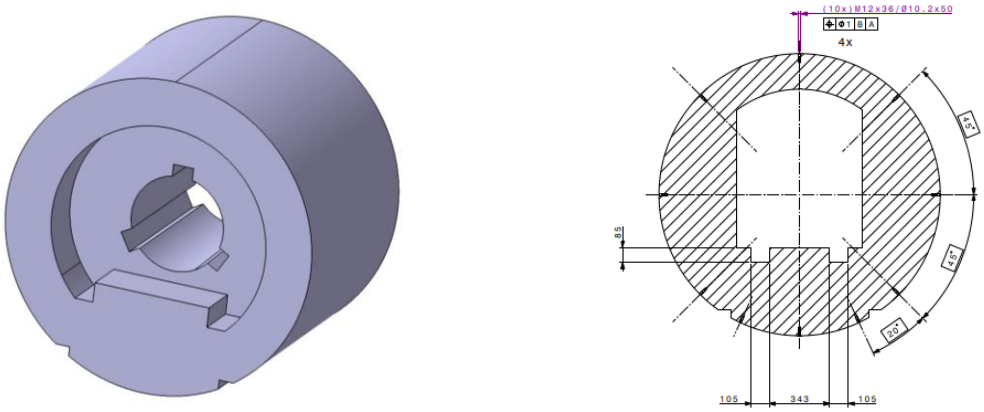

Figure 8-8: 3D view of the ATLAS Toroid shielding plug (JTT, in grey). Only the first of the four disks is shown. For present LHC configuration (left) the disk is a single block, while it will be modified for the HL-LHC (right) will be modified and the shielding will be done in two parts: an outer cylinder with a tailored bore, and an internal block attached to the JFC2 module (Figure 8-9).

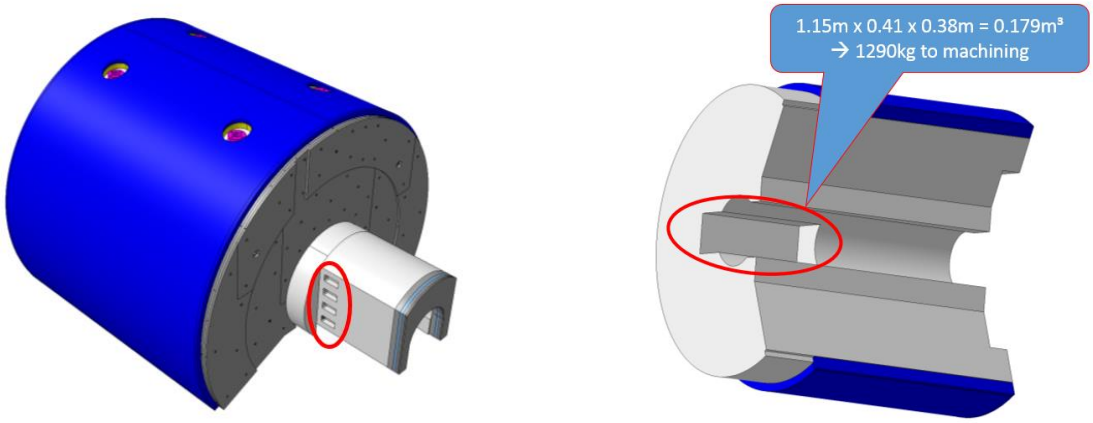

Figure 8-9. Left: 3D view of the ATLAS JFC2 module. Presently the module is a cylindrical shaped block, while for the HL-LHC an “extra nose” shielding will be bolted to fill the gap required in JTT for the detector opening without removing VAX. Right: proposal for machining JFC3 subject to ATLAS agreement.

Figure 8-10. Left: View of the “extra nose” shielding (3 tons) manufactured by VMV METAL Ltd (Bulgaria) during LS2. Right: New 11-ton ATLAS Toroid shielding plug (JTT), manufactured by PAEK (Pakistan).

8.2.1.2 The TAXS absorber and the relocated VAX in CMS/P5

As is the case for ATLAS, in CMS large shielding structures are situated surrounding the TAS and beampipe in the forward regions. Although conceptually similar, the mechanics are different and opening of these large, cantilevered structures is done by rotating them, using a “classical” hinged system. The updated layout for the CMS experiment is shown in Figure 8-12.

The assembly module for the vacuum equipment is similar to that for ATLAS, with minor modifications to adopt it to the shielding layout. As for ATLAS, there are some conflicts with the presently installed shielding that can be resolved with minor modifications:

A new plug for the fix iron nose will be built and shielding elements of the rotating shielding will be either removed or modified to allow the integration of the displaced VAX equipment. There is no further conflict with the detector opening as the new module will occupy basically the volume of the presently installed support module, shown in yellow in Figure 8-14 and Figure 8-16. The installation of the vacuum equipment (all metal gate valves-quick connectors), bellows and VAX module on the new beam pipe support will require the relocation of the services (Grey beam over the support at Figure 8-16 left). The passage of the services is challenging but possible using the channels on the Fixed Iron Nose (FIN) left open when the rotating shielding closes.

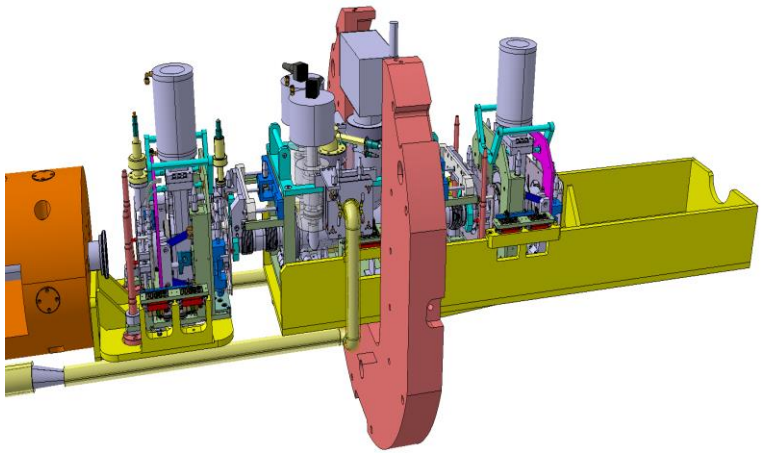

Figure 8-11: Right- cut of the Vacuum module assembly (VAX) installed on the IP side of the TAXS with all-metal gate valves.

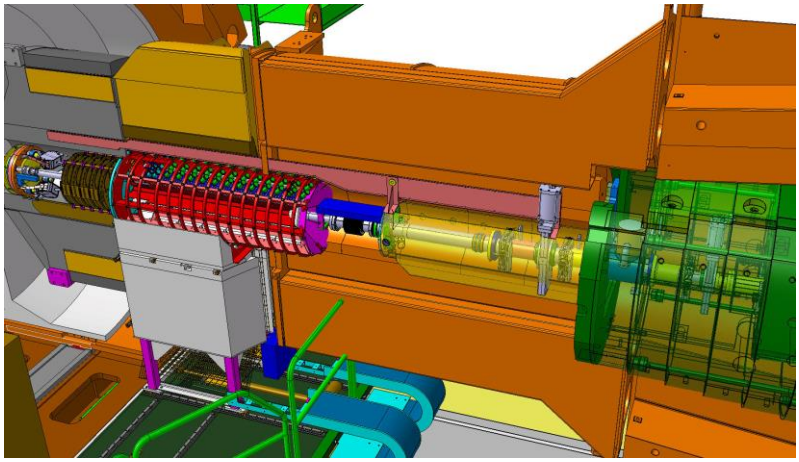

Figure 8-12: 3D view of the CMS forward shielding region with the TAXS and vacuum module. The layout corresponds to the Run 3 configuration. The TAXS absorber is located on the right inside the Fixed Iron Nose shielding (FIN, in green) and the surrounding rotating shielding (in orange). The relocated vacuum assembly module (VAX) on the IP side is shown inside the baseplate support (transparent yellow).

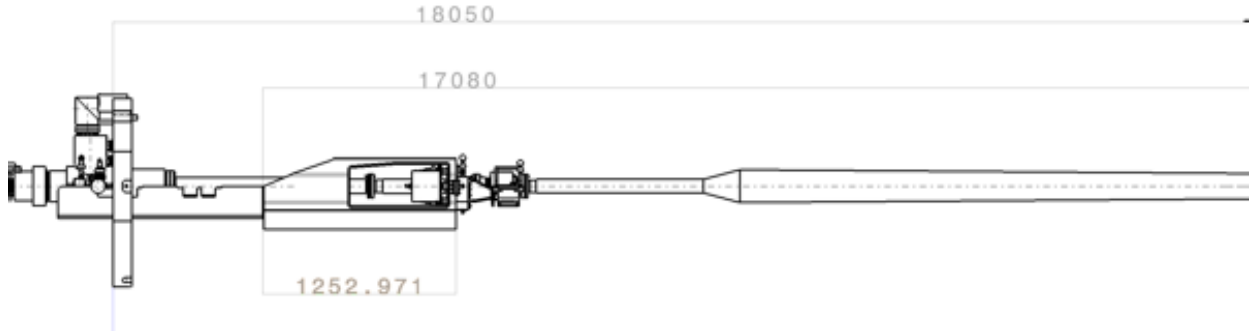

Figure 8-13: 2D drawing of the CMS beam pipe forward region. The new VAX support will extend until 17080 from the IP and will serve as a connection for the new relocated ion pump cantilever support (1253 mm in length towards the IP from the 17080 VAX support interface plate).

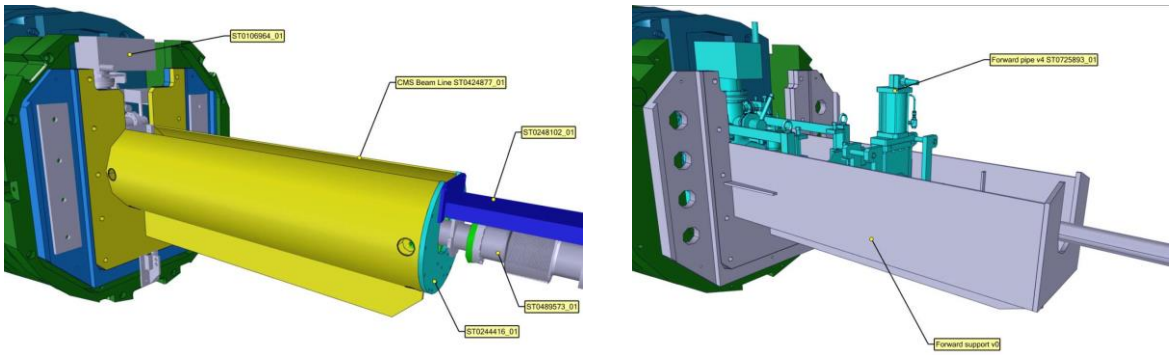

Figure 8-14: Left:3D view of the current CMS beam pipe support (yellow) in front of TAS. Right: the new VAX support structure (grey) will support the relocated VAX equipment (blue) and the ion pump cantilever support. The layouts correspond to the open detector configuration.

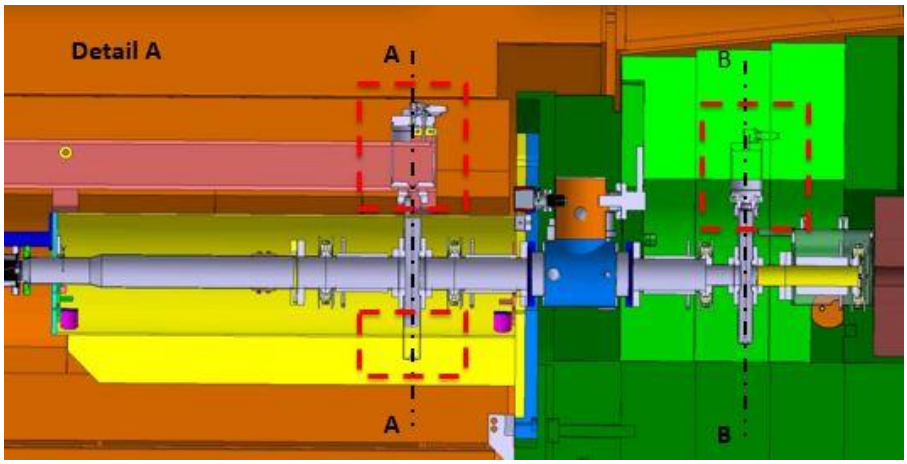

Figure 8-15: Cut of the CMS forward shielding showing the relocated VAX inside the yellow beam pipe support module. The end of the TAXS is shown at the right end. The required modifications in the Forward shielding (orange) and Fixed Iron nose (green) are highlighted by the dashed red boxes. Details of the beam pipe support and the cable tray required to be modified are shown on the left.

Figure 8-16: Photos showing the CMS forward shielding during access. The small rotating shielding is open, showing the yellow beam pipe support module. Details of the beam pipe support (yellow structure at the tip of the cylindrical tallow support) and the cable tray (Aluminium structure over the yellow support) to be modified are shown on the right picture.

8.2.2 The neutral particle passive absorbers - TAXN, TANB

A TAXN absorber will be installed on both sides of IP1 and IP5 located between the separation/recombination dipole pair D1 and D2 and contain the transition from the single common beam pipe to the two separate pipes for the incoming/outgoing beams, replacing the existing TAN absorbers. The TANB absorbers are new elements in the LHC tunnel and were already installed during LS2 on both sides of P8, located in front of the separation/recombination dipole D2. Differently from the TAN and TAXN, the TANB is situated away from the recombination Y chamber.

8.2.2.1 The TAXN for IP1 & IP5

The design of the new TAXN absorbers for P1 and P5 (Figure 8-17) is based on that of the presently installed TAN, with the following modifications and improvements:

- In the HL-LHC layout, the position of the TAXN is displaced by approximately 14 m towards the IP compared to the present situation, and the available longitudinal space is reduced by approx. 160 mm.
- The vacuum chamber has a fixed aperture, which combined with a specially designed TCLX collimator with movable jaws just downstream towards D2, provides the maximum protection efficiency at all beam optics scenarios for the HL-LHC. The chamber will be NEG-coated and the TAXN will provide enhanced baking capabilities (250°C with a 50°C/h heating rate).
- Active water cooling will be required to dissipate the expected approx. 1.8 kW of deposited heating power from the beam, expected during the HL-LHC operation including safety margins which allows for operation up to ultimate luminosities of $7.5 \times 10^{34}\,\mathrm{cm}^{-2}\,\mathrm{s}^{-1}$. The expected peak dose is 4.5 Gy for 3000 fb^{-1} (see Ref. [13]).
- Improvements in the mechanical design of the absorber will be incorporated to the design in order to allow optimized installation and maintenance activities.
- A dedicated slot for beam instrumentation for luminosity monitoring (BRAN) will be maintained, whereas the BRAN will adapt its transversal dimensions to the HL-LHC optic configuration (aperture and beam distance inside TAXN).

- A Zero Degree Calorimeter (ZDC) will be integrated in a dedicated slot inside the TAXN. ZDC will adapt its transversal dimensions to the HL-LHC optic configuration (aperture and beam distance inside TAXN).
- The TAXN will reuse most of the external shielding of the TAN and will act as support for nearby vacuum equipment. Support feet will allow the TAXN to be compatible with remote alignment.

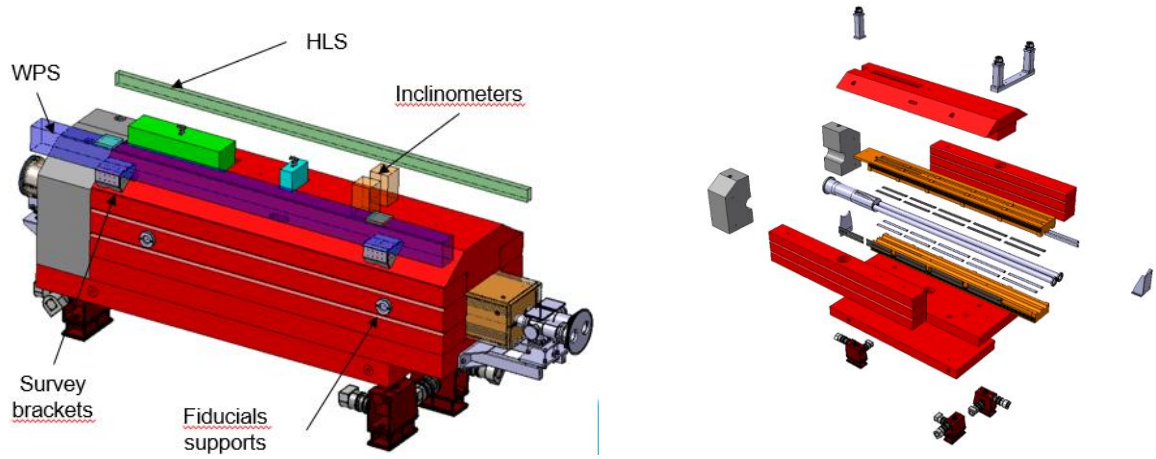

Figure 8-17: Left: 3-D drawing of the TAXN and its surrounding equipment. Right: Exploded view of the TAXN. Y chamber (grey) is surrounded by the Cu absorber (orange) embedded onto a heating jacket (not shown) for bake-out purposes. This subsystem is itself enclosed in the TAN steel shielding (red). Ancillaries as feet (remotely aligned), heating strips, cooling pipes, alignment supports, and marble blocks are also shown. The top lid is being redesigned to be compatible with the BRAN luminosity detector and Zero Degree Calorimeter (ZDC).

Since the first version of the TDR, several important changes affected the TAXN design: The external steel shielding from the TAN (shown in red in Figure 8-18) will be reused, allowing a waste reduction of 100 Tonnes (25 Tonnes per TAN), and the alignment feet will be remotely actuated as it will be the case for the surrounding elements.

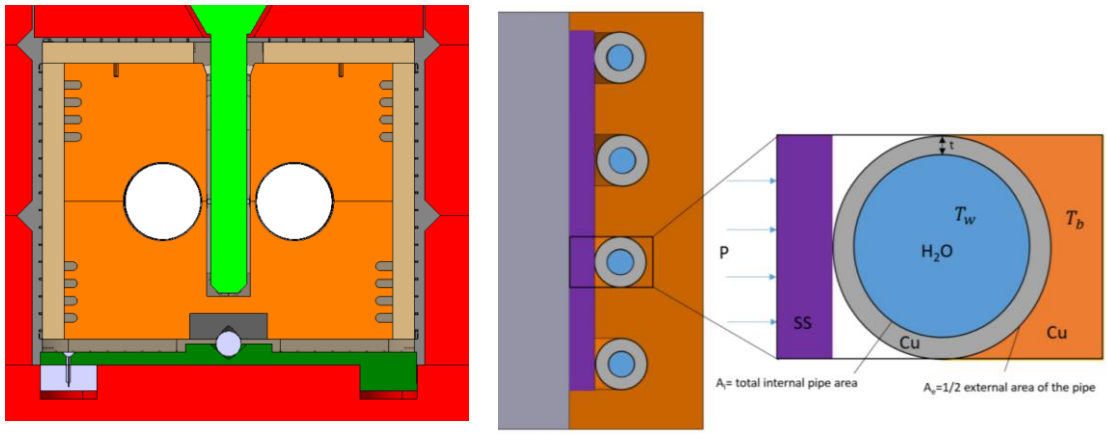

Figure 8-18: Left: Front view of the absorber inside the TAXN (non-IP side). Parallel vacuum chambers are embedded onto the Cu absorber (orange), containing the water cooling pipes at its lateral edges. In light brown, the heating jacket surrounds the subsystem. A removable insert (green) was designed to be compatible with the Zero Degree Calorimeter (ZDC). Right: Detail of the cooling principle, with stainless steel channels allowing water flow.

At the beginning of 2020, ATLAS and CMS requested the space for a ZDC detector. Some changes in the absorber were performed, and the external shielding will still be kept with the exception of the top cover,

(a new one will be manufactured to be compatible with the BRAN and ZDC). Changes in the surrounding tunnel equipment (mainly cable routing, rack location and handling with remotely actuated cranes) are currently under revision. Figure 8-19 shows the TAXN integration drawings with the present tunnel equipment.

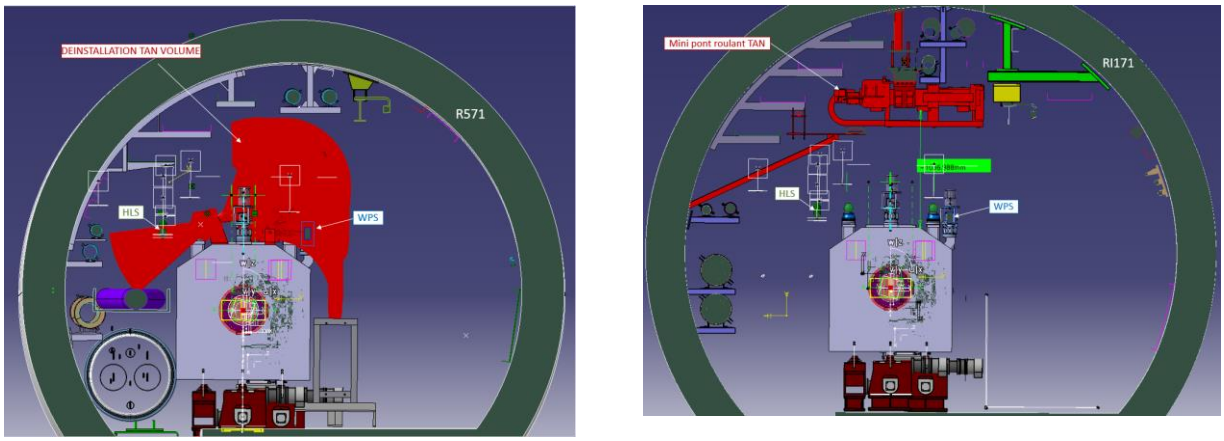

Figure 8-19: View of the TAXN inside the LHC tunnel and current auxiliary cranes used for handling the forward detectors inside TAXN. Left: CMS crane path will collide with surrounding equipment (mainly alignment wire positioning system). Right: ATLAS crane principle will be kept.

The TAXN design is described in detail in the Technical Specifications Documents for P1 and P5 [14] respectively, while its interfaces with surrounding equipment including ZDC and BRAN detectors are described in Ref. [20]. Conceptual description, technical requirements and design parameters of the recombination chamber (Y-chamber) which will be installed during LS3 inside the TAXN absorber are described in a separate document released by WP12 [18]. The key design and operation parameters are shown in Table 8-4 and Table 8-5.

Table 8-4: Key design parameters for the TAXN of P1 and P5 (under approval).

Parameter	**Unit**	**Value**
Aperture separation (from the transition point) entrance end	 mm mm	 151.1 161.1
TAXN length from flange to flange	mm	4300
Total absorber length (minimum)	mm	3310
Internal absorber length	mm	2400
Length of separated pipes	mm	3450
Maximum TAXN width	mm	1150
Maximum TAXN height (from two beam centreline)	mm	550
Shielding radius (from two beam centreline)	mm	530
Nominal beam height from floor	mm	1100/950
Beam tube facing IP (two beams in one tube) Inner diameter Thickness Flange size	 mm mm	 250 2 DN273
Beam tube away from IP (two beams in two tubes) Inner radius Thickness	 mm mm	 88 1.5
Vacuum chamber to alignment fiducial tolerance	mm	± 1
Supports range of motion	mm	± 10.0 [h & v]
Absorber cooling		Demin. Water

Table 8-5: TAXN operational parameters.

Characteristics	Units	Value
Absorbed collision power at 5×10^{34} cm^{-2} s^{-1} 7.5×10^{34} cm^{-2} s^{-1}	kW	 1.2 1.8
Maximum internal beam tube temperature	C	50

The TAXN absorber length has been optimised for radiation shielding and starting from the current TAN design, as studies performed by WP10 [21] have shown that the protection levels for the region are adequate. Indeed, the fact that the power deposition inside the TAXN for the worst case of p-p operation is highly peaked at the side of beam entry allowed a reduction in length for the absorber, as shown in Figure 8-20.

The aperture of the Y-chamber inside the TAXN has been set to 85 mm after several studies proving that the gain in protection to the D2 assembly in case of a smaller aperture would be minor (around 2 W reduction, which represents about 10% of the total input power). Manufacturing tolerances could lead to a small increase of this aperture (i.e 88 mm)

These studies also show that a shorter absorber can be equally efficient, gaining about 1m in longitudinal length (see Figure 8-21). Shorter options would be feasible using a denser material such as Tungsten, however, using Tungsten as the core absorber material may increase manufacturing and technical challenges (both thermal & mechanical) compared to copper. Therefore, so this possibility is kept as an option for the final technical design of the absorber if available space due to integration of surrounding equipment becomes critical.

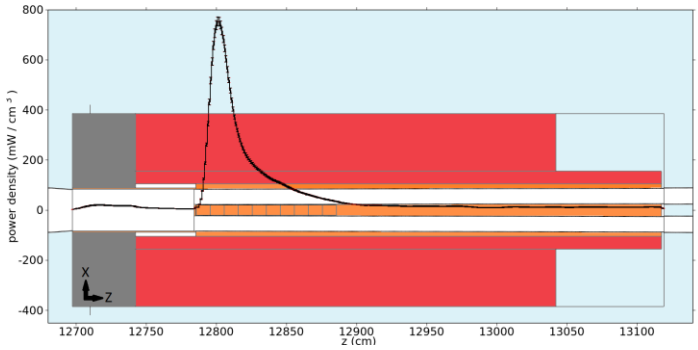

Figure 8-20: TAXN geometry showing the peak power deposition profile in case of a Cu absorber. Most of the power is deposited in the first part of the absorber.

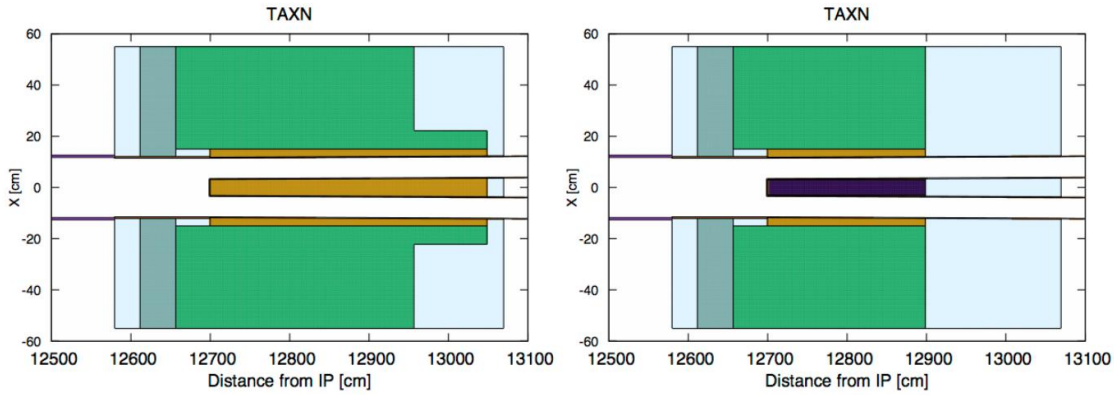

Figure 8-21: TAXN geometry using different material for the core absorber: Cu (left), Inermet180 (right). Maintaining the same efficiency (approx. 22-25 λ_{int}) a gain in length of 1.5m can be obtained.

8.2.2.2 The TANB for IP8

During the LHC design stage, it was estimated that absorbers would only become necessary for luminosities above $L = 10^{33}$ cm^{-2} s^{-1}. The original request by LHCb was for luminosities of up to $L = 4 \times 10^{32}$ cm^{-2} s^{-1}, thus IR8, where the LHCb experiment is located, could be designed without absorbers. More detailed studies on energy deposition in IR8 [16] have been made recently, to assess to which extent absorbers are required for the luminosity upgrade in IR8 with luminosity up to $L_{HL} = 2 \times 10^{33}$ cm^{-2} s^{-1}.

With $L_{HL} = 2\times10^{33}$ cm^{-2}s^{-1} and the inelastic cross section $\sigma_{pp} = 85$mb, there will be 1.7×10^{8} inelastic collisions per second at the interaction point of LHCb. The inelastic collision power is carried off by neutrals (mostly neutrons and photons) and charged particles (mostly pions and protons), that leave in both directions from the IP. Detailed Fluka simulations have estimated the energy deposition around IP8 at 2×10^{33} cm^{-2} s^{-1} luminosity without TAS and compared it to that at IP1 and IP5 at 1×10^{34} cm^{-2} s^{-1} luminosity with TAS. The studies have shown that the TAS is only really effective as protection for Q1. The energy deposition in the triplet depends on the crossing angle in IP8. Changing the beam screen orientation has a negligible effect on the energy deposition. As conclusion, the LHCb luminosity upgrade with 2×10^{33} cm^{-2} s^{-1} appears to be operable without a TAS installation, and that instead a protection (in the form of a minimal TAN scenario) is recommended to reduce the heat load on the D2 magnets to well below their quench level.

Several energy deposition studies with different configurations of absorbers and masks situated in specific locations upstream of D2, as shown in Figure 8-22 and Figure 8-23 were performed: a classical TAN located at the Y chamber, a cold mask placed inside the D2 and a “mini-TAN” situated at ~ 1.9 m from the D2-IP face. The studies showed that protection levels of the latest are the highest, and thus, a “mini-TAN” (TANB) with a minimum size of 340 × 200 mm with a 500 mm long Inermet180 absorber situated at ~ 1.9 m from the D2-IP face would efficiently protect the D2 from the interaction debris at the foreseen luminosity of 2×10^{33} cm^{-2} s^{-1} for LHCb (See Figure 8-23).

The integration of the TANB in the current LHC lay-out required the relocation of the BPM’s situated between D2 and the TCTPH and the change of some vacuum elements (bellows & beam pipe). The TANB was successfully installed as the first HL-LHC element in the LHC tunnel during LS2 [19].

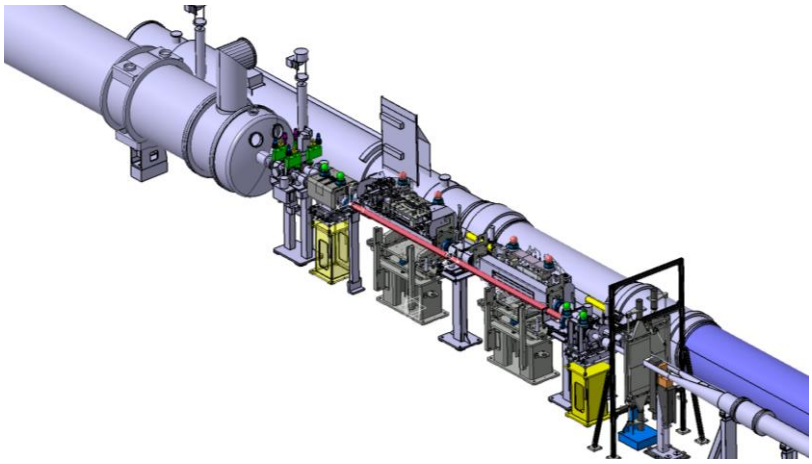

Figure 8-22: 3D layout of the D2 region after LS2. The new TANB (above located on top of yellow support on the left) is situated between D2 and the TCTPH collimator. BPM’s (located on top of above yellow support on the right) are relocated to the vicinity of the Y-chamber, shown on the right side of the picture.

Thermal analysis has been performed showing that the TANB will not need to be water-cooled (estimated heat deposition is below 20 W).

The total weight of the new equipment is around 800 kg and was transported as a single piece.

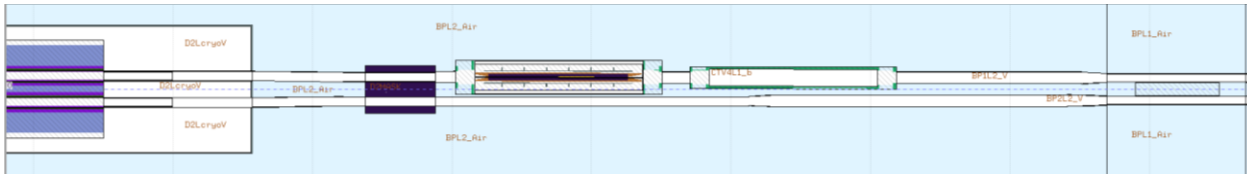

Figure 8-23: 2D layout (top view) of the D2 region as considered for the FLUKA analysis. The new TANB (-black) is situated between D2 (white) and the TCTPH collimator. Y-chamber is shown on the right side of the picture.

An innovative alignment plate with all the actuators situated in the transport side of the tunnel has been developed (see Figure 8-24 and Figure 8-25) and was installed to support the TANB, in order to reduce dose to personnel during future alignment operations of the TANB absorbers and the relocated BPM assemblies. Alignment will be manual, although automation could be developed and implemented at later stages.

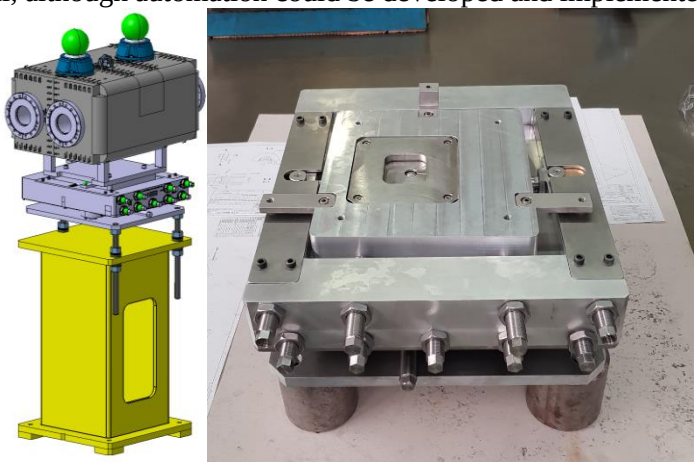

Figure 8-24: Left: 3D drawing of the TANB as installed in LSS8. The inner part is made of high-density tungsten, while the surrounding box provides baking capabilities. Right: TANB alignment plate, with all the actuators situated at the transport side to reduce dose to personnel.

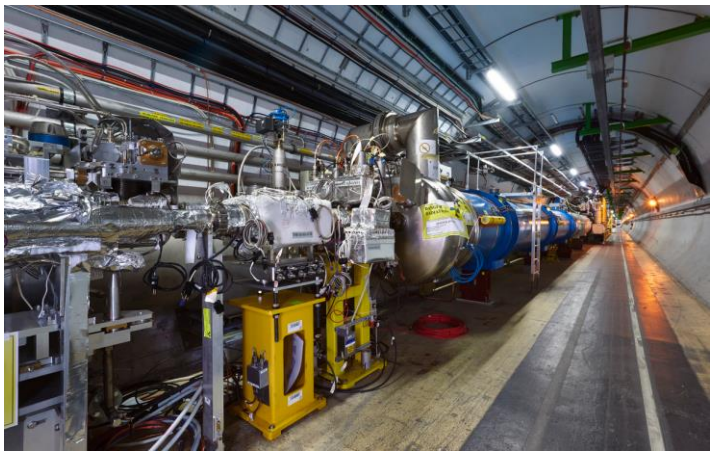

Figure 8-25: One of the 2 TANB installed in LSS8 (1 per side). The alignment plate can be seen (actuators protruding from the black label between the TANB and the standard yellow support).

8.3 Experimental beampipe modifications

The situation of the beam pipes of the experiments, all modified (or being modified) from the original LHC start, is reported in Table 8-6. No further modification is foreseen for the HL-LHC.

Table 8-6: Original and reduced inner beam pipe radii located at the IPs vicinity.

IP	Original r_{min} [mm]	Reduced r_{min} [mm]	Experiment	When
1	29	23.5	ATLAS	LS1
2	29	19 (central part)	ALICE	LS2
5	29	21.7	CMS	LS1 & LS2
8	5	3.5	LHCb, VELO	LS2

The activation levels in the experimental beam pipes, in particular for the high-luminosity experiments ATLAS and CMS, and the activation levels in vacuum chambers and the central tracking detectors need to be considered already during Run 3 but become significant in particular after a few years of operation in Run 4 at high-luminosity. The development of special handling tools and careful planning during maintenance activities and final dismantling will be needed to minimize the dose during interventions.

8.3.1 Beam pipe for ATLAS

For ATLAS, the central beryllium beam vacuum chamber of 7.382 m length and placed around the interaction point was exchanged with a new one with a reduced aperture of 47 mm to accommodate the new inner pixel detector layer (IBL) as shown in Figure 8-26 [7]. Preparations for a new, all-silicon inner tracker scheduled for installation during LS3 will continue in LS2 [17].

The conical vacuum chambers up to the forward TAS absorber were also exchanged to new aluminium ones in order to minimize the material activation and dose during interventions. The already installed permanent bake-out system is maintained. The last part of the conical chambers upstream of the TAS and the chamber support system would have to be exchanged during LS3 to adapt to the relocated VAX, with new apertures and layout as explained in Section 8.2.1.1.

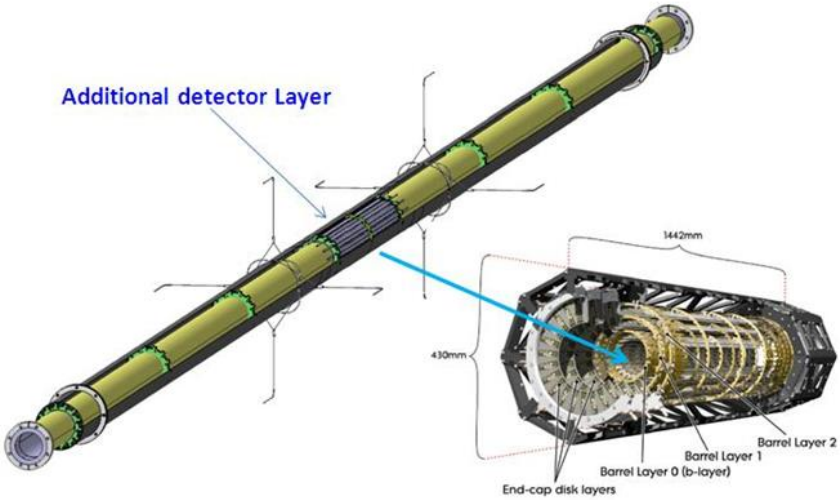

Figure 8-26: The updated ATLAS central vacuum chamber and the new inner detector.

8.3.2 Beam pipe for CMS

A new 6.24 m long central beryllium vacuum chamber will be installed in CMS during LS2 with the same aperture as the previous one installed during LS1 (i.e. 43.5 mm), but without the conical ends as depicted in Figure 8-27.This central pipe will be compatible with the existing Pixel detector and also with the new Inner Tracker detector currently under design for the Phase 2 upgrade [3]. A smaller bellow at 3.2 m from the IP has been designed to match the reduced diameter of the next Endcap beampipe section and the supports have been adapted to the new geometry.

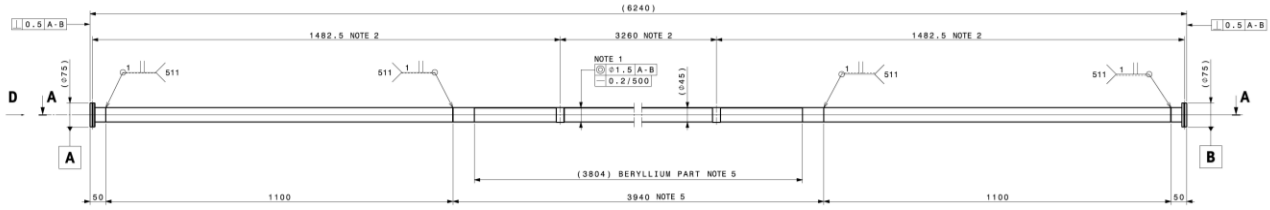

Figure 8-27: The updated CMS central vacuum chamber.

The conical vacuum chambers up to the forward TAS absorber will be exchanged to aluminium ones during LS2 to minimize activation and dose during interventions and a new beam-pipe support will be installed at 15.6 m from the IP, replacing the one currently located at 13.5 m from the IP. As for ATLAS, the last section (forward pipe) will be further modified during LS3 to adopt to the new layout and apertures for the HL-LHC operation. No permanent bake-out system is installed. The pumping station presently installed at the end of the experiment will be moved forward towards the TAS region as indicated in Figure 8-28 and Figure 8-13.

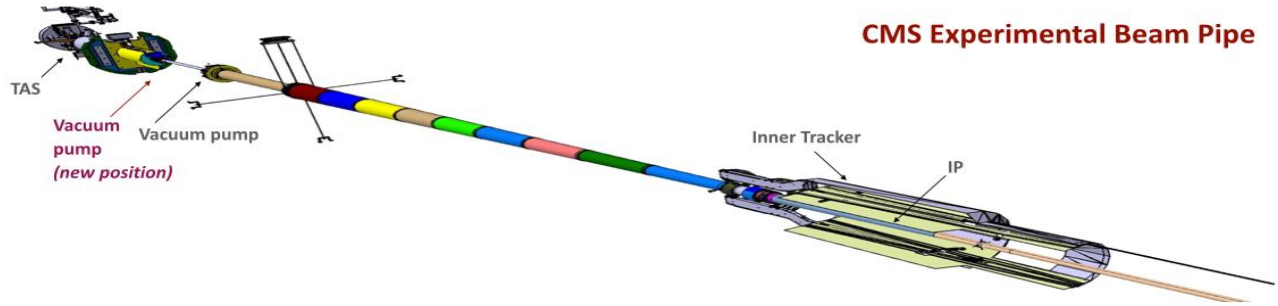

Figure 8-28: The full CMS vacuum chamber layout (single side) from the IP to the TAS. The present and future position of the proximity pumping station is indicated.

8.3.3 Beam pipes for ALICE and LHCb

New reduced-aperture central vacuum chambers will be installed during LS2 for ALICE and LHCb. The new ALICE beampipe geometry was officially approved in the LMC meeting in September 2014. While LHCb will follow a major upgrade in LS2 [4] to meet the new experimental challenges due to the increased luminosity, some changes described in Ref. [4] are still under approval.

After LS2 upgrade (both for ALICE and LHCb), no further changes to the experimental vacuum chamber geometry and layout is needed for the HL-LHC operation, although the vacuum chambers in the matching sections of IR1 and IR5 will still need modifications.

At LHCb the Vertex Locator (VELO), which allows for precise measurements of primary and displaced vertices of short living particles, is one of the detectors that will be upgraded in LS2. The LHCb updated VELO detector will operate in the same mode as presently: open to 30 mm aperture during injection, ramp, squeeze and adjust, but it will move closer to the beam axis, from the current 8.4 mm to 3.5 mm, once stable physics mode is established in the machine, coping with higher radiation and data rates

8.4 References

[1] ATLAS Phase-II Upgrade Scoping Document, CERN-LHCC-2015-020.

[2] Technical proposal for the upgrade of the CMS detector through 2020, CMS Collaboration, CERN-LHCC-2011-006.

[3] Technical Proposal for the Phase-II Upgrade of the CMS Detector, J. Butler *et. al*, CERN-LHCC-2015-010. LHCC-P-008.

[4] Framework TDR for the LHCb Upgrade: Technical Design Report, CERN-LHCC-2012-007.

[5] A. Santamaría *et al.*, Machine Protection from Fast Crab Cavity Failures in the High Luminosity LHC, Proc. IPAC 2016, DOI: 10.18429/JACoW-IPAC2016-TUPMW025.

[6] K. Sjobak *et al.*, Time Scale of Crab Cavity Failures Relevant for High Luminosity LHC, 7th IPAC, Busan, Korea, 8 - 13 May 2016, DOI: 10.18429/JACoW-IPAC2016-TUPMW025.

[7] M. Galilee, Reduction of ATLAS VI Diameter, EDMS 1230222.

[8] Atlas shielding project web page link.

[9] I. Bergstrom, H. Vincke, 39th HL-LHC WP8 meeting. INDICO: 539877.

[10] E. Hoyer *et al.*, Interface Specification LHC IP1/IP5, Front Quadrupole Absorbers (TAS), EDMS: 111998.

[11] Target Absorber for IP1 Insertion Region Secondary - Conceptual Specifications, EDMS: 1361111.

[12] Target Absorber for IP5 Insertion Region Secondary - Conceptual Specifications, EDMS: 1361109.

[13] IP1 Neutral Beam Absorber - Conceptual Specifications, EDMS: 1361107.

[14] IP5 Neutral Beam Absorber - Conceptual Specifications, EDMS: 1361109.

[15] C. Adorisio, Overview of activation of LHC elements to be disassembled 48th HL-LHC Integration Meeting, INDICO: 502039.

[16] F. Cerutti, 45th HL-LHC WP15 Integration meeting & 40th HL-LHC WP8 Meeting, INDICO: 545143.

[17] ATLAS Collaboration, Technical Design Report for the ATLAS Inner Tracker Strip Detector, CERN-LHCC-2017-005.

[18] P. Santos Diaz, IP1&5 recombination chamber conceptual design, EDMS: 1824656.

[19] F. Sanchez Galan et al., Installation of a TANB in A4R8 and A4L8 and Related layout Modifications, EDMS: 1970117.

[20] P. Santos Diaz, M. de la Aleja Cabana, M. Mendes, TAXN interfaces to BRAN and ZDC, EDMS: 2349145.

[21] M. Sabate-Gilarte, F. Cerutti, Energy deposition in optics v1.5 and possible layout optimizations, 9th HL-LHC Collaboration meeting, Fermilab, INDICO: 806637.

Chapter 9

Cryogenics for the HL-LHC

S. Claudet[1*], *G. Ferlin*[1], *E. Monneret*[1], *A. Perin*[1], *O. Pirotte*[1], *M. Sisti*[1] *and R. Van Weelderen*[1]

[1]CERN, Accelerator & Technology Sector, Switzerland
[*]Corresponding author

9 Cryogenics for the HL-LHC

9.1 Overview

The upgrade of the cryogenics for the HL-LHC will consist of the following:

- The design and installation of two new cryogenic plants at P1 and P5 for high luminosity insertions. This upgrade will be based on a new sectorization scheme aimed at separating the cooling of the magnets in these insertion regions from the arc magnets and considering the newt feedboxes and superconducting links located in underground infrastructures.
- The design and installation of a new cryogenic distribution lines (QXL) at P1 and P5 in the LHC tunnel and in a new underground service galleries.
- The upgrade of the existing cryogenic plant (QSRA and QURA) cooling the LHC sector 3-4 located at P4.
- The cryogenic design support for superconducting devices, such as magnets, crab cavities, superconducting links, and the hollow electron lenses.

Some other options such as new cryogenic circuits at P7 for the HTS links and displaced current feedboxes or a new cryoplant in P4 have been discarded.

9.2 LHC machine upgrades

9.2.1 Upgraded beam parameters and constraints

The main parameters impacting on the cryogenic system are given in Table 9-1. With respect to the nominal beam parameters, the beam bunch population will double and the luminosity in the detectors of the high luminosity insertions at P1 and P5 will be multiplied by a factor 5.

Table 9-1: LHC upgraded beam parameters for 25ns bunch spacing

Parameter	**Unit**	**Nominal LHC**	**Nominal HL-LHC**
Beam energy, E	TeV	7	7
Bunch population, N_b	protons/bunch	1.15×10^{11}	2.2×10^{11}
Number of bunches per beam, n_b	-	2808	2748
Luminosity, L	$cm^{-2}\ s^{-1}$	1×10^{34}	5×10^{34}
Bunch length	ns	1.04	1.04

These upgraded beam parameters will introduce new constraints to the cryogenic system.

- The collimation scheme must be upgraded. As some of the new collimators will work at room temperature but be installed on the cold region, cryogenic bypasses are required to guarantee the continuity of the cryogenic and electrical distribution.
- Hollow electron lenses will be installed for halo control.
- The increase of the level of radiation to the electronics could possibly require relocating power convertors and related current feedboxes. New superconducting links will be required to connect the displaced current feedboxes to the magnets.
- To improve the luminosity performance by addressing the geometric luminosity reduction factor and possibly allowing the levelling of the luminosity, cryo-modules of crab-cavities (CC) will be added at P1 and P5.
- Finally, the matching and final focusing of the beams will require completely new insertion cryo-assemblies at P1 and P5.

9.3 Temperature level and heat loads

Heat loads to the cryogenic system have various origins and uncertainties. The heat loads deposited in the accelerator are the result of physical mechanisms, which are classified as static, resistive, beam-induced, collision-induced, or radiofrequency-induced. The nomenclature is based on the LHC Design Report [1].

An important effort has been done during the last years to estimate the future HL-LHC heat loads [2]. The heat loads values in Table 9-2 are categorized by temperature level and heat load type. Table 9-3 reports the heat load values for group of users. It indicates the total contribution from static, dynamic (nominal/ultimate), total load (nominal/ultimate) and design values.

Table 9-2: “Nominal heat load” table for the LSS.R5 for the HL-LHC. Preliminary values.

Component	**Q1**	**Q2A**	**Q2B**	**Q3**	**CP**	**D1**	**Intercon.**	**DFX**	**DFM**	**D2**	**CC**
Length (m) (thermal shield)	10.140 (10.640)	9.785	9.785	10.140	6.01 (6)	7.370	6.930 (6 unit *)	2.535 (3.034)	4.000	13.025 (14.025)	2 module units †
Cold Mass											
Temperature (K)	1.9	1.9	1.9	1.9	1.9	1.9	1.9	4.5	4.5	1.9	2
Total Heat Load (W)	138.9	122.7	157.5	163.9	97.4	97.1	38.2	4.1	4.5	46.7	89.9
Avg. Heat Load (W/m)	13.7	12.5	16.1	16.2	16.2	13.2	5.5 W pu	1.6	1.1	3.6	45.0 W pu
Static (W/m)	1.7	1.7	1.7	1.7	1.8	2.2	0.3 W pu	1.6	1.1	0.6	18.9 W pu
Resistive (W/m)	0.7	0.4	0.4	0.7	3.9	0.1	0.0 W pu	0.0	0.0	0.0	0.0 W pu
Beam Induced (W/m)	0.3	0.2	0.2	0.3	0.0	0.1	2.2 W pu	0.0	0.0	0.2	0.0 W pu
Collision Induced ‡ (W/m)	11.0	10.3	13.8	13.5	10.5	10.7	3.0 W pu	0.0	0.0	2.8	0.0 W pu
RF Cavity (W/m)	-	-	-	-	-	-	-	-	-	-	26.1 W pu
Beam Screen											
Temperature (K)	60-80	60-80	60-80	60-80	60-80	60-80	60-80	-	-	4.5-20	4.5-20
Total Heat Load (W)	223.1	97.3	144.8	133.0	66.9	74.0	375.8	0.0	0.0	49.8	46.0
Avg. Heat Load (W/m)	22.0	9.9	14.8	13.1	11.1	10.0	54.2 W pu	0.0	0.0	3.8	23.0 W pu
Static (W/m)	0.1	0.1	0.1	0.1	0.2	0.2	0.0 W pu	0.0	0.0	0.0	9.3 W pu
Resistive (W/m)	0.0	0.0	0.0	0.0	0.0	0.0	0.0 W pu	0.0	0.0	0.0	13.6 W pu
Beam Induced (W/m)	5.1	2.9	4.4	5.1	0.6	2.3	42.4 W pu	0.0	0.0	3.7	0.0 W pu
Collision Induced ‡(W/m)	16.8	6.9	10.2	7.9	10.3	7.6	11.9 W pu	0.0	0.0	0.2	0.0 W pu

Component	Q1	Q2A	Q2B	Q3	CP	D1	Intercon.	DFX	DFM	D2	CC
Thermal Shield											
Temperature (K)	60-80	60-80	60-80	60-80	60-80	60-80	60-80	60-80	60-80	60-80	60-80
Total Heat Load (W)	66.6	53.2	53.2	54.3	133.8	103.2	22.2	24.9	28.0	133.1	609.0
Avg. Heat Load (W/m)	6.3	5.4	5.4	5.4	22.2	14.0	3.2 W pu	8.2	7.0	9.5	304.5 W pu
Static (W/m)	6.3	5.4	5.4	5.4	22.2	14.0	3.2 W pu	8.2	7.0	9.5	206.9 W pu
RF Cavity (W/m)	-	-	-	-	-	-	-	-	-	-	97.6 W pu

"-" = not applicable; W pu = Watts per unit.
* Length of each interconnection unit is 1 m, except between Q3-CP which is 1.8 m and CP-D1 which is 1.13 m.
† A module unit contains 2 crab cavities.

Table 9-3: Total heat loads divided by group of users, LSS.R5 and IP5. Preliminary values.

Group*	IT	D2	CC	LSS_R5		IP5	
Cold mass length (m)	62.7	17	-	79.7		159.4	
Thermal shield length (m)	63.7	18	-	81.7		163.4	
Number of units (-)	-	-	2	2 (CC)		4 (CC)	
Cold Mass							
Temperature (K)	1.9	1.9	2	1.9-2		1.9-2	
Total Design + flash (W)	1416.7	100.2	149.6	1667		3333	
Total Design (W)	1173.3	83.0	127.6	1384		2768	
Total Ultimate (W)	1103.4	68.7	89.9	1262		2524	
Total Nominal (W)	779.4	50.7	89.9	920		1840	
Dynamic - Ultimate (W)	1033.4	54.4	52.2	1140		2280	
Dynamic - Nominal (W)	709.4	36.4	52.2	798		1596	
Static (W)	70.0	14.3	37.7	122		244	
Beam Screen							
Temperature (K)	60-80	4.5-20	4.5-20	60-80	4.5-20	60-80	4.5-20
Total Design (W)	1685.0	74.7	97.0	1685	172	3367	343
Total Ultimate (W)	1424.1	50.9	46.0	1424	97	2846	194
Total Nominal (W)	1115.0	49.8	46.0	1115	96	2228	192
Dynamic - Ultimate (W)	1415.8	50.9	27.3	1416	78	2830	156
Dynamic - Nominal (W)	1106.7	49.8	27.3	1107	77	2211	154
Static (W)	8.4	0.0	18.7	8	19	17	37
Thermal Shield							
Temperature (K)	60-80	60-80	60-80	60-80		60-80	
Total Design (W)	744.9	229.6	913.5	1967		3935	
Total Ultimate (W)	496.6	153.1	609.0	1312		2623	
Total Nominal (W)	496.6	153.1	609.0	1312		2623	
Dynamic - Ultimate (W)	0.0	0.0	195.2	195		390	
Dynamic - Nominal (W)	0.0	0.0	195.2	195		390	
Static (W)	496.6	153.1	413.8	1116		2233	

(*) *italic* values are indicating Design Heat Load values

The design heat load values consider margins and technological requirements. They can be calculated by using the following equations:

$$\dot{Q}_{installed} = MAX\left[F_{ov} \cdot \left(F_{un} \cdot \dot{Q}_{static} + \dot{Q}_{dynamic\ nominal}\right)\ ;\ F_{un} \cdot \dot{Q}_{static} + \dot{Q}_{dynamic\ ultimate}\right] \quad (9\text{-}1)$$

$$\dot{Q}_{installed} = MAX\left[F_{ov} \cdot \dot{Q}_{nominal} \; ; \; \dot{Q}_{ultimate}\right])$$

The first equation is valid for the cold mass (1.9–2 K) and beam screens (4.5–20 K and 60–80 K). The second equation is valid for the thermal shield (60–80 K) and current leads (20–293 K). A detailed study is available on [2]. Figure 9-1 gives a global view of the heat load at 1.9 K.

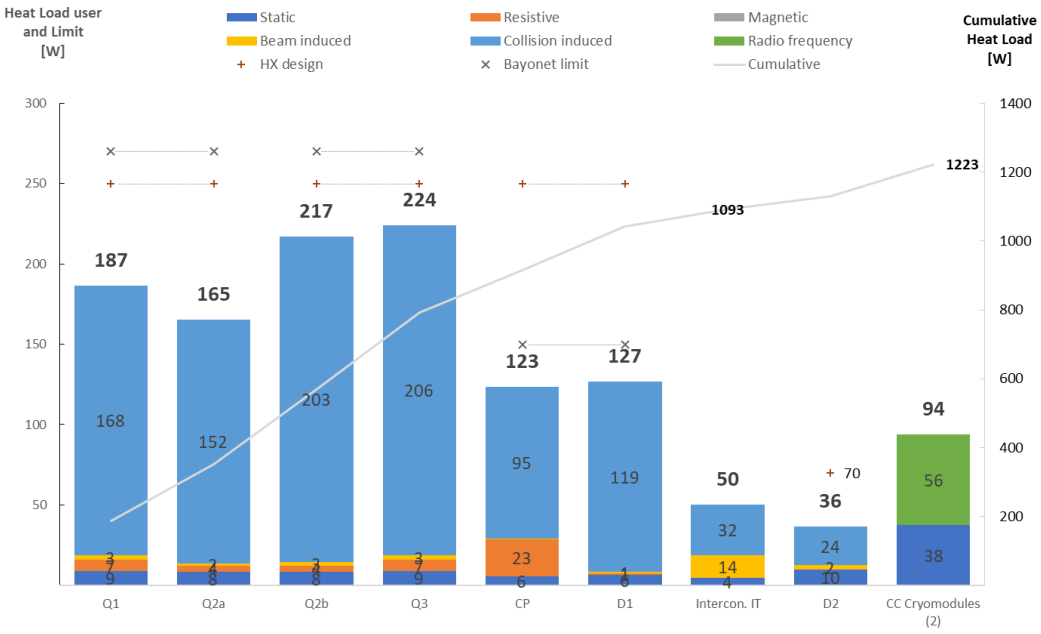

Figure 9-1:Total heat load for users at 1.9 K. Preliminary values.

9.4 Impact on existing sector cryogenic plants

With new cryogenic plants dedicated to the cooling of cryogenic equipment in P1 and P5, the cooling duty of the existing sector cryogenic plants will be reduced and more equally distributed. Figure 9-2 and Figure 9-3 shows the required cooling capacities for the different temperature levels and compares them to the nominal cooling requirements and to the installed capacities. The low-load sectors equipped with upgraded ex-LEP cryogenic plants have lower installed capacity than the four cryogenic plants specially ordered for the LHC high-load sectors. For the HL-LHC, sufficient capacity margin still exists providing that the beam scrubbing of dipole beam-screens is efficient (dipole off).

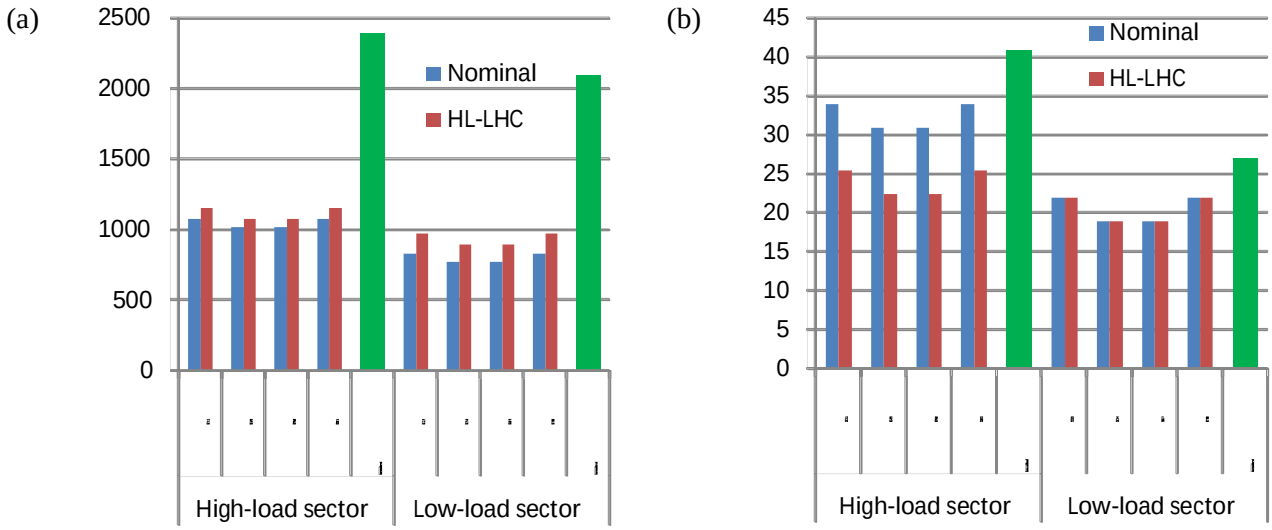

Figure 9-2: Cooling capacity requirement of sector cryogenic plants. (a) Cold mass; (b) current leads

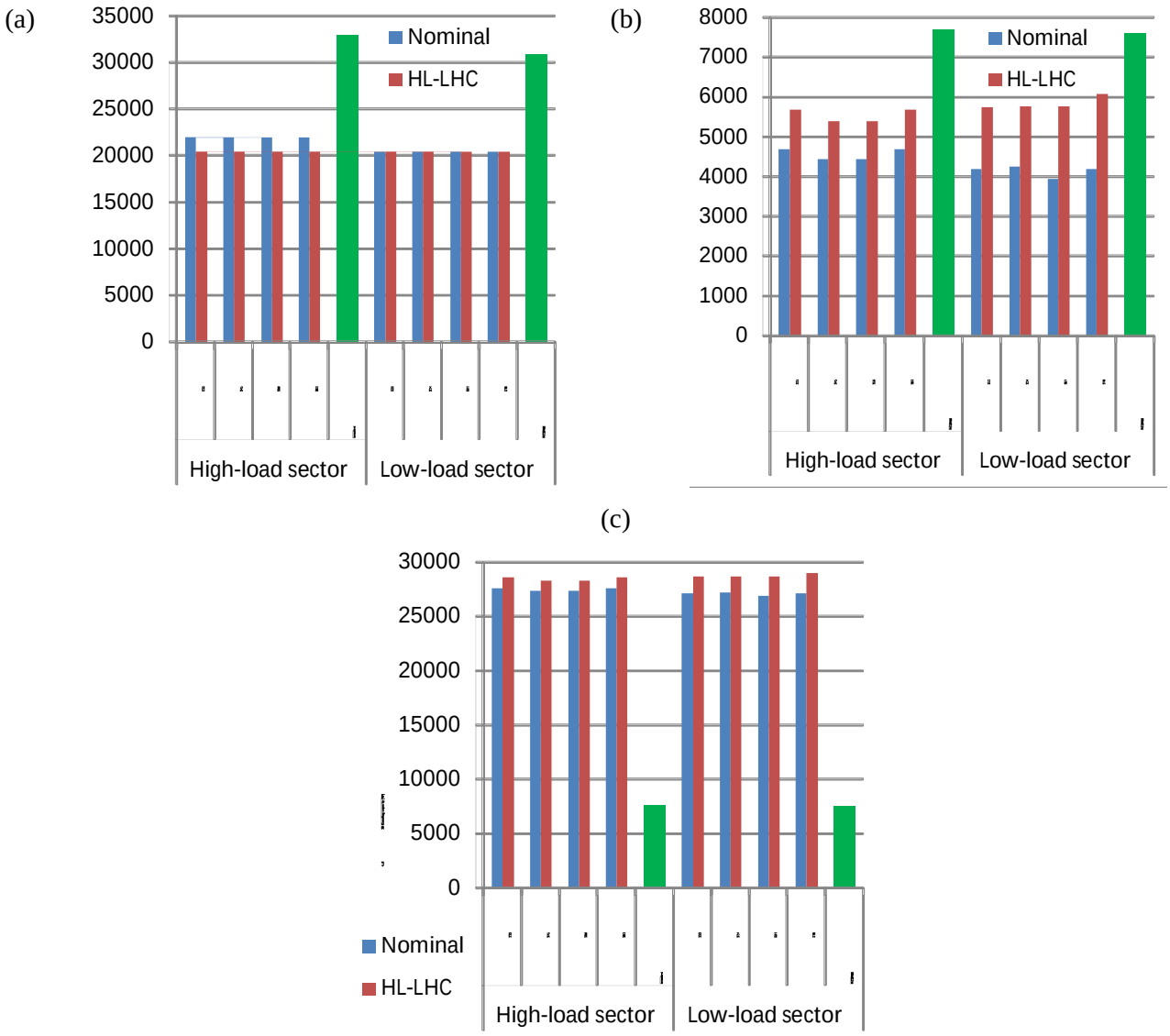

Figure 9-3: Cooling capacity requirement of sector cryogenic plants. (a) thermal shields; (b) beam screen (dipole off); (c) beam screen (dipole on).

9.5 Point 4 cryogenics

The initial baseline considered the installation of a new cryoplant in P4. Later on, was decided to evaluate an alternative scenario for the refrigeration part. The alternative scenario consisted of an upgrade of one of the existing refrigerator of P4 (equivalent of 2 kW@4.5 K with respect to the existing plant capacity of 16.5 kW@4.5 K) [6] to fulfil the required cooling capacity of existing SRF modules with sufficient margin, while keeping or adapting the distribution system depending on the alternative. As a complement, a new mobile refrigerator with a cooling capacity allowing RF tests of a single cryo-module during long shut-downs was then considered, as all other cryogenic sub-systems would be stopped for maintenance and major overhauling, but was finally abandoned.

The upgrade of the ex-LEP refrigerator included mainly:

- Replacement of 7 expansion turbines.
- Modification of one existing turbine.
- Modification of the required piping inside the boxes or for instrumentation and service panels.

The upgrade was successfully completed during the Long Shutdown 2.

The modification of the cryogenic distribution line to allow the installation of the hollow electron lenses is under study. The schematic layout can be seen in Figure 9-4 [5].

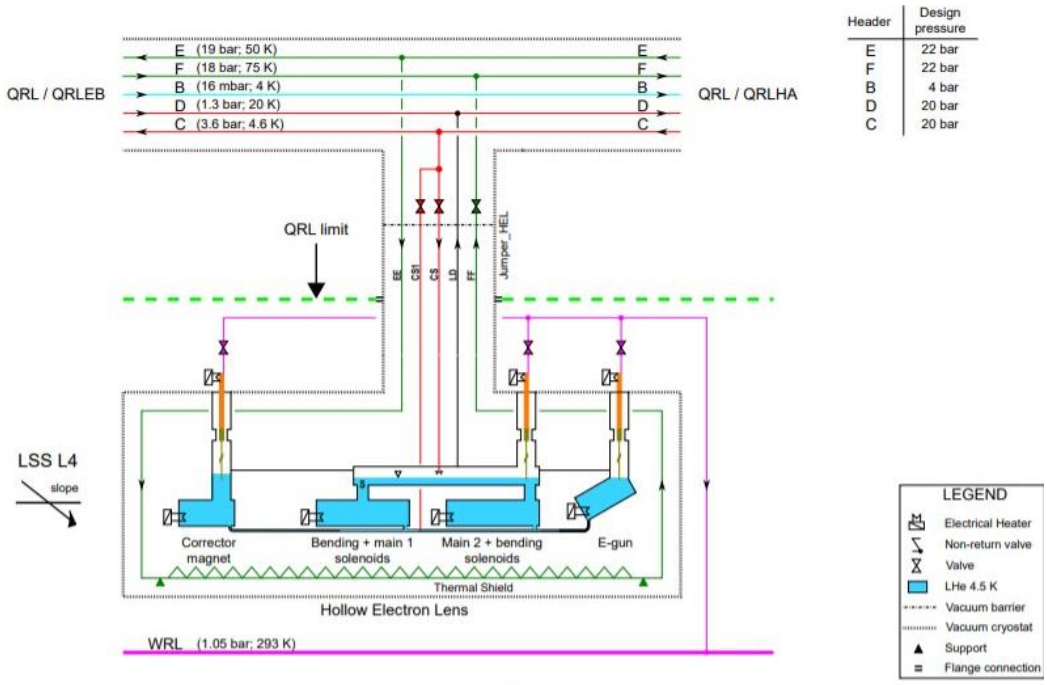

Figure 9-4: Layout of the possible cryogenic layout at P4 (Hollow e-lens)

9.6 New cryogenics for high luminosity insertions at Point 1 and Point 5

The new HL-LHC cryogenic system will require new cryo-plants of about 15 kW at 4.5 K including 3 kW at 1.8 K. They will encompass new refrigeration plants and distribution lines. Figure 9-5 illustrates the architecture of the system A full analysis of both systems have been done in order to optimize the cost and the sourcing strategy.

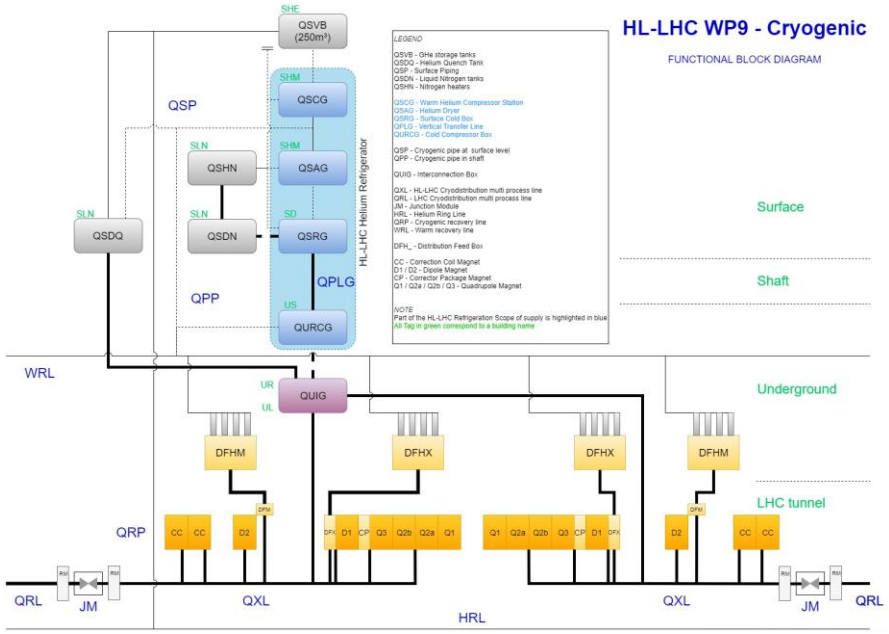

Figure 9-5: HL-LHC Cryogenic architecture at P1 and P5

The main components of the new helium refrigeration system are [7]:

- The compressor station (QSCG).
- A dryer system (QSAG).
- The 4.5 K cold box (QSRG) including 80 K and 20 K absorbers and a liquid helium phase separator.
- A cryogenic vertical transfer line (QPLG) in a shaft connecting the 4.5 K surface cold box to the 1.8 K cold box located in an underground cavern.
- A 1.8 K cold box (QURCG) including the cold compressors and a phase separator.

Each HL-LHC helium refrigerator shall:

- Provide cooling to different magnets with an equivalent capacity of about 3 kW at 1.8 K.
- Supply an average helium mass flow rate of approximatively 10 g/s at 4.5 K for the beam screens and recover it at around 20 K.
- Provide cooling to the Distribution Feed Boxes (DFH) with a liquefaction flow rate of 25 g/s.
- Supply an average helium mass flow rate of approximatively 100 g/s at 60 K for various thermal shields and recover it at around 80 K, for a corresponding cooling capacity of 10 kW.
- Allow control of supply temperature between 300 K and 10 K during cool down of magnets.
- Accommodate heat load variation from 20 to 100 % in less than one hour twice a day.

Regarding the new distribution system it shall [8]:

- Distribute helium from the refrigerator to the different machine components in the temperature range from 4 K to 350 K with a maximum allowable pressure of 25 bar absolute.
- Control the helium flow to and from users as required for multiple operating modes.
- Have a maximum heat load for lines below 20 K ($Ø_{eq}$ ~320 mm) lower than 0.5 W/m.
- Have a vacuum vessel diameter ranging from ~650 mm to ~770 mm.
- House five inner headers ranging from ISO DN40 to DN300 and an actively cooled thermal shield.
- Integrate approximately 200 cryogenic control valves and interface to users via 32 feeding points.

Figure 9-7 illustrates the cryogenic distribution architecture while the following details provide details on the layout for the different components.

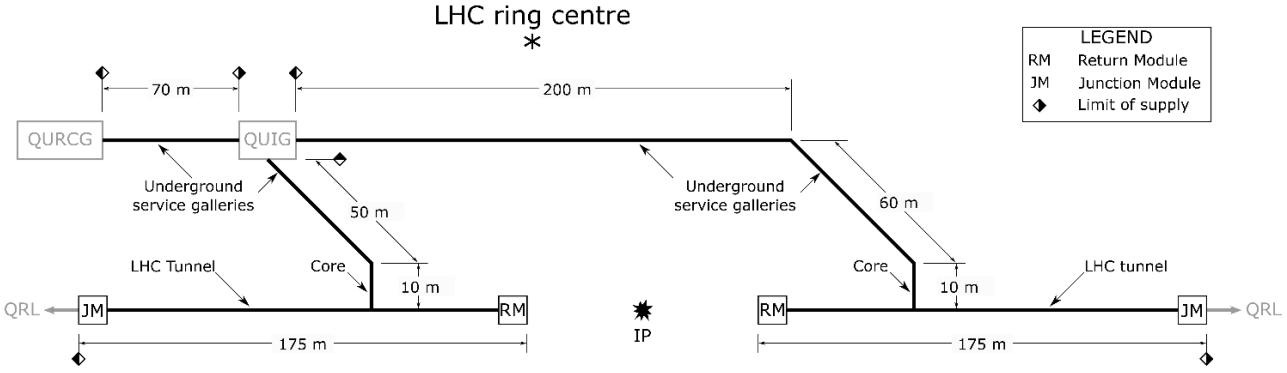

Figure 9-6: Schematic of the cryogenic distribution architecture [8]

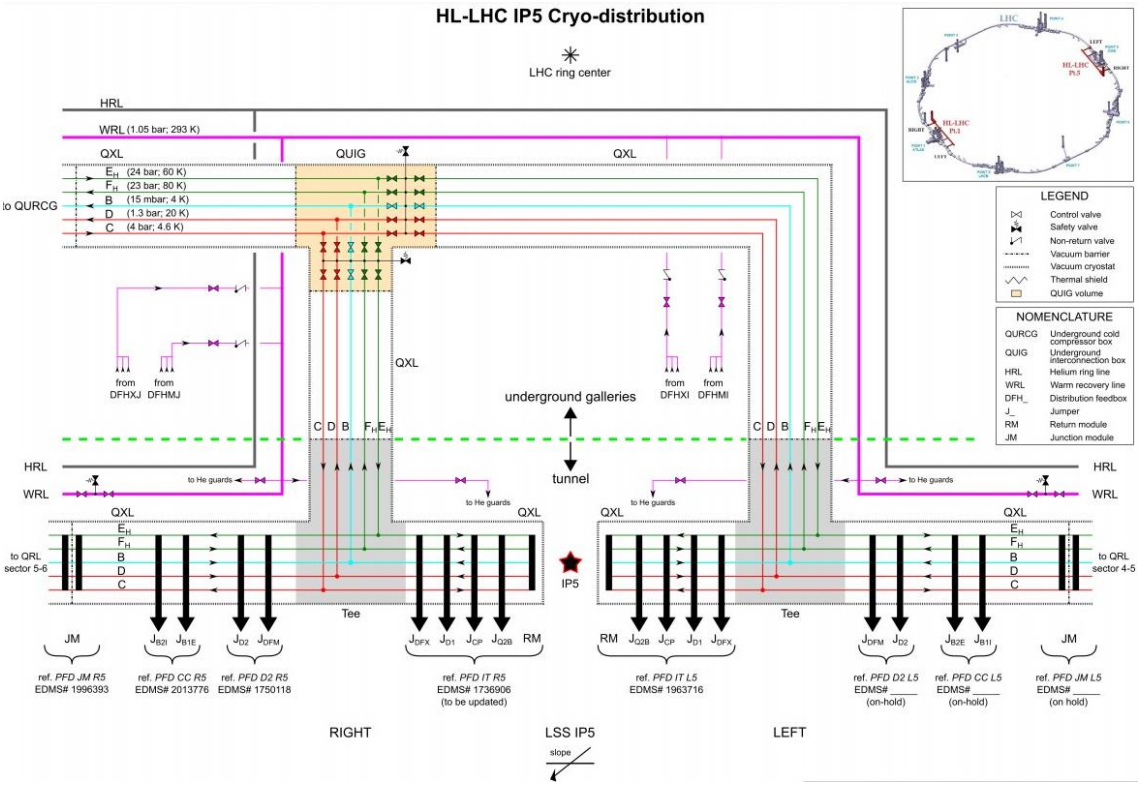

Figure 9-7: Layout of the IP5 Cryodistribution [9].

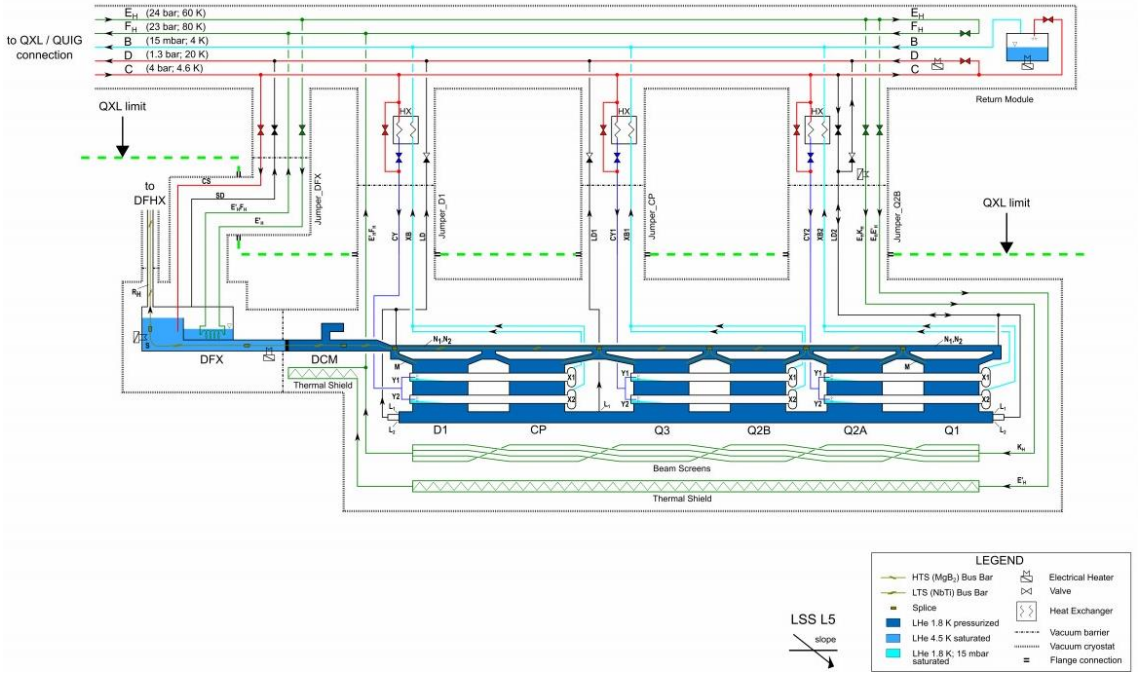

Figure 9-8: Detail of the distribution for the IT magnets, CP and D1. [10]

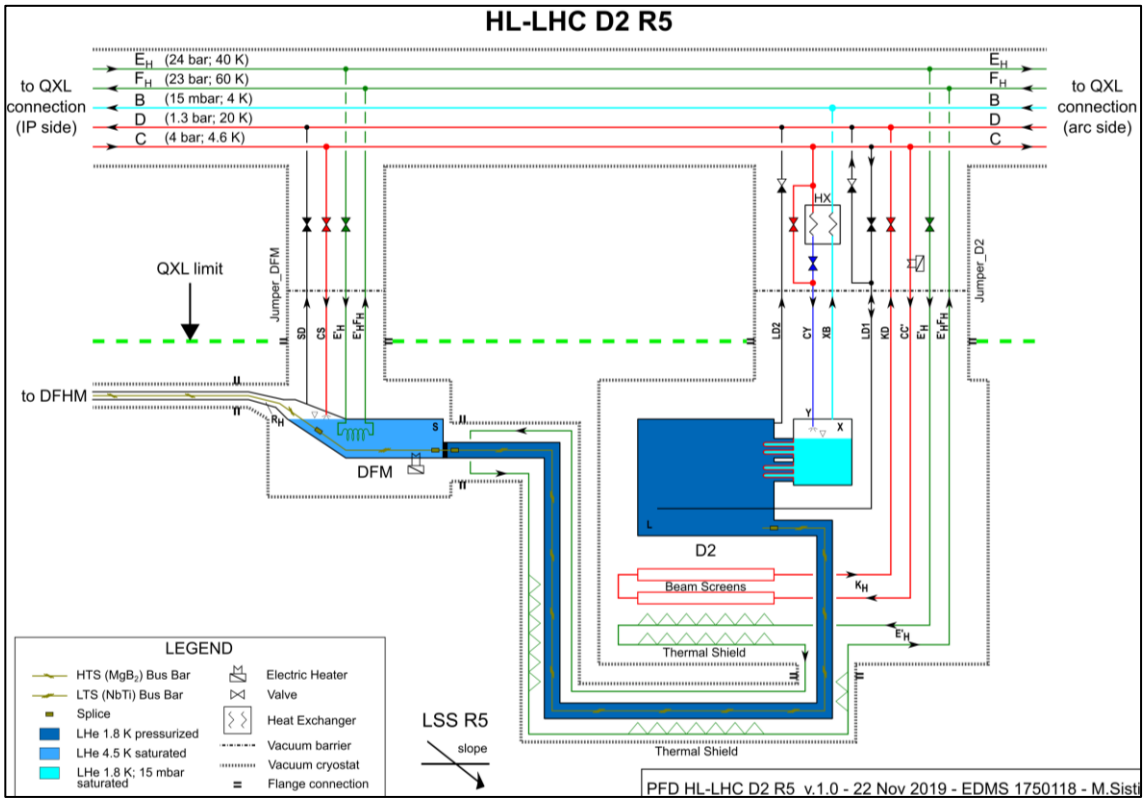

Figure 9-9: Detail of the distribution for the D2 magnet. [11]

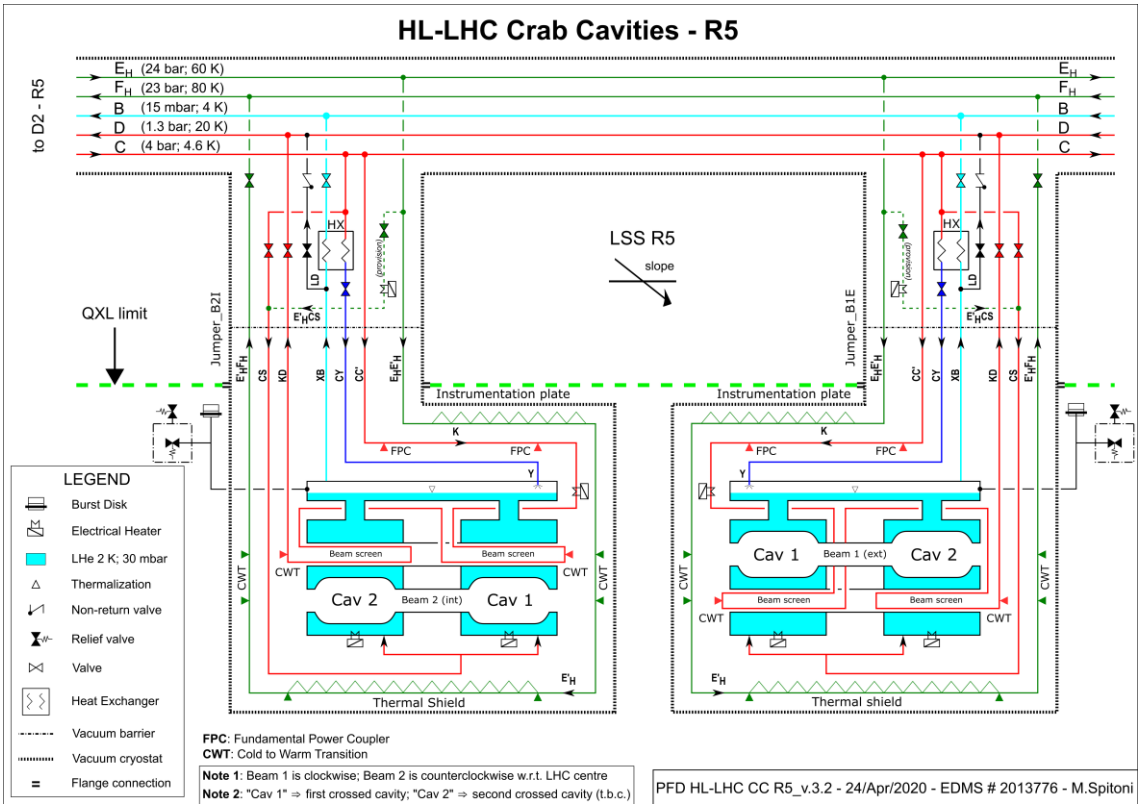

Figure 9-10: Detail of the distribution for the Crab Cavities [12].

Process flow diagrams for the Distribution Feed boxes are available on Refs. [13] [14].

9.7 References

[1] LHC Design Report Volume I - The LHC Main Ring. Chapter 11. CERN, 2004, EDMS: 445856.
[2] Updated heat load tables for the LSS.R5 for the HL-LHC, EDMS: 1610730.
[3] Process flow diagram of HL-LHC IT L5, EDMS: 1963716.
[4] Cryo distribution IP5, EDMS: 2025508.
[5] Process Flow Diagram of HL-LHC Hollow e-Lens in P4, EDMS: 2314734.
[6] IT-4472 Upgrade of the ex-LEP Refrigerator for HL-LHC - Point 4, EDMS: 2001440.
[7] MS-4631 HL-LHC He Refrigerators, EDMS 2382454.
[8] MS-4630 Supply of the Cryogenic Distribution Lines for the HL-LHC at P1 and P5, EDMS: 2381328.
[9] Process flow diagram of HL-LHC IP5, EDMS: 2025508.
[10] Process flow diagram of HL-LHC IT L5, EDMS: 1963716.
[11] Process flow diagram of HL-LHC D2 L5, EDMS: 1750118.
[12] Process flow diagram of HL-LHC Crab Cavities R5, EDMS: 2013776.
[13] Process flow diagram of HL-LHC DFX L5, EDMS: 2322140.
[14] Process flow diagram of HL-LHC DFM DSHM/DFHM R5, EDMS: 2373843.

Chapter 10

Energy deposition and radiation to electronics

F. Cerutti[1*], *R. Garcia Alia*[1*], *G. Lerner*[1], *M. Sabaté Gilarte*[1, 2] *and A. Tsinganis*[1†]

[1]CERN, Accelerator & Technology Sector, Switzerland
[2]University of Seville, Spain
[†] ELI Beamlines, Czech Republic
[*]Corresponding authors

10 Energy deposition and radiation to electronics

10.1 Energy deposition

10.1.1 Characterization of the radiation source

Proton–proton inelastic collisions taking place inside the four LHC detectors generate a large number of secondary particles with an average multiplicity of approximately 120 per single proton–proton interaction with 7 TeV beams, but with very substantial fluctuations over different events. Moving away from the interaction point (IP), this multiform population evolves, even before touching the surrounding material, because of the decay of unstable particles (in particular neutral pions decaying into photon pairs). Figure 10-1 illustrates the composition of the debris at 5 mm from the point of a 14 TeV centre of mass collision, featuring a ∼30% increase in the number of particles, due to the aforementioned decays, and a clear prevalence of photons (almost 50%) and charged pions (∼35%).

Most of these particles are intercepted by the detector and its forward region shielding, releasing their energy within the experimental cavern. However, the most energetic particles, emitted at small angles with respect to the beam direction, travel farther inside the vacuum chamber and reach the accelerator elements, causing a significant impact on the magnets along the insertion regions (IRs), in particular the final focusing quadrupoles, their associated corrector units, and the separation dipoles. Figure 10-1 also shows the breakdown of the debris components going through the aperture of the Target Absorber Secondaries (TAS), a protection element installed at 20 m from the IP on each side of the high luminosity detectors (ATLAS in IR1 and CMS in IR5) and consisting of a 1.8 m long copper core, featuring in the HL era a circular aperture of 60 mm diameter.

Despite the fact that the number of particles per collision leaving the TAS aperture is more than one order of magnitude lower than the total number of debris particles, they carry about 80% of the total energy, implying that 40% of the released energy at the IP exits on each side of the experiments. At the nominal HL-LHC luminosity (5×10^{34} cm^{-2} s^{-1}), this represents about 3800 W per side that is inevitably impacting upon the LHC elements and consequently dissipated in the machine and in the nearby equipment (e.g. electronics, racks, etc.) and in the tunnel walls.

It is fundamental to study how these particles are lost in order to implement the necessary protections for shielding sensitive parts of the LHC machine. For this purpose, Monte Carlo simulations of particle interactions with matter play an essential role, relying on a detailed implementation of physics models and an accurate 3D description of the region of interest [1][2].

In addition to the luminosity debris, which dominates energy deposition in the vicinity of the collision points, regular and accidental beam losses represent other relevant sources of radiation. In particular, beam halo particles caught in the collimators (see Chapter 5) initiate hadronic and electromagnetic showers, mainly in the betatron and momentum cleaning IRs, but also from the tertiary collimators around the experiments. The same happens with injection and dumping protection devices (see Chapter 14). Moreover, secondary particle showers are also originated by beam interactions with the residual gas inside the vacuum chamber along the length of the accelerator, as well as with dust fragments falling into the beam path.

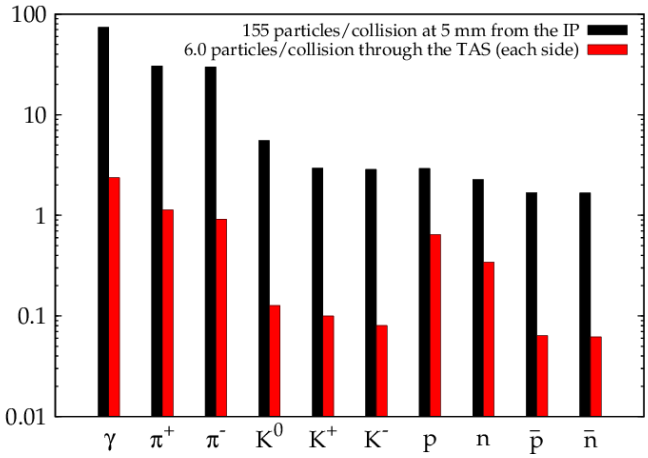

Figure 10-1: Breakdown of the debris particles per single proton–proton inelastic interaction at 5 mm from the interaction point (black) and at the exit of each 60 mm TAS aperture (red). Calculations have been carried out with FLUKA [3-8], as for all simulation results presented in this Chapter.

10.1.2 Triplet and separation dipole protection

As previously mentioned, the TAS absorber represents the interface between the detector and the accelerator on each side of the ATLAS and CMS caverns. On the other hand, its protection role is not needed for luminosities up to 0.2×10^{34} cm^{-2} s^{-1}, as in the LHCb insertion. In fact, the TAS effectiveness is limited to the first quadrupole, since its geometrical shadow gets soon spoiled by the effect of the magnetic field that bends a significant fraction of charged debris particles coming through its aperture, in particular high energy pions, against the quite larger quadrupole aperture. For this reason, the backbone element for the protection of the string of magnets up to the separation dipole (D1) is rather the beam screen equipped with dedicated tungsten alloy absorbers along its length. These absorbers are made of Inermet 180, which has a density of 18 g cm^{-3}, and reach their maximum thickness (of 16 mm in the first quadrupole Q1 and 6 mm elsewhere) at the magnet mid-planes, where the energy deposition is concentrated, as shown in 10-2.

In the latter, one can see that the beam screen structure is not in thermal contact with the magnet cold mass, allowing to evacuate its significant fraction of absorbed power at a different temperature. In fact, for an instantaneous luminosity of 5×10^{34} cm^{-2} s^{-1}, the total power collected by the 60 m long string of magnets amounts in the worst case (namely for vertical crossing) to more than 1200 W and is almost equally shared between the beam screen structure and the cold masses. For horizontal crossing, the total load is 6% less.

The combination between the focusing-defocusing field configuration and the crossing plane yields a characteristic longitudinal profile for the peak dose (and power density) in the superconducting coils, as reported in Figure 10-3 for the HL-LHCv1.3 optics with a 255 μrad half-angle and round beams at the IP.

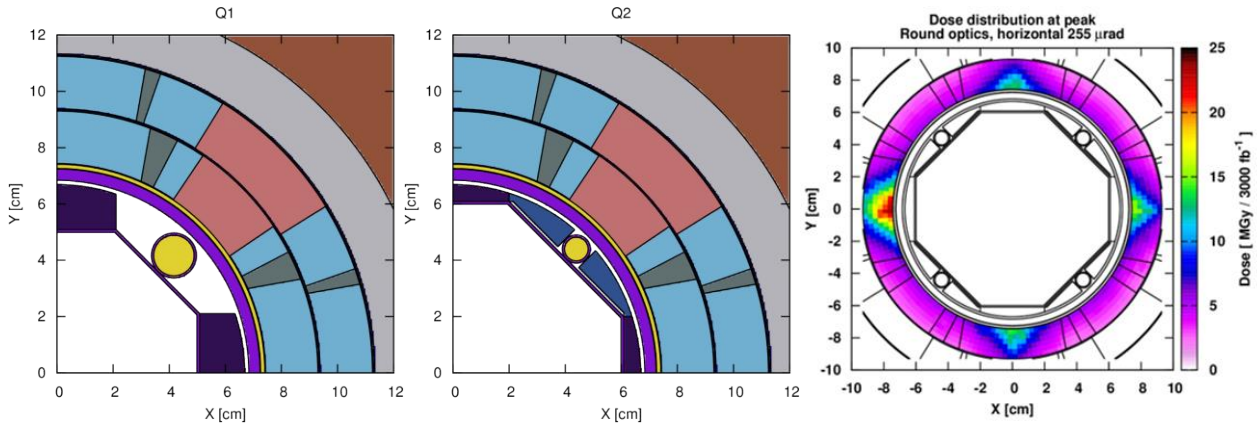

Figure 10-2: Cross-section of (a) the two modules of the first triplet quadrupole (Q1) and (b) all the other quadrupoles (Q2-Q3). The extension of the Inermet absorbers (dark blue) around the Helium (yellow) channel at 45º, implemented from Q2 onwards in alternation with pumping slot gaps, can be noted. The stainless steel cold bore is in violet, the Nb_3Sn coils are in light blue, the copper wedges are in dark grey, the titanium alloy poles are in red, the aluminium collar is in light grey, and the iron yoke is in brown. (c) Dose distribution in the coils at the IP end of the second Q2 module (Q2B) for horizontal crossing, representing the most exposed location.

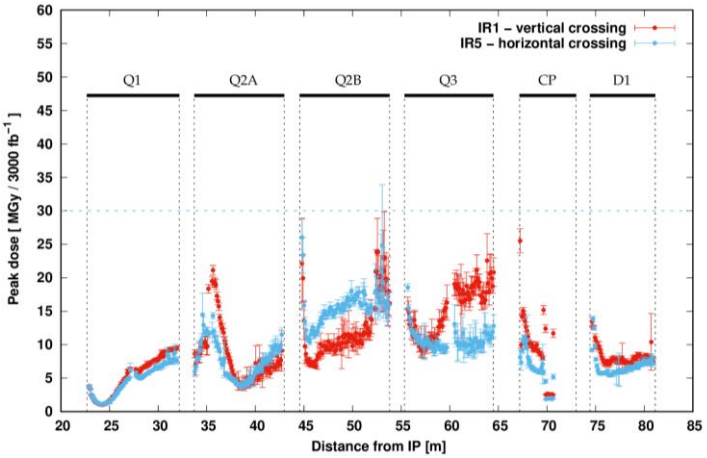

Figure 10-3: Peak dose profile in the superconducting coils of the single bore magnet string after 3000 fb^{-1}, for vertical (red) and horizontal (blue) crossing. The values are obtained by radially averaging over the innermost layer (≤ 3mm). Error bars indicate the statistical uncertainty. The discontinuity of the red points at the extremities of the orbit corrector dipoles in the CP and Q2A assembly is due to the fact that the inner coil layer, oriented to give a horizontal kick, intersects there the vertical plane. An analogous topological effect applies to the extremities of the superferric skew quadrupole at 70 m from the IP.

After the HL-LHC upgrade, the weakest point becomes the Q2B IP extremity for horizontal crossing, due to the effect of the preceding interconnect, where the amount of absorbing material is limited. A careful optimization of the interconnect design (see Figure 10-4), allowing for the extension of the Inermet absorbers as well as their installation in the embedded Beam Position Monitor (BPM), brought the maximum dose expectation down to 26 MGy for the nominal target of 3000 fb^{-1}, which is a level deemed to be sustainable by the coil insulator. However, the radiation resistance of the latter is challenged by the scaling to nearly 35 MGy for the ultimate goal of 4000 fb^{-1}, as indicated in Table 10-1.The target tolerances in the interconnect and BPM alignment do not affect the gain provided by this optimization. On the other hand, the maximum power density (radially averaged over the cable width) is predicted not to reach 3 mW/cm^3 at 5×10^{34} cm^{-2} s^{-1}, therefore

remaining below the Nb_3Sn (NbTi) quench limit of more than 60 mW/cm^3 (20-30 mW/cm^3) [9] with a considerable margin.

The coils of the three nested orbit correctors, located on different ends of the Q2A and Q2B cryostats and in the Corrector Package, are exposed to a lower dose if their inner layer is oriented in order to produce a vertical field, i.e. a horizontal kick, as assumed in Figure 10-3. It has to be noted that in such a configuration the inner layer crosses anyway the vertical plane at the magnet extremities, while remaining outside of it for most of the dipole length. In the case of the third corrector, this implies that for vertical crossing a dose of 25 MGy is locally reached on the IP side.

Table 10-1: Maximum dose (MGy) in the coils of the elements of the Q1–D1 string for the nominal and ultimate integrated luminosity targets.

Magnet	**3 ab^{-1}**	**4 ab^{-1}**	**Magnet**	**3 ab^{-1}**	**4 ab^{-1}**
Q1A	6.5	8.5	Q1B	9.5	13
Orbit Corrector	18.5	24.5	Q2A	21	28
Q2B	26	34.5	Orbit Corrector	< 25	< 33
Q3A	18.5	24.5	Q3B	22	29
Orbit Corrector	25.5	34	Superferric Correctors	12.5	16.5
D1	14	18.5			

Out of the nine superferric magnets of the Corrector Package, detailed dose distributions were calculated only for the skew quadrupole, whose maximum value of 12–13 MGy, found again at the magnet extremity where the coils traverse the vertical and horizontal planes, is not expected to be approached in the following short correctors.

Some margin to reduce the maximum accumulated dose, and so to increase the triplet lifetime, can be obtained if operating at minimal crossing angle with the envisaged levelling schemes, which yield a 10% improvement. Moreover, a transverse IP displacement in the crossing plane along the direction opposite to the beam transverse momentum, which is equivalent to a triplet displacement in the direction of the latter, has been found to have the potential for a further substantial gain, up to a 50% lifetime increase for a 2 mm displacement.

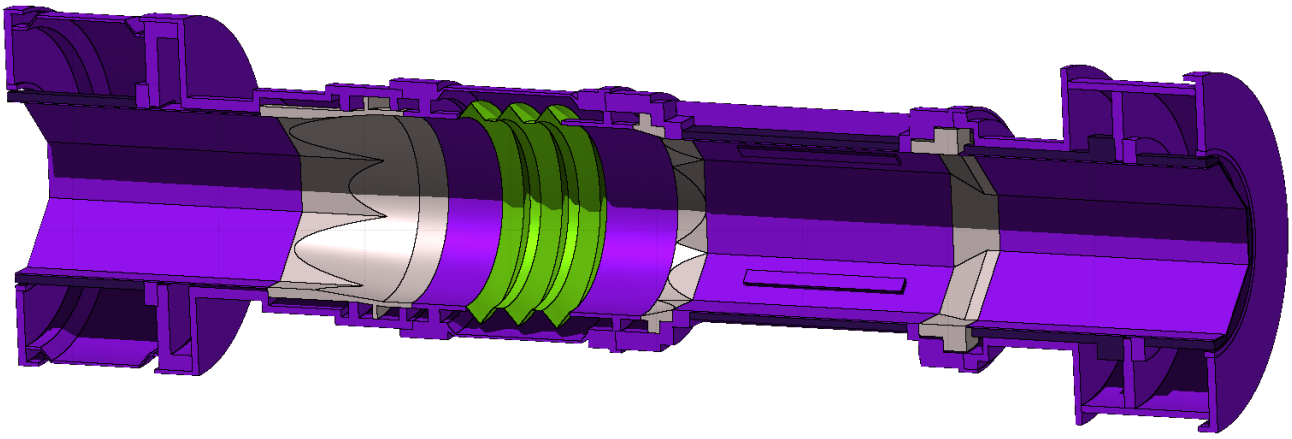

Figure 10-4: FLUKA model of the triplet interconnect, including an octagonal BPM.

10.1.3 Matching section protection

The transition from the single bore hosting the two counter-rotating beams to the two separate beam chambers (referred to as Y chamber) is embedded in the TAXN (Target Absorber Neutral, previously named simply TAN for the LHC layout), another massive absorber, with a 3.3 m long copper core, aimed at intercepting the neutral component of the collision debris, mostly photons and neutrons. The TAXN absorber provides a substantial protection to the double bore recombination dipole (D2) and the four main quadrupole assemblies of the matching section (see Figure 10-5), including dipole correctors.

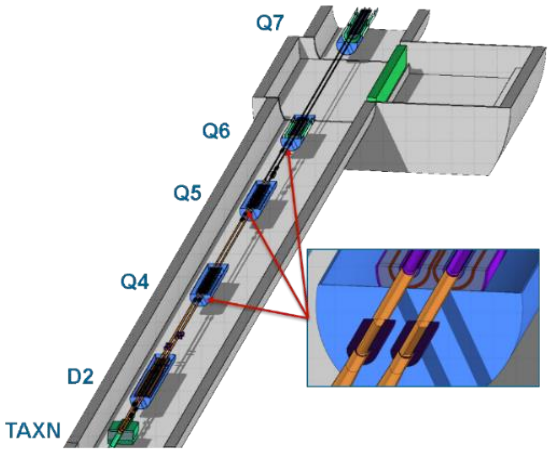

Figure 10-5: Geometry model of the future matching section layout. The frame zooms in on the additional TCLM masks.

However, the HL-LHC layout features a shorter D1–D2 distance, implying a lower beam separation in the TAXN, coupled to a very significant enlargement of its twin pipes, due to optics requirements. These design changes, together with an almost double-crossing angle and an important increase of the mechanical aperture of the upstream elements, lead to a weakening of the TAXN effectiveness. In fact, apart from the luminosity rise, the number of debris particles entering the matching section per primary collision is much larger than in the case of the current machine. This is illustrated in Figure 10-6, where the debris particle distribution at the exit of the TAXN outgoing beam pipe is shown for both the LHC and the HL-LHC. The number of protons is increased by about 30% (from 0.12 to 0.16 protons/collision), while the number of photons and neutrons is about seven times higher (from 0.06 to 0.41 particles/collision). Moreover, the beam size enlargement at this location implies that a collimator set at the same aperture in beam σ is less effective in intercepting debris particles, as clearly revealed in the figure by the number of particles left inside the beam envelope.

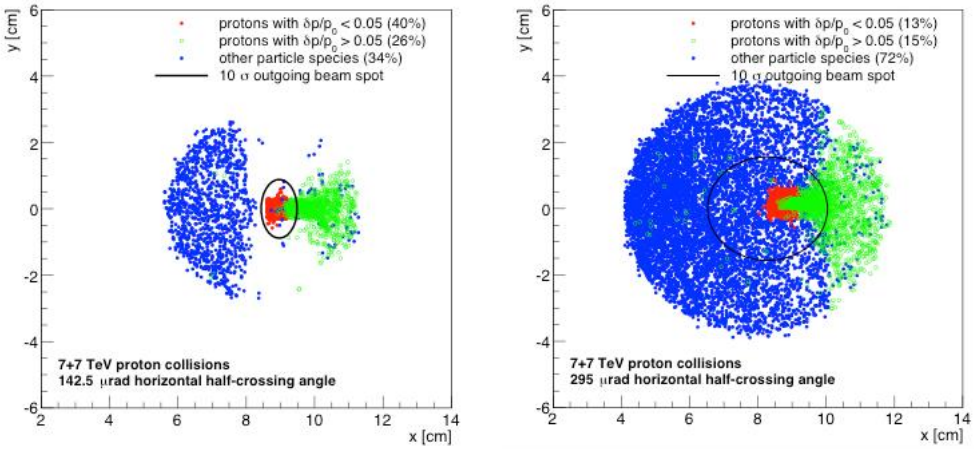

Figure 10-6: Debris particle distribution at the exit of the outgoing beam pipe of the TAXN, (left) for the LHC; (right) for the HL-LHC. Red points indicate protons with magnetic rigidity within 5% with respect to beam protons and green points indicate protons with lower magnetic rigidity. Blue points indicate neutral particles (photons and neutrons). The same number of collisions is simulated in both cases. The black ellipse shows the 10 σ outgoing beam envelope for round beam optics.

Therefore, the cold magnet shielding has to be strengthened, by complementing the TCL (Target Collimator Long) physics debris collimators on the outgoing beam with 1 m long tungsten alloy warm masks put in front of the cryostats and matching the aperture of the following beam screen, without altering the magnet design. Additionally, the first collimator, located between TAXN and D2, requires a special design with thicker jaws (TCLX4), in order to assure an adequate transverse coverage. The incoming beam pipe benefits from the

presence of the TCT (Target Collimator Tertiary) collimators that, while cleaning by design the incoming halo, also play a role in intercepting the debris propagating in the opposite direction. This scheme prevents the risk of debris induced quenches, keeping the power density in the coils below 1 mW/cm^3 for the reference luminosity of 5×10^{34} cm^{-2} s^{-1}, with the three TCL collimators set at 14 σ, equivalent to 21, 7 and 3 mm half gaps, respectively. Corresponding dose values after 3000 fb^{-1} are predicted to remain below 10 MGy, except for the D2, locally exceeding by 15% that limit as reported in Table 10-2. Nevertheless, the value locally reachable in the coils on the IP end of the Q4 cryostat, not closely preceded by a collimator, critically depends on the accuracy of the aperture and transverse alignment of the upstream mask, considering that a 2 mm discrepancy can lead it beyond 30 MGy.

Table 10-2: Maximum dose [MGy] in the coils of the elements of the D2 assembly for the nominal and ultimate integrated luminosity targets.

Magnet	**3 ab^{-1}**	**4 ab^{-1}**	**Magnet**	**3 ab^{-1}**	**4 ab^{-1}**
D2	11.5	15	Correctors	< 5	< 6

Figure 10-7 clearly shows that the leakage through the TAXN is minimized in case of vertical crossing, where the main spot in between the TAXN twin apertures is produced by neutral particles (photons and neutrons) hailing from the IP. Its vertical position reflects the crossing angle polarity. A further hot spot can be recognized on the lower edge of the outgoing beam bore (at positive x), due to protons far enough from the beam energy so that they are bent by the triplet quadrupoles on the side opposite to the crossing angle and then moved by the separation dipole in the external direction. For horizontal crossing, the neutral cone from the IP has instead a significantly larger overlap with the outgoing beam aperture, inducing in the D2, which is the most exposed magnet collecting of a total power amounting to 33 W, twice as much its load for vertical crossing.

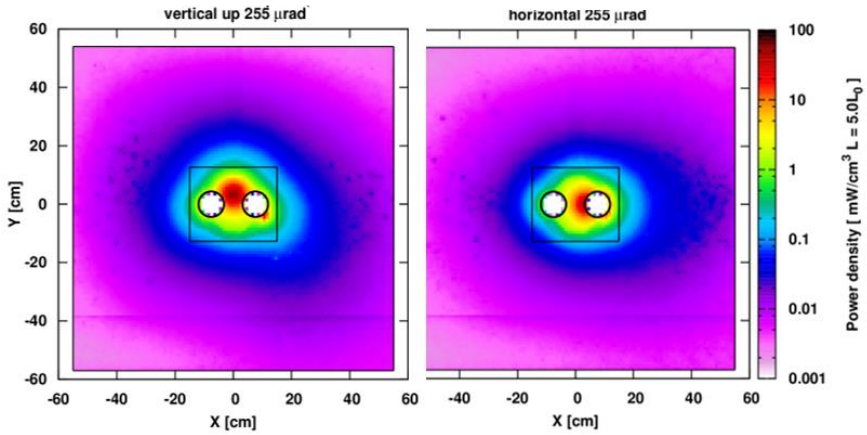

Figure 10-7: Absorbed power density distribution in the most impacted TAN slice, for vertical (left) and horizontal (right) beam crossing.

10.1.4 Dispersion suppressor protection

The most forward TCL collimator, in the straight section Half-Cell 6, provides a good cleaning of the initial part of the Dispersion Suppressor (DS), where the beam lines get bent through the LHC main dipoles and no layout modification is planned for the HL-LHC era. This is illustrated in Figure 10-8, where the progressive collimator closure translates into a substantial reduction in the number of debris particles impacting the beam screen. The tighter half gap considered in the figure is meant to indicate the cleaning sensitivity, but cannot be operationally adopted, since it would break the collimator hierarchy and, moreover, would excessively expose the metallic jaws to accidental events, such as an asynchronous beam dump. Anyway, beyond the TCL6 range, far losses are expected in the DS odd half-cells, according to the periodicity of the single turn dispersion, as regularly observed already in the LHC operation. In fact, they originate from protons subject to diffraction at

the IP, affected by a magnetic rigidity deficit of the order of 1% and therefore destined to touch the horizontal boundary of the mechanical aperture towards the centre of the ring.

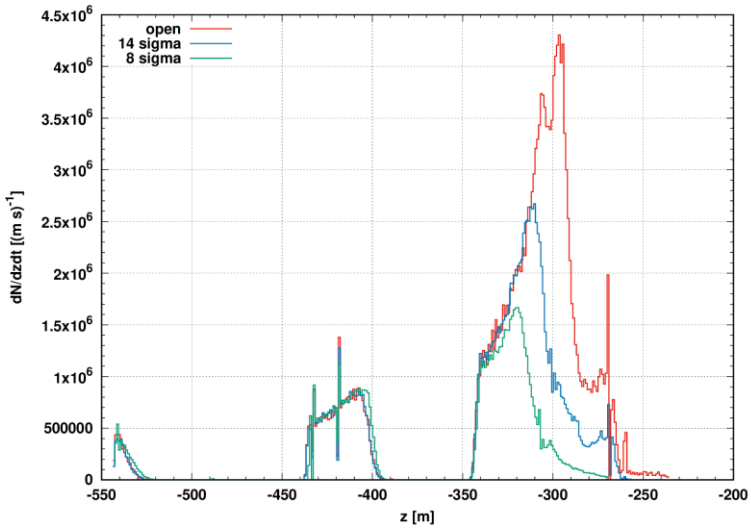

Figure 10-8: Loss maps in the DS for different TCL6 settings, normalized to the nominal instantaneous luminosity of 5×10^{34} cm^{-2} s^{-1}.

As a consequence, maximum doses at the level of 20 MGy are predicted to be accumulated in the superconducting coils of the Half-Cell 9 for a 3000 fb^{-1} integrated luminosity. On top of that, actual imperfections in the machine aperture may locally worsen the picture. Such values are deemed to be excessive for the dipole corrector in the Half-Cell 9 on the left of IP1 and IP5 (considering the layout asymmetry), due to its lower radiation resistance, and mitigation actions are being considered. Respective peak power densities appear less severe, being of the order of 1 mW/cm^3 for the reference instantaneous luminosity of 5×10^{34} cm^{-2} s^{-1}.

10.2 Radiation to electronics

10.2.1 Introduction

A specific problem is represented by the sensitivity of electronics to radiation. The above described particle debris emerging from the IP (together with the additional loss contribution from beam-gas interactions, which however is not expected to bring a significant increase) will impact equipment in the LHC tunnel and areas adjacent to it (UJs, RRs). Installed (present or future) electronic systems (e.g. controls, powering, protection…) are either fully commercial or based on commercial-off-the-shelf (COTS) components, both possibly affected by radiation. This includes the immediate risk of single event effects (SEE) and a possible direct impact on beam operation, as well as in the long-term cumulative dose effects (impacting the component/system lifetime) that additionally have to be considered.

For the tunnel equipment in the existing LHC, radiation was only partially, and relatively late, considered as a design criterion prior to construction. Most of the equipment placed in adjacent and partly shielded areas was neither conceived nor tested for their actual radiation environment. Therefore, given the large amount of electronics being installed in these areas, in 2008 a CERN-wide project called Radiation To Electronics (R2E) [10] was initiated to quantify the danger of radiation-induced failures and to mitigate the risk for beam operation to below one failure per week. The respective mitigation process, mainly through shielding and relocation, was based on a detailed analysis of the radiation fields involved, intensities and related Monte Carlo calculations; radiation monitoring and benchmarking; the behaviour of commercial equipment/systems and their use in the LHC radiation fields; as well as radiation tests with dedicated test areas and facilities [10][11].

In parallel, radiation-induced failures were analysed in detail in order to confirm early predictions of failure rates, as well as to study the effectiveness of implemented mitigation measures. Figure 10-9 shows the actual number of SEE failures measured during 2011 and 2012 operations, the achieved improvement (note that the failure rate measured during 2011 already benefitted from mitigation measures implemented during 2009 and 2010), as well as the goal for operation after LS1 and during the HL-LHC era. As can be seen in Table 10-3, the ~0.5 dumps/fb^{-1} objective was reached for the 2016-18 LHC operation period in Run 2, after the LS1 relocation, shielding and upgrade activities.

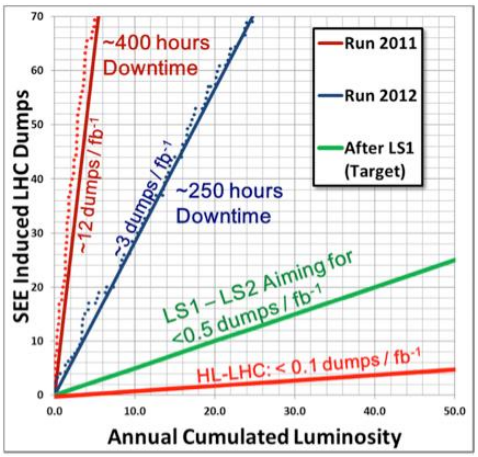

Figure 10-9: LHC beam dumps due to single event effects against beam luminosity. Dots (2011 and 2012) refer to measurements, whereas lines show annual averages for both past and future operations.

Aiming for annual luminosities of 250 fb^{-1}, it is clear that machine availability has to be maximized during the HL-LHC period in order to successfully achieve the physics goal. This implies that existing electronics systems are either installed in fully safe areas, sufficiently protected by shielding, or are made adequately radiation tolerant.

Table 10-3: Number of R2E suspected dumps during Run 2 operation.

Year	R2E dumps				Integrated Luminosity (fb^{-1})	R2E dumps per fb^{-1}
	QPS	EPC	Other	Total		
2015	2	5	-	7	4.2	1.7
2016	0	6	-	6	40	0.15
2017	1	10	-	11	50	0.22
2018	14	11	3	28	60	0.46

The last statement implies that existing equipment, as well as any future equipment that may be installed in R2E critical areas, must be conceived in a specific way.

Radiation damage to electronics is often considered in satellite and human space flight and was also to different degrees of detail regarded in the LHC experiment electronics design and qualification. However, it is important to note that the radiation environment encountered at the LHC accelerator, the high number of electronics systems and components partly exposed to radiation, as well as the actual impact of radiation-induced failures, differ strongly from the context of satellite and human space flight applications. While design, test, and monitoring standards are already well defined for the latter, additional constraints, but in some cases also simplifications – mainly related to the ability of upgrading equipment and improving the related radiation tolerance at regular intervals - have to be considered for the accelerator environment.

The mixed particle type and energy field encountered in the relevant LHC areas is composed of charged and neutral hadrons (protons, pions, kaons, and neutrons), photons, electrons, and muons ranging from thermal energies up to the GeV range. This complex field has been extensively simulated by the FLUKA Monte Carlo code and benchmarked in detail for radiation damage issues at the LHC [12][13]. As discussed above, the observed radiation is due to particles generated by proton–proton (or ion–ion) collisions in the LHC

experimental areas, distributed beam losses (protons, ions) around the machine, and to beam interaction with the residual gas inside the beam pipe. The proportion of the different particle species in the field depends on the distance and angle with respect to the original loss point, as well as on the amount (if any) of installed shielding material. In this environment, electronics components and systems exposed to a mixed radiation field will experience three different types of radiation damage: displacement damage, damage from the total ionizing dose (TID), and Single Event Effects (SEEs). The latter range from single event or multiple bit upsets (SEUs or MBUs), transients (SETs) up to possible destructive latch-ups (SELs), destructive gate ruptures, or burn-outs (SEGRs and SEBs).

The first two groups are of cumulative nature and are measured through TID and non-ionizing energy deposition (non-ionizing energy losses (NIEL), generally quantified through accumulated 1 MeV neutron equivalent fluence), where the steady accumulation of defects causes measurable effects that can ultimately lead to device failure. As for stochastic SEE failures, they form an entirely different group, since they are due to ionization by a single particle and are able to deposit sufficient energy to perturb the operation of the device. They are characterized in terms of their probability of occurring as a function of accumulated high energy (> 20 MeV) hadron (HEH) fluence, incorporating also the weighted contribution of lower energy neutrons [14]. The probability of failure will strongly depend on the device as well as on the flux and nature of the particles.

10.2.2 Radiation environment and effects during Run 2

During Run 1 and Run 2 LHC operation, the radiation levels in the LHC tunnel and in the (partly) shielded areas have been extensively measured using the CERN RadMON system [15], which is dedicated to the analysis of radiation levels possibly impacting installed electronics equipment. In combination with other radiation monitors (e.g. Beam Loss Monitors, optical fibres) and FLUKA calculations, the radiation levels in the machine can be accurately measured and linked with the operational parameters of the machine.

Table 10-4 summarizes the level of accumulated HEH fluence measured during the Run 2 nominal operation years for the most critical LHC areas where electronics equipment is installed and that are relevant for the HL-LHC project. The HEH fluence measurements are based on the RadMON reading of the SEUs of SRAM memories whose sensitivity has been extensively calibrated in various facilities. In the case of LHC tunnel locations, RadMONs are typically placed below the interconnects (at 70 cm from the floor level) and are therefore slightly more exposed than the electronic racks themselves, which are located below the magnets.

Moreover, in the RE alcoves, which are shielded galleries next to the LHC ARCs, the measured levels by the RadMONs on the tunnel side of the alcoves are, as expected, compatible with those of the arc RadMONs in the tunnel itself. Inside the alcove, the vast majority of RadMONs measure no SEU events at all, setting an upper limit to the annual fluence of 10^6 HEH/cm^2/yr. Therefore, in practical terms such values are compatible with surface level cosmic neutron flux.

It is worth noting that the changes during Run 2 in the annual radiation levels of the RRs and Cells 8/9 of the Dispersion Suppressor in IP1 and IP5 are mainly related to the different Roman Pot and TCL6 configurations. For the HL-LHC, the situation will be that all TCL debris collimators (4, 5 and 6) will be in closed position (14σ) therefore protecting Half-Cell 8 (and partially 9) in the DS at the expense of generating large radiation levels in the RRs. It is worth noting that during 2018, operation with the TCL6 open reduced the radiation levels in the IP1 and IP5 RRs, but increased them in Half-Cell 8 and beginning of Half-Cell 9 of the DS, leading to an overall increase in the R2E events per unit integrated luminosity, as reflected in Table 10-3.

Likewise, the 2018 increase in the annual radiation levels in IP7 (both RR and DS) is related to the increase of a factor ~3 of protons lost in the primary collimation system in 2018 with respect to 2016 and 2017 due to the reduced dynamic aperture linked to the crossing angle and beta-star reduction.

Table 10-4: HEH levels in different LHC locations critical for electronics operation as measured during Run 2 with the RadMON system.

LHC area	Zone Type	2016 (HEH/cm^2)	2017 (HEH/cm^2)	2018 (HEH/cm^2)
UJ14/161	Shielded	8.3×10^8	8.9×10^8	2.7×10^8
RR13/17	Shielded	5.4×10^7	3.9×10^8	1.6×10^8
UJ56	Shielded	6.7×10^8	8.1×10^8	8.5×10^8
RR53/57	Shielded	1.9×10^8	5.1×10^8	3.9×10^8
UJ76	Shielded	3.4×10^7	7.9×10^7	1.7×10^8
RR73/77	Shielded	1.6×10^7	1.8×10^7	6.6×10^7
UX85	Shielded	5.3×10^8	4.7×10^8	6.0×10^8
US85	Shielded	1.4×10^8	1.2×10^8	1.4×10^8
IP1 Half-Cell 8	Tunnel (DS)	9.9×10^8	8.5×10^8	1.7×10^{11}
IP5 Half-Cell 8	Tunnel (DS)	3.2×10^8	4.9×10^8	1.3×10^{11}
IP1 Half-Cell 9	Tunnel (DS)	3.7×10^{10}	1.0×10^{10}	2.9×10^{10}
IP5 Half-Cell 9	Tunnel (DS)	4.1×10^{10}	3.4×10^{10}	5.2×10^{10}
IP7 Half-Cell 9	Tunnel (DS)	7.3×10^8	2.1×10^8	7.3×10^8
IP1 Half-Cell 11	Tunnel (DS)	6.0×10^{10}	7.8×10^{10}	4.5×10^{10}
IP5 Half-Cell 11	Tunnel (DS)	3.4×10^{10}	5.1×10^{10}	5.2×10^{10}
Rest of DS and ARC	Tunnel	$\sim 5 \times 10^7$		

10.2.3 FLUKA R2E simulations for IP1 and IP5

In combination with projections based on presently measured radiation levels and expected future scaling, FLUKA simulations are an essential tool in defining radiation levels for future operation, especially for cases involving new layouts and/or beam optics scenarios.

Dedicated maps of R2E relevant quantities in the tunnel and adjacent areas of the high luminosity experimental insertions (IP1 and IP5), in their HL-LHC configuration, are available through FLUKA simulations. A first study focused on the energy deposition and R2E relevant levels in the inner triplet and matching section, extending up to 260m from the IPs, up to Half-Cell 7 [16]. In this area, the radiation levels in the HL-LHC tunnel at locations relevant for the equipment (i.e. 1.6m from the beam line) and for the full operational period (3000 fb^{-1}) will be mostly above 10 kGy and 10^{13} n_{eq}/cm^2, reaching maximum values of over an order of magnitude larger. Therefore, such values clearly exclude the use of accelerator systems based on commercial electronic components, and dedicated Application Specific Integrated Circuits (ASIC) and other radiation hardened by design components would need to be developed for such applications.

A case of special interest in this region are the radiation levels immediately downstream D1, a suitable location for the cold bypass diodes protecting the inner triplet magnet circuit. Provided the electrical parameters of such high-current diodes are expected to degrade with radiation, thus potentially compromising the integrity of the machine, a dedicated radiation level study was carried out to define the radiation hardness targets for the diode. The main results of such study are shown in Figure 10-10, reflecting that a potentially adequate location for the diode from a radiation environment perspective would be around 83m from the IP. At this location, the neutron equivalent fluence (main contributor of the diode degradation) is at a stable minimum of $\sim 2 \times 10^{14}$ n/cm^2, and the ionizing dose is below 50 kGy, before abruptly increasing due to the absence of the shielding provided by the D1 magnet structure.

[1] The apparent reduction in the HEH hadron levels in 2018 in UJ14/16 is attributed to the direct measurement of the R-factor (contribution of thermal neutrons to the total SEU rate) which, as not measurable in previous years, was assumed as a worst-case value in terms of respective HEH flux.

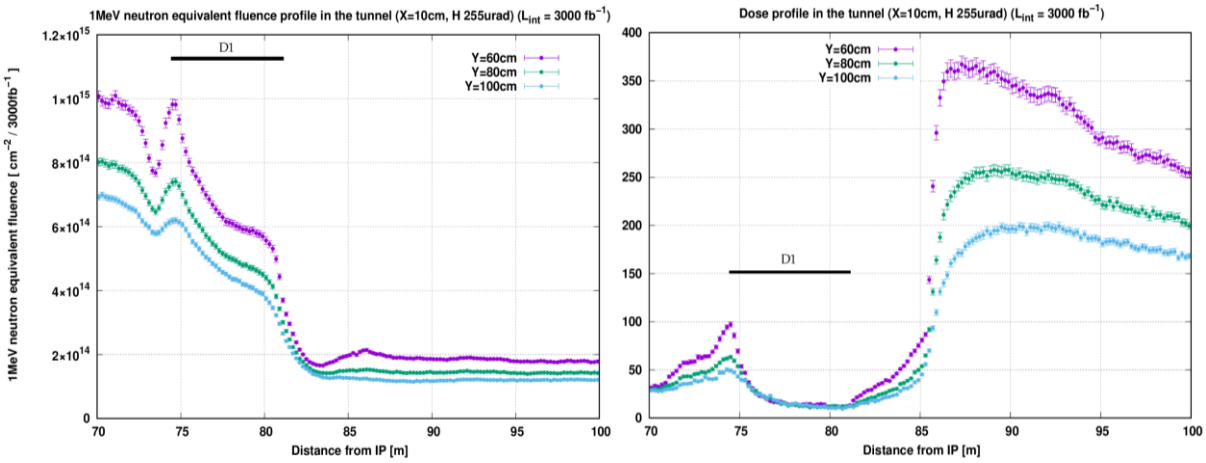

Figure 10-10: Simulated radiation levels in terms of 1-MeV neutron equivalent (left) and TID (right) for 3000 fb^{-1} HL-LHC operation near D1, at beam level in the horizontal direction perpendicular to the beam (X=0) and at different vertical positions (Y=60, 80 and 100 cm) for horizontal, IP5 crossing.

Owing to the harsh radiation environment in the LHC inner triplet and matching section, electronic systems for the machine elements installed in this area (e.g. inner triplet magnets) are hosted in the shielded alcoves. The latter are known as UJ (Junction Chamber) and UL (Liaison Gallery between Underground Works) in the case of the heavily shielded areas near the IPs; and as RRs for the lightly shielded areas roughly 240–260 m away from the IP. According to the dedicated FLUKA simulations, taking into account the detailed layout and beam optics aspects of the HL-LHC, the expected radiation levels in the shielded areas around IP1 and IP5 are summarized in Table 10-5.

Table 10-5: Expected annual radiation levels in IP1/IP5 shielded alcoves for the HL-LHC operation. Further details of the HL-LHC radiation environment are provided in Ref. [17].

Location	**HEH fluence (HEH/cm^2/yr)**	**TID (Gy)**	**1-MeV neutron equivalent fluence (cm^{-2})**
UJ14/16/56	3×10^9	6	5×10^{10}
UL14/16	1.2×10^8	< 1	$< 10^{10}$
RR13/17	1.4×10^{10}	25	7×10^{10}

An important implication of such levels is that equipment installed in the UJ and RR shielded areas will not only need to be tolerant to SEEs, but also qualified for cumulative TID and DD degradation, as the specified radiation levels for the HL-LHC are of a magnitude that implies potential lifetime issues for commercial parts. For the LHC, only the electronics installed in the tunnel was concerned about cumulative damage, the shielded electronics being mainly designed and qualified against SEEs.

Moving further away from the IP, as of Half-Cell 8 included, the LHC tunnel starts to host electronic racks for a broad variety of equipment (power converters, quench protection system, vacuum, cryogenics, beam instrumentation…). As shown in Section 10.1.2 related to the Run 2 operation, the Dispersion Suppressors of IP1 and IP5 are amongst the most hostile radiation areas with active commercial electronics in operation. Despite the robust radiation design of many of these systems, the 2018 experience in particular has shown that both SEE and lifetime radiation effects in this area of the machine can have a strong impact on the availability of the different systems and in turn that of the accelerator as a whole.

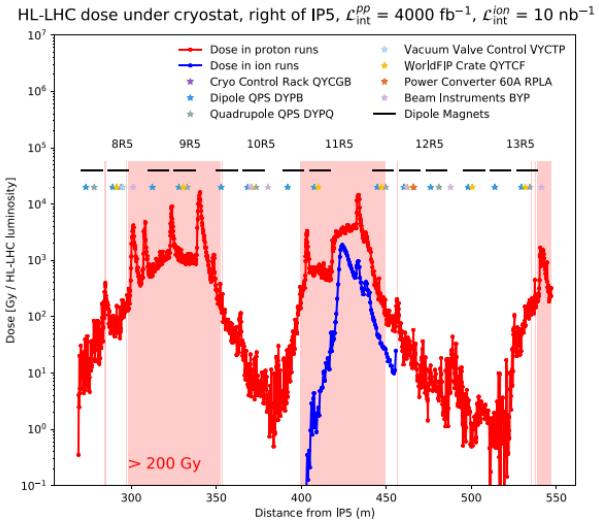

Figure 10-11: Simulated TID distribution for the equipment rack locations (70 cm below the beam) for both proton (4000 fb^{-1}) and ion (10 nb^{-1}) HL-LHC operation in IP1/5.

This will be even more the case for the HL-LHC, where losses in the DS, in fist approximation, are expected to increase with the integrated luminosity. The results of the dedicated FLUKA studies for this area of the machine, taking the protons lost on the beam screen from a first step simulation starting from the collisions in the IP, and propagating them and their produced showers in a second step, are shown in Figure 10-11. The radiation levels (e.g. dose) are scored below the magnets, at the location of the electronic racks, and both for proton and ion operation. As can be seen, whereas the ion losses, deriving from Bound Free Pair Production processes in the IP, are mainly located in the interconnect cryostat, losses during proton operation will affect very large portions of Half-Cells 9 and 11 hosting racks. Therefore, electronic designs for the latter will either need to be more robust than the present LHC tunnel qualification limit of 200 Gy, or racks will require relocation, often implying a significant cost, especially in terms of cabling.

10.2.4 Radiation hardness assurance implications

The radiation levels near IP1 and IP5 (Dispersion Suppressor and shielded areas), as well as elsewhere in the machine (not directly covered in this report but described as radiation level specifications in Ref. [17]) pose a serious threat and constraint to the operation of electronics for critical HL-LHC systems. As a complementary activity to Work Package 10 in the HL-LHC, who is responsible for the definition of the expected radiation levels and validation of the related Radiation Hardness Assurance of the equipment; the Radiation to Electronics (R2E) project at CERN provides, in parallel to the HL-LHC, the necessary support for the actual electronic component selection and circuit architecture definition, as well as for the radiation qualification, both at component and system level.

The selection and qualification of the critical parts for a radiation tolerant system needs to be performed at a very early stage of the project, as the outcome of the radiation tests on the component can have a decisive impact on the system design. Radiation testing at component level is typically carried out using 200 MeV proton beams at the Paul Scherrer Institute (PSI), as well as in the CHARM mixed-field facility, both covering all three effects of radiation: TID, displacement damage and Single Event Effects. The cumulative radiation level targets will depend on the specific applications, but for parts of possible use across multiple HL-LHC systems, 1 kGy and 10^{13} n_{eq}/cm^2 are typically applied. For pure TID tests, the cobalt-60 facility at CERN provides a highly accessible and practical option. As for SEE testing, the upper limit to the acceptable cross-section will depend on the criticality of the part and the system, however values as low as ~10^{-13} cm^2/device may be required (as was the case e.g. for the analog-to-digital converter of the FGClite power converter controls system).

According to the expected HL-LHC radiation levels and availability objectives, the following Radiation Hardness Assurance (RHA) considerations apply:

- Radiation levels in the tunnel, especially in the DS areas exposed to high losses, will reach the HL-LHC lifetime values of ~1 kGy, therefore considerably exceeding the expected radiation lifetime of equipment presently installed in the machine, and posing a critical constraint to the selection of the system's architecture and selection of commercial components;
- Radiation levels in the UJ and RR shielded areas (~50–100 Gy for the full HL-LHC operation) will not only involve a threat in terms of Single Event Effects, but also related to commercial component lifetime.

Owing to the challenging radiation level and system availability requirements, as well as the very broad range and quantity of electronic components and systems installed in radiation areas, the component level radiation testing described above needs to be complemented with system level testing. The latter is performed in the CHARM facility at the PS East Area experimental complex, providing a unique opportunity of irradiating full-scale accelerator systems in representative functional and radiation conditions, and constituting the final RHA validation step before being approved for installation in radiation areas.

10.3 References

[1] N.V. Mokhov and I.L. Rakhno, Mitigating radiation loads in Nb_3Sn quadrupoles for the CERN Large Hadron Collider upgrades, *Phys. Rev. ST Accel. Beams* **9** (2006), DOI: 10.1103/PhysRevSTAB.9.101001.

[2] L.S. Esposito, F. Cerutti and E. Todesco, Fluka Energy Deposition Studies for the HL LHC, Conf. Proc. C130512, 2013, pp.TUPFI021.

[3] G. Battistoni *et al.*, Overview of the FLUKA code, Annals of Nuclear Energy 82 (2015), DOI: 10.1016/j.anucene.2014.11.007.

[4] T.T. Bohlen *et al.*, The FLUKA Code: Developments and Challenges for High Energy and Medical Applications, Nuclear Data Sheets 120, 211-214, 2014, DOI: 10.1016/j.nds.2014.07.049.

[5] V. Vlachoudis, FLAIR: A powerful but user friendly graphical interface for FLUKA, Proc. Int. Conf. Mathematics, Computational Methods & Reactor Physics, Saratoga Springs, New York, 2009, on CD-ROM, American Nuclear Society, LaGrange Park, IL, 2009, ISBN: 978-0-89448-069-0.

[6] A. Mereghetti *et al.*, The FLUKA LineBuilder and Element DataBase: Tools for Building Complex Models of Accelerator Beam Lines, IPAC2012, Conf. Proc. C1205201, 2012, pp.WEPPD071.

[7] S. Roesler, R. Engel and J. Ranft, The Monte Carlo event generator DPMJET-III, Proc. Monte Carlo 2000 Conference, Lisbon, October 23-26 2000, A. Kling, F. Barao, M. Nakagawa, L. Tavora, P. Vaz eds., Springer-Verlag Berlin, pp. 1033-1038, 2001, DOI: 10.1007/978-3-642-18211-2_166.

[8] A. Fedynitch, Cascade equations and hadronic interactions at very high energies, PhD Thesis, CERN-THESIS-2015-371.

[9] P.P. Granieri and R. van Weelderen, Deduction of Steady-State Cable Quench Limits for Various Electrical Insulation Schemes With Application to LHC and HL-LHC Magnets, *IEEE Transactions on Applied Superconductivity* **24**, (2014) 4802806, DOI: 10.1109/TASC.2014.2299797.

[10] R2E website. www.cern.ch/r2e.

[11] M. Brugger *et al.*, R2E Experience and outlook for 2012, Proc. LHC Performance workshop, Chamonix 2012, pp 13-18.

[12] K. Roed *et al.*, FLUKA simulations for SEE studies of critical LHC underground areas, *IEEE Trans. Nucl. Sci.* **58**, (2011) 932, DOI: 10.1109/TNS.2010.2097605.

[13] M. Battistoni *et al.*, FLUKA capabilities and CERN applications for the study of radiation damage to electronics at high-energy hadron accelerators, *Prog. Nucl. Sci. Tech.*, 2010, PNST10184-R1.

[14] K. Roed *et al.*, Method for Measuring Mixed Field Radiation Levels Relevant for SEEs at the LHC, *IEEE Trans. Nucl. Sci.* **59**, 2012, 1040, DOI: 10.1109/TNS.2012.2183677.

[15] G. Spiezia *et al.*, A New RadMon Version for the LHC and its Injection Lines, *IEEE Trans. Nucl. Sci*. **61**, (2014) 3424, DOI: 10.1109/TNS.2014.2365046.

[16] R. García Alía *et al*., "LHC and HL-LHC: Present and Future Radiation Environment in the High-Luminosity Collision Points and RHA Implications," in IEEE Transactions on Nuclear Science, vol. 65, no. 1, pp. 448-456, Jan. 2018, DOI: 10.1109/TNS.2017.2776107.

[17] G. Lerner *et al*., "HL-LHC Radiation level specification document", EDMS: 2302154.

Chapter 11

11 T dipole and new connection cryostat for the dispersion suppressor collimators

F. Savary[1*] *and D. Schoerling*[1]

[1]CERN, Accelerator & Technology Sector, Switzerland
[*]Corresponding author

11 11 T dipole and connection cryostat for the dispersion suppressor collimators

11.1 Introduction

In Run 3 the intensity of the ion beams (usually Pb ions) for ion–ion collisions is planned to be increased by a factor of three: from 40×10^9 to 120×10^9 circulating particles. This intensity increase will amplify the losses in the cold zone at P2 and P7 and may drive the beam induced heat losses in the main dipoles in the dispersion suppressor (DS) region above the quench limit. To avoid limiting the machine performance during ion operation due to this effect, various countermeasures have been studied, and the solution chosen was to intercept these diffractive losses via warm absorbers, so-called TCLDs (Target Collimator Long Dispersion) suppressors, left and right of the LHC interaction points P2 and P7.

The concerns about diffractive losses of the Run 3 ion as well as later physics runs are reinforced by the high diffractive losses in IR7 collimators for the proton runs with beam intensity above nominal. At HL-LHC intensity, after LS3, a TCLD in the dispersion suppressor region left and right of IR7 is needed. For Run 3 intensity, with bunch populations of 1 - 1.7 10^{11} p we will be probably in a grey area, given by the uncertainties of the simulations. The paramount importance of the proton run (a limitation in DS losses would directly affect directly the luminosity reach of the ATLAS and CMS experiments), has reinforced the decision of advancing the installation of the 11 T and associated TCLD collimators to intercept the diffractive losses in the DS for both, ion and protons run. A detailed description for the reasons of the change for P2 and P7 is given in Refs. [1] and [2], respectively.

For P2, a detailed analysis of the losses has shown that the most effective place to install the TCLDs is at the centre position of the existing connection cryostats (LEBR.11L2, LECL.11R2). The positions are:

- LEBR.11L2: distance from IP2: - 432.1047 m, distance from IP1 (DCUM): 2900.2557 m.
- LECL.11R2: distance from IP2: 419.33 m, distance from IP1 (DCUM): 3751.6904 m.

This change requires the removal of the present so-called ‘empty’ cryostat LEBR.11L2 and the installation of the connection cryostat full assembly at the LEBR place. The assembly is composed of two new connection cryostats (shorter in length), with a bypass cryostat installed between them. After that, installation of a new TCLD collimator between the two connection cryostats follows. WP11 delivers the two new connection cryostats and the bypass cryostat. A detailed description of the required changes in the LHC is given in Ref. [3].

For P7, it was found that the only effective and available place to install the collimator is at the position of an existing main dipole magnet (MB). In order to make the installation of a TCLD at such a location possible and considering technological constraints, magnets with a nominal operating field of 11 T based on Nb_3Sn

technology were proposed and consequently developed. By replacing MBs (nominal field of 8.33 T), with 11 T dipoles, also called MBH, the same integrated field can be generated on a length which is around 3.5 m shorter. This gained space is sufficient to place a by-bass cryostat with a TCLD collimator assembly. For reasons of beam dynamics (reduction of the orbit excursion with respect to the ideal trajectory) and to reduce the technology risk associated with the innovative and relatively expensive Nb_3Sn superconductor, it was decided to split the MBH into two straight magnets of 5.5 m length each, with the bypass and collimator module installed in the middle. The development of the MBH magnet was initiated at FNAL in October 2010 and in the middle of 2011 at CERN. The performed R&D at FNAL and at CERN is discussed in detail in Refs. [4] and [5], respectively.

The final number and position of MBs and the scope of the project at both FNAL and CERN was realigned due a re-evaluation of heat deposition, modified beam optics, and a change in the funding profile. In August 2019, the final baseline for the installation of the MBHs was formally approved [6]. According to this baseline, the standard LHC dipole magnets MB.A9L7 (LBBRB.9L7) and MB.A9R7 (LBARA.9R7) are replaced with MBHs. The positions are (virtual interconnect plane, upstream B1):

- MB.A9L7 (LBBRB.9L7): distance from IP7: -323.629 m, distance from IP1 (DCUM): 19670.5334 m, half-cell 9.L7, called following P7 left side.
- MB.A9R7 (LBARA.9R7): distance from IP7: 307.969 m, distance from IP1 (DCUM): 20302.1314 m, half-cell 9.L7, called following P7 right side.

In detail, the changes comprise the removal of the present MBs, the installation of the 11 T dipole full assembly at the MB place. The assembly is composed of two dipoles and a bypass cryostat in the middle, providing cryogenic and electrical continuity between them. After that, the installation of a new TCLD collimator between the two magnets will follow. A detailed description of the required changes in the LHC is given in Ref. [2].

11.2 The connection cryostat full assembly

On both sides of IR2, the existing connection cryostat cryo-assembly will be replaced with a string of three independently installed and aligned cryo-assemblies: two of these will be new connection cryostats (QEP), with a bypass cryostat (QEN) installed between them. This new assembly will be called connection cryostat full assembly. There are two types of cold masses per cryo-assembly: the cold mass QEP_001 that will be installed on the left hand side of the collimator (for an observer looking from the centre of the accelerator), and the cold mass QEP_002 that will be installed on the right hand side of the collimator. These cold masses will have all the features to make their installation compatible with the location of the collimators on either side of the IR2. The QEP cold mass assembly has a length of 5309 mm between the datum plane C and L at the end covers. The QEPs need to be compatible with the LHC lattice and its main systems. They will be connected in series with the MBs and MQs. The cold mass of the QEP is made of a mechanical structure holding several pipes ensuring continuity of the cryogenic circuits. Specific busbars are installed inside the cold mass for continuity of the main and auxiliary powering circuits. The mechanical structure is based on three 25 mm thick stainless-steel plates assembled with screws to form an H type beam. This beam is reinforced by intermediate plates to ensure mechanical stability of the assembly when loaded. A cross-section through the QEP is shown in Figure 11-1.

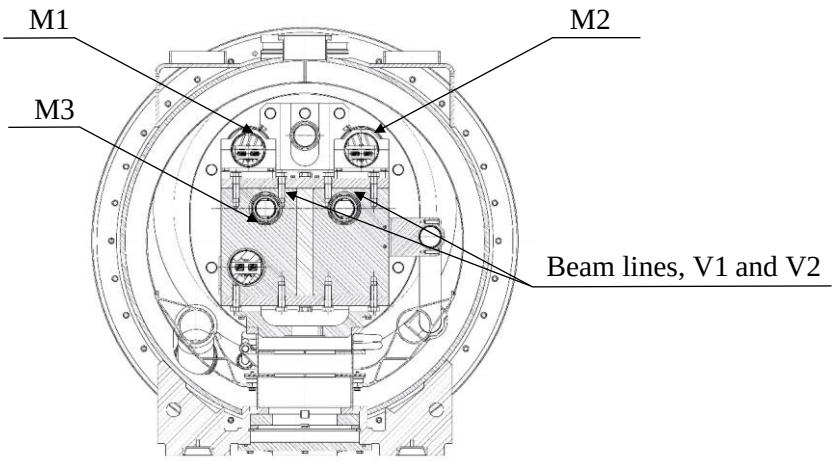

Figure 11-1: Cross-section of the QEP.

The cold mass is finished by a flat plate on the side of the assembly facing the existing MBs or MQs (see Figure 11-2) and by a dished end of a larger diameter on the side of the assembly facing the collimator (see Figure 11-3).

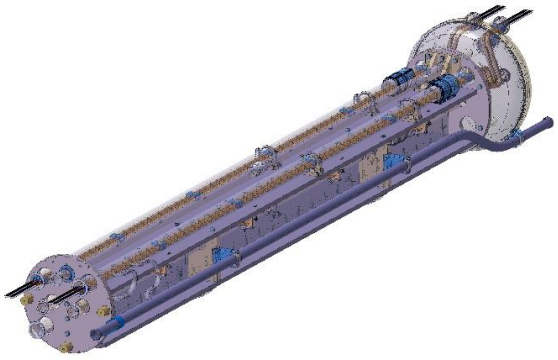

Figure 11-2: QEP Cold Mass (MBs side)

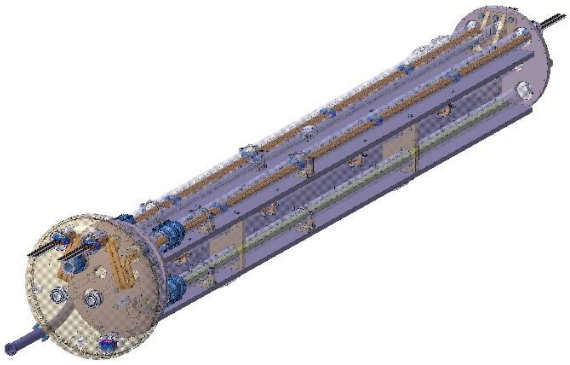

Figure 11-3: QEP Cold Mass (QEN side)

The cryogenic circuit is composed of three pipes housing the main busbars and a heat exchanger pipe connected to a “shuffling module” composed of two dished ends. On the MBs or MQs side, the pipes housing the busbars are placed in the same position as in a standard interconnection. On the collimator side, the busbars are placed further away from the beam lines to allow the routing of the busbars across the bypass cryostat. The shuffling module is made large enough to hold the lyras of the busbars and is used also to make the transition between the position of the busbar in a standard interconnection and their position in the bypass cryostat.

The QEP will be equipped with the same cold bore tube and beam screen as the present connection cryostats to facilitate integration. The cold bore is installed inside a larger pipe hydraulically connected to the main cryogenic circuit of the QEP to ensure low temperature cryo-pumping on the beam vacuum surface. This configuration guarantees the temperature of the cold bore walls to be at 1.9 K in operation.

Contrary to the connection cryostats installed presently in the LHC, which features a Pb shielding for protecting the busbars and downstream magnet from particle radiation, the QEP has no such shielding installed, as it was deemed not necessary (see Ref. [7]).

The main parameters of the QEP are listed in Table 11-1.

Table 11-1: Main parameters of the QEP.

Characteristics	Unit	Value
Cold bore tube inner diameter/thickness	mm	50/1.5
Number of apertures	-	2
Distance between apertures at room temperature/1.9 K	mm	194.52/194.00
Cold mass physical length (between datum planes C and L)	m	6.252
Cold mass weight	kg	~2000
Nominal operating current (main circuit busbars)	kA	11.85
Operating temperature	K	1.9
Heat exchanger hole inner diameter	mm	60
Heat exchanger distance from centre (same position as in the MB)	mm	180

Full reference to the integration is given in Ref. [8] and the information for installation in the HL-LHC is provided in Ref. [3].

11.3 The 11 T dipole full assembly

A main dipole cryo-magnet assembly (MB) will be replaced with a string of three independently installed and aligned cryo-magnet assemblies: two of these will each house an 11 T dipole, referred to below as the MBH, with a bypass cryostat installed between them. This new assembly will be called 11 T dipole full assembly. The bypass cryostat ensures the continuity of the cryogenic and electrical circuits and comprises cold to warm transitions on the beam lines in order to create a room temperature vacuum sector sufficiently long to install the TCLD. The TCLD is supported directly from the tunnel floor so as not to be affected by deformations of the cryostat vacuum vessels due to alignment or pressure-induced forces. A pair of MBHs will provide an integrated field of 119 T·m at the nominal operating current of the MBs, 11.85 kA. This corresponds to a nominal magnetic flux density of 11.23 T at the centre of the bore. This goal shall be obtained with a margin of ~20% on the magnet load line. A detailed description of the 11 T magnet is provided in the next Section.

Figure 11-4 shows a schematic layout of the string of cryo-assemblies composing the 11 T dipole full assembly, which will replace a main dipole cryo-magnet assembly. The cryostat for the MBH follows the same design and fabrication principles as the other arc cryostats. It complies with the static heat loads specified by the Heat Load Working Group [9]. Standard LHC cryostat performance in terms of alignment tolerances and geometrical stability are ensured. The design of the bypass cryostat is compatible with the integration of the collimator and of the RF-shielded gate valves at the extremity of the cold-to-warm transitions shown in Figure 11-5. All cryogenic lines and powering busbars have their continuity ensured across the bypass cryostat. Enlarged end covers at the extremity of the MBH cold mass interfacing with the collimator allows for all lines to run straight across the bypass cryostat as illustrated in Figure 11-6.

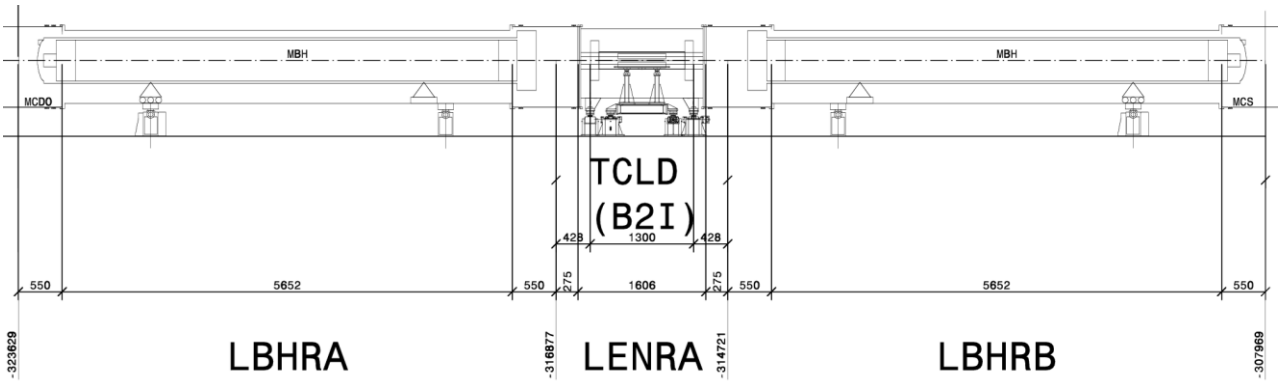

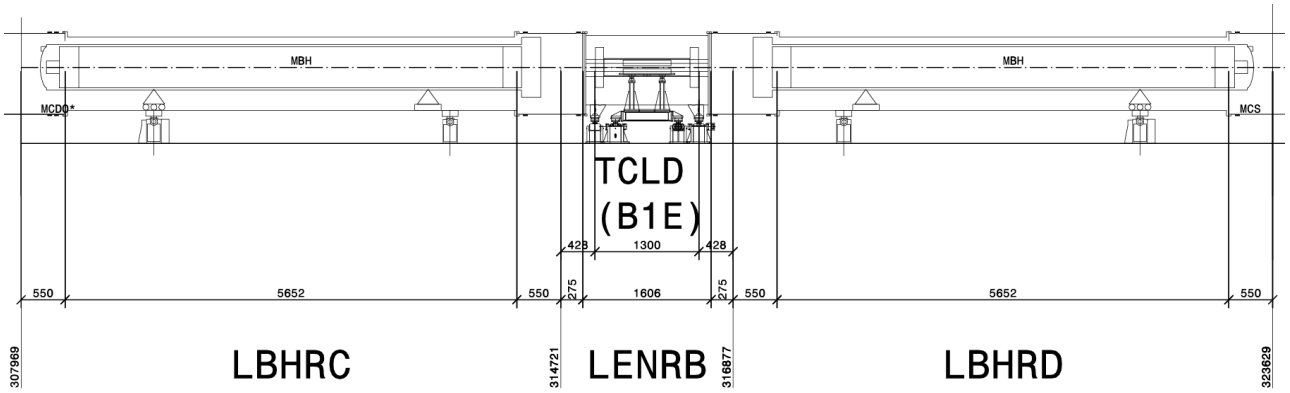

Figure 11-4: Section of the HL-LHC layout for P7 left (from LHCLSSH_0013, top) and P7 right (from LHCLSSH_0014, bottom).

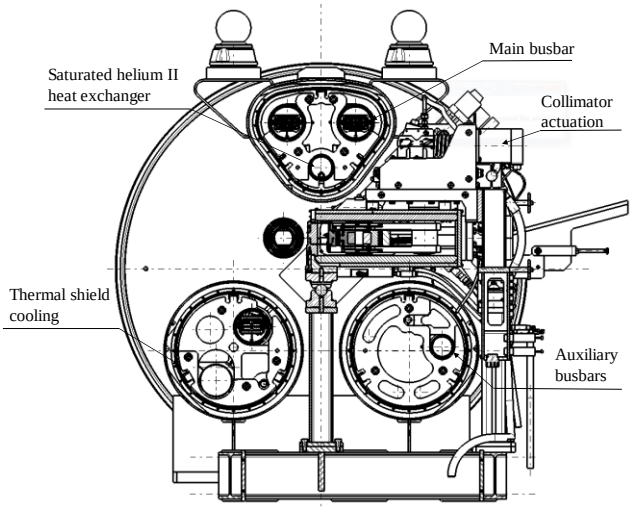

Figure 11-5: Cross-section of the bypass cryostat and collimator. The three main busbar lines have been moved away from the beam lines radially in order to create space for the collimator and the beam vacuum sector valves.

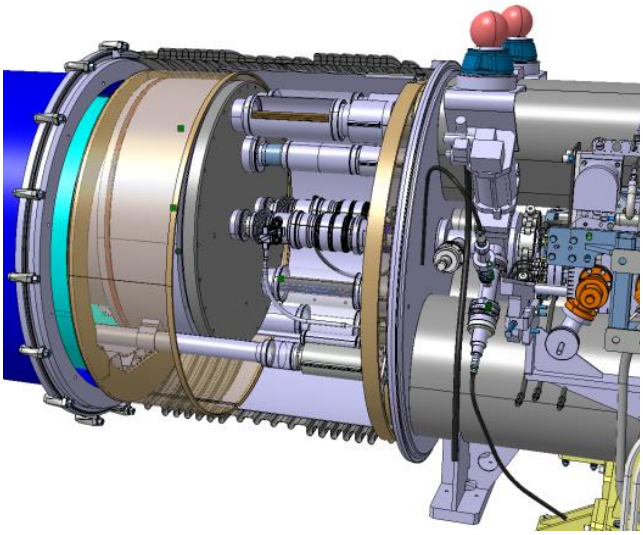

Figure 11-6: View of the enlarged cold mass end cover and the interconnection to the bypass cryostat .

The main parameters of the 11 T dipole full assembly are given in Table 11-2. The dimensions of the cryogenic pipes are equivalent to those of a standard LHC arc continuous cryostat.

Table 11-2: Main parameters of the 11 T dipole full assembly.

Characteristics	Value (mm)
Total length including interconnects	15660
Upstream cryostat length between interconnect planes	6752
Downstream cryostat length between interconnect planes	6752
Bypass cryostat length between interconnect planes	2156
Beam line cold bore diameter (inner)	50
Length of room temperature beam vacuum sector measured between cold-to-warm transition flanges	1230
Compatible active length of the collimator jaws	600

The design of the 11 T dipole full assembly is based on the following baseline.

- The length of the jaws of the collimator is 600 mm and this is valid for all the locations envisaged for installation, in particular for proton and ion cleaning (see Chapter 5).
- The interface between the cold beam lines of the MBH cryostats and the beam vacuum sector of the collimator requires sectorization by RF-shielded gate valves.
- As opposed to other collimators in the machine, residual radiation to personnel is assumed compatible with the removal and installation of the TCLD collimator without remote handling equipment. Given the integration constraints in the LHC dispersion suppressors, the design of a collimator compatible with remote handling is most likely not achievable.
- Radiation doses on the cryostat throughout the HL-LHC lifetime are compatible with the usage of LHC standard cryostat materials.
- Magnetic shielding is not required on the bypass cryostat. It is assumed that the magnetic field created by the busbar currents will not be detrimental to the accuracy of the TCLD instrumentation and controls.

11.3.1 The 11 T dipole

The design of the MBH is based on the two-in-one concept, i.e. the cold mass comprises two apertures in a common yoke and shell assembly, as shown in Figure 11-7. There are two types of cold mass per 11 T dipole full assembly, the cold mass LMBHA that will be installed on the left-hand side of the collimator (for an observer looking from the centre of the accelerator), and the cold mass LMBHB that will be installed on the right-hand side of the collimator. These cold masses will have all the features to make them compatible to the installation locations on either side of IP7.

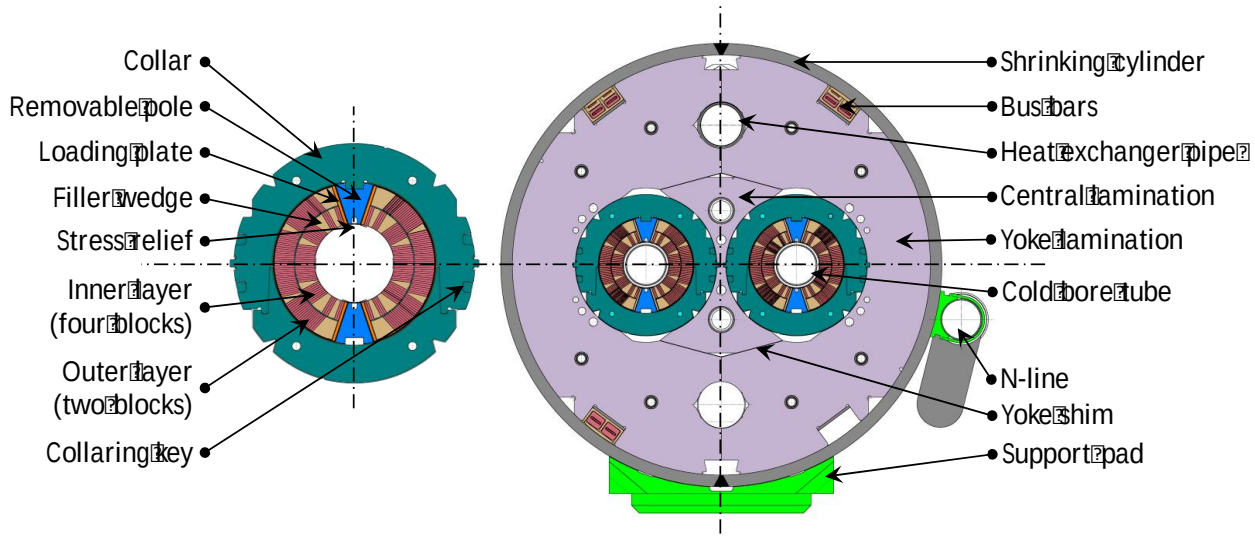

Figure 11-7: Cross-section through (left) the 11 T dipole collared coil; (right) the cold mass assembly.

The LMBH cold masses have a length of 6.252 m between the datum planes C and L that are shown on the end covers, see Figure 11-8 and Figure 11-9. The coils have a length of 5.4568 m without the outermost end spacers (called saddles), and 5.599 m with the saddles, see Figure 11-10. A pair of MBHs is needed to produce an integrated field of 119 T·m at 11.85 kA, which corresponds to the bending strength of the MB. The MBHs need to be compatible with the LHC lattice and its main systems. They will be connected in series with the MBs main dipole circuit. A detailed description of the design, technology and the performance of short models and a first full-scale prototype is given in Ref. [5]. A full-scale series magnet has been manufactured. This magnet was fully qualified for installation. After its initial training and a thermal cycle, this magnet reached nominal operating conditions without quench.

The parameters of the strands and the Rutherford cable were selected based on the required number of ampere-turns to generate the requested integrated transfer function (ITF) under the 20% operating margin, the available coil space, and the maximum number of strands possible in the cabling machine. For this last constraint, the most stringent limits were between CERN (40 strands), and FNAL (42 strands). The selected strand diameter was 0.7 mm, with a cable mid-thickness of 1.25 mm and 1.3 mm before and after reaction. As baseline strand, used for all MBH to be installed in the HL-LHC the conductor RRP 108/127 was chosen. An overview of the different conductors used for models and a discussion on the selection of this option is provided in Ref. [5]. The optimization of the cable parameters was done jointly by FNAL and CERN [10], and included the selection of the cable cross-section geometry and compaction to achieve good mechanical stability of the cable and acceptable critical current degradation (less than 10%), incorporating a stainless-steel core (25 μm thickness), and preserving a high residual resistivity ratio (RRR) of the Cu matrix (RRR larger than 100 in extracted strands).

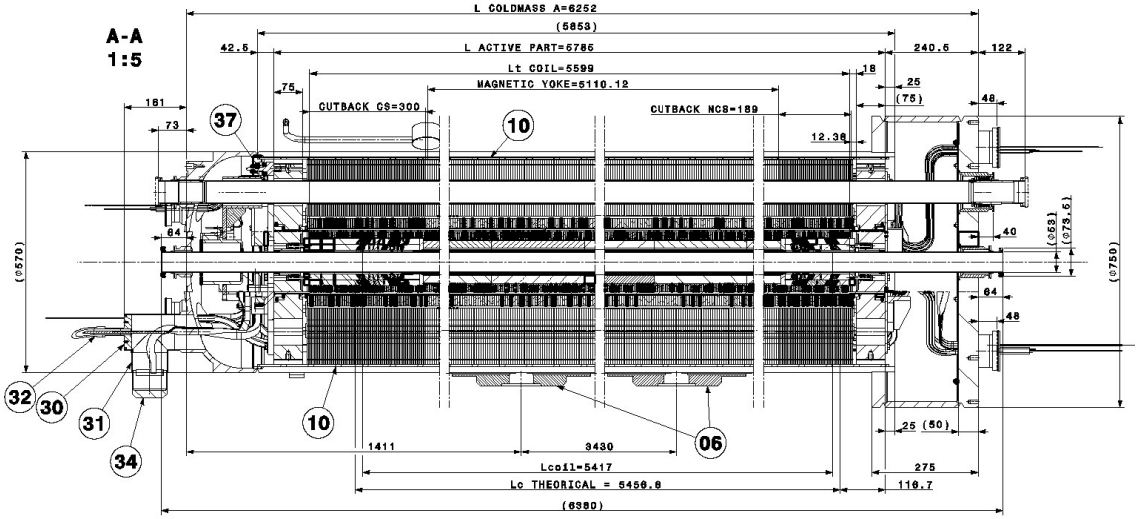

Figure 11-8: Longitudinal section of the cold mass assembly LMBHA (LHCLMBH_0001)

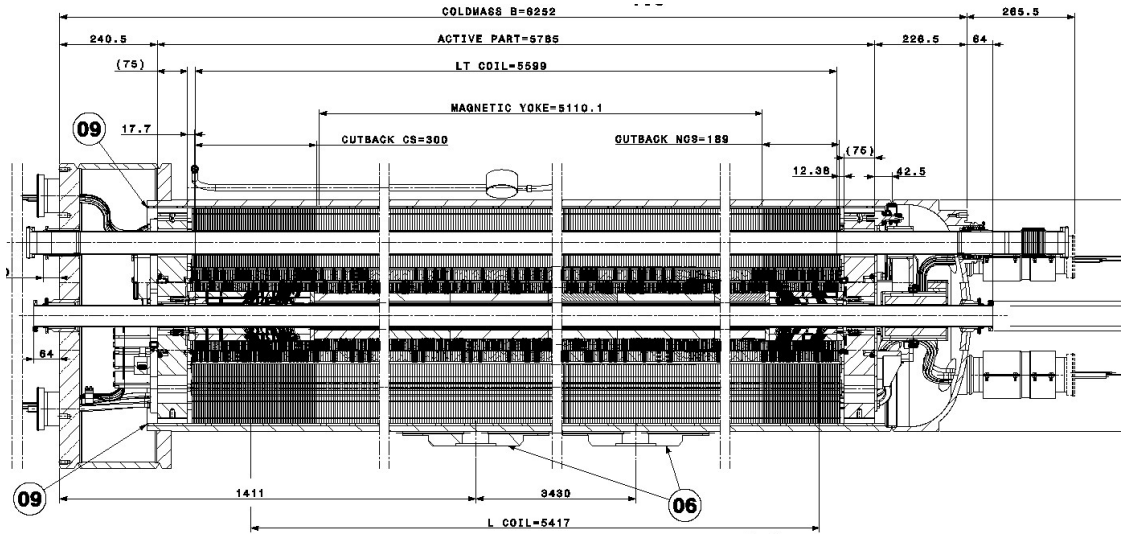

Figure 11-9: Longitudinal section of the cold mass assembly LMBHB (LHCLMBH_0002)

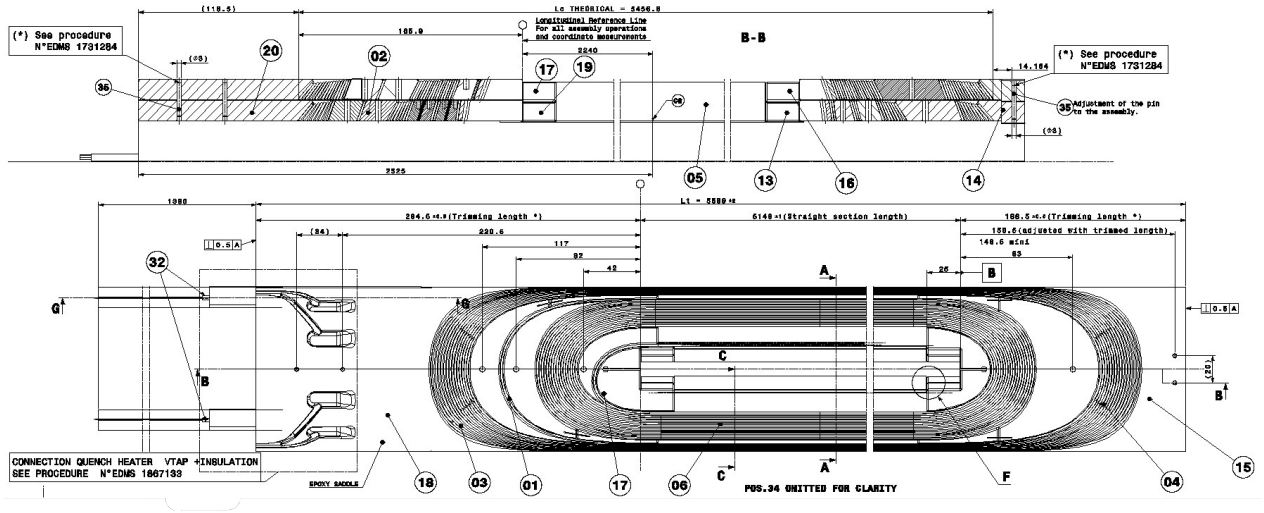

Figure 11-10: Top and side views of the coil (LHCMBH_C0005)

The first 11 T dipole series magnet was cold tested (aka S1 – MBHB-002) in Summer 2019 [11]. After the first cool down, MBHB-002 reached 11950 A (nominal current of 11850 A + 100 A margin) after 2 quenches (quench #1: 7.2 kA, #2: 11.1 kA) at 1.9 K. During the remainder of the first and second cool down, MBHB-002 always performed stable and without quench. In twothe two cold test periods cool downs combined, the magnet was ramped 370 times including 340 fast cycles. Also, at 4.5 K the nominal current + margin was reached without quench in after both cool downs. Multiple holding current tests with up to 12 hours at nominal current showed stable magnet behaviour. The results of this cold testing in combination with conform electrical high-voltage testing, have qualified this magnet for installation in the HL-LHC.

The next series magnets, S2 – MBHA-001, S3 – MBHA-002, and S4 – MBHB-003, were also tested. S2 and S4 with satisfactory results during the initial training, and S3 with unsatisfactory results, as illustrated in Figure 11-11. The magnet S3 has shown limitation in one of the coils, even if it reached 11.95 kA.

Subsequently, during the following cool downs, the magnet S2 has also shown degradation of its performance after the third cool down, CD3, with further degradation after the fourth cool down, CD4, as shown in Figure 11-12. Whereas the magnet S4 has shown degradation after the second cool down, CD2, as shown in Figure 11-13. Investigations and analysis work are on-going in order to understand the cause of the degradations observed after powering and thermal cycles.

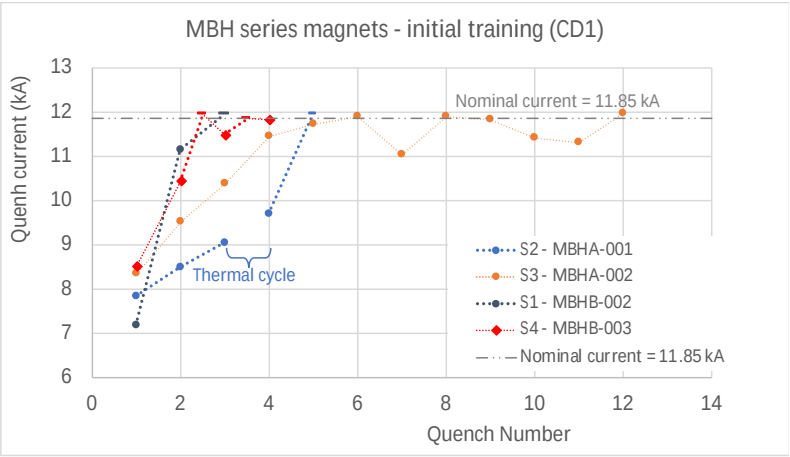

Figure 11-11: Initial training of the first 4 series magnets, i.e. first cool down or CD1. The straight markers mean no quench (S1, S2, and S4). For the magnet S2, the initial training, CD1, was interrupted in order to replace the capillary tube of the IFS because of a suspicion of electrical fault, and the cold tests were resumed after replacement of the capillary tube

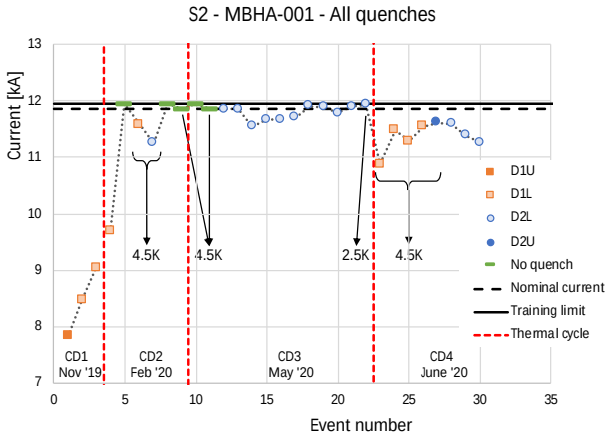

Figure 11-12: All quenches history of the magnet S2, from CD1 to CD4. Unless otherwise stipulated on the graph, the test temperature is 1.9K. The straight markers mean no quench.

D1U denotes upper coil of Aperture 1, and D1L lower coil of Aperture 1. D2U denotes upper coil of Aperture 2, and D2L lower coil of Aperture 2

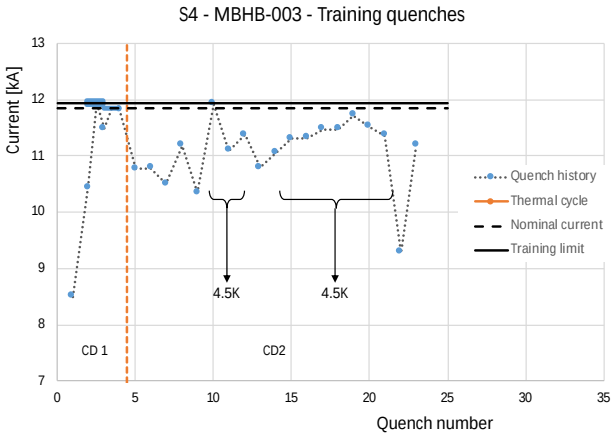

Figure 11-13: Training quenches of the magnet S4, for CD1 and CD2. Unless otherwise stipulated on the graph, the test temperature is 1.9K. The straight markers mean no quench

The main parameters of the MBH, the cryogenics, the strand and the cable are listed in Table 11-3.

Table 11-3: Main parameters of the MBH.

	Characteristics	Unit	Value
Magnet parameters	Aperture	mm	60
	Number of apertures	-	2
	Distance between apertures at room temperature/1.9 K	mm	194.52/194.00
	Cold mass outer diameter	mm	570
	Magnetic length	m	5.307
	Coil physical length, as per magnetic design	m	5.457
	Magnet physical length: active part (between the end plates)	m	5.785
	Magnet physical length: cold mass (between datum planes C and L)	m	6.252
	Cold mass weight	kg	~ 8000
	Nominal operatingoperation current	kA	11.85
	Bore field at nominal current	T	11.23
	Peak field at nominal current	T	11.77
	Operating temperature	K	1.9
	Load line margin	%	20
	Stored energy/m at I_{nom} in both apertures	MJ/m	0.896
	Differential inductance/m at I_{nom}	mH/m	11.97
	Number of layers	-	2
	Number of turns (inner/outer layer)	-	56 (22/34)

	Characteristics	Unit	Value
Cryogenics	Heat exchanger hole diameter	mm	60
	Heat exchanger distance from centre (same position as in the MB)	mm	180
	Cold bore tube inner diameter/thickness (same as in the MB)	mm	50/1.5
	Gap CBT to coil	mm	2.7
Strand	Superconductor	-	Nb_3Sn
	Strand diameter before reaction	mm	0.700 ± 0.003
	Number of strands per cable	-	40
	Cu to non-Cu ratio	-	1.15 ± 0.10
	Effective filament size D_{eff}	μm	< 41
	Cu RRR, reacted but not cabled	-	> 150
	Minimum strand critical current, I_c, without self-field correction (12 T, 4.222 K)	A	438
	Minimum strand current density, J_c, at 12 T, 4.222 K	A/mm^2	2560
Cable	Cable insulation thickness per side azimuthal, before/after reaction	mm	0.155/0.100
	Cable bare width before reaction	mm	14.7
	Cable bare mid-thickness before reaction	mm	1.25
	Cable bare width after reaction	mm	15.08
	Cable bare mid-thickness after reaction	mm	1.30
	Keystone angle RRP 108/127 before reaction	degree	0.79
	Keystone angle RRP 108/127 after reaction	degree	0.81
	Cable unit length for the two layers (no layer jump splice)	m	~650
	Cu RRR, extracted from cable after reaction	-	> 100

11.3.2 RB circuit changes

To avoid deformation changes of the beam-closed orbit of the beams, the integrated transfer function of a pair of MBHs shall be identical to that of the MB. However, this is not possible across the entire range of current during ramping up to nominal current, as shown in Figure 11-14. The design is such that a pair of MBHs provides the same integrated field of 119 T·m as a standard MB at the nominal current of 11.85 kA.

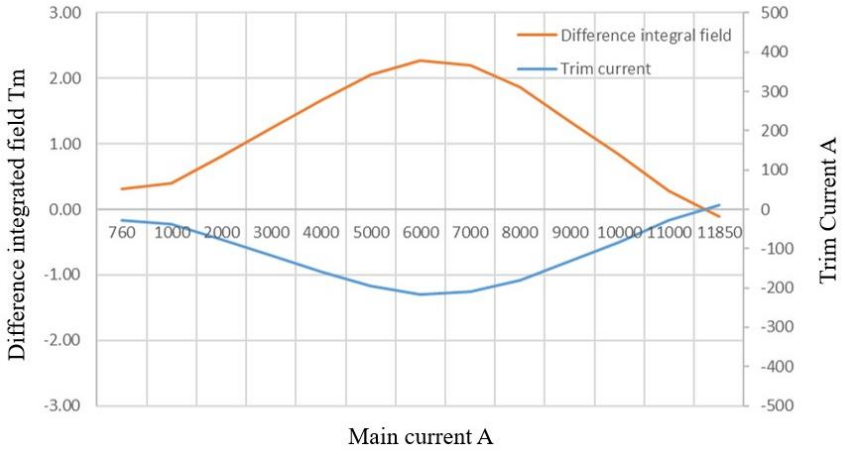

Figure 11-14: Difference in integrated field between a pair of MBHs and an MB, both delivering 119 T·m at 11.85 kA and the trim current needed to correct the difference at currents below 11.85 kA .

The MBH is stronger at lower currents (it has more turns) with a peak difference in integrated field around 6.5 kA. This can be mitigated by adding a dedicated trim power converter for ± 250 A / ± 10 V. In the absence of trim current, the resulting orbit distortion could be mitigated by means of the standard orbit correctors in the LHC lattice. Note that the MBH is assembled as a type A dipole magnet but replaces in circuit RB.A67 a MB of type B. Therefore, the circuit is adapted such that the MBH is connected into the 'A type' circuit part, leading to an asymmetric number of magnets left and right of the energy extraction. This asymmetry is considered uncritical. The MBH will be protected with quench heaters and a bypass diode operating at cold, integrated with the cold mass assembly. One bypass diode is installed for the two MBHs of an 11 T dipole full assembly, similar to the protection scheme of the MBs. The main circuit parameters are provided in Table 11-4. Further details on this circuit including all relevant references are provided in Chapter 6.

Table 11-4: RB circuit characteristics in the current LHC configuration and after the introduction of 11 T dipole full assembly for circuits RB.A67 and RB.A78.

	Circuit	**LHC Configuration**	**HL-LHC Configuration**
Maximal Required PC Voltage	RB.A67 - RB.A78	171 V	171.6 V
Total Circuit Inductance (L_{TOT})	RB.A67 - RB.A78	15.708 H	15.734 H
Circuit Time Constant (τ)	RB.A67 - RB.A78	15700s	15740s
Energy Extraction Time Constant	RB.A67 - RB.A78	112s	113s
Maximum Common Voltage of the Trim Circuit in Case of Energy Extraction	RB.A67 - RB.A78	420 V	431 V
Maximum Common Voltage of the Trim Circuit in Case of Energy Extraction + Earth Fault	RB.A67 - RB.A78	910 V	910 V

11.3.3 Instrumentation

The instrumentation foreseen in the 11 T dipole full assembly is much reduced when compared to that installed in the MBH models (1 to 2 m in length) and prototypes (full length). However, it is significantly increased when compared to the instrumentation of the standard LHC dipole of type MB that will be replaced.

The voltage taps installed along the electrical circuit are used to detect quenches in the coils and to monitor the electrical resistance of the splices between the different coils and bus bars as well as , and the electrical resistance of the joints which are part of the diode leads. The present scheme uses one V-Tap on each side of each splice in the cold mass assembly. The 14 V-Taps distributed along the dipole and spool pieces circuits inside an MBA (respectively 10 for an MBB) amount to 30 in the LMBHA, and 18 in the LMBHB. They are shown in Figure 11-15 with "EExxx" labels. This figure illustrates the 13 kA circuits, the integration of the trim circuit, and the associated V-Taps. Eighteen V-Taps are used to monitor the Nb-Ti to Nb-Ti and Nb-Ti to Nb_3Sn splices between the poles and apertures. The LMBHA cold mass is equipped with 6 additional V-Taps to monitor the joints along the diode and trim circuits, and 2 I-Taps, which can be used for specific quality control tests. Four additional wires for the MCDO and 2 for the MCS spool pieces circuits are installed respectively in LMBHA and LMBHB, as shown in Figure 11-16.

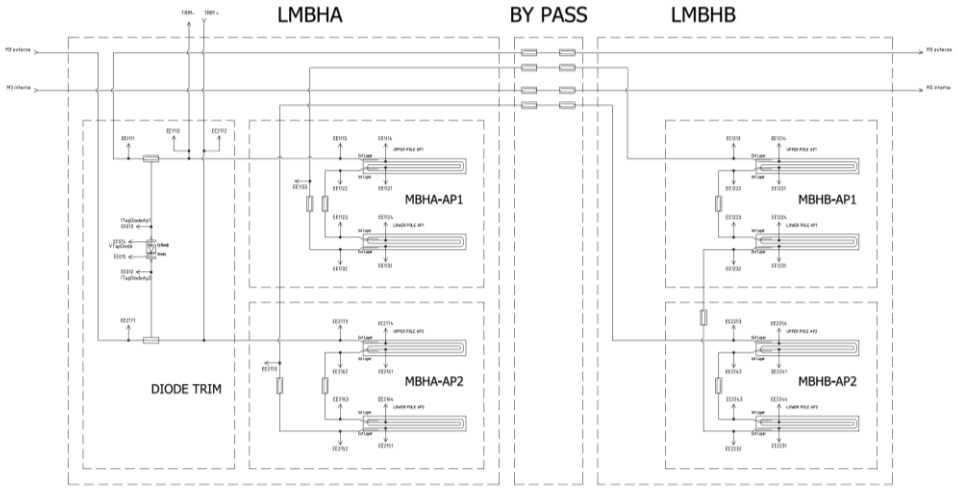

Figure 11-15: Instrumentation scheme in the main/trim circuits of the 11 T dipole full assembly substituting a standard MB (type A or type B)

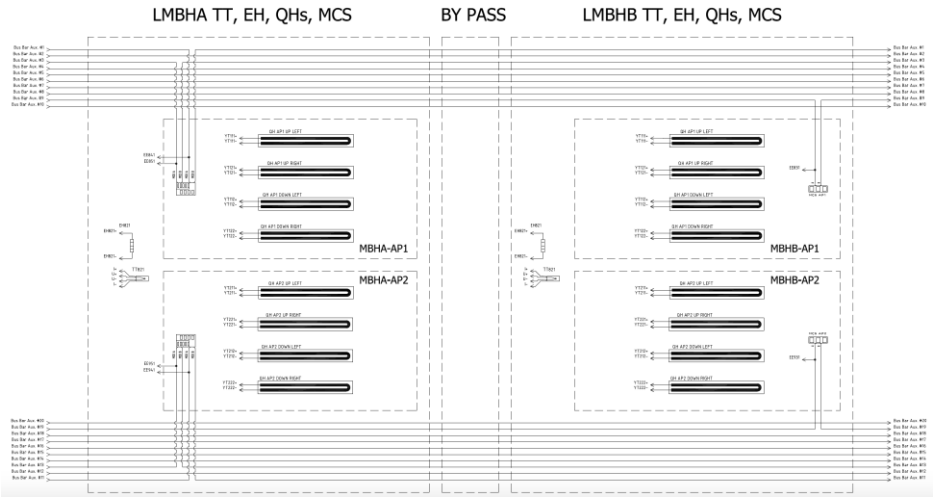

Figure 11-16: Instrumentation scheme for the temperature sensor, cryo-heater, spool pieces, and quench heaters in the 11 T dipole full assembly substituting a standard MBA.

11.3.4 Cryo-heater

A cryo-heater is installed at the bottom of each LMBHA and LMBHB cold mass on the magnet end plate at the connection side. It can be used during warm-up phases to vaporise the helium possibly remaining in the cold mass. The powering circuit of the cryo-heater comprises 2 wires.

11.3.4.1 Temperature sensor

In each LMBHA and LMBHB cold mass, a temperature sensor is attached to the lower part of the yoke, inside the magnet 2 m away from the end plate, on the connection side. It is the same as those used in the MBs (type CERNOX™). Each temperature sensor is equipped with 4 wires arranged in a cable.

11.3.4.2 Instrumentation and feed-through system

The instrumentation feed-through system (IFS) provides the path for the cabling of the electrical and cryogenic instrumentation and quench heaters via a capillary tube running from the cold mass envelope to the envelope of the cryostat.

For the sake of standardization, the design of the cover flange will be the same as that the one used in the MBs. It is equipped with 40 feedthrough pins for high-voltage and low-voltage signals. Therefore, two cover flanges (and two IFS boxes) are needed for each MBH. Moreover, because the section of the 16 quench heater wires has been increased, and there are more wires in the LMBHA, it was decided to increase the inside diameter of the capillary tube from 10 mm (which is the case in the MBs) to 12 mm.

11.3.5 Impact on beam dynamics

The bending angle of the beam is kept the same thanks to the same integrated field generated by the pair of 5.5 m-long 11 T dipoles as by a standard main dipole magnet (MB).

The field quality is worse than for the one of a standard MBs, in particular the sextupole component b_3 is larger. The latest field quality table of the 11 T dipoles can be found in Ref. [12] and the field quality of each MBH will be measured in detail at cold. Beam dynamics studies [13] have shown that the expected field quality is such to leave dynamic aperture essentially unaffected, both at injection and collision energy, given the limited number of magnets which will be installed.

The field stability is similar, as the 11 T dipoles are connected in series with the MBs, so the main current in all magnets is identical during standard operation. The trim power converters have a marginal impact. The flux jump amplitudes are too small to have a significant impact on orbit and emittance. Short lifetime dips are however to be expected, even if their amplitude should not present a risk for operation.

The same type and number of spool pieces as currently installed in the MBs will be installed in the 11 T dipoles (LBBRB.9L7: MCS, for symmetry reason a MCDO will be installed but not connected to the circuit to mimic the type B dipole; LBARA.9R7: MCS and MCDO).

Unlike the main dipoles, the 11 T magnets are straight. The exact installation position considering the sagitta is given in the layout database.

11.3.6 Operation under radiation

The MBH will, inevitably, see a shower of particles from the DS collimator. The dose estimates at the foreseen locations of the 11 T dipole full assemblies around IP7, including at the level of the cold diode, have been computed in Ref. [14]. The peak dose in the coils remains below 2 MGy and will be limited to few kGy at the level of the cold diode. These predictions rely on the assumption that 10^{17} protons are lost in IR7. These levels of radiation are acceptable for the magnet components.

11.3.7 Installation and dismantling

Full reference for the integration is given in Ref. [15] and the information for installation in the HL-LHC is provided in Ref. [2].

11.3.8 Cryogenics

11.3.8.1 Cooling

Although the cooling layout is similar to that of an MB, the heat extraction capacity in the MBH is quite different from the MBH due to construction specificities of the Nb_3Sn coils, in particular because they are impregnated and can function for coil temperatures exceeding the lambda point of helium (2.17 K). In both magnet cases, the cold source is formed by a bayonet heat exchanger protruding the upper yoke-hole. Whereas the MB has radial connections open to helium from the annular space in between the coil-inner layer and beam-pipe to this cold source, the coils of the MBH do not. Adding such radial connections in sufficient amount for a measurable improvement in effective cooling, specifically through the titanium pole of the coils, is for the moment considered not feasible. Therefore, instead of radially, the heat extraction for temperatures below the lambda point will take place via conduction over the magnet length through the helium contained in the annular

space between beam-pipe and inner-coil layer towards the magnet ends. Given a cold bore of 54.5 mm diameter (53 mm + Kapton® insulation), an inner coil diameter of 59.8 mm and a magnet length of 5.5 m, the maximum heat extraction capacity at 2.1 K is evaluated to 1.7 W/m (9.3 W total). This is approximately a factor 3 above the requirement. Therefore, radial cooling channels through the coil will not be required as long as the annular space around the beam pipe towards the magnets-ends remains unobstructed and thus free for the helium. In addition, for coil temperatures exceeding the lambda point the MBH will be able to conduct heat away through the outer coil surface across the electrical insulation layers. Assuming an electrical insulation equivalent to ~600 µm of Kapton, the heat exchange coefficient is approximately 7.7 W/K.m for the two apertures combined, i.e., 21 W per two apertures and over 5.5 m length for outer layer coil temperatures 0.5 K above the helium bath temperature.

11.3.8.2 Quench-induced pressure

In the absence of radial escape channels for the helium from the annular space around the beam-pipe an assessment of possible pressure build-up in this area has to be made. This with reference to experience with the MBs where, in case this radial escape path was blocked, dangerously high pressures develop [16][17]. We do not expect this to be an issue due to the fact that:

- The Nb_3Sn coil is fully impregnated, thus eliminating the effects due to helium in close contact with the cable;
- The helium escape path along the annular space around the beam-pipe is much wider than in the MB;
- The escape path is much shorter as the magnet is only ~5.5 m long.

11.4 Inventory of units to be installed and spare policy

Besides the units required for installation (see Section 11.1) one full spare assembly of the connection cryostat full assembly and the 11 T dipole full assembly will be produced. The components for the full assembly spare unit of the connection cryostat are available, the spare full assembly of the 11 T dipole magnets is planned to be finalized in 2021.

11.5 Quality assurance

The fabrication of the parts of the 11 T dipole full assembly and of the connection cryostat full assembly comply with the HL-LHC Quality Assurance Plan, whose implementation started at the beginning of the prototyping phase. A dedicated Quality Assurance team ensures systematic update of the relevant documentation: drawings, test reports, technical specifications, work instructions, and Manufacturing and Inspection Plans (MIP). The documentation is classified in the CERN reference databases, EDMS and CDD, where it can be easily retrieved.

Each production step is checked and documented following the MIP in order to provide adequate traceability level for each performed operation.

11.6 References

[1] R. Bruce *et al.*, Installation in IR2 of dispersion suppressor collimators (TCLD), EDMS: 1973010.

[2] D. Schoerling *et al.*, Installation of the 11 T Dipole Full Assembly in LHC P7 (HL-LHC WP11), EDMS: 1995306.

[3] D. Schoerling *et al.*, Installation of the Connection Cryostat Full Assembly in the LHC P2 (HL-LHC WP11), EDMS: 1973010.

[4] Zlobin A.V. (2019) Nb_3Sn 11 T Dipole for the High Luminosity LHC (FNAL). In: Schoerling D., Zlobin A.V. (eds) Nb_3Sn Accelerator Magnets. Particle Acceleration and Detection. Springer, Cham, DOI: 10.1007/978-3-030-16118-7_8.

[5] B. Bordini *et al.* (2019) Nb_3Sn 11 T Dipole for the High Luminosity LHC (CERN). In: Schoerling D., Zlobin A.V. (eds) Nb_3Sn Accelerator Magnets. Particle Acceleration and Detection. Springer, Cham, DOI: 10.1007/978-3-030-16118-7_9.

[6] Summary of the 382nd LMC Meeting held on 21st August 2019, INDICO: 847537.

[7] C. Bahamonde and A. Lechner, Needs for shielding in the connection cryostats in IR2 DS, 14th TCC, 01/09/2016, INDICO: 559125.

[8] M. Gonzalez de la Aleja, WP11: Point 2 Connection Cryostat Full Assembly Integration Study, EDMS: 1904996.

[9] Heat Load Working Group, web page.

[10] A.V. Zlobin *et al*, Design and fabrication of a single-aperture 11 T Nb_3Sn dipole model for LHC upgrades. IEEE Trans Appl Supercond 22(3):4001705, 2012, DOI: 10.1109/tasc.2011.2177619.

[11] G. Willering *et al*., Cold powering tests, HCLMBHB001-CR000002, EDMS: 2211895.

[12] S. Izquierdo Bermudez, Field quality table, Intranet field quality web page.

[13] L. Fiscarelli *et al*., Field Quality of MBH 11 T Dipoles for HL-LHC and Impact on Beam Dynamic Aperture, IEEE Trans. Appl. Supercond. 28 4004005, DOI: 10.1109/TASC.2018.2792424.

[14] C. Bahamonde Castro, R2E levels for installation of 11T in cell 9, 62nd TCC meeting, INDICO: 776391.

[15] M. Gonzalez de la Aleja (WP15), WP11: 11 T Dipole full assembly integration study, EDMS: 1904620.

[16] Lebrun, P. *et al*., Investigation of quench pressure transients in the LHC superconducting magnets, 15th International Cryogenic Engineering Conference, Genoa, 1994, pp.705-708. CERN-AT-94-16-CR-MA.

[17] Wahlström, T., Investigation of quench pressure transients in the LHC superconducting magnets, 1994, CERN-AT-94-46.

Chapter 12

Vacuum system

V. Baglin[1*], *P.* Chiggiato[1], *C. Garion*[1] *and G. Riddone*[1]

[1]CERN, Accelerator & Technology Sector, Switzerland
[*]Corresponding author

12 Vacuum system

12.1 Overview

The luminosity upgrade programme (HL-LHC) requires modifications of the present LHC's vacuum system, in particular in the triplets, crab cavities, matching section and experimental areas. Such modifications must follow guidelines similar to those followed for the present machine. The increased stored current implies a higher thermal power in the beam screen from the image current moving along with the stored particles and stronger synchrotron radiation (SR) and electron cloud (EC) effects, which in turn translate into higher degassing rates.

One of the main tasks of the HL-LHC vacuum work package is to produce new beam screens in the new superconducting (SC) Inner Triplet (IT) and D1-D2 magnets together with the vacuum layout along the Insertion Region (IR). It is also necessary to assemble and insert with the beam screens high-density shielding material into IT magnets. This is mandatory for protecting the magnets from collision debris coming from the experiments' interaction points (IPs). A balance between cold bore size and vacuum pumping system is defined based on experience gained with the present machine and recent advances with new materials. Indeed, a number of new ideas have emerged recently for the mitigation of the e-cloud effect in cryogenic beam pipes: amorphous carbon (a-C) coating for which validation is ongoing and laser structured surface currently under study.

The change of the aperture of the IT at IR1 and IR5 implies that the experimental vacuum chambers of CMS and ATLAS require a review of aperture, impedance, and vacuum (dynamic and static). The forward regions of CMS and ATLAS will need to be adapted to cope with the new beam geometry in IR1 and IR5. New vacuum systems at the tunnel/cavern interfaces are needed to mitigate the additional activation from the increased luminosity. New access procedures and tooling will be also needed to allow the minimization of the integrated dose to personnel. With the HL-LHC, less flexibility will be available for the optics of LHCb and ALICE; therefore, the vacuum chambers at IR2 and IR8 must be validated for operating conditions to ensure that these chambers do not impose a limitation. *In-situ* a-C coating of the beam screens of the IT magnets, located in LSS2 and 8, is under validation to reduce the electron cloud heat load onto the cryogenic system. Finally, positions of mechanical supports, pumps, and gauges must be analyzed to ensure that layouts are optimized for the new machine configuration. Bake-out equipment will be redefined depending on activation and specific needs. To deliver good vacuum conditions, all chambers held at room temperature must be treated with Non-Evaporative Getter (NEG), to provide low dynamic outgassing with large pumping speed and to minimize secondary electron yield (SEY), to reduce electron cloud effects.

12.2 Beam vacuum requirements

The HL-LHC beam vacuum system must be designed to ensure the required performance when beams with HL-LHC nominal parameters circulate ($L_{peak} = 5 \times 10^{34}$ cm^{-2} s^{-1}, $L_{int} \sim 3$ ab^{-1}). By using engineering margins, the system must be designed for the HL-LHC ultimate performance ($L_{peak\ ult} = 7.5 \times 10^{34}$ cm^{-2}s^{-1}, $L_{int\ ult} \sim 4$ ab^{-1})[1].

The vacuum system must be designed

- to avoid pressure runaway induced by ion-stimulated desorption,
- to satisfy the vacuum lifetime,
- and to provide low background to the experiments induced by beam-gas collisions.

The design considers the effects of synchrotron radiation, electron cloud, and ion-stimulated desorption from the walls. Heat load onto the beam vacuum chamber walls or flanges and beam impedance effects must also be taken into account [2].

The system must be compatible with the global LHC impedance budget and the designated machine aperture.

The average gas density along the ring must satisfy a maximum level of heat load into the cold mass as defined by the 100 h vacuum lifetime due to nuclear scattering, i.e. less than 1.2×10^{15} H_2 molecules m^{-3} equivalent in the LHC [3]. The corresponding heat load into the cold mass is therefore limited to ~ 80 mW/m when both beams circulate. Since this acceptable gas density limit decreases proportionally to the inverse of the beam current, the HL-LHC vacuum lifetime is set to 200 h. Table 12-1 gives the molecular gas densities yielding a 100 h vacuum lifetime in the LHC and 200 h vacuum lifetime in the HL-LHC assuming the presence of a single gas species in the vacuum system.

Table 12-1: Single gas species molecular gas density (m−3) to satisfy 100 h vacuum lifetime in the LHC and 200 h vacuum lifetime in the HL-LHC [3].

Machine	**I A**	**H_2 m^{-3}**	**CH_4 m^{-3}**	**H_2O m^{-3}**	**CO m^{-3}**	**CO_2 m^{-3}**
LHC	0.58	1.2×10^{15}	1.8×10^{14}	1.8×10^{14}	1.2×10^{14}	7.9×10^{13}
HL-LHC	1.09	6.4×10^{14}	9.6×10^{13}	9.6×10^{13}	6.4×10^{13}	4.2×10^{13}

The average gas density along IR1, IR2, IR5, and IR8 must also ensure that the background to the LHC experiments remains at acceptable levels [4][5]. In the absence of specified values from the LHC experiments themselves, the LHC design value will be scaled to the HL-LHC parameters as shown in Table 12-2 where the gas density is expressed in H_2 equivalent. Therefore, for HL-LHC, the designed average gas density in the IR1&5 (mainly dominated by the cryo-elements and other beam equipment such as collimators, masks etc.) equals 2.8×10^{12} H_2 equiv/m^3 which correspond to a pressure of 1×10^{-10} mbar assuming the solely presence of hydrogen in the vacuum system.

Table 12-2**:** H_2 equivalent gas density (H_2 equiv/m^3) design value for the LHC high luminosity experiment and IRs [4][5]and for the HL-LHC.

Machine	**I A**	**ATLAS H_2 equiv/m^3**	**CMS H_2 equiv/m^3**	**IR1&5 H_2 equiv/m^3**	**IR2&8 H_2 equiv/m^3**
LHC	0.58	1.5×10^{11}	3.1×10^{12}	5.3×10^{12}	6.5×10^{12}
HL-LHC	1.09	8.0×10^{10}	1.6×10^{12}	2.8×10^{12}	3.5×10^{12}

12.3 Vacuum layout

The vacuum layout must ensure the vacuum requirements for circulating beams with the HL-LHC nominal parameters. The system must be designed for the HL-LHC ultimate luminosity, without margin.

- All beam vacuum elements must be leak tight (leak rate less than 10^{-11} mbar. ℓ/s He equivalent), clean according to CERN vacuum standards, and free of contamination *e.g.* grease, oil, fingerprints.
- According to the LHC baseline [3], the vacuum system in the Long Straight Sections (LSS) must be sectorized with gated valves, see in Figure 12-1 a schematic of the HL-LHC sectorisation on the left side of IP1 and 5. The vacuum sectorization is delimited by cold-to-warm transitions, length of vacuum sectors, or specificity of components (fragility, maintenance, etc.) [6].
- Vacuum sector valves must be installed at each cold-to-warm transition in order to decouple the room temperature and cryogenic temperature vacuum systems during bake-out, cool-down, installation, and commissioning phases.
- The distance between the vacuum sector valve and the cold-to-warm transition must be minimized in order to reduce the length of the beamline that is not baked-out in situ.
- Dedicated vacuum instrumentation must be provided close to and on both side of each sector valve for beam interlocking and along any vacuum sector for diagnostics.
- Sector valves must be remotely controlled and interlocked in order to dump the circulating beam in the case of malfunctioning. The LHC and the HL-LHC vacuum sectorizations delimit two types of vacuum system:
  - room temperature vacuum system,
  - cryogenic temperature vacuum system.

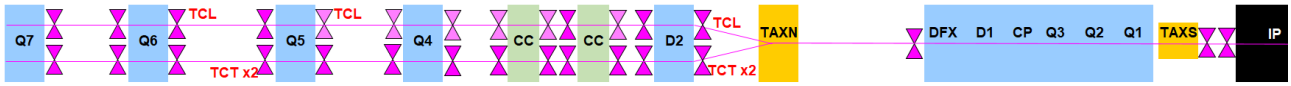

Figure 12-1: Schematic of the HL-LHC vacuum sectorisation of all the cryo-elements from the interaction point (IP) to Q7.

- The vacuum system shall be integrated in the tunnel and cavern volumes with the permanent/mobile bake-out system, bake-out racks, quick flanges collars, mobile pumping systems, and diagnostics systems. The corresponding space must be reserved into the tunnel integration to allow a proper access and operation of the vacuum system. At present, detailed studies were conducted for the TAXS, DFX, TAXN-D2 and CC areas, see e.g.[48].
- Integration studies must also be performed for installation and un-installation phases of equipment to identify potential conflicts.
- Integration and installation drawings must be circulated and validated before installation in the tunnel and caverns.
- The vacuum chamber aperture is defined by the beam optics system, the beam impedance, by machine protection, and background considerations of the experiments. The aperture of the vacuum chamber must not be the limiting aperture [49].
- All components to be installed into the vacuum systems must be approved and their vacuum performance validated before installation.
- A maximum number of LHC beam vacuum components will be reused for the HL-LHC upgrade. The present vacuum layout design foresees to reuse about 56 sector valves, 120 vacuum chambers and 144 vacuum modules.

- High radiation areas along the LSS identified at an early stage of the design, highlighted positions where remote handling/tooling might be preferred and positions where instrumentation must be radiation resistant [15]. The present vacuum layout design foresees remote handling in the TAXS area (see Section 12.5) and remote tooling for the DFX and TAXN-D2 areas.
- When needed, irradiation tests of specific components (instruments, bake-out jackets, cables, electronics, O-rings, etc.) must be conducted to demonstrated that they meet the radiation dose specifications.
- The vacuum work package spares policy follows the general A&T sector policy. The defined spares policy benefits from large quantity orders, in particular for highly specialized equipment such as beam screens, cold bores, cold warm transitions and standard equipment such as modules, vacuum chambers, sector valves etc [20].
- Similar to the LHC construction, cryogenic elements must be installed first, then room temperature vacuum sector valves, followed by completion of the room temperature vacuum sectors.
- Time, resources, and space to allow the temporary storage of LHC vacuum components, which need to be dismounted to allow the HL-LHC infrastructure modifications and equipment installation, will be evaluated in the next phase of the project.

12.3.1 Room temperature vacuum system

Standard vacuum chambers and vacuum modules will connect the machine components. Similar to the LHC vacuum system, all components must be bakeable (230°C ±20°C for NEG coated vacuum chambers and 300°C ±20°C for uncoated stainless-steel beam pipes). The vacuum system layout is designed to fulfil the stated requirements throughout a full run [3][25].

The current LHC circular vacuum chambers variants are 80 mm, 100 mm, 130 mm, and 212 mm ID: any further variants needed for the HL-LHC will be kept to the minimum necessary. The present HL-LHC vacuum layout, still under development, requires the introduction of 150 mm, 250 mm ID as new circular vacuum chamber standard to accommodate the required beam aperture between D1 and D2 [21].

An exception is the recombination chambers installed into the TAXN absorber, which by definition is not circular. The present HL-LHC recombination chamber, still under development, is based on two 88 mm ID chambers, installed coaxially to the beam path, merging into a 250 mm ID chamber [22].

Vacuum chamber transitions (VCT), which give offsets and adaptations between pipe apertures, must be integrated into the concerned equipment by the equipment owners themselves at the early design stage, e.g. beam monitors, superconducting cavities, quadrupole masks, etc. in agreement with the vacuum, surface and coating group of the CERN Technology department. The present HL-LHC vacuum layout requires the production of 4 VCTs to accommodate 250/212 mm apertures and 212/150 mm apertures.

The vacuum chambers are aligned within ±3 mm accuracy. Better tolerance will require the installation of survey targets on the vacuum chamber, their fiducialisation and their alignment with the support of the survey team. In this latter case, the vacuum equipment may be aligned within ±0.2 mm accuracy at best. Alignment of other equipment is the responsibility of the survey team.

Remotely aligned components require a radial stroke of ±2.5 mm by design. Therefore, all transitions between remotely aligned components and fixed components shall have a deformable RF bridge. The present vacuum layout design foresees two remotely aligned sector valve assemblies located upstream and downstream to D2. The other vacuum components have large enough apertures to remain fixed to the ground or are supported by remotely aligned components to be compatible with the full remote alignment system (FRAS) [50][51].

The supporting system of the new HL-LHC room temperature vacuum component is based on an upgrade version of the LHC supporting system, ALARA approach and FRAS requirements. Specific supports

are under design for new vacuum chamber standards, vacuum components located next to deformable RF bridges and remotely aligned sector valve assemblies. Upgraded supports are foreseen for some LHC-like sector valve assemblies and vacuum chambers. In the ALARA context, some supporting system may be aligned during initial installation and allow a disconnection / reconnection of the vacuum device without further re-alignment.

The choice of the vacuum chamber material between Cu-alloy and stainless steel (either Cu coated or bare) is dictated by beam impedance and production constraints. In the LHC, ID apertures up-to 130 mm are made of bulk Cu. Al- alloys are preferred in high-radiation areas.

Connections between equipment must be made by ConFlat® bolt technology unless radiation issues and/or remote handling require the use of quick-release flanges with, for example, chain clamps.

12.3.2 Cryogenic temperature beam vacuum system

The cryogenic beam vacuum system must be tightly decoupled by sector valves from the room temperature vacuum system. Dedicated instruments must be provided close to the sector valves to allow atmospheric evacuation roughing, monitoring, and safety against overpressure of the beam vacuum vessel.

A cold-to-warm transition must be integrated into the cryogenic beam vacuum sector at each extremity of the cryogenic system.

A continuous cold bore, i.e. without penetrating welds between the beam vacuum and helium enclosure, ensures leak-tightness between the superfluid helium and beam vacuum along the cryogenic beam vacuum sector. The LHC nominal cold bore temperature is 1.9 K in the arcs.

A beam screen must be inserted into the cold bore to extract the beam-induced heat load at a temperature higher than 1.9 K. The beam screen must be perforated with slots (4% transparency in the LHC arcs) to allow pumping into the cold bore space [3]. The LHC beam screen operates from 5 K to 20 K. The HL-LHC beam screens of the IT quads, corrector package and D1 will operate at a higher temperature, between 60 K and 80 K [52], to cope with the much higher heat load (15–25 W/m). When required, in situ heating of the LHC beam screen up to 90 K, with cold bore < 3 K, is used to flush the condensed gas present on the beam screen inner surfaces towards the cold bore. Owing to the presence of a-C coating, the value is increased to 120 K for the HL-LHC beam screens [52]. This heating cycle may be performed after a long technical stop or even between physics fills. For the new beam screens built for the HL-LHC project, the surface area of the beam screen perforation will be scaled to the HL-LHC parameters, hence doubled, and therefore increased as compared to the LHC.

When a cold bore operates at 4.5 K, cryo-absorbers are installed outside the beam screen in order to provide hydrogen pumping speed and capacity [3]. Cryo-absorbers are mandatory for cold bores operating above 2.8 K. Cryo-absorbers shall be placed outside the beam screen and thermally anchored on it. In situ heating of the beam screen up to 90 K is required for the cryo-absorbers regeneration [3].

In the cold part of the LHC, the maximum length without beam screen is less than 1 m (with the exception of superconducting cavities). This LHC design value will be scaled to the HL-LHC parameters and therefore reduced.

For the HL-LHC, the beam screen aperture is derived from beam optics and magnet aperture inputs, for details see Table 12-3 and Table 12-4 in the beam screen design section.

12.4 Insulation vacuum

The insulation vacuum system ensures the performance of the cryogenic system by eliminating the heat losses due to gas convection. The insulation vacuum systems under the responsibility of TE-VSC include the cryogenic distribution line (QRL) and cryogenic machine components up to a vacuum barrier, but exclude transfer lines outside the LHC tunnel and those of the experimental cavern, unless specifically agreed with the equipment owner.

The requirements of the insulation vacuum system for the HL-LHC can be summarized as follows:

- the pressure must be below 10^{-5} mbar;
- the helium leak rate, at the component level, must be below 10^{-10} mbar ℓ/s;
- it must be compatible with the LHC insulation vacuum system [3];
- it must be built with the same standards used for the LHC insulation vacuum system.

The QRL and the magnet cryostats are mechanically connected via specific bellows and pipes assemblies called jumpers. However, the insulation vacuum of the QRL and continuous cryostat is sectorized through vacuum barriers. There is no sectorization of the QRL in the LSS of the LHC. Sectorization of the HL-LHC cryostats shall ensure that longitudinal leak location techniques can be employed. Connection to cryo-plant or transfer lines outside the LHC tunnel shall be delimited by vacuum barriers.

Figure 12-2 shows, for the present baseline, a schematic of the insulation vacuum equipment which is under the scope of WP12. These components are in connection with the beam vacuum on one side and delimitated by a vacuum barrier on the other side. Equipment over the vacuum barrier are outside the scope of WP12. The purpose of this geographical separation is to ensure that any malfunctioning of an insulation vacuum sector, under the responsibility of VSC, will not alter the beam vacuum performance. The present layout, still under study, foresees the creation of 11 insulation vacuum subsectors per IP side (the LHC has only 5 insulation vacuum sectors per IP side).

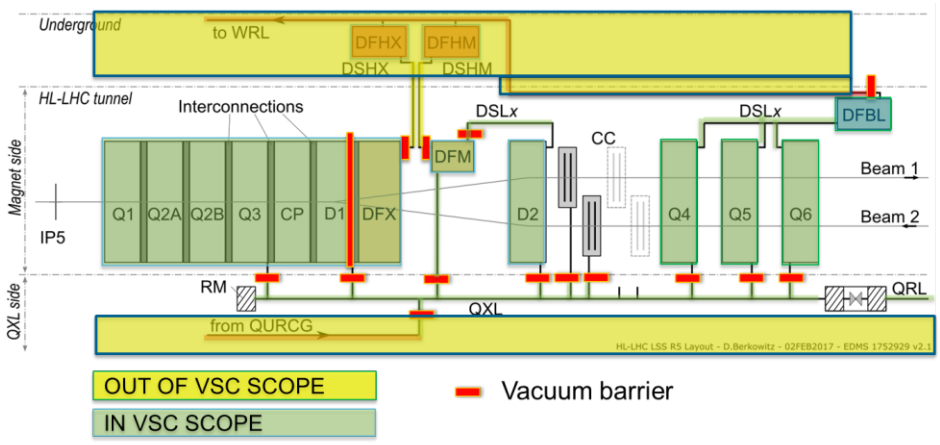

Figure 12-2: Schematic of the HL-LHC insulation vacuum layout. Insulation vacuum equipment under the VSC scope (defined by the vacuum barrier position) are highlighted in green.

The insulation vacuum relies on cryopumping during normal operation. Fixed turbomolecular pumping groups are used for pumping before cool-down. This system also mitigates the impact of possible helium leaks during operation, therefore runs constantly. Such pumps are also used for the detection of helium or air leaks. Dedicated pumping ports are employed for rough pumping groups, pressure gauges, pressure relief valves, longitudinal leak localization techniques, and additional pump placement in case of operational leaks. A bypass equipped with isolation valves is installed between subsectors. The standard for pumping ports is the ISO-K DN 100 flange. Each insulation vacuum volume must be equipped with pressure relief valves. Elastomer seals (Viton, NBR) are used where system disassembling is necessary (interconnections, instrumentations, etc.).

For the HL-LHC project, in high radiation areas, specific seals (metals or hard-rad polymers) have to be installed on new equipment and be used to replace standard seals on any retained equipment.

12.5 Experimental vacuum system

The experimental vacuum system is located between Q1L and Q1R of each interaction point. Similarly to the LSS, the vacuum layout of each experimental vacuum system must ensure the vacuum requirements when

beams with the HL-LHC nominal parameters circulate. The system shall be designed for the HL-LHC ultimate performance, without margin [25]. Therefore, all constraints and requirements defined in Section 12.3 apply also in this Section.

During long beam stops (> 10 days), ultra-pure neon venting is needed to protect the fragile experimental vacuum chambers from deformations caused by possible mechanical shocks. The baseline is that there will be no work in the vicinity of the vacuum chambers while they are under vacuum.

The vacuum chamber supporting system must be compatible with standard activities performed in the experimental cavern during short stops (e.g. winter technical stops). In particular, no personnel are allowed in the vicinity of the beam pipe (< 2 m radius) during these phases.

As for the present LSS vacuum system, all machine components operating at room temperature must be bakeable and NEG coated.

Accidental or scheduled air venting for repair or maintenance of any of the vacuum sectors of the experimental vacuum system implies a complete NEG recommissioning of the beam pipes, i.e. two bake-out cycles, the first for the bake-out of the metallic part, the second for NEG activation.

12.5.1 High luminosity experiments: ATLAS and CMS

ATLAS and CMS LHC vacuum layout drawings are described in Refs. [7] and [8] and not discussed here. The secondary particles absorber, TAXS, is located at the interface between the tunnel and the experimental cavern.

At the tunnel extremity, as shown in Figure 12-3, left side, the instrumentation of the Q1–TAXS areas is minimized to prevent from personnel access after the installation. The present baseline foresees a simple connecting bellow and two ion pumps between Q1 and TAXS chambers. The connecting bellow is surrounded by an insulating vacuum to minimise the impact of potential leaks into the beam vacuum system.

At the cavern extremity, a complete and robust decoupling between the two complex and delicate IT and experimental vacuum sectors, is obtained by two vacuum sector valves sitting almost side by side, see Figure 12-3, right. The vacuum sector defined by these two sector valves is named hereafter ‘buffer’.

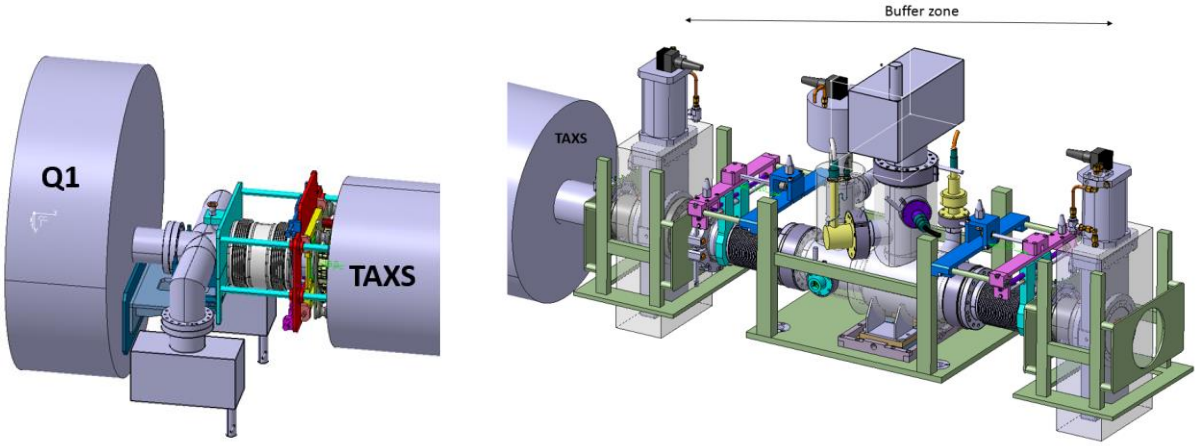

Figure 12-3: Schematic of the HL-LHC high luminosity experiments instrumentation areas. Left, connection between Q1 and TAXS. Right, buffer zone between sector valves.

On both sides of ATLAS and CMS caverns, a vacuum system is installed in the buffer zone to allow neon venting, pump-down and vacuum commissioning during NEG activation of the ATLAS and CMS experiment. A rupture disk is also installed in this system to protect the experimental vacuum chambers in case of liquid helium inrush.

The following are required to avoid personnel intervention in a high radiation area:

- A pumping and neon venting systems will be installed in the buffer zone on both sides of ATLAS during LS3 to complement the left-hand side [9].
- Remote tooling and handling are foreseen to avoid personnel intervention [15]. Quick type flanges are mandatory. Welds are preferred to flanges.
- Installed components must be robust: in particular, sliding fingers in RF bridges are forbidden.

The bake-out system must be permanent and fully integrated with the other systems from the design phase.

It is assumed that the ATLAS central beam pipe inner diameter, as installed during LS1, remains the same until at least LS4 [9].

According to Ref. [10], the following are assumed.

- The CMS central beam pipe inner diameter, as installed during LS2 remains the same until at least LS4.
- End cap, HF, CT2, and forward pipes of the CMS vacuum system will be upgraded to Al bulk material during LS2. No mechanical intervention between +/- 16 from the IP is therefore expected during LS3.
- A permanent bake out system will be installed at CMS during LS2, with the exception of the central Be chamber.

Since the TAS needs to be replaced during LS3, and a new ‘buffer zone’ will be installed, the vacuum system located inside the experimental cavern needs to be adapted and recommissioned, i.e. requiring NEG activation even if no changes to the vacuum system inside the cavern is foreseen.

12.5.2 ALICE and LHCb experiments

ALICE and LHCb vacuum systems are not part of the HL-LHC upgrade. However, their vacuum system is still upgraded during LS2 and LS3. The interested reader may refer to Refs. [11][12][13] and [14] for detailed documentation.

12.6 Beam screen design

Beam screens are inserted into cryogenic cold bores to guarantee the vacuum performance. They are part of the LHC vacuum system baseline [1]. The HL-LHC beam screen must be compatible with vacuum, impedance and cryogenic, including e-cloud, requirements of LHC [3][25].

In order to operate properly, the beam vacuum system must be evacuated, before cool-down, for, at least, five consecutive weeks, to allow the outgassing rate of adsorbed water to be reduced to acceptable levels.

During cool-down of a cryogenic system, the cold bore must be cooled first to minimize gas condensation onto the beam screen.

In the case where gas condenses onto the beam screen during operation, e.g. after a magnet quench, a transfer of this gas towards the cold bore via beam screen heating may be needed. This procedure should be carried out in a couple of days.

The HL-LHC beam screen must be inserted during the cryostating phase prior to tunnel installation. The surface of the beam screens must be kept clean during assembly. This implies that the beam screen is installed at the last stage of cryostating. Without specific tooling, procedures and approval from the vacuum group, no probe or device can be inserted into the vacuum system once the beam screens are installed.

The cooling tubes must be dimensioned to allow a proper cooling of the system during operation within the limits defined above.

According to vacuum standards, full penetrating welds are forbidden in the vessel wall separating the beam vacuum and helium enclosures.

Depending on the location, two types of beam screens exist: shielded and non-shielded beam screens. The shielded beam screens intercept part of the debris produced at the high luminosity IPs, thereby protecting the cold masses from radiation-induced damaged. In Q1, the beam screen surface shall withstand a dose of 1 GGy during its lifetime.

The selected beam screen material is P506 non-magnetic stainless steel, same material as present LHC beam screens. Copper is co-laminated with the stainless steel for impedance reasons. The thickness of the Cu layer is 75 μm.

Amorphous carbon (a-C) coating is the baseline for the inner surface of the HL-LHC shielded and non-shielded beam screens. Due to a-C's properties, electron multipacting suppression in these HL-LHC components and photon stimulated gas load comparable to copper are expected [26][27]. Amorphous carbon coating will be applied to the HL-LHC beam screens when needed for the reduction of heat load to cryogenic systems, reduction of background to experiment, and/or beam physics requirements.

The present state of the art of the in-situ coating process has led to the decision to produce during LS2 a-C coating of beam screens located in Q5R2, Q6R2, Q6L8 and Q5L8 of the LHC [23]. The parameters used for this coating are a first layer of 150 nm thick Ti, to provide adherence and to reduce the beam screen outgassing during coating, and a 50 nm thick, top layer of carbon. During the deposition of the carbon layer, Ti is also deposited to provide pumping during the coating process of hydrogen and water molecules to keep the maximum secondary electron yield below 1.1. The overall thickness of the Ti layer will not exceed 500 nm in order to maintain the overall impact on impedance negligible [24].

Amorphous carbon coating shall be the last step of beam vacuum preparation before lowering the magnet into the tunnel, avoiding any subsequent insertion of tooling or other devices into the beam vacuum line.

For IP2 and IP8, in situ coating of the present beam screen (or alternatively laser surface structuring) must be studied and conducted during the long shutdown (LS2 and LS3). If in situ coating or other treatments are not possible, removal of the magnet cryostat will be considered to allow beam screen exchange. The present baseline foresees the in-situ coating of the four ITs and six standalone magnets, namely D1Q3Q2Q1L2, D1Q3Q2Q1R2, D2Q4R2, Q5R2,Q6R2, Q6L8, Q5L8, D2Q4L8, D1Q3Q2Q1L8, D1Q3Q2Q1R8 [28].

For IP1 and IP5, new beam screens will be coated during RUN 3 and reused beam screen will be coated at the surface during LS3 for upgrade of the magnets. The present baseline foresees the coating of the following new magnets: D2L1, D1CPQ3Q2Q1L1, D1CPQ3Q2Q1R1, D2R2 and D2L5, D1CPQ3Q2Q1L5, D1CPQ3Q2Q1R5, D2R5. The coating of the LHC upgraded magnets is planned for Q5L1, Q4L1, Q4R1, Q5R1 and Q5L5, Q4L5, Q4R5, Q5R5 [28]. The beam screens of the non-crabbed beam pipes inside the crab-cavity cryomodules are also coated [53].

Laser treated surfaces are considered as an alternative treatment to the a-C coating for electron multipacting mitigation. The technology is presently under development for a potential laser treatment of some LHC beam screens [29]. The process offers the advantage to be held under atmospheric pressure but still needs studies to mitigate the dust production and impedance aspects.

In the LHC arcs, a sawtooth structure was produced on the beam screen walls (dipoles and quadrupoles). The structure was designed to intercept the synchrotron radiation at perpendicular incidence to decrease the photoelectron yield and forward scattering of light. Owing to reduced synchrotron radiation in the LSS, such a specific structure was not required for the new HL-LHC beam screens.

12.6.1 Shielded beam screen

The HL-LHC shielded beam screens are to be inserted into the HL-LHC D1, CP and FT of LSS1 and LSS5. These beam screens ensure the vacuum requirements, the shielding of the cold mass from physics debris, and the screening of the 1.9 K cold bore cryogenic system from beam-induced heating.

As a baseline, the shielded beam screen is assumed to fulfil the vacuum requirements with a-C coating operating at a higher temperature than 5-20 K [16]. Recent laboratory studies have demonstrated that a possible operating temperature of the a-C coated shielded beam screen range from 60 to 80 K [30][53].

The selected shielding material is a tungsten heavy alloy, Inermet® 180. It is a sintered tungsten-based composite material with around 95 wt% of tungsten, 3.5 wt% of nickel and 1.5 wt% of copper. The electrical, thermal, magnetic and mechanical properties of the materials from different suppliers have been measured at room and cryogenic temperatures [17]. In the 60–80 K range, Inermet® 180 has an electrical resistivity of 4 10^{-8} Ω.m, a magnetic susceptibility in the order of 10^{-4} and a thermal conductivity of 75 W m^{-1} K^{-1}.

The shielding is made of 40 cm long tungsten alloy blocks, which must be accommodated on the beam screen structure [18]. Figure 12-4 shows a concept based on a mechanical assembly of the tungsten absorbers [19].

As for the standard LHC beam screen, the shell is perforated with oblong holes (slots) to provide sufficient pumping speed of the desorbed gas. These slots are screened by a shield to prevent the cold bore surface from electrons bombardment. The inner side of this electron shield is coated with a-C [28].

The pumping speed of the beam screen slots, computed with Molflow, equals 600 ℓ/s per meter of tube for nitrogen at 20°C. The electron shields reduce this pumping speed to 430 ℓ/s per meter of tube, slightly larger than the LHC arc beam screen-electron shield assembly (365 ℓ/s per meter of tube for nitrogen at 20°C) [31]. The shielded beam screen transparency set to 2% provides a total surface area for the slot of 60 cm^2/m.

The cooling is provided by four 10 mm diameter tubes. Copper strips are installed between the absorbers and the cooling tubes to assure a good heat transfer.

The tungsten blocks are positioned on the beam screen by pins, welded onto the shell. Dedicated slots are used on one side of the block to allow differential thermal contraction.

The beam screen is supported in the cold bore by a titanium spring ceramic ball system [32]. Vibration study has been carried out [33]. Natural frequency of the first mode is expected at around 13 and 20 Hz for the Q1 and Q2, respectively. High damping occurs due to Coulomb friction and magnetic forces.

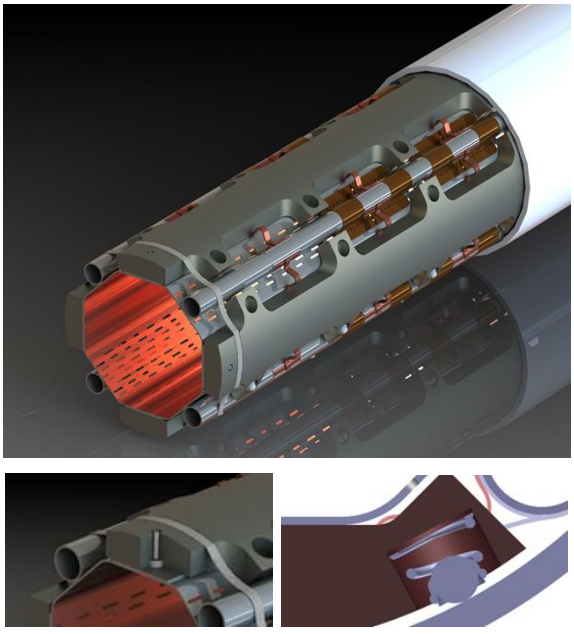

Figure 12-4: Mechanical design of the beam screen with tungsten shielding (for illustration, one electron shield has been removed from the top image to show the slots behind). Top image, cold bore and beam screen assembly, bottom images, details of the tungsten supporting structure (left) and beam screen supporting system (right).

During a magnet quench, the fast decay of the magnetic field leads to the development of Foucault currents that induce Laplace forces, especially in high electrical conductivity material such as copper. A thermomechanical model was developed to study the effect on the structure of a magnet quench [34]. The behaviour of the assembly is driven by the 75 μm thick copper layer and the tungsten alloy absorbers; the typical electrical resistivity is in the order of 2.10^{-10} Ω.m and 4.10^{-8} Ω.m, respectively. The temperature dependence and magneto-resistivity have been considered. Dynamic behaviour and self-inductance effects are implemented in the model as well.

For Q1, the specific resultants of the e.m. forces, per quadrant, are around 40 N/mm and 230 N/mm for the copper layer and tungsten absorbers, respectively.

The beam screen assembly has been designed to be elastic and therefore, during a magnet quench, the tungsten absorbers go in contact with the 4 mm thick cold bore, which can withstand the high magnetic forces. The maximum contact force between the tungsten and the cold bore is around 350 N/mm. The maximum Von Mises stress in the cold bore is around 520 MPa which is below the yield strength (860 MPa). The maximum stress in the beam screen wall is around 580 MPa, whereas the yield stress is around 1150 MPa.

The mechanical assembly is also designed to be compatible with the Coupling Loss Induced Quench (CLIQ) system that is based on a fast transient alternating current unbalanced between the different coils of the magnet. The current evolution being non-monotonic leads to an inversion of the Laplace force direction. For the beam screen and in particular for the tungsten blocks, this induces torques of respectively, 700 N.m and 580 N.m, per beam screen meter, for the absorbers and beam screen tube [35]. The behaviour with fast discharge also in presence of CLIQ has been validated on a Q1 short model test [36].

The heat deposited on the tungsten absorbers is transferred by thermal links to the cooling tubes, in which a helium flow is imposed. The specific thermal load for the whole beam screen is 25 Wm^{-1} and 15 Wm^{-1}, for the Q1 and Q2 beam screens, respectively. A detailed parametric thermal analysis has been also carried out based on [34].

Along the magnet string, the operating temperature windows for the beam screen copper inner layer is 60–80 K. The 20 K temperature increase above the 60 K gas inlet is due for 15 K to the longitudinal temperature gradient along the triplet between Q1 and D1, and for 5 K to the transversal temperature gradient, i.e. between the helium and the copper inner layer. A temperature difference between the helium and the absorbers of up 15.8 K is expected for the Q1 whereas the variation for the copper layer is assessed below 1 K, Figure 12-5.

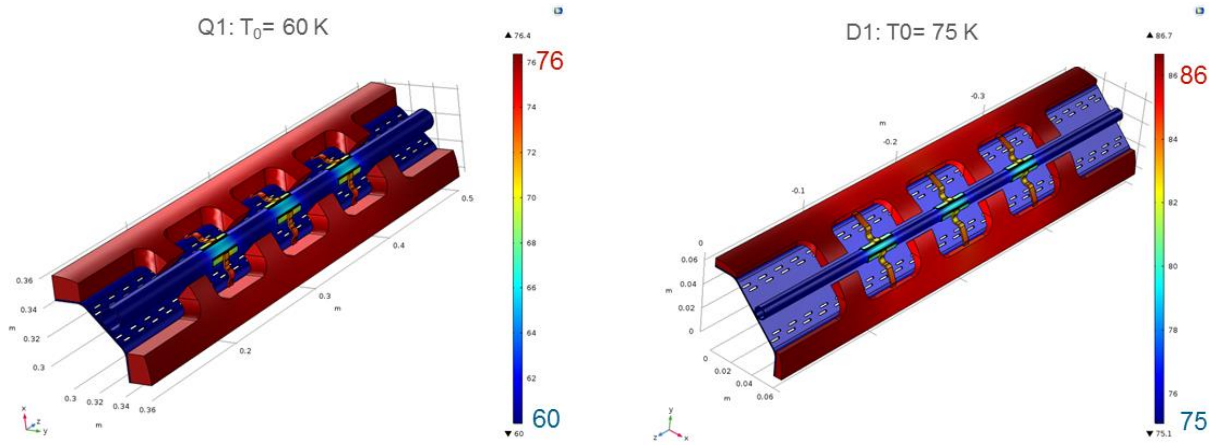

Figure 12-5: Expected temperature field for the Q1 and Q2 beam screens.

The heat transfer is ensured by thermal links in copper, 5 mm^2 cross-section (5 mm width; 1 mm thickness: 2 × 0.2 mm + 6 × 0.1 mm multilayer). Three pairs of links are brazed on the tungsten absorbers. On the other side, an interface plate, 30 mm long, in colaminated copper/P506 stainless steel is welded on

the cooling tube, see Figure 12-6 left side. The thermal behaviour has been assessed on small samples and on a representative 80 cm long beam screen prototype, Figure 12-6, right side.

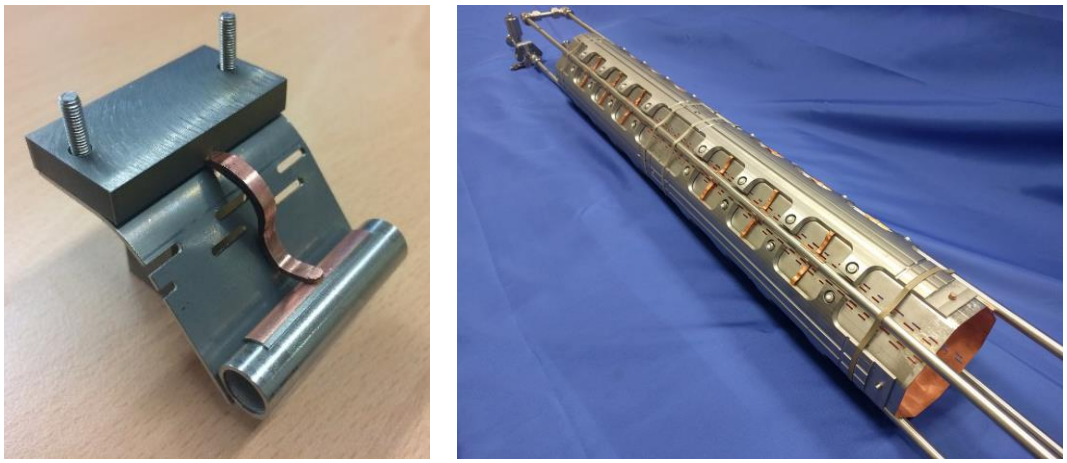

Figure 12-6: Samples and prototype used for the heat transfer assessment.

Different cooling configurations have been considered before selecting the most appropriate one [37]. A good agreement with the simulations has been obtained and a temperature difference between helium and the internal surface of the beam screen tube below 0.5 K has been achieved.

The overall heat load from the beam screens to the 1.9 K cold bore is expected to remain within the cryogenic budget. The heat is transferred by both conduction through the titanium springs and ceramic balls and by radiation. The heat transfer by conduction through the supporting system has been assessed by both simulations and measurements on a dedicated mock-up [54].

A heat load to the cold bore of 5 to 8 m W/spring has been measured for absorber temperatures between 60 to 90 K. Results are in good agreement with simulations [38] and a low dependence with the compression force has been also observed [37]. The laboratory test on the beam screen prototype has confirmed that the heat load to the cold bore remains below the cryogenic budget of 500 m W/m in the HL-LHC operating windows with 50% margin and ultimate conditions. Non-nominal conditions (point-like direct contact between the beam screen and the cold bore, uneven heat loads) have been assessed as well [39].

The main mechanical parameters have been also derived. Table 12-3 summarise the main dimensions and tolerances for the design and construction of the IT, CP and D1 assembly [40].

Table 12-3**:** Cold bores and beams screens main dimensions and tolerances of the IT, CP and D1 assembly of LSS1 and LSS5 [40].

	Cold bore		**Beam screen**						
	Inner Diameter	Thickness	Nominal aperture* H(V) ; ±45º	Vertical tolerance		Horizontal tolerance		Cooling tube Nb×OD×thickness	Shielding maximum Thickness
				Shape	Positioning**	Shape	Positioning**		
Q1	136.7 H8	4 0/+0.5	99.7; 99.7	±1.15	-1.23/+0.15	±1.1	±0.65	4 × 10 × 1	16
Q2a	136.7 H8	4 0/+0.5	119.7; 110.7	±1.15	-1.05/+0.11	±1.1	±0.65	4 × 10 × 1	6
Q2b	136.7 H8	4 0/+0.5	119.7; 110.7	±1.15	-1.05/+0.11	±1.1	±0.65	4 × 10 × 1	6
Q3	136.7 H8	4 0/+0.5	119.7; 110.7	±1.15	-1.05/+0.11	±1.1	±0.65	4 × 10 × 1	6
CP	136.7 H8	4 0/+0.5	119.7; 110.7	±1.15	-1.05/+0.11	±1.1	±0.65	4 × 10 × 1	6
D1	136.7 H8	4 0/+0.5	119.7; 110.7	±1.15	-1.05/+0.11	±1.1	±0.65	4 × 10 × 1	6

* Cu layer thickness, thermal contraction, self-weight deformation not accounted.

** One additional support, 0.25 radial clearance between the support and the cold bore.

The cold bore inner diameter is set to 136.7 mm all along the magnet string. The beam screen nominal aperture is reduced in Q1, positioned at 40 m from the interaction point, to allow the insertion of thicker tungsten shielding for better magnets protection.

Finally, The magnetic frequency response of the shielded beam screen was studied in detail for the specification of the power converter performance [41].

12.6.2 Non-shielded beam screen

The HL-LHC non-shielded beam screens are to be inserted into the HL-LHC D2, Q4 and non-crabbed lines of LSS1 and LSS5. If needed, new beam screens will be inserted in Q5 and Q6 of LSS1 and LSS5 and D1, DFBX, and IT of LSS2 and LSS8. Such beam screens (equipped with hydrogen cryosorbers when used for the 4.5 K cold masses of Q4, Q5 and Q6 [42]) ensure the vacuum requirements together with screening of the cold bores from beam-induced heating.

As a baseline, the a-C beam screen is assumed to fulfil its vacuum requirements with a-C coating operating at 5–20 K [16].

Table 12-4 gives the main dimension of the cold bore and beam screens of the LSS1 and LSS5 for the present designs of D2 and the non-crabbed line and for Q4, Q5 and Q6 based on the LHC design [43]. All beam screens, except Q6, are a-C coated. The beam screens of Q5 and Q6, equipped with hydrogen cryosorbers, are recovered from the LHC matching section.

Table 12-4**:** Cold bores and beams screens main dimensions and tolerances of the D2, non-crabbed line, Q4, Q5 and Q6 assemblies of the LSS1 and LSS5 [43].

Machine	**Cold bore**		**Beam screen**			
	ID/OD	**ID tolerance**	**a-C coated**	**Shape**	**H(V); ±45º ID/OD**	**Radial ID; Between flats ID**
D2	94.5/100	1.10	Yes	Non regular octagonal	87.4; 77.6	-
Non-crabbed line	84/88	0.20	Yes	circular	69.9/72.1	-
Q4	62.98/66.5	0.38	Yes	racetrack	-	57.8; 48.0
Q5	50/53	0.35	Yes	racetrack	-	45.1; 35.3
Q6	50/53	0.35	No	racetrack	-	45.1; 35.3

12.6.3 Vacuum beam line interconnection

The HL-LHC shielded beam screens are to be inserted into the HL-LHC D1, CP and IT region of LSS1 and LSS5. Beam vacuum interconnections ensure the continuity of the beam vacuum envelope, a smooth transition between adjacent beam screens, and the electrical continuity of the image current.

Figure 12-7 shows the present design of the vacuum beam line interconnection (length = 1000 mm) which integrate a non-deformable RF bridge and tungsten shielding for better cold mass protection against the debris produced at the IP [47].

The beam screens are fixed on one side to the cold mass; on the other side, compensation bellows between the beam screen extremity and the cold mass has to be integrated to cope with the differential thermal displacements between the beam screens and the cold mass.

The four 10 mm diameter cooling tubes are routed along the interconnect, connecting the upstream to the downstream beam screen. Through-wall welds on the helium circuit are forbidden in the beam vacuum. Automatic welds have to be used in the insulation vacuum.

A new type of non-sliding RF fingers (deformable RF bridge) are implemented and are being developed [44].

The vacuum beamline interconnections in the triplets integrate BPMs as well.

A tungsten shielding is also integrated into the interconnection around the beam position monitor body and at the beam screen extremity on the non-IP side to further increase the protection of the cold mass against the collision debris [45].

Finally, a-C coating of the vacuum beam interconnection is required to reduce the beam-induced heat load on the cryogenic system [46]. For this purpose, the coating of the interconnection line, including for the BPM body and the deformable RF bridge, will be done in the laboratory during the construction phase.

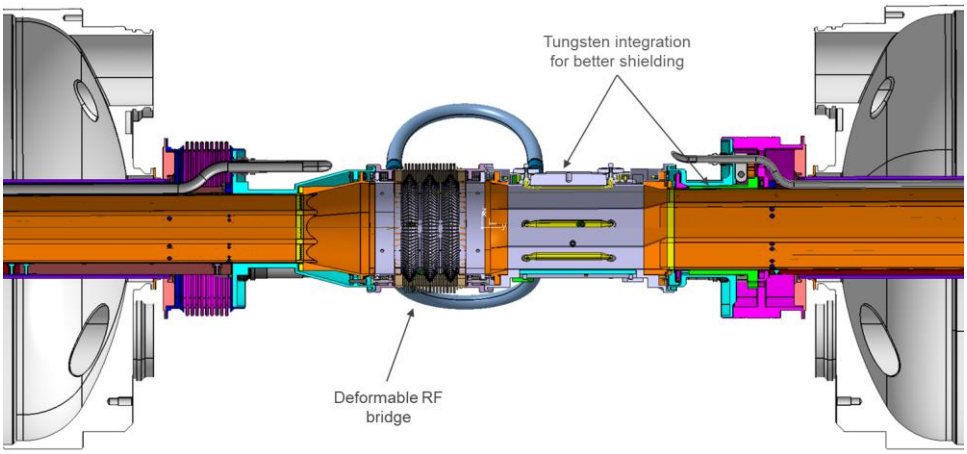

Figure 12-7: Vacuum beam line interconnection [44].

12.6.4 Cold-to-warm transitions

The HL-LHC cold-to-warm transitions design are based on the LHC machine. They are placed at each cryostat extremity. They must be made of a rigid tube to avoid the introduction of a RF bridge in the cryostat. For this reason, a bellow is welded at the external envelope of the cryostat to compensate from the cold mass length contraction during cool-down. The maximum acceptable length without beam screen shall be less than 1 m to prevent from pressure runaway. Therefore, longer cold-to-warm transitions require specific designs to satisfy this condition. The cold-to-warm transition of beam screen operating in the 5–20 K range, shall be thermally anchored to the cryostat thermal screen. Other cold-to-warm transitions designed for beam screens operating at higher temperature (60–80 K) do not require thermal anchoring to the cryostat thermal screen.

At present, the Q1 cold-to-warm transition integrates a beam position monitor. The D1 cold-to-warm transition is placed after at an extension of the helium vessel designed to provide vacuum pumping. Cold-to-warm transitions at other locations are under study.

12.7 References

[1] L. Rossi, Status of HiLumi: from design study to construction project, 5th Joint HiLumi LHC-LARP Annual Meeting 2015, INDICO: 400665.

[2] O. Gröbner, Overview of the LHC vacuum system. *Vacuum* **60**, 2001, DOI: 10.1016/S0042-207X(00)00240-2.

[3] LHC Design Report, 2004, DOI: 10.5170/CERN-2004-003-V-1.

[4] A. Rossi, Residual Gas Density Estimations in the LHC Insertion Regions IR1 and IR5 and the Experimental Regions of ATLAS and CMS for Different Beam Operations, 2004, LHC Project Report 783.

[5] A. Rossi, Residual gas density estimations of the LHC experimental interaction regions. CERN LHC Project Report 674 (2003), EDMS: 410413.

[6] Model of LSS layout LHCLJV_L0011, EDMS: 356208.

[7] ATLAS vacuum layout Q1/Q1. LHCVC1__0007, EDMS: 1317281.

[8] CMS LS2 vacuum layout Q1/Q1. LHCVC5__0009, EDMS: 1992313.

[9] J. Sestak, LHC experimental beam vacuum consolidation and upgrade ATLAS experiment, EDMS: 2234763.

[10] J. Sestak, LHC experimental beam vacuum consolidation and upgrade CMS experiment, EDMS: 2234765.

[11] ALICE vacuum layout Q1/Q1. LHCVC2__0008, EDMS: 2046454.

[12] J. Sestak, LHC experimental beam vacuum consolidation and upgrade LHCb experiment, EDMS: 2234767.

[13] LHCb vacuum layout Q1/Q1. LHCVC8B_0151, EDMS: 932121.

[14] J. Sestak, LHC experimental beam vacuum consolidation and upgrade ALICE experiment, EDMS: 2234762.

[15] C. Adoriso, HL-LHC residual dose rate estimations in the LSS1 and LSS5 (from TAXS up to Q7), 7th HL-LHC Annual Meeting, Madrid, Spain, EDMS: 1868872.

[16] HL-LHC Decision Management: Temperature beam screens Q1 to Q6. EDMS: 1601082.

[17] C. Garion *et al.*, Material characterisation and preliminary mechanical design for the HL-LHC shielded beam screens operating at cryogenic temperatures, Advances in Cryogenic Engineering - Materials: International Cryogenic Materials Conference, Tucson, AZ, USA, 28 Jun - 2 Jul 2015. DOI: 10.1088/1757-899X/102/1/012013.

[18] C. Garion *et al.*, Preliminary design of the high-luminosity LHC beam screen with shielding, 6th International Particle Accelerator Conference, 2015, DOI: 10.18429/JACoW-IPAC2015-MOBD1.

[19] R. Kersevan *et al.*, Preliminary design of the HiLumi-LHC triplet area beam screen. 5th International Particle Accelerator Conference, Dresden, Germany, 2014, DOI: 10.18429/JACoW-IPAC2014-WEPME048.

[20] V. Baglin, G. Riddone, The spare needs for HL-LHC: what is needed that is not covered yet by the LHC spare policy / HL_LHC operation, EDMS: 2045659.

[21] R. Tavares Rego, HL-LHC Vacuum Layout LSS5, EDMS: 2045739.

[22] P. Santos Diaz, J. Hansen, IP1&5 recombination chamber conceptual design, EDMS: 1824656.

[23] P. Costa Pinto et al. ECR: Amorphous carbon coating in standalone magnets of the LHC in IR2 and IR8 during LS2, EDMS: 1983116.

[24] S. Antipov, Impact of a-C coating on impedance, 124th HiLumi WP2 Meeting, INDICO:741104.

[25] V. Baglin *et al*., Vacuum System in: High-Luminosity Large Hadron collider (HL-LHC) Preliminary Design Report pp. 195-205, DOI: 10.5170/CERN-2015-005.195.

[26] R. Salemme et al., Vacuum performance of amorphous carbon coating at cryogenic temperature with presence of proton beams. Proc. of IPAC 2016, DOI: 10.18429/JACoW-IPAC2016-THPMY007.

[27] A. Krasnov *et al*, Results on a-C tubes subjected to synchrotron radiation, 8th HL-LHC Annual Meeting, CERN, Geneva, Switzerland, INDICO:742082.

[28] V. Baglin, P. Chiggiato. Preparation of the ECR regarding the modification of the HL-LHC base line for a-C coating. 46th HL-LHC Technical coordination Committee, INDICO:705929.

[29] M. Sitko *et al*. Towards the implementation of laser engineered surface structures for electron cloud mitigation, Proc. of IPAC 2018, Vancouver, Canada, DOI: 10.18429/JACoW-IPAC2018-TUZGBE3.

[30] V. Baglin, Towards final validation of new temperature of beam screen for triplets, 8th HL-LHC Annual Meeting, CERN, Geneva, Switzerland, INDICO:742082.

[31] R. Kersevan. Private communication, September 2018.

[32] C. Garion, Design and behaviour of 3D printed elastic components for HL-LHC shielded beam screen, EDMS: 2001118.

[33] C. Garion, Vibrations of the HL-LHC shielded beam screens, EDMS: 2031211.

[34] M. Morrone, Thermomechanical study of complex structures in the aperture of superconducting magnets: application to the design of the High-Luminosity LHC shielded beam screen, CERN-THESIS-2018-052.

[35] C. Garion, Design and tests of the shielded beam screen, 7th HL-LHC Annual Meeting, Madrid, Spain, INDICO: 647714.

[36] M. Morrone, Quench test of the HL-LHC beam screen in the MQXFS4b magnet, TE Technical Meeting, CERN, Geneva, Switzerland, INDICO: 776870.

[37] P. Borges de Sousa et al, Parametric study on the thermal performance of beam screen samples of the High-Luminosity LHC Upgrade, IOP Conf. Ser. Mater. Sci. Eng. 278, 2017, DOI: 10.1088/1757-899X/278/1/012053.

[38] C. Garion, Design and tests of the shielded beam screen, 7th HL-LHC Annual Meeting, Madrid, Spain, INDICO: 647714.

[39] P. Borges de Sousa, Thermal qualification of the HL-LHC beam screens for the inner triplets, TE Technical Meeting, CERN, Geneva, Switzerland, INDICO: 762917.

[40] C. Garion, Mechanical design of the triplet cold bore and beam screen, 6th HL-LHC Annual Meeting, Paris, France, INDICO: 549976.

[41] M. Morrone *et al*, Magnetic frequency response of High-Luminosity Large Hadron Collider beam screens, Phys. Rev. Accel. Beams 22, 2019, DOI: 10.1103/PhysRevAccelBeams.22.013501.

[42] Full Remote Alignment Study (FRAS) And Matching Section Optimization Targets, and advancement report, P. Fessia et al. 54th HL-LHC Technical Coordination Committee, CERN, INDICO: 747490

[43] N. Kos *et al*, Beam screen for the LHC long straight sections, EDMS: 334961.

[44] C. Garion, Design of the compensation system for the HL-LHC cold beam vacuum interconnections, EDMS: 2012795.

[45] F. Cerutti *et al*, Recap of energy deposition and radiation damage, 7th HL-LHC Annual Meeting, Madrid, Spain. INDICO: 647714.

[46] G. Iadarola *et al*, Beam induced heat loads on Hl-LHC beam screens, 7th HL-LHC Annual Meeting, Madrid, Spain, INDICO: 647714.

[47] C. Garion, Status of beam screen, cold bore, interconnect and CWT design & production, 8th HL-LHC Annual Meeting, CERN, Geneva, Switzerland, INDICO: 742082.

[48] V. Baglin and G. Riddone, HL-LHC WP12 Vacuum & Beam Screen technical update, 99th HL-LHC Technical Coordination Committee, EDMS: 2363271.

[49] R. Tavares Rego, General methodology for vacuum equipment mechanical aperture computation, EDMS: 1999375.

[50] P. Fessia, H. Mainaud Durand, Functional specification full remote alignment system, EDMS: 2166298.

[51] V. Baglin, J. Hansen, G. Riddone, Vacuum: full remote alignment system. Review of HL-LHC alignment and internal metrology, CERN, 25th August 2019, EDMS: 2219953.

[52] V. Baglin. Shielded beam screens operating temperature for the triplets, corrector package and D1, EDMS: 2112891.

[53] V. Baglin, A. Carvalho, G. Riddone, Vacuum for HL-LHC CC. International review of the crab cavity system design and production plan for the HL-LHC, CERN, 19-21 June 2019, INDICO: 787363

[54] P. Borges de Sousa *et al*, Study on heat transfer between the High-Luminosity LHC beam screens and the He II cooled beam tube. IOP Conf. Ser.: Mater. Sci. Eng. 502, 2019, DOI: 10.1088/1757-899X/502/1/012088.

Chapter 13

Beam instrumentation and long-range beam–beam compensation

R. Jones[1], E. Bravin[1], T. Lefevre[1] and R. Veness[1]*

[1]CERN, Accelerator & Technology Sector, Switzerland
[*]Corresponding author

13 Beam instrumentation and long-range beam–beam compensation

13.1 Introduction

The extensive array of beam instrumentation with which the LHC is equipped has played a major role in its commissioning, rapid intensity ramp-up and safe and reliable operation. Much of this equipment will need consolidation by the time the LHC enters the High-Luminosity (HL) era, while the upgrade itself brings a number of new challenges.

The installation of a completely new final focus system in the two high-luminosity LHC insertions implies the development of new beam position monitors to equip the upgraded quadrupole magnets. As well as replacing the 10 current beam position monitors, six additional beam position monitors will be added per interaction region, to further improve beam control at the collision point.

The use of crab cavities for luminosity enhancement implies a need for new instrumentation in order to allow for the optimisation of their performance. This requires intra-bunch measurement of transverse position on a turn-by-turn basis. Several diagnostic systems are being investigated as candidates to perform this task, including very high bandwidth pick-ups and a streak camera installation making use of synchrotron light.

The installation of a hollow electron lens for cleaning the beam halo has added to the beam diagnostic challenges of high-luminosity LHC. Not only must the beam halo be measured, but a good concentricity and alignment between the electron and proton beam must be ensured. A coronagraph based on synchrotron light is therefore under study with the aim of being able to image the halo at a level of 10^{-5} of the core intensity, while a gas curtain monitor is being developed to align the electron and proton beams within the hollow electron lens. The latter will use a high-density, supersonic, gas sheet to allow a two-dimensional image of both beams to be created via luminescence.

Upgrading the LHC also provides the opportunity of developing new instrumentation to address areas identified as currently lacking adequate diagnostics. This includes a non-invasive, beam-size measurement system capable of delivering data throughout the LHC acceleration cycle, with a prototype beam gas vertex detector already being tested for this purpose.

An upgrade or consolidation is envisaged for several other systems, including the main beam position monitoring system, the beam loss measurement system, the luminosity measurement system, and the synchrotron light monitor.

This workpackage also covers the study of possible technologies for long–range beam-beam compensation.

13.2 Beam loss measurement

Monitoring of beam losses is essential for the safe and reliable operation of the LHC. The beam loss monitor (BLM) system provides knowledge on the location and intensity of such losses, allowing an estimation to be made of the energy dissipated in the equipment throughout the accelerator. This information is used for machine protection, to optimise beam conditions, and to track the radiation dose to which equipment has been exposed. The BLM system consists of nearly 4000 ionisation monitors distributed around the machine [1]. These are located at all probable loss locations, with the majority mounted on the outside of quadrupole magnets. While the existing system is globally believed to meet the needs of the HL-LHC, some upgrades will nevertheless be required.

The quench level signals estimated for 7 TeV running are, for some detectors, very close to the noise level of the acquisition system. This is mainly determined by the length of cable required to bring the signal from the radiation hard, ionisation chamber detector to the radiation sensitive front-end electronics. This is not an issue for the detectors in the arcs, as the current electronics are qualified for use in low radiation environments and can therefore be placed close to the detectors. For the detectors in the interaction and collimation regions, however, this is not the case, with some 250 channels affected. Development has therefore begun to implement the readout electronics in a radiation hard Application Specific Integrated Circuit (ASIC) that could sit near each detector, eliminating the need for long cables.

Two technologies are being studied for this ASIC, current to frequency conversion, as is used in the standard LHC ring beam loss system, and a sigma-delta implementation. The final ASIC will need to cover a 180 dB dynamic range (corresponding to a current range from 1 pA – 1 mA) with a 10 μs integration time and target a radiation tolerance of 1 MGy. This ASIC will use standard 130 nm CMOS technology (known to be radiation tolerant to 2 MGy) and be housed in a standard 64 pin Quad Flat Package (10 × 10 mm). Each chip will have two analogue readout channels, triplicated digital circuitry with majority voting, and double communication channels for redundancy [2].

13.2.1 Changes from the initial HL-LHC TDR

In the original TDR it was proposed to investigate possible options for placing radiation detectors inside the cryostat of the triplet magnets as close as possible to the superconducting coils. The dose measured by such detectors would then correspond much more precisely to the dose deposited in the coils, allowing the system to prevent quenches and distinguish between beam loss and luminosity debris. Silicon and diamond detectors were investigated for this purpose, with both shown to be capable of operating in such an environment [3]. However, recent studies using the updated HL-LHC optics and including the tungsten shielding in the beam screen, have demonstrated that there is little difference in the loss patterns measured by such detectors and the standard beam loss monitors external to the cryostat [4]. The option of installing cryogenic beam loss monitors in the HL-LHC triplets is therefore abandoned.

The prototype beam loss monitor ASIC described in the original TDR used what is now outdated 250 nm CMOS technology. A complete redesign was therefore required to use standard 130 nm technology. This gave the chance to investigate alternative topologies, with both a sigma/delta and current to frequency method now being studied. The final choice of technology will be taken after fully testing prototype versions of each ASIC.

13.3 Beam position monitoring

With its 1070 monitors, the LHC Beam Position Monitor (BPM) system is the largest BPM system in the world [5]. Based on the Wide Band Time Normalizer (WBTN) principle [6], it provides bunch-by-bunch beam position over a wide dynamic range (~50 dB). Despite its size and complexity (3820 electronic cards in the accelerator tunnel and 1070 digital post-processing cards in surface buildings) the performance of the system during the first LHC physics runs has been excellent.

13.3.1 Current performance and limitations

The short-term reproducibility of orbit measurements using the LHC beam position monitors has been determined to be better than 20 μm [7]. The main limitation on the accuracy is linked to temperature dependent effects in the acquisition electronics, which can generate offsets of up to a millimetre if left uncalibrated. Temperature controlled racks have been installed to limit this effect, but drifts of several tens of micrometres are still observed. The non-linearity of the BPMs located near the interaction points has also proven to be problematic, in particular for accurate measurements during the beta-squeeze and during machine development periods. A new correction algorithm has therefore been developed, based on electro-magnetic simulations, with the aim of bringing the residual error down to below 20 μm over ~70% of the useable BPM aperture [8]. As they detect both beams, these BPMs also suffer from cross-coupling of the signals induced, which is something that is being addressed for the HL-LHC.

13.3.2 A high-resolution orbit measurement system for the HL-LHC

At the start of the HL-LHC era, the existing BPM system will have been operational for over 15 years, using components that are over 20 years old. A completely new read-out system is therefore being developed to replace these ageing electronics. It will be heavily based on digital signal processing, directly sampling opposite electrode outputs on a single channel, making use of recent advancements in high resolution, fast sampling analogue to digital conversion technology and the radiation hard, high speed optical transmission systems developed for the LHC experiments. The aim will be to provide a high reliability system with improved long-term stability and reproducibility.

13.3.3 High directivity strip-line pick-ups for the HL-LHC insertion regions

In the BPMs close to the interaction regions, the two beams propagate in the same vacuum chamber. Strip-line pick-ups acting as directional couplers are therefore used to provide the position signals of both beams. The particularity of such a BPM is that signal from the beam only appears at the upstream port, with little contribution at the downstream port. The same BPM can therefore be used to measure both beams. However, when the two beams pass through the BPM at nearly the same time, there is still some interference due to the imperfect directivity (some signal still appearing at the downstream port) of the strip-line. In the current strip-line BPMs there is only a factor 10 isolation between the upstream and downstream signals, making it difficult for such a BPM to measure beams with significantly different intensities or large position offsets. The effect can be minimised by installing the BPMs at a location where the two counter-propagating beams do not meet. This is a constraint included in both the present and future layout, but which cannot be satisfied for all BPM locations. The ideal longitudinal location corresponds to $(1.87 + N \times 3.743)$ m from the IP where N is an integer, providing a maximum separation of 12.5 ns between signals. Any deviation from this will diminish the ability of the system to distinguish one beam from the other. For the current HL-LHC layout the temporal separation between the two beams at the locations of the BPMs varies from 3.9 ns, for the BPMs installed on the Q1 and Q2a magnets, up to 10.5 ns for the BPM installed on the corrector package.

As part of the critical beam position system required to maintain optimised collisions in the HL-LHC these components need to be highly reliable and maintenance-free. The system should be able to measure the average beam position (i.e. orbit) for each beam with a resolution of 1 μm and with a medium term (fill to fill) reproducibility of 10 μm [7].

The BPMs in front of the Q2a, Q2b, Q3, the triplet corrector package, and D1 magnets require tungsten shielding close to the beam screen aperture to minimise the integrated radiation dose deposited in these magnets due to luminosity debris. This implies rotating the electrodes by 45° to allow the insertion of tungsten shielding in the median planes of both horizontal and vertical axes. A mechanical re-design, coupled with extensive electro-magnetic simulation, is therefore being performed to optimise the directivity under these constraints.

Six directional strip-line BPMs of three different types are foreseen on each side of the high-luminosity insertions. A cold BPMQSTZA without tungsten shielding in front of Q1; 5 cold BPMQSTZB (Figure 13-1) with tungsten shielding: in front of Q2A, between Q2A and Q2B, in front of Q3, between Q3 and the corrector package, and in front of D1.

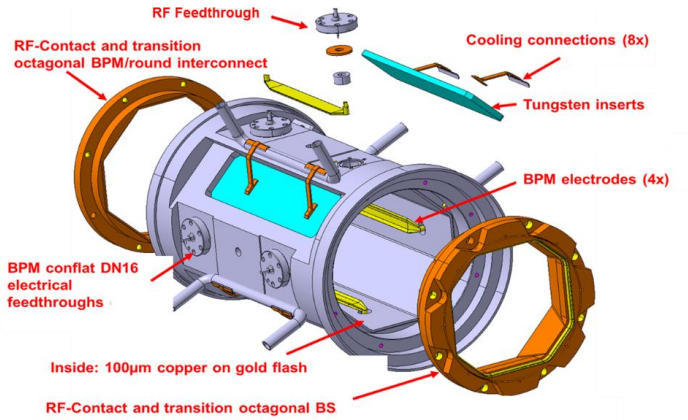

Figure 13-1: Mechanical design of the BPMQSTZB stripline beam position monitor for the HL-LHC.

The signal from all of these BPMs will be extracted using eight semi-rigid, radiation-resistant coaxial cables per BPM. Two feedthroughs with four coaxial cable connections each will be integrated into the cryostats of the Q1, Q2a, Q2b, Q3, corrector package and D1 magnets. The outputs of these feedthroughs will be connected to standard ½″ coaxial cables taking the signal to the electronics in the UJ/US.

A total of 24 new strip-line BPMs will be installed in the high-luminosity insertions as part of the HL-LHC upgrade (Table 13-1).

13.3.4 Button electrode beam position monitors for the HL-LHC insertion regions

Two new, cold, button BPMs will be added inside each D2 cryostat, liberating space currently taken by warm button BPMs in front of the D2 magnet. Two different types, for the internal / external beam, may be required due to asymmetric welding interfaces. The BPTX trigger BPM for the experiments, currently in front of Q4, will need to be redesigned or relocated due to aperture considerations.

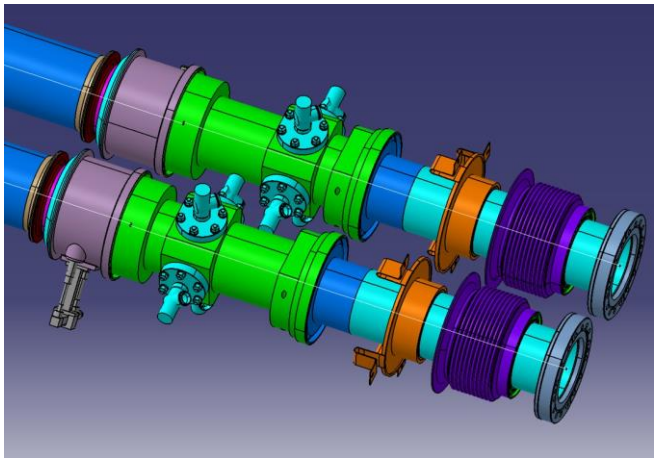

Figure 13-2: Layout of the BPMQBCZA and BPMQBCZB D2 button beam position monitors for the HL-LHC.

A total of 8 new button BPMs will be installed in the high-luminosity insertions as part of the HL-LHC upgrade (Table 13-1).

Table 13-1: Summary of Q1-Q5 BPM locations and types Left and Right of IP1 and IP5 for the HL-LHC

Code	Location	Distance from IP (m)	Aperture (mm)	Warm or cold	Stripline or button	Tungsten shielding	Electrode position	Parasitic bunch crossing timing (ns)	New or existing
BPMQSTZA	Q1 (IP side)	21.853	Octagonal 101.7 / 99.7	Cold	Stripline	No	0° / 90°	3.92	New
BPMQSTZB	Q2B (IP side)	33.073	Octagonal 112.7 / 119.7	Cold	Stripline	Yes	45° / 135°	3.92	New
BPMQSTZB	Q2B (IP side)	43.858	Octagonal 112.7 / 119.7	Cold	Stripline	Yes	45° / 135°	6.82	New
BPMQSTZB	Q3 (IP side)	54.643	Octagonal 112.7 / 119.7	Cold	Stripline	Yes	45° / 135°	9.72	New
BPMQSTZB	CP (IP side)	65.743	Octagonal 112.7 / 119.7	Cold	Stripline	Yes	45° / 135°	10.52	New
BPMQSTZB	D1 (IP side)	73.697	Octagonal 112.7 / 119.7	Cold	Stripline	Yes	45° / 135°	7.36	New
BPMQBCZA BPMQBCZB	D2 (arc side)	151.930	Round Ø 90	Cold	Button	No	0° / 90°	N/A	New
BPTX	Between crabs & Q4	169.024 (not final)	Round Ø 80	Warm	Button	No	0° / 90°	N/A	Existing
BPMYA BPMYB	Q4 (arc side)	182.312	Round Ø 61	Cold	Button	No	0° / 90°	N/A	Existing
BPMYA BPMYB	Q5 (arc side)	210.171	Round Ø 61	Cold	Button	No	0° / 90°	N/A	Existing

13.3.5 Collimator beam position monitors

All next generation collimators in the LHC will have button electrodes embedded in their jaws (Figure 13-3) for on-line measurement of the jaw to beam position [9]. These are fitted with an orbit measurement system based on a compensated diode detector scheme [10], which has been demonstrated to be simple and robust, and to provide a position resolution at the sub-micron level. This will provide a fast and direct way of positioning the collimator-jaws and subsequently allow constant verification of the beam position at the collimator location, improving the reliability of the collimation system as a whole.

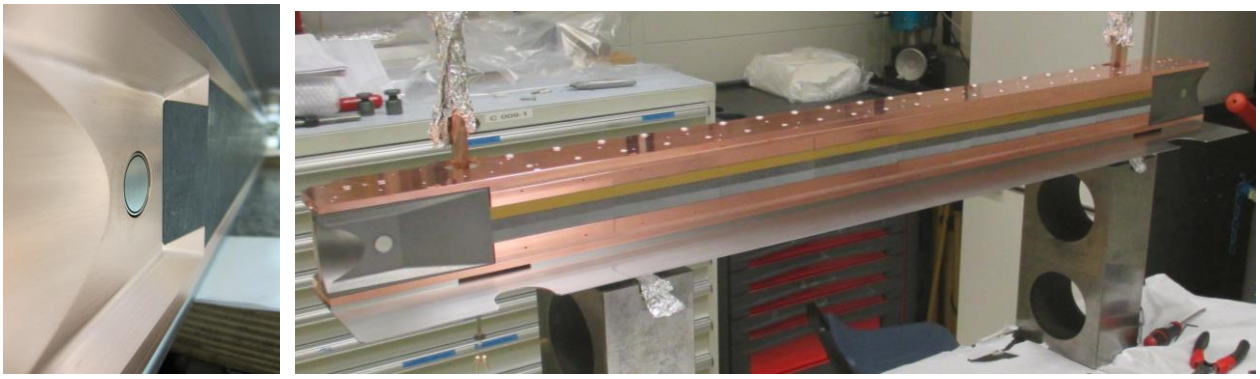

Figure 13-3: Photograph of TCSP collimator button BPM (left) and a test assembly (right).

The collimator BPM hardware, i.e. the button electrode located in the jaw, the cable connecting the electrode to the electrical feedthrough mounted on the vacuum enclosure, the feedthrough itself, the quick connect flange on the support and the cable connections to the standard cable patch panel, have all been chosen to withstand the radiation dose of 20 MGy expected during the lifetime of the collimator.

13.3.6 Changes from the initial HL-LHC TDR

The following changes have been made with respect to the original TDR:

- New BPMs are not required for Q4 and Q5 due to the decision to re-use the current magnets.
- The warm BPMs of D2 are moved into the cryostat to free additional space in front of D2.
- The warm BPMQSWZA after D1 is removed as it brings little additional information and is difficult to incorporate into the fully remote alignment system.
- Tungsten shielding is added to all BPMs of type BPMQSTZB to reduce the number of variants and simplify production. This more than offsets the additional cost of adding the tungsten to all these BPMs.
- The baseline electronic acquisition system is now based on digital signal processing techniques, directly sampling opposite electrode outputs on a single channel and making use of recent advancement in high resolution, fast sampling analogue to digital conversion technology and the radiation hard, high speed optical transmission systems developed for the LHC experiments.

13.4 Beam profile measurements

The LHC is currently fitted with a host of beam size measurement systems used to determine beam emittance. These different monitors are required in order to overcome the specific limitations of each individual system. Wirescanners are used as the absolute calibration reference but can only be operated with a low number of bunches in the machine due to intensity limitations linked to wire breakage and the quench limits of downstream magnets. A cross-calibrated synchrotron light monitor is therefore used to provide beam size measurements, both average and bunch-by-bunch, during nominal operation. However, the small beam sizes achieved at 7 TeV, the multiple sources of synchrotron radiation (undulator, D3 edge radiation, and central D3 radiation), and the long optical path required to extract the light imply that the correction needed to obtain an absolute value is of the same order of magnitude as the value itself. This relies on an excellent knowledge of all error sources to obtain meaningful results and excludes continuous measurement during the energy ramp.

A third system initially installed was an ionisation profile monitor foreseen to provide beam size information for lead ions at injection, where there is insufficient synchrotron light. However, with intense proton beams the monitor suffered from excessive, impedance related, radio-frequency heating and had to be removed.

Whilst efforts are ongoing to improve the performance of all the above systems, alternative techniques to measure the transverse beam size and profile are also under study for the HL-LHC, in particular during the ramp, as this is crucial for understanding the emittance evolution of the beam throughout the acceleration cycle and hence to optimise the final luminosity achievable.

13.4.1 A beam gas vertex profile monitor

The VELO detector of the LHCb experiment has shown how beam gas interactions can be used to reconstruct the transverse beam profile of the circulating beams in the LHC [11]. Currently under study is whether a simplified version of such a particle physics tracking detector can be used to monitor the beams throughout the LHC acceleration cycle. Such a concept has, up to now, never been applied to the field of beam instrumentation, mainly because of the large amount of data treatment required. However, the advantages compared to standard beam profile measurement methods are impressive: high-resolution profile reconstruction, single-bunch measurements in three dimensions, quasi non-destructive, no detector equipment

required in the beam vacuum, high radiation tolerance of the particle detectors and accompanying acquisition electronics.

Unlike LHCb, where the detector is placed very close to the beam and can therefore only be used during stable beams, the aim with the Beam Gas Vertex profile monitor (BGV) is to design a robust instrument that can be used for beam size measurements throughout the LHC cycle. Its final specifications are to provide:

- transverse bunch size measurements with a 5% resolution within 1 minute;
- average transverse beam size measurements with an absolute accuracy of 2% within 1 minute.

Prototyping of such a detector began in 2012 in collaboration with the LHCb experiment, the École Polytechnique Fédérale de Lausanne and RWTH Aachen. The system was installed on the left-hand side of LHC IP4 on Beam 2 in 2015 (Figure 13-4) and made operational for data taking in 2017–2018. The main subsystems are: a neon gas target at a pressure of ~5×10^{-8} mbar; a thin aluminium exit window; tracking detector based on scintillating fibre modules read out by silicon photomultipliers; hardware and software triggers; and a readout and data acquisition system based on that used for LHCb. As the tracking detector is external to the vacuum chamber, no movable parts are required.

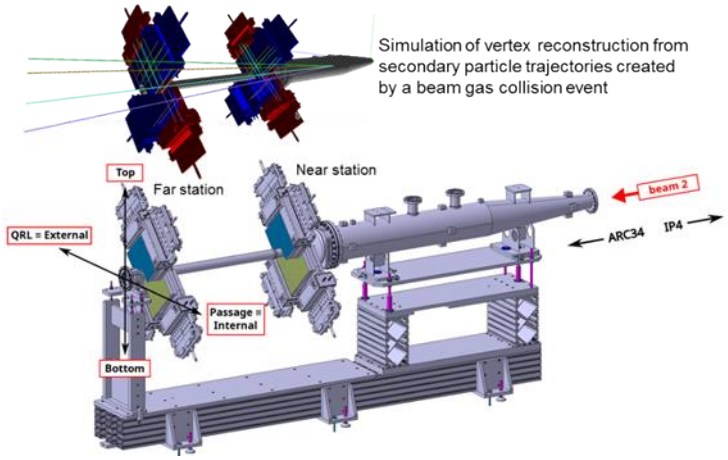

Figure 13-4: The principle and design of the prototype LHC beam gas vertex detector.

The installed prototype has demonstrated the ability to measure both the horizontal and vertical beam size independently, with a precision better than 3% for an integration time of less than a minute [12]. This allows beam size monitoring during all operational phases, including the energy ramp, for which there is currently no other instrument that can make a measurement of the beam size for high intensity physics beams.

The encouraging results and experience gained with the prototype has led to continued R&D on such a monitor, to develop two, fully optimised systems for installation on both beams as part of the baseline HL-LHC project. Various new concepts are being investigated [13] including the possibility to confine the gas target using gas-jet technology already being developed for the HL-LHC (see Section 13.8), using three tracking planes incorporating multi-pattern gaseous detectors and deploying a radiation tolerant readout electronics using standard components that can be maintained in the longer term.

13.4.2 Changes from the initial HL-LHC TDR

In the original TDR it was foreseen to install a copy of the first system during LS2, so as to equip both beams. Instead, since the initial system is not maintainable for the longer term, the project will now fund two new systems that will be optimised for performance and maintainability and installed during LS3.

13.5 Halo diagnostics

One of the major challenges for high intensity accelerators is the control of beam losses. In the case of the HL-LHC, the stored energy per beam is of the order of 700 MJ while the collimation system can sustain a maximum of 1 MW continuous power deposition. For this reason, it is vital to study and understand loss dynamics. An important mechanism for slow losses consists of populating the beam "halo", i.e. populating the periphery of the phase-space with particles at large amplitudes (by IBS, beam-gas collisions, resonances etc.). These halo particles then gradually increase their amplitude due to the non-linearity of the optics until they hit a collimator. Measurement of the beam halo distribution is important for understanding this mechanism and hence to minimise its effect. Moreover, in the HL-LHC, crab cavities will be used to counter the geometric luminosity loss factor introduced due to the increased crossing angle. In case of failure of a crab cavity module the whole halo may be lost in a few turns. If the halo population is too high this can cause serious damage to the collimation system or to other components of the machine. The total halo population that can be absorbed by the collimation system in case of a fast loss is of the order of few 10^{-5} of the nominal beam intensity. The halo monitor for the HL-LHC should thus be able to observe the halo at a level of 10^{-5} of the peak bunch intensity.

Most diagnostics used for transverse beam profile measurement could be adapted for halo measurement. For the LHC this consists of beam imaging using synchrotron radiation, wire-scanners, ionisation profile monitors and the new technique based on beam-gas vertex reconstruction. However, halo measurements using synchrotron radiation seem the most promising.

13.5.1 Halo measurement using synchrotron radiation imaging

Halo measurement using synchrotron radiation can be achieved using one of the following techniques:

- High dynamic range cameras
- Core masking and standard cameras
- Performing an X-Y scan of the image plane with a photo-detector located behind a pinhole
- Single photon counting with a pixelated photo-detector

The limiting factor in all cases is likely to be the unavoidable presence of diffused synchrotron light coming from reflections in the vacuum chamber or optics, diffusion by dust particles, and diffraction. The first two can be mitigated with an appropriate surface treatment and a clean, hermetic setup, although diffusion by scratches and defects on the optical components cannot be entirely removed. Diffraction, however, is a physical limitation.

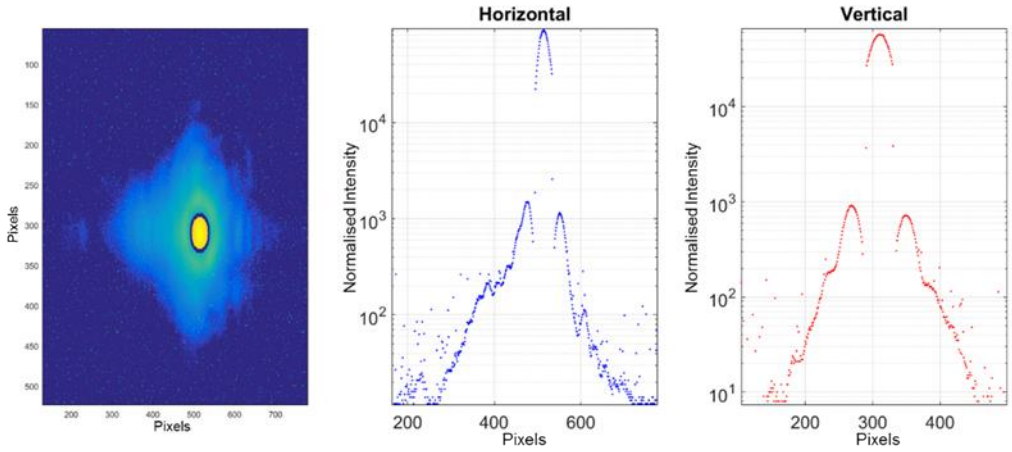

Figure 13-5: Combined core and halo measurement showing a dynamic range of ~10^4.

To overcome the problem of diffraction, halo measurement using a coronagraph technique is under study, and a prototype, using components from a similar system installed on the Photon Factory at KEK, is

currently installed in the LHC [14]. By combining a core image (without the coronagraph mask in place) with a halo image (with the coronagraph mask in place) a combined beam profile measurement is obtained (Figure 13-5). This shows that the current, prototype system is capable of detecting halo at the level of 10^{-4}. In order to push this further a new design is underway, exploiting a Cassegrain reflector telescope to allow for higher magnification, and therefore capable of achieving the specified contrast of 10^{-5}. This is foreseen to replace the first prototype for testing during LHC Run 3, on the existing optical table exploiting the light from the D3 magnet (at top energy) and undulator (at injection energy).

To measure the halo at this very low level, a dedicated light extraction path is mandatory to minimise the number of optical elements. The current prototype installation can therefore only be used during machine development periods when the standard beam size observation is not required. The final, optimised versions of the coronagraph will require new, specifically built synchrotron radiation lines. Integration studies are currently underway to incorporate a second synchrotron radiation line per beam, using the radiation produced by the D4 separation magnets near the RF insertion in Point 4. The light will be extracted via an in-vacuum mirror to a new optical table located below the beampipe (as is currently the case for the existing lines). This will only provide halo measurements at top energy as, in the absence of an undulator near the D4 magnet, there is insufficient light generated at injection energy. The option of installing an undulator (at present not in the baseline) upstream of D4 is retained to allow additional diagnostics at injection energy, with the possibility of using permanent magnets being considered.

13.6 Diagnostics for crab cavities

The crab cavities for the HL-LHC will enhance luminosity by countering the geometric reduction factor caused by the large crossing angle. These cavities will be installed around the high-luminosity interaction points (IP1 and IP5) and used to create a transverse bunch rotation at the IP. The head and tail of each bunch is kicked in opposite transverse directions such that the incoming bunches will cross parallel to each other at the interaction point. These position bumps which vary along the length of the bunch are closed by crab-cavities acting in the other direction on the outgoing side of the interaction region. If the bumps are not perfectly closed the head and tail of the bunch will travel on different closed orbits around the ring which could lead to unwanted emittance blow-up, and more importantly to beam loss at locations with aperture restrictions. Two monitors capable of measuring the closure of the head-tail bump and any head-tail rotation or oscillation outside of the interaction regions are therefore included in the HL-LHC baseline: an electromagnetic monitor; a streak camera using synchrotron light, which is also capable of providing accurate longitudinal profiles.

13.6.1 Bunch shape monitoring using electro-magnetic pick-ups

Electromagnetic monitors for intra-bunch diagnostics are already installed in the LHC [15]. These so-called “Head-Tail” monitors mainly provide information on instabilities and have a bandwidth up to several GHz. Similar monitors were essential to understand and optimise the first ever use of crab cavities in a proton synchrotron during the 2018 tests of the HL-LHC prototypes in the CERN-SPS accelerator.

To better understand instabilities in the HL-LHC and to help with the tuning of the crab-cavities a higher granularity within the bunch (bandwidth > 5 GHz) is desirable, along with better position resolution. The current HL-LHC baseline foresees the installation of pick-ups based on electro-optical crystals in combination with laser pulses, with a prototype recently tested on the CERN-SPS in collaboration with Royal Holloway University of London, UK [16]. Four such monitors, two per beam with 90° phase advance between pick-ups, are foreseen be installed in LSS4. The exact locations will depend on the final optics configuration.

Studies are also continuing to improve the existing electromagnetic pick-ups, including the optimisation of the pick-up design and the testing of faster acquisition systems, which would become the fallback option should the electro-optical pick-ups not reach the required sensitivity and resolution.

13.6.2 Bunch shape monitoring using streak cameras

The use of synchrotron light combined with a streak camera is complementary to electromagnetic or electro-optical pick-ups for high-resolution temporal imaging, being able to also provide detailed longitudinal bunch profile information. Using an optical system to re-image the synchrotron light at the entrance of a streak camera allows the transverse profile of the beam to be captured in one direction (horizontal or vertical) with a very fast time resolution (below the picosecond level). Such a system can be used to observe a number of beam parameters simultaneously: bunch length, transverse profile along the bunch, longitudinal coherent motion, head-tail motion etc. The main limitations of the streak camera are the repetition rate of the acquisition, typically less than 50 Hz, and the limited length of the recorded sample, which is given by the CCD size. The latter can be improved by using double scan streak cameras. Considering a CCD with 1000 × 1000 pixels working at 50 Hz and adjusting the optical magnification and scan speed such that the image of each bunch covers an area of about 100 × 100 pixels one could record a maximum of 100 bunch images per 20 ms, i.e. 5000 bunches per second. This is clearly just an optimistic upper limit with other factors likely to reduce this value but indicates that a complete snapshot of all circulating bunches could be acquired within a reasonable time.

The longitudinal resolution of around 50 ps required for the HL-LHC is rather easy to achieve using streak cameras, where measurements down to the sub-picosecond are now possible. In terms of transverse resolution two distinctions have to be made:

- The resolution when measuring beam width. This is affected by diffraction due to the large relativistic gamma of the beam, with the diffraction disk of the same order as the beam size. Measurement of the absolute transverse beam size will therefore not be very precise.
- The resolution when measuring centroid motion, i.e. the centre of gravity of the beam. This is not directly affected by the diffraction, which produces a symmetrical blur, and therefore the resolution for this type of measurement will be much better.

As head-tail motion is essentially a centroid motion, the streak camera should be able to achieve the resolution of a few percent of the beam sigma necessary to quantify any residual non-closure of the crab cavity bumps. However, in order to measure this, the phase advance between the crab cavities and the light extraction point would need to be optimised which is not the case with the current HL-LHC optics. It is therefore still being investigated how much of an effect could be detected with such a system.

Streak cameras are expensive and delicate devices not designed for the harsh environment inside an accelerator. Radiation dose studies are therefore required in order to verify if a streak camera can be installed directly in the tunnel or if it has to be housed in a dedicated hutch in an equipment gallery. The latter would imply an optical line to transport the synchrotron light from the machine to the camera, for which initial integration studies have already been performed.

13.7 Luminosity measurement

The measurement of the collision rate at the luminous interaction points is very important for the regular tuning of the machine. Accurate information about the instantaneous luminosity is provided by the LHC experiments once stable collisions are established, but this information is often not available during commissioning, machine development periods or during the initial process of bringing the beams in collision. Simple, reliable, collision-rate monitors are therefore needed for the HL-LHC, similar to those presently available for LHC operation. This measurement is currently provided by measuring the flux of forward neutral particles generated in the collisions using fast ionisation chambers installed inside the TAN neutral collision debris absorbers. As these absorbers will be re-designed for the completely different HL-LHC geometry in this region (TAXN), new, adapted luminosity monitors will need to be produced. Integration in the TAXN is not trivial due to space constraints, and the measurement is complicated by the fact that the shower is asymmetric for horizontal crossing, leading to a dependence of the measured flux on the crossing angle (Figure 13-6).

There are several drawbacks with the current ionisation chambers, notably the need for a circulating gas circuit and the fact that the front-end amplifiers have to be placed as close as possible to the detector in a very high radiation area, making repairs difficult. A different technology, Cherenkov radiation, is therefore being studied to provide this measurement for the HL-LHC. Prototypes, with Cherenkov radiation produced in both air and fused silica rods, have been tested in the LHC during Run 2 to try to qualify the system for use in a region where the radiation dose will reach 180 MGy per year. The results indicate that the high radiation affects both systems, leading to a continuous degradation of the mirrors used in the air monitor, and a change in transmission of the fused silica rods. However, almost all of the transmission loss in the fused silica occurs within the first 10 fb^{-1}, with transmission remaining stable beyond this while still producing sufficient light. This technology therefore looks promising as the baseline for the luminosity monitors of the HL-LHC [17].

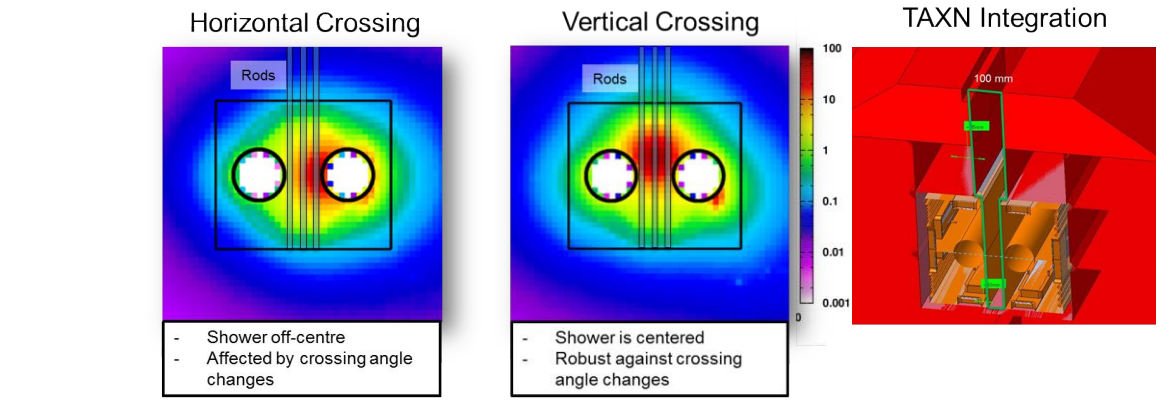

Figure 13-6: (a) Prototype installation in the LHC TAN; (b & c) Secondary shower map at the TAXN for horizontal and vertical crossing; (d) Space for integration of the Cherenkov rods in the TAXN

13.7.1 Changes from the initial HL-LHC TDR

In the original TDR it was foreseen to install ionisation chambers similar to those already operating in LHC. However, the disadvantages of these monitors led to R&D on new techniques, resulting in a successful validation of Cherenkov detectors, which are now the baseline for the luminosity monitors of the HL-LHC.

13.8 Gas jet diagnostics

With a hollow electron lens being added to the HL-LHC collimation system, research and development is underway to ensure that such an electron lens can be fitted with adequate diagnostics. One requirement is the on-line monitoring of the position of both the electron and proton beams, to ensure that the low energy, hollow electron beam is always concentric about the high-energy proton beam. This requires a non-invasive monitor capable of providing a simultaneous, two-dimensional image of both beams. In addition, this measurement must be made in close proximity to the solenoid field constraining the electron beam, preventing the use of charged particles as an observable.

An instrument is being developed through collaboration with GSI (Darmstadt, Germany) and the Cockcroft Institute/University of Liverpool (UK) to image fluorescence generated by the interaction between these beams and a thin, supersonic, gas curtain [18]. By tilting this ‘Beam Gas Curtain’ (BGC) with respect to the beam axis, a two-dimensional image of both beams can be obtained in much the same way as with a traditional, solid screen beam observation system. The instrument consists of the following main components:

- a gas generation stage with a supersonic gas nozzle followed by three skimmers which select and shape the gas jet;
- an interaction chamber where the high energy proton beam and low energy hollow electron beam interact with the gas jet;

- an optical system for image generation;
- an exhaust chamber which pumps the residual gas jet and contains gas jet diagnostics.

There are a number of key developments required for this instrument. It is important to select a working gas that is compatible with the NEG-coated, ultra-high vacuum system of the LHC, whilst still producing an adequate fluorescence signal from the interaction of both keV electrons and TeV protons, preferably from the spectral line of a neutral atom or molecule to avoid image distortion from electric and magnetic fields. It is also necessary to study the production of a dense supersonic gas curtain whilst minimising the background gas load to the vacuum system, and to develop a radiation-hard imaging system that is efficient for both the electron and proton excited fluorescence signals.

Although no fluorescence cross-section data exists for protons impacting neutral gases at 7 TeV, extrapolation from lower energy experiments indicate that for the gases of choice, neon, or argon, these will be between 20-30 times lower than for the low energy electrons. This, however, is compensated by the small transverse size of the proton beam, with detection of a few hundred photons considered sufficient to assess the proton beam position and shape. The electron beam is distributed over a much larger area, and it is therefore estimated that ~10^4 photons will be needed for the same purpose. Since the total electron and proton beam currents are of the same order of magnitude (~5 A for electrons and ~1 A for protons) the total integration times should be similar and of the order of 1 s.

A prototype is currently under construction with plans to install and validate this technology for operation on high energy proton beams during Run 3 of the LHC (see Figure 13-7).

Figure 13-7: Exploded view of prototype to be installed for testing in the LHC during Run 3.

13.9 Long-range beam–beam compensation

The simulated strong effect of the LHC long-range interactions on beam stability led to a proposed long-range beam-beam compensation for the LHC based on current-carrying wires [19]. As of today, this equipment is not part of the HL-LHC baseline, however studies, construction of a number of prototypes, tests in LHC with beam, and a final conceptual design for the HL-LHC are supported by the project. The aim is to be ready with a validated solution in case of need, e.g. for operation with flat beams and/or if there is a shortfall in crab cavity performance.

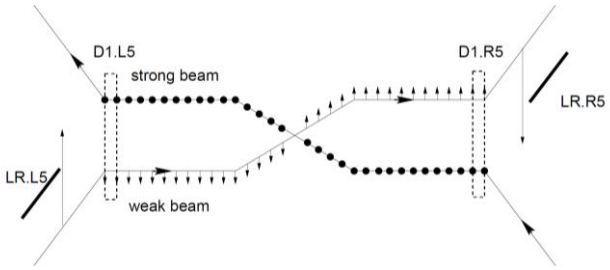

Figure 13-8: Illustration of the compensation principle. Here LR.L5 and LR.R5 indicate schematically the potential position of compensating wires.

13.9.1 Long-range beam–beam demonstrator

One of the few solid objects that can approach the beam accurately to within 10 σ or less are the LHC collimators. By embedding a wire in such a collimator, it is possible to use the collimator as a host for a demonstrator version of a long-range beam-beam compensator. The best compensation effect in this scenario is obtained by a wire in the tertiary collimators (TCT) located just in front of the D2 magnet. A 1 m long wire at this location would require a DC current of some 180 A at a distance of 9.5 σ to the beam or over 200 A at a distance of 11 σ. These values correspond to a symmetric layout with one compensator left of the IP and another on the right-hand side, a set-up that is necessary since the ratio of the horizontal and vertical beta functions are not equal at the TCT locations.

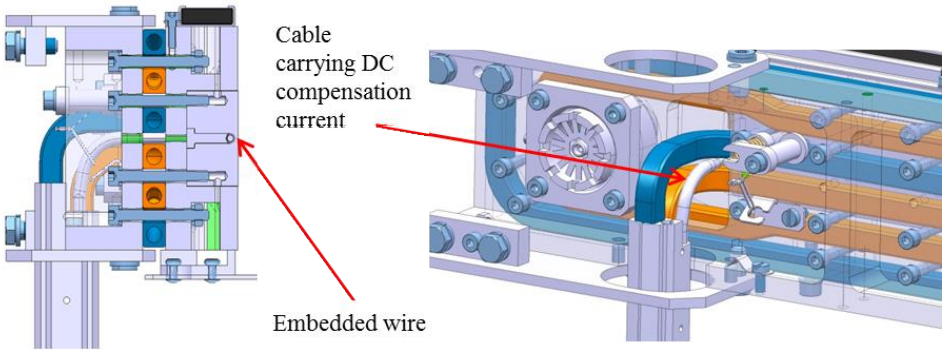

Figure 13-9: Technical drawing of the wire-in-jaw collimator design.

Integration of DC-powered wires into collimator jaws (Figure 13-9) was the only possibility to make realistic beam tests before embarking on a final implementation of the wires for high-luminosity operation. This integration itself required the solution of many important technical issues:

- no interference of the wires with the nominal operation of the collimators;
- transfer of 1 kW resistive heat loss in the wire by heat conduction to the water-cooled collimator jaw;
- shielding of the wire from the beam with a thin metallic layer for impedance reasons.

These were all successfully solved with four such wires now installed for testing in the LHC, along with the necessary DC cables and power converted infrastructure [20].

Machine experiments performed in 2017 and 2018 with these wires have clearly demonstrated long-range compensation [21]. Studies are therefore ongoing to complete a conceptual design for optimised beam-beam compensators for the HL-LHC.

13.10 Changes from the initial HL-LHC TDR

In the original TDR it was foreseen to study a high current electron beam as an alternative to a solid, current carrying wire in order to allow a much closer approach to the beam. However, recent results from the wire-in-

jaw long-range compensators in the LHC accompanied by updated simulations, show that this is not necessary, and that adequate compensation can still be achieved at distances compatible with the collimation hierarchy. This favours the possibility of using of solid wires for the final system, a technology that is much cheaper and easier to integrate than high current electron beams.

13.11 References

[1] C. Zamantzas *et al.*, "The LHC beam loss monitoring system commissioning for 2010", Proc. Evian Workshop on LHC Commissioning, 19-20 Jan 2010, DOI: oai:cds.cern.ch:1281617.

[2] L. Giangrande, "ASICs for the BLM system upgrade", INDICO: 742082.

[3] M. Bartosik *et al.*, "Beam loss monitors for the cryogenic LHC magnets", Proc. IBIC2015, Melbourne, Australia, 13-17 Sept 2015, DOI: 10.18429/JACoW-IBIC2015-MOPB042.

[4] A. Tsinganis, F. Cerutti, A. Lechner, A. Mereghetti, Y. Zou, "Detection of beam losses in the triplet and cold BLM sensitivity", INDICO: 647714.

[5] E. Calvo *et al.*, "The LHC orbit and trajectory system", Proc. DIPAC03, Mainz, Germany, 2003, p. 187, CERN-AB-2003-057-BDI.

[6] D. Cocq, "The Wide Band Normaliser: A New Circuit to Measure Transverse Bunch Position in Accelerators and Colliders", Nucl. Instrum. Methods Phys. Res. A 416, 1998, CERN-SL-98-064-BI.

[7] J. Wenninger, "BPM performance for operation In LHC Run 1 and Run 2", INDICO: 716801.

[8] A. Nosych, "Geometrical non-linearity correction procedure of LHC beam position monitors", EDMS: 1342295.

[9] G. Valentino *et al.*, "Final implementation, commissioning, and performance of embedded collimator beam position monitors in the Large Hadron Collider", Phys. Rev. Accel. Beams 20, 2017, DOI: 10.1103/PhysRevAccelBeams.20.081002.

[10] M. Gąsior *et al.*, "First Operational Experience with the LHC Diode ORbit and OScillation (DOROS) System", Proc. IBIC'16, Barcelona, Spain, Sep. 2016, DOI: 10.18429/JACoW-IBIC2016-MOPG07.

[11] LHCb Collaboration, "Absolute luminosity measurements with the LHCb detector at the LHC", J. Instrum. **7** (2012) P01010, IOP and SISSA, DOI: 10.1088/1748-0221/7/01/P01010.

[12] A. Alexopoulos *et al.*, "Non-invasive LHC transverse beam size measurement using inelastic beam–gas interactions", Phys. Rev. Accel. Beams 22, 042801, DOI: 10.1103/PhysRevAccelBeams.22.042801.

[13] R. Kieffer *et al.*, "The Beam Gas Vertex profile monitoring station for HL-LHC", Proc. IPAC2019, Melbourne, Australia, 19-24 May 2019, DOI: 10.18429/JACoW-IPAC2019-WEPGW082.

[14] G. Trad *et al.*, "First observation of the LHC beam halo using a synchrotron radiation coronagraph", Proc. IPAC2017, Copenhagen, Denmark, DOI: 10.18429/JACoW-IPAC2017-TUOAB2.

[15] T. Levens, K. Lasocha and T. Lefevre, "Recent Developments on Instability monitoring at the LHC", Proc. IBIC2016, Barcelona, Spain, 11-15 Sept. 2016, DOI: 10.18429/JACoW-IBIC2016-THAL02.

[16] S.M. Gibson *et al.*, "Enhanced bunch monitoring by interferometric electro-optic methods", Proc. IPAC2018, Vancouver, BC, Canada, 2018, DOI: 10.18429/JACoW-IPAC2018-WEPAL073.

[17] M. Palm, "Update on Luminosity monitoring for HL-LHC", INDICO: 742082.

[18] R. Veness *et al.*, "Development of a beam-gas curtain profile monitor for the high-luminosity upgrade of the LHC", Proc. IBIC2018, Shanghai, China, DOI: 10.18429/JACoW-IBIC2018-WEPB16.

[19] J.-P. Koutchouk, "Principle of a correction of the long-range beam-beam effect in LHC using electromagnetic lenses", 2000, LHC-Project-Note-223.

[20] A. Rossi, "Wire: Brief status of hardware/controls and tests done/to be done", INDICO: 615088.

[21] G. Sterbini *et al.*, "First results of the compensation of the beam-beam effect with DC wires in the LHC", Proc. IPAC2019, Melbourne, Australia, DOI: 10.18429/JACoW-IPAC2019-WEYYPLM3.

Chapter 14

Beam injection and dumping systems

C. Bracco[1*], *M. J. Barnes*[1] *and A. Lechner*[1]

[1]CERN, Accelerator & Technology Sector, Switzerland
[*]Corresponding author

14 Beam injection and dumping systems

14.1 Overview

The beam transfer into the LHC is achieved by the two transfer lines TI2 and TI8, together with the septum and injection kickers, plus associated systems to ensure the protection of the LHC elements in case of a mis-steered beam. The foreseen increase in injected intensity and brightness for the HL-LHC means that the protection functionality of the beam-intercepting devices (TDI) needs upgrading [1]. In addition, the higher beam current significantly increases the beam-induced power deposited in many elements, including the injection kicker magnets in the LHC ring.

The beam dumping system is also based on DC septa and fast kickers, with various beam intercepting protection devices including the beam dump block. Again, the significant change in the beam parameters for the HL-LHC implies redesign of several of the dump system devices, both because of the increased energy deposition in the case of direct impact and because of increased radiation background that could affect the reliability of this key machine protection system [1].

Since the last version of the HL-LHC Technical design report [2] several changes occurred. HiRadMat tests allowed to finalise the choice on the materials of the absorbing blocks and the back-stiffener of the injection dump (TDIS). The modification and displacement towards the IP of the auxiliary injection protection collimator (TCLIA) in Point 2, to increase the ZDC acceptance, is now part of the HL-LHC baseline. As a result of the successful tests on an upgraded injection kicker prototype, the series production of the MKIs with Cr_2O_3 coated chambers and modified beam screen was also approved and is in the project baseline. New failure types of the dilution kickers (MKB) and different weaknesses of the beam dump block itself (robustness of the different components plus vibrations) were found. Mitigation measures to improve the reliability of the MKBs will be put in place in LS2 but further upgrades of the full system are needed for a fully safe operation with the HL-LHC beams.

14.2 Beam injection systems

The layout of the LHC injection region and the associated protection devices is shown schematically Figure 14-1. The beam to be injected passes through five horizontally deflecting steel septum magnets (MSI) and receives a total kick of 12 mrad. Four vertically deflecting kickers (MKI) merge the beam on to the LHC closed orbit by applying a total kick strength of 0.85 mrad. Uncontrolled beam losses resulting from MKI errors (missing pulses, erratic, partial, badly synchronized, or wrong kick strength) could result in serious damage to the downstream equipment. In particular the superconducting separation dipole D1, the triplet quadrupole magnets near the ALICE and LHCb experiments or the magnets in the arcs of the LHC machine itself could be directly hit by the beam. Also, particle showers, generated by proton losses, could damage components of

the detectors which are close to the beam pipe. Precautions must therefore be taken against damage and magnet quenches and collimators and dumps are placed at key locations in the injection regions.

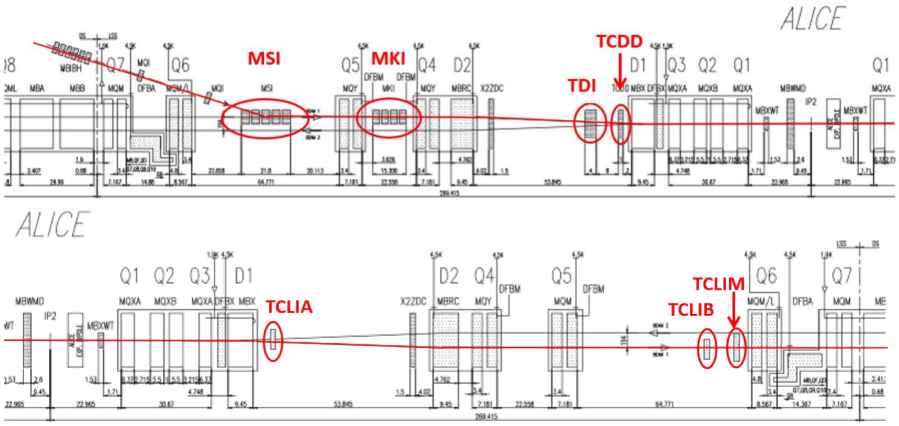

Figure 14-1: Overview of the present injection system into the LHC and the associated protection devices (Beam 1, IR2). The beam is injected from the left-hand side.

14.2.1 Upgrade of the injection dump TDIS

The present TDI is a movable two-sided vertical absorber which is installed at about 90° betatron phase advance from the injection kicker. Its main purpose is to protect machine elements in case of MKI malfunctions and timing errors. The TDI is also used to intercept bunches during the set-up or commissioning of the injection system with low intensity beam (one bunch of 5×10^{9} - 1×10^{10} ppb).

The jaws of the TDIs presently installed in the LHC are 4.185 m long and accommodate blocks of graphite (6 × 47.1 cm), aluminium (1 × 60 cm) and CuCr1Zr (1 × 70 cm). The two latter blocks are retracted by 2 mm with respect to the graphite to avoid direct beam impact on these materials, which could lead to an excessive heating and stresses of these blocks. During the first years of the LHC operation, the TDIs in both IR2 and IR8 injection insertions were affected by several anomalies including outgassing, vacuum spikes, structural damage of the beam screens and elastic deformation of the jaws due to beam induced RF heating during the fills. Several hardware changes were already applied during the first long shutdown (LS1) and the following winter stops to mitigate the encountered problems [3]. Despite a visible reduction of the beam induced jaw deformation and of the vacuum activity, it was decided to develop a new improved design in terms of mechanics, robustness, reliability, setup accuracy, impedance and operational aspects in view of operation with higher intensity and brightness beams after LS2.

Instead of having one long jaw, the new TDI (called TDIS, where the “S” stands for Segmented) will comprise three shorter absorbers (~1.6 m each) accommodated in separate tanks (see Figure 14-2). The jaws of each module will all be identical except for the active absorber material. For robustness reasons, the two upstream modules will accommodate low-Z graphite absorber blocks (SIGRAFINER R7550, 1.83 g/cm3). The third module is foreseen to host higher-Z absorber materials (Ti6Al4V and CuCr1Zr) to better absorb and efficiently attenuate the particle showers from the low-density upstream blocks.

The correct positioning of the TDIS jaws around the beam is vital for machine protection. Each module will be independently movable and redundant position measurements will be performed and checked via the Beam Interlock (BIS) and the Beam Energy Tracking Systems (BETS). The jaws of the third module will be slightly retracted compared to the upstream jaws to avoid direct beam impact on the higher-Z absorber blocks.

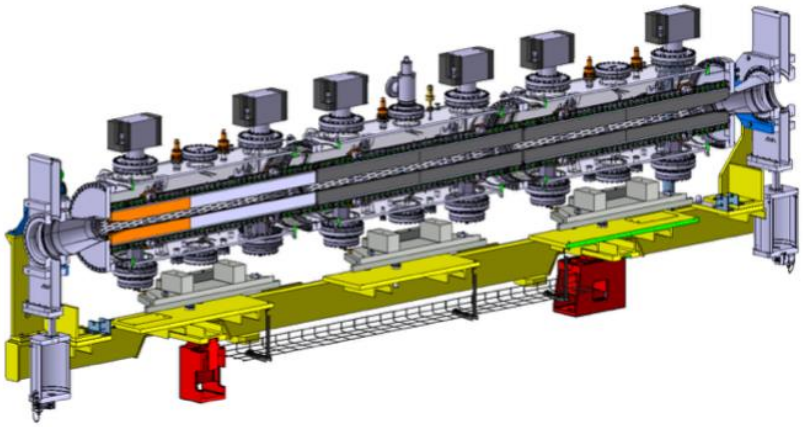

Figure 14-2: The longitudinal cross-section of the new TDIS showing the modules composed by different materials. The first two module jaws, starting from the right side of the figure, are made of graphite R7550 (dark grey), the last module is made of Ti6Al4V (light grey) and CuCr1Zr (orange).

14.2.2 Supplementary shielding of D1 coils

A complementary mask (TCDD in IR2 and TCDDM in IR8) is installed directly in front of the superconducting D1 separation dipole to prevent damage of the coils due to secondary showers from the TDIS in case of MKI failure, see Figure 14-1. Detailed particle simulations [4] showed that the most efficient way to further reduce the energy deposition on D1, and possibly limit the risk of quench, consists in installing additional mask-like stainless-steel protection elements directly inside the insulation vacuum of the D1 cryostat. This solution offers the advantage of intercepting shower particles closer to the magnet without affecting the present machine aperture (Figure 14-3).

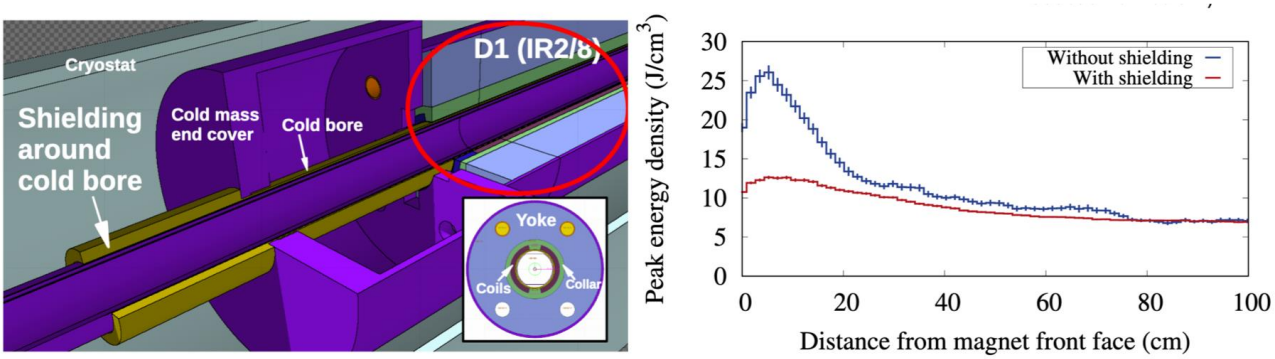

Figure 14-3: 3D model of D1 cryostat where the additional shielding is installed around the cold bore to reduce the energy deposition on the magnet coils in case of injection failure (left). The expected reduction in the peak energy is also shown (right).

14.2.3 Displacement of auxiliary injection protection collimator TCLIA

The TCLIA is an auxiliary collimator which provides additional protection from mis-kicked beam in case of MKI failures. This device is set at an aperture of ±6.8 σ (for the nominal LHC emittance of 3.5 mm mrad) during the injection process. Once the injection is completed and the MKIs are in standby, the TCLIA is opened to parking position in order not to represent anymore an aperture bottleneck. The present maximum aperture at parking (±28 mm) and the longitudinal position of the TCLIA limits the maximum crossing angle to ≤ 60 µrad (Figure 14-4) and thus the Zero-Degree-Calorimeter (ZDC) of ALICE [5]. This is not compatible with operation with 50 ns bunch spacing (i.e. the present baseline for the HL-LHC Pb−Pb physics operation) where an angle ≥ 100 µrad is needed. Studies were performed and it was found that the maximum TCLIA

opening can be increased to 59 mm. Moreover, it was decided to move the collimator by 2.2 m towards the IP. These modifications will allow achieving a crossing angle of 102.4 µrad as required for 50 ns bunch spacing operation.

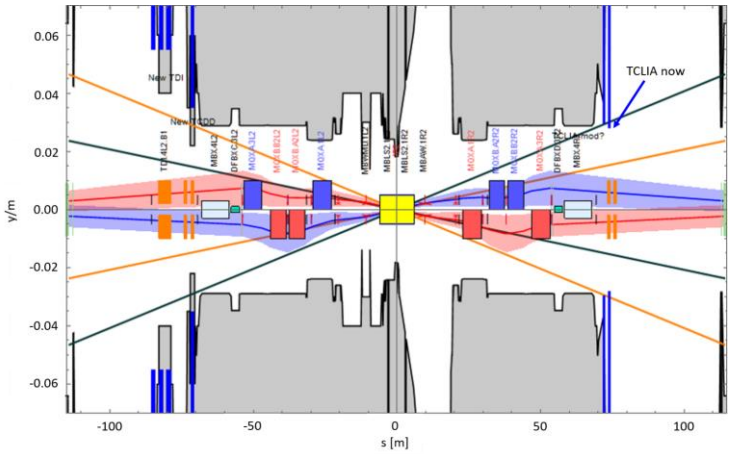

Figure 14-4: IR2 aperture layout and 100 µrad neutron cone from IP2. The present TCLIA, even when fully opened to parking position, is in the line of sight of the ZDC.

14.2.4 Upgrade of the injection kickers MKIs

The injection kicker magnets are transmission line type magnets, each with 33 cells consisting of a U-core ferrite between two high voltage (HV) conducting plates [6]. To limit the longitudinal beam coupling impedance and thus heating, while allowing a fast magnetic field rise-time, an extruded ceramic tube (99.7% alumina) with up to 24 screen conductors lodged in its inner wall is placed within the aperture of each MKI magnet. A set of toroidal ferrite rings is mounted around each end of the alumina tube, outside of the aperture of the magnet to damp low-frequency resonances. To ensure reliable operation of the MKI magnets, the temperature of the ferrite yokes must not exceed their Curie point, which is ~125°C for the ferrite used. At this temperature, the magnetic properties of the ferrite are temporarily compromised, and the beam cannot be injected.

Both the MKI kickers installed in IR2 and IR8 prior to LS1 encountered a number of issues which affected operation. These include beam-induced heating, electrical flashovers, beam losses and electron cloud related vacuum pressure rise [7] with electrical breakdown and surface flash-over. A prototype MKI, with a 50 nm thick Cr_2O_3 coating applied by magnetron sputtering to the inner part of the alumina tube, was installed in IR8 during the winter stop between 2017 and 2018 [8]. A rapid reduction of the dynamic vacuum and faster conditioning with respect to the original design was observed during the scrubbing run and in operation. In addition, the Cr_2O_3 coating has not resulted in a statistically significant change in the number of UFOs (macro particles falling into the beam).

The beam screen of all the MKIs was upgraded during LS1 to allow the full complement of 24 screen conductors to be installed. The modified design allowed the surface flashover rate to be further reduced [6]. The post-LS1 design also resulted in a considerable reduction of beam induced power deposition in the ferrite yoke [9] and no limitation was encountered in operation during Run 2 [10]. A further reduction in the yoke temperature was observed in the IR8 prototype where the beam screen was modified to reduce the total power loss and move the main losses from the yoke to the ferrite rings [11]. Thermal simulations were carried out to confirm that the calculated power losses for Run 2 agreed with the temperatures measured during LHC operation. A good agreement was found, and no issues were foreseen since a maximum temperature of 110°C was calculated in the first cell at the upstream end of the upgraded magnet [10]. However, for operation with the HL-LHC type beams, the power deposition in the MKI is expected to be a factor of four greater than for LHC nominal beam parameters, which would be unacceptably high with the existing design [12]. Studies showed that, following the redistribution of power from the yoke to the ferrite rings, an active water cooled

system just of the ferrite rings is sufficient to keep the temperature of the full magnet well below 100°C also for the HL-LHC beams [13]. A complete prototype with Cr_2O_3 coated chambers, upgraded beam screen with active cooling of the ferrite rings, the so called "MKI cool" (Figure 14-5 shows the modified beam screen at the beam entrance of the "MKI cool" [6]), will be installed and tested in the LHC for the final validation during Run 3 before launching the upgrade of the full MKI series.

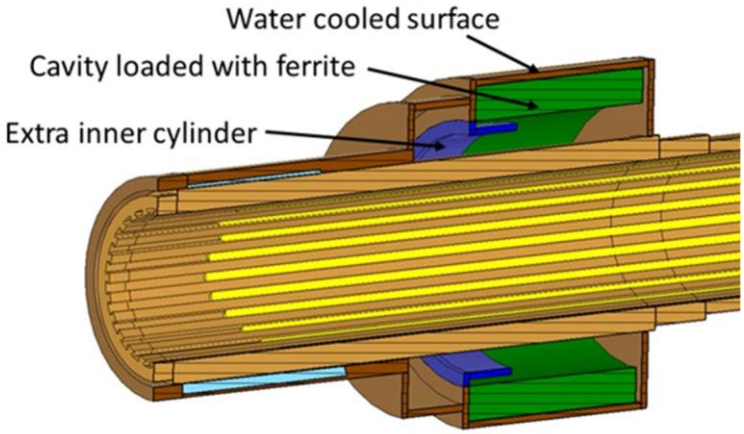

Figure 14-5: Simplified schematic illustration of the upstream end of the beam screen to be implemented in the "MKI Cool" that will be installed during LS2.

14.3 Beam dumping system

Each beam is extracted from the LHC ring, by means of fifteen pulsed extraction kickers (MKD) and DC septum magnets (MSD) located in a dedicated insertion of the LHC (IR6, schematic view in Figure 14-6, towards a long drift chamber and a graphite absorber dump block (TDE). A system of four horizontal (MKBH) and six vertical (MKBV) dilution kickers is powered with anti-phase sinusoidal currents to sweep the beam over the front face of the TDE in order to reduce the deposited energy density.

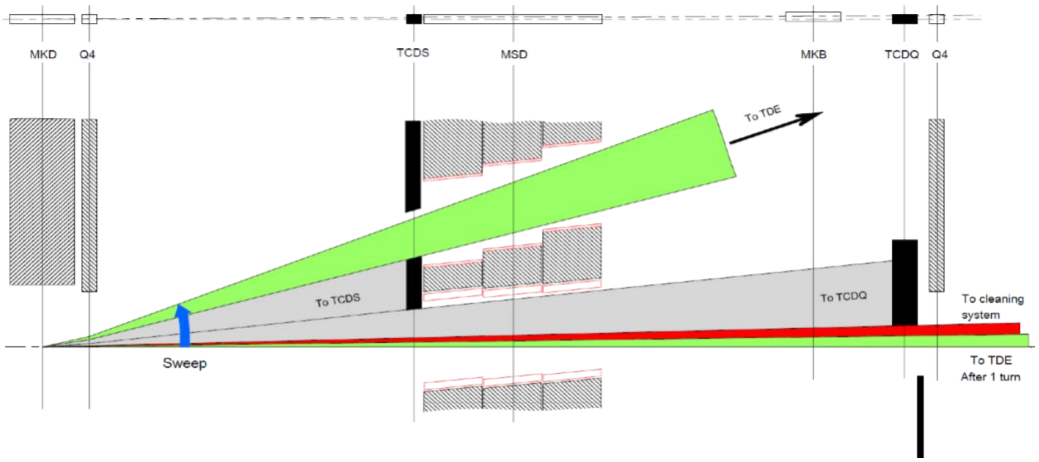

Figure 14-6: Overview of the LHC extraction region (Point 6)

To avoid losses during the rise time of the LHC MKD, a 3 μs long abort gap in the circulating bunch pattern is kept free of particles. So-called asynchronous beam dumps can be caused by loss of synchronisation of the MKD rise time with the abort gap, e.g. in case of failure of the Trigger Synchronisation Unit (TSU), or by the erratic pre-firing of an extraction kicker. In these cases, the beam can be swept over the machine aperture and dedicated absorber blocks are installed in the LHC extraction region to protect the down-stream elements.

14.3.1 Beam dump system absorbers TCDQ and TCDS

Several failure modes exist in the synchronization system and in the kicker switches that could lead to an asynchronous dump where part of the beam would be swept across the LHC aperture. Without dedicated protection devices this would lead to massive damages. The protection devices against asynchronous beam dump damages are: the TCDS, which is a fixed absorber that directly protects the downstream extraction septum MSD and the TCDQ, which is a movable absorber that protects the superconducting quadrupole Q4 and further downstream elements, including the arc and the tertiary collimators (TCTs) around the experiments. A fixed mask (TCDQM) is installed right upstream of Q4 to intercept secondary particle showers and thus reduce the energy deposition in the superconducting coils. The TCDQ was already upgraded in LS1. The new design, which is described in detail in Ref. [14], includes an extension of the absorber length from 6 m to 9 m, and the replacement of the higher density graphite absorber material with different grades (1.4 g/cm^3 and 1.8 g/cm^3) of carbon fibre composites (CfC). This design was supposed to be compatible with operation with the HL-LHC beams. During the reliability runs performed in 2015 a new type of MKD erratic firing (Type 2), with a different rise time than the standard one (Type 1), was identified. This case is more critical since a higher number of bunches can impact the TCDQ with a large density close to the jaw surface (see Figure 14-6). New studies were carried out to verify the robustness of the TCDQ also for this new failure scenario. Depending on the optics, the TCDQ jaw will have to be set at an aperture which could vary between 2.5 mm and 3.9 mm. No damage is expected if the TCDQ sits at ≥ 3 mm from the beam while, for smaller gaps, the peak dose could go above 2.7 kJ/g (Figure 14-7) corresponding to a temperature ≥ 1500°C. The present knowledge of the material properties at such temperature is quite poor and does not allow to exclude possible failures. A further TCDQ upgrade is not part of the HL-LHC baseline and presently, alternative mitigations (i.e. Type 2 erratic prevention, improved monitoring of the local orbit, suitable optics conditions, etc.) are being evaluated.

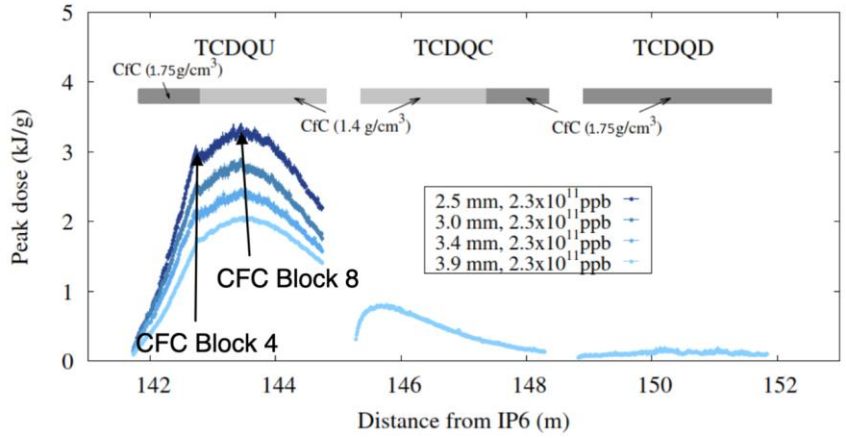

Figure 14-7: Peak dose along the TCDQ modules in case of asynchronous beam dump with the TCDQ sitting at different apertures depending on the optics requirements.

The BETS monitors the position of the TCDQ as a function of the beam energy. This HW interlock was implemented in LS1 to have a redundant check of the TCDQ positioning in case of failure of the standard control system. This forbids moving the TCDQ outside pre-defined thresholds at fixed energy and might be a limitation for the ATS optics when the β-function at the TCDQ changes during the squeeze and the protection element should vary its position accordingly. In case this affects the HL-LHC β^* reach, the BETS should be upgraded to allow for TCDQ movements during the squeeze. This activity is not part of the present baseline.

The robustness of the TCDS and the protection of the MSD magnets, in case of an asynchronous beam dump with the full intensity HL-LHC beams, was verified for all types of erratics. A maximum energy density of 2.5 kJ/cm^3 (giving a maximum temperature of ~1150°C) was calculated in the low-density blocks (graphite and CFC) and of ≥ 1 kJ/cm^3 in the Ti block. Thermo-mechanical studies indicate that the Ti block will experience plastic deformation and some low-Z blocks could fail due to the high stresses and elevated temperatures reached. The calculated energy deposition at the first downstream MSD septum corresponds to a

temperature increase of less than 100 K (~130°C absolute temperature). This temperature is not critical concerning possible changes in the magnetic properties of the steel (up to 150°C is considered acceptable). Moreover, the peak temperature is reached in a peripheral part of the yoke so that no issue is expected for the insulation of the coils. Further studies are needed to evaluate if a temperature increase of up to 100 K could induce a deformation of the vacuum chamber of the circulating beam. Moreover, FLUKA and ANSYS calculations have to be performed to quantify the temperature increase of the water in the MSD cooling pipes and thus to evaluate the pressure rise and the consequent risk of shock-waves. The TCDS upgrade is included in the HL-LHC baseline.

14.3.2 The beam dump TDE

The LHC beam dump consists of an upstream window made of carbon-carbon composite on a thin stainless steel foil, a ~8 m long graphite dump core, a downstream Ti window and is kept under N_2 gas at higher than atmospheric pressure. The TDE and its entrance and exit windows will need to withstand the repeated dumps of high intensity HL-LHC beams. Simulation studies show that, in case of a regular dump of the HL-LHC beams a peak temperature of ~1800°C (a factor ~2 higher than for the LHC Run 2 beams) will be reached in the core. In case of failure of the dilution kickers, the sweep pattern is altered (Figure 14-8) and significantly higher temperatures and stresses can be reached. The originally assumed worst case failure scenario was the loss of two MKBs due to either the erratic firing of one kicker and perfect phase opposition with the remaining ones or a flashover simultaneously affecting two MKBs sharing the same vacuum tank. In addition, due to the smaller number of horizontal modules, their contribution in case of a failure is more critical and, for the given dilution pattern, the system is more sensitive to the loss of horizontal dilution. In case of two missing horizontal MKBs, the peak temperature can go up to 2800°C for these failure cases. No information is available about the core material behaviour at this temperature and mechanical characterisation studies are being performed to evaluate if any modification of the present design is needed.

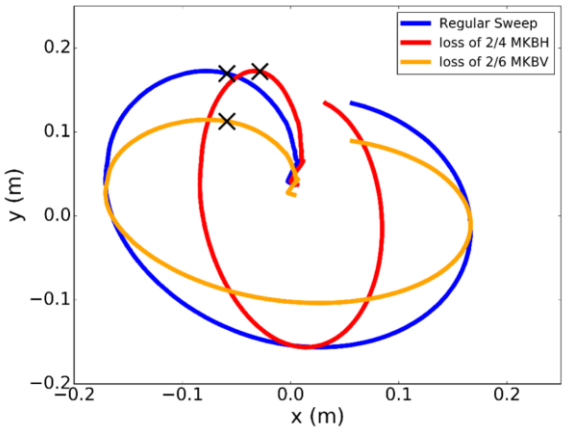

Figure 14-8: Simulated beam sweep patterns at the dump for a regular sweep (blue) and the failure cases of 2 out of 4 horizontal (red) and 2 out of 6 vertical dilution kickers missing (orange). The positions of highest energy deposition are marked with a black cross.

The expected stress level at the present windows, also in nominal operational conditions, would be too high to insure a long term and reliable operation with the HL-LHC beams. For this reason, they will be upgraded already in Run 3 to ensure their survival also in case of dumps with two missing MKBs.

Moreover, during Run 2, a series of N_2 leaks appeared at the flange connections and were ascribed to large vibrations of the whole dump due to beam energy transfer during high intensity dumps.

No dump upgrade was originally included in the HL-LHC baseline since detailed studies, identifying weaknesses and defining needed modifications, were missing. Studies evaluating all limitations are under way and the goal is to have all the information required for defining the complete upgrade strategy at hand by 2021

in order to define the upgrade layout and to be ready for installation in LS3. The HL-LHC project committed to upgrade the dump with the help of the Russian in-kind contribution.

14.4 LBDS kickers, generators, and control system

A number of erratic triggers due to electric breakdowns and unexpected failures were encountered during reliability runs, tests and operation with beam of the LBDS kickers.

The breakdowns were located at regions with large electrical fields of around 3 MV/m at the edges of the insulators in the generators. A redesign of the switch stacks of the MKD generators is ongoing with the aim of keeping the electrical field below 1.5 MV/m in all areas in order to allow reliable operation at 7 TeV. Moreover, the upgraded system is compatible with operation at the ultimate energy of 7.5 TeV. The replacement of the generator switch stacks is foreseen for LS2. Simultaneously, the power triggering and re-triggering system of the MKD switches will be upgraded. The power triggers are presently rated at a current of 500 A and a dI/dt of 400 A/μs for a voltage of 3.5 kV. The upgraded system will double the current and almost double the dI/dt for a reduced voltage of 3.0 kV. The new parameters are better in line with the specifications of the manufacturer, will increase the lifetime of the GTO switches, will result in a shorter rise time, and will make the power trigger less sensitive to radiation. The re-trigger system triggers all the extraction and dilution kickers as quickly as possible in case of an erratic closing of an extraction kicker switch. The present re-trigger delay is about 900 ns and the aim is to try to reduce it even further to minimise the load on the TCDQ and the ring elements, in particular the tertiary collimators, in case of an asynchronous dump. Also the diagnostic tool (IPOC [15]) will be upgraded and a sparking activity surveillance system will be implemented to monitor the status of the generators, allow to react in case of signs of nonconformity and provide statistics for a better understanding of the correlation between sparks and erratics. At the same time, the electronics of the re-triggering system, which is becoming obsolete, will be replaced.

Beside Type 2 erratics for the MKDs, unexpected failures affected also the dilution kickers. In particular, the parasitic electromagnetic coupling, through the re-triggering line, caused the firing of neighbouring MKB generators [16]. This event, combined with anti-phase could determine the loss of more than two MKBs, which was identified as the worst failure scenario in the original design of the system.

Moreover, up to three MKBVs were lost, on one occasion, due to a flash-over propagation with some delay and anti-phase in two kickers sharing the same vacuum tank. All these cases might have dramatic effects on the beam dump when operating with the HL-LHC beams, in particular in case of MKBH failures. Different upgrade scenarios for the dilution system are being considered [17]. The MKBH generators will be upgraded to reduce their operational voltage (presently higher than the MKBV voltage due to the lower number of MKBHs). A new re-triggering system for all the MKBs will be put in place to eliminate the risk of anti-phase in case of erratics. Different sweep patterns are then expected at the dump depending on the delay between the erratic and the execution of a synchronous dump as shown in Figure 14-9. The consequent energy deposition on the dump windows and the core are being evaluated for all possible relative delays. Finally, it is proposed to install two additional MKBHs per beam since this is the only fully reliable solution to reduce the risk and the sensitivity to any possible failure and opens the possibility to increase the nominal sweep pattern to reduce the stresses on the dump also during nominal operation. The HL-LHC project has approved the upgrade and implemented it through the Russian in-kind contribution. The installation is foreseen for LS3.

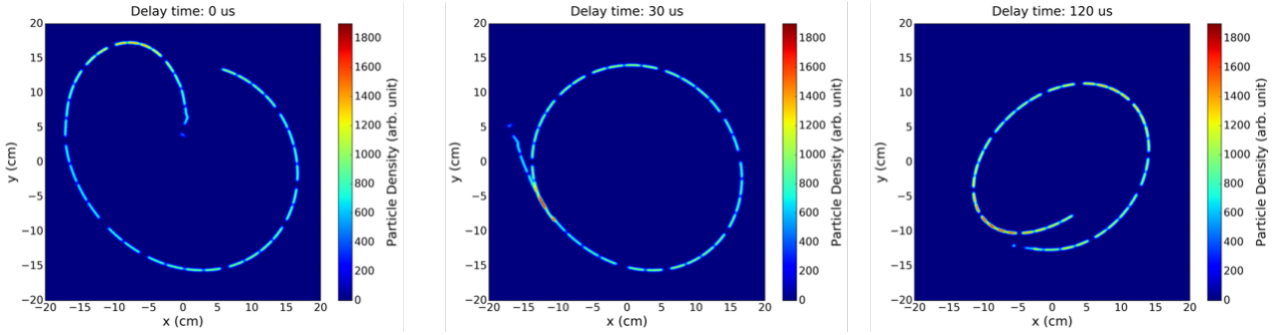

Figure 14-9: Simulated sweep patterns in case of MKB re-triggering for different delays between the erratic event and the synchronous dump execution.

14.5 Acknowledgments

W. Bartmann, M. Calviani, D. Carbajo Perez, E. Carlier, L. Ducimetiere, M.I. Frankl, B. Goddard, N. Magnin, A. Perillo Marcone, T. Polzin, V. Rizzoglio, V. Senaj, L. Vega, V. Vlachodimitropoulos and C. Wiesner.

14.6 References

[1] J. Uythoven *et al.*, Upgrades to the injection and beam dumping systems for the HL-LHC project, Proc. 5th International Particle Accelerator Conference, Dresden, Germany, 15 - 20 Jun 2014, DOI: 10.18429/JACoW-IPAC2014-MOPRO032.

[2] G. Apollinari *et al.*, High-Luminosity Large Hadron Collider (HL-LHC): Technical Design Report V. 0.1, DOI: 10.23731/CYRM-2017-004.

[3] A. Lechner *et al.*, Protection of Superconducting Magnets in Case of Accidental Beam Losses During HL-LHC injection, Proceedings of IPAC, Richmond, USA, 2015, DOI: 10.18429/JACoW-IPAC2015-TUPTY049.

[4] A. Lechner *et al.*, TDI Past observations and improvements for 2016, 6th Evian Workshop on LHC beam operation, Evian Les Bains, France, 15 - 17 Dec 2015, pp.123-130, CDS: 2294666.

[5] J. Jowett, ALICE ZDC aperture requirements, EDMS: 1830131.

[6] M.J. Barnes *et al.*, Reduction of Surface Flashover of the Beam Screen of the LHC Injection Kickers, 4th International Particle Accelerator Conference, Shanghai, China, 12 - 17 May 2013, pp.735, CDS: 1574591.

[7] M.J. Barnes *et al.*, Upgrade of the LHC injection kicker magnets, Proceedings of IPAC, Shanghai, China, 12 - 17 May 2013, pp.729, CERN-ACC-2013-0077.

[8] M.J. Barnes *et al.*, An upgraded LHC injection kicker magnet, Proceedings of IPAC, Vancouver, Canada, 2018, DOI: 10.18429/JACoW-IPAC2018-WEPMK003.

[9] M.J. Barnes *et al.*, Operational experience of the upgraded LHC injection kicker magnets during Run 2 and future plans, 8th International Particle Accelerator Conference, Copenhagen, Denmark, 14 - 19 May 2017, DOI: 10.1088/1742-6596/874/1/012101.

[10] L. Vega Cid *et al.*, Preliminary design of a cooling system for the LHC injection kicker magnets, Proceedings of IPAC, Vancouver, Canada, 2018, DOI: 10.18429/JACoW-IPAC2018-WEPMK001.

[11] M.J. Barnes et al., Exchange of LHC kicker magnet MKI2B, EDMS: 2049157.

[12] V. Vlachodimitropoulos *et al.*, Longitudinal impedance analysis of an injection kicker magnet, Proceedings of IPAC, Vancouver, Canada, 2018, DOI: 10.18429/JACoW-IPAC2018-WEPMK002.

[13] L. Vega Cid *et al.*, Conception and design of a cooling system for the LHC injection kicker magnets, *Nucl. Instrum. Methods Phys. Res., A* 916, 296-305, 2019, DOI: 10.1016/j.nima.2018.11.007.

[14] R. Versaci *et al.*, LHC asynchronous beam dump: Study of new TCDQ model and effects on downstream magnets, CERN, Geneva, Switzerland, 2012, CERN-ATS-Note-2012-084-MD.

[15] N. Magnin *et al.*, Internal Post Operation Check system for kicker magnet current waveforms surveillance, Proceedings of ICALEPCS2013, San Francisco, CA, USA. pp.moppc029.

[16] C. Wiesner *et al.*, LHC beam dump performance in view of the high luminosity upgrade, 8th IPAC, Copenhagen, Denmark, 2017, DOI: 10.18429/JACoW-IPAC2017-WEPIK033.

[17] C. Wiesner *et al.*, Upgrade of the dilution system for HL-LHC, Proceedings of IPAC, Vancouver, Canada, 2018, DOI: 10.18429/JACoW-IPAC2018-MOPMF062.

Chapter 15

Integration, (de-)installation and alignment

P. Fessia[1*] *and H. Mainaud Durand*[1]

[1]CERN, Accelerator & Technology Sector, Switzerland
[*]Corresponding author

15 Integration, (de-)installation and alignment

15.1 Overview

The HL-LHC will require modifying the machine and infrastructure installations of the LHC in several points along the Accelerator Ring, in particular: P1, P2, P4, P5, P6, P7 and P8.

Part of the modifications and improvement in P2, P4, P7 and P8 shall be completed during Long Shutdown 2 (LS2) and be operational for LHC Run 3, while the largest part of the interventions will take place in Long Shutdown 3 (LS3) and they will affect primarily P1, P4, P5, P6 and P7. The activities required point by point will be therefore listed and analysed here below.

The Project evolution has allowed and obliged to revise and refine the previous integration plan. Here below the main changes are singled out

- Point 1 and Point 5
    - The LHC Machine layout has been made compliant with the optics version 1.4 that integrates the deployment of the Full Remote Alignment and the results of the matching section optimization. The present layout is based on updated and refined equipment designs considering the progress of the engineering design of each system. This includes in particular: magnet cryostats, DFX, Crab Cavity cryo-modules, collimators that have all seen important evolution in their design.
    - The system optimization implied a revision of the localization of some of the equipment, i.e. the power converters feeding the circuits of the Higher Order correctors magnets that are in the Corrector Package have been moved from the new HL-LHC underground infrastructures to the service alcoves of the LHC tunnel.
    - Following the refinement of the services design and the machine equipment requirements, the full integration in the new HL-LHC underground infrastructures has been reviewed. The integration activity in this area is strictly linked to the finalization of the construction design of the caverns that are being built during LS2.
    - In a similar way, and for the same reasons, the integration of the new surface buildings and the connecting technical galleries has been revisited in detail, leading to an optimization in the gallery topology and refinement in the building design.
- Point 4:
    - The cryogenic system upgrade at Point 4 has been reviewed. In order to support the operation in Sector 3-4 (that is fed by a refrigerator unit inherited from the LEP machine) the refrigerator will be upgraded, but without impacting the cryogenic distribution network. The previously foreseen mobile

refrigerator that was foreseen to cool the LHC RF accelerating cavities for testing and conditioning purposes has been abandoned.

- The conceptual design of the Hollow-Electron Lenses has been integrated in the tunnel together with their services validating the design choices.

- Point 6
  - The previous foreseen upgrade of the Q5 units has been abandoned. The presently installed units will be operated in the HL-LHC configuration as they currently are in the existing LHC configuration.
  - The horizontal beam dump dilution kicker system is planned to be upgraded with the installation of 1 additional kicker module for each beam.
  - The Beam Dump block will be upgraded already in LS2 with new upstream windows. Additionally, the dump block will be mechanically separated from the beam dump line and its support system modified to allow for an improved absorption of the shock waves during beam impact.
  - The entire Beam Dump block is planned to be replaced during LS3 in preparation for the HL-LHC exploitation.

15.2 Point 1 and Point 5

The largest part of the new equipment required to meet the HL-LHC performance objectives will be installed at P1 and P5. The items to be installed and actions to be carried out are listed below and are applicable to both points, if not otherwise specified. The list is organized by geographical areas.

15.2.1 LHC machine tunnel

De-installation:

- All the accelerator equipment from the interface with the experimental cavern (TAS included) until the Q6 (excluded) needs to be removed from the Interaction region on the Right and Left side of the IP (so defining a “Q6L-Q6R” zone).
- In a similar way, all the cabling in the Q6L-Q6R region has to be removed. The present cables and optical fibres will be of three families:
  - Cabling linked to LHC equipment in this area and that has therefore to be de-installed and to be replaced with the new HL-LHC equipment (ex. triplets, D1, D2 magnets and their ancillary equipment).
  - Cabling linked to the machine equipment not affected by the HL-LHC modifications, but that are passing through the Q6L-Q6R region and that need to be de-installed to permit the execution of the Civil Engineering (CE) activities in the area.
  - General services and safety systems cabling passing through the Q6L-Q6R region.
- In the same area, the present QRL will also have to be removed. A new return module will be installed in the region between the Crab Cavities and the Q4. This element will allow separation of the coolant flows coming from the LHC QRL and the one of the new HL-LHC QXL. The HL QXL will feed the part of the machine from Q1 to the Crab Cavities included. This return module should also provide the possibility, if required, to connect the LHC QRL with the HL QXL, ensuring an increased level of redundancy in the system. The LHC QRL between the Crab Cavities and the Q6 will be reassembled re-using as much as possible the previous QRL elements but re-installed in order to cope with the different optical positions of the Q4 and Q5 magnets.
- It will be necessary to remove all the services linked to the above mentioned equipment that will be de-installed, and also all the services that could obstruct the opening of the vertical cores that will link the

HL-LHC new infrastructures with the LHC tunnel (e.g. cables trays, cooling pipes, ventilation ducts, part of monorail system, etc.).

- Opening of the vertical cores linking the HL-LHC new infrastructures with the LHC tunnel: these cores will be not excavated when the new main HL-LHC cavern will be created, but only later at the start of LS3 and therefore after the completion of LHC Run 3. The activity will take place well after the completion of the underground HL-LHC complex.

Preparation for re-installation:

- Minor works could be necessary in order to prepare the tunnel floor and wall to receive the installation of the new equipment (for larger and dedicated CE activities see the next paragraphs).
- Re-install the general services and safety system cables with their needed supports and ancillaries.
- Re-install general services equipment previously dismounted (e.g. cooling pipes, ventilation ducts, part of monorail system, safety equipment, etc.).

Installation of the new equipment, probably in the following sequence:

- TAXS (the installation of the TAXS will take place from the experimental caverns of P1 and P5 and the therefore this activity is strictly linked with the upgrade program of the experiments);
- QXL with related valve and service modules;
- Magnets, Crab Cavities, TAXN and collimators support systems;
- Magnets, Crab Cavities and TAXN;
- distribution feedboxes (DFX) for the Q1 to D1 magnet system and distribution feedboxes (DFM) for the D2 magnet;
- Super Conducting (SC) link section from the DFM till the D2;
- Collimators.

The sequence of installation of the vertical SC links (DSHX and DSHM) to be connected to the DFX and DFM still needs to be assessed according to the options retained for their routing.

Figure 15-1: 3D integration model of the high-luminosity insertion regions of IR1 and IR5 of the HL-LHC machine. From left to right: Q1, Q2, Q3, D1, Corrector Package, DFX, DFM, TAXN and collimators, D2, 2 Crab Cavities cryo modules, Q4.

15.2.2 Existing LHC tunnel service areas

The caverns hosting the Matching section power converters (named with code RR) on both sides of IP1 and IP5 will need to be re-organized, and in particular the following actions will be necessary:

- De-install the power converters and other related systems (e.g. the quench detection system) linked to the powering of the removed LHC D2 magnet as it will be fed via a new SC link (DSHM) and the related DFM.

- Re-organize the remaining equipment in order to have the most efficient space occupation, increase if necessary and possible the radiation shielding, and place the most radiation-sensitive equipment in the most protected areas. Possible replacement of equipment with new, radiation-tolerant designs can be envisaged.

In the bypass caverns around the experiments of Point 1 and Point 5 (named USC55, UL14 and UL16) the presently installed power converters (dedicated to feed the LHC final focus quadrupoles) will be removed. Racks belonging to the magnet protection system and low current power converters (120 A and 200 A) will be installed at those locations.

At present, no CE work interventions are foreseen in the RRs areas.

15.2.3 The new HL-LHC underground service areas

15.2.3.1 General concepts

The installation of the new cryogenic plants in points 1 and 5 provide independent cooling capacity to feed the final focus and the part of the matching section till the D2 including the Crab Cavities.

The lower corresponding cold boxes will be installed in new underground caverns. The maximum difference in level between the lower cold box outlet and the new QXL distribution line shall be less than 20 m. Points that need to be considered:

- The above-mentioned maximum allowed height difference of 20 m.
- The need to build connection galleries to distribute the cryogenic fluids from the cold box to the left and right of the IP.
- The advantage for the Crab Cavities to have the RF equipment installed in the proximity, providing easier exploitation, and simplifying the equipment installation.
- The possible synergy with the magnet power converter system installation.
- The lack of space to integrate the RF waveguides or coaxial lines in the LHC tunnel.

For the construction of the new underground caverns and galleries, the HL-LHC project has identified the following list of systems that need to be integrated:

- The cold boxes and the connection to the QXL.
- The RF ancillaries (powering and control, space will be reserved for a possibly doubling of the HL-LHC baseline Crab Cavities system at a later moment of the HL-LHC operation).
- The magnet power converters.
- The systems required for connecting the power converters to the magnets (distribution boxes and superconducting links).
- The related technical services (cooling and ventilation, electrical supply, access control systems, technical networks, etc.).
- The necessary safety related equipment (smoke extraction, firefighting equipment safety room, etc.).
- Main part of the magnet protection system, of the survey electronics and of the beam instrumentation electronics.

The installation approach shall guarantee the access to the power converters, the relevant part of the RF ancillaries and to the survey and beam instrumentation electronics also during periods with beam present in the machine (‘beam-on’). The underground cavern location/design and the equipment installation implies that none or only very limited amounts of radiation will come from the LHC to the new areas and that there will be no risk of oxygen deficiency in case of He release from the cryogenic system installed in the LHC machine.

The proposed solution has been identified with the nick name of “double decker” (See Figure 15-2 and Figure 15-3). Superconducting links and the RF ancillaries will be installed in the UAs that extend from the UR gallery (located parallel to the LHC machine tunnel at a distance of about 40 m) to the top of the LHC machine in a vertical point as close as possible to the equipment that needs to be connected. In this connection point, the rock layer between the LHC tunnel vault and the UL galleries will be about 7 m. Vertical cores will provide the path through which the cryogenic lines, the SC links and the RF powering will descend towards the LHC tunnel. To guarantee escape paths to safe areas for all the envisaged incident scenarios it has been decided to build two escape ways (UPR) joining the UA extremities to the LHC tunnel.

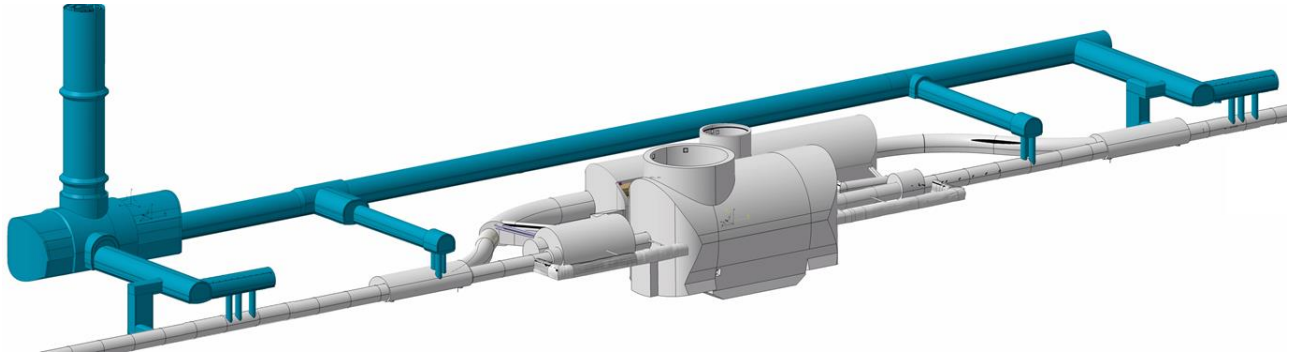

Figure 15-2: Axonometric view of the HL-LHC underground Civil Engineering infrastructures as it would appear in IP5.

The main elements of the new underground structures and their code names are visible in Figure 15-3:

- PM: shaft joining the surface to the underground structure.
- US: cavern for the installation of the cryogenic cold box.
- UW: physically part of the US caverns, but separated from it by a fire-resistant wall, the UW will house cooling and ventilation equipment.
- UR: gallery parallel to the LHC tunnel, about 40 m away, and extending from the location of the Crab Cavities system on the right of the IP to the point where the Crab Cavities are installed on the left of the IP. Approximately 300 m long.
- UA: two galleries per LHC point, distributed symmetrically with respect to the IP and joining the URs to a position on top of the Crab Cavities installed in the LHC tunnel.
- UL: two galleries per LHC point, distributed symmetrically with respect to the IP and joining the URs to a position on top of the DFX (near the D1 magnet) installed in the LHC tunnel.
- UPRs: safety exists joining the UAs with the LHC tunnel and providing a second escape way towards the main LHC tunnel in case the PM could not be reachable.

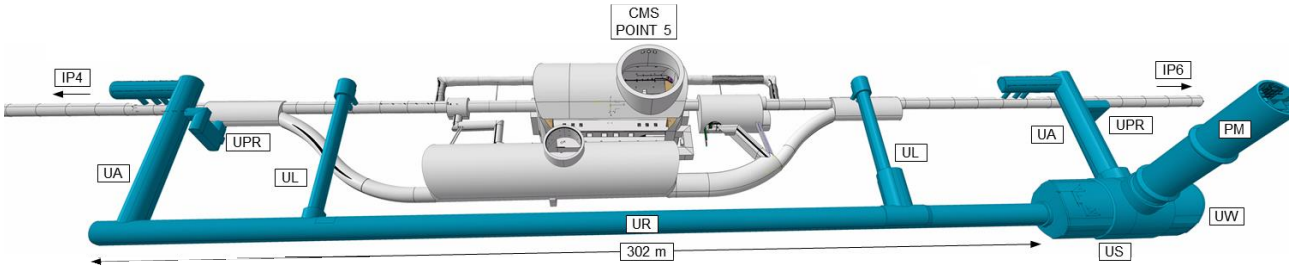

Figure 15-3: Top view of the HL-LHC underground Civil Engineering infrastructures as it would appear in IP5 with the relevant underground code names.

In the following paragraph the installation approach for the many equipment will be discussed.

15.2.3.1 The cryogenic installation

The HL-LHC lower cold box cryo-line (see Figure 15-4) will join the distribution box in the alcove of the nearest UL. From this distribution box, two cryo-lines will exit feeding the QXLs left and right of the IP. The first one would run along the UL and connect into the LHC tunnel via a vertical core. The second will run through the UR length and then (as for the first one) will join the other UL and will descend down through the core to be connected to the LHC QXL.

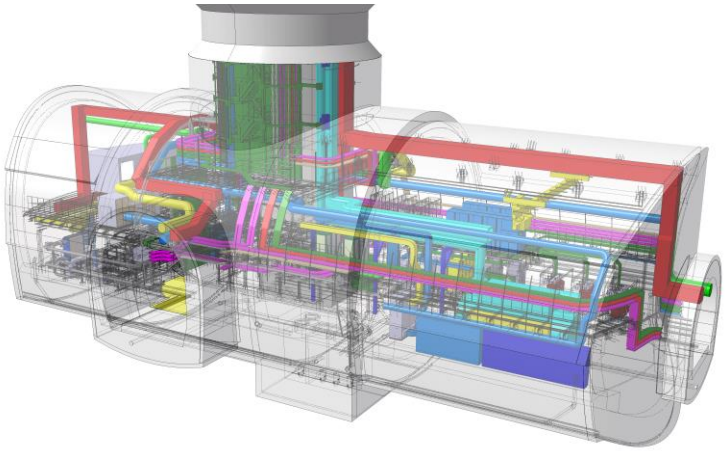

Figure 15-4: The cavern (US) hosting the cold box (in the image in light blue on the front right) with other technical services.

15.2.3.2 The superconducting links

There are four Superconducting links per IP, two per IP side. The largest in section (code name DSHX) will connect the dedicated current leads system (code name DFHX) to the distribution feed box in the LHC tunnel (code name DFX) in order to feed the superconducting magnets installed from Q1 to D1. The second one, smaller in section, but longer, (code name DSHM) will connect the current leads (installed in the DFHM) to the distribution feed box DFM dedicated to feed the D2 magnet along with its correctors.

The DFHX and DFHM will be installed in the URs near the power converters that will feed them and as close as possible to the ULs (Figure 15-5). The Superconducting links will reach, through the UL and together with the cryo-lines, the vertical crossing of the LHC and then will descend down through cores to be connected to the DFX and DFM that will be installed in the LHC tunnel on top of the beam line for the DFX and on top of the D2 for the DFM (Figure 15-6).

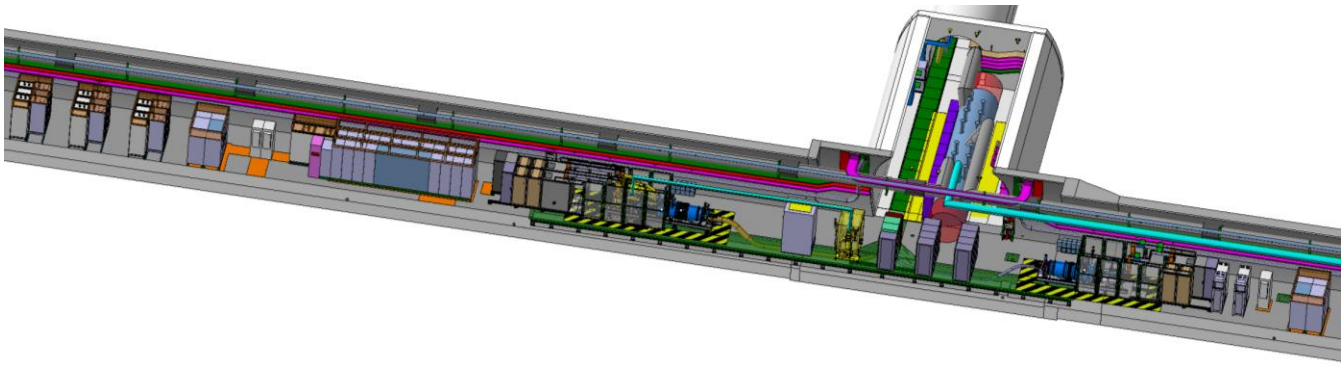

Figure 15-5: Installation of the DFHX and DFHM in the UR and routing of the SC links towards the UL. Externally, with respect to the two feed boxes, the Power Converters connected to the relevant circuits are installed. The related Energy Extraction units, when present, share the same locations.

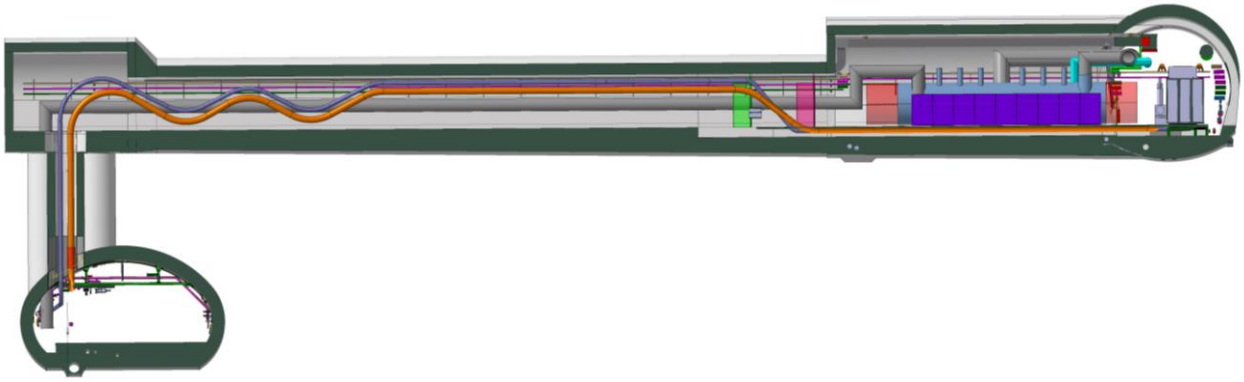

Figure 15-6: The UL gallery with the routing of the cryogenic and Superconducting link towards their vertical connection with the LHC machine tunnel.

15.2.3.3 The Power converters

The power converters connected to the DFHX and DFHM will be installed in the URs (8) in the vicinity of these two units and connected via a network of warm cables, water cooled cables, solid copper bus bar and switches (CDBs) assuring personnel safety via through an electrical separation of the magnet string during interventions and ELQA campaigns. The power converters are the main source of space requirement and of ventilation cooling capacity requirement in the URs. Therefore, any possible optimisation on the electrical scheme (reduction of the number of circuits or of the circuit current) will have a relevant impact on the underground space requirement and on the required ventilation cooling capacity to be installed in the URs.

15.2.3.4 The RF ancillaries

The waveguides joining the RF superconducting cavities to the circulator will require two large cores per IP side (Figure 15-7). The two safety escape ways (UPR) to the LHC tunnel will represent the two paths through which radiation could propagate from the LHC machine into the UA and therefore to the UR. The foreseen layout is:

- Vertically to the position of the Crab Cavities in the LHC tunnel, three large cores will be drilled: two for the Crab Cavity feeding (each one housing two waveguides), one for the instrumentation and control cables. The latter will also house some recently added small piping (warm cryogenic piping, water, and compress air)
- Opposite to the Crab Cavities, the waveguides will exit inside the UA tunnels, running parallel and on the top of the LHC tunnel and separated from it by about 7 m of rock.
- In the UA tunnels the waveguides will be connected to the respective loads and circulators. These elements are not radiation sensitive and therefore they will be installed just at the exit of the cores or further inside the UAs. Such arrangement will allow reducing the waveguide length, facilitating the installation of the maze required for radiation attenuation.

A maze will be installed at the junction of the gallery and the UAs in order to reduce the influx of radiation to a level allowing access during beam operation also in case of accidental beam loss scenarios (defined by the Radio Protection as the theoretical loss of the full beam intensity on a massive block placed under the entrance of the cores along the LHC beam trajectory). Solid-state amplifiers and RF power supplies will be installed in the UAs, between the maze and the junction between the UAs and the URs, and they will be connected to the circulator by coaxial cables. The RF control racks will be placed in a shielded Faraday cage. The safety escape ways (UPRs) have been designed in order to fulfil the same radiological requirements.

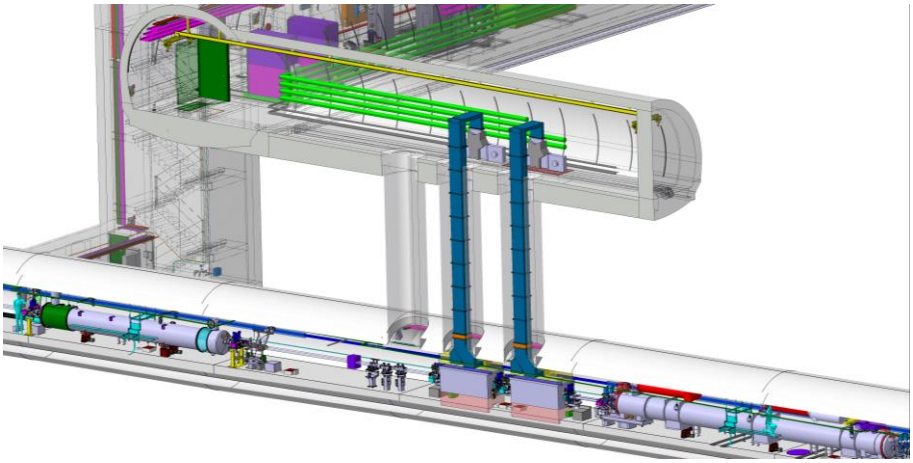

Figure 15-7: The axonometric view of the UA with the waveguides providing RF powering to the Crab Cavities installed in the LHC and the tetrodes installed along the UA.

15.2.4 New surface installation

With the adoption of the double decker solution, all the systems directly linked with the HL-LHC machine equipment will be installed underground with the exception of the warm compressors of the cryogenic plants. On the surface it will be necessary to construct, both at Point 1 and Point 5, new buildings to host the general services. Detailed descriptions of these buildings and of the equipment to be installed there are not the objective of this Chapter, and therefore the description will be limited to the list of the required buildings and their main functions:

- SD: access to the PM shaft connecting the surface to the new underground US-UR complex;
- SU: ventilation service building;
- SE: electrical service building;
- SHM: compressor building;
- SF: cooling towers.

In addition, various technical galleries and concrete platforms for equipment support to be installed in open air will be required.

The layouts for the Point 1 and Point 5 are depicted in Figure 15-8 and Figure 15-9.

Figure 15-8: The LHC Point 1 with the new HL-LHC surface buildings in orange. Simple concrete slabs are highlighted in yellow.

Figure 15-9: The LHC Point 5 with the new HL-LHC surface buildings in orange. Simple concrete slabs are highlighted in yellow.

15.2.4.1 Activity sequence considerations

Concerning the execution of the underground works, vibration propagation studies and LHC optics studies have revealed the elevated risk to perturb LHC beam operation if the activities of excavation would be performed during LHC Runs. Consequently, the project has anticipated the majority of excavation during the LS2 in order to avoid any risk for LHC operations. In order to avoid interference of the main HL-LHC CE activities with the LHC tunnel in the LS2, the completion (opening) of the vertical cores between the new underground infrastructures and the LHC tunnel will be dug and finished only during LS3.

For what concerns the installation, while the sequence of interventions on the underground LHC installed equipment (in LHC and RR Tunnels) is quite clear and linked to the end of the LHC Run 3, the sequence for the other installation and surface CE activities is still under evaluation.

15.3 Point 2

In order to limit the heat deposition from secondary beams on the superconducting magnets during the ion run, TCLD collimators in the dispersion suppressor will also be installed in P2 (Chapter 5). The installation will take place only in one slot on each side of the IP (presently occupied by the interconnection cryostat LECL.11L2 and LECL.11R2, in the regions from 419 m to 432 m from the IP on each side). The initially proposed strategy relying on the installation of two 11 T units with the related by-pass and TCLD collimators has been changed in replacing the interconnection cryostat with a modified version of the by-pass cryostat developed for the TCLD collimator installation in P7 (chap.11). This approach is much more cost effective, and it has been made possible thanks to the study and tests performed during Run 2 that have confirmed the possibility to steer the secondary ion beam to be intercepted by the TCLDs installed in these locations.

In Point 2 it will be also necessary to upgrade the primary injection absorbers (TDIS). The new TDIS will be at the same position as the present TDI as it needs to be at 90° betatron phase advance relative to the MKIs. To equip the two injection regions, two TDISs units are required. They will be installed in the Long Straight Sections (LSS) in IP2 left side (82 m from the IP) and the other in IP8 right side (78 m from the IP). The intervention at Point 2 will be completed by the movement of the TCLIA by 2.2 meters towards the IP (auxiliary collimator). This change is performed to increase the acceptance of the Zero-Degree Calorimeter of ALICE.

All installation in IP2 will take place and be completed during LS2.

15.4 Point 4

15.4.1 Cryogenic system upgrade

P4 will receive an upgrade of the cryogenic system to address the additional cryogenic load from the new installations.

15.4.2 New beam line elements

The following elements are foreseen to be installed in the long straight section at Point 4 for the HL-LHC. Their installation will take place in LS2 and LS3:

- **Synchrotron light diagnostics:** New synchrotron light diagnostics, looking at photon emission from the D4 bending magnet. It will be installed on the beam heading to IP4 and it will also include a new extraction mirror located ~20 m from D4 toward D3 and an optical path to bring the synchrotron light to a light detector located in a hutch in the UA gallery. The optical line will be installed through a duct to be drilled in the shielding wall. This installation is foreseen on both beams, one on each side of IP4.
- **Synchrotron light monitors**: The present synchrotron light monitor's undulator magnet, installed on the beams heading away from IP4, will be upgraded and optical hutches will be installed in in the UA's galleries. This will require to install an optical path and drilling the corresponding ducts in the RA-UA shielding walls.
- **High Bandwidth BPM:** To support the Crab Cavity operation in Pt1 and Pt5, two High Bandwidth BPMs will be installed on each beam and on each side of IR4, substituting the current head-tail monitors.
- **Hollow Electron lenses**: They will complete the collimation system by providing an active control of the beam halo population and therefore the beam loss rate in the collimation regions of IR3 and IR7. The Hollow Electron lenses will be equipped with BGC (Beam Gas Curtain) monitors to visualize the position of the beams and their overlap inside the equipment. A prototype of the BGC will be already installed in LS2 for development purpose.

The Hollow Electron lenses require transverse space that is only available in the central region of the long straight section at IP4, between D3 Left and D3 Right, where the beam separation is 420 millimetres.

15.5 Point 6

Quench tests and optics optimization have led to reconsider the necessity to increase the nominal field of the two Q5 units installed left and right of IP6. Therefore, there is no more necessity to intervene on the cryogenic distribution line and on the Q5 assemblies to lower their operating temperatures to 1.9 K.

The horizontal beam dump dilution kicker system is planned to be upgraded with the installation of two additional kicker modules. The Beam Dump block will be upgraded already in LS2 with new upstream vacuum windows. The entire Beam Dump block is planned to be replaced during LS3 in preparation for the HL-LHC exploitation. The impact on integration and installation of these activities planned for LS3 is object of ongoing studies.

15.6 Point 7

In order to protect the superconducting magnets (by excessive heat deposition from off-momentum proton leakage from the main collimator system itself), some special collimators (TCLD) must be installed in the dispersion suppression region, i.e. in the continuous arc cryostat. The installation of these collimators will take place during LS2.

In order to cope with the proton losses in the dispersion suppressor area it has been decided to install two TCLD collimators on each side of the IP. In order to do so it will be necessary to:

- Remove MB.A9L7 and the symmetric MB.A9R7.
- Substitute each removed dipole with a unit composed of two 11 T dipoles (Chapter 11) separated by a cryogenic bypass.
- Install the TCLD collimator on top of the cryogenic bypass (Chapter 5).

The magnet installation will also require a new dedicated quench protection system and a trim circuit with its own power converter. The 600 A power converter for the trim circuit will be installed in the nearby RRs.

15.7 Point 8

As mentioned in the Point 2 activity description, a new primary injection absorbers (TDIS) will be installed also in Point 8 in the LSS.

In addition, as LHCb will see the delivered luminosity increased after the Long Shutdown 2, two absorbers of neutral debris are necessary to protect the D2 magnets. The two masks denominated TANB will be installed at ±119 meters symmetrically with respect to IP8. In order to increase their efficiency, it is necessary to displace the horizontal and vertical tertiary collimator installed in the zone in order to create the space as near as possible to the magnet to be protected.

All equipment in P8 will be installed during LS2.

15.8 Alignment and internal metrology

15.8.1 General objectives, requirements, and constraints

The HL-LHC performance heavily relies on precise and accurate alignment of the magnets, RF systems and beam diagnostics components. The alignment and internal metrology of these components can be divided into three steps: the fiducialisation, the absolute alignment of the components w.r.t. the underground geodetic network (“standard alignment”) and the relative alignment (“smoothing”) of the components using sensors and actuators to determine their position and re-adjust them remotely.

In the HL-LHC, the monitoring of cold masses inside each cryostat of the inner triplet combined with the continuous determination of the position of each cryostat, will considerably improve the alignment of the inner triplet compared to the LHC era. This new instrumentation will allow monitoring the cold mass displacements occurring after cool-down, due to mechanical stresses. The mechanical axes of the magnets from Q1 to Q5 shall be included in a cylinder with a radius of 0.10 mm. The fitting of all mechanical axes of these magnets located on the right side of the IP shall be included in a cylinder with a radius of 0.15 mm w.r.t. magnets located on the left side of the IP (Figure 15-10) [1].

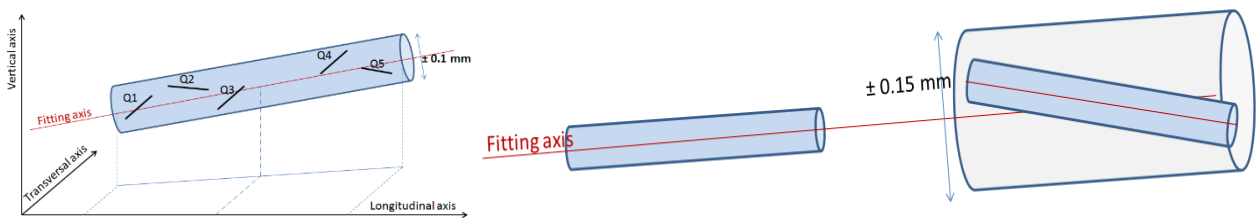

Figure 15-10: The HL-LHC alignment requirements

The Full Remote Alignment (FRA) of all the components from Q1 to Q5 will provide the capability to perform a complete and rigid remote alignment from the CCC of all the components of ±2.5 mm, if the machine components are misaligned w.r.t. the detector inner tracker [2]. Such correction will be applied after having circulated a first pilot beam that will provide a unique and efficient reference. The FRA will also allow correcting ground motions remotely during one year of operation to another. A thorough study performed on all the intermediary components has classified the machine components as capable to accept misalignments of ±2.5 mm (“ remote alignment compatible”) w.r.t their adjacent components (e.g. vacuum components with sufficient aperture) or needing to be equipped, as the main components, with remote adjustment and position determination capabilities [3].

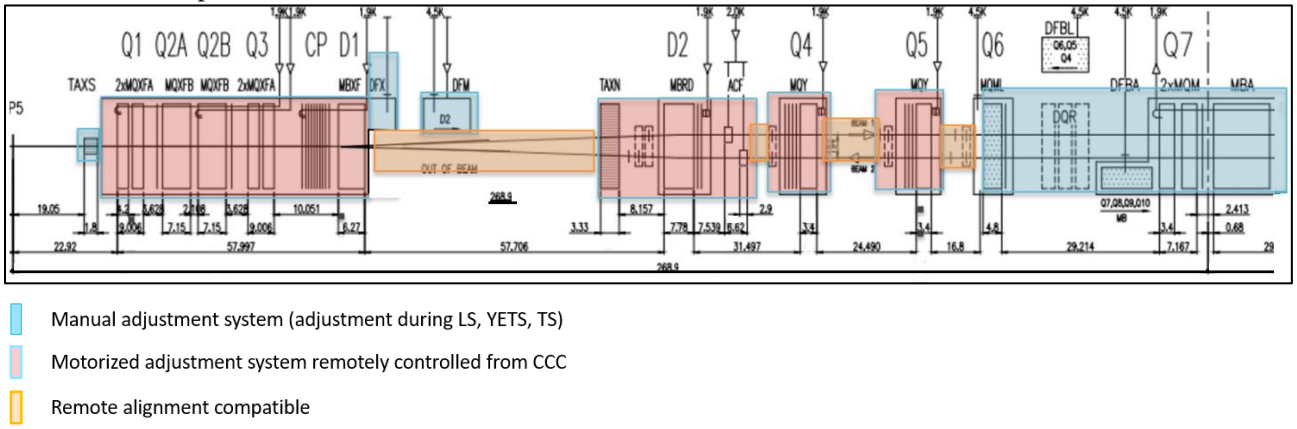

Figure 15-11: Full Remote Alignment system applied to the HL-LHC 1.4 optics

On top of the increase of the window for machine operation, the FRA will allow a reduction of radiation doses taken by surveyors. It will decrease the required strength of orbit correctors and will provide an increased level of machine flexibility. In addition, the derived equipment simplification has opened up the possibility to re-optimize the matching sections leading to the present HL-LHC optics v1.4.

15.8.2 Internal metrology

The determination of the coordinates of the fiducials (or alignment targets), located on the vacuum vessel of the cryo-assembly magnets, w.r.t. the as-built mechanical and magnetic axis of the quadrupoles and dipoles, is the basic information necessary for all further alignment actions and it is the object of the fiducialisation process [3][4]. Each cryostat will be equipped with redundant 1.5-inch fiducials. Considering the lessons learnt from the LHC, the following improvements of the internal metrology will be implemented:

- The straightness of the cold mass and the position of the vacuum pipe will be controlled during the manufacturing phase of the cold masses.
- The position of the cold mass inside the cryostat will be controlled after the manufacturing phase within an uncertainty of measurement of ±0.1 mm.
- Additional reference points on the cold mass extremities will increase redundancy and allow to re-fiducialise the magnets in-situ if needed and to perform additional geometrical controls of the interconnection areas.
- The positions of the fiducial targets on the cryostats and of the interface points with the jacks will be measured and re-adjusted if needed after magnet assembly to allow for the full range of the alignment system.
- The same procedure as in the LHC will be carried out to determine the mechanical position of the BPM, the beam screens and the cartography at the ends of each cryo-assembly [5].

15.8.3 Internal monitoring of cold masses and crab cavities inside their cryostat.

As described in Ref. [1], the position of the mechanical axis of each Inner Triplet magnet, w.r.t. the fiducials installed on top of the cryostat, will have to be known within ±0.1 mm (1σ). Such budget of error includes the error of fiducialisation and the error of the cold mass monitoring.

To fulfil such requirements, it is proposed to use Fourier analysis-based Frequency Scanning Interferometry (FSI) [6]. This system performs absolute distance measurements between the ferule of one optical fiber and multiple targets. This CERN designed FSI has the advantage of being less sensitive to the variations of intensity of the reflected optical signal.

The position of the cold mass inside its cryostat will be monitored at three sections by four distance measurements (Figure 15-12). The optical fiber is inserted in a feedthrough on the cryostat; the mechanical reference of the optical fiber has been determined during the calibration process w.r.t. external targets placed on the feedthrough. Once the cryostat is installed in the accelerator tunnel, the position of these targets will be determined in the machine reference frame by laser tracker measurements, and consequently it will provide the position of the "zero" for the optical fibers in such a frame. Each section of the cold mass is equipped with four targets, installed on a specific support developed to avoid cryo-condensation and designed to keep each target at a temperature above 200 K. Validation tests conducted with such a configuration demonstrated that the center of each section could be determined within a standard deviation of 0.1 mm (1σ) in the referential frame of the cryostat [7].

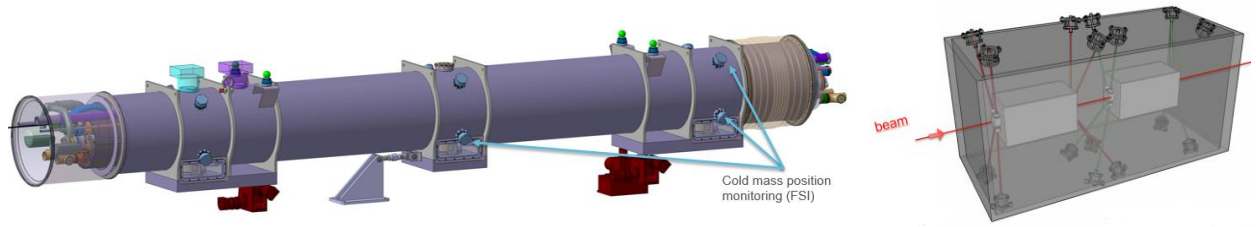

Figure 15-12: FSI lines of sight in Inner Triplet quadrupoles (left) and crab cavities (right)

The position of each crab cavity inside its cryostat will be monitored through two sections performing four distance measurements between the cryostat and targets installed on the flange of the dressed cavity (Figure 15-12). Tests performed in real conditions in the SPS tunnel demonstrated that the relative position of the cavities could be monitored within a few micrometers and their absolute position in the tunnel reference frame could be determined within an accuracy of 50 μm [7].

15.8.4 Standard alignment

In order to assure similar beam geometry for the HL-LHC as during the LHC era the underground network will be re-determined in the area where new components will be installed. The network will be derived from the old components prior to their dismounting as their position is known in the context of beam operation / performance. Later, this re-determined underground network will be used for the preparatory works, once the old components are removed from the tunnel. Initially, the marking on the floor of the position of the new elements will take place, following the strategy used in the LHC [8] and then, the heads of jacks will be positioned within ±2 mm w.r.t. their theoretical position with the adjustment screws in their middle range. Once the jacks are at their nominal position, they will be sealed on the floor [9].

Traditionally, in accelerators, the alignment of the cryo-assembly magnets is carried out in two steps: the initial alignment and the smoothing (relative alignment of cryo-assembly magnets w.r.t. each other, not considering the underground geodetic network any more as reference). In the case of HL-LHC, only the first step will be carried out using standard alignment measurements [10]. The second step will be performed using sensors and actuators.

The initial alignment will take place once the magnets have been installed on their jacks before the interconnection and cool-down operations are completed. Each cryostat will be aligned independently w.r.t.

the underground geodetic network using its external fiducials within ±0.25 mm (1σ). Once the initial alignment completed, the interconnection phase will start.

15.8.5 Alignment sensors and actuators

To determine remotely the position of each cryo-magnet assembly or intermediary components (as collimators), each component will be equipped with two capacitive Wire Positioning Sensors (WPS). The two WPS provide four degrees of freedom by measuring the transverse (horizontal and vertical) offsets with respect to a stretched wire: pitch and yaw rotations, vertical and radial translations, within a micrometric accuracy. The roll angle will be determined either by Hydrostatic Levelling Sensors (HLS) (three HLS sensors in that case will determine the vertical distance to a water surface within a micrometric accuracy providing redundancy in the vertical translation and pitch rotation), or by a radiation hard inclinometer when space is limited on the component. The longitudinal position of each component will be determined by FSI measurements between a reference point fixed to the floor and the cryostat interface. On the triplets, an inclinometer will be added to provide redundancy in the roll determination.

Diagnostic devices associated with each alignment system will carry out the remote validation of the sensors. Prototypes are already in place in the LHC.

To link radially the tunnel on both sides of experimental areas, a wire will be stretched in a gallery parallel to the LHC tunnel around IP1 and IP5 [11]. A combination of WPS sensors and FSI measurements will provide the six distance measurements between tunnel and parallel gallery wires. Left and right sides will be linked vertically by HLS sensors as can be seen in Figure 15-13 [12].

The WPS and HLS sensors installed in the experimental area will provide machine references in the experimental areas, to align the TAXS using standard instrumentation.

The remote adjustment of the components according to 5 degrees of freedom will be achieved dependent on the component, either by motorized jacks or by a standardized adjustment platform equipped with permanent motors. In both cases, the motorization solution shall fulfil the following requirements: a resolution of displacement below 10 µm, over a stroke of ±5 mm. The remote adjustment system shall provide a high stiffness to the cryostat support, with the first Eigenfrequencies as high as possible.

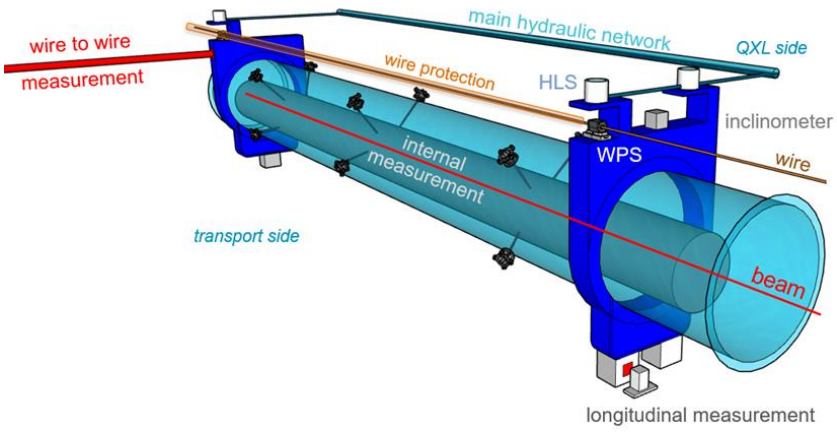

Figure 15-13: Alignment sensor configuration

The standardized adjustment platform is a CERN universal solution for the alignment of light weight components: the knobs interfaces of all adjustment axes will be located towards the transport area, with a simplified and intuitive kinematics allowing performing its adjustment without complicated algorithms [13]. The platform can be configured in three versions: manual (adjustment acting on knobs), semi manual (adjustment by plugging motors temporarily) or automatized (equipped with permanent motors). The objective of using the same platforms below all the components is to limit the doses taken by the surveyors [14].

During the Long Shutdowns, the components with no remote adjustment capability will have their position controlled, using laser trackers in an automatize mode.

15.9 References

[1] Fitterer, M. *et al*., Crossing scheme and orbit correction in IR1/5 for HL-LHC, 16th IPAC, Richmond, VA, USA, 3-8 May 2015, DOI: 10.18429/JACoW-IPAC2015-TUPTY036.

[2] Herty A. *et al*., HL-LHC Full Remote Alignment Study, IPAC 2019, Melbourne, 2019, DOI: 10.18429/JACoW-IPAC2019-THPGW057.

[3] Fessia P., Mainaud durand H., Full Remote Alignment System, EDMS: 2166298.

[4] Missiaen D., Quesnel J.-P., Fiducialisation of the LHC cryo-dipole magnets, EDMS: 110632.

[5] High-Luminosity Large Hadron Collider (HL-LHC): Preliminary Design Report, DOI: 10.5170/CERN-2015-005.

[6] Sosin M. *et al*., The frequency sweeping interferometry for robust and reliable measurements in harsh accelerator environment, SPIE Optics + Photonics, San Diego, USA, 2019, DOI: 10.1117/12.2529157.

[7] Rude V. *et al*., Frequency Scanning Interferometry to monitor the position of accelerators components inside their cryostat for the HL-LHC project, IWAA 2018, FNAL, Batavia, USA, 2018, DOI: 10.18429/JACoW-IPAC2018-WEPAF068.

[8] Quesnel J.-P., Schmitt J., Marking on the floor in the LHC and transfer tunnels (TI2 & TI8)- Interface specification, EDMS: 311753.

[9] Quesnel J.-P., Positioning of the jacks of the cryomagnets, EDMS: 311752.

[10] Quesnel J.-P., The first positioning of the LHC cryomagnets (Arcs and DS), EDMS: 311755.

[11] Mainaud Durand H., Alignment requirements for the LHC low beta triplets, EDMS: 344496.

[12] Mainaud Durand H. *et al*., HL-LHC requirements and associated solution, IPAC 2017, Copenhagen, Denmark, 2017, DOI: 10.18429/JACoW-IPAC2017-TUPIK085.

[13] Herty A. *et al*., Technical challenges for HL-LHC alignment and associated solutions, IWAA 2018, FNAL, Batavia, USA, 2018.

[14] Sosin M. *et al*., Design and study of a 6 Degree of Freedom universal adjustment platform for HL-LHC components, IPAC 2019, Melbourne, Australia, 2019, DOI: 10.18429/JACoW-IPAC2019-THPGW058.

Chapter 16

IT string and hardware commissioning

M. Bajko[1*] *and M. Pojer*[1*]

[1]CERN, Accelerator & Technology Sector, Switzerland
[*]Corresponding authors

16 IT string and hardware commissioning

16.1 The HL-LHC IT string layout

16.1.1 Introduction and goal of the HL-LHC IT string

The HL-LHC IT string (IT string) is a test stand for the HL-LHC, whose goal is to validate the collective behaviour of the IT magnets and circuits in conditions as near as possible to the operational ones. Each individual magnet circuit will be powered through a SC link and its associated current leads up to the ultimate operational current while cooled to 1.9 K in liquid helium. The test stand will be installed in the building 2173 (SM18) and will use magnets, superconducting (SC) link, current leads, power converters and protection equipment designed for the HL-LHC with their final design, and usable for the HL-LHC. The test bench will allow a real size training for the installation and alignment, the validation of the electrical circuits, the protection scheme of the magnets, and the SC link. At this occasion, all subsystem owners will be able to fine-tune their set up and to complement or change when necessary, before they are finally installed into the HL-LHC. The powering procedures will be written and validated during the tests. These tests will also improve our knowledge of every single component and will give us the opportunity to optimize the installation and hardware commissioning procedures.

16.1.2 Description of the HL-LHC IT string

The HL-LHC IT string will be composed of the cryo-magnet assemblies called Q1, Q2a, Q2b, Q3, CP and D1 (Figure 16-1). In total, 21 superconducting magnets using Nb-Ti or Nb_3Sn technology will be required to set-up the HL-LHC IT String.

In the IT string, as for the HL-LHC, the magnets will be powered via a SC link (DSH) by standard HL-LHC power converters. The circuit will also include the current leads and the water-, air- cables or bus bars between the power converter and the leads passing through the so called disconnector boxes (DCB).The DCBs are placed in the vicinity of the power converters allowing the safe separation of the electrical circuits while necessary. The SC link will be connected to the bus bars of the magnets via a dedicated equipment called DFX.

Cold diodes will provide decoupling between cold and warm parts of the circuit and limit the over-currents in the superconducting bus bars and link conductors. The diode assembly will be located in between D1 and the DFX, in order to be accessible for maintenance and replacement. For this reason, a dedicated box, as a part of the so-called D1-DFX Connection Module, operating at 1.9 K, will be installed into the IT string.

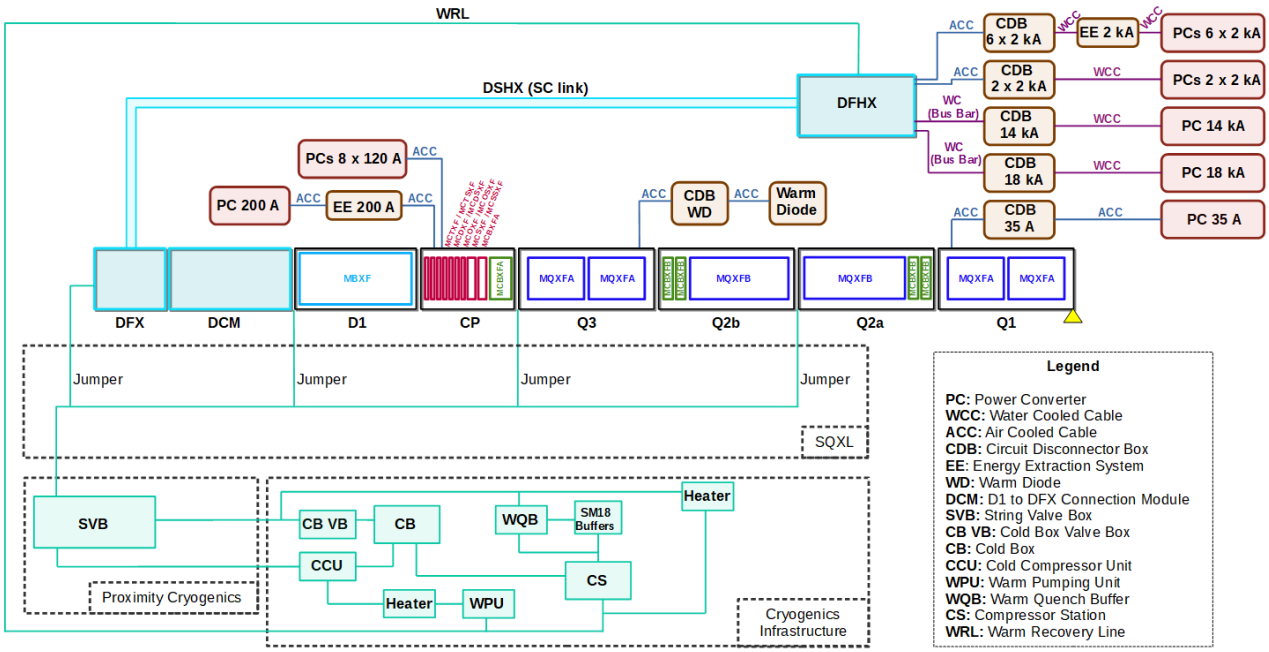

Figure 16-1: Schematic view of the IT string.

The cooling of the magnets will be done via a dedicated cryogenic valve box and will be a new additional “client” for the SM18 cryogenic installations sharing the cooling and pumping capacity with the RF and magnet testing. As such, the cryogenic equipment cannot be re-used in the HL-LHC.

16.1.3 Location of the IT tring test stand

For practical reasons, the IT string will be installed in SM18 that is housing the cryogenic powering test facility of the RF cavities and SC magnets for both the LHC and the HL-LHC. The integration of the test stand in the SM18 is shown in Figure 16-2.

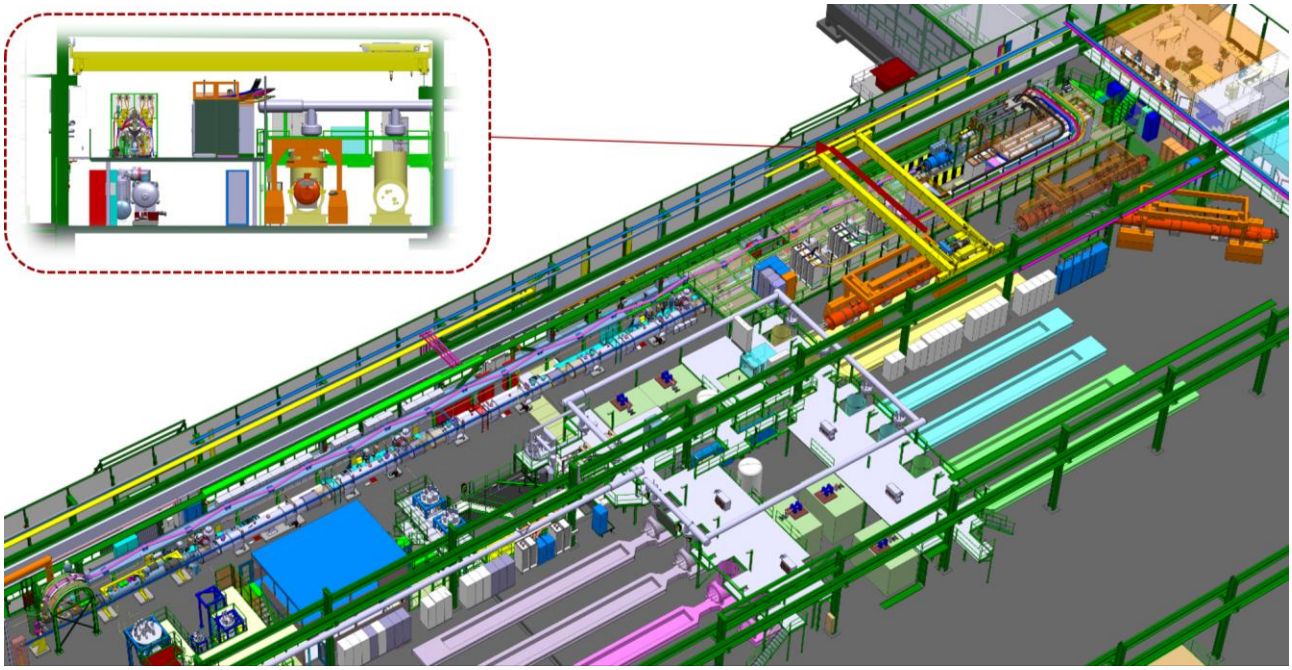

Figure 16-2: Integration of the IT string. Top left picture: cross-section view. Bottom: top view of the string assembly.

The powering system is centralised on a metallic bridge between the wall and the present structure holding the electrical racks of the horizontal magnet test benches.

16.1.4 Time scale of the IT string test stand

One of the main goals of the IT string is to test and confirm the nominal operational conditions and the collective behaviour of the entire IT setup, before the installation of the magnets and main components into the LHC tunnel. The delivery schedule of the cold masses is the key element defining the starting date for the installation fixed for the end of 2021. The IT string will be active until October 2023 as it is shown in Figure 16-3. During this extended period under study, the string will not be in operation, but will stay available in case of new tests are required.

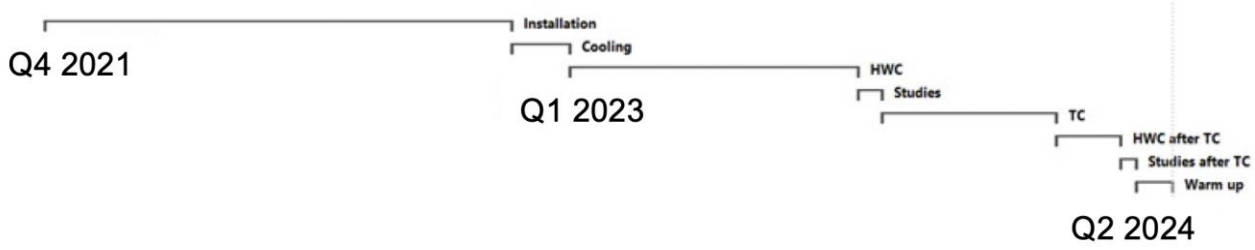

Figure 16-3: Delivery schedule of the cryo-magnet assemblies for the IT string.

16.1.5 Technical infrastructure for the IT string test stand

The main components of the IT string technical infrastructure are:

- The cryogenic cooling system.
- The water-cooling system.
- The electrical powering system from the general network.

The SM18 test hall area is equipped with technical infrastructure that will serve the IT string test. Its capacity however is not sufficient when shared between the other activities: the RF cavity and SC magnet tests. The HL-LHC SC magnets and links production qualification will require approximately 100 tests for magnets and 20 for SC links in the period between 2019 and 2025. The test stands should also assure the testing of the spare LHC magnets (estimated to 50 tests) during the same period. In view of these activities, the existing infrastructure has to be upgraded.

16.1.5.1 Cryogenic cooling system upgrade

The estimated needs of cryogenic cooling of the IT string are 12 g/s for cooling and 6 g/s for pumping. The cryogenic powering tests of the LHC and the HL-LHC magnets are scheduled at the same time. These considerations implied the need of an upgrade in the liquid helium (LHe) production system from the present 27 g/s to 60 g/s. Using the present installations and combining the two warm pumping units, the total of 12 g/s capacity is used for magnet and/or IT string testing at 1.9 K operation. The upgrade started in 2019.

16.1.5.2 Water cooling system upgrade

16.1.5.2.1 Demineralised water system

The HL-LHC magnets are powered with currents higher than those of the present LHC magnets. Therefore, the power converters and associated installations needing water cooling require a higher quantity of demineralised water. Consequently, the demineralised water production was upgraded to a system that is able to deliver 138 m^3/h. The upgrade of the demineralised water system was successfully completed in 2016.

16.1.5.2.2 Primary water system

With the increased need of demineralised water and upgraded cryogenic cooling system, the need for primary water also increases. The SRF, the SC magnets and the IT string cooling capacity will be double of the present 1.6 MW, while the cryogenic upgrade will require an increased capacity from 2.5 MW to 6 MW. The primary water system was upgraded in 2019.

16.1.5.3 Electrical powering system upgrade

The IT string consumption is estimated to 1 MVA. It is going to be connected, together with the new Cluster F 20 kA power converter to the new transformer of 3 MVA capacity leaving approximately 1 MVA free power for future needs. The installation of the new 3 MVA transformer was completed in 2019.

16.1.6 Installation and dismounting of the IT string

The heaviest and largest objects will be installed, positioned, and aligned with dedicated equipment. The option to handle the cryo-assemblies with the specific handling tools (different from those used for the LHC magnet installations) is under study. The slope of the tunnel will not be reproduced for the string as none of the main users have requested it.

16.2 Preliminary test program for the IT string

16.2.1.1 Performance test of components before installation into the IT string

Each individual component will be tested before its installation in the IT string. The responsible institute will test magnets at their premises and/or at CERN at nominal operational condition (or equivalent). The individual magnets will be powered up to their ultimate current and at each step of the test, their electrical integrity will be checked. Voltage test procedure will follow exactly the one applied in the accelerator according to the table defined in Chapter 6.

16.2.1.2 Electrical circuit integrity test

The typical High Voltage Qualification (ElQA) test will be performed at the specified level of voltage for each step and each circuit. The continuity of the instrumentation and protection system wiring will be verified. The IT string will allow the testing of the revised and adapted ELQA procedures for the HL-LHC.

16.2.1.3 Cryogenic system test

The cryogenic system test will focus on the cool-down of the magnet chain and the thermal behaviour after the quench of the cold and warm powering systems, composed by magnets, bus bars, cold diodes, SC links, cold boxes, current leads, warm cables and power converters.

16.2.1.4 Vacuum system test

The IT string will not be equipped with beam screen and therefore there is no test planned to verify heat deposition. Those verifications will be done offline. The insulation vacuum will be qualified with leak tests and tests of different sealing options. Also, there will be no separation between beam and cryostat vacuum. Lack of beam screen and vacuum separations are maybe the most important deviations from the operational configuration. The decision was taken to limit the cost and in view of the experience accumulated with LHC, which is still very relevant for the vacuum system of the IT triplet.

16.2.1.5 Powering of the IT magnets

The HL-LHC will require the development of new power converters, a high precision 20 kA 2-quadrant power converter, and the magnets will be powered singularly (for the independent magnets) or in series (for the Q1

to Q3 assembly), adjusted with 3 trim circuits. The IT string will be the first and unique occasion for testing the series powering before the real powering in the tunnel.

The cold powering system is composed mainly of the HTS current leads and the SC link, which relies on cooling with helium gas. The gas has a temperature range from 4.2 K up to 35 K - 50 K. The use of MgB_2 and HTS materials enables safe operation of the superconducting components, for which a temperature margin of at least 10 K is guaranteed. Although the SC link will go through qualification test before the IT string tests, the complete warm and cold powering circuit will be only tested in the IT string before their installation into the LHC tunnel.

The most critical aspects that the IT string will address are the cooling performance of the cold part of the circuits, the electro-magnetic cross talk between circuits inside the SC link, and the protection of the circuits while using the new protection scheme that includes the CLIQ system for the magnets. The IT string will also allow the qualification of the individual splices of the interconnections between magnets and cold powering system.

16.2.1.6 Magnet protection system test

The protection system of the magnets is relying on quench heaters and/or the Coupling Loss Induced Quench (CLIQ) system. A careful protection system test has to be performed before powering the magnets at low and intermediate current. Specifically, for Nb_3Sn magnets, it was found that flux jumps appear in the low and medium current range, with amplitudes ranging from 10 mV up to 2 V, and characteristic times of 10 to 20 ms. The quench detection will be done with the universal QPS (uQPS) as planned for the HL-LHC. This system will be only tested on a complete circuit in the IT string.

16.2.1.7 Interlock test

The interlock system validation will be one of the most critical tests. The HL-LHC interlock system will integrate and handle, with a given logic, signals from all subsystems. The overall system test will be only possible in the IT string, as the interlock system used on the benches for the test of individual cryo-magnet assemblies is a dedicated one, not necessarily working in the same conditions as in the tunnel.

16.2.1.8 DAQ test

As for the interlock system, the DAQ of the IT string will be the one associated to the uQPS.

16.2.1.9 Performance tests

During the performance tests, we will investigate the capability of the different subsystems to work together and within the specified conditions.

16.2.1.10 Quality assurance

The IT string will give the opportunity to validate and test all Quality Control (QC) steps and installation and test procedures.

16.3 Hardware commissioning in the tunnel after LS3

16.3.1 Commissioning of the superconducting circuits

16.3.1.1 Electrical Quality Assurance tests

As stated in Ref. [1], the objective of the ElQA tests is to release each individual superconducting circuit for powering, to gather all the necessary electrical parameters for operation, and to track all data acquired and to manage the related non-conformities.

16.3.1.1.1 ElQA at warm

At the end of the installation and connection of all magnets, resistance measurements and a high voltage qualification of all circuits will be performed: to check whether the circuit is closed; to determine a reference resistance value at warm; and to validate the galvanic insulation versus ground. The values of voltages to be applied and the maximum acceptable leakage current values are reported in the Chapter 6 and may dynamically evolve according to experience gained with prototypes and IT string commissioning.

16.3.1.1.2 ElQA at cold

Similar tests will be performed at cold, with larger test voltages applied. The circuits and the corresponding link will be cooled down to their nominal temperature. For the high voltage qualification of all lines, the tests will be performed to validate the galvanic insulation versus ground and the capacity of all lines to withstand the mutual high voltages developed during a fast change of current in the different circuits (typically during a fast abort or quench).

The high voltage qualification also includes testing of all the elements that are electrically connected to the tested circuit. Such elements are:

- the instrumentation and feedthrough systems.
- the magnet protection units.
- the temperature sensors with the related tunnel cabling and electronics.
- the tunnel cabling for routing the voltage taps used for the protection of the superconducting circuits.

In addition, transfer function measurements will be performed, with the aim of determining the impedance as a function of the frequency. The results of these measurements are used to spot possible inter-turn shorts, and for the power converter team to adjust the regulation of the power converters.

16.3.1.2 Powering tests

The HL-LHC magnets present several peculiarities [2] that have to be kept in mind for their commissioning. The most relevant are: the fact that the vast majority of magnets will be cooled down to 1.9 K (with only a small number of matching section magnets at 4.5 K); that Nb_3Sn will be used extensively for the first time; that the current of the inner triplet will be the highest in the machine (18 kA); and, importantly, that some of the high current magnets will be protected only via energy extraction in a dump resistor without quench heaters. In addition, the powering scheme of the inner triplet will be different from the present one with implications in case of a quench of one of the magnets (see Chapter 3). There will be 11-T magnets in the DS where NbTi and Nb_3Sn magnets will be powered in series with the difference of a trim power converter locally feeding the 11 T (to compensate for the different transfer functions) through resistive current leads, identical to those used to power the arc 60 A circuits.

The powering of all circuits up to nominal current will be done in steps. At the end of each step, online and offline analyses are performed by equipment owners and protection experts to assess the performance of all hardware in the circuit. In particular, for the powering of individual circuits, several cycles at different current levels will be performed to study the performance of the magnets, the efficiency of the protection mechanisms (by provoking fast aborts and even quenches), and to check all functionalities of the powering interlocks and of the power converters (via provoked powering failures).

A typical series of tests includes:

- at minimum operational current, testing of the full interlock chain, with the verification of cryogenic signals, power permit, powering failure, circuit quench transmission, and fast power abort requests.
- at low current, a check of the power converter performance and verification of all protection functionalities, by means of provoked slow and fast power aborts, with energy extraction.

- repetition of a series of power aborts and simulation of quenches from progressively higher current levels, with more and more energy stored (e.g. 25%, 50%, and 100% of the nominal stored energy).

Before starting a new powering test, all previous tests must have been validated. The validation includes approval by power converter and powering interlock experts, magnet owners, and protection experts. Cryogenics experts should also confirm the correct operation of their installations and instrumentation. The criteria for approval, the parameters, and the relevant information to be stored will be discussed in due time.

After the individual test of all circuits up to the design current, the common powering of a set of circuits will be done for magnets that are in the same cryogenic envelope and are powered from the same link (usually referred to as the powering of a group of circuits). The objective of this simultaneous powering is to validate operation of all magnets in nominal conditions; current cycles similar to those applied in normal operation should be used for the powering of a group of circuits. Important at this stage is the behaviour with combined powering in critical conditions, such as the fast power abort of a circuit when the others are at full current. For the inner triplets, in particular, quenching in a triplet quadrupole might induce a quench in a nearby quadrupole or corrector if the current in this related circuit is not extracted fast enough. These tests should be performed on all the magnets and could well trigger the change of detection thresholds and protection configurations. Once more, all tests should be approved by a group of experts and recorded for future reference.

Particular attention also has to be paid to those circuits that are not equipped with heaters and are protected by energy extraction on a dump resistor. For such circuits, a precise estimate of the energy deposited during a quench has to be made, not only in the case of bench tests, but also in the more severe conditions of combined powering in the tunnel. Eventually, the protection threshold should be adapted to reduce energy deposition and improve magnet safety during powering.

16.3.1.3 Magnet training

Operations at 7 TeV will hopefully be established during Run 3. In the process, extensive experience will be gained with the required dipole training to get to the requisite current level. The effects of a full thermal cycle will also be given by commissioning following LS2. A sound estimate of the number of quenches required following LS3 will thus be possible and well optimized procedures will be in place to assure an effective retraining campaign. Sufficient time should be foreseen in the schedule for this phase.

16.3.2 Hardware commissioning of the HL collimation system

At the HL-LHC, the requirements for hardware commissioning of mechanics and controls of the collimation system will be essentially equivalent to those of Run 2 and Run 3. Required tools are expected to be well debugged and validated by the time of the HL-LHC. The collimator settings, controls, and operational sequences should be extensively re-tested during the hardware commissioning and cold-checkout phases [3]. A dedicated test to address the reproducibility of collimator movements during critical operational sequences (such as the ramp) will be performed. At this stage, the collimators should have been fully installed and the local collimator controls in the tunnel fully validated. Unlike other hardware commissioning tests (such as the magnets), most of the collimation commissioning can be done parasitically, the main exception being the testing of the interlock system where the beam interlock system (BIS needs to be available.

Before beam is injected into the machine, the machine protection (MP) functionality of the collimation system must be guaranteed. Each collimator is connected to the BIS and has more than 20 interlocks that will need to be verified. The jaw positions and collimator gaps are monitored via six linear variable differential transformer (LVDT) sensors. These signals are interlocked with inner and outer limit values, making a total of 12 interlocks per collimator. In addition, there are a total of six energy-dependent and β^*-dependent limit functions and an interlock to protect from ‘local’ mode collimation control. The temperature of the collimators is also monitored and interlocked with minimum and maximum adjustable thresholds independently for five sensors per collimator. After successful results from these tests, the system will be ready to allow beam into the machine.

The new design of the TCLD collimator to be installed between two short 11-T dipoles and the connection cryostats around IR2 has been finalized. These collimators feature the latest design improvements, including embedded BPMs for fast alignment, and will be commissioned for the first time in LS2. New hardware will have to be part of the hardware commissioning as well. In particular, crystal primary collimators and the hollow electron beams. At this stage, the final implementation of interlocking aspects for these devices is not yet finalized.

16.3.3 Commissioning of the cryogenic systems

The HL-LHC foresees numerous modifications of the cryogenic system [4]. The operation of the resultant system, together with the time needed to qualify and tune the system, will be detailed once the design is definitive. Provisionally, an approximate time of three weeks is considered to be mandatory to commission the system for the superconducting magnets.

16.3.4 Commissioning of the crab cavities

As for all elements in the LHC, the crab cavities will be tested on the surface at the SM18 facility to nominal specification prior to its installation in the tunnel. One such prototype was installed in the SPS for a complete qualification of the standard two-cavity module with LHC-type beams in 2018 [4] and the installation of the other complete prototype is planned for beam tests in the SPS during Run 3.

The commissioning of the crab cavity system is differentiated into two main phases: cavity conditioning up to nominal operating voltage including the associated ancillary system (high power RF, cryogenics, vacuum) followed by RF commissioning with beam. Once the cryomodules are stable at 2 K, the RF conditioning is expected to take several weeks and is assumed to be within the hardware commissioning period.

Concerning the commissioning of the cryogenics, the correct operation of the cooling loops and the capacity will be verified, together with the expected behaviour of the instrumentation; proper verification criteria and sequence will be defined at later time with input from the qualification of the cryogenic-module on the surface tests. The vacuum integrity and the vacuum interlocks will be tested as well, which should cut the RF power in case of issues and during cavity conditioning.

The conditioning of the cavities will first be performed on the surface, but the commissioning of the low-level RF system (the tuning control, the regulation loop around the amplifier, plus the RF feedback) was validated in the SPS for the first time in its nominal configuration. A detailed procedure for the verification of all functionalities and the summary of issues and performance is available at Ref. [4].

All possible RF manipulations and synchronization with the main RF system in P4 is foreseen for the LHC operation cycle will first be performed without beam. An important verification concerns the efficiency of the fast feedback of the cavity field. The delay loops in the SPS between the two cavities was arranged to mimic the cavity setup in the LHC to both ensure the fast and independent control of the cavity set point voltage and phase, and the slower loop to regulate the cavities on either side of the IP. This is essential to ensure machine protection in the event of an abrupt failure of one of the cavities.

16.4 Commissioning with beam

Beam commissioning is not formally part of the HL-LHC construction project. After HWC the machine will be handed over to the HL-LHC operations team (BE department). A skeleton plan is shown in Table 16-1.

The initial commissioning phase should evolve through initial set-up, system commissioning through the nominal cycle, standard measurement and correction, set-up of protection devices, and validation. It is a relatively complex phase with necessary interplay between the various teams to allow beam-based commissioning of systems such as tune and orbit feedbacks, transverse dampers, RF, etc. under appropriate conditions at the various phases of the operational cycle.

Table 16-1: Outline of initial commissioning following LS3.

Phase	Key objectives
Injection and first turn	Injection region aperture, injection kicker timing
Circulating beam	RF capture, beam instrumentation, initial parameter checks
450 GeV initial commissioning	Transfer line and injection set-up, orbit,
450 GeV measurements and setup	Beam instrumentation, optics, aperture, collimation, LBDS
450 GeV two-beam operation	Separation bump checks, beam instrumentation
Ramp	Snapback, chromaticity control, orbit, and tune feedbacks
Flat-top checks	Collimation, optics, orbit, decay
Squeeze	Optics, collimation set-up
Validation	Loss maps, asynchronous dumps
Collide	First stable beam with a low number of bunches

The aims of the initial commissioning phase are as follows.

- Establish nominal cycle with a robust set of operating parameters. This will include commissioning of the squeeze to an appropriate β* with measurement and correction of the optics and key beam parameters at each stage. One should not expect to probe the limits of the HL-LHC parameter space at this stage.
- Measure and correct the optics. Measure the aperture.
- Set-up injection, beam dump, and collimation, and validate set-up with beam.
- Commission beam-based systems: transverse feedback, RF, injection, beam dump systems, beam instrumentation, and orbit and tune feedbacks.
- Commission and test machine protection backbone with beam.
- Check the understanding of magnet model and higher order optics.

The initial commissioning phase is performed at low intensity, with a low number of bunches, and a generally safe beam. The output of this phase is taken to be first collisions in stable beams with a small number of bunches. Following this, pilot physics can be delivered with up to 100 widely spaced bunches. Scrubbing will then be required before entering the intensity ramp-up phase. Scrubbing could well follow the two-stage approach deployed following LS1. This approach is outlined below.

- Initial scrubbing with 25 ns beam following initial commissioning opening the way for a period of 25 ns operation with non-nominal batch spacing.
- Initial intensity ramp-up with 25 ns is then foreseen. During this stage, system commissioning with higher intensity continues (instrumentation, RF, injection, beam dumps, machine protection, vacuum, etc.). Variables at this stage include bunch intensity, batch structure, number of bunches and emittance. Physics fills can be kept reasonably short. The intensity ramp-up is performed in a number of clearly defined steps with associated machine protection and other checks. This phase will be used to characterize vacuum, heat load, electron cloud, losses, instabilities, UFOs, and impedance.
- Thereafter a further scrubbing period with 25 ns and possibly the doublet beam is foreseen.
- This is followed by an intensity ramp-up with 25 ns dictated by electron cloud conditions, with further scrubbing as required. Past experience indicates that a sustained period of physics in the presence of electron cloud will be needed.

Important beam-related characteristics such as lifetime, beam loss through the cycle, stability, quench levels, and UFO rates will only become fully accessible with an increase in bunch intensity and number of bunches during the intensity ramp-up phase.

16.5 References

[1] M. Bednarek *et al.*, ElQA qualification of the superconducting circuits during hardware commissioning, LHC-DE-TP-0007, EDMS: 788197.

[2] G. Apollinari, I. Bejar Alonso, O. Brüning, P. Fessia, M. Lamont, L. Rossi, L. Tavian (Eds.), Chapter 3, High-Luminosity Large Hadron Collider (HL-LHC): Technical Design Report V.0.1, DOI: 10.23731/CYRM-2017-004.

[3] Th. Weiler *et al.*, LHC Collimation system hardware commissioning, 22nd Particle Accelerator Conference, Albuquerque, NM, USA, 25 - 29 Jun 2007, pp.1625, DOI: 10.1109/PAC.2007.4440844.

[4] G. Apollinari, I. Bejar Alonso, O. Brüning, P. Fessia, M. Lamont, L. Rossi, L. Tavian (Eds.), Chapter 9, High-Luminosity Large Hadron Collider (HL-LHC): Technical Design Report V.0.1, DOI: 10.23731/CYRM-2017-004.

[5] R. Calaga, *et al*., The SPS Tests of the HL-LHC Crab Cavities,9th International Particle Accelerator Conference, IPAC 2018, Vancouver, BC, Canada, DOI: 10.18429/JACoW-IPAC2018-TUPAF057.

Chapter 17

Technical infrastructure

L. Tavian[1*], *M. Battistin*[1], *S. Bertolasi*[1], *C. Bertone*[1], *B. Di Girolamo*[1], *N. Dos Santos*[1], *K. Foraz*[1], *T. Hakulinen*[1], *P. Mattelaer*[1], *P. Muffat*[1] *and P. Pepinster*[1]

[1]CERN, Accelerator & Technology Sector, Switzerland
[*]Corresponding author

17 The HL-LHC technical infrastructure

The HL-LHC technical infrastructure includes the civil engineering, the electrical distribution, the cooling & ventilation, the access & alarm system, the technical monitoring, the transport, the logistics, the storage, and the operational safety.

17.1 Civil engineering

17.1.1 Introduction

In terms of civil engineering, the needs of the HL-LHC machine are, to a large extent, similar to the LHC machine, which was a considerable extension carried out between 1998 and 2005 of the previous LEP tunnel built in in the 1980's. These needs consist principally of access shafts from the surface to the underground areas together with various underground caverns and tunnels that, to distinguish from the LHC beam tunnel, we will call galleries. Buildings are required on the surface for housing compressors, ventilation equipment, electrical equipment and helium and nitrogen tanks.

The HL-LHC construction work will be split between two existing experimental sites, LHC Point 1 for the ATLAS experiment, located in Switzerland, and LHC Point 5 for the CMS experiment, located in France, and will include underground and surface works at both points.

The underground work at each point will consist of a shaft, a cavern, a power converter gallery, service galleries, safety galleries and vertical cores that link the new galleries to the existing LHC infrastructure. The civil engineering work encompass both the primary concrete and steel structures of the surface and underground structures as well as the secondary steel structures within the buildings and caverns. At both locations, some of the new work will be located close to existing LHC infrastructure. Hence, special protective measures must be taken in order to minimise impact on the operation of the LHC and on the LHC infrastructure itself.

To fulfil the HL-LHC timeline the majority of the construction will be completed in a 5-year period. Activities started in 2018 with the excavations of the shafts starting from the surface. The remaining underground excavation work close to the LHC tunnel area was scheduled during LS2, when the LHC operation is stopped, and the less invasive concreting and finishing of the underground work is scheduled during 2020–2021. The surface work is scheduled to take place from late 2019 to the end of 2022. Staged handovers of the new buildings are planned. The only construction work that is scheduled outside of this 5-year period are the drilling of the linkage cores from the new HL-LHC infrastructure into the existing LHC tunnel, which is scheduled for early 2025 when the LHC is again not operational during LS3. The objective is to also construct the safety galleries that connect the HL-LHC underground structures to the existing LHC

tunnel during LS2 and have them operational during infrastructure installation that will take place during the LHC Run 3.

17.1.2 Underground work

For the HL-LHC additional underground space is required for services. The dimensions of underground structures specified for Point 1 and Point 5 are detailed in Table 17-1. However, for the HL-LHC there is no requirement for additional underground spaces as experimental caverns. As shown in Figure 17-1 the underground work consists of the structures described hereafter.

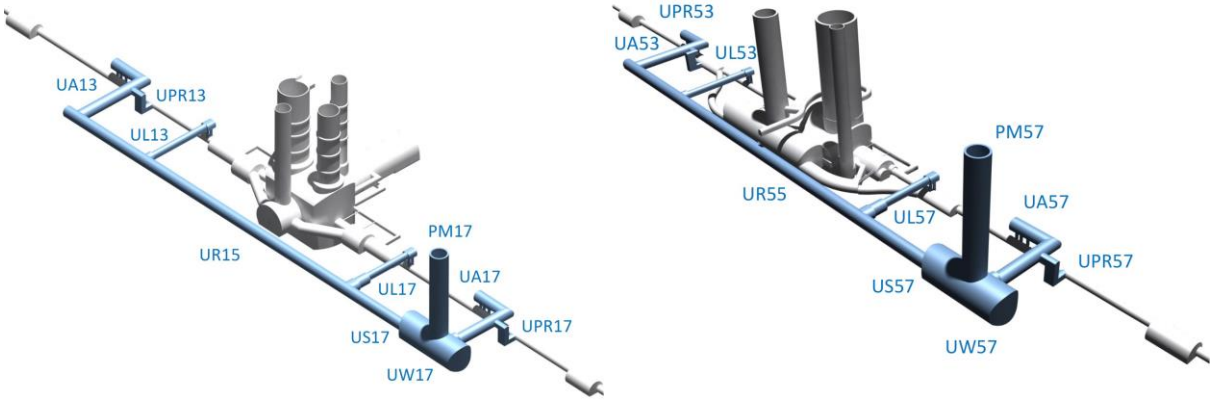

Figure 17-1: Point 1 (left) and Point 5 (right) indicative underground axonometric

Table 17-1: Underground structure dimensions at Point 1 (Point 5 if different)

Building Code	Building Name	Length (m)	Inside Width (at floor level) (m)	Height (m)	Radius (m)	Floor Area (m^2)	Volume (m^3)
PM	Shaft	-	-	72.0 (82.2)	5.00	79	5690 (9490)
US/UW	Cavern	46.3	14.7	11.2	8.00	681	6 924
UR	Power converter gallery	302.0	5.0	4.7	2.90	1522	7 013
UL	SC cryo link galleries	53.7	3.7	3.3	1.55	198	618
UA	RF galleries	68.1	5.7	4.4	2.90	389	1 579
UPR	Safety galleries	51.1 (54.3)	2.5	2.50	-	128 (136)	286 (304)

The shaft (PM) connects the surface with the underground area. A lift in the shaft provides day-to-day personnel and equipment access; it is housed in leak tight concrete modules which are over-pressurized with respect to the ambient pressure. Aa staircase is also included in these concrete modules. At the bottom and top of the shaft, there are pressurized safe rooms. All cryogenic, power and ventilation connections between the surface and the cavern pass through the shaft.

The underground caverns are made up of two portions: the US and the UW. They house the cryogenic equipment and other technical services. A concrete wall separates the US and UW portions. In the UW and large part of the US, there is a first floor supported by a steel structure to provide a two-storey facility.

The UR gallery, approximately 300-m long and placed parallel to the LHC tunnel, mainly houses the power converters and the electrical current feed boxes of the superconducting magnets. It is connected to the LHC tunnel via the service galleries.

Four service galleries (UA and UL) provide the connection from the UR gallery to the existing LHC tunnel for Point 1 and Point 5 each, via the vertical linkage cores. The UA galleries will house the RF equipment of the crab-cavities and the UL galleries will house the cryogenic distribution system and the superconducting links.

Vertical cores, of approximately 1 m diameter each, are required to pass services from each of the four service galleries to the existing LHC tunnel. These linkages allow connecting the newly installed services to the new systems (superconducting magnets, cryogenic distribution lines and RF cavities) that occupy the Long Straight Sections (LSS) in the existing LHC tunnel.

Finally, a safety gallery (UPR) for personnel is required to connect each UA gallery directly to the existing LHC infrastructure.

17.1.3 Surface work

All LHC buildings keep their present functionality during the HL-LHC era. In addition, some new buildings are required at Point 1 and Point 5. The surface work at each point is made up of 5 new buildings, a combination of steel and concrete structures, as well as technical galleries, concrete slabs, roads, drainage, and landscaping. At present, it is anticipated that the buildings would generate an additional 6200 m^2 of floor area. The dimensions for the surface structures at Point 1 and Point 5 are specified in Table 17-2. The corresponding site layouts are shown in Figure 17-2 and Figure 17-3. The surface works consist of the structures described hereafter.

The head-shaft building (SD) covers the PM shaft; a steel frame building is envisaged. The floor slab of the building requires technical galleries to allow cables, pipes, and other services to pass from the PM shaft to the service gallery and other adjacent buildings.

The ventilation building (SU) is required to house the equipment needed for the heating, ventilation, and air conditioning of the underground infrastructure. The building is constructed in reinforced concrete to minimise noise levels outside the building. The building is split into two sections that house compressors and air handling units, respectively.

The electrical building (SE) is used to house electrical equipment. The building includes a low voltage room, a high voltage room and a small room for UPS battery storage.

The cooling tower building (SF) is required to extract the heat loads from the equipment and is constructed in reinforced concrete. The building is split into two zones, one for the two cooling towers, and one for the pump room. This building is partially equipped with a steel mezzanine structure. Chemical products for water treatment are stored in a dedicated external container, which requires a dedicated concrete slab.

The compressor building (SHM) houses the warm compressors of the cryogenic plant. It is constructed in reinforced concrete. This building is partially equipped with steel mezzanine structures.

The technical galleries (SL) run just below ground level between the buildings in order to provide a route for power supplies, cryogenics, and cooling pipes. The siting of the new technical galleries is optimised such that there is no interference with existing services. There are some openings required in the roof of the galleries to provide access for the installation of services, extraction points and escape points. Some technical galleries are connected to existing buildings and galleries. The galleries must be watertight and are foreseen in reinforced concrete.

The helium tank platform (SHE) is a concrete foundation for placing 2 helium tanks on. The support for the tanks is based on a steel frame that is connected to the foundation using anchor bolts that can transfer seismic loads to the slab. A crash barrier is required around the structure.

The nitrogen tank platform (SLN) is a concrete slab for placing large nitrogen tanks on. The support for the tanks is based on a steel frame that is connected to the slab using anchor bolts that can transfer seismic loads to the slab. A crash barrier is required around the structure.

The harmonic filter slab will house the electrical equipment needed for the power quality of the electrical network. In addition, a slab for a new electrical sub-station housing a transformer is required at Point 5. The slabs at Point 5 are not included in the WP17.1 scope and are part of the WP17.2.

New roads and car parks are required to provide transport links to the new buildings. At Point 1, the existing terrain level is modified to create a platform at approximately the elevation of the ATLAS site. Spoils excavated from the underground structures are used to construct this platform.

Finally, required drainage for all the new surface and underground structures is fully integrated into the existing drainage system

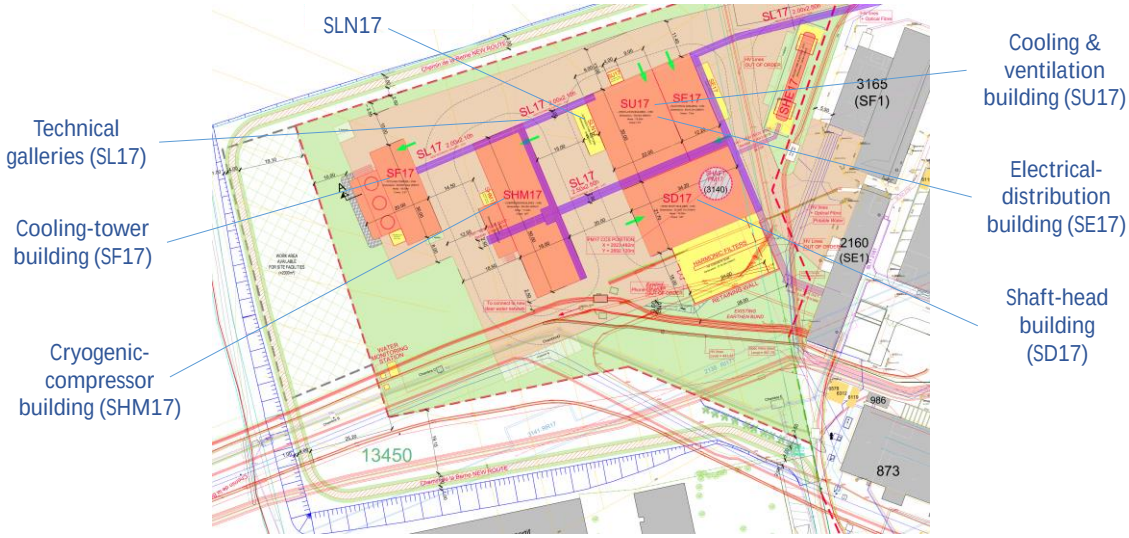

Figure 17-2: Point 1 surface layout

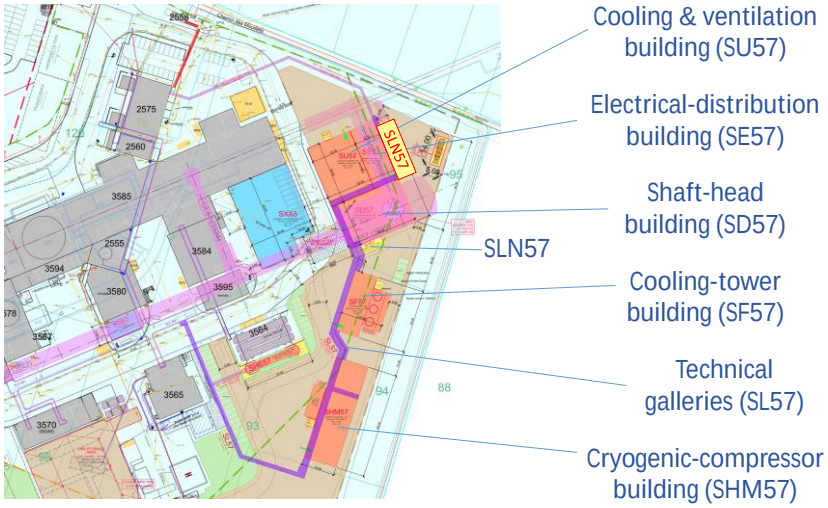

Figure 17-3: Point 5 surface layout

Table 17-2: Point 1 surface building characteristics (Point 5 if different)

Building Code	Building Name	Length (m)	Width (m)	Height (m)	Floor Area (m^2)	Volume (m^3)
SD	Head shaft building	32.0	20.0	16.0	640	10 200
SU	Ventilation building	30.0	22.0	13.5	660	8 910
SE	Electrical building	29.5	10.5	7.0	310 (352)	2 170 (2460)
SF	Cooling towers	19.0	18.1	7.7	344	2 648
SHM	Compressor building	56.0	16.0	10.9	896	9 770

17.1.4 Vibration risk to the LHC during construction

The impact of the HL-LHC construction on the LHC operation is a key constraint of the civil engineering of the HL-LHC project. It has been concluded that excavation of the caverns and various service galleries close to the LHC tunnel cannot take place whilst the machine is in operation. Hence, these activities have been scheduled during LS2. The decision was taken at the end of 2015 and required advancing the whole HL-LHC civil engineer by two years with respect to the original plan. The shaft has been located as far as possible from the triplets and is located 40 m from the existing infrastructure; its construction has been deemed possible whilst the LHC was running, during the last year of Run 2 (2018). The experience proved that this decision was right since no problem of vibrations has been actually affected the LHC operation. The concreting/finishing phase of the underground construction will be completed in 2021: again, we do not expect any issue for the LHC operation due to vibrations from this construction phase.

17.2 Electricity

17.2.1 Objective

This Section outlines the new infrastructures needed for the HL-LHC in terms of electrical distribution, optical fibre infrastructure, Direct Current (DC) distribution and signal cabling. The design principles presented in the document are based on the requirements formulated by the users in 2016. A recent revision of the user-load requirement might imply some modifications of the electrical distribution system. A more detailed description can be found in [1].

17.2.2 Requirements and constraints

From an environmental point of view, the new electrical infrastructure required for the HL-LHC may imply risks in term of noise. The noise level generated by electrical equipment, such as transformers or switchgear, have been provided to an acoustic consultant, which has performed studies both for surface and underground installations. In addition, all the distribution transformers (excepted for the 66/18 kV transformer at Point 5) installed in the context of the HL-LHC will be of dry type and therefore do not create problems in relation to oil pollution.

The schedule for the work outlined in the next Sections is strictly related to the hand-over of the surface buildings and underground structures foreseen by the project.

Part of the work related to the transport and distribution infrastructure, such as the installation of the infrastructures in the new underground caverns and surface buildings, can be carried out during the run of the accelerators. A large part, especially related to the modifications to existing infrastructure, needs to be executed during an Extended Year End Technical Stop (E)YETS or during a Long Shutdown (LS) when the accelerators are not being operated.

In Point 1, the constraints related to the construction of the new buildings require the displacement of existing power cables and optical fibres, which was executed during the EYETS 2016 in order to limit the risk of loss of availability of user systems.

In order to minimize the impact of cumulated dose received during the future maintenance interventions and to adequately select the components to be installed in the radiation areas, the radiation data collection has started and is under analyse in collaboration with HSE-RP. The installation work in the LHC tunnel is organized in campaigns according to the correspondent activities and following the ALARA (*As Low As Reasonably Achievable*) principle to minimize the cumulated dose received by the participants.

It is necessary to underline that the technical solutions specified by the users have an important impact on both power requirements and integration in underground facilities. For example, in the case of radio frequency (RF) systems, the worst-case scenario in terms of power consumption and integration is represented by the use of power amplifiers with IOT technology, while the best-case scenario is represented by the use of

Solid State Power Amplifiers (SSPA). While the HL-LHC baseline after the C&SR4 includes SSPAs for the crab cavities, the design described in this document is still based on the use of IOTs which is the more demanding reference from the integration point of view and foresees to supply 4 crab-cavity modules per Point.

The following Sections cover the design principles related to the distribution network, which covers 18 kV, 3.3 kV and 400 V as well as optical-fibres and DC cables. The design principles used for the distribution network are the same at Point 1 and 5, allowing an important level of standardization, and are based on the present LEP and LHC principles for what concerns power transmission.

17.2.3 User electrical load forecast at Point 1 and Point 5

The load forecast of the HL-LHC project has been evaluated by the main users (cryogenics, radiofrequency, power converters, cooling and ventilation) and is summarized in Table 17-3. The differences between the two Points are due to additional building electrical heating at Point 5.

At Point 1, the HL-LHC loads are fed via the existing transformer EHT102/1E, which has sufficient design margins to supply these extra HL-LHC loads as well as extra loads due to the ATLAS detector upgrade. The Point 5 of LHC is presently supplied via an existing 18 kV 15 MVA line coming from LHC Point 6. This existing line is definitely not adapted to the new loads foreseen at Point 5, both for the HL-LHC and the CMS detector upgrade. Consequently, a new 66 kV line coming from LHC Point 6 is foreseen in the CERN consolidation plan (i.e. outside of the HL-LHC project scope). On the Point 5 site, a new electrical substation equipped with a 66/18 kV electrical transformer of 38 MVA must be added and is part of the WP17.2 scope.

Table 17-3: HL-LHC loads in Point 1 and Point 5

		Point 1				**Point 5**			
User	**Location**	**(kW)**	**(kvar)**	**(kVA)**	**cos(phi)**	**(kW)**	**(kvar)**	**(kVA)**	**cos(phi)**
Cryogenic system	SHM	5000 (5320)	2967 (3157)	5814 (6186)	0.86	5000 (5320)	2967 (3157)	5814 (6186)	0.86
Ventilation	SE	8 (36)	4 (27)	9 (45)	0.9 (0.8)	8 (36)	4 (27)	9 (45)	0.9 (0.8)
Ventilation	SU	32 (44)	16 (33)	36 (55)	0.9 (0.8)	32 (44)	16 (33)	36 (55)	0.9 (0.8)
Ventilation	SF	49 (51)	24 (38)	55 (64)	0.9 (0.8)	43 (221)	21 (166)	48 (276)	0.9 (0.8)
Ventilation	UW	62 (20)	30 (15)	69 (25)	0.9 (0.8)	62 (20)	30 (15)	69 (25)	0.9 (0.8)
Ventilation	SHM	31 (32)	15 (24)	35 (40)	0.9 (0.8)	31 (32)	15 (24)	35 (40)	0.9 (0.8)
Ventilation	UR	0 (32)	0 (24)	0 (40)	0.9 (0.8)	0 (32)	0 (24)	0 (40)	0.9 (0.8)
Ventilation	UA	0 (6)	0 (5)	0 (8)	0.9 (0.8)	0 (6)	0 (5)	0 (8)	0.9 (0.8)
Ventilation	US	0 (6)	0 (5)	0 (8)	0.9 (0.8)	0 (6)	0 (5)	0 (8)	0.9 (0.8)
Cooling	SU	606 (566)	293 (425)	673 (708)	0.9 (0.8)	606 (566)	293 (425)	673 (708)	0.9 (0.8)
Cooling	SF	549 (520)	266 (390)	610 (650)	0.9 (0.8)	549 (520)	266 (390)	610 (650)	0.9 (0.8)
Cooling	UW	164 (138)	79 (104)	182 (173)	0.9 (0.8)	164 (138)	79 (104)	182 (173)	0.9 (0.8)
Radiofrequency	UR/UA	807 (444)	265 (146)	849 (468)	0.95	807 (444)	265 (146)	849 (468)	0.95
Radiofrequency	US/UA	807 (444)	265 (146)	849 (468)	0.95	807 (444)	265 (146)	849 (468)	0.95
Power converters	UR	1300 (1014)	700 (814)	1368 (1300)	0.95 (0.75)	1300 (1014)	700 (814)	1368 (1300)	0.95 (0.75)
Cold powering	UR	0 (20)	0	0 (20)	1	0 (20)	0	0 (20)	1
Machine protection	UR	0 (24)	0 (12)	0 (27)	0.9	0 (24)	0 (12)	0 (27)	0.9
Survey		0 (65)	0 (31)	0 (72)	0.9	0 (65)	0 (31)	0 (72)	0.9
EL network Control		0 (2)	0	0 (2)	1	0 (2)	0	0 (2)	1
Transport		0 (316)	0 (204)	0 (376)	0.78	0 (316)	0 (204)	0 (376)	0.78
Various	Surface Underg.	1000	800	1281	0.78	1000	800	1281	0.78
(xxx): Revised estimate		10416 (10100)	5725 (6398)	11830 (11956)		10913 (10300)	5965 (6548)	12383 (12205)	

17.2.4 Power quality at Point 1 and Point 5

The operation of the HL-LHC accelerator imposes the need for excellent power quality. In particular the power converters, controlling DC currents with highest precision of a few ppm are very sensitive to power quality issues. Consequently, to compensate for the reactive power consumption of the HL-LHC load, and to filter the higher frequency harmonics, two new high-pass filters are required at Point 1 and Point 5. Each of these harmonic filters will be switched individually by a dedicated 18 kV circuit breaker, allowing to adapt the reactive power generation. The ratings of the components for these two harmonic filters will be based on CERN's standardised harmonic filter design. The achieved power quality level will be in conformity with the requirements of the CERN LHC Engineering Specification EDMS113154 and with the international standard IEC 61000-2-4 Class 1. Table 17-4 gives the main characteristics of these filters.

Table 17-4: Main characteristics of harmonic filters

Location	Reactive power rating of filter #1 (Mvar)	Reactive power rating of filter #2 (Mvar)	Connected to substation
Point 1	6	6	EMD8/1E
Point 5	6	4	EMD2/5E

17.2.5 User electrical load forecast at Point 4

Following a Decision Management Report to not install at Point 4 the mobile helium refrigerator presently used for the SPS test station of crab-cavity cryo-modules, no additional electrical load is required at Point 4.

17.2.6 High voltage distribution network

The detailed single line diagrams are given in [2] and [3] for Point 1 and Point 5 respectively. As previously mentioned, the 18 kV and 3.3 kV distribution in Point 1 and Point 5 are designed to be as similar as possible. The main users are the cryogenic systems (SHM), the cooling and ventilation (SU, SF, UW), the radio frequency system (UA) and the power converters (UR).

The electrical-distribution building (SE) contains 3 rooms. The first room, called SEH, hosts 18 kV and 3.3-kV switchgear. The second room, called SES, hosts 18 kV and 3.3 kV protection relays, 400 V main and secondary distribution switchboards (normal and secured network), safety lighting power sources and distribution switchboards, 48 VDC system (chargers and distribution), UPS units, equipment control/supervision racks and emergency stop rack. The third, smaller room, hosts batteries for the 48 VDC system and the UPS.

In the US cavern, a fireproof safe room is created to host all safety-related equipment. The safe room contains main and secondary secured switchboards, 48 VDC systems (chargers, distribution, and batteries) and emergency stop racks.

The equipment to be installed in SE buildings, safe rooms and underground facilities has been defined and integrated in the 3D model on the basis of EL known needs, user requirements and affinity with existing LHC installations.

17.2.7 Low voltage distribution network

The low voltage distribution topology is based on the one currently used for the LHC and based on the available amount of information provided at this stage by the users. Four main functional networks are foreseen to be distributed in most of the surface and underground buildings: general services, machine network, secured network (backed-up by diesel generators) and uninterruptible power supplies network (UPS).

In Point 1, the General Services Network is fed by one 18/0.4 kV transformer, located outside SE17, and supplied by the 18 kV switchgear EMD1/1E installed in SE1. The main 400 V distribution switchboard

EBD1/17E feeds all general services sub-switchboards installed inside surface buildings and underground facilities. The Machine network is fed by several 18/0.4 kV transformers distributed along the machine buildings; on the secondary side of each transformer, one main 400 V switchboard will distribute the power to various users. The low voltage distribution network is described in Ref. [4] for Point 1 (Point 5 follows the same principles).

17.2.8 Secured power systems

This Section describes the design principles of the low voltage distribution related to the diesel generators, the UPS systems and 48 VDC systems.

In Point 1 and Point 5, the load forecast is estimated to 167 kW dedicated to ventilation safety systems and lifts and does not indicate the need of a major modification of the existing infrastructure. In Point 1, the secured network dedicated to the HL-LHC loads is fed by one 18/0.4 kV transformer, located outside SE17, and supplied by the 18 kV switchgear EFD1/1E installed in SE1. The main 400 V distribution switchboard ESD1/17E feeds all secured sub-switchboards installed inside surface buildings and underground facilities. In Point 5, the estimated loads imply the replacement of the existing diesel generator which is limited to 78 kW or the installation of a new one (space has been reserved for this scope). The distribution principle will be similar to the one described above for Point 1.

The UPS network is constituted by several UPS units (double-conversion AC/DC) associated with batteries and 400-V distribution switchboards. The UPS have a 10-minute autonomy; underground UPS will be installed with N+1 redundancy. The UPS and related switchboards are installed and rated according the user needs. Depending on this, the UPS can be installed with a centralised configuration, in which a single UPS supplies different functional equipment, or with a single unit dedicated to a specific user. The load forecast, presented in Table 17-5, highlights the needs of UPS in both Point 1 and Point 5.

Table 17-5: Load forecast for the UPS in LHC1 and LHC5

	Location	**P1 P (kW)**	**P5 P (kW)**	**Comment**
Power converters	UR	86	86	1kW/ converter
	SR	10	10	IOT option
Radio Frequency	UR	70	70	Tetrode option
Cryogenic Systems	SHM	5	5	Extrapolated from LHC
	SDH	5	5	Extrapolated from LHC
	US	10	10	Extrapolated from LHC
Interlock and Energy extraction	UR	65	65	Redundant powering with 2 UPS lines, 10 min autonomy
Cooling & Ventilation		0	0	
Total		251	251	

In addition to the networks described above, a 48 VDC network supplies the auxiliaries of high voltage switchgears and low voltage switchboards, the emergency stop systems and Scada-related equipment. The 48 VDC network is constituted by Ni-Cd batteries, distribution switchboards and battery chargers fed by 400 V secured network. Only WP17.2 equipment is connected to the 48 VDC network.

17.2.9 Safety systems

Dedicated emergency lighting systems are installed in every surface and underground facility. The emergency lighting system is activated in the event of a power failure or a scheduled test. For the underground facilities, it is foreseen to install a centralized and redundant system, with two different and independent sources, separate fireproof cabling, and specific luminaires. Surface buildings, more likely, are equipped with safety luminaires for an emergency evacuation. These luminaires have their own batteries and act in the event of a power failure or a scheduled test. The lighting levels and distribution are according to the last safety norms applicable at CERN.

The emergency stop system, so-called AUG, is constituted by two racks: one in the surface building SE and one in the safe room inside the US cavern. Surface buildings and underground facilities are subject to the action of Emergency Stop Buttons, which act on the 18 kV distribution network. In the event that an AUG is activated, the CERN fire brigade is called immediately (Level 3 alarm) and all electrical powers are lost until their restoration by the stand-by duty service. A risk assessment shall be conducted in accordance with IS5 to decide the scope of services affected by an AUG action.

17.2.10 SCADA System

The electrical equipment of the CERN power distribution network is interfaced with the existing SCADA system, referred to as ENS, Electrical Network Supervision, which provides the CERN Control Centre (CCC) and the electrical operation personnel with remote monitoring, control facilities, alarm information and historical archiving. The SCADA system supervision covers from simple status signals to digital protection relays as well as UPS and battery chargers. Control channels permit remote actions mainly on circuit-breakers, UPS, and battery chargers. Majority of devices involved at various levels are synchronised from Time Servers through NTP protocol. In addition to the conversion of multiple communication protocols from field equipment towards the upstream IEC870-5-104, RTUs allow for a second level of supervision in the major substations through local SCADA software. The implementation is “stand-alone”, remaining fully operational in the event of unavailability of the external informatics infrastructure or main SCADA system. In the context of the HL-LHC, two new RTU will be installed per LHC point (1 and 5), one in the SE building and one in the US cavern, centralizing the supervision of electrical equipment respectively in all new surface and underground buildings.

The main SCADA system, Siemens WinCC OA based (formerly known as PVSS) runs on 2 LINUX servers in a redundant hot-standby configuration. The system is integrated with existing CERN facilities for long term archiving and logging, for alarms and for data exchange with other applications and control systems.

17.2.11 High current DC cabling

In the HL-LHC Project, high Direct Current (DC) cables are used between the power converters and the superconducting-circuit current leads, which are integrated in the DFH or cryo-magnet assemblies. Those chlorine-free power cables are either conventional (air-cooled) or water-cooled depending on the current requirements. The design of the terminations is adapted to the power converters and to the current leads of the DFBs. Table 17-6 and Figure 17-4 show the intensity of the current requested and the cross-section of the cables. Conventional Air Cooled Cable (ACC) are used for the following intensities: 35, 120, 200 and 600 A. The cross-section of the conventional DC cables is defined in the Reference Database, which contains all information related to the Electrical DC Circuits. Their installation is included in the machine cabling campaigns. Water-Cooled Cables (WCC) are used for high current DC interconnections between the power converters and the circuit disconnector boxes, located in the UR galleries of the points 1 and 5 of LHC. The WCCs concern the following intensities: 2, 13 and 18 kA. The cooling of the cables is assured by the circulation of demineralized water inside the cable hose. This technology is well known at CERN and currently used in all the points of the LHC. For the other circuits Q4, Q5, Q6 and their correctors, the existing DC cables already installed in the RRs are reused.

The bending radius of the cables is given in Table 17-6. Due to the configuration of the civil engineering of the UR building, the 18 kA link is composed of 2 cables of 1300 mm^2 in parallel for each one of the polarities to limit the height necessary for the bending radius of the cables. The space required for the links has been reserved in the integration database. The supports of the cables located above the power converters and the current leads have to be carefully designed in order to avoid stress on the equipment and connectors and to allow easy operation. According to the actual layout, the main characteristics and the total length of the DC cables are shown in Table 17-7. The lengths are identical for both sides of each Point. In the UR, the cable resistive losses are 420 kW per Point dissipated in the demineralized water and 30 kW per Point dissipated the UR ventilation system.

	Copper section [mm²]	Length of the cable above the lug h: [mm]	Minimum bending radius r: [mm]	External diameter [mm]
18 kA	2x1300	500	800	2x95
13 kA	2000	500	800	115
6 kA	1000	500	700	95
2 kA	500	500	500	70
600 A	400	300	300	36
200 A	95	200	200	25
120 A	70	150	150	22

Table 17-6: Intensity requested and cross-section of the cables

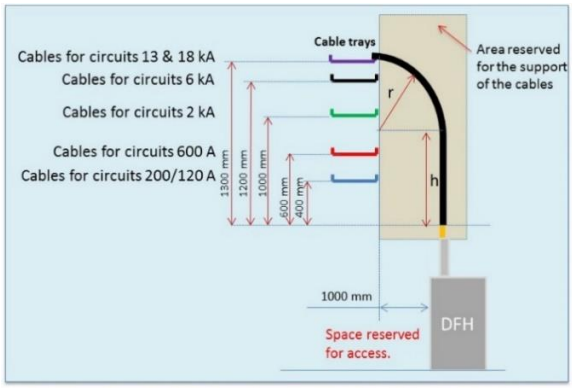

Figure 17-4: Bending radius of the DC cables

Table 17-7: DC cable characteristics

Optic	Magnet	PC location	CL location	Current (kA)	# of circuits per side	Cu section (mm²)	Unit cable length (m)	# cable per polarity	# of sides	Total cable length (m)	Type
Q1-Q2a-Q2b-Q3	MQXFA / MQXFB	UR	UR (DFHX)	18	1	1300	42	2	4	672	WCC
Trim Q1		UR	UR (DFHX)	2	1	500	60	1	4	480	WCC
Trim Q3		UR	UR (DFHX)	2	1	500	28	1	4	224	WCC
Corrector	MCBXFBV	UR	UR (DFHX)	2	2	500	64	1	4	1024	WCC
Corrector	MCBXFBH	UR	UR (DFHX)	2	2	500	66	1	4	1056	WCC
Corrector	MCBXFAV	UR	UR (DFHX)	2	1	500	70	1	4	560	WCC
Corrector	MCBXFAH	UR	UR (DFHX)	2	1	500	72	1	4	576	WCC
D1	MBXF	UR	UR (DFHX)	13	1	2000	44	1	4	352	WCC
D2	MBRD	UR	UR (DFHM)	13	1	2000	36	1	4	288	WCC
Correct D2	MCBRD	UR	UR (DFHM)	0.6	4	400	24	1	4	768	ACC
Kmod Q1a		LHC UJ	IT cryostat	0.035	1	20	120	1	4	960	ACC
CP	MQSXF	LHC UL & UJ	IT cryostat	0.2	1	120	75	1	4	600	ACC
CP	MCSXF / MCSSXF	LHC UL & UJ	IT cryostat	0.12	2	50	75	1	4	1200	ACC
CP	MCOXF / MCOSXF	LHC UL & UJ	IT cryostat	0.12	2	50	75	1	4	1200	ACC
CP	MCDXF / MCDSXF	LHC UL & UJ	IT cryostat	0.12	2	50	75	1	4	1200	ACC
CP	MCTXF	LHC UL & UJ	IT cryostat	0.12	1	50	75	1	4	600	ACC
CP	MCTSXF	LHC UL & UJ	IT cryostat	0.12	1	50	75	1	4	600	ACC
11 T trim		LHC RR	11 T cryostat	0.25	1	50	80	2	2	640	ACC
11 T Dipole	MBH	LHC UA	LHC DFBA	Re-use of existing DC cables							
Q4	MQYY	LHC RR	RR (DFBL)								
Correct Q4	MCBYY	LHC RR	RR (DFBL)								
Q5	MQY	LHC RR	RR (DFBL)								
Correct Q5	MCBY	LHC RR	RR (DFBL)								
Q6	MQML	LHC RR	RR (DFBL)								
Correct Q6	MCBC	LHC RR	RR (DFBL)								

17.2.12 Optical fibre infrastructure

The optical fibre infrastructure provides optical fibre links across the CERN site, including in-between surface and underground buildings. The infrastructure is also distributed in each of the LHC service areas and along the LHC arcs. This infrastructure services a variety of systems (Cryogenics, Beam Interlock, LASS, Evacuation, Power converters, IT Network, GSM, TETRA, and others). A new portion of the optical fibre infrastructure is deployed for the HL-LHC with the same topology and installation techniques as the existing one, for each of the LHC service areas. The optical fibre capacity is dimensioned according to the received requests and calculated spare capacity in the same proportion as in the existing LHC service areas). The current requests are in a phase of studies and discussions and concern the general optical fibre infrastructure, the controls for electrical distribution network, the IT Network, the crab-cavities monitoring and the magnet cold mass monitoring. The topology of the current optical fibre infrastructure is based on a star-point distribution. For the new distribution, the topology will be mirrored from the existing infrastructure in the LHC service areas. The new distribution includes also main linking paths between the existing and the new star-points. A redundancy path to the surface is also created over the new pit. This configuration will allow creating redundancy paths for critical systems and serving locally new systems that could be added later.

17.2.13 Signal cabling

Signal cabling includes the installation of electrical cables for data transfer and control for the various user systems. It typically comprises a very large volume of cables to be installed in multiple cabling campaigns. The signal cabling definition and installation for the users is outside the WP17.2 scope and is included in the scope of the different work packages. However, the resources required to supervise the signal cabling is included in the WP17.2. The signal cables are grouped together on the same cable ladder independently of the systems they serve. The vast majority of the signal cables are screened, which limits crosstalk and electro-magnetic interference. Cables for those systems that are particularly sensitive to those effects are pulled on a separated cable ladder. The requested connectors are mounted at each end and then protected from dust. Each installed cable is visually checked and tested for insulation and continuity and the wiring convention is verified.

17.3 Cooling and ventilation

17.3.1 Framework for cooling and ventilation installations

The Cooling and Ventilation installation at Point 1 and Point 5 are mostly the same. The only difference between the two installations consists in the heating solution for the air-handling units: at Point 1 (in Switzerland) electrical heaters are not allowed. A dedicated extension of the superheated water network is used instead. At Point 5 (in France) there is no superheated water network, and the national law allows electrical heaters and this solution has been used here.

The design of the CV installation is done according to the 2016 user-load input data. A recent revision of the user-load requirement will be subject to an update of the cooling and ventilation system.

17.3.2 Primary water cooling

A new 3-cell cooling tower (n + 1 redundancy) of 5 MW each will be installed at each Point. The total cooling power requirements are listed in Table 17-8. The water supply temperature will vary between 20°C and 25°C. The primary water flowrate is based on 8 K temperature difference between supply and return. Three circuits will distribute the primary water in a duty and standby (1 + 1) arrangement. The pump heads are selected to provide approximately 300 kPa (3 bar) at the connexion point of each user equipment. The new plant room will house the three couples of redundant pumps, the sand filtration, and frost protection systems. The pipeline will be made of stainless steel and distributed in the various buildings using technical galleries. The water treatment station is located in a special chemical container to limit the risk of pollution.

Table 17-8: Overall cooling power requirements at Point 1

Location	Final user	Cooling power (kW)	User total (MW)	Design (MW)
UW	Power Converters Water-cooled cable Machine protection RF IOTs, drivers, circulators HV power supply Cryogenics	272 (205) 420 (420) 78 (0) 664 (352) 184 (424) 70 (50)	1.7 (1.5)	1.94*
SHM, SD	Cryogenics	5200 (5200)	5.2 (5.2)	6.0*
SU	Chillers	950 (587)	1.0 (0.6)	1.0

*: Including 15 % of margin

(xxx): Revised estimate

The general P&ID schematic of the cooling installation of the HL-LHC (LHCF31990027) is presented in the Annex of this document. Figure 17-5 shows the corresponding water-cooling architecture.

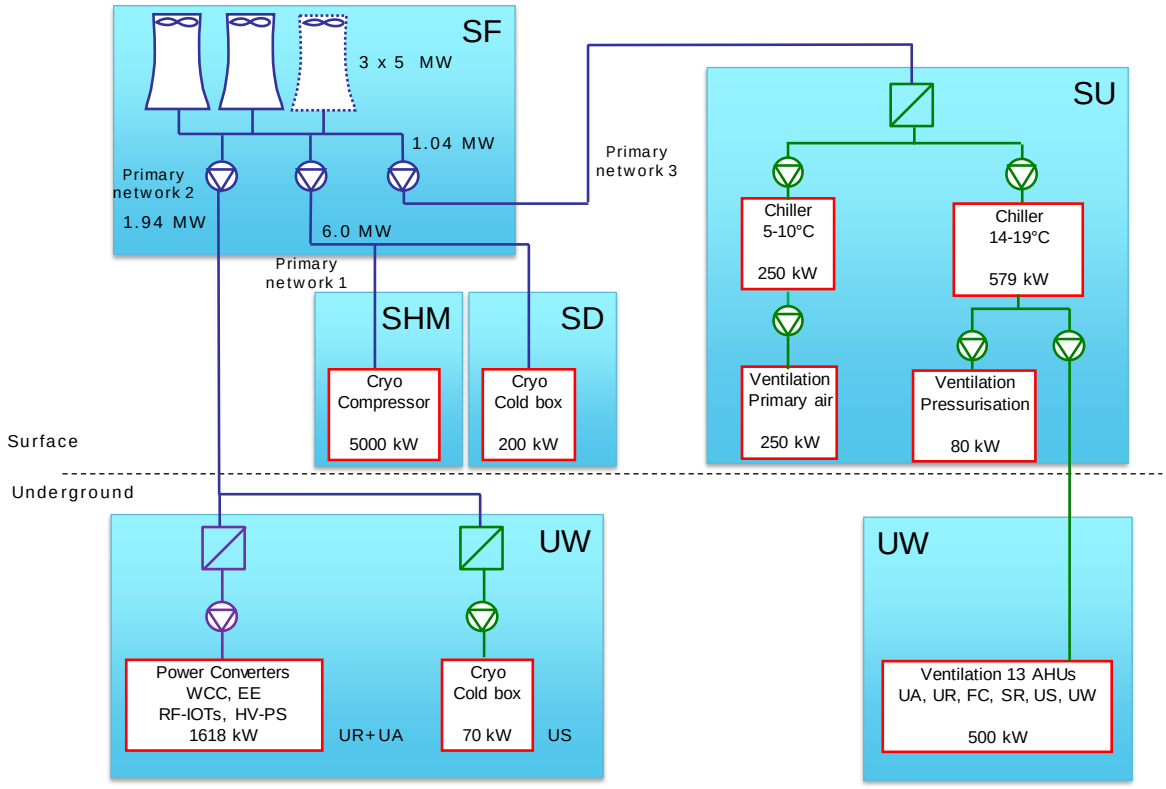

Figure 17-5: Water cooling architecture

17.3.3 UW secondary water cooling

The cold compressors of the cryogenic system are cooled by a dedicated raw-water cooling station in the UW cavern part. It will include a heat exchanger of 80 kW and a duty and standby pump.

One demineralised water-cooling circuit is installed to service all the underground installation. It will cool the power converters, the machine protection system, the water-cooled cables in the UR and the IOTs RF system in the UA. The station will include one heat exchanger (1.75 MW), a duty and standby pump and a demineraliser. The water conductivity is maintained below 0.8 µS/cm.

17.3.4 Chilled and mixed water

The chilled water production plant is dedicated to the fresh air treatment only because of its de-humidification needs. It will be located in SU17. The mixed-water production plant is also located in SU17. Table 17-9 gives the number, the unit capacity, the operating temperature, and the buffer-tank volume of the chillers as well as the distribution pump number and distribution pipework inner diameters. The pipework is in stainless steel thermally insulated.

17.3.5 Hot water for air handling units (Point 1 only)

The CERN Meyrin superheated water network is available close to the HL-LHC site. A hot water production station is installed to distribute hot water to the air-handling units located in the surface building of the HL-LHC complex at Point 1. Electrical heaters will guarantee heating power at Point 5 instead.

Table 17-9: Chiller cooling circuit characteristics

Production plant	Chiller number	unit capacity (kW)	Buffer tank volume (m^3)	Supply temp (°C)	Return temp (°C)	Distribution pump number	Distribution pipe diameter (mm)
Chilled water for fresh air handling units	2*	310 (200)	3	6	12	2*	DN80
Mixed water for surface air handling units	3*	430 (200)	5	14	20	2*	DN80
Mixed water for underground air handling units						2*	DN125

*: including 1 unit in standby for redundancy

(xxx): Revised estimate

17.3.6 Firefighting network

A firefighting water pipe is installed in the PM for the underground areas. A surface and underground firefighting water network (DN100) is installed to supply hose reels and firefighting Storz-55 connections. The network is connected to the existing firefighting networks at Point 1 and Point 5 which are supplied by the raw water pipework embedded in the LHC tunnel. At Point 5, the two rising pumps (in duty and standby configuration) located in the UJ56 shall be upgraded to increase their unit flowrate from 50 to 120 m^3/h.

17.3.7 Compressed air

The compressed air is distributed from the existing LHC network which has sufficient capacity and margin to ensure the HL-LHC needs. The compressed air network will be made of galvanised steel or stainless steel and will distribute compressed air to buildings and underground areas.

17.3.8 Clean and wastewater

A main clean water sump is located at the lowest part of the new underground areas (US) in order to collect all the infiltration or accidental water release. A duty and standby pump will lift the clean water to the surface drainage network. Secondary water sumps are located at the lowest part of the UR (Point 1 only) and of the UPRs. A duty and standby pump will lift the clean water to the main US water sump. A wastewater pit and duty and standby pumps will lift the wastewater to the surface wastewater network.

17.3.9 Underground air handling units

Figure 17-6 shows the underground ventilation architecture. Table 17-10 gives the main characteristics of the air-handling units of the underground areas including the ambient temperature range to be maintained, the total cooling capacity to be installed, the number/flow-rate/size/location of the ventilation units as well as the

diameter of the supply/return ducts. The air supply and return ducts have regular spaced duct mounted grids. The underground air-handling units use mixed-water produced by the chillers located in the SU building and they are not fitted with any heating battery. For the UR, the ventilation system consists of six ventilation units located as close as possible of the equipment generating the heat load. These UR units will not be equipped with ducts, they will recirculate the air locally taking the warm air from the top part of the tunnel and supplying cold air at the level of the floor.

The two Faraday cages located in the US and in the UR have two dedicated air-handling units (one duty and one standby unit for redundancy). Some fresh air is directly supplied into the cages for hygienic purpose. The safe room located in the US has two dedicated air-handling units (one duty and one standby unit for redundancy). The two units are physically located in two different fire-compartments (one in the US and one in the UW part of the cavern). The hydrogen potentially produced by the batteries in the safe room is continuously extracted and diluted in the main ventilated US/UW volumes. The over pressurisation will be ensured.

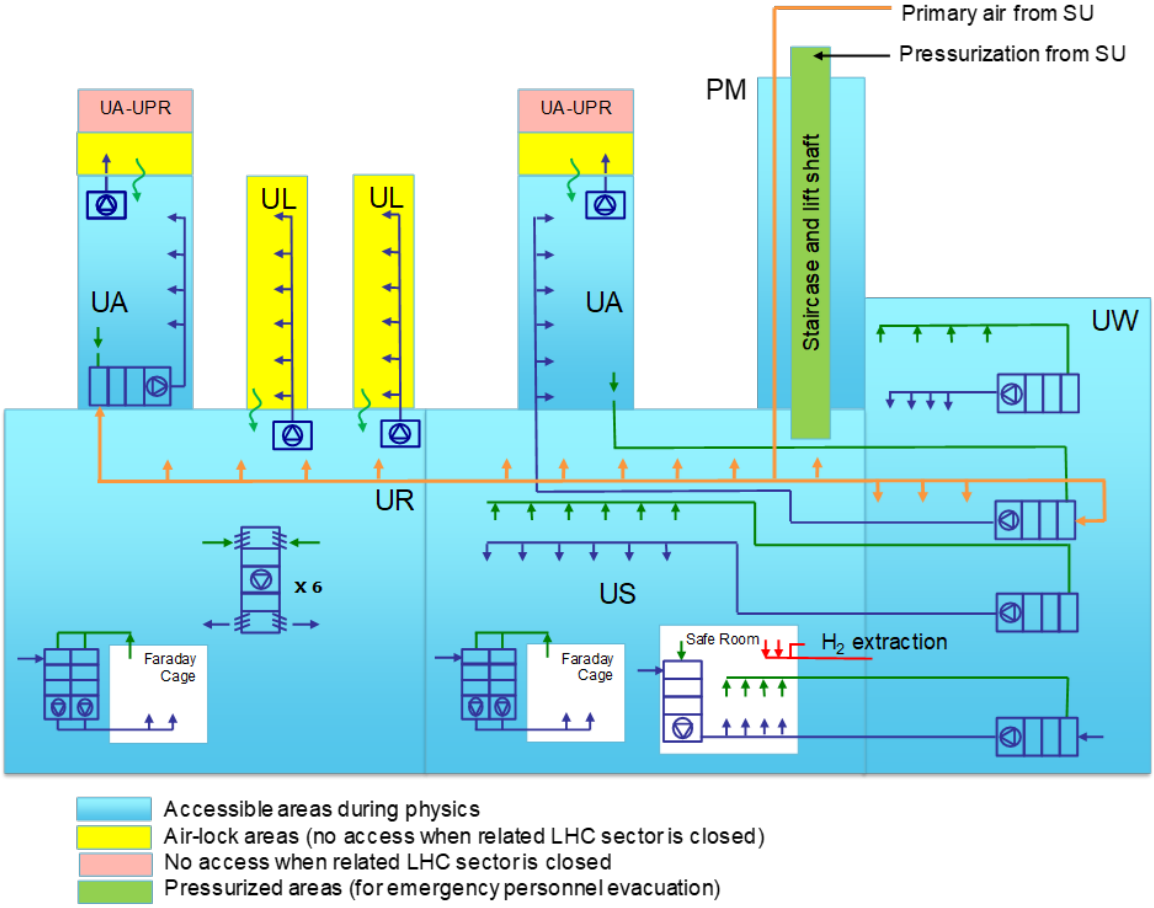

Figure 17-6: Underground ventilation architecture

Table 17-10: Underground air-handling-unit characteristics

Ventilated area	Temp range (°C)	Total cooling capacity (kW)	Units	Unit flow-rate [m3/h]	Unit size Lxlxh (m)	Unit location	Cooling water type	Supply/return duct diameter (mm)	Supply air temp (°C)
UR	14-25	190 (164)	6	8'500	1.65 x 1.35 x 3.5	UR	Mixed	n/a	
UAx3	14-25	60 (52)	1	11'000	5.0 x 2.6 x 1.65	UAx3	Mixed	630	
UAx3 **		0 (4)				UAx3			
UAx7	14-25	60 (52)	1	11'000	5.0 x 2.6 x 1.65	UAx7	Mixed	630	
UAx7 **		0 (4)				UAx7			
US	14-25	47 (32)	1	9'500	4.0 x 1.65 x 1.65	UW	Mixed	630	
UW	14-25	15 (7)	1	3'000	3 x 1.35 x 1.2	UW	Mixed	400	
US Faraday cage	20-22	8 (7)	2*	2'500	1.35 x 0.85 x 2.5	US	Mixed	400/350	15
UR Faraday cage	20-22	8 (7)	2*	2'500	1.35 x 0.85 x 2.5	UR	Mixed	400/350	15
Safe room	18-23	10 (7)	2*	1'500	1.35 x 0.85 x 2.5	US-UW	Mixed	400/200	16

*: including 1 unit in standby for redundancy

** behind mobile shielding

(xxx): Revised estimate

17.3.10 Primary-air distribution

The primary-air is distributed either to the underground air-handling units or directly to the rooms (see Figure 17-7). The primary air is distributed by one duty and one standby air handling unit located in the SU. Table 17-11 gives the main characteristics of the corresponding air-handling units including the unit cooling capacity to be installed, the number/flow-rate/size/location of the units, the air dew-point temperature to be guarantee, the expected dehumidification rate, as well as the diameter of the supply duct, which has to be thermally insulated. For cooling, each unit uses chilled water produced by the chillers located in the SU building. For heating, two hot water batteries (Point 1) and electrical heaters (Point 5) are implemented. The air-intake and supply ducts are thermally insulated.

Table 17-11: Primary air-handling-unit characteristics

Location	Unit cooling capacity (kW)	Units	Unit flow-rate (m^3/h)	Unit size Lxlxh (m)	Cooling water type	Supply duct*** inner diameter (mm)	Fresh air dew-point (°C)	Dehumidification rate (kg/h)	Heating** capacity (kW)
SU	200 (200)	2*	16'000	5.0 x 2.0 x 1.65	Chilled	800	12	80	2 x 120

*: including 1 unit in standby for redundancy

**: hot water at P1 and electrical heater at P5

***: thermally insulated

(xxx): Revised estimate

17.3.11 Staircase, lift shaft and air-lock pressurization

The PM staircase and lift shaft must be permanently over-pressurized in order to guarantee a safe evacuation of personnel in case of fire or ODH alarm. In addition, air-lock areas must be over-pressurized at 25 Pa with respect to the LHC tunnel and the HL-LHC galleries in order to guarantee that contaminated LHC tunnel air is not entering the new HL-LHC areas, which are in personnel access mode during physics. Table 17-12 gives the main characteristics of the pressurization systems (see Figure 17-7). Duty and standby units located in the SU insure the safe pressurisation including the lift exit in the US (see Figure 17-7). Both units will be equipped

with a hot water battery (Point 1) or an electrical heater (Point 5). Only one of them is fitted with a mixed-water battery produced by the chillers located in the SU. The air-intake and supply ducts are thermally insulated. Two redundant ventilation systems assure the pressurisation of the airlock installed at the end of the UA galleries. The units will take air from the UA tunnel to pressurise the air-lock areas. On the same principle, two redundant ventilation systems assure the pressurisation of the airlocks installed in the UL galleries.

Table 17-12: Pressurization system characteristics

Location	**Unit cooling capacity (kW)**	**Units**	**Unit flow-rate (m^3/h)**	**Unit size Lxlxh (m)**	**Cooling water type**	**Supply duct*** diameter (mm)**	**Unit heating** capacity (kW)**
Staircase SU duty unit	75 (60)	1	12'000	5.0 x 2.0 x 1.65	Mixed	800	130
Staircase SU standby unit	n/a	1	12'000	5.0 x 2.0 x 1.65	n/a		130
UAx3 air lock	n/a	2*	200		n/a	n/a	n/a
UAx7 air lock	n/a	2*	200		n/a	n/a	n/a
ULx3 air lock	n/a	2*	1000		n/a	250	n/a
ULx7 air lock	n/a	2*	1000		n/a	250	n/a

*: including 1 unit in standby for redundancy

**: hot water at P1 and electrical heater at P5

***: thermally insulated

(xxx): Revised estimate

17.3.12 Heating, ventilation, and air-conditioning (HVAC) for surface buildings

The required outside fresh air will be provided by the ventilation systems in all the surface buildings. Figure 17-7 shows the architecture of the ventilation in the surface buildings. Table 17-13 gives the characteristics of the HVAC for the surface buildings including the building volume, the temperature range to be maintained, the required cooling/heating capacity, the number of units, the unit flow-rate and size, as well as the supply/return duct inner diameter. The air-intake ducts are thermally insulated. The HVAC units run in free cooling mode to save energy, except the SU unit, which is designed to run both with mixed water and in free cooling. The over-pressure will be released using several static exhausts (or louvered penthouse) located on the roof.

In the SHM building, the air return duct has regularly spaced duct mounted grids. The air supply is distributed through low velocity displacement units located on the ground floor level. The SE building is divided in two parts for the low voltage (LV) and high voltage (HV) electrical equipment. On the LV side the air supply is distributed under the false floor, the return air is taken from the top of the room. On the HV side the air is extracted from the top of the room; heat-pumps (Pt1) or heaters (Pt5) assure a minimum temperature inside both rooms. In the SF building, the air supply duct has regularly spaced duct mounted grids. The air return is done in bulk directly in the mixing plenum. In the SU building, the air return is done in bulk from the top of the room. The air supply is distributed through low velocity displacement units located on the ground floor level. This building houses as well the air-handling units for the ventilation of the SD, for tunnel primary fresh air, for the pressurisation of the staircase and lift shaft and one air-handling unit for the air heat recovery. Finally, in the SD building, the air supply and return ducts have regular spaced duct mounted grids.

Table 17-13: HVAC characteristics of surface buildings

Location	Building volume (m^3)	Temp range (°C)	Total cooling capacity (kW)	Units	Unit flow-rate (m^3/h)	Unit size Lxlxh (m)	Cooling water type	Supply/return duct diameter (mm)	Unit heating** capacity (kW)
SHM	7'125	18-26	200 (200)	1	60'000	9.0 x 3.0 x 6.0	free cooling	1350	200
SE HV room	1000	18-35	0 (0)	2*	2'500	1.2 x 1.35 x 3.0	free cooling	n.a.	10
SE LV room	500	18-35	11 (19)	2*	11'000	1.35 x 0.85 x 2.5	free cooling	n.a.	10
SF	1'600	18-35	30 (25)	1	15'000	5.0 x 1.65 x 2.0	free cooling	800/600	16
SU	6'006	18-30	47 (53)	1	34'000	5.0 x 1.65 x 2.0	Mixed and free	1'000	28
SD	3328	18-35	10 (10)	1	12'000	4.0 x 1.65 x 1.65	free cooling	710	26

*: including 1 unit in standby for redundancy

**: hot water at P1 and electrical heater at P5

(xxx): Revised estimate

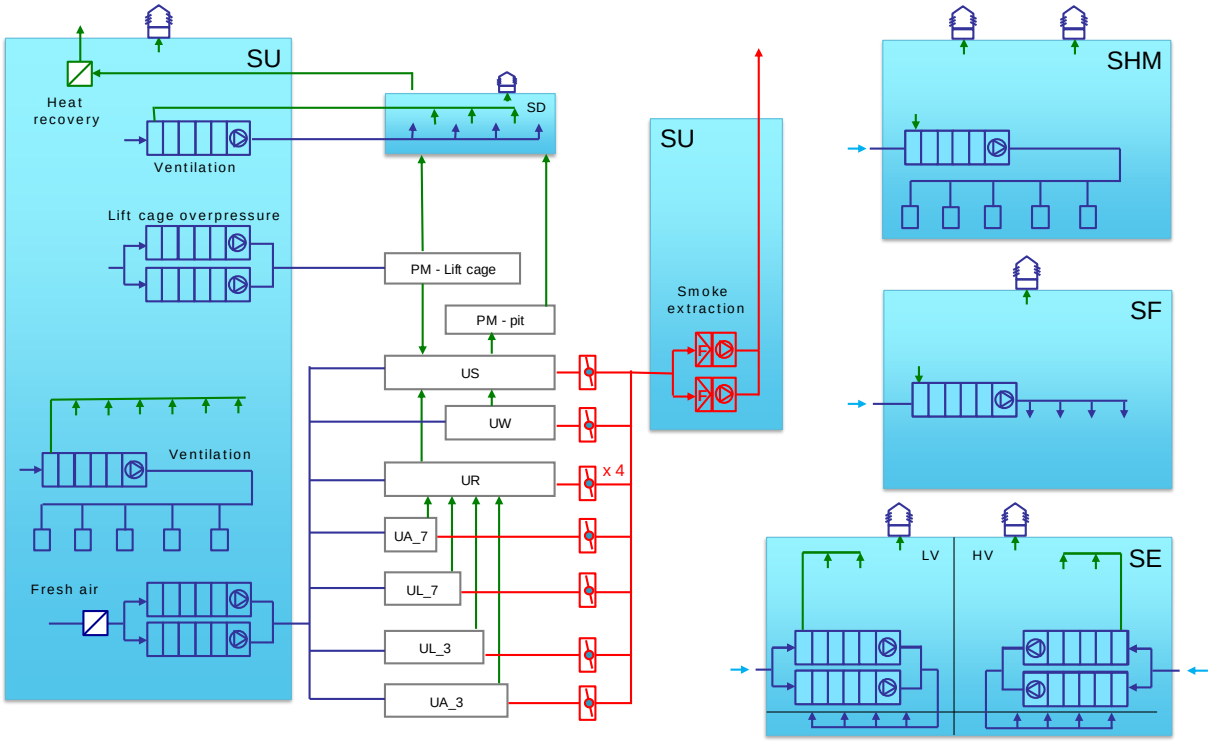

Figure 17-7: Ventilation architecture of surface buildings and smoke extraction

17.3.13 Smoke extraction

Each of the buildings SHM, SU, SD, SE and SF are equipped with a dedicated and independent smoke extraction system. The smoke extraction is ensured by natural ventilation using dedicated sky domes. The free opening areas will respect 1/200 of the floor area of each building. Mechanical air intake dampers are installed in addition to the access doors where needed in order to have less than 10 meters without an air intake entry. The static exhaust(s) and air intake damper(s) will be operated using a firemen cubicle located at the entrance of each building.

Two fans of 36000 m^3/h each are installed out of the SD to assure the smoke extraction form the underground buildings. The fans are F400 120 rated (according to EN 12101) and hardwired to the SMSC (Système de Mise en Sécurité). The fresh air intake comes naturally from the PM shaft. In addition, motorised fresh air dampers are installed in the SD to facilitate the fresh air entry into the shaft. A calcium silicate duct rated REI90 600°C in multi-compartment sections and RE90 600°C in single-compartment sections collects the smoke in the underground buildings. A fire-resistant door is installed in the middle of the UR galleries; the door is motorised and opens to assure the fresh air intake in some smoke extraction scenarios. Smoke curtains are installed in various positions on the vault of the gallery to define smoke retention areas. Smoke resistant dampers are installed in the ductwork in the appropriate locations to allow the extraction of the smoke in the targeted area. Figure 17-7 shows the smoke-extraction architecture.

17.4 Access and alarm systems

17.4.1 Objective

The HL-LHC project includes many modifications to the current LHC installations. On the one hand, large new surface buildings will be constructed and new underground areas excavated for the new equipment, and, on the other hand, existing LHC equipment will be upgraded, such as the inner triplet areas of Point 1 and 5. New types of equipment (e.g. crab cavities) as well as higher prompt and residual radiation levels due to the increased luminosities around interaction points require a re-evaluation of risks around these sections of the LHC tunnel. The new underground areas must be constructed so as to fulfil the regulations for fire and radiation safety as well as for oxygen deficiency hazards.

This Section enumerates the modifications to the current LHC access and safety systems (LASS/LACS) including integration of the new underground installations at LHC Points 1 and 5. It contains also the modifications and new installations of alarm systems and other associated safety systems. All alarm systems send Level-3 alarms to the fire brigade for immediate interventions via the CERN Safety Alarm Monitoring system (CSAM). Table 17-14 gives the synthesis of the estimates for the principal safety, access, and alarm equipment by system.

17.4.2 Requirements and constraints

Installation of safety and access systems poses no particular environmental concerns. The LHC is a CERN Beam Facility, and as such, the provisions laid out in the November 15th, 2010 tripartite agreement in matters of radiation protection and radiation safety fully apply. Namely, the LHC personnel safety systems are subject to joint inspection visits by the competent Host State authorities. Safety document “CERN Safety Code E – Fire protection” specifies that installed equipment shall follow the regulations of the host states on their respective territories. In order to treat the LHC and the HL-LHC as a whole, a formal derogation will be put in place to treat the HL-LHC as a French installation for this purpose.

Access and safety systems are designed to be operational constantly 24/7, with the exception of clearly defined maintenance windows. During maintenance, the installed systems may need to be accessed and access control functionality replaced by temporary measures, as applicable. During normal operation, these systems are for the most part operated remotely, but may require underground access for corrective actions. The safety report “Emergency Preparedness of the HL-LHC Underground Service Areas” [3] defines the precise needs in terms of safety functions and safety systems.

Access and safety systems may be sensitive to single event upsets caused by LHC operation and to degradation due to high radiation fields. For these reasons, all equipment not required close to high radiation areas, must be located at a safe distance from such areas. High magnetic fields can cause magnetic locks and electric motors to malfunction. Therefore, all access doors should preferably be located at a safe distance from magnetic fields. All safety and access systems require their own control cabling between the equipment and the control racks. This cabling is to be installed within dedicated safety cables trays, as is the case in the LHC.

In addition, the LACS and CSAM require network connectivity via the CERN Technical Network, which must be present close by so as to only require connection via an Ethernet patch cable.

Table 17-14: Synthesis of the estimates for the principal safety, access, and alarm equipment by system (total quantity for the 2 Points)

Equipment	System	Q
Interlocked end-of-zone door (grating) in the UL	LASS	4
Interlocked end-of-zone/ventilation door (solid) in the UA	LASS	4
Interlocked sector door (grating) in UPR	LASS	4
Supervised ventilation/overpressure door in the UPR	LASS	4
Interlocked ventilation door in the UL	LASS	4
Interlocked ventilation door in the UA	LASS	4
Key-operated switch box for arming patrol in a sector (UA, UL, UPR)	LASS	16
Equipment rack for cabling, relays, PLC I/O modules	LASS	4
RF EIS : Elements acting on RF powering	LASS	4
Personnel Access Device (PAD) including iris scanner	LACS	2
Material Access Device (MAD) including video surveillance	LACS	2
Equipment rack including badge readers, interphone, panel-PC	LACS	2
Access point video surveillance camera	LACS	4
Non-interlocked but supervised door at top of pit	LACS	2
Fire detector	Fire Detection	220
Fire central concentrating several detectors	Fire Detection	4
Red telephones (direct line to the fire brigade with alarm)	Emergency Comm	50
Secure communication equipment (TETRA)	Emergency Comm	2
CSAM rack: Secure delivery of level 3 alarms to the fire brigade	CSAM	2
ODH detector and warning	ODH Detection	74
ODH central	ODH Detection	6
Evacuation siren in underground areas	Evacuation	40
Evacuation central	Evacuation	2
CROME monitoring station for detection of ambient radioactivity	Radiation Monitoring	8
Alarm unit for CROME monitoring station	Radiation Monitoring	8
Simple access-controlled door	SUSI	24
Non-access controlled but supervised door (emergency exit)	SUSI	12
Video surveillance camera of the buildings and sites	SUSI	30

17.4.3 Power distribution

Access and safety equipment are generally powered by CERN secure power grid (ESD). All critical functions are also secured by uninterruptible power supplies (UPS).

17.4.4 Access safety system

The LHC Access Safety System (LASS) is the main safety system ensuring personnel safety in the various operational modes of the LHC (e.g., general access, commissioning, powering, beam operations). The LASS consists of two diverse and redundant safety chains for the critical operations. The main safety logic is implemented using Siemens safety PLCs. Interlocking of the exterior envelope is also doubled by a redundant cabled loop using relay-based logic in order to ensure that no intrusion into the controlled areas can go unnoticed even in case of a potential unsafe failure of the PLC equipment. The HL-LHC requires the new

important safety elements (EIS) to be installed into the LHC tunnel and the access galleries include access safety elements (EIS-a) as well as machine and optional beam safety elements (EIS-m and EIS-f, respectively). EIS-a consists of access doors and patrol boxes. Concerning the access doors, the instrumentation and controls of the doors are part of the WP17.4 scope; the supply and installation of the doors are part of the WP17.10. Figure 17-8 shows the underground access zoning and access elements. The cabling of the new EIS to the LASS site PLC is implemented directly via existing pathways in the LHC (EIS-a/m) and possibly via the new HL-LHC service areas (EIS-m). If a connection via the HL-LHC service areas is eventually required, a LASS rack with remote I/O units connecting to LASS site PLCs will be installed on the surface of the new HL-LHC access pits (PM17 and PM57). The total number of elements to be installed at the two sites is:

- 8 interlocked end-of-zone doors to isolate the LHC tunnel and service areas from the new HL-LHC underground galleries (UA, UL). Due to lack of space in the UA galleries, the end-of-zone doors there will also serve as ventilation doors (solid construction), whereas in the UL galleries they are of grating type.
- 4 interlocked sector doors to isolate the LHC tunnel from the UPR safety exits. These sector doors are of grating type and are installed at the lower parts of the UPR. They include opening devices and patrol boxes on both sides.
- 4 interlocked ventilation doors in the UL galleries.
- 4 overpressure doors in UPR galleries giving towards the LHC tunnel and in series with the sector doors. These doors are interlocked by the powering interlock (PIC) during the powering phase II and simply supervised with alarm during beam.
- 4 interlocked ventilation doors in UA galleries.
- 8 individual patrol boxes at suitable locations according to new zoning (UA, UL, UPR).
- EIS for the RF of the crab cavities. The exact type and number of these elements will depend on the risk analysis.

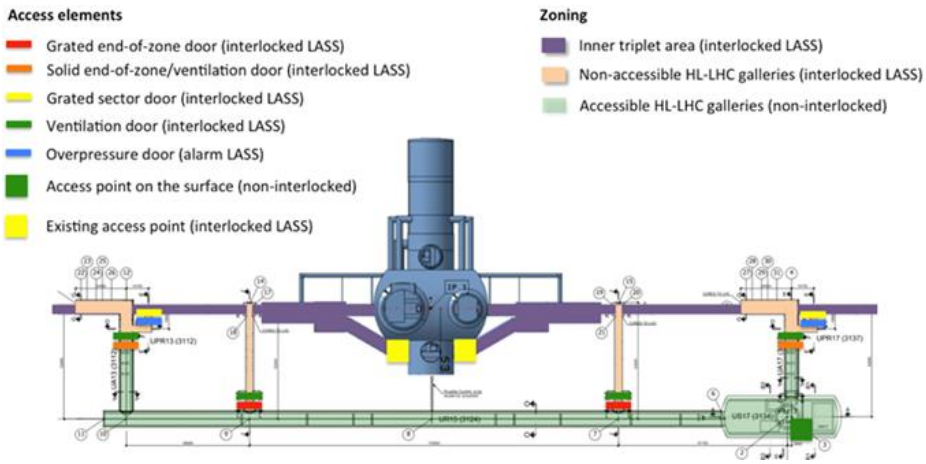

Figure 17-8: Underground access zoning and access elements at Point 1. Zoning of Point 5 will be similar as applicable with the exception of existing access point and service tunnel locations.

17.4.5 Access control system

Concerning underground access, the LHC Access Control System (LACS) manages access to the controlled areas according to access modes given by the LASS. The LACS reads the user badges, checks the access rights, verifies the user identity via biometric check, and lets the user pass if all access conditions are fulfilled. Access to interlocked areas may be possible either in general mode or in restricted mode. Restricted mode is meant for accessing the machine in ready-for-beam conditions, and the user must be in possession of a safety token

and the attached restricted mode key. The safety token will ensure that the beam cannot be entered into the machine until the token is returned to its place in the token distributor. The new normally accessible underground areas of the HL-LHC will be of non-interlocked type, which means that no safety tokens are necessary. The equipment to be installed in the LACS access points at PM17 (building SD17) and PM57 (building SD57) are the Personnel Access Device (PAD) including the iris scanner and the Material Access Device (MAD) including video surveillance and personnel detection inside the MAD. In addition, LACS equipment rack at the access point includes badge readers, intercoms, and a panel-PC for information display, but without a safety key distributor. A video surveillance is available both on the outside and inside of the access points. Finally, a supervised, but non-interlocked, access door provides a second emergency evacuation path from the top of the pit.

Access control in the surface buildings is implemented via the SUSI system, which comprises badge readers and video surveillance both inside and outside of the buildings.

17.4.6 Automatic fire detection system

The Automatic Fire Detection (AFD) system consists of detectors of various kinds (point detectors and/or air sampling networks), located in specific areas to detect the presence of smoke. These detectors are connected to Control and Indicating Equipment (CIE) located in one of the surface buildings. If a fire or smoke hazard is detected, the CIE generates Level-3 alarms and launches automatic safety functions. Fire detection is installed in all underground areas. The UR gallery will be equipped with smoke curtains designed to divide the gallery into zones that can contain smoke from a localized fire until smoke extraction can be activated on that zone. Fire detection is also installed in all surface buildings. A reservation is made for an optional installation of fire detection also in the inter-building technical galleries.

17.4.7 Emergency telephones

The underground areas will be equipped with emergency telephones (so-called red telephones) at regular intervals (~70 m), which provide a level-3 alarm and a direct telephone connection to the fire brigade.

17.4.8 CSAM and MMD

The CERN Safety Alarm Monitoring system (CSAM) is the primary safety system for delivering level-3 alarms to the CERN fire brigade. The LSAC (Local Safety Alarm Controller) PLC receives all the relevant Level-3 alarms within that area and delivers them to the fire brigade via diverse and redundant signal chains. The MMD (Multi-purpose Monitoring Device) is used to deliver alarms of level-2 and below directly to the TI operators via TIM. The CSAM and MMD systems include the cable infrastructure required to connect all Level-3 alarms to CSAM and other alarms to MMD. To accommodate the new alarms, the acquisition capacity of these systems at Point 1 and Point 5 will need to be increased.

17.4.9 TETRA and GSM

The TETRA secure communication system is installed and maintained by IT/CS. However, certain alarms from the TETRA system are transmitted via the CSAM system. As the TETRA uses the same infrastructure as the standard CERN GSM network (leaky feeders), the GSM infrastructure will be installed at the same time.

17.4.10 Automatic ODH detection

The Automatic ODH detection system consists of oxygen sensors located in specific areas to detect an oxygen deficiency due to a gas release. These sensors are connected to a Control and Indicating Equipment (CIE). If an ODH is detected, the CIE generates Level-3 alarms and launches automatic safety functions, automatic emergency evacuation, and ODH flashing lights. In the new underground areas, ODH detection is installed in the service caverns (US) as well as in the galleries UR, UA, UL, and UPR. ODH sensors are installed

approximately at every 50 m in linear galleries and according to need in more complex spaces. ODH detection is to be installed in the head shaft building (SD) housing the cold boxes, in the compressor building (SHM) as well as in the inter-building technical galleries.

17.4.11 Radiation monitoring

As the accessible non-interlocked areas of the underground HL-LHC galleries are adjacent to some of the most radioactive areas of the future HL-LHC beam line, online monitoring of radiation is required at the end-of-zone doors of the interlocked zones. 4 CROME monitors with associated alarm units will be installed per site in the immediate vicinity of the end-of-zone doors in the UA and the UR next to the UL galleries.

17.4.12 Automatic protection system

The automatic protection safety system launches safety functions in case of fire or ODH detection. These functions are compartmentalization, evacuation, and smoke extraction. If necessary, the CERN fire brigade has the possibility of triggering these functions remotely from CCC or SCR and the possibility to sound safety instructions to the HL-LHC area remotely from CCC and SCR.

17.4.13 Evacuation system (safety sound system)

The emergency evacuation system is a part of the automatic protection system. It consists of audible evacuation signals triggered either automatically by another safety system or manually by pushing one of the evacuation buttons installed within the area in question. The evacuation system is to be installed in all underground areas.

17.5 Monitoring and operation of general services

17.5.1 Objective

All installed equipment is monitored for important operational data, events, and alarms. The low-level monitoring of each subsystem depends on the exact equipment and data collection framework used by that subsystem. Delivery of high-level surveillance and alarm information to CERN TI operators is realized via the CERN Technical Infrastructure Monitoring system (TIM), which acquires the required data items and alarms from the local SCADA-systems or directly from the monitored equipment, as applicable. This Section describes the general monitoring framework of TIM, into which the various subsystems are to be connected and the installation of standard network services.

17.5.2 TIM infrastructure adaptations

While TIM is capable of connecting to many different equipment and existing SCADA systems to access data of various types, it is always possible that some application-specific development to the core system will be necessary to fully support the control system to be connected to TIM.

17.5.3 Subsystem configuration and development

The main bulk of work consists of the owners of various HL-LHC subsystems to set up monitoring of the important parameters of their systems in such a way that they can be read by TIM data acquisition modules. The following steps are necessary for setting up TIM monitoring of a device:

- Definition of the monitored device variables and making them available for readout via network.
- Definition of the tags in the TIM system to correspond to the variable to read. This step consists of defining a hierarchical tag name corresponding to the device in question, defining the data acquisition method and address, and defining the operator action in case of an alarm.
- Building TIM graphical visualization based on the registered tags.

Setting up of monitoring of the devices belonging to the various equipment groups is carried out in collaboration with the equipment group in question and the TIM team.

17.5.4 Networking

Networking will be installed in both the surface buildings and the underground structures. This covers cabled connections to CERN General Purpose Network (GPN) and Technical Network (TN) as well as Wi-Fi connections in selected areas.

In underground areas, cabled connections are provided at regular distances in the galleries so that modern network-connected equipment can take advantage of it. Wi-Fi coverage is provided. This requires installation of a Starpoint rack at approximately every 70–80 meters. As the UPR has to be operational before the deployment of the networks inside the HL-LHC galleries, dedicated UPR networks are deployed from the LHC tunnel.

All surface buildings will have cabled connections at regular distances. Wi-Fi coverage will be limited to the more frequented areas (control rooms, rack areas, etc.).

17.6 Transport

17.6.1 Objective

The scope of transport covers the surface transport & handling, the transfer to the underground facility and the transport & handling in the tunnels and caverns.

This Section lists the new transport and handling equipment that will be required in the new facilities for HL LHC installation. This document does not include anything concerning the dismantling and installation of components in the existing LHC facilities.

17.6.2 Requirements and constraints

The supply, including the installation, shall comply in all respects with the CERN safety rules. The CERN safety rules are available under the Refs. [6][7] and [8].

As for the LHC, the tight schedule and the large quantity of items to be transported will require fully integrated logistics for the transport on the surface and even more stringent co-ordination underground. The general means of transport and handling of equipment, together with the organisation necessary to bring the equipment to its final destination is directly inherited from LHC.

Articulated vehicles with hydraulic suspension are used for the road transport. The ROCLA vehicles are used to transport the cold masses and cryomagnets in SM18 and SMA18. Mobile cranes (CERN or externally rented) is used to install big elements such as helium tanks and transformers. Exceptional transport is rarely used and is done via one of CERN specialised contractors.

Two temporary storage platforms (including in the WP17.9 scope) are required in Point 1 and Point 5 to allow transit of equipment and for logistic reasons. The use of a heavy haulage external company is foreseen with the direct consequence of having to park on site trucks and mobile cranes with high-payloads. The pavement in these zones shall withstand a load of 300 kN/axle.

No specific requirement for new special transport equipment underground has been identified at this stage (apart from the EOT cranes in the cavern). Preliminary studies show that existing CERN transport equipment fulfils most requirements for transport underground in tunnels and galleries (electric tractors, trailers, forklifts, etc…). Detailed integration studies to define precise volume reservation for transport shall be conducted once the layout is finalized to contribute to the optimization process.

The new HL-LHC infrastructures are designed in a way that workers involved in transport and handling operations cannot be exposed to the risk of exposure to ionising radiation.

17.6.3 Lifts

The specifications are based on LHC 3-t lifts (e.g. PM54, and PM15); the capacity / dimensions of these lifts cover 90% of transport requirements. The safety requirement covers LHC specific risks (over pressurized shafts in case of fire or He leak) and they will be fed by UPS and have a safe level-3 communication with the fire brigade so that they will be used as evacuation exits in case of incident in the underground facility. The lifts components will be the same as for LHC lifts (the 6 LHC 3-t lifts will be replaced by 2021) for improving availability (common spare parts, better training/performance of maintenance services). No specific constraints of dimensions or any specific additional requirements with respect to LHC lift have been identified at that stage. Table 17-15 gives the main lift characteristics. The lift concrete casing will be equipped with periodic grating doors for access.

Table 17-15: Main lift characteristics

Location	Capacity (kg)	Travel Height (m)	Door width (m)	Door height (m)	Speed (m/s)	Cabin dimensions (m)		
						Length	Width	Height
PM17/57	3000	72.5	1.9	2.7	1.6	2.7	1.9	2.7

17.6.4 Electric travelling cranes

The overhead cranes preliminary design for surface buildings & caverns are based on requirements from users, including size and weight of biggest/heaviest object to be transported to define parameters such as clearance under hook, span, and length. These designs integrate technical and legal requirements for the crane installation, operation, and maintenance, such as the clearance above the cranes and the catwalk to provide access to the rails and to the machinery. Table 17-16 list the cranes main characteristics. For more detailed information (e.g. reactions on rails) please refer to the general layout drawing of each building.

Table 17-16: Main overhead travelling cranes

Location	Capacity (t)	Height Hook (m)	Lifting Height (m)	Hopper (m)		Speed (m/min)	
				Rail length	Span	Max	Min
SHM17 / 57	20	6	6	50	15	5	0.25
SD17 / 57	25	10	100	28.4	16.1	20 (without load) 10 (with load)	0.5
SF17 / 57	3.2	9	9	23	10	5	0.25
SU17 / 57	7.5	8	8	16	14	5	0.25
US17 / 57	5	7.5	7.5	26	12	5	0.25
UW17 / 57 (top)	3.2	3.2	3.2	15	6	5	0.25
UW17 / 57 (floor)	3.2	3.2	3.2	15	6	5	0.25

17.6.5 Manual overhead travelling cranes

All UA galleries will be permanently equipped with manual overhead travelling (MOT) cranes travelling on rails to allow for handling and transport of the RF components. Table 17-17 gives the characteristics of the UA cranes.

In both Points 1 and 5, one UL gallery will be permanently equipped with manual cranes travelling on rails to allow for handling and transport during maintenance of cryogenic components. Table 17-17 gives the main characteristics of the UL MOT cranes.

Table 17-17: MOT crane characteristics

Location	User	Capacity (t)	Length (m)	Width (m)
UA13 / 17 / 53 / 57	RF	1	26	5
UL17 / 57	Cryogenics	1	12	2

17.6.6 Hoists

Water sumps are equipped with heavy lifting pumps that need to be maintained. The supports for the hoist are permanently installed on site. Only one hoist unit is requested, that will be used on demand and moved from one point to another.

The equipment, tools, and materials necessary for the maintenance of the equipment located in the UW cavern upper floor are transported from the US side. A small tremie with a dedicated 500 kg hoist will be permanently installed to lift the tools and consumables to the US top floor that communicates with the UW top floor through a door in the separation wall.

In the SHM buildings, a hoist on a rail is required to transfer the load in the second bay of the building. Table 17-18 gives the hoist characteristics in the different location

Table 17-18: Hoist for the lifting pumps of the water sumps

Location	User	Capacity [t]
US17 / 57	Cooling & ventilation	0.5
US-UW17 / 57	Cooling & ventilation	0.5
SHM17 / 57	Cryogenics	1.5

17.6.7 Drawbridges

For installation of the large cooling & ventilation equipment's and all heavy equipment's located in the UW upper floor, two 5-t drawbridges will be permanently installed inside the shaft of the US caverns in point 1 and 5. (They are kept in vertical position closed during normal operation. When equipment needs to be transported to the UW upper floor, the drawbridges are lowered in the loading bay open and provide a platform that is accessible with the SD building cranes.)

17.6.8 Shielding

All UA galleries will be equipped with 12-t mobile-shielding doors with electrical motors. The dimensions (based on preliminary studies) are: 2 m x 0.8 m x 2.8 m. The ground rails are not included and are provided by WP17.1. In addition, 102 t of steel and 48 t of concrete blocks are used in the construction of shielding walls in the UL galleries.

17.6.9 Tooling for transport

Special tooling is required for cold box handling, QRL sections, electrical racks, etc… No specific requirement for special transport vehicle has been identified yet at this stage. The necessity of special vehicles or trailers be for sure appear in the detail design phase.

17.6.10 Studies

The following Computer Aided Design (CAD) studies shall be conducted for simulation of transport scenarios, for integration studies to define precise volumes reservation for transport and for the design of new tooling and special equipment's (e.g.: lifting beam, supports, etc…).

17.7 Logistics and storage

17.7.1 Objective

The HL-LHC project will bring an increase of activity in logistics services. The objective of sub-work-package 17.9 is to adapt the logistics capacity to foreseen workload coming during the project period, both in terms of FTEs and storage space.

17.7.2 Logistics services

The following services are impacted by the HL-LHC project:

- Shipping & waste: Administrative work linked to import activities (transport management from suppliers to CERN, customs clearance, VAT exoneration documentation) and waste traceability requested by the French and Swiss authorities.
- Goods Reception: CERN official order matching and registration, quantitative control, packaging control, establishment of eventual reserves and responsibilities in case of damage.
- Internal distribution: deliveries of goods and material from goods receptions and Stores to any locations at CERN and vice versa.
- Stores - Product management: Supply and demand management for standard items. Price inquiries, replenishment, order follow-up.
- Stores - Warehousing: Qualitative reception for standard items, put-away, picking.
- Storage areas**:** Operation of storage areas for radioactive and conventional materials.

The HL-LHC project planning suggested a significant increase in the logistics services from 2017 to S1/2026:

- Wastes will be generated on CERN site from the beginning of the construction.
- Increase of official orders and imports foreseen implying extra administrative work and movements in goods receptions.
- Increase of internal distributions from goods reception/Stores to CERN points. Logistic reinforcement might be necessary.
- Increase in volume for strategic standard materials from CERN Stores inducing extra work both for product management and in the warehouses.
- Extra movements foreseen in storage areas.

17.7.3 Conventional and radioactive storage

Both conventional and radioactive storage space is needed in current buildings. A new “flex” building of 10000 m^2 has been made available in 2018. The “flex” building includes both conventional and light radioactive storage space. During LS2, the building will be managed by the LS2 team, which will also include the HL-LHC activities that will take place in that shutdown. SMB department will take over the operation of the building after LS2. The shift of the LS3 is impacting the storage need as the ready-for -installation equipment shall be stored during one additional year.

Concerning conventional storage, existing buildings (897, 917 and 957, 954, SAX area), the temporary storage structures at Point 1 & 5 (see below) and the new “flex” building will offer enough capacity to cope with the HL-LHC project. The actual requested space for conventional storage consists of 2 surfaces at Point 1 and 5, each one will be between 200 to 250 m^2 (needed between LS2 and LS3). The modalities for implementation and the functional specifications are still to be defined. Two temporary storage platforms are required in Point 1 and Point 5 to allow transit of equipment and for logistic reasons. The use of heavy haulage external company is foreseen with the direct consequence of having to park on site trucks and mobile cranes with high-payloads. The pavement in these zones shall withstand a load of 300 kN/axle. Only the installation of the structure is included in the sub-WP17.9.

Radioactive storage covers only storage of radioactive equipment (e.g. spares), and not radioactive waste, which is managed by HSE-RP. For information, radioactive storage is not possible outside CERN. Table 17-19 gives the preliminary forecast for RP storage. Pallet storage is included in the figures for LS3, which will reduce the need of space.

Table 17-19: Preliminary study using forecasts collected via HSE-RP in 2015

TOTALs	Per period (m^2)	Integral (m^2)
End 2016	36	36
LS2	17.1	53.1
LS3	497.86	550.96

The existing radioactive storage buildings (954 and 955) did not have remaining floor areas before the availability of the new “flex” building. To free space, the new “flex” building allows the storage of light-radioactive equipment. The threshold for light radioactivity has been established allowing the transfer to the “flex” building of equipment equivalent to about 150 m^2. Further optimization will be needed because the available space does not satisfy yet the HL-LHC project storage need of about 500 m^2.

17.8 Operational safety

17.8.1 Objective

The scope of the operational safety is the procurement and installation of doors in the caverns and underground galleries, of smoke curtains in underground galleries, of large sectional doors for surface buildings, of fire fighting vehicles in the UA galleries, of fire extinguishers. In addition, resources for RP operational support, safety coordination and safety inspection are also included in this scope.

17.8.2 Doors and curtains

Doors and their corresponding frames are required to guarantee the sectorization, the safety and the evacuation of personnel in the caverns and underground galleries. Table 17-20 gives the characteristics of the doors included in the scope.

Table 17-20: Characteristics of doors and curtains

Type	Location	Total number	Opening size L x H (m)	CE interface size	resistant category		Comment
					Fire	Pressure	
Ventilation and fire-resistant door	UA airlock system	4	1.3 x 2.4	R 3.2 m	EI 120	n/a	
Ventilation and end-of-zone door	UA airlock system	4	1.3 x 2.4	R 3.2 m	n/a	n/a	
End-of-sector door	UPR LHC side	4	1 x 2.1	1.16 x 2.2	n/a	n/a	Grating
Fire- & pressure-resistant door	UPR LHC side	4	1 x 2.1	1.08 x 2.2	EI 120	60 mbar	
Fire-resistant door	UR	2	2.8 x 2.8	R 2.9 m	EI 90	n/a	
Fire-resistant door	UW	4	3 x 3	3.1 x 3.05	EI 90	n/a	1/3 - 2/3
Fire-resistant door	Safe-room	2	2 x 2.45	2.1 x 2.5	EI 120	n/a	
End-of-zone door	UL	4	1.1 x 2.15	R 1.6 m	n/a	n/a	Grating
Ventilation door	UL	4	1.1 x 2.15	R 1.6 m	n/a	n/a	
Ventilation and fire-resistant door	US lift sas	2	2 x 2.65	2.1 x 2.7	EI 120	n/a	
Sectional door	SD	2	6 x 6	n/a	n/a	n/a	wall mounted
Sectional door	SF	2	4 x 4	n/a	n/a	n/a	wall mounted
Sectional door	SHM	2	5 x 5	n/a	n/a	n/a	wall mounted
Sectional door	SHM (CV room)	2	4 x 5	n/a	n/a	n/a	wall mounted
Sectional door	SU	2	5 x 5	n/a	n/a	n/a	wall mounted
Smoke curtain	UR	6	n/a	R 2.9 m	EI 90	n/a	
Smoke curtain	UA entrance	4	n/a	R 3.2 m	EI 90	n/a	
Smoke curtain	UL entrance	4	n/a	R 1.6 m	EI 90	n/a	
Noise curtain	SHM	2	5 x 5	n/a	n/a	n/a	

17.8.3 Firefighting equipment

Four firefighting vehicles are located in the UA galleries on the UPR side. These vehicles are composed of a tractor and a trailer. In addition, fire extinguishers are periodically distributed in underground structures and surface buildings. Table 17-21 gives the number of extinguishers to be installed.

Table 17-21: Number of extinguishers per Point

Location		**Underground**	**SU**	**SD**	**SE**	**SF**	**SHM**	**Total**
# extinguishers per Point	5 kg CO_2	14	5	3	4	2	4	32
	9 kg CO_2	2	0	0	0	0	0	2

17.8.4 RP support, safety coordination and safety inspections

The radioprotection activities, like controls, transport, reception, and storage of waste, are supported via a service contract. The safety coordination supports the installation activities. During these periods, the category of the installation worksite will be “Technical Stops”. The safety inspections, like electrical, crane, pressure-test inspection, are supported via a service contract.

17.9 Reference

[1] *S. Bertolasi et al*. Technical design report EN-EL for HL-LHC, EDMS: 1688633.

[2] EN-EL, “18 kV distribution HL-LHC1 project”, EDMS: LHCEM_1005 rev.AA.

[3] EN-EL, “18 kV distribution HL-LHC5 project”, EDMS: LHCEM_5003 rev.AA.

[4] EN-EL, “Low voltage distribution HL-LHC1 project”, EDMS: LHCEB_1208.

[5] *T. Otto*, Emergency Preparedness of HL-LHC Underground Service Areas, EDMS: 1610772.

[6] Safety rules Web page.

[7] Host states http://hoststates.web.cern.ch/hoststates/en/Welcome.html.

[8] Prestations sur le site du CERN - Working on the CERN site, EDMS: 1155899.

Chapter 18

Controls technologies

J. Serrano[1*]

[1]CERN, Accelerator & Technology Sector, Switzerland
[*]Corresponding author

18 Controls technologies

18.1 Overview

By the time of the commissioning and subsequent operation of the HL-LHC, many of the physical elements of the control system will have been upgraded due to obsolescence. This applies particularly to the front and back end CPUs and storage. It is not, however, foreseen that the overall control system strategy and architecture will change in its conceptual structure during this period, and many parts of the current controls infrastructure will still be sufficient for the HL-LHC needs. Nevertheless, three areas have been identified as having to be addressed so that the control system can respond to the new challenges presented by the HL-LHC upgrade project.

During operation of the HL-LHC there will be an increase of radiation in some areas, which will trigger re-designs and relocation of electronics currently installed close to beam line elements (see Chapter 10 and 19). The HL-LHC project will also require the installation of new, more powerful Nb_3Sn magnets that will raise the need for more diagnostics data (i.e. higher data rates) in subsystems such as the quench detection system and the cold powering system. Higher data rates will also be needed during the commissioning of the HL-LHC, as equipment groups will need to fine-tune their systems and will therefore require access to the full diagnostics capabilities of their systems. In order to assure correct functionality up to the end of the HL-LHC operational period with ultimate performance, it is important to be conservative regarding the design choices and to share proven solutions as much as possible. This approach assures that proven solutions persist and that all design efforts can be concentrated on making a few designs very robust instead of spreading efforts into a large number of sub-optimal designs.

The increase in data bandwidth needs triggered by the HL-LHC is an overarching theme in this work package. It has an effect on the electronics interfacing to the accelerator components, on the communication technologies used to get the data out of those crates towards higher layers of the control system, and finally on the solutions used to store the data in the logging system and, later, to extract it and analyse it in an efficient way.

18.2 Control technologies

18.2.1 Data logging

Development of the next generation accelerator logging systems (NXCALS) has started, and the aim is to have a new Logging system with equivalent functionality as today but with significantly easier scalability, faster data extraction and analysis performance.

Following past experience, we are expecting a massive increase in the volume of data to be logged as a direct result of installing, commissioning and then operating the HL-LHC as well as of numerous consolidation actions across the various equipment systems presently installed in the LHC. Figure 18-1 shows the growth in

data logged post LS1 as a result of updates to various LHC systems, most notably the LHC quench protection system (QPS), and the need to increase data rates to better understand the operational behaviour of the machine.

Based on user input and given the extensive hardware and operational changes foreseen for the HL-LHC, we must be prepared for similar or even greater increases in the amount of data collected in the logging system in the HL-LHC era. We foresee the need to install additional, properly dimensioned, hardware in 2025, to be ready for use in 2026 to support the HL-LHC hardware commissioning followed by beam commissioning.

In addition to the need for additional storage, it is critical to develop and deploy a new software infrastructure to properly support the users of the foreseen data sets. In order to properly validate the behaviour and performance requirements with realistic data and use cases *prior* to the HL-LHC commissioning period, the deployment of this software should take place before the start of Run 3.

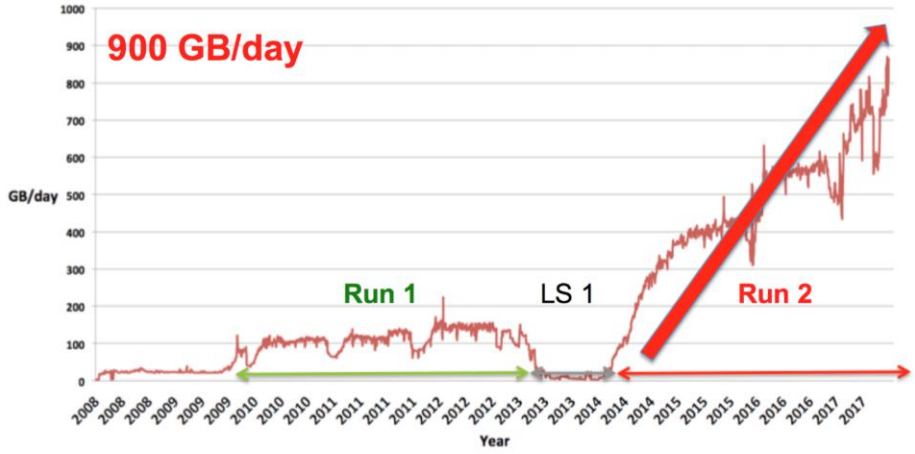

Figure 18-1: Storage evolution.

In recent years, the so-called “Big Data” technology landscape has evolved significantly to support large-scale data logging and analysis, opening up new possibilities to perform efficient analysis of large data sets. To gain experience with these technologies and help choose a direction for NXCALS, a Proof of Concept (PoC) Logging System was developed in collaboration with IT-DB in early 2016. This PoC was based on the open-source Apache Hadoop technology - as a replacement for the current Oracle-based CALS [1] system. The PoC work clearly demonstrated the potential to successfully replace the current system and improve performance and scalability for an overall lower hardware cost than the current system (not considering the Oracle Licensing costs). Subsequently, the approval by CERN management led to the full-scale development of NXCALS.

The NXCALS system is based on a microservices architecture. The aim of this is to be able to more easily upgrade or replace different aspects of the system in the future as necessary, without being forced to put in place a completely new system. From a technology perspective, NXCALS is based on in-house developments combined with open-source software such as Hadoop (HDFS and HBase), Kafka, Spark, and Jupyter notebooks.

The core technologies used in NXCALS are based on the concept of “horizontal scalability”, which essentially means the ability to increase performance by adding more resources to the underlying infrastructure. From this perspective, the NXCALS system has the potential to adapt to the required performance needs of the future, provided sufficient resources can be financed and that sufficient physical hosting capacity is available.

In terms of potential data analysis performance, a key difference in NXCALS with respect to the CALS system is a change in paradigm. With the CALS system, users first extracted the data and then performed the analysis on their local machines. With the NXCALS system, users seeking high levels of data analysis performance need to submit their analysis algorithms to be executed directly on the NXCALS cluster, using

Spark, and then retrieve only the results. This change of paradigm has already revealed cases where analysis times can be reduced from several days to less than an hour.

18.2.2 New distributed I/O tier

The HL-LHC will place challenging demands on data acquisition to/from the accelerator components which need to be controlled and diagnosed, such as the new Nb_3Sn magnets. The need for larger amounts of diagnostics information will result in a requirement for more throughput in the lower layers of the control system and will therefore affect the electronics in this tier and the communication links used to send the information up the controls stack. The current controls architecture has front-end computer systems (VME or PICMG 1.3) with a large variety of reusable electronic cards to control accelerator components by sending and receiving data and carrying out calculations in real-time. In the LHC, these front-end computers typically drive some kind of fieldbus, which connects to Input/Output (I/O) modules sitting close to the accelerator, as shown in Figure 18-2. Historically, there has been much less sharing and reuse of design effort in this lower Distributed I/O Tier (DI/OT) than in the front-end tier.

For the HL-LHC, the proposal is to extend the sharing model of the front-ends to the DI/OT layer. The electronics in this layer is designed to transmit data as fast as possible to/from actuators and sensors attached to accelerator components. These I/O modules are connected to a smaller number of high-performance front-end computers which process the data and perform the necessary calculations. By collaborating with equipment groups and providing a service in this I/O layer analogous to that of the front-end tier, we will ensure a uniform level of quality and increase overall availability of electronics deployed in this tier, including those subject to radiation [2].

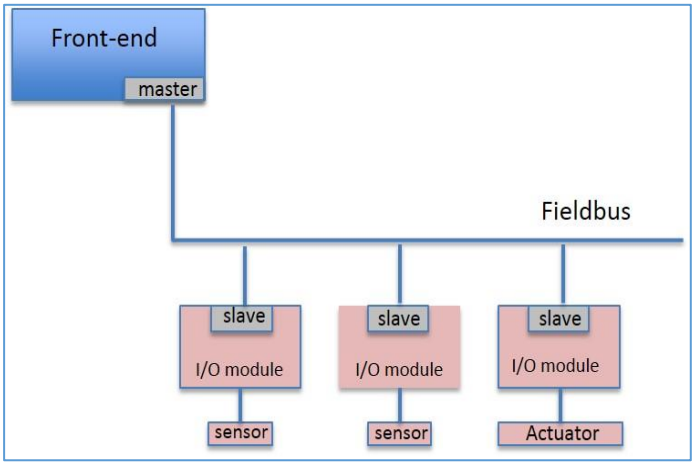

Figure 18-2: Proposed controls architecture.

As shown in Figure 18-3, the DI/OT kit will be modular, allowing different applications to benefit from common infrastructure at different levels. It will consist of a 3U Europe crate and a passive backplane conforming to the CompactPCI Serial standard. The standard specifies PCIe as the main protocol to be used in communication through the backplane. PCIe is, however, unnecessarily complex for our needs and an attempt to implement it for the DI/OT system could compromise radiation tolerance. We therefore decided to use the basic physical infrastructure of CompactPCI Serial without following further prescriptions on protocols. A simple serial protocol (such as high-speed SPI) will be used instead, with support for automatic discovery of hardware modules. The controller slot in the crate will host the so-called system board, which communicates with other boards through the backplane and with the upper layers of the control system through a fieldbus interface. In order to support different fieldbus technologies, the system board features an FMC (VITA 57) slot, and different communication mezzanines can be plugged in that slot. There will be different boards for radiation and non-radiation areas. Those meant to operate in radiation environments will be optimised for radiation tolerance, so simplicity will be a major design goal, at the expense of performance. The system board variant meant to operate in non-radiation environments will be more complex and capable. The project includes

the development of a radiation-tolerant (rad-tol) switching AC/DC power converter, whose design will be made generic enough so that parts of it can be reused in other projects (e.g. FGCs).

The modularity of this kit caters for different needs in equipment groups. Survey, for example, will use the full kit, including the crate, rad-tol system board and WorldFIP communication mezzanine. They will design their own add-in boards in 3U Europe format to interface with their sensors and actuators. The BLM, BPM and other systems have a need for their own dedicated crate and system board, and they will insert one of the communication mezzanines on it for basic remote diagnostics and slow control. The non-radiation-tolerant variant will be used in the Full Remote Alignment System. A short summary of foreseen uses can be seen in Table 18-1.

Table 18-1: Foreseen uses of DI/OT electronics.

System	Components	Locations
Survey	50 full DI/OT crates and 30 crates with PSU only	UA galleries and RRs
FRAS	18 racks populated with electronics	UR15, US15, UR57, UL557
WIC	50 DI/OT crates	TI2, TI8, TT40, TT41
PIC	36 DI/OT crates	RR13/17, RR53/57, RR73/77, UA23/27, UA43/47, UA63/67, UA83/87
BLM	60 radiation-tolerant WorldFIP mezzanines	SPS
BPM	Potentially 500 radiation-tolerant WorldFIP mezzanines	LHC arcs and Dispersion Suppressors

The DI/OT kit will offer general services like remote monitoring of the platform (temperatures, fan speeds, voltages, and currents…) and remote re-programming of the Field Programmable Gate Arrays (FPGA). It will also benefit from a specific effort on increasing reliability and availability. Another important part of the monitoring infrastructure will be the measurement and reporting of radiation in the location of each crate, through the inclusion in each chassis of a generic radiation monitoring module supported by the R2E working group.

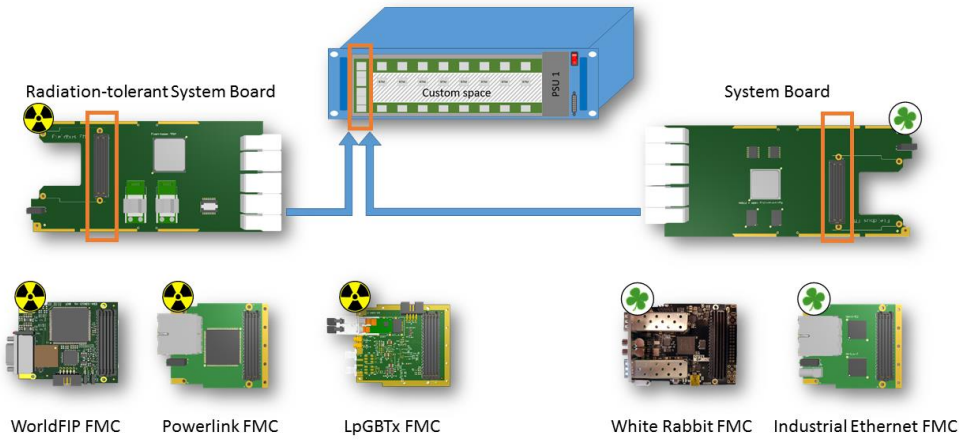

Figure 18-3: Modular DI/OT kit, including radiation and non-radiation-tolerant variants.

18.2.3 A new high-speed radiation-tolerant fieldbus

For HL-LHC the QPS system needs to accommodate the new Nb_3Sn magnets in points 1, 5 and 7. The newly developed Universal Quench Detection System has much increased data acquisition capabilities, rendering the current solution based on WorldFIP sub-optimal, due to the very low available bandwidth (2.5 Mbps maximum) for the transmission of the acquired logging and Post mortem data.

The QPS electronics in points 1 and 5 will be installed in radiation-free zones, however the RR alcoves in point 7 may pose some low (< 1–2 Gy/year) radiation-tolerance constraints, which should be considered when proposing a new fieldbus for the HL-LHC era.

A re-usable standards-based solution will serve also other users and will help increase overall quality and therefore availability. An industrial, Ethernet-based solution with 100 Mbps bandwidth, µs synchronization and supporting 50 slaves/segment is proposed , so it can be considered as a candidate for the QPS electronics and any other subsystem needing faster data transfer rates than what WorldFIP can provide. After a market review including leading Industrial Ethernet technologies such as Profinet and EtherCAT, we decided to design a radiation-tolerant implementation of Ethernet Powerlink. This is the only popular fieldbus technology featuring an open-source implementation of its stack unencumbered by patents and other obstacles. It is important to have full control of these sources because radiation-tolerance is achieved through logic triplication and voting in a flash-based FPGA. This requires a certain degree of introspection in the design so as to be able to test different strategies for triplication and evaluating which ones work best.

The basic technologies used for rad-tol digital design in this work package are mature and well tested for doses of a few hundred Gy. For pure logic, triplication inside a flash-based FPGA, followed by voting, can effectively mitigate the effects of Single Event Upsets (SEUs). Systems involving soft-cores running software are a bit more involved because of the various places at which redundancy can be inserted. Figure 18-4 shows the most likely scenario for the implementation of a rad-tol Powerlink stack inside an FPGA. A RISC-V [3] core is triplicated and runs software stored in Error-Correcting Code (ECC) memory. The data for the program resides in a separate ECC RAM block. This basic building block can then be re-used in other projects needing a small microcontroller running software of moderate complexity in a radiation environment. The main challenge in our context is to implement the open-source Powerlink stack, originally developed to run in desktop systems with no memory limitations, in the amount of memory available in typical flash-based FPGAs.

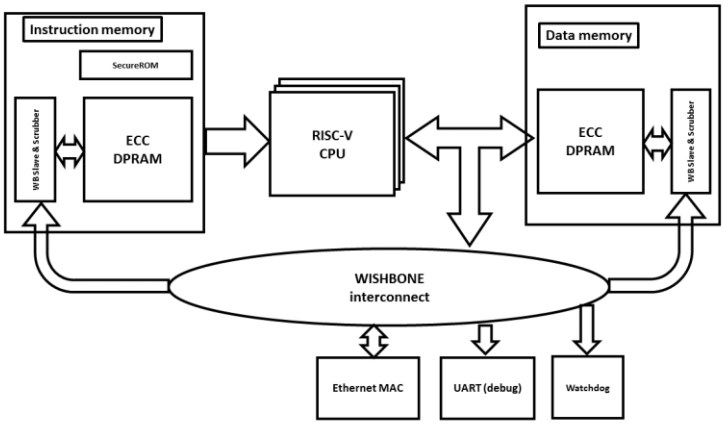

Figure 18-4: Simplified block diagram of the rad-tol Ethernet Powerlink implementation.

The Powerlink mezzanine (Figure 18-5) will bridge the gap between users who are satisfied with the limited bandwidth of WorldFIP and streaming-like multi-Gb/s applications, which will use the LpGBTx chip designed in the EP Department at CERN. Powerlink being a standard, it is relatively easy to find commercial off-the-shelf solutions for the master side of the fieldbus, including PCIe add-in boards hosted in Linux PCs and also bus masters in Programmable Logic Controllers (PLCs). This illustrates a common theme in this work package: using industry standards as far as possible to benefit from a set of verified solutions and customising them only as needed.

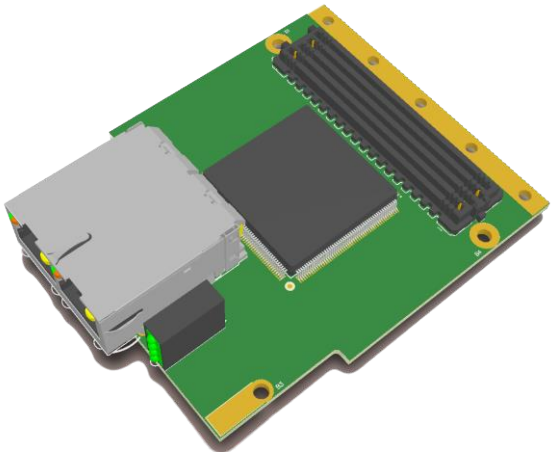

Figure 18-5: 3D model of the Powerlink mezzanine.

18.3 References

[1] The CERN Accelerator Logging Service - 10 Years in Operation: A Look at the Past, Present and Future C. Roderick, *et al*. 14th International Conference on Accelerator & Large Experimental Physics Control Systems, San Fran, USA, 2013, CDS: tuppc028.

[2] Plans at CERN for electronics and communication in the Distributed I/O Tier G. Daniluk *et al*., ICALEPCS 2017, Barcelona, Spain, 2017, DOI: 10.18429/JACoW-ICALEPCS2017-THPHA071.

[3] Open hardware repository web page.

Chapter 19

Safety

T. Otto[1*], *C. Adorisio*[1], *C. Gaignant*[1], *A. Infantino*[1*] *and M. Maietta*[1]

[1]CERN, Accelerator & Technology Sector, Switzerland
[*]Corresponding authors

19 Safety

19.1 Overview

CERN declares in its Safety Policy [1] that it will ensure the best possible protection in health and safety matters of all persons participating in the Organization's activities or present on its site, as well as of the population living in the vicinity of its installations, limit the impact of the Organization's activities on the environment, and guarantee the use of best practice in matters of Safety.

A safety organisation accompanies the life cycle of every large project, such as the HL-LHC, to ensure that the Organization's Safety objectives are met. This Chapter describes the safety assessment process applied to the deliverables of the HL-LHC project. As the methods to achieve the safety objectives differ between occupational and operational Safety and Radiation Protection (RP), the two subjects are treated in distinct Subsections.

19.2 Radiation protection considerations

19.2.1 Design constraints and the "As Low As Reasonably Achievable" (ALARA) principle

Design constraints for new or upgraded facilities should ensure that the exposure of persons working on CERN sites, the public, and the environment will remain below the specified dose limits [2] under normal as well as abnormal conditions of operation, and that the optimization principle is implemented [3][4]. In particular, the following design constraints apply:

- The design of components and equipment must be optimized such that installation, maintenance, repair, and dismantling work does not lead to an effective dose, e.g. as calculated with Monte Carlo simulations, exceeding 2 mSv per person and per intervention. The design is to be revised if the dose estimate exceeds this value for cooling times compatible with operational scenarios.
- The annual effective dose to any member of a reference group outside of the CERN boundaries must not exceed 10 μSv. The estimate must include all exposure pathways and all contributing facilities.
- The selection of construction material must consider activation properties to optimize dose to personnel and to minimize the production of radioactive waste. In order to guide the user, a web-based code (ActiWiz) is available for CERN accelerators [5].

Proton–proton collisions in the LHC experiments produce a secondary radiation field that penetrates into the adjacent accelerator tunnels and can cause severe activation of beam-line elements. Consequently, in such areas the design of components and infrastructure has to be optimized to follow the As Low As Reasonably Achievable (ALARA) principle. The optimization of the design for later interventions is an

iterative process: dose equivalent maps per unit time of exposure (called dose rate maps below) of the concerned area(s) are compiled from measurements and/or simulations with Monte Carlo particle transport codes such as FLUKA [6][7]. Based on these maps, the individual and collective doses of the intervention teams are calculated by using an intervention plan that then allows identification of and optimization of critical work steps in order to reduce doses to intervening personnel. If the latter involves a change in design or work scenario, then doses are re-evaluated by repeating the above steps.

19.2.2 Residual dose rate predictions for the Long Straight sections in Point 1 and 5

Residual dose rate maps were calculated with FLUKA for the part of the Long Straight Sections (LSS) in Point 1 (P1) and 5 (P5) that extend from the Target Absorber Secondary (TAXS) up to quadrupole Q7 in Cell 7, according to the latest HL-LHC layout (optic v1.5). Activation in LSS1 and LSS5 is dominated by the debris coming from p-p collisions at 14 TeV centre-of-mass energy in the interaction point of the two high-luminosity experiments ATLAS and CMS. Other type of losses such as injection losses, losses during ramp and squeeze are therefore not considered in the calculation, since their contribution to activation can be assumed negligible with respect to collision losses, and the generated high energy secondary radiation field, during stable beams. However, those losses might be the dominant source term in other points of the machine, e.g. in the collimation regions of IR3 and IR7 or the beam-gas interactions in the arc. The contributions from losses of the beam directed towards the interaction point (IP) and beam–gas interactions are not considered.

An up to date FLUKA model, also including the new HL-LHC galleries, was used to update existing RP studies. Both horizontal crossing (IP1) and vertical crossing (IP5) schemes where simulated. New/updated elements were included in the simulations, such as the latest design of the TAXN shielding, the full model of the crab cavities and the DFX. DPMJET-III [8] was used as the event generator. Results were normalized accordingly to the forecast operation conditions (peak luminosity and integrated luminosity) shown in Figure 1-8 of Ref. [9], referring to the so called “ultimate HL-LHC parameters”. These operation conditions represent the worst-case scenario in terms of radiation protection constraints. Therefore, an ad-hoc FLUKA irradiation profile was built in order to model the HL-LHC operation, as shown in Figure 19-1.

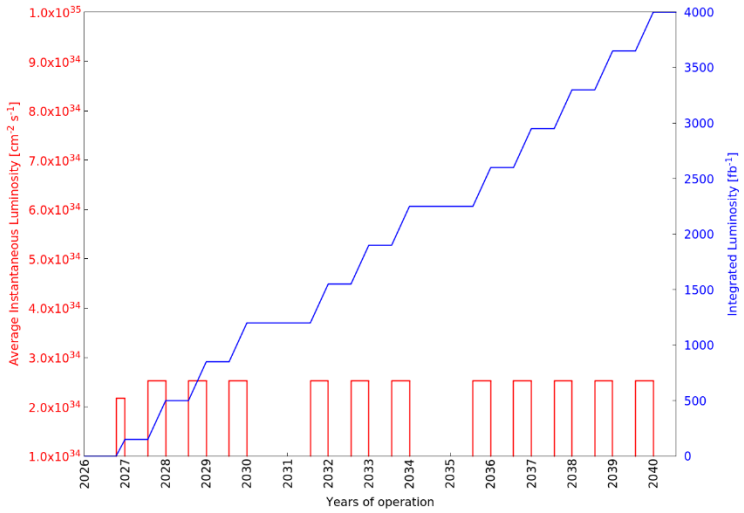

Figure 19-1: Assumed (worst-case) irradiation profile for the HL-LHC operation.

The irradiation profile assumed 160 days of proton-proton physics and a total integrated luminosity of 4000 fb^{-1} over the entire lifetime of the HL-LHC machine: an average integrated luminosity of 350 fb^{-1} per year was assumed and the average instantaneous luminosity was calculated, assuming an inelastic p-p cross-section of 80 mb [10]. The very last 12 hours were assumed to consist of a fill with the maximum levelled luminosity (accordingly to Figure 1-8, [9]) to be conservative for short-lived radionuclides [11]. In addition, two Long Showdowns (LS) of a duration of one year were assumed, namely LS4 and LS5.

As mentioned above, three-dimensional residual dose rate maps were calculated for the entire area from around 14 m distance from the interaction point up to around 270 m distance (i.e. from the TAXS to Q7). The coverage of the 3D mesh included also additional areas, such as ULs, UJs, UPRs, RRs. Six different cooling times were considered covering all typical intervention scenarios: 1 hour, 1 day, 1 week, 4 weeks (assumed equal to one month), 4 months, and 1 year after the last HL-LHC operational period. To give examples for the available results, residual dose rates are reported in the following as two-dimensional maps for a one-month cooling time as well as 1D-profile plots for four different cooling times (1 week, 1 month, 4 months, and 1 year). The values correspond to the average over 40 cm around the beam pipe height (y = 0) and, for the 1D-profile plots, between 40–50 cm distances from the outer surface of any equipment on the tunnel side (on average, x = -100 cm from the machine axis, i.e. x = 0).

Figure 19-2 shows the ambient dose equivalent rate maps after one month of cooling time during the first Long Shutdown during the HL-LHC era, LS4, in LSS1 (upper plot) and in LSS5 (bottom plot). Both plots refer to the right side of the LSS: while close to the beam line (x = ±100 cm) the dose rate maps are symmetric with respect to the IP, differences can be appreciated only in the ULs, UJs and UPRs, and particularly for Point 5 due to the asymmetric infrastructure layout of the UJs. The detailed maps for both left and right side can be found in Ref. [12]. The main difference in between the two ambient dose equivalent rate maps of Figure 19-2 is due to the different crossing angle plane, as well as the different infrastructure layout for what concerns the side alcoves and tunnels.

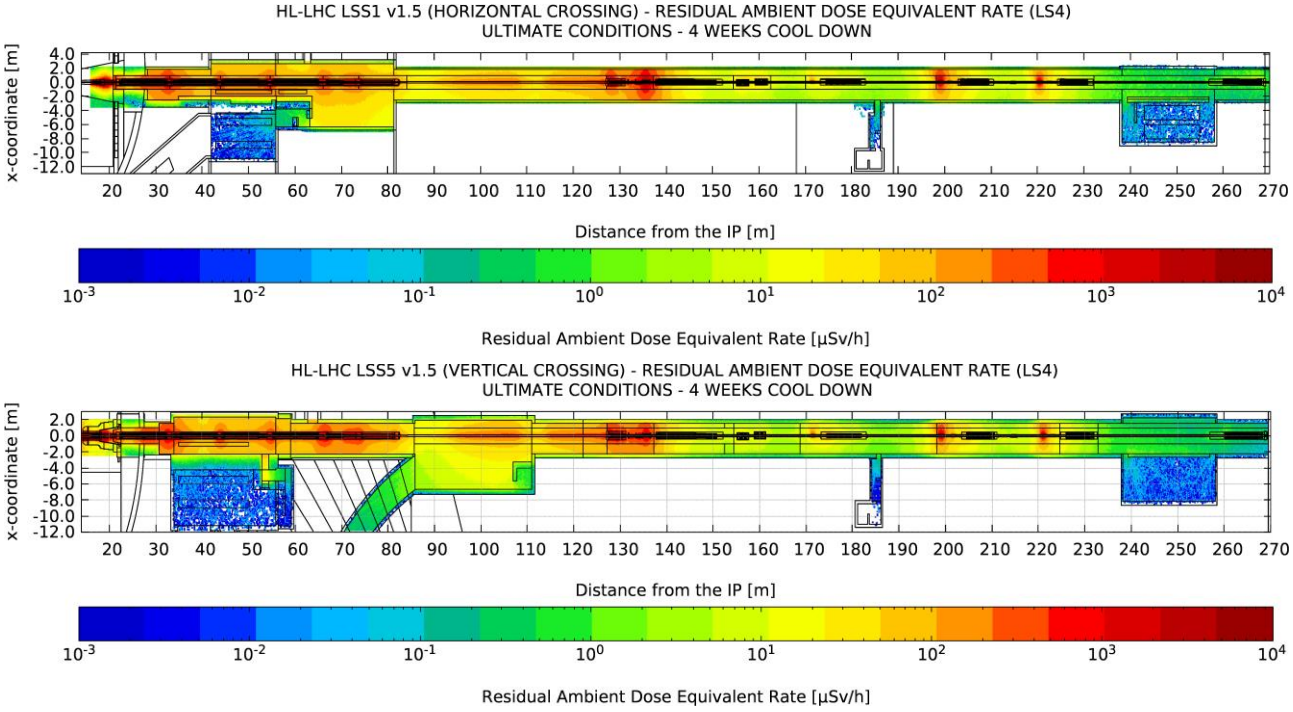

Figure 19-2. Ambient dose equivalent rate maps in the LSS1 (top plot) and in LSS5 (bottom plot) after one-month cooling time during LS4 (ZX plane). The residual dose in the vertical dimension is averaged on 40 cm around the beam pipe (y = 0). The highest dose levels are reached (from left to right) at the TAXS, the Inner-Triplet, the TAXN, and the TCL collimators.

Figure 19-3 shows the ambient dose equivalent rate profile in the aisle at a working distance from the machine elements (~40 cm from the outer surface) at four different cooling times: these cooling times are considered as reference for maintenance interventions in the machine tunnel during the scheduled technical stops, end of the year technical stops and long shutdowns. The higher residual dose rates are typically around the elements closest to the IP, such as the inner triplet, and corresponding to the connections between elements, where the shielding effect due to self-absorption of the element is less effective. In addition, high residual dose rates can be found in correspondence of the TAXN and the TCLX collimators. As shown in Figure 19-3, in

case of horizontal crossing, the TCLX4 plays a significant role in protecting the downstream elements, becoming the most active object in the LSS1.

Figure 19-4 shows the radiation level calculated for LSS5. The main difference from the LSS1 values in Figure 19-3 comes from the different crossing scheme in IP5 and, consequently, the different losses on the TCLX4. The inner triplet region shows comparable levels.

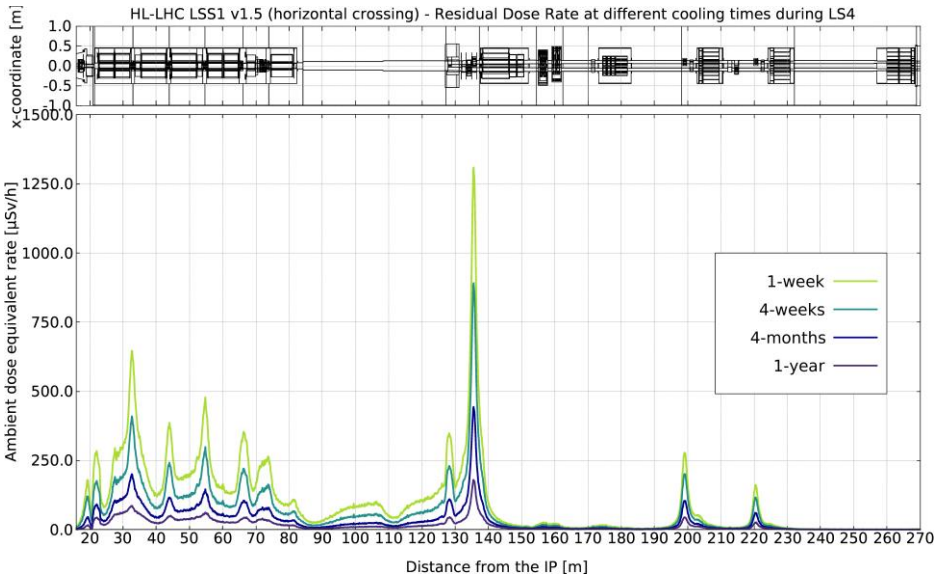

Figure 19-3: Ambient dose equivalent rate profile in the LSS1 at different cooling times during LS4 (z-coordinate). The values correspond to the average over 40 cm around the beam pipe height (y = 0) and between 40–50 cm distances from the outer surface of any equipment on the tunnel side (on average, x = -100 cm from the machine axis, i.e. x = 0).

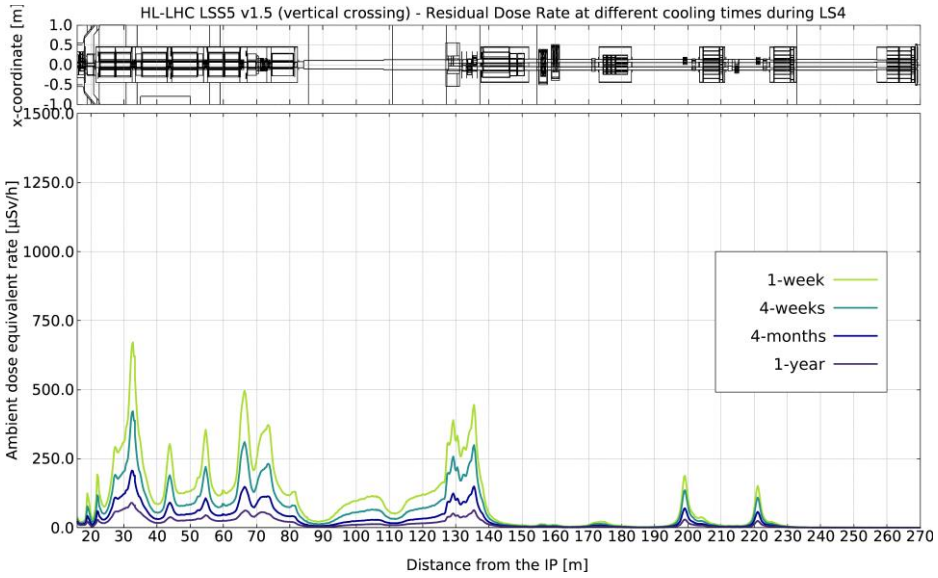

Figure 19-4: Ambient dose equivalent rate profile in the LSS5 at different cooling times during LS4 (z-coordinate). The values correspond to the average over 40 cm around the beam pipe height (y = 0) and between 40–50 cm distances from the outer surface of any equipment on the tunnel side (on average, x = -100 cm from the machine axis, i.e. x = 0).

19.2.3 Radiological risk assessments for the new underground infrastructures in Points 1 and 5

Access to the new US, UR and UA service galleries is foreseen during beam operation (See Chapter 15). For this reason, the radiological impact of the machine operation on the personnel has to be assessed. The UL galleries will be closed during the machine operation, apart from one, in which the first 12 m will be accessible. Two radiological risks have been addressed and will be described here after: air activation and stray radiation.

Risks due to activated air can be either due to direct activation of air inside the new infrastructures by stray radiation or due to streaming of activated air from the LHC tunnel into the new service areas. While the former is expected to be negligible the latter is prevented by static and dynamic confinement of the LHC tunnel air with ventilation doors and ventilation schemes that ensure a lower pressure in the LHC tunnel.

Stray radiation levels will impact the radiological classification of the new service areas. It is foreseen to classify them as Supervised Radiation Areas, similar to any other service area of the LHC. Two different scenarios have been studied, stray radiation during normal operation of the machine and an accidental scenario, represented by one full 7 TeV proton beam lost in a bulky object in front of the most exposing connection to the galleries. The ultimate luminosity and beam intensity are considered (7.5×10^{34} cm^{-2} s^{-1} and 2808 bunches at 2.2×10^{11} protons per bunch).

The dose limits follow from the radiological classification as Supervised Radiation Area. During normal operation of the accelerator, in the new service galleries the ambient dose equivalent rate has to be as low as reasonably possible (ALARA principle) and, in any case, it has to be lower than 15 μSv/h, the limit for non-permanently occupied workplaces. In the accident scenario, the effective dose received by personnel must not exceed the legal annual limit for the class B radiation worker, i.e. 6 mSv.

A standalone geometry model (Figure 19-5), updating the one reported in Ref. [13], of these galleries was developed and used for the shielding studies, such as the choice of the material for the stairs [14]. The model includes the UR and the UA service galleries including the UPR connections, the UA elbow on top of the LHC tunnel with 5 connection cores, and a portion of the LHC tunnel where a tungsten target (100 cm long, 10 cm diameter) is placed in front the UPR-LHC to simulate the accidental loss of the full 7 TeV proton beam on a massive element.

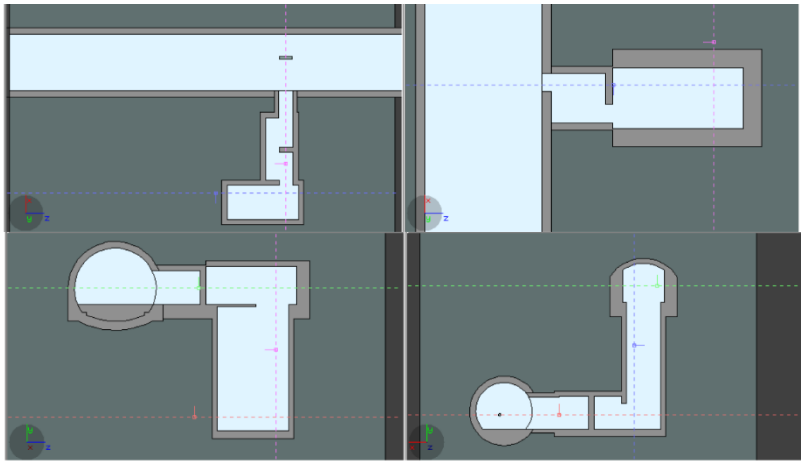

Figure 19-5. Different sections of the FLUKA model of the UPR17. Top-left: top view LHC tunnel-UPR17; Top-right: top view UPR17-UA17 junction; Bottom-left: side view UPR17-UA17 junction; Bottom-right: side view LHC tunnel-UPR17 junction. The stairs are not visible in these sections. A dedicated FLUKA input file has been created for the UPR13, UPR57 and UPR53.

In order to reduce the radiation streaming through the cores connecting the UA elbow to the LHC, two concrete shielding walls are placed at the end of the UA gallery next to the UA elbow. These two walls will be 40 cm think with a sliding door allowing access to the elbow when the accelerator machine is not operating.

In the following, as example, only the results for the UPR17 are reported. The results for the others UPRxx can be found in Ref. [14]. Figure 19-6 and Figure 19-7 show the ambient dose equivalent maps at the UPR17-LHC and UPR17-UA17 interface respectively. The transmission through the implemented infrastructure, from the LHC tunnel to the closest accessible area in the new UA17 gallery (UPR17-UA17 interface), is estimated to about $3x10^{-8}$, where the ambient dose equivalent level drops to <0.3 mSv (Figure 19-8).

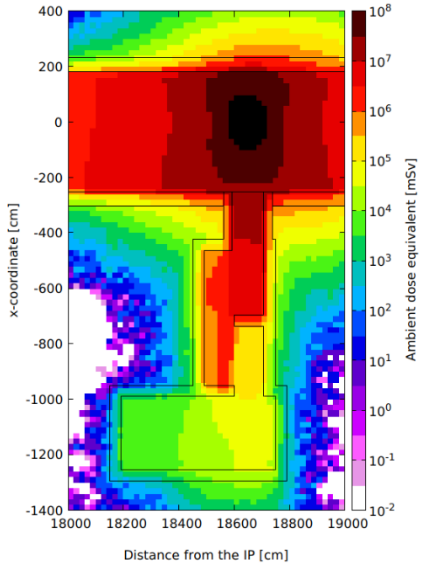

Figure 19-6. Prompt ambient dose equivalent maps for the UPR17-LHC interface considering the full loss of the 7 TeV proton beam on a massive element ($2808 \times 2.2 \times 10^{11}$).

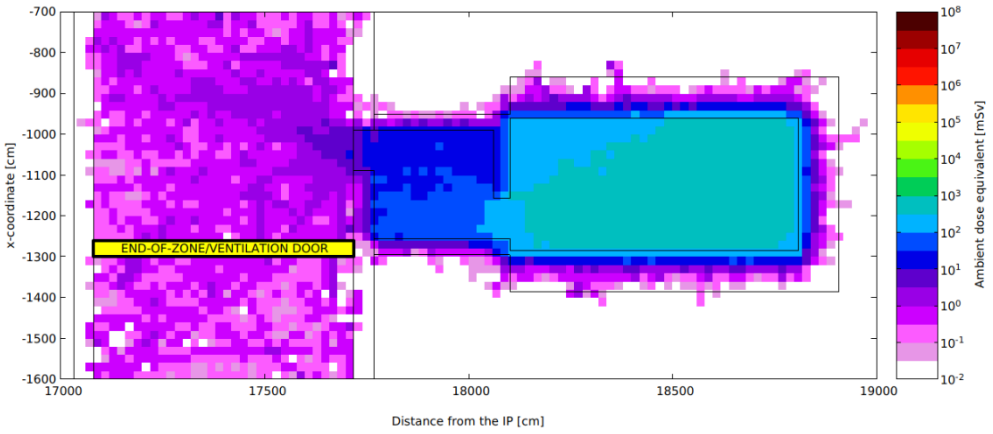

Figure 19-7. Prompt ambient dose equivalent maps for the UPR17-UA17 interface considering the full loss of the 7 TeV proton beam on a massive element ($2808 \times 2.2 \times 10^{11}$).

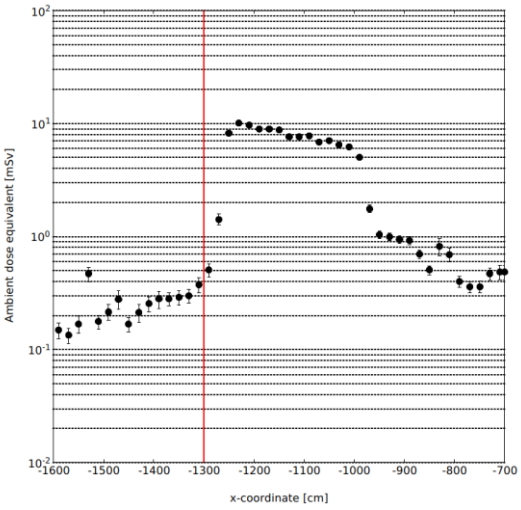

Figure 19-8: Prompt ambient dose equivalent profile along the UA17 tunnel for the full 7 TeV proton beam being lost ($2808 \times 2.2 \times 10^{11}$). The red line indicates the approximate location of the end-of-zone door. Ambient dose scored at 40 cm from the door. Δy = 300 cm, Δz = 600 cm.

During machine operation, the maximum dose rate next to the tunnel wall is 50 Sv/h, which after applying the attenuation factor of $3x10^{-8}$, leads to a value of 1.5 μSv/h ambient dose equivalent rate due to stray radiation in the closest accessible point of the new underground gallery.

19.2.4 Activation studies for the excavation of the new underground galleries in P1 and P5

In order to assess the level of activation of the spoil coming from the excavation of the new underground galleries, the results obtained with the FLUKA Monte Carlo code (particle fluence spectra) have been used as input for the ActiWiz3 Creator © code.

An activated material is defined as radioactive if the specific or total activity of any radionuclides of artificial origin exceed the corresponding clearance limit, i.e.:

$$\sum_{i=1}^{n} \frac{a_i}{LL_i} < 1 \qquad (19\text{-}1)$$

where a_i is the specific activity (Bq/g) or the total activity (Bq) of the i^{th} radionuclide of artificial origin in the material, LL_i is the respective CERN clearance limit for the radionuclide i in the material and n is the number of radionuclides present.

During last end of the year technical stop of the LHC machine, some concrete and rock samples were extracted from the LHC tunnel wall, in the place where the excavation will occur. γ-spectrometry measurements were performed on the rock and concrete samples, after a cooling time of about 3 months. The activation of the samples was also evaluated using ActiWiz3 Creator code. The results are reported in Table 19-1, in the form of the sum of specific activity over clearance limit.

Table 19-1: Activation level of concrete and soil samples as measured by the γ-spectrometry and calculated using the ActiWiz3 Creator© code.

$\sum_i \frac{a_i}{LL_i}$	**3 months cooling time**		
UPR	**γ spectrometry measurements**	**ActiWiz3 Creator©**	
		only γ	**full**
concrete	1.15E-01	9.70E-02	*4.96E-01*
soil	8.17E-03	5.30E-03	*1.65E-02*

In the last column of Table 19-1, the results of all the radionuclides is reported, including the ones that cannot be measured with the γ-spectrometry technique. The γ results, second and third column Table 19-1, are in good agreement. The induced radionuclide list calculated is reported in Table 19-2 with the contributing percentages to the sum; the most contributing radionuclide in both cases is Ca-45, which is a pure β-emitter, thus not measurable with the γ-spectrometry technique.

The activity over limit sum was evaluated for the spoils coming from the excavation of the new underground galleries where they are connected to the existing LHC tunnel. The results of the calculation, for the first three meters of excavation spoils is reported in Figure 19-9, for one and four months cooling times; the first meter of excavated spoils will be radioactive, the second and the third meters are below the legal limits in both the cases.

Table 19-2: Contributing percentage of the induced radionuclide

	Contribution to $\sum_i \frac{a_i}{LL_i}$	**Contribution to $\sum_i \frac{a_i}{LL_i}$**
Radionuclide	**Concrete sample**	**Soil sample**
Ca-45	80%	68%
Na-22	7%	28%
Zn-65	3%	
Fe-55	3%	
S-35	1%	2%
Mn-54	1%	

$\sum_i \frac{a_i}{LL_i}$	***LS2***	
UPR	ActiWiz 3 Creator©	
	1 month	4 months
1st meter	5.19E+00	4.15E+00
2nd meter	3.19E-01	2.90E-01
3rd meter	1.87E-02	1.70E-02

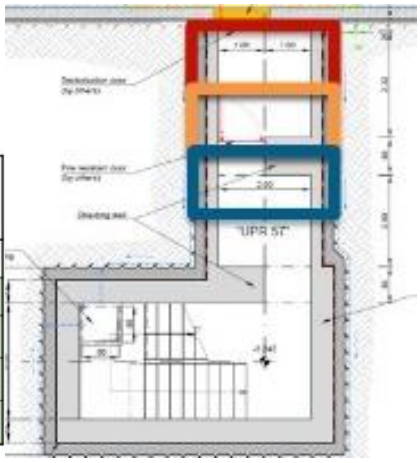

Figure 19-9: Expected activation level of excavated spoils.

19.2.5 Preliminary residual dose rate prediction for the Long Straight Section in Point 8

A preliminary activation study, considering the LSS left of IP8, has been performed to give guidelines for the design of the new neutral absorber, TANB (See Chapter 8). Different design options have been evaluated, with and without shielding. Figure 19-10 shows the FLUKA geometry model and the TANB model used for the study.

Residual dose rate maps were calculated with FLUKA for the part of LSS in Point 8 that extends from the warm dipole MBXWH on the left of IP8 up to the dipole D2 in Cell 4 left. As for P1 and P5, the simulations were performed for the high energy secondary radiation field arising from p–p collisions at 14 TeV centre-of-mass energy as it dominates the activation in these areas. Results were normalized to the nominal LHC peak luminosity value of 2×10^{33} cm^{-2} s^{-1}, using DPMJET-III as the event generator. The irradiation profile considered was based on the operational scenarios reported in Ref. [1] and consists in two operational runs (Run 3 and Run 4) of three years each, at nominal peak luminosity and a total integrated luminosity per run of 25 fb^{-1} with a composition of 5 fb^{-1}/10 fb^{-1}/10 fb^{-1} over the three operational years of each run.

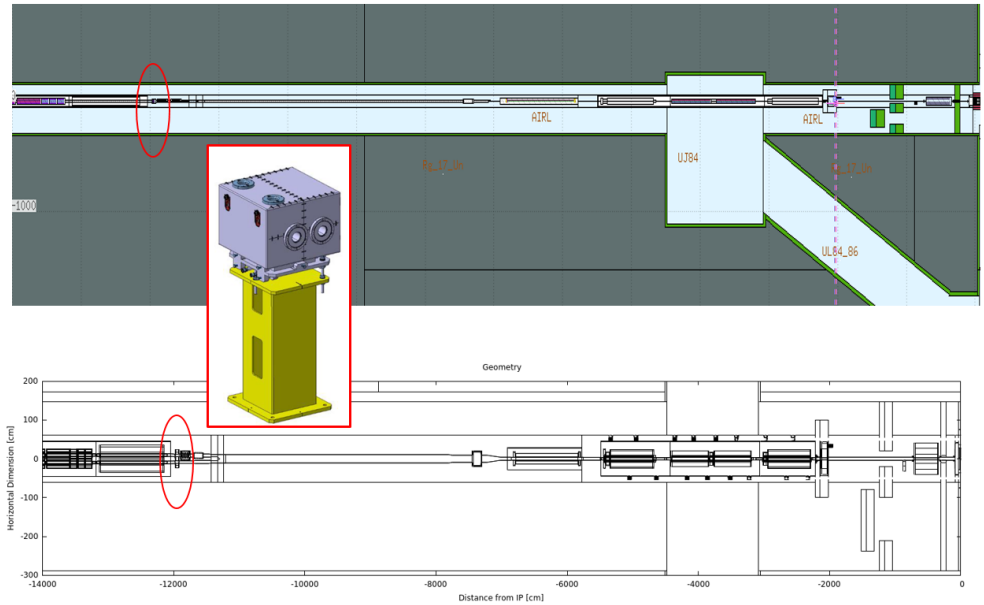

Figure 19-10. FLUKA geometry model of the LSS left of IP8 and the TANB model.

Figure 19-11 shows the ambient dose equivalent rate map after one month of cooling time during the LS3, and Figure 19-12 shows the ambient dose equivalent rate profile in the aisle at a working distance from the machine elements at four different cooling times (1 week, 1 month, 4 months and 1 year), which are typical cooling times for maintenance interventions in the machine tunnel during the scheduled technical stops, end of the year technical stops and long shutdowns. The higher residual dose rates are around the elements closest to the IP (elements on the right in the figures) where the highest levels in the aisle correspond to the connections between elements, where the shielding effect due to self-absorption of the element is less effective, and in cell 4 where there is the Y chamber, the TCT collimators and the TANB absorber.

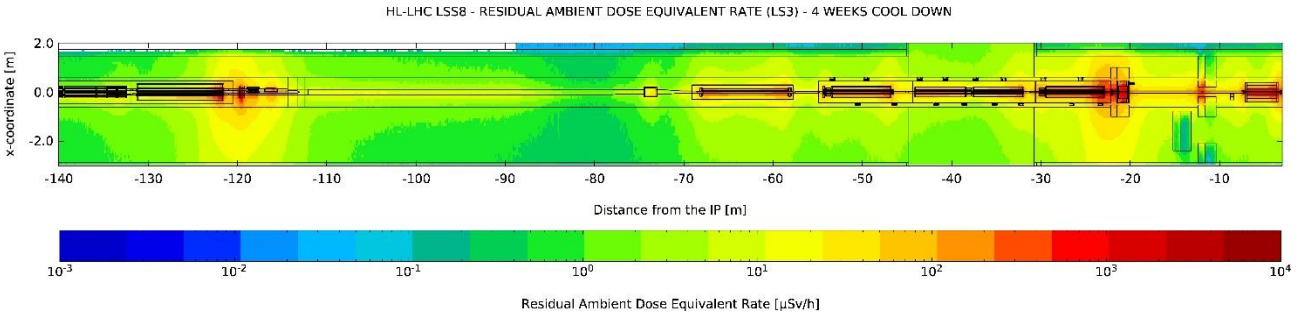

Figure 19-11. Ambient dose equivalent rate map in the LSS8 left after one-month cooling time during LS3. The residual dose in the vertical dimension is averaged on 30 cm around the beam pipe.

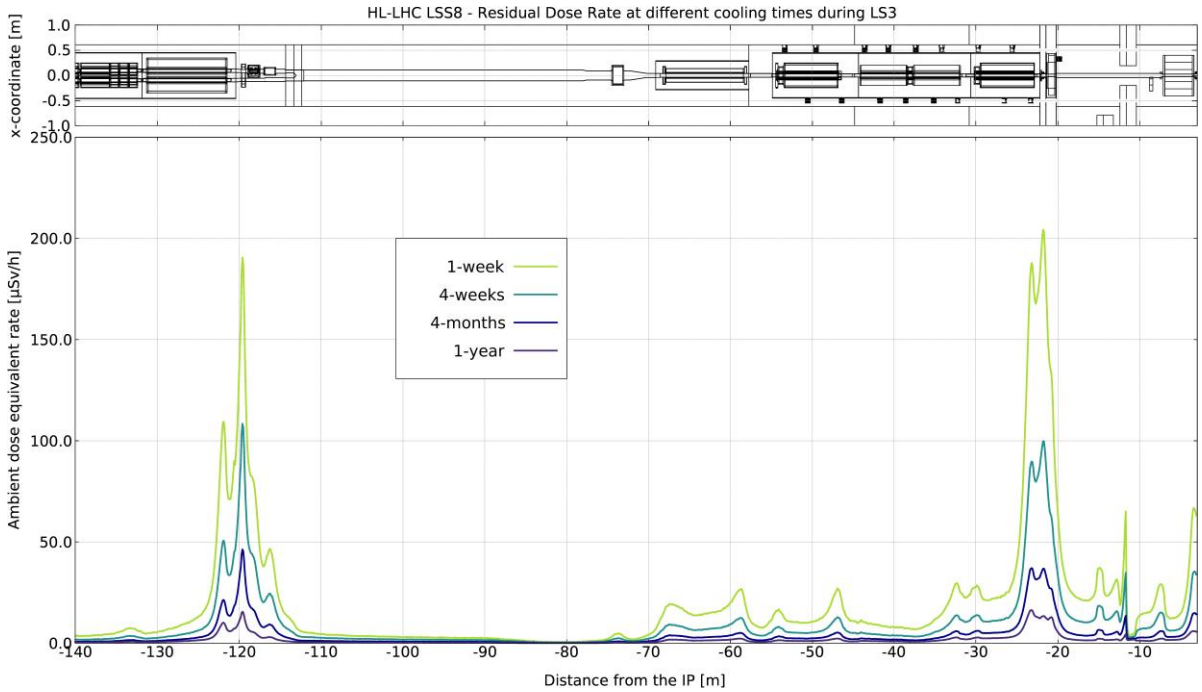

Figure 19-12. Ambient dose equivalent rate profile in the LSS8 left at different cooling times during LS3. The residual doses in the horizontal and vertical dimensions are averaged on 30 cm.

Figure 19-13 shows the ambient dose equivalent rate profiles in the aisle at a working distance from the TANB and adjacent equipment corresponding to three different material shielding options of the absorber: stainless steel, cast iron, marble and without shielding. The advised design option is the one without shielding.

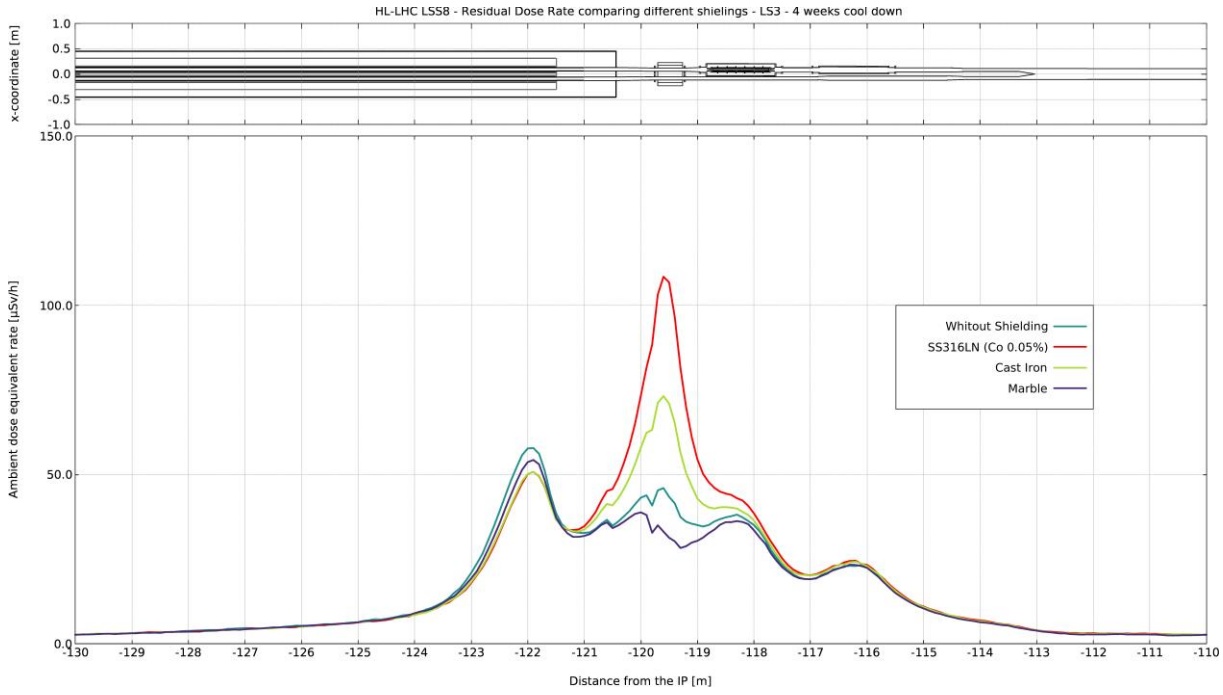

Figure 19-13. Ambient dose equivalent rate profiles around TANB, for different shielding options at 1-month cooling time during LS3. The residual doses in the horizontal and vertical dimensions are averaged on 30 cm.

19.3 Occupational, Operational, Radiation Safety, and Safety Conformity

19.3.1 Introduction

Safety of a facility can be highlighted from different perspectives: first, there is a temporal distinction between the project phase, the operational phase and later the decommissioning phase. Second, one can distinguish between the conformity aspect of Safety (the project's deliverables shall comply with Safety regulations, standards and recommendations), the aspects of workplace safety (the prevention of professional accidents and professional illness by instructing, training and protecting workers), and operational safety (definition and approval of technical and organisational measures to ensure a safe operation of a facility), including radiation safety.

This Section highlights the strategies developed to ascertain compliance of the HL-LHCs hardware with Safety Standards and regulations. Workplace safety is not particular to the HL-LHC project, but part of the hierarchical responsibility of the executive departments and units.

19.3.2 Project safety at CERN

A project pools together resources from numerous, specialised organisational units from all over CERN in a Matrix structure in order to achieve its objectives. A specific organisation is put into place for projects, including the project's Safety aspects [16]. The project leader assumes responsibility for the Safety of the Project, however, neither he, nor the Project organisation substitute the Hierarchical Line of Safety Responsibility that is mandatory at CERN [1][18]. The organisational units participating in the project retain responsibility for results, both technical and in matters of Safety. An example is the delivery of accelerator components, meeting applicable safety standards, and best safety practice during their production. The project's responsibility is the provision of the necessary means to meet the technical and safety objectives, in form of manpower, budgets and a common safety organisation.

In a larger project, the project leader is advised to appoint a Project Safety Officer (PSO) [16][18] to assist him with his Safety responsibilities.

The central Health, Safety and Environmental Protection (HSE) unit has the role to establish a regulatory framework for Safety within CERN, to advise organisational units and projects on its implementation, and to monitor the installation of special equipment and activities by safety clearances and inspections.

The Departmental Safety offices are already involved during the project phase, so that they can advise on the design and operational aspects. Indeed, the risk owners remain the Departments which is particularly true as soon as the project organisation stands down at the beginning of the operational phase.

19.3.3 Safety documentation

The decisions taken on behalf of Safety during the project phase need to be documented and archived properly for future lifecycle phases of the equipment built under the HL-LHC project. One of the PSO's tasks is therefore to oversee the edition of the Safety Documentation, in parallel with the project's development. In this function, the PSO collaborates closely with the work package leaders and project engineers, and with members of the HSE unit (HL-LHC HSE Correspondents and HSE experts).

For the HL-LHC project, it has been decided to create a safety documentation that follows the project breakdown structure. The safety documentation is recorded in the System Safety Assessment (SSA) form, with a content agreed between the project and the HSE unit. The SSA form is a living document, accompanying the equipment during the life cycle, after which it will be archived with the equipment's documentation. The aim is that during the operational phase of the equipment, this document is updated for each modification so that the hazards and risks can be re-evaluated regularly. The SSA for each equipment or assembly is archived under the "Safety" heading in the Workpackage's EDMS space. Safety documents pertaining to individual assets

(e.g. one specific magnet from the series) are stored with the asset's technical documentation in the Equipment Management Folder (MTF) database.

The first step of the safety documentation consists in the production of a hazard register, between a Project Safety Officer and the Work Package Leader and engineers [17] and based on an agreed table of potential hazards [19]. Targeted hazards are those that may appear during installation, operation, maintenance, and dismantling of the equipment. For many hazards, "standard best practice" from CERN safety regulations or national rules or recommendations can be applied to suppress them. The hazard register and the mitigation measures are recorded in the SSA and submitted for review to the HSE unit. The HSE unit may accept it, and then the Project Safety Officers will monitor the implementation of the mitigation measures by the Work Packages. Where standard best practice is not sufficient to mitigate a hazard, the HSE unit may decide that the equipment has "Major Safety implications (mSi)". Based on the hazard register and the risk assessment, the HSE unit will finally define "Safety Checks" which have to be fulfilled before the equipment receives "Safety Clearance" and can be installed and operated in the accelerator.

Equipment or systems with "major safety implications" include deliverables from collaboration partners that are external to the EU and thus not able to certify conformity with EU directives as well as equipment employing novel technologies not documented in the safety literature, such as the crab cavities or the cold powering system. In these cases, a dedicated risk assessment will be performed by the Project Safety Officers in collaboration with the work package leader and engineers. It is documented either in in the SSA or in a dedicated safety report. Examples are given below. Other risks requiring dedicated analysis and reporting are those which may lead to helium release and oxygen deficiency.

19.3.4 Conformity with safety standards

The likelihood of equipment failure leading to an accident or occupational illness is reduced by installing only equipment that meets published Safety regulations and standards. These regulatory documents draw on the pooled experience in workplace safety of panels of experts working on behalf of the public authorities. CERN has adopted the Essential Safety Requirements (ESR) of the European Directives as the safety standard for its technical equipment. These requirements are met by an equipment that is constructed following the applicable Harmonised European Norms (EN), technical standards, but the compliance can also be achieved by other means.

Other sources of Safety regulations and standards may be national regulations of a Host State, or specific regulations at CERN, which are published in form of a Safety Regulation (SR) or a General Safety Instruction (GSI) [20].

19.3.5 Examples - superconducting magnets, cold powering and crab cavities

Two HL-LHC WPs will produce superconducting magnets, based either on Nb_3Sn or Nb-Ti conductor technology. WP11 provides 11-T superconducting magnets produced at CERN. WP3 is relying on contributions from partners in Italy, France, Spain, U.S.A., Japan, and China. The cold masses of superconducting magnets are pressure vessels. Their safety is ascertained world-wide by legal prescriptions, backed by mandatory industrial standards. They differ in certain details from the prescriptions in the European Directives and harmonised standards. It would be prohibitively expensive in terms of budget and time to assess conformity of their contributions with European Standards, and this assessment would not add significantly to the quality and the safety of the equipment received. It has therefore been agreed upon between the project and the HSE unit to deviate in this aspect from a strict adherence to the European Safety Directives. The HSE unit will act as a de facto Notified Body with regard to the assessment of the conformity of the deliverables to the ESR. On the basis of an inspection checklist [21] drawn up by the project and the HSE unit that sets out the minimum requirements relating to the equipment, the HL-LHC HSE Correspondents make an evaluation if the conformity assurance methods put in place by countries using other standards are suitable to meet the Essential Safety Requirements of the European Directive. It may decide compensatory measures throughout the lifecycle of the equipment to proceed with the next steps of manufacture if necessary. Documents to be delivered for

the Safety Checks are described in Ref. [21]. The roles and responsibilities of the manufacturer, the importer and the HSE unit are precisely defined within a formal agreement written and signed by the three parties [22].

The high-current magnets in the HL-LHC inner triplets and in part of the matching section are powered from the new underground galleries by a superconducting link. The link is made from a MgB_2 superconducting cable, cooled by gaseous helium. The advantage of this scheme is that the feedboxes hosting the current leads are not exposed to ionising radiation (which is the case of present LHC DFBX and DFBM) and that they can be inspected during the operation of the accelerator. The price to pay is, however, that a fully powered, superconducting system is partly installed in an accessible part of the underground structures. A feedbox in the accessible service tunnel will make the link between busbars or water-cooled cables and the superconducting MgB2 cable. This cable will be guided in a superconducting link cryostat of up to 90 m length to the LHC tunnel. There, a second feedbox will make the electrical connection to the superconducting magnets. The cold powering will rely on European In-kind contributions to manufacture the interconnection cryostats which are pressure vessels. The EU manufacturer will choose the conformity assessment process according to the category level of the equipment and deliver it to CERN with an EU certificate of conformity with the stamp of the nominated Notified Body. Once the interconnection cryostats are delivered to CERN, the HSE unit will make a complementary conformity assessment before connecting pipes and assembling the equipment in the tunnel.

A failure mode and effects analysis (FMEA) has identified the maximum credible incidents (MCI) of the cold powering system. The information from this analysis is used in the design process of the safety devices (pressure relief valves and burst disks) which must assure that only the limited amount of gaseous helium contained in the link cryostat can be released to the accessible parts of the underground galleries during an MCI [23]. The outcome of this study will also be used to define and implement other technical protection and organizational measures to ensure a safe operation of the superconducting link when work is simultaneously being performed in the accessible service galleries (e.g. deflectors, ventilation, and maintenance procedures).

WP4 provides Crab Cavities to the project, RF devices which improve the overlap of the proton bunches in the interaction points and thus increase luminosity. They present several challenges for Safety compliance: the cavities are cryogenic devices and therefore pressure vessels, constructed from the non-standard material Niobium. In addition, some of the deliverables are supplied by non-EU countries. Similar to the procedure outlined for superconducting magnets, an approval process for this non-standard equipment was defined with the HSE unit, which defined a number of Safety Checks in order to grant clearance for the Crab Cavities. This process was applied to the first prototype of a Double Quarter Wave cavity, which was successfully tested in the SPS accelerator in 2018.

19.4 References

[1] CERN, “CERN Safety Policy”, EDMS: 1416908.

[2] CERN, “CERN Safety Code F”, EDMS: 335729.

[3] CERN, “ALARA rule applied to interventions at CERN”, EDMS: 1751123.

[4] CERN, “ALARA Review Working Group. Final report”, 2013. EDMS: 1244380.

[5] C. Theis and H. Vincke, “ActiWiz – optimizing your nuclide inventory at proton accelerators with a computer code,” in Proceedings of the ICRS12 conference, 2012, Nara, Japan, Progress in Nuclear Science and Technology, Volume 4 pp. 228-232, 2014, DOI: 10.15669/pnst.4.228.

[6] A. Ferrari, P.R. Sala, A. Fassò, and J. Ranft, “FLUKA: a multi-particle transport code”, 2005, DOI: 10.5170/CERN-2005-010.

[7] T. Böhlen, F. Cerutti, M.P.W. Chin, A. Fassò, A. Ferrari, P.G. Ortega, A. Mairani, P.R. Sala, G. Smirnov and V. Vlachoudis, “The FLUKA Code: Developments and Challenges for High Energy and Medical Applications,” Nuclear Data Sheets 120, 211-214, 2014, DOI: 10.1016/j.nds.2014.07.049

[8] S. Roesler, E. Enge and J. Ranft, The Monte Carlo Event Generator DPMJET-III, Vols. in Proceedings of the Monte Carlo 2000 Conference Lisbon, October 23-26, A. Kling, F. Barao, M. Nakagawa, L. Tavora and P. Vaz, Eds., Springer-Verlag Berlin, 2001, DOI: 10.1007/978-3-642-18211-2_166

[9] G. Apollinari, I. Bejar Alonso, O. Bruning, P. Fessia, M. Lamont, L. Rossi and L. Tavian, High Luminosity Large Hadron Collider (HL-LHC): Technical Design Report V.0.1., 2017, DOI: 10.23731/CYRM-2017-004

[10] Csörgő, T. *et al*., "Elastic Scattering and Total Cross-Section in p+p reactions measured by the LHC Experiment TOTEM at sqrt(s) = 7 TeV," in XLI International Symposium on Multiparticle Dynamics, 2012, DOI: 10.1143/PTPS.193.180

[11] V. Kouskoura and R. Froeschl, "Radiological Source Terms for the FIRIA ATLAS Pilot Case," CERN, Geneva, 2020.

[12] A. Infantino and M. Maietta, "Radiation levels in HL-LHC LSS1 and LSS5: update to optics v1.5, EDMS: 2405113.

[13] C. Adorisio, "HL-LHC - Residual Dose Rate Estimations in the LSS1 and LSS5 (from TAXS up to Q7)", EDMS: 1868872.

[14] A. Infantino, "HL-LHC UPR underground galleries: review of the ambient dose equivalent rate during operation", EDMS: 2212147.

[15] E. Thomas, "LHCb request for running at 'nominal' LHC luminosity", 5th Joint HiLumi LHC-LARP Annual Meeting, 2015, INDICO: 400665.

[16] CERN, "Safety Regulation SR-SO "Responsibilities and Organisational Structure in Matters of Safety at CERN", EDMS: 1389540.

[17] T. Otto and F. Viggiano, "Hazard Classification for Technological processes in TE Department", EDMS: 1586444.

[18] CERN, "General Safety Instruction GSI-SO-7", EDMS: 1410233.

[19] CERN, "HL-LHC Hazard Identification Table", EDMS: 1361970.

[20] CERN, "Safety Procedure SP-R1 "Establishing, updating, and publishing CERN Safety Rules", EDMS: 872057.

[21] CERN, HSE, "HL-LHC requirements for Cat IV pressure equipment", EDMS: 2087591.

[22] CERN, "Agreement for compliance of LMBXF cold masses supplied by KEK with CERN Safety Rules", EDMS: 2052040.

[23] T. Otto and N. Grada, "Preliminary Assessment of the Cryogenic Releases from Cold Powering in HL-LHC Underground Areas", EDMS: 1974133.

List of machine and beam parameters

A. List of machine and beam parameters

A.1. Main machine parameters

Table A-1: HL-LHC nominal machine parameters for proton operation [1]

		Injection	Collision
Geometry			
Ring circumference	(m)	26658.883	26658.883
Ring separation in arcs	(mm)	194	194
Bare inner vacuum screen height in arcs	(mm)	46.5	46.5
Effective vacuum screen height (incl. tol.)	(mm)	44.04	44.04
Bare inner vacuum screen width in arcs	(mm)	36.9	36.9
Effective vacuum screen width (incl. tol.)	(mm)	34.28	34.28
Main magnets			
Number of main bends		1232	1232
Length of main bends	(m)	14.3	14.3
Field of main bends	(T)	0.535	8.33
Bending radius	(m)	2803.95	2803.95
Lattice			
Maximum dispersion in arc (H/V)	(m)	2.42/0.28	2.72/0.80
Minimum dispersion in arc (H/V)	(m)	0.96/−0.28	0.56/−0.50
Maximum β in arc (H/V)	(m)	178/179	592/593
Minimum β in arc (H/V)	(m)	31.2/31.7	24.1/25.1
Minimum β in IP1/2/5/8*	(m)	6/10/6/10	0.15/10/0.15/1.5
Horizontal tune		62.27	62.31
Vertical tune		60.295	60.32
Momentum compaction (B1/B2)	[10^{-4}]	3.478/3.476	3.485/3.480
Slip factor η (B1/B2)	[10^{-4}]	3.435/3.432	3.485/3.480
Gamma transition γ_{tr} (B1/B2)		53.62/53.64	53.56/53.61
RF System			
Revolution frequency	(kHz)	11.2455	11.2455
RF frequency	(MHz)	400.789	400.790
Harmonic number		35640	35640
Total RF voltage**	(MV)	8	16
Synchrotron frequency	(Hz)	66.0	23.8
Bucket area	(eVs)	1.38	7.63
Bucket half height ($\Delta E/E$)	[10^{-3}]	0.965	0.343
Crab Cavities			
RF frequency	(MHz)	400.789	400.790
Max. Total RF voltage (per IP)	(MV)	6.8	6.8

*The horizontal and vertical β functions are equal at the IP.

** Injection requires the so-called half-detuning scheme while energy ramp, flattop, and collision require full detuning scheme (see chapter 4).

Table A-2: HL-LHC nominal machine parameters at the collision points for proton operation. The crossing angle and separation refer to Beam 1 if not specified otherwise [1].

		Injection	**Collision**
Interaction data			
Number of collision points		NA	4
Half crossing angle at the IP for ATLAS (IP1) [a]	(μrad)	+295 (H)	+250 (H)
Half parallel separation at the IP for ATLAS (IP1)[b]	(mm)	+2.0 (V)	0.0 (V)
Half external crossing angle at IP for ALICE (IP2)[b,c]	(μrad)	-170 (V)	-170 (V)
Half crossing angle at the IP for ALICE (IP2)[b,c,d]	(μrad)	-170 ∓ 1089 (V)	-170∓70 (V)
External parallel angle at the IP for ALICE (IP2)[e]	(μrad)	-40 (H)	0 (H)
Angle at the IP for ALICE (IP2)	(μrad)	-40∓4.5(B1H)//40±4.5(B2H)	∓0.3(B1H)//±0.3(B2H)
Half parallel separation at the IP for ALICE (IP2)[e]	(mm)	+3.5 (H)	+0.138[f] (H)
Half crossing angle at the IP for CMS (IP5)[b]	(μrad)	+295 (V)	+250 (V)
Half parallel separation at the IP for CMS (IP5)[b]	(mm)	-2.0 (H)	0.0 (H)
Half external crossing angle at the IP for LHCb (IP8)[a]	(μrad)	-170 (H)	-200 (H)
Half crossing angle at the IP for LHCb (IP8)[c,d]	(μrad)	-170∓2100 (H)	-200∓135 (H)
External parallel angle at the IP for LHCb[e] (IP8)[e] [4]	(μrad)	-40 (V)	0
Angle at the IP for LHCb (IP8) [4]	(μrad)	-40∓28(B1V)//40±28(B2V)	∓1.8(B1V)//±1.8(B2V)
Half parallel separation at IP for LHCb (IP8)[e] [4]	(mm)	-3.5 (V)	-0.031/-0.035[g] (V)
Minimum β at IP1 and IP5 (H/V)	(m)	6/6	0.15/0.15
β at IP2 (H/V)	(m)	10/10	10/10
β at IP8 (H/V)	(m)	10/10	1.5/1.5

[a] The sign is defined by the LHC geometry.
[b] The other sign is possible and not correlated with other sign choices.
[c] The crossing angle in IP2 and IP8 is the sum of an external crossing angle bump and an 'internal' spectrometer compensation bump and it depends on the spectrometer polarity [2]. The external bump extends over the triplet and D1 and D2 magnets. The internal spectrometer compensation bump extends only over the long drift space between the two triplet assemblies left and right from the IP. For IP2 the vertical external crossing angle sign can be changed (but it is not strictly necessary) and therefore the sign of the internal and external angle can be chosen to be the same. This is not possible for IP8 as the sign of the crossing angle must be compatible with the recombination scheme. For IP2 and IP8 the value of the external crossing angle is given to provide the maximum crossing angle at the IP for the so-called "positive" polarity of the spectrometer [3]. The convention for the spectrometer polarity sign is that it is positive for a negative sign of the "internal" crossing angle at the IP.
[d] The first value corresponds to the so-called "positive" polarity of the spectrometers [3].
[e] The other sign is possible but the sign of the parallel angle and separation are correlated for the same IP.
[f] This corresponds to a full separation of 4.8 σ required to reduce the luminosity down to 10^{31} cm^{-2} s^{-1} for the nominal bunch population at the beginning of the stable beam period both for the positive and negative polarity of the spectrometer. The standard filling scheme has been considered.
[g] This corresponds to a full separation of 2.8/3.1 σ required to reduce the luminosity down to 2×10^{33} cm^{-2} s^{-1} for the nominal bunch population at the beginning of the stable beam period for the positive and negative polarity of the spectrometer, respectively. The standard filling scheme has been considered.

A.2. Proton-beam parameters in collision

Table A-3: HL-LHC nominal parameters for 25 ns operation [5][6] for two production modes of the LHC beam in the injectors described in Ref. [7] and for the alternative scenario 8b+4e [7] [8] [9].

Parameter	HL-LHC (standard)	HL-LHC (BCMS)[#]	HL-LHC (8b+4e)[@]
Beam energy in collision (TeV)	7	7	7
Particles per bunch, N [10^{11}]	2.2	2.2	2.2
Number of bunches per beam	2760	2744	1972
Number of collisions in IP1 and IP5[*]	2748	2736	1960
N_{tot} [10^{14}]	6.1	6.0	4.3
Beam current (A)	1.10	1.10	0.78
Half-crossing angle in IP1 and IP5 (μrad)	250	250	250
Minimum norm. long-range beam–beam separation (σ)	10.5	10.5	10.5
Minimum β^* (m)	0.15	0.15	0.15
ε_n (μm)	2.50	2.50	2.50
ε_L (eVs)	3.03	3.03	3.03
R.M.S. energy spread [10^{-4}] (q-Gaussian distribution)	1.1	1.1	1.1
R.M.S. energy spread [10^{-4}] (FWHM equiv. Gaussian)	1.29	1.29	1.29
R.M.S. bunch length (cm) (q-Gaussian distribution)	7.61	7.61	7.61
R.M.S. bunch length (cm) (FWHM equivalent Gaussian)	9.0	9.0	9.0
IBS horizontal (h)	16.5	16.5	16.5
IBS longitudinal (h)	19.2	19.2	19.2
Radiation Damping time (h)	26	26	26
Piwinski parameter	2.66	2.66	2.66
Total reduction factor R_0 without crab cavities at min. β^*	0.342	0.342	0.342
Total reduction factor R_1 with crab cavities at min. β^*	0.716	0.716	0.716
Beam–beam tune shift/IP [10^{-3}]	8.6	8.6	8.6
Peak luminosity without crab cavities L_{peak} [10^{34} cm^{-2} s^{-1}]	8.11	8.07	5.78
Peak luminosity with crab cavities $L_{peak}\times R_1/R_0$ [10^{34} cm^{-2} s^{-1}]	17.0	16.9	12.1
Events/crossing w/o levelling and without crab cavities	212	212	212
Levelled luminosity [10^{34} cm^{-2} s^{-1}]	5.0	5.0	3.8
Events/crossing μ (with levelling and crab cavities)[‡]	131	132	140
Max. line density of pile-up events during fill [evts/mm]	1.28	1.29	1.37
Levelling time (h) (assuming no emittance growth)[‡]	7.2	7.2	6.4
Number of collisions in IP2/IP8	2492/2574[**]	2246/2370[**]	1178/1886[**]
N at injection [10^{11}][††]	2.30	2.30	2.30
Maximum number of bunches per injection	288	240	224
N_{tot}/injection [10^{13}]	6.62	5.52	5.15
ε_n at SPS extraction (μm)[‡‡]	2.10	1.70	1.70

[#]BCMS parameters are only considered as a backup scenario set in case one encounters larger-than-expected emittance growth in HL-LHC during injection, ramp, and squeeze

[@]The 8b+4e variant represents a back-up scenario for the baseline 25ns operation in case of electron cloud limitations.

[*]Assuming one less batch from the PS for machine protection (pilot injection, transfer line steering with 12 nominal bunches) and non-colliding bunches for experiments (background studies, etc.). Note that due to RF beam loading the abort gap length must not exceed the 3 μs design value.

[‡]The total number of events/crossing is calculated with an inelastic cross-section of 81 mb, while 111 mb is assumed as a pessimistic value for calculating the proton burn off and the resulting levelling time [10][11].

[**]The lower number of collisions in IR2/8 compared to the general-purpose detectors is a result of the agreed filling scheme, aiming as much as possible at an equal sharing of collisions between the experiments.

[††]An intensity loss of 5% distributed along the cycle is assumed from SPS extraction to collisions in the LHC.

[‡‡]A transverse emittance blow-up of 10–15% on the average H/V emittance in addition to that expected from intra-beam scattering (IBS) is assumed (to reach 2.5 μm of emittance in collision for 25 ns operation).

A.3. Proton-beam parameters at LHC injection (after capture)

Table A-4: HL-LHC nominal parameters at injection (after capture) for 25 ns operation [5][6]for two production modes of the LHC beam in the injectors described in [7] and for the alternative scenario 8b+4e [7][8][9]. The longitudinal parameters have been revised with respect to previous documents.

Parameter	HL-LHC (standard)	HL-LHC (BCMS)#	HL-LHC (8b+4e)@
Beam energy (TeV)	0.45	0.45	0.45
Relativistic gamma	479.6	479.6	479.6
Particles per bunch, N [10^{11}]	2.30	2.30	2.30
Number of bunches per beam	2760	2744	1972
N_{tot} [10^{14}]	6.3	6.3	4.5
Beam current (A)	1.14	1.14	0.82
Stored energy per beam (MJ)	46	46	33
ε_n (μm)	2.1	1.7	1.7
ε_L (eVs)	0.57	0.57	0.57
R.M.S. energy spread [10^{-4}] (q-Gaussian distribution)**	3.1	3.1	3.1
R.M.S. energy spread [10^{-4}] (FWHM equiv. Gaussian)**	3.4	3.4	3.4
R.M.S. bunch length (cm) (q-Gaussian distribution)**	7.8	7.8	7.8
R.M.S. bunch length (cm) (FWHM equivalent Gaussian)**	9.2	9.2	9.2
IBS horizontal (h)	4.7	3.0	3.0
IBS longitudinal (h)	3.5	2.7	2.7

#BCMS parameters are only considered for injection and as a backup parameter set in case one encounters larger-than-expected emittance growth in the HL-LHC during injection, ramp and squeeze.
@The 8b+4e variant represents a back-up scenario for the baseline 25ns operation in case of electron cloud limitations.
** Before IBS emittance blow-up takes place.

A.4. Required proton beam parameters at SPS extraction

Table A-5: Required beam parameters at SPS extraction for 25 ns operation [5][6] for two production modes of the LHC beam in the injectors described in [7] and for the alternative scenario 8b+4e [8][9].

Parameter	HL-LHC (standard)	HL-LHC (BCMS)#	HL-LHC (8b+4e)@
Beam energy (TeV)	0.45	0.45	0.45
Particles per bunch, N [10^{11}]††	2.30	2.30	2.30
Maximum number of bunches per injection	288	240	224
Max N_{tot}/extraction [10^{13}]	6.62	5.52	5.15
ε_n (μm)‡‡	2.1	1.7	1.7
ε_L (eVs)[a]	0.57	0.57	0.57
R.M.S. energy spread [0.0001] [a]	2.5	2.5	2.5
R.M.S. bunch length (cm) [a]	12.4	12.4	12.4

#BCMS parameters are only considered as a backup scenario set in case one encounters larger-than-expected emittance growth in the HL-LHC during injection, ramp and squeeze.
@The 8b+4e variant represents a back-up scenario for the baseline 25ns operation in case of electron cloud limitations.
††An intensity loss of 5% distributed along the cycle is assumed from SPS extraction to collisions in the LHC.
‡‡A transverse emittance blow-up of 10–15% on the average H/V emittance in addition to that expected from intra-beam scattering (IBS) is assumed (to reach 2.5 μm of emittance in collision for 25 ns operation).
[a] These represent the average values including 10% voltage of 4th harmonic system. Calculations are performed without including intensity effects. A spread of ±10% in longitudinal bunch length and of ±10% in R.M.S. energy spread has to be expected, resulting in a ±20% spread in longitudinal emittance.

A.5. Ion-beam parameters in collision

Table A-6: Key LHC design parameters for Pb operation from [12] compared with the achieved parameters in 2018 and the HL-LHC design values [13].

Parameters	**Nominal LHC (design report)**	**2018 achieved**	**HL-LHC (LIU baseline)**
Beam energy in collision (Z TeV)	7	6.37	7
Particles per bunch, N [10^7]	7	23	18
Number of bunches per beam	592	733	1240
Colliding pairs at IP1/5	< 592	733	976-1240[1]
Colliding pairs at IP2	592	702	976-1200[1]
Colliding pairs at IP8	0	468	0-716[1]
Total intensity N_{tot} [10^9]	41.4	169	223
Beam current (mA)	6.12	24.9	33.0
Stored beam energy (MJ)	3.8	13.9	20.5
Minimum β^* (m)	0.5	0.5	0.5
Normalized emittance ε_n (μm)	1.5	2.3	1.65
Longitudinal emittance ε_L [eVs/charge]	2.50	2.33	2.42
RMS energy spread [10^{-4}]	1.08	1.06	1.02
RMS bunch length (cm)	8.07	8.24	8.24
Half-crossing angle at IP2 (μrad) (external,net)	110,40	137,60	170,100
Peak luminosity [10^{27} cm^{-2} s^{-1}]	1.0	-	-
Levelled luminosity IP1/5 [10^{27} cm^{-2} s^{-1}]	-	6.13	6.4
Levelled luminosity IP2 [10^{27} cm^{-2} s^{-1}]	-	1.0	6.4
Levelled luminosity IP8 [10^{27} cm^{-2} s^{-1}]	-	1.0	1.0
Typical levelling time IP2 (h)	-	7	1.5
Maximum number of bunches per injection	54	42	56

[1] The values give the range over the filling schemes considered in Ref. [13].

A.6. Main insertion region magnet parameters

Table A-7: New or refurbished quadrupoles for the HL-LHC in IR1 and 5. “Beam stay clear” indicates the minimum aperture available for the beam considering the tolerance on the mechanical deformations of the nominal beam screen inner shape.

	Inner triplet (single aperture)			**Matching section (two-in-one)**	
Magnet	Q1	Q2	Q3	Q4	Q5
Number per side per insertion	2			1	
Type	MQXFA	MQXFB	MQXFA	MQY	MQML
Magnetic length (m)	4.2	7.17	4.2	3.4	4.8
Maximum Gradient	132.2			160	160
Coil aperture (mm)	150			70	56
Aperture separation	NA			194	
Operating temperature	1.9			4.5	
Beam screen shape	Octagon			Rectellipse	
Nominal beam screen aperture (mm)	99.7 (H/V)/ 99.7 (45°)	119.7 (H/V)/ 110.7 (45°)		60.2 (d)/50.4 (g)	47.5 (d)/37.7 (g)
Beam stay clear (mm)	94.94 (H/V)/ 94.94 (45°)	115.3 (H/V)/ 106.3 (45°)		57.8 (d)/48 (g)	45.1 (d)/35.3 (g)
Alignment tolerances (R/H/V) (mm)	0.6/1.0/1.0			0.84/1.26/0.6	
Beam screen orientation (plane of smaller gap)				L.B1: V L.B2: H R.B1: H R.B2: V	

The description of the shapes is made by providing the dimensions corresponding to the horizontal (H)/vertical (V) and 45° cuts for octagons; diameter (d) and gap (g) for rectellipse [12]; radius for circles. The orientation of the rectellipse cross section depends on the IP side and beam type and it has been chosen to optimise the beam aperture in collision. The alignment tolerances are represented as a racetrack shape of radius (R), horizontal (H), vertical (V) extent, respectively. The values provided include ground motion and fiducialization tolerances [1], although they are going to be reviewed in the context of the full remote alignment system.

Table A-8: Separation and corrector dipole magnets for the HL-LHC in IR1 and 5. The order of the correctors has to be considered starting from the IP towards the arcs.

	Separation/recombination dipoles		**Orbit correctors**				
Assembly	D1	D2	Corrector Package	Q2	D2	Q4	Q5
Number per side per insertion	1	1	1	2	2	3	1
Configuration			HV nested	HV nested	L.B1: VH L.B2: HV R.B1: VH R.B2: HV consecutive	L.B1: VHV L.B2: HVH R.B1: HVH R.B2: VHV consecutive	L.B1: V L.B2: H R.B1: H R.B2:V
Type	MBXF	MBRD	MCBXFA	MCBXFB	MCBRD	MCBY	MCBC
Magnetic length (m)	6.27	7.78	2.2	1.2	1.89	0.9	0.9
Integrated field (Tm)	35.08	35.08	4.5	2.5	5.0	2.5	2.33
Coil aperture (mm)	150	105	150	150	105	70	56
Aperture separation (mm)	NA	188	NA	NA	188	194	194
Operating temperature (K)	1.9					4.5	
Beam screen shape	Octagon	Octagon	Octagon	Octagon	Octagon	Rectellipse	Rectellipse
Nominal beam screen aperture (mm)	119.7 (H/V)/ 110.7 (45°)	87.45 (H/V)/ 77.55 (45°)	119.7 (H/V)/ 110.7 (45°)	119.7 (H/V)/ 110.7 (45°)	87.45 (H/V)/ 77.55 (45°)	60.2 (d)/ 50.4 (g)	47.5 (d)/ 37.7 (g)
Beam stay clear	115.3 (H/V)/ 106.3 (45°)	82.7 (H/V)/ 72.5 (45°)	115.3 (H/V)/ 106.3 (45°)	115.3 (H/V)/ 106.3 (45°)	82.7 (H/V)/ 72.5 (45°)	57.8 (d)/ 48 (g)	45.1 (d)/ 35.3 (g)
Alignment tolerances (R/H/V) (mm)	0.6/1.0/1.0	0.84/1.36/1.0	0.6/1.0/1.0	0.6/1.0/1.0	0.84/1.36/1.0	0.84/1.26/0.6	
Beam screen orientation (plane of smaller gap)						L.B1: V L.B2: H R.B1: H R.B2: V	

Table A-9: New superferric correctors for the HL-LHC [15][16]. The order (from left to right) follows the order of installation from the IP.

Number	1	1	1	1	1	1	1	1	1
Number of poles	4	12	12	10	10	8	8	6	6
Normal/skew	Skew	Normal	Skew	Normal	Skew	Normal	Skew	Normal	Skew
Name	MQSXF	MCTXF	MCTSXF	MCDXF	MCDSXF	MCOXF	MCOSXF	MCSXF	MCSSXF
Magnetic length (m)	0.401	0.470	0.099	0.146	0.146	0.145	0.145	0.167	0.167
Integrated field (mT m) at 50 mm	700	86	17	37	37	69	69	95	95
Aperture (mm)	150								
Operating temp.(K)	1.9								
Beam screen shape	Octagon								
Nominal beam screen aperture (H/V) (mm)	119.7 (H/V)/ 110.7 (45°)								
Beam stay clear (mm)	115.3 (H/V)/ 106.3 (45°)								
Alignment tolerances (R/H/V) (mm)	0.6/1.0/1.0								

A.7. Expected field quality for the new insertion-region magnets

In this section the error tables used in the tracking simulations (as described in Chapter 2, Section 2.3.2) for the various classes of new magnets are collected. The error tables can be found under /afs/cern.ch/eng/lhc/optics/HLLHCV1.0/errors2.

The expected field quality of each of the triplet magnets MQXFA and MQXFB at injection and top energy is presented in Table A-10 and Table A-11, respectively. The contributions from the body of the magnets and of the fringe fields at the Connection Side (CS) and Non-Connection Side (NCS) are indicated. The magnetic lengths of the magnets body and of the fringe fields are listed in

Table A-12.

Table A-10: Expected field quality (Systematic – S, Uncertainty – U, Random – R) at injection energy for the IT magnets (r_0 = 50 mm).

	Body			CS	NCS		Body			CS	NCS
	S	U	R	S	S		S	U	R	S	S
a_2	0.000	0.000	0.000	-31.342	0.000	b_2	0.000	0.000	10.000	0.000	0.000
a_3	0.000	0.650	0.650	0.000	0.000	b_3	0.000	0.820	0.820	0.000	0.000
a_4	0.000	0.650	0.650	0.000	0.000	b_4	0.000	0.570	0.570	0.000	0.000
a_5	0.000	0.430	0.430	0.000	0.000	b_5	0.000	0.420	0.420	0.000	0.000
a_6	0.000	0.310	0.310	2.209	0.000	b_6	-21.300	1.100	1.100	8.943	-0.025
a_7	0.000	0.190	0.190	0.000	0.000	b_7	0.000	0.190	0.190	0.000	0.000
a_8	0.000	0.110	0.110	0.000	0.000	b_8	0.000	0.130	0.130	0.000	0.000
a_9	0.000	0.080	0.080	0.000	0.000	b_9	0.000	0.070	0.070	0.000	0.000
a_{10}	0.000	0.040	0.040	0.065	0.000	b_{10}	3.890	0.200	0.200	-0.189	-0.821
a_{11}	0.000	0.026	0.026	0.000	0.000	b_{11}	0.000	0.026	0.026	0.000	0.000
a_{12}	0.000	0.014	0.014	0.000	0.000	b_{12}	0.000	0.018	0.018	0.000	0.000
a_{13}	0.000	0.010	0.010	0.000	0.000	b_{13}	0.000	0.009	0.009	0.000	0.000
a_{14}	0.000	0.005	0.005	-0.222	0.000	b_{14}	0.210	0.023	0.023	-0.545	-1.083
a_{15}	0.000	0.000	0.000	0.000	0.000	b_{15}	0.000	0.000	0.000	0.000	0.000

Table A-11: Expected field quality (Systematic – S, Uncertainty – U, Random – R) at top energy for the IT magnets (r_0 = 50 mm).

	Body			CS	NCS		Body			CS	NCS
	S	U	R	S	S		S	U	R	S	S
a_2	0.000	0.000	0.000	-31.342	0.000	b_2	0.000	0.000	10.000	0.000	0.000
a_3	0.000	0.650	0.650	0.000	0.000	b_3	0.000	0.820	0.820	0.000	0.000
a_4	0.000	0.650	0.650	0.000	0.000	b_4	0.000	0.570	0.570	0.000	0.000
a_5	0.000	0.430	0.430	0.000	0.000	b_5	0.000	0.420	0.420	0.000	0.000
a_6	0.000	0.310	0.310	2.209	0.000	b_6	-0.640	1.100	1.100	8.943	-0.025
a_7	0.000	0.190	0.190	0.000	0.000	b_7	0.000	0.190	0.190	0.000	0.000
a_8	0.000	0.110	0.110	0.000	0.000	b_8	0.000	0.130	0.130	0.000	0.000
a_9	0.000	0.080	0.080	0.000	0.000	b_9	0.000	0.070	0.070	0.000	0.000
a_{10}	0.000	0.040	0.040	0.065	0.000	b_{10}	-0.110	0.200	0.200	-0.189	-0.821
a_{11}	0.000	0.026	0.026	0.000	0.000	b_{11}	0.000	0.026	0.026	0.000	0.000
a_{12}	0.000	0.014	0.014	0.000	0.000	b_{12}	0.000	0.018	0.018	0.000	0.000
a_{13}	0.000	0.010	0.010	0.000	0.000	b_{13}	0.000	0.009	0.009	0.000	0.000
a_{14}	0.000	0.005	0.005	-0.222	0.000	b_{14}	-0.870	0.023	0.023	-0.545	-1.083
a_{15}	0.000	0.000	0.000	0.000	0.000	b_{15}	0.000	0.000	0.000	0.000	0.000

Table A-12: Estimated magnetic lengths of the triplet magnets' body and fringe fields at the connection (CS) and non-connection (NCS) sides.

	Magnetic length		
Magnet	Body	CS	NCS
MQXFA	3.459	0.4	0.341
MQXFB	6.409	0.4	0.341

The expected field quality of the MBXF magnet at injection and top energy is presented in Table A-13 and Table A-14, respectively.

Table A-13: Expected field quality errors (Systematic – S, Uncertainty – U, Random – R) at injection energy for the MBXF magnets (r_0 = 50 mm).

	S	U	R		S	U	R
a_2	0.000	0.679	0.679	b_2	0.000	0.200	0.200
a_3	0.000	0.282	0.282	b_3	-16.000	0.727	0.727
a_4	0.000	0.444	0.444	b_4	0.000	0.126	0.126
a_5	0.000	0.152	0.152	b_5	-0.500	0.365	0.365
a_6	0.000	0.176	0.176	b_6	0.000	0.060	0.060
a_7	0.000	0.057	0.057	b_7	0.900	0.165	0.165
a_8	0.000	0.061	0.061	b_8	0.000	0.027	0.027
a_9	0.000	0.020	0.020	b_9	-0.660	0.065	0.065
a_{10}	0.000	0.025	0.025	b_{10}	0.000	0.008	0.008
a_{11}	0.000	0.007	0.007	b_{11}	0.440	0.019	0.019
a_{12}	0.000	0.008	0.008	b_{12}	0.000	0.003	0.003
a_{13}	0.000	0.002	0.002	b_{13}	0.000	0.006	0.006
a_{14}	0.000	0.003	0.003	b_{14}	0.000	0.001	0.001
a_{15}	0.000	0.001	0.001	b_{15}	-0.040	0.002	0.002

Table A-14: Expected field quality errors (Systematic – S, Uncertainty – U, Random – R) at top energy for the MBXF magnets (r_0 = 50 mm).

	S	U	R		S	U	R
a_2	0.000	0.679	0.679	b_2	0.000	0.200	0.200
a_3	0.000	0.282	0.282	b_3	-0.900	0.727	0.727
a_4	0.000	0.444	0.444	b_4	0.000	0.126	0.126
a_5	0.000	0.152	0.152	b_5	0.000	0.365	0.365
a_6	0.000	0.176	0.176	b_6	0.000	0.060	0.060
a_7	0.000	0.057	0.057	b_7	0.400	0.165	0.165
a_8	0.000	0.061	0.061	b_8	0.000	0.027	0.027
a_9	0.000	0.020	0.020	b_9	-0.590	0.065	0.065
a_{10}	0.000	0.025	0.025	b_{10}	0.000	0.008	0.008
a_{11}	0.000	0.007	0.007	b_{11}	0.470	0.019	0.019
a_{12}	0.000	0.008	0.008	b_{12}	0.000	0.003	0.003
a_{13}	0.000	0.002	0.002	b_{13}	0.000	0.006	0.006
a_{14}	0.000	0.003	0.003	b_{14}	0.000	0.001	0.001
a_{15}	0.000	0.001	0.001	b_{15}	-0.040	0.002	0.002

The Expected field quality of the MBRD magnets at injection and top energy is presented in Table A-15 and Table A-16, respectively.

Table A-15: Expected field quality errors (Systematic – S, Uncertainty – U, Random – R) at injection energy for the MBRD magnets (r_0 = 35 mm). The systematic error represents the value of the multipole for the V1 aperture and that for V2 can be derived from the well-known symmetries for 2-in-1 magnets.

	S	U	R		S	U	R
a_2	0.000	0.679	0.679	b_2	-5.000	0.200	0.200
a_3	0.000	0.282	0.282	b_3	-19.000	0.727	0.727
a_4	0.000	0.444	0.444	b_4	2.000	0.126	0.126
a_5	0.000	0.152	0.152	b_5	3.000	0.365	0.365
a_6	0.000	0.176	0.176	b_6	2.000	0.060	0.060
a_7	0.000	0.057	0.057	b_7	1.300	0.165	0.165
a_8	0.000	0.061	0.061	b_8	1.000	0.027	0.027
a_9	0.000	0.020	0.020	b_9	0.520	0.065	0.065
a_{10}	0.000	0.025	0.025	b_{10}	0.000	0.008	0.008
a_{11}	0.000	0.007	0.007	b_{11}	0.000	0.019	0.019
a_{12}	0.000	0.008	0.008	b_{12}	0.000	0.003	0.003
a_{13}	0.000	0.002	0.002	b_{13}	0.000	0.006	0.006
a_{14}	0.000	0.003	0.003	b_{14}	0.000	0.001	0.001
a_{15}	0.000	0.001	0.001	b_{15}	0.000	0.002	0.002

Table A-16: Expected field quality errors (Systematic – S, Uncertainty – U, Random – R) at top energy for the MBRD magnets (r_0 = 35 mm).

	S	U	R		S	U	R
a_2	0.000	0.679	0.679	b_2	1.000	1.000	1.000
a_3	0.000	0.282	0.282	b_3	1.000	1.667	1.667
a_4	0.000	0.444	0.444	b_4	-3.000	0.600	0.600
a_5	0.000	0.152	0.152	b_5	-1.000	0.500	0.500
a_6	0.000	0.176	0.176	b_6	2.000	0.060	0.060
a_7	0.000	0.057	0.057	b_7	2.000	0.165	0.165
a_8	0.000	0.061	0.061	b_8	1.000	0.027	0.027
a_9	0.000	0.020	0.020	b_9	0.500	0.065	0.065
a_{10}	0.000	0.025	0.025	b_{10}	0.000	0.008	0.008
a_{11}	0.000	0.007	0.007	b_{11}	0.030	0.019	0.019
a_{12}	0.000	0.008	0.008	b_{12}	0.000	0.003	0.003
a_{13}	0.000	0.002	0.002	b_{13}	0.000	0.006	0.006
a_{14}	0.000	0.003	0.003	b_{14}	0.000	0.001	0.001
a_{15}	0.000	0.001	0.001	b_{15}	0.000	0.002	0.002

The expected field quality of the MCBXFA and MCBXFB magnets at nominal field is presented in Table A-17.

Table A-17: Expected field quality errors for the MCBXFA and MCBXFB magnets (r_0 = 50 mm) for the two orientations (horizontal and vertical) at top energy.

	MCBXFA		MCBXFB			MCBXFA		MCBXFB	
	H	V	H	V		H	V	H	V
a_2	0.00	0.00	0.00	0.00	b_2	0.00	0.00	0.00	0.00
a_3	0.00	20.12	0.00	-10.33	b_3	-16.65	0.00	17.37	0.00
a_4	0.00	0.00	0.00	0.00	b_4	0.00	0.00	0.00	0.00
a_5	0.00	-3.04	0.00	-3.60	b_5	-0.35	0.00	2.49	0.00
a_6	0.00	0.00	0.00	0.00	b_6	0.00	0.00	0.00	0.00
a_7	0.00	-3.98	0.00	-3.26	b_7	0.98	0.00	0.62	0.00
a_8	0.00	0.00	0.00	0.00	b_8	0.00	0.00	0.00	0.00
a_9	0.00	-0.62	0.00	-0.58	b_9	0.07	0.00	-0.75	0.00
a_{10}	0.00	0.00	0.00	0.00	b_{10}	0.00	0.00	0.00	0.00
a_{11}	0.00	0.02	0.00	0.12	b_{11}	4.30	0.00	3.60	0.00
a_{12}	0.00	0.00	0.00	0.00	b_{12}	0.00	0.00	0.00	0.00
a_{13}	0.00	0.00	0.00	0.00	b_{13}	0.00	0.00	0.00	0.00
a_{14}	0.00	0.00	0.00	0.00	b_{14}	0.00	0.00	0.00	0.00
a_{15}	0.00	0.00	0.00	0.00	b_{15}	0.00	0.00	0.00	0.00

The expected field quality for the MCBRD correctors is being evaluated.

A.8. Expected field errors for the crab cavities

The expected RF multipoles for the DQW (providing vertical kick) and RFD (providing horizontal kicks) cavities normalized to a RF voltage of 10 MV are listed in Table A-18 and Table A-19, respectively.

Table A-18: Expected integrated RF multipoles normalized to a RF voltage of 10 MV for the DQW crab cavities (r_0 = 30 mm) in mT m/m^{n-1} as defined in [17] and updated in [18].

	Re	Im		Re	Im
a_2	0	0	b_2	6	-2
a_3	1506	27	b_3	0	0
a_4	0	0	b_4	2106	-539
a_5	N/A	N/A	b_5	N/A	N/A
a_6	N/A	N/A	b_6	N/A	N/A

Table A-19: Expected integrated RF multipoles normalized to a RF voltage of 10 MV for the RFD crab cavities (r_0 = 30 mm) in mT m/m^{n-1} as defined in [17] and updated in [18].

	Re	Im		Re	Im
a_2	0	0	b_2	0	0
a_3	0	0	b_3	-522	-56
a_4	0	0	b_4	-914	-36
a_5	N/A	N/A	b_5	N/A	N/A
a_6	N/A	N/A	b_6	N/A	N/A

The expected RF integrated normal and skew decapolar and dodecapolar components are not available yet.

A.9. References

[1] E. Métral *et al.*, Update of the HL-LHC operational Scenarios for Proton Operation, CERN-ACC-NOTE-2018-0002.

[2] O. Brüning and W. Herr, R. Ostojic, A beam separation and collision scheme for IP2 and IP8 at the LHC for optics version 6.1, LHC Project Report 367.

[3] Spectrometer bumps and polarities Guide.

[4] S. Fartoukh, LHCb crossing scheme for Run II & III, LHC Machine Committee Meeting n. 167, 19/6/2013.

[5] R. Tomás Garcia, Update of HL-LHC parameters and operational scenarios (protons), 104th Technical Coordination Committee, 28th May 2020, INDICO: 921722.

[6] HL-LHC Technical Coordination Committee Parameter Table v. 7.1.1 (29/07/2020), TCC Web page

[7] G. Arduini, O. Brüning, R. De Maria, R. Garoby, S. Gilardoni, B. Goddard, B. Gorini, M. Meddahi, G. Rumolo and R. Tomás, Beam parameters at LHC injection, CERN-ACC-2014-0006.

[8] R. Tomás *et al.*, HL-LHC: Exploring alternative ideas, Proc. Review of LHC and Injector Upgrade Plans Workshop (RLIUP), Archamps, France, 29–31 October 2013, CERN–2014–006, pp. 119-126 DOI: 10.5170/CERN-2014-006.119.

[9] H. Damerau *et al.*, LIU: Exploring Alternative Ideas, Proc. Review of LHC and Injector Upgrade Plans Workshop (RLIUP), Archamps, France, 29–31 October 2013, CERN–2014–006, pp. 127-137, DOI: 10.5170/CERN-2014-006.127

[10] The ATLAS and CMS Collaborations, Expected pile-up values at HL-LHC, ATL-UPGRADE-PUB-2013-014, CERN (30 September 2013).

[11] D. Contardo, private communication, 3 December 2014.

[12] O. Brüning, P. Collier, P. Lebrun, S. Myers, R. Ostojic, J. Poole and P. Proudlock (Eds.), LHC Design Report, v.1: the LHC Main Ring, 2012, CERN-2004-003-V-1.

[13] R. Bruce et al., HL-LHC operational scenario for Pb-Pb and p-Pb operation, CERN-ACC-2020-0011.

[14] J.-B. Jeanneret, Geometrical tolerances for the qualification of LHC magnets, LHC-PROJECT-Report-1007.

[15] E. Todesco, M. Sorbi, HL-LHC ECR - WP3 Change Of Quadrupole, Sextupole, Octupole And Decapole Correctors Integrated Field - LHC-M-EC-0002, EDMS: 1963788.

[16] J. Oliveira, M. Amparo Gonzalez De La Aleja Cabana, Final confirmation of dimension of magnetic length of Corrector Package, INDICO: 774098.

[17] A. Grudiev, J. Barranco, R. Calaga, R. De Maria, M. Giovannozzi, and R. Tomas, “Study of Multipolar RF Kicks from the Main Deflecting Mode in Compact Crab Cavities for LHC”, in Proc. 3rd Int. Particle Accelerator Conf. (IPAC'12), New Orleans, LA, USA, May 2012, paper TUPPR027, pp. 1873-1875.

[18] R. Calaga, “Latest info on field quality for crab cavities”, Presentation in the 152nd HL-LHC WP2 Meeting, 02/07/2019, INDICO: 826475.

Acronyms

B. HL-LHC acronyms

Acronym	Term
a-C	Amorphous carbon
ADC	Analogue to digital converter
ADT	Transverse damper
AFD	Automatic Fire Detection
ALARA	As low as reasonable achievable
ASIC	Application specific integrated circuit
ATS	Achromatic telescopic squeezing
AUG	Emergency stop buttons
BBLR	Beam-Beam Long Range
BCAM	Brandeis CCD Angle Monitor
BCMS	Bach compression and beam merging scheme
BCS	Bardeen-Cooper-Schrieffer
BCT	Bidirectional Controlled Thyristor
BDS	Beam Dump System
BETS	Beam energy tracking system
BFPP	Bound-free pair production
BGC	Beam Gas Curtain
BGV	Beam gas vertex profile monitor
BIS	Beam interlock system
BLM	LHC beam loss monitoring system
BPM	Beam position monitor
BRAN	TAN luminosity monitor
BS	Beam screen
BSRT	Synchrotron radiation telescope monitor
CALS	CERN accelerator logging system
CARE	Coordinated Accelerator Research in Europe
CC	Crab cavities
CCC	Connection cryostats
CCT	Costheta design
CCB	Cold compressor box
CDB	Circuit Disconnector Boxes
CDD	CERN design directory
CDP	Conductor development programme
CFC	Carbon fibre carbon composites
CLIQ	Coupling loss induced quench
CMM	Coordinate Measurement Machines
CMOS	Complementary metal-oxide-semiconductor
C.O.M.	Centre-of-mass

COTS	Commercial-off-the-shelf
CSAM	CERN Safety Alarm Monitoring system
CtC	Cost to completion
CW	Continuous wave
CVD	Chemical vapour deposition
DA	Dynamic Aperture
DAC	Digital-to-analog converter
DAQ	Data acquisition
DCCT	DC Current Transformer
DF	Distribution feedbox
DFBAM	Distribution feedbox for arc – IR 7/L
DFBAN	Distribution feedbox for arc – IR 7/R
DIOT	Distributed I/O Tier
DOE	Department of Energy
DPA	Displacements-per-atom
DQW	Double quarter wave cavity
DSs	Dispersion suppressors
DVB	Cryogenic distribution valve box
DWR	Extraction resistors
EC	Electron cloud
ECT	Endcap Toroid
EE	Energy extraction systems
ElQA	High voltage qualification
EMD	Electromagnetic dissociation
EN	European Norm
EOT	Electric overhead travelling crane
ERA	European Research Area
ESR	Essential Safety Requirements
ESFRI	European Strategy Forum on Research Infrastructure
EUCARD	Enhanced European Coordination for Accelerator Research and Development
EYETS	Extended yearly technical stop
FGC	Function Generator/Controller
FMCM	Fast magnet current change monitors
FNAL	Fermi National Accelerator Laboratory
FPC	Fundamental power coupler
FPGA	Field programmable gate array
FRAS	Full remote alignment system
FSI	Frequency Scanning Interferometry
FT	Focusing triplet
FWDs	Free-wheeling diodes
FWTs	Free-wheeling thyristors
GPN	General Purpose Network
GSI	General Safety Instruction

HDR	High dynamic range
HEB	Hollow electron beam
HEH	High Energy Hadron
HEL	Hollow Electron Lenses
HEP	High Energy Physics
HFM	High-field magnet
HIF	Hazard Identification Form
HL-LHC	High Luminosity Large Hadron Collider
HOM	High-order modes
HTS	High temperature superconductor
HLS	Hydrostatic Levelling Sensor
IBL	Inner pixel detector layer
IBS	Intra-beam scattering
ID	Inner diameter
IES	Important safety element
IFS	Instrumentation feed-through system
IOT	Inductive Output Tubes
IP	Interaction point
IR	Insertion Region / Interaction Region
IT	Inner triplet
ITF	Integrated Transfer Function
LACS	LHC Access Control System
LARP	US LHC Accelerator Research & Development Program
LASS	LHC Access Safety System
LBDS	LHC beam dumping system
LBS	LHC background study working group
LCB	Lower cold box
LIU	LHC Injector complex Upgrade
LLRF	Low level RF
LMBHA/B	Cold mass 11 T
LRBB	Long-range beam–beam
LS[X]	Long technical Shutdown [Id Number]
LSA	Launch Safety Agreement
LSB	Least Significant Bit
LSS	Long Straight Section
LVDT	Linear variable differential transformer
MB	Main LHC dipoles
MBH	11 T dipole
MBU	Multiple bit upsets
MCDO	Magnet corrector decapole/octupole
MCS	Magnet corrector sextupole
MD	Machine development
MFB	Multi-cavity feedback

MIM	Multi-band instability monitor
MIMO	Multiple Input Multiple Output
MKB	Diluter dump kicker
MKD	Beam dump kicker
MLI	Multi-Layer Insulation
MKI	Magnet injection kicker
MMD	Multi-purpose Monitoring Device
MP3	Magnet circuits, powering and performance panel
MP	Machine Protection
MPP	Machine protection panel
MPS	Machine protection system
MQY	Insertion region wide aperture quadrupole
MS	Matching section or Member States
NEG	Non-evaporable getter
NIEL	Non-ionizing energy losses
NIMS	National Institute of Materials Science
NMS	Non-Member States
NXCALS	Next generation Accelerator Logging Systems
P[#]	LHC Point [Number of the Point]
P5	Particle Physics Project Prioritization Panel
PIC	Powering interlock system
PIT	Powder-in-tube process
PLC	Programmable logic controller
PSM	Project Steering Committee
PSO	Project Safety Officer
PU	Pile-up
QEN	Bypass cryostat
QDS	Quench detection system
QPS	Quench protection system
QRL	LHC cryogenic distribution line
QV	Quench buffer
QXL	HL-LHC cryogenic distribution line
r.m.s.	Root mean square
R2E	Radiation To Electronics
RAMSES	Radiation Monitoring System
RF	Radio frequency
RFD	RF dipole cavity
RHQT	Rapid-heating, quenching transformation
RRP	Restacked rod process
RRR	Residual resistivity ratio
SC	Superconductor
SCL	Superconducting link
SCRF	Superconducting radio frequency

SEE	Single event effects
SET	Single event transients
SEU	Single bit upsets
SEY	Secondary electron yield
SFP	Small Form-factor Pluggable
SIL	Safety integrity level
SISO	Single Input Single Output
SM	Service module
SPS	Super Proton Synchrotron
SPT	Scheduled proton physics time
SR	Synchrotron radiation
SRF	Superconducting radio frequency
SSAP	Solid State Power Amplifiers
TANB	Target Neutral Absorber P8
TAXN	Target absorber for insertion region neutrals
TAXS	Target absorber for insertion region secondary
TCAP	Target collimator absorber passive
TCC	Technical Coordination Committee
TCDQ	Collimator for Q4 protection
TCL	Long collimator
TCLA	Target collimator long absorber
TCLD	Auxiliary collimators in DS area
TCPP	Primary collimator with BPM
TCSG	Target collimator secondary graphite
TCSMP	Secondary collimator metallic prototype
TCSP	Secondary collimator with pick-up
TCSPM	Secondary collimator with pick-up metallic
TCT	Target collimators tertiary
TCTP	Target collimator tertiary with pick-up
TCTPM	Target collimator tertiary with pick-up metallic
TDE	Target dump for ejected beam
TDI	Beam absorber for injection
TID	Total ionizing dose
TIM	Technical Infrastructure Monitoring system
TMCI	Transverse mode coupling instability
TN	Technical Network
TS[X]	Technical stop [Id number]
TSU	Trigger Synchronisation Unit
UA[X]	Service and access tunnel [point number]
UCB	Upper cold box
UFO	Falling particles
UJ[X]	Service cavern [point number]
UPS	Uninterruptable power supplies

UQDS	Universal Quench Detection System
US AUP	US HL-LHC Accelerator Upgrade Project
VCT	Vacuum chamber transition
VDWB	Vacuum – dump lines – window
VELO	Vertex locator
WBTN	Wide band time normalizer
WCC	Water Cooled cables
WCS	Warm compressor station
WIC	Warm magnet interlock system
WPS	Wire Positioning Sensors
YETS	Year-end technical stop

Glossary and definitions

C. Glossary and definitions

Term	**Definition**
β^*	Optical β-function at the IP.
η	Machine slip factor.
η_D	Normalized dispersion, $\eta D = D/\sqrt{\beta}$, where D is the machine dispersion.
γ	Optic gamma function, $\gamma(s) = (1 + \alpha 2(s))/\beta(s)$ where $\beta(s)$ is the optical betatron function along the machine and $\alpha(s) = -\frac{d\beta}{2\,ds}$.
γ_r	The relativistic gamma factor.
Abort gap	Area without any bunches in the bunch train that fits the time required for building up the nominal field of the LHC dump kicker.
Arc	The part of the ring occupied by regular half-cells. Each arc contains 46 half cells. The arc does not contain the dispersion suppressor.
Arc cell	Consists of two arc half-cells and presents the basic period of the optic functions.
Arc half-cell	Periodic part of the LHC arc lattice. Each half-cell consists of a string of three twin aperture main dipole magnets and one short straight section. The cryo magnets of all arc half-cells follow the same orientation with the dipole lead end pointing upstream of Beam 1 (downstream of Beam 2).
Availability	Is the Scheduled proton physics time (SPT) minus the time assigned to faults and fault recovery. It is normally expressed as a percentage of the SPT. Edge effects (e.g. recovery from access, the pre-cycle) should be fully included in the assigned fault time.
Batch	PS batch: train of 72 bunches that is injected into the SPS in one PS to SPS transfer. SPS batch: Train of 4 × 72 or 3 × 72 bunches that is injected into the LHC in one SPS to LHC transfer.
Beam 1 and Beam 2	Beam 1 and Beam 2 refer to the two LHC beams. Beam 1 circulates clockwise in Ring 1 and Beam 2 circulates counter clockwise in Ring 2. If colours are used for beams, Beam 1 is marked blue and Beam 2 is marked red.
Beam cleaning	Removal of the large amplitude (larger than 6 σ) particles from the beam halo. The LHC has two beam cleaning insertions: one is dedicated to the removal of particles with large transverse oscillation amplitudes (IR7) and one dedicated to the removal of particles with large longitudinal oscillation amplitudes (IR3). These insertions are also referred to as the betatron and momentum cleaning or collimation insertions.
Beam crossing angle	Dedicated orbit bumps separate the two LHC beams at the parasitic beam crossing points of the common beam pipe of Ring 1 and Ring 2. The crossing angle bumps do not separate the beams at the IP, but only at the parasitic crossing points. These orbit bumps generate an angle between the orbit of Beam 1 and Beam 2 at the IP. The full angle between the orbit of Beam 1 and Beam 2 is called the crossing angle. In IR2 and IR8 the crossing angle orbit bumps consist of two separate contributions. One external bump generated for the beam separation at the parasitic beam crossing points and one internal bump generated by the experimental spectrometer and its compensator magnets. The LHC baseline foresees vertical crossing angles in IR1 and IR2 and horizontal crossing angles in IR5 and IR8.
Beam half-life	Time during beam collision after which half the beam intensity is lost.

Beam screen	Perforated tube inserted into the cold bore of the superconducting magnets in order to protect the cold bore from synchrotron radiation and ion bombardment.
Beam types	**Pilot beam:** consists of a single bunch of 0.5×10^{10} protons. It corresponds to the maximum beam current that can be lost without inducing a magnet quench. **Commissioning beam:** beam tailored for a maximum luminosity with reduced total beam power (i.e. increased operational margins related to beam losses and magnet quenches) and possibly smaller beam sizes (i.e. increased mechanical acceptance in terms or the transverse beam size and larger tolerances for orbit and β-beat). **Intermediate beam:** beam tailored for a high accuracy of the beam measurements with reduced total beam power (i.e. increased operational margins related to beam losses and magnet quenches). **Nominal beam:** beam required to reach the design luminosity of $L = 10^{34}$ cm^{-2} s^{-1} with $\beta^* = 0.55$ m ($\rightarrow$ normalized emittance $\varepsilon_n = 3.75$ μm; $N_b = 1.15 \times 10^{11}$; $n_b = 2808$). **Ultimate beam:** beam consisting of the nominal number of bunches with nominal emittances (normalized emittance of 3.75 μm) and ultimate bunch intensities ($I = 0.86$ $A \rightarrow N_b = 1.7 \times 10^{11}$). Assuming the nominal value of $\beta^* = 0.55$ m and 2808 bunches, the ultimate beam can generate a peak luminosity of $L = 2.3 \times 10^{34}$ cm^{-2} s^{-1} in the two high luminosity experiments.
BPM	Beam position monitor.
Bunch	Collection of particles captured within one RF bucket.
Bunch duration	The bunch duration is defined as $$\sigma_t = \frac{\sigma_s}{v},$$ where σ_s is the bunch length and v is the speed of the particles in the storage rings.
Bunch length	The bunch length is defined as the r.m.s. value of the longitudinal particle distribution in one RF bucket. The bunch length is denoted as σ_s.
Busbar	Main cable that carries the current for powering the magnets outside the magnet coil.
Channel	The two apertures of the double bore magnets form two channels through the LHC. Each arc has one outer and one inner channel.
Cold mass	The cold mass refers to the part of a magnet that needs to be cooled by the cryogenic system, i.e. the assembly of magnet coils, collars, iron yoke, and helium vessel.
Crossings	The two machine channels cross at the experimental insertions, i.e. at IP1, IP2, IP5, and IP8.
Cryo-magnet assembly	Complete magnet system integrated into one cryostat, i.e. main magnet coils, collars and cryostat, correction magnets, and powering circuits.
DA	See dynamic aperture
Damper	Transverse or longitudinal feedback system used to damp injection oscillations and/or multi-bunch instabilities of a beam.
Damping time	Time after which an oscillation amplitude has been reduced by a factor $1/e$. **Longitudinal emittance damping time:** Half of the longitudinal amplitude damping time for a Gaussian approximation of the bunch distribution. **Transverse emittance damping time:** half of the transverse amplitude damping time for a Gaussian approximation of the transverse bunch distribution. If no explicit mentioning of the types of damping times is given the damping times refer to the amplitude damping times.

Decay and snap back	Persistent current decay is a change in the persistent current contribution to the total magnetic field in superconducting magnets powered at constant current (e.g. at injection). This effect varies among magnets and is a function of the powering history (i.e. previous current cycles). When the magnet current is changed (e.g. during the acceleration ramp) the magnetic field comes back to the original value before the decay. This effect is called snap back and occurs for the LHC main dipole magnets within the first 50 A change of the LHC ramp.
Dispersion suppressor	The dispersion suppressor refers to the transition between the LHC arcs and insertions. The dispersion suppressor aims at a reduction of the machine dispersion inside the insertions. Each LHC arc has one dispersion suppressor on each end. The length of the dispersion suppressors is determined by the tunnel geometry. Each LHC dispersion suppressor consists of four individually powered quadrupole magnets that are separated by two dipole magnets. This arrangement of four quadrupole and eight dipole magnets is referred to as two missing dipole cells. For the machine lattice these two missing dipole cells are referred to as one dispersion suppressor. However, reducing the dispersion at the IPs to zero requires a special powering of two more quadrupole magnets on each side of the arc. In terms of the machine optics the dispersion suppressor refers therefore to the two missing dipole cells plus one additional arc cell.
Dogleg magnets	Special dipole magnet used for increasing the separation of the two machine channels from standard arc separation. The dogleg magnets are installed in the cleaning insertions IR3 and IR7 and the RF insertion IR4.
Dynamic aperture	Maximum initial oscillation amplitude that guarantees stable particle motion over a given number of turns. The dynamic aperture is normally expressed in multiples of the RMS beam size (σ) and together with the associated number of turns.
Eddy currents	Eddy currents are screening currents that tend to shield the interior of a conductor or a superconducting cable from external magnetic field changes. In the case of a strand the eddy currents flow along the superconducting filaments in the strand (without loss) and close across the resistive matrix of the strand (copper for the LHC). In the case of a cable the eddy currents flow along the strands (without loss) and close resistively at the contact points among strands in the cable. Eddy currents are also referred to as coupling currents.
Energy spread	The energy spread is defined as the 'RMS' value of the relative energy deviations from the nominal beam energy in a particle distribution. The energy spread is denoted as $\sigma_{\delta E/E0}$.
Experimental insertion region	Insertion region that hosts one of the four LHC experiments.
Filament	Superconducting filaments are fine wires of bulk superconducting material with typical dimension in the range of a few microns. The superconducting filaments are embedded in the resistive matrix in a strand.
Hourglass effect *H*	Luminosity loss due to longitudinal modulation of beta function over the length of the bunch for small β^*.
Insertion region (IR)	Machine region between the dispersion suppressors of two neighboring arcs. The insertion region consists of two matching sections and, in the case of the experimental insertions, of two triplet assemblies and the separation/recombination dipoles.
Interaction point (IP)	Middle of the insertion region (except for IP8). In the insertions where the two LHC beams cross over, the IP indicates the point where the two LHC beams can intersect.

	In IR8 the experimental detector is shifted by 3/2 RF wavelength and the IP refers to the point where the two LHC beams can intersect and does not coincide with the geometric centre of the insertion.
Ions	The LHC foresees collisions between heavy ions, $^{208}Pb^{82+}$ (fully stripped) during the first years (208 is the number of nucleons, 82 the number of protons of this particular nucleus).
Ions, nominal scheme	Approximately 600 bunches per beam, with 7×10^7 Pb ions each, are colliding at 2.76 TeV/u to yield an initial luminosity of $L = 1.0 \times 10^{27}$ cm^{-2} s^{-1} where $\beta^* = 0.5$ m.
Ions, early scheme	Approximately 60 bunches per beam, with 7×10^7 Pb ions each, are colliding to yield an initial luminosity of $L = 5.0 \times 10^{25}$ cm^{-2} s^{-1} with ($\beta^* = 0.5$ m).
Lattice correction magnets	Correction magnets that are installed inside the short straight section assembly.
Lattice version	Lattice version refers to a particular hardware installation in the tunnel. It is clearly separated from the optics version and one lattice version can have more than one optics version.
Left, right	See the definition under 'right and left'.
Long-range interactions	Interaction between the two LHC beams in the common part of Ring 1 and Ring 2 where the two beams are separated by the crossing angle orbit bumps.
Long straight section (LSS)	The quasi-straight sections between the upstream and downstream dispersion suppressor of an insertion, including the separation/recombination dipole magnets.
Longitudinal emittance	The longitudinal emittance is defined as: $\epsilon_s = 4\pi\sigma_t\sigma_{\delta E/E0}E_0,$ where σ_t is the bunch duration in seconds, and $\sigma_{\delta E/E0}$ the relative energy spread.
Luminosity half-life	Time during beam collision after which the luminosity is halved. The luminosity half-life is generally smaller than the beam half-life.
Luminous region	The 3D distribution of the collision event vertices.
Luminosity reduction	**Geometric luminosity reduction factor due to beam offset *R*:** Reduced beam overlap due to transversal offset of collisions, frequently used for reduction of luminosity (levelling) and Van der Meer scans. Luminosity reduction factor due to crossing angle *S*: reduced beam overlap due to tilted bunch shape due to crossing angle. Total luminosity reduction factor $F = R^*H^*S$ (Strictly speaking here there is no direct multiplication, but provides a reasonable indication of the different contributions, while dominated by the crossing angle contribution).
Machine cycle	The machine cycle refers to one complete operation cycle of a machine, i.e. injection, ramp-up, possible collision flat-top, ejection, and ramp-down. The minimum cycle time refers to the minimum time required for a complete machine cycle.
Machine statistics	Run time: annual time allocated to running with beam [days]. Scheduled physics time: annual time allocated to physics (excluding initial beam commissioning, scrubbing, TS, recovery from TS, MDs, special physics) [days]. Physics efficiency: time with both beams present and stable beams, versus scheduled physics time [%]. Machine availability: time during which the machine is in a state allowing operations to take beam and run through a nominal physics cycle, versus run time [%].

	Turnaround time: time between the end of one and the start of the next physics run/data taking by the experiments (delimited by the loss of beam presence/beam dump back to declaration of stable beams) [hours]. Recovery time: time between the end of one cycle and the readiness for injection of new particles for the next cycle (delimited by the loss of beam presence/beam dump and resumption of the normal operational cycle) [hours].
Magnet quench	Loss of the superconducting state in the coils of a superconducting magnet.
Main lattice magnets	Main magnets of the LHC arcs, i.e. the arc dipole and quadrupole magnets.
Matching section	Arrangement of quadrupole magnets located between the dispersion suppressor and the triplet magnets (or the IP for those insertions without triplet magnets). Each insertion has two matching sections: one upstream and one downstream from the IP.
n_1	The effective mechanical aperture n_1 defines the maximum primary collimator opening in terms of the r.m.s. beam size that still guarantees a protection of the machine aperture against losses from the secondary beam halo. It depends on the magnet aperture and geometry and the local optics perturbations.
N_b	Number of particles per bunch.
n_b	Number of bunches per beam.
Nominal bunch	Bunch parameters required to reach the design luminosity of L = 1034 cm−2 s−1 where β* = 0.55 m. The nominal bunch intensity is N_b = 1.15 × 1011 protons.
Nominal powering	Hardware powering required to reach the design beam energy of 7 TeV.
Normalized transverse emittance	The beam emittance decreases with increasing beam energy during acceleration and a convenient quantity for the operation of a hadron storage rings (and linear accelerators) is the ‘normalized emittance’ defined as $$\epsilon_n = \epsilon\gamma_r\beta_r,$$ where γ_r and β_r are the relativistic gamma and beta factors $$\beta_r = \frac{v}{c}$$ $$\gamma_r = \frac{1}{\sqrt{1-\beta_r^2}}$$ where v is the particle velocity and c the speed of light in vacuum. The nominal normalized transverse emittance for the LHC is ε_n = 3.75 μm.
Octant	An octant starts in the center of an arc and goes to the centre of the next downstream arc. An octant consists of an upstream and a downstream half-octant. A half-octant and a half-sector cover the same part of the machine even though they may not have the same number.
Optical configuration	An optical configuration refers to a particular powering of the LHC magnets. Each optics version has several optical configurations corresponding to the different operational modes of the LHC. For example, each optics version has a different optical configuration for injection and luminosity operation, and for luminosity operation the optics features different optical configurations corresponding to different β^* values in the four experimental insertions of the LHC.
Optics version	The optics version refers to a consistent set of optical configurations. There can be several different optics versions for one lattice version.
Pacman bunches	Bunches that do not experience the same number of long-range beam–beam interactions left and right from the IP.

Parallel separation	Dedicated orbit bumps separate the two LHC beams at the IP during injection, ramp, and the optics squeeze. The total beam separation at the IP is called the parallel separation. The LHC baseline foresees horizontal parallel separations in IR1 and IR2 and vertical separations in IR5 and IR8.
Parasitic crossing points	Positions in the common part of the Ring 1 and Ring 2 where the two beams can experience long-range interactions.
Persistent currents	Persistent currents are eddy currents with (ideally) infinitely long time constants that flow in the bulk of the superconducting filaments of a strand and tend to shield the interior of the filament from the external magnetic field changes. These screening currents close inside the superconducting filament, with zero resistance (in steady state). Hence, for practical purposes, they do not decay in time and for this reason they are referred to as 'persistent'.
Physics efficiency	Is the fraction of the Scheduled proton physics time **(**SPT) spent in Stable Beams
Physics run	Machine operation at top energy with luminosity optics configuration and beam collisions.
Pile-up	**Event pile-up μ:** number of visible inelastic proton–proton interactions in a given bunch crossing. Average pile-up: mean value of the pile-up over a fill (averaged over all bunchcrossings). Peak pile-up: maximum pile-up in any bunch crossing at any time (usually at the start of the fill). Peak average pile-up: mean pile-up at the beginning of the fill. It corresponds to the peak luminosity of the fill. In practice, it is determined as the maximum of the pile-up values obtained by averaging over all bunch crossings within time intervals of typically one minute. Average pile-up density: number of inelastic proton–proton interactions in a given bunch-crossing divided by the size of the luminous region in Z.
Pilot bunch	Bunch intensity that assures no magnet quench at injection energy for an abrupt loss of a single bunch but is still large enough provide BPM readings. The pilot bunch intensity of the LHC corresponds to 0.5×10^{10} protons in one bunch.
Piwinski parameter	Parameterization of reduced beam overlap due to finite crossing angle.
Ramp	Change of the magnet current. During the beam acceleration the magnets are 'ramped up' and after the end of a physics store the magnets are 'ramped down'.
Resistive matrix	One of the two main constituents of the strand. The resistive matrix embeds the filaments in the strand and provides a low resistance current shunt in case of quench (transition of superconducting material to the normal state).
RF bucket	The RF system provide a longitudinal focusing that constrains particle motion in the longitudinal phase space to a confined region called the RF bucket.
Right, left	Describes the position in the tunnel relative to an observer inside the ring looking out (same definition as for LEP).
Ring 1 and Ring 2	There are two rings in the LHC, one ring per beam. Ring 1 corresponds to Beam 1, which circulates clockwise, and Ring 2 corresponds to Beam 2, which circulates counter-clockwise in the LHC.
Satellite bunch	Collection of particles inside RF buckets that do not correspond to nominal bunch positions. The nominal bunch spacing for the LHC is 25 ns, while the separation of RF buckets is 2.5 ns. In other words, there are nine RF buckets between two nominal LHC bunch positions that should be empty.

Scheduled proton physics time	Is the time scheduled in a given year for high luminosity proton physics. It does not include initial re-commissioning, special physics runs, ions, machine development (MD), and technical stops. It does include the intensity ramp-up following re-commissioning at the start of the year
Sector	The part of a ring between two successive insertion points (IP) is called a sector. Sector 1-2 is situated between IP1 and IP2.
Separation/recombination magnets	Special dipole magnets left and right from the triplet magnets that generate the beam crossings in the experimental insertions.
Short straight section (SSS)	Assembly of the arc quadrupole and the lattice corrector magnets. Each SSS consists of one quadrupole magnet, one beam position monitor (BPM), one orbit corrector dipole (horizontal deflection for focusing and vertical deflection for defocusing quadrupoles), one lattice correction element (i.e. trim or skew quadrupole elements or octupole magnets). and one lattice sextupole or skew sextupole magnet.
Special straight section (SPSS)	Quadrupole assemblies of the insertion regions. The SPSS features no lattice corrector and sextupole magnets and has only orbit correction dipole magnets and BPMs.
Spool piece correction magnets	Correction magnets directly attached to the main dipole magnets. The spool piece correction magnets are included in the dipole cryostat assembly
Strand	A superconducting strand is a composite wire containing several thousands of superconducting filaments dispersed in a matrix with suitably small electrical resistivity properties. The LHC strands have Nb-Ti as their superconducting material and copper as the resistive matrix.
Superconducting cable	Superconducting cables are formed from several superconducting strands in parallel, geometrically arranged in the cabling process to achieve well-controlled cable geometry and dimensions, while limiting strand deformation in the process. Cabling several strands in parallel results in an increase of the current carrying capability and a decrease of the inductance of the magnet, easing protection. The LHC cables are flat, keystoned cables of the so-called Rutherford type.
Super pacman bunches	Bunches that do not collide head-on with a bunch of the other beam in one of experimental IPs.
Synchrotron radiation damping times	**Longitudinal amplitude damping time:** the ratio of the average rate of energy loss (energy lost over one turn divided by the revolution time) and the nominal particle energy. **Transverse amplitude damping time:** time after which the transverse oscillation amplitude has been reduced by a factor $1/e$ due to the emission of synchrotron radiation. For a proton beam it is just twice the longitudinal amplitude damping time due to the emission of synchrotron radiation. If no explicit mentioning of the types of damping times is given the damping times refer to the amplitude damping times.
TAN	Target absorber neutral: absorber for the neutral particles leaving the IP. It is located just in front of the D1 separation/recombination dipole magnet on the side facing the IP.
TAS	Target absorber secondaries: absorber for particles leaving the IP at large angles. It is located just in front of the Q1 triplet quadrupole magnet on the side facing the IP.
Transverse beam size	The transverse beam size is defined as the r.m.s. value of the transverse particle distribution.

Transverse emittance	The transverse emittance is defined through the invariance of the area enclosed by the single particle phase space ellipse. The single particle invariant under the transformation through the storage ring is given by $$A = \gamma x^2 + 2\alpha x x' + \beta x'^2,$$ where α, β, and γ are the optical functions. The area enclosed by the single particle phase space ellipse is given by $$\text{area of ellipse} = \pi A$$. For an ensemble of particles the emittance is defined as the average of all single particle invariants (areas enclosed by the single particle phase space ellipsoids divided by π). The transverse betatron beam size in the storage ring can be written in terms of the beam emittance as $$\sigma_{x,y}(s) = \sqrt{\beta_{x,y}(s)\epsilon_{x,y}},$$ where $\beta_{x,y}$ (s) is the optical β-function along the storage ring. The transverse emittance is given by the following expression: $$\epsilon_z = \sqrt{\langle z^2\rangle\langle z'^2\rangle - \langle zz'\rangle^2}; z = x, y,$$ where it is assumed that the particle coordinates are taken at a place with vanishing dispersion and where ⟨ ⟩ defines the average value of the coordinates over the distribution. z and z' are the canonical transverse coordinates ($z = x,y$).
Triplet	Assembly of three quadrupole magnets used for a reduction of the optical β-functions at the IPs. The LHC triplet assembly consists in fact of four quadrupole magnets, but the central two quadrupole magnets form one functional entity. The LHC has triplet assemblies in IR1, IR2, IR5, and IR8.
Tune	Number of particle trajectory oscillations during one revolution in the storage ring (transverse and longitudinal).
Turnaround time	Is defined as the time taken to go from Stable Beam mode back to Stable Beam mode in the absence of significant interruptions due to fault diagnosis and resolution
Ultimate bunch intensity	Bunch intensity corresponding to the expected maximum acceptable beam–beam tune shift with two operating experimental insertions. Assuming the nominal emittance (normalized emittance of 3.75 μm) the ultimate bunch intensity corresponds to 1.7×10^{11} protons per bunch.
Ultimate powering	Hardware powering required to reach the ultimate beam energy of 7.54 TeV, corresponding to a dipole field of 9 T.
Upstream and downstream	Always related to the direction of one of the two beams. If no beam is specified, then Beam 1 is taken as the default. This implies that stating a position as being ‘upstream’ without indicating any beam is equivalent to stating that the position is to the left.

Index

L

M

O

P

Q

R

S

U

V

W